Advances in Experimental Medicine and Biology 977

Howard J. Halpern
Joseph C. LaManna
David K. Harrison
Boris Epel *Editors*

Oxygen Transport to Tissue XXXIX

Springer

Advances in Experimental Medicine and Biology

Volume 977

More information about this series at: http://www.springer.com/series/5584

Howard J. Halpern • Joseph C. LaManna
David K. Harrison • Boris Epel
Editors

Oxygen Transport to Tissue XXXIX

Springer

Editors
Howard J. Halpern
Department of Radiation and Cellular Oncology
Center for EPR Imaging In Vivo Physiology
University of Chicago
Chicago, IL, USA

David K. Harrison
Microvascular Measurements
St. Lorenzen, Italy

Joseph C. LaManna
Department of Physiology and Biophysics
Case Western Reserve University School of Medicine
Cleveland, OH, USA

Boris Epel
Department of Radiation and Cellular Oncology
Center for EPR Imaging In Vivo Physiology
University of Chicago
Chicago, IL, USA

ISSN 0065-2598 ISSN 2214-8019 (electronic)
Advances in Experimental Medicine and Biology
ISBN 978-3-319-55229-3 ISBN 978-3-319-55231-6 (eBook)
DOI 10.1007/978-3-319-55231-6

Library of Congress Control Number: 2017941513

Printed on acid-free paper

This Springer imprint is published by Springer Nature
The registered company is Springer International Publishing AG
The registered company address is: Gewerbestrasse 11, 6330 Cham, Switzerland

Preface

This volume is the publication of papers presented at the 44th annual meeting of the International Society on Oxygen Transport to Tissue, ISOTT, held in Chicago, IL, USA, from July 10 to July 14, 2016. I believe it represents a wonderful variety of perspectives focusing on a great deal of the areas of research on the transport of oxygen to tissues. The work presented has been subjected to peer review by the leading experts in this area. Through the review by members internationally recognized for their contribution to the field, the science therein is of the highest quality.

The meeting involved 105 scientists from 60 institutions in 15 countries from North America, Asia, and Europe. Given the busy schedules of many of the best-known participants, topics were spread throughout the meeting. In the best tradition of ISOTT, this allowed presentations and presenters to mingle with researchers from intellectually distant backgrounds. The exotic spice of new ideas was thereby mingled with the broth of established understanding to stimulate the true value of this meeting: innovation.

The meeting keynote presentation was given by Greg Semenza, who at the time had not yet won the Lasker Award for 2016, detailing the latest research on molecular biology of the required organismal response to low levels of local oxygenation. From molecular biology to individual human response, to oxygen changes monitored by optical/near-infrared spectroscopy/tomography, to novel electron resonance spectroscopy and spectroscopic imaging, to progress in blood substitute research, retinal physiology, etc., the quality and innovation of the research and those involved in it were outstanding and exciting. In-depth presentations from our internationally recognized experts accompanied wide-ranging shorter presentations. As in recent past meetings, poster information was communicated to the meeting attendees as a whole with succinct poster summary presentations that allowed our participants to focus on the novel, compelling the poster sessions.

In addition to the presentation of science, the history of ISOTT has revolved about the opportunities that the meeting and its venue provided for productive scientific exchange between attendees. The location of the meeting at a boutique in the heart of Chicago's Miracle Mile provided relaxed access to the most diverse restaurants, from small inexpensive but high-quality quiet venues to some of the finest in the

world. Here, in-depth discussions could extend into the evening free of constraint. The history of the city, considered by many to be the architectural capital of the USA, was elucidated during the Chicago River tour. The vistas provided by the 95th floor banquet, the weather performance of a July storm with its second-order (and perhaps third-order) rainbow after dinner, and the city fireworks that followed gave the muscular sense of one of America's signature cities. This seemed a superb setting for the optimum exchange of science and the engendered friendship.

We acknowledge the excellent support of the members of the Department of Radiation and Cellular Oncology including Mert Vincent, Matthew Maggio, Emily Toops, Eugene Barth, Richard Miller, and Feya Epel for help in the preparation of the meeting materials and for ensuring the smooth running of the meeting. Our ISOTT treasurer, Dr. Peter Keipert, provided financial wisdom through the preparative stages of the meeting. Members of our Local Organizing Committee, our Scientific Committee, the ISOTT Executive Board, and the session chairs and cochairs burnished the roster of presenters and disciplined our exciting sessions. Those who presented at the meeting need our particular gratitude for insight at the heart of the meeting. We thank those of our participants who submitted their work as scientific publications. We especially thank our reviewers of the submitted papers who provided wisdom and insight without which the meeting would not have been such a success and the papers which have issued in this volume so important.

Chicago, IL, USA

Boris Epel
Howard J. Halpern

Acknowledgments

As president of the 2016 Meeting of the International Society on Oxygen Transport to Tissue, held on July 10–14, 2016, in Chicago, USA, I would like to gratefully acknowledge the support of our sponsors.

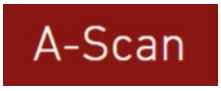

A-Scan LLC
http://www.ascan-llc.com/

Bruker Corporation
https://www.bruker.com/

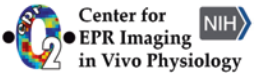

NIH Center for EPR Imaging and In vivo Physiology
http://epri.uchicago.edu/

Department of Radiation and Cellular Oncology
https://radonc-sites.uchicago.edu/

ISS
http://iss.com/

Panel of Reviewers

Reviewer	Affiliation
Linda Ahnen	University Hospital Zurich, Switzerland
Gemma Bale	University College London, UK
Leif Bülow	Lund University, Sweden
Alexander Caicedo	Katholieke Universiteit Leuven, Belgium
Bryan Clifford	University of Illinois at Urbana–Champaign, USA
Gareth Eaton	University of Denver, USA
Martyna Elas	Jagiellonian University, Poland
Boris Epel	University of Chicago, USA
Ann B. Flood	EPR Center at Dartmouth, Hanover, USA
Leonard Fru	University of Wisconsin, Madison, USA
Michal Gonet	Jagiellonian University, Poland
Howard J. Halpern	University of Chicago, USA
David K. Harrison	Microvascular Measurements, St. Lorenzen Italy
David Highton	National Hospital for Neurology and Neurosurgery, London, UK
Fahmeed Hyder	Yale University, USA
Kyung Kang	University of Louisville, USA
Peter E. Keipert	Keipert Corp. Consulting, San Diego, USA
Periannan Kuppusamy	EPR Center at Dartmouth, Hanover, USA
Joseph C. LaManna	Case Western Reserve University, Cleveland, USA
Frédéric Lange	University College London, UK
Terence Leung	University College London, UK
Lin Li	University of Pennsylvania, USA
Qi Liu	Northwestern University, USA
Molly Lockart	The University of Alabama, USA
Arnulf Mayer	University Medical Center, Mainz, Germany
Andreas Metz	University of Bern, Switzerland
Subhabrata Mitra	University College London, UK
Paul Okunieff	University of Florida, USA
Takuya Osawa	Juntendo University, Japan

George Perdrizet	University of California San Diego, USA
Pong Phan	University College London, UK
Sally Pias	New Mexico Tech, USA
Michelle Puchowicz	Case Western Reserve University, Cleveland, USA
Anne Reimann	University of Halle, Germany
Pang Dong Ryu	Seoul National University, Republic of Korea
Guennadi Saiko	Ryerson University, Canada
Kaoru Sakatani	Nihon University School of Medicine, Japan
Wilson Schreiber	EPR Center at Dartmouth, Hanover, USA
John Severinghaus	University of California San Francisco, USA
Kwang Sup Soh	Seoul National University, Republic of Korea
Witold Subczynski	Medical College of Wisconsin, USA
Harold Swartz	EPR Center at Dartmouth, Hanover, USA
Ileas Tachtsidis	University College London, UK
Rong-Wen Tain	ETH Zurich, Switzerland
Shun Takagi	Waseda University, Japan
Eiji Takahashi	Saga University, Japan
Tomotaka Takeda	Tokyo Dental College, Japan
Oliver Thews	University of Halle, Germany
Peter Vaupel	University Medical Center, Mainz, Germany
Martin Wolf	University of Zurich, Switzerland
Ursula Wolf	University of Bern, Switzerland
Kui Xu	Case Western Reserve University, Cleveland, USA
Technical Reviewer	
Laraine Visser-Isles	Rotterdam, the Netherlands
Eileen Harrison	St. Lorenzen, Italy


44th Meeting of the International Society on Oxygen Transport to Tissue
July 10–14, 2016, Chicago, IL

Local Organizing Committee

Howard J. Halpern, University of Chicago
Hao F Zhang, Northwestern University
Joseph Culver, Washington University in St. Louis
Boris Epel, University of Chicago

Scientific Committee

Hao F Zhang, Northwestern University, USA
Joseph Culver, Washington University in St. Louis, USA
Qingming Luo, Huazhong University of Science and Technology, China
Lin Z. Li, University of Pennsylvania, USA
Kyung A. Kang, University of Louisville, USA
Joseph C. LaManna, Case Western Reserve University, USA
Harold M. Swartz, Dartmouth College, USA
Clare Elwell, University College, London, UK
Peter Keipert, Sangart, Inc., San Diego, USA
Peter Vaupel, University of Mainz Medical Center, Germany
Oliver Thews, University of Mainz Medical Center, Germany
Paul Okunieff, University of Florida College of Medicine, USA
John Severinghaus, University of California San Francisco, USA

ISOTT Officers and Executive Committee

Presidents

Name: Howard J. Halpern
Country: USA
Telephone: (+1) 773-702-6871
Fax: (+1) 773-702-5940
Email: h-halpern@uchicago.edu

Past Presidents

Name: Qingming Luo
Country: China
Telephone: (+86) 27-8779-2033
Fax: (+86) 27-8779-2034
Email: qluo@mail.hust.edu.cn

Name: Lin Z. Li
Country: USA
Telephone: (+1) 215-898-1805
Fax: (+1) 215-573-2113
Email: linli@mail.med.upenn.edu

President-Elect

Name: Oliver Thews
Country: Germany
Telephone: (+49) 345-557-4048
Fax: (+49) 345-557-4019
Email: oliver.thews@medizin.uni-halle.de

Secretary

Name: Oliver Thews
Country: Germany
Telephone: (+49) 345-557-4048
Fax: (+49) 345-557-4019
Email: oliver.thews@medizin.uni-halle.de.

Treasurer

Name: Peter E. Keipert
Country: USA
Telephone: (+1) 858-699-4789
Fax: (+1) 858-792-7489
Email: peterkeipert@gmail.com

Head of Publication Committee

Name: Joseph C. LaManna
Country: USA
Telephone: (+1) 216-368-1112
Fax: (+1) 216-368-1144
Email: joseph.lamanna@case.edu

Chairman, Knisely Award Committee

Name: Duane F. Bruley
Country: USA
Telephone: (+1) 410-313-9939
Fax: F: (+1) 410-313-9939
Email: bruley33@verizon.net

Executive Committee

Alexander Caicedo-Dorado, Belgium
Boris Epel, USA
Ann B. Flood, USA
Malou Friedrich-Perrson, Sweden
Kyung A. Kang, USA
George A. Pedrizet, USA
Pan Dong Ryu, Republic of Korea
Eiji Takahashi, Japan
Ursula Wolf, Switzerland
Karen A. Yilmaz, USA

ISOTT Award Winners

The Melvin H. Knisely Award

The Melvin H. Knisely Award was established in 1983 to honor Dr. Knisely's accomplishments in the field of the transport of oxygen and other metabolites and anabolites in the human body. Over the years, he has inspired many young investigators, and this award is to honor his enthusiasm for assisting and encouraging young scientists and engineers in various disciplines. The award is to acknowledge outstanding young investigators. This award was first presented during the banquet of the 1983 annual conference of ISOTT in Ruston, Louisiana. The award includes a Melvin H. Knisely plaque and a cash prize.

Melvin H. Knisely Award Recipients

1983 Antal G. Hudetz (Hungary)
1984 Andras Eke (Hungary)
1985 Nathan A. Bush (USA)
1986 Karlfried Groebe (Germany)
1987 Isumi Shibuya (Japan)
1988 Kyung A. Kang (Korea/USA)
1989 Sanja Batra (Canada)
1990 Stephen J. Cringle (Australia)
1991 Paul Okunieff (USA)
1992 Hans Degens (the Netherlands)
1993 David A. Benaron (USA)
1994 Koen van Rossem (Belgium)
1995 Clare E. Elwell (UK)
1996 Sergei A. Vinogradov (USA)

1997 Chris Cooper (UK)
1998 Martin Wolf (Switzerland)
1999 Huiping Wu (USA)
2000 Valentina Quaresima (Italy)
2001 Fahmeed Hyder (Bangladesh)
2002 Geofrey De Visscher (Belgium)
2003 Mohammad Nadeem Khan (USA)
2004 Fredrick Palm (Sweden)
2005 Nicholas Lintell (Australia)
2006 –
2007 Ilias Tachtsidis (UK)
2008 Kazuto Masamoto (Japan)
2009 Rossana Occhipinti (USA)
2010 Sebatiano Cicco (Italy)
2011 Mei Zhang (USA)
2012 Takahiro Igarashi (Japan)
2013 Malou Friederich-Persson (Sweden)
2014 David Highton (UK)
2015 Alexander Caicedo Dorado (Belgium)
2016 Sally Pias (USA)

The Dietrich W. Lübbers Award

The Dietrich W. Lübbers Award was established in honor of Professor Lübbers's long-standing commitment, interest, and contributions to the problems of oxygen transport to tissue and to the society. This award was first presented in 1994 during the annual conference of ISOTT in Istanbul, Turkey.

Dietrich W. Lübbers Award Recipients

1994 Michael Dubina (Russia)
1995 Philip E. James (UK/USA)
1996 Resit Demit (Germany)
1997 Juan Carlos Chavez (Peru)
1998 Nathan A. Davis (UK)
1999 Paola Pichiule (USA)
2000 Ian Balcer (USA)
2001 Theresa M. Busch (USA)
2002 Link K. Korah (USA)
2003 James J. Lee (USA)

2004 Richard Olson (Sweden)
2005 Charlotte Ives (UK)
2006 Bin Hong (China/USA)
2007 Helga Blockx (Belgium)
2008 Joke Vanderhaegen (Belgium)
2009 Matthew Bell (UK)
2010 Alexander Caicedo Dorado (Belgium)
2011 Malou Friedrich (Sweden)
2012 Maria Papademetriou (UK)
2013 Nannan Sun (China/USA)
2014 Felix Scholkmann (Switzerland)
2015 Shun Takagi (Japan)
2016 Gemma Bale (UK)

The Britton Chance Award

The Britton Chance Award was established in honor of Professor Chance's long-standing commitment, interest, and contributions to the science and engineering aspects of oxygen transport to tissue and to the society. This award was first presented in 2004 during the annual conference of ISOTT in Bari, Italy.

Britton Chance Award Recipients

2004 Derek Brown (Switzerland)
2005 James Lee (USA)
2006 Hanzhu Jin (China/USA)
2007 Eric Mellon (USA)
2008 Jianting Wang (USA)
2009 Jessica Spires (USA)
2010 Ivo Trajkovic (Switzerland)
2011 Alexander Caicedo Dorado (Belgium)
2012 Felix Scholkmann (Switzerland)
2013 Tharindi Hapuarachchi (UK)
2014 Anne Riemann (Germany)
2015 Wenhao Xie (China)
2016 Linda Ahnen (Switzerland)

The Duane F. Bruley Travel Awards

The Duane F. Bruley Travel Awards were established in 2003 and first presented by ISOTT at the 2004 annual conference in Bari, Italy. This award was created to provide travel funds for student researchers in all aspects of areas of oxygen transport to tissue. The awards signify Dr. Bruley's interest in encouraging and supporting young researchers to maintain the image and quality of research associated with the society. As a cofounder of ISOTT in 1973, Dr. Bruley emphasizes cross-disciplinary research among basic scientists, engineers, medical scientists, and clinicians. His pioneering work constructing mathematical models for oxygen and other anabolite/metabolite transports in the microcirculation, employing computer solutions, was the first to consider system nonlinearities and time dependence, including multidimensional diffusion, convection, and reaction kinetics. It is hoped that receiving the Duane F. Bruley Travel Award will inspire students to excel in their research and will assist in securing future leadership for ISOTT.

The Duane F. Bruley Travel Award Recipients

2004	Helga Blocks (Belgium), Jennifer Caddick (UK), Charlotte Ives (UK), Nicholas Lintell (Australia), Leonardo Mottola (Italy), Samin Rezania (USA/Iran), Ilias Tachtsidis (UK), Liang Tang (USA/China), Iyichi Sonoro (Japan), Antonio Franco (Italy)
2005	Robert Bradley (UK), Harald Oey (Australia), Kathy Hsieh (Australia), Jan Shah (Australia)
2006	Ben Gooch (UK), Ulf Jensen (Germany), Smruta Koppaka (USA), Daya Singh (UK), Martin Tisdall (UK), Bin Wong (USA), Kui Xu (USA)
2007	Dominique De Smet (Belgium), Thomas Ingram (UK), Nicola Lai (USA), Andrew Pinder (UK), Joke Vanderhaegen (Belgium)
2008	Sebastiano Chicco (Italy)
2009	Lei Gao (UK), Jianting Wang (USA), Obinna Ndubuizu (USA), Joke Vanderhaegen (Belgium)
2010	Zareen Bashir (UK), Tracy Moroz (UK), Mark Muthalib (Australia), Catalina Meßmer (USA), Takashi Eriguchi (Japan), Yoshihiro Murata (Japan), Jack Honeysett (UK), Martin Biallas (Switzerland)
2011	Catherine Hesford (UK), Luke S. Holdsworth (UK), Andreas Metz (Switzerland), Maria D. Papademetriou (UK), Patrik Persson (Sweden), Felix Scholkmann (Switzerland), Kouichi Yoshihara (Japan)
2012	Allann Al-Armaghany (UK), Malou Friederich-Persson (Sweden), Tharindi Hapuarachchi (UK), Benjamin Jones (UK), Rebecca Re (Italy), Yuta Sekiguchi (Japan), Ebba Sivertsson (Sweden), Andre´ Steimers (Germany)

2013 Allann Al-Armaghany (UK), Gemma Bale (UK), Alexander Caicedo Dorado (Belgium), Luke Dunne (UK)
2014 Geraldine De Preter (Belgium), Benjamin Jones (UK), Stefan Kleiser (Switzerland), Nassimsadat Nasseri (Switzerland), Marie-Aline Neveu (Belgium), Shinsuke Nirengi (Japan), Takuya Osawa (Japan)
2015 Nannan Sun (China), Gemma Bale (UK), Chenyang Gao (China), Guennadi Saiko (Canada), Kuangyu Shi (Germany), Phong Phan (UK), Chae Jeong Lim (Korea)
2016 Isabel De Roever (UK), Yuya Enokida (Japan), Jingjing Jiang (Switzerland), Frédéric Lange (UK), Andreas J Metz (Switzerland), Shun Takagi (Japan)

Kovach Lecture

The Kovach Lecture is presented periodically to honor a career dedicated to oxygenation research. Arisztid Kovach was a world-renowned cardiovascular physiologist and one of the early leaders of ISOTT. This lecture is dedicated to his remarkable scientific and teaching career.

Kovach Lecture Recipients

2011 John Severinghaus
2012 Peter Vaupel
2013 No Recipient
2014 Edwin Nemoto
2015 No Recipient
2016 No Recipient

Contents

Part I
Cell Metabolism, Tissue Oxygenation and Treatment

Chapter 1
Oxygen Sensing by the Carotid Body: Past and Present

Nanduri R. Prabhakar and Ying-Jie Peng

Abstract It is now well established that carotid bodies are sensory organs for monitoring arterial blood oxygen levels and trigger reflexes that are critical for maintaining homeostasis during hypoxemia. This review article provides a brief account of the early studies leading to the discovery of the carotid body as a sensory receptor and addresses current views of O_2 sensing mechanism(s) in the carotid body and their physiological importance.

Keywords Gasotransmitters • Carbon monoxide • H_2S • Hypoxia • Ion channels

1 Introduction

The carotid body (also called *glomus caroticum*) is a small organ located at the bifurcation of the internal and external carotid artery. The discovery of carotid body as a sensory organ for detecting arterial blood O_2 levels opened a new area in physiology. This review article provides a brief account of the history of the discovery of the carotid body as a sensory organ and current concepts of O_2 sensing by the carotid body. A detailed account of the history of discovery of the carotid body and advances in carotid body physiology can be found in recent review articles [1, 2].

2 Discovery of Carotid Bodies as an O_2 Sensing Organ

Pflüger, a German physiologist, as early as 1868, reported that hypoxia stimulates breathing [3]. This finding spurred investigations to identify the structures that "sense" systemic O_2 levels and trigger physiological responses. Although studies between the 18th and 20th centuries identified a structure resembling "ganglion"

N.R. Prabhakar (✉) • Y.-J. Peng
Institute for Integrative Physiology and Center for Systems Biology of O_2 Sensing, Biological Sciences Division, University of Chicago, Chicago, IL 60637, USA
e-mail: nanduri@uchicago.edu

H.J. Halpern et al. (eds.), *Oxygen Transport to Tissue XXXIX*, Advances in Experimental Medicine and Biology 977, DOI 10.1007/978-3-319-55231-6_1

[4], or a "gland" [5] at the bifurcation of the common carotid artery, no physiological function was assigned to this organ.

Fernando de Castro at the Cajal Institute, Madrid, Spain, showed that the carotid body is a complex structure comprised of small blood vessels, axons of the sympathetic nerves, glandular cells which were innervated by glossopharyngeal nerve fibers. He concluded that the carotid sinus nerve innervating the carotid body is sensory in nature and glomus cells are of secretory phenotype, and proposed that the carotid body detects the chemical composition of arterial blood i.e., chemical sensing, and that the information is transmitted to the nerve terminals [6–10].

In the 1920s, Jean-Francois Heymans and Corneille Heymans in Belgium, while studying reflex regulation of blood pressure from the sino-aortic region, found that hypoxia-induced stimulation of breathing was abolished after sectioning carotid sinus nerves. Their studies led to the proposal that the carotid sinus was the seat of pressor receptors, and the chemical composition of arterial blood is sensed by the carotid body [11–18]. Thus, both Fernando De Castro and Heymans' group independently discovered the sensory nature of the carotid body. Cornielle Heymans was awarded the Nobel Prize in Physiology & Medicine in 1938 and he was nominated by the Hungarian Professor Mansfeld. Unfortunately, nobody nominated De Castro for the Nobel Prize. However, the Nobel Citation duly acknowledged the contributions of Fernando De Castro [1].

Between 1930 and 1939, three groups of investigators including G. Stella from Padova, Italy, Pierre Rijlants, Ghent, Belgium, Y. Zotterman, G. Lilljestrand, and U.S. von Euler in Stockholm, independently recorded the electrical activity from the carotid sinus nerve [19]. These studies showed that asphyxia, hypoxia and hypercapnia, all increased carotid body sensory nerve activity. The study by von Euler et al. [20] further established stimulus-response of the carotid body response to hypoxia and CO_2.

A prevailing view in the 1930s was that brain senses the chemical composition of arterial blood and evokes physiological responses. Consequently, many physiologists doubted the theory that the carotid body is a sensory organ for monitoring arterial blood gas composition. Corneille Heymans, shortly after the discovery of the carotid body function, joined the Western Reserve University in Cleveland to work with Carl Wiggers, a renowned physiologist, who made seminal contributions to cardiovascular physiology. Upon hearing C.F. Heymans' discovery of the sensory nature of the carotid body, Wiggers commented that "no text book ever said that". However, Wiggers arranged an experiment for Heymans to prove his claim about the sensory function of the carotid body. Heymans demonstrated hypoxia-induced hyperventilation was abolished after bilateral ablation of carotid sinus nerves. Seeing this experiment, Wiggers commented "Yes…. The dog is right … and text books are wrong". Goran Liljestrand, who was Professor of Physiology at Karolinska Institute, Stockholm also doubted the theory of chemical sensing by the carotid body. In 1935, Zotterman presented recordings of the carotid body sensory activity at the Physiological Society meeting in Stockholm, and Liljestrand gave up his opposition and joined Zotterman and Ulf von Euler in the experiments characterizing the carotid body sensory nerve response to hypoxia and CO_2, which

were published in 1939 [20]. In 1940, Henderson at Yale listened to Zottermans' gramophone recordings of the carotid body sensory nerve activity and – he too gave up his opposition. Carl F. Schmitt in Philadelphia, however, did not give up his resistance until 1959. However, he subsequently withdrew his opposition at the Montreal International Congress of Physiology [19].

3 Current Views on Carotid Body O_2 Sensing

A substantial body of evidence accumulated during the subsequent years suggests that glomus cells are the primary site of transduction and they work in concert with the nearby afferent nerve ending as a "sensory unit" [2]. Much attention has been focused on delineating the mechanism(s) of hypoxic sensing by the carotid body and identifying the potential O_2 sensor. Given that the carotid body responds to hypoxia within a few seconds, it is likely that the transduction process involves changes in existing proteins rather than *de novo* protein synthesis [21].

Emerging evidence in the past few years suggests that hypoxic sensing by the carotid body chemoreceptor utilizes biochemical mechanisms involving O_2-dependent interplay between two gaseous messengers, carbon monoxide (CO) and hydrogen sulfide (H_2S). CO is generated during the enzymatic degradation of heme by heme oxygenases 1 and 2(HO-1and HO-2) [22]. HO-1 is an inducible isoform and HO-2 is constitutively expressed in various tissues, including the carotid body [23–25]. HO-2 is the primary enzyme contributing to CO generation in the carotid body [26]. Hypoxia leads to a graded reduction of CO levels in the carotid body [27], suggesting that CO generation from HO-2 is sensitive to changes in O_2. The inherent O_2 sensitivity of HO-2 requires two cysteine residues (Cys^{265}, and Cys^{282}) in the heme regulatory motif [26]. With intact Cys^{265} and Cys^{282} residues, HO-2 exhibits low affinity for O_2 ($K_m = 65 \pm 5$ mmHg), whereas mutation of Cys^{265} and Cys^{282} dramatically increases O_2 affinity ($K_m = 25 \pm 3$ mmHg). Physiological studies showed that CO signaling during normoxia inhibits CSN activity [25, 27].

Under hypoxic conditions, CO-dependent inhibition is released, leading to carotid body activation. CO mediates carotid body activation by increasing the synthesis of H_2S. Glomus cells express cystathionine-γ-lyase (CSE), an enzyme that catalyzes H_2S generation [28, 29]. Hypoxia increases H_2S generation in the carotid body in a graded manner, and this response is markedly attenuated or absent following pharmacological blockade or genetic ablation of CSE activity [28]. However, the increased H_2S generation is not due to a direct effect of hypoxia on CSE, rather it is due to reduced CO levels and the resulting decrease in protein kinase G (PKG)-dependent phosphorylation of CSE (Fig. 1.1). Carotid body activation by hypoxia is severely impaired with genetic or pharmacological blockade of CSE [28], suggesting that CSE-derived H_2S mediates increased carotid body sensory nerve activity by hypoxia.

How might H_2S stimulate the carotid body sensory nerve activity? The current consensus is that hypoxia depolarizes glomus cells leading to Ca^{2+}-dependent

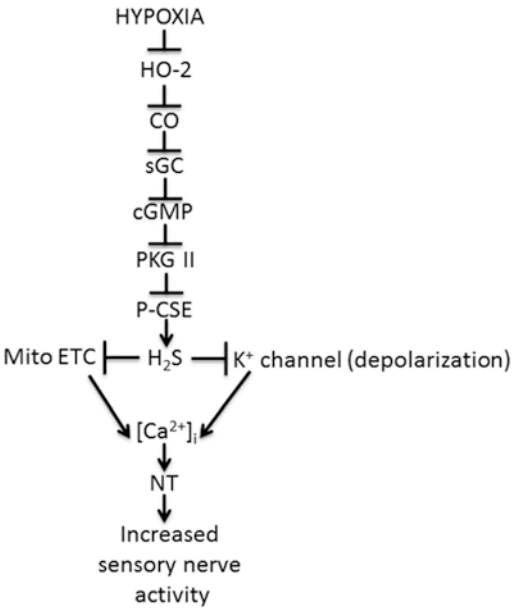

Fig. 1.1 The O_2 sensing and signaling pathway in the carotid body. Schematic presentation of CO-regulated H_2S generation in glomus cells of the carotid body and its impact on sensory nerve activity. *HO-2* heme oxygenase 2, *CO* carbon monoxide, *sGC* soluble guanylate cyclase, *cGMP* cyclic gunosine monophosphate, *PKG- II* protein kinase G-II, *P-CSE* phosphorylated cystathionine-ϒ-lyase, *Mito ETC* mitochondrial electron transport chain, *H_2S* hydrogen sulfide, *$[Ca^{2+}]_i$* intracellular calcium concentration, *NT* neurotransmitter

release of excitatory neurotransmitters, which by stimulating the afferent nerve ending increase carotid sinus nerve activity [2]. Consistent with this possibility, H_2S depolarizes glomus cells, which appears to be in part due to inhibition of either a TASK-like K^+ conductance [30], or inhibition of Ca^{2+}-activated K^+ channel activity [29, 31]. H_2S increases $[Ca^{2+}]_i$ in glomus cells and hypoxia-induced transmitter secretion is nearly absent in CSE –null glomus cells [32]. In addition, H_2S might act on mitochondrial electron transport chain glomus cells [30] (Fig. 1.1).

4 Physiological Implications of Carotid Body O_2 Sensing by Gasotransmitters

The chemosensory reflex is a critical regulator of autonomic functions [2]. A recent study examined the importance of gaso transmitter signaling in the carotid bodies in Spontaneous Hypertensive (SH), Brown Norway (BN), and Sprague-Dawley (SD) rats [27]. Compared to SD rats, SH rats displayed *augmented* and BN rats *attenuated* carotid body responses to hypoxia. The exaggerated chemosensory response in SH rats was associated with elevated basal and hypoxia-induced H_2S levels and markedly reduced CO levels in the carotid body. Treating SH rats, with L-propargylglycine (L-PAG), an inhibitor of CSE, or with CORM-2, a CO donor, eliminated hypersensitivity of the carotid body to hypoxia. Remarkably, L-PAG treatment markedly reduced the magnitude of hypertension in SH rats, suggesting

that elevated H_2S signaling in the carotid body contributes to the pathogenesis of hypertension in SH rats.

In contrast, the impaired carotid body response to hypoxia in BN rats was associated with elevated CO and reduced H_2S levels as compared to SD rats. The chemosensory reflex was nearly absent in BN rats, as evidenced by the absence of ventilatory and sympathetic nerve stimulation by low O_2. Treating BN rats with an HO inhibitor, which reduced CO levels, restored the carotid body response to hypoxia comparable to that seen in SD rats, improved ventilator adaptations to hypoxia, and prevented pulmonary edema in response to hypobaric hypoxia [27]. Taken together, these findings suggest that dysregulation of CO-H_2S signaling in the carotid body leads to pathological consequences.

Acknowledgments The research in our laboratory is supported by grants from National Institutes of Health, Heart, Lung and Blood Institute PO1-HL-90554 and UH2-HL-123610.

References

1. de Castro F (2009) Towards the sensory nature of the carotid body: Hering, de Castro and Heymansdagger. Front Neuroanat 3:23
2. Kumar P, Prabhakar NR (2012) Peripheral chemoreceptors: function and plasticity of the carotid body. Compr Physiol 2:141–219
3. Pflüger E (1868) Ueber die Ursache der Athembewegungen, sowie der Dyspnoë und Apnoë. Pflügers Arch Gesamte Physiol Meschen Tiere 1:61–106
4. Taube H (1743) Dissertationem inauguralem de vera nervi inter costalis origine
5. Kohn A (1900) Ueber den bau und die entwicklund der sogenannten carotisdruse. Archiv Mik Anat Entwick 56:81–148
6. De Castro F (1923) Evolución de los ganglios simpáticos vertebrales y prevertebrales. Conexiones y citotectonia de algunos grupos de ganglios en el niño y hombre adulto. Trab Lab Invest Biol Univ Madrid 20:113–208
7. De Castro F (1925) Technique pour la coloration du système nerveux quand il est pourvu de ses étuis osseux. Trav Lab Rech Biol 23:427–446
8. De Castro F (1926) Sur la structure et l'innervation de la glande intercarotidienne (glomus caroticum) de l'homme et des mammiferes et sur un nouveau systeme de l'innervation autonome du nerf glossopharyngien. Trav Lab Rech Biol 24:365–432
9. De Castro F (1928) Sur la structure et l'innervation du sinus carotidien de l'homme et des mammifères. Nouveaux faits sur l'innervation et la fonction du glomus caroticum. Trav Lab Rech Biol 25:331–380
10. De Castro F (1929) Ueber die Struktur und innervation des glomus caroticum beim Menschen aund bei den Säugetieren. Anatomisch-experimentelle Untersuchungen. Z Anat Entwicklungsgesch 89:250–265
11. Heymans C (1929) Le sinus carotidien, zone reflexogene regulatrice du tonus vagal cardiaque du tonus neurovasculaire et deI'adrenalinosecretion. Arch Int Pharmacodyn Ther 35:269–313
12. Heymans C, Bouckaert JJ (1930) Sinus caroticus and respiratory reflexes. J Physiol 69:254–266
13. Heymans C, Bouckart JJ, Dautrebande L (1930) Sinus carotidien et réflexes respiratoires. II. Influences respiratoires réflexes de l'acidôse de l'alcalose, de l'anhydride carbonique, de l'ion hydrogéne et de l'anoxémie: Sinus carotidiens et échanges respiratoires dans le poumons et au delá des poumons. Arch Int Pharmacodyn 39:400–448

14. Heymans C, Bouckaert JJ, Dautrebande L (1931) Au sujet du mécanisme de la bradycardie provoquée par la nicotine, la lobéline, le cyanure, le sulfure de sodium, les nitrites et la morphine, et de la bradycardie asphyxique. Arch Int Pharmacodyn 41:261–289
15. Heymans C, Bouckaert JJ, Regniers P (1933) Le Sinus Carotidien. G. Doin, Paris, pp 1–334
16. Heymans C, Bouckaert JJ, von Euler US et al (1932) Sinus carotidiens et reflexes vasomoteurs. Arch Int Pharmacodyn 43:86–110
17. Heymans J, Heymans C (1927) Sur les modifications directes et sur la regulationreflexede l'activitie du centre respiratory de la tete isolee du chien. Arch Int Pharmacodyn Ther 33: 273–372
18. Heymans C, Ladon A (1925) Recherches physiologiques et pharmacologiques sur la tête isolée et le centre vague du chien. I: Anémie, asphyxie, hypertension, adrénaline, tonus pneumogastrique. Arch Int Pharmacodyn 30:145
19. Zotterman Y (1979) Opening remarks. In: von Euler C, Lagercrantz H (eds) Central nervous control of mechanisms of breathing. Peragam Press, Oxford/New York/Toranto/Sydney/Paris/ Frankfort, pp 1–2
20. von Euler US, Liljestrand G, Zotterman Y (1939) The excitation mechanism of the chemoreceptors of the carotid body. Scand Arch Physiol 83:132–152
21. Prabhakar NR, Semenza GL (2015) Oxygen sensing and homeostasis. Physiology (Bethesda) 30:340–348
22. Maines MD (1997) The heme oxygenase system: a regulator of second messenger gases. Annu Rev Pharmacol Toxicol 37:517–554
23. Mkrtchian S, Kahlin J, Ebberyd A et al (2012) The human carotid body transcriptome with focus on oxygen sensing and inflammation – a comparative analysis. J Physiol 590:3807–3819
24. Ortega-Saenz P, Pascual A, Gomez-Diaz R et al (2006) Acute oxygen sensing in heme oxygenase-2 null mice. J Gen Physiol 128:405–411
25. Prabhakar NR, Dinerman JL, Agani FH et al (1995) Carbon monoxide: a role in carotid body chemoreception. Proc Natl Acad Sci U S A 92:1994–1997
26. Yuan G, Vasavda C, Peng YJ et al (2015) Protein kinase G-regulated production of H2S governs oxygen sensing. Sci Signal 8:ra37
27. Peng YJ, Makarenko VV, Nanduri J et al (2014) Inherent variations in CO-H2S-mediated carotid body O2 sensing mediate hypertension and pulmonary edema. Proc Natl Acad Sci U S A 111:1174–1179
28. Peng YJ, Nanduri J, Raghuraman G et al (2010) H2S mediates O-2 sensing in the carotid body. Proc Natl Acad Sci U S A 107:10719–10724
29. Li Q, Sun B, Wang X et al (2010) A crucial role for hydrogen sulfide in oxygen sensing via modulating large conductance calcium-activated potassium channels. Antioxid Redox Signal 12:1179–1189
30. Buckler KJ (2012) Effects of exogenous hydrogen sulphide on calcium signalling, background (TASK) K channel activity and mitochondrial function in chemoreceptor cells. Pflugers Arch 463:743–754
31. Telezhkin V, Brazier SP, Cayzac SH et al (2010) Mechanism of inhibition by hydrogen sulfide of native and recombinant BKCa channels. Respir Physiol Neurobiol 172:169–178
32. Makarenko VV, Nanduri J, Raghuraman G et al (2012) Endogenous H2S is required for hypoxic sensing by carotid body glomus cells. Am J Physiol Cell Physiol 303:C916–C923

Chapter 2
Predicted Decrease in Membrane Oxygen Permeability with Addition of Cholesterol

Gary Angles, Rachel Dotson, Kristina Bueche, and Sally C. Pias

Abstract Aberrations in cholesterol homeostasis are associated with several diseases that can be linked to changes in cellular oxygen usage. Prior biological and physical studies have suggested that membrane cholesterol content can modulate oxygen delivery, but questions of magnitude and biological significance remain open for further investigation. Here, we use molecular dynamics simulations in a first step toward reexamining the rate impact of cholesterol on the permeation of oxygen through phospholipid bilayers. The simulation models are closely compared with published electron paramagnetic resonance (EPR) oximetry measurements. The simulations predict an oxygen permeability reduction due to cholesterol but also suggest that the EPR experiments may have underestimated resistance to oxygen permeation in the phospholipid headgroup region.

Keywords Molecular dynamics simulation • Oximetry • Electron paramagnetic resonance (EPR) • Resistance to permeation • Tempocholine

1 Introduction

Here, we discuss work implicating membrane cholesterol as a hindrance to oxygen transport on the cellular level and consider related biomedical implications. Further, we offer atomic resolution insight into prior electron paramagnetic resonance (EPR) based estimates of membrane oxygen permeability and resistance to permeation.

Though cholesterol is a normal constituent of higher eukaryotic membranes [1] and lung surfactant [2], its influence on oxygen diffusion is not fully understood. The cholesterol content of normal cells varies widely but often falls in the range 20–40 mol% [1]. Normal red blood cells contain about 50 mol% cholesterol, or a 1:1 ratio of cholesterol with phospholipid [3].

G. Angles • R. Dotson • K. Bueche • S.C. Pias (✉)
Department of Chemistry, New Mexico Institute of Mining and Technology (New Mexico Tech), 801 Leroy Place, Socorro, NM 87801, USA
e-mail: sally.pias@nmt.edu

H.J. Halpern et al. (eds.), *Oxygen Transport to Tissue XXXIX*, Advances in Experimental Medicine and Biology 977, DOI 10.1007/978-3-319-55231-6_2

The complexity of biological membranes makes drawing conclusions regarding cholesterol's influence on permeability particularly difficult, as cholesterol itself is inhomogeneously distributed within the membrane and plays a substantial role in raft formation and stabilization [1]. Lateral inhomogeneity of cholesterol content likely impacts oxygen transport, giving rise to regions of greater and lesser permeability [4–6]. Further, measuring *intracellular* oxygen, as distinct from extracellular oxygen, presents a substantial methodological challenge [7], not to mention the potential difficulty of tracking oxygen movement and partitioning within cells.

A few cellular studies have successfully characterized transmembrane oxygen diffusion with varying membrane cholesterol content and have suggested that cholesterol reduces the rate of transmembrane oxygen flow [7, 8]. Yet, generalization of the findings would require further detail regarding membrane composition and organization for the cells studied. Prior biophysical studies have strongly suggested that membrane cholesterol content directly reduces oxygen permeability [5, 6, 9]. Subczynski and colleagues have used EPR spin-label oximetry data to estimate permeability coefficients, which describe the rate of diffusional flux across a membrane. However, approximations inherent in the method limit the accuracy of the permeability values to ±30% [9].

Computer simulations of molecular dynamics provide a particularly valuable means of attaining atomic-resolution insight into biological processes in which molecular structural behavior plays a significant role. The current work represents a first step toward reevaluating the rate impact of membrane cholesterol on oxygen permeability. We present resistance to permeation curves calculated from all-atom molecular dynamics simulations and compare the curves with published data from EPR probe-based oximetry. Then, we provide preliminary evidence indicating that the base-level permeability of membrane phospholipids may be lower than generally assumed.

2 Methods

To examine membrane oxygen permeability with atomic resolution, we conducted all-atom molecular dynamics simulations. These were performed with the GPU-enabled version of Amber 14 biomolecular modeling software [10, 11], utilizing the equilibration strategy and simulation conditions reported previously [17]. Here, we feature simulations using the Amber Lipid14 force field and cholesterol extension [12, 13], along with the TIP3P explicit water model [14] and in-house O_2 parameters [17]. A tempocholine spin label moiety was modeled using Lipid14 force field atom types. The tempocholine moiety and glycerol backbone were charge-fitted according to the Amber Lipid Framework modular scheme [15].

Data from three simulation systems are reported here, with each system consisting of 128 lipid molecules, total, along with 35 water molecules per lipid. 31 or 35 O_2 molecules were included, to reach a concentration of 200 mM for the entire system (lipid and water). This high O_2 concentration enables relatively rapid sampling

of the configurational space and provides results comparable to those obtained with only one O_2 molecule (data not shown). As a simplified representation of the bulk lipid fraction of animal cell membranes, we used the highly abundant phospholipid 1-palmitoyl,2-oleoylphosphatidylcholine (POPC) for all three simulation systems: (1) pure POPC, (2) POPC mixed in a 1:1 ratio with cholesterol ("POPC/cholesterol"), and (3) POPC with one tempocholine-1-palmitoyl-2-oleoylphosphatidic acid ester (T-PC) molecule per leaflet. All simulations were conducted at a constant pressure of 1 atm and at a fixed temperature of either 37 or 25 °C.

From duplicate 300-ns POPC and POPC/cholesterol simulations at 37 °C, we estimated resistance to permeation curves for oxygen according to the method of Marrink and Berendsen, using the relative local free energy calculated from the depth-dependent oxygen concentration, along with an estimate of the depth-dependent diffusion coefficient based on the local mean-squared displacement along the bilayer normal [16]. From two POPC simulations incorporating two explicit T-PC molecules and run at 25 °C, we observed the probe orientational behavior over 100 ns. Data are shown for one representative simulation from each set of duplicates.

3 Results and Discussion

Simulation resistance to permeation curves for POPC and POPC/cholesterol (Fig. 2.1a) predict fairly similar permeabilities for both bilayers, given comparable areas under the resistance to permeation curves. This similarity was initially puzzling because prior EPR experiments had estimated POPC/cholesterol to be about three times less permeable to oxygen than pure POPC [9]. Our simulation systems show strong agreement with other experimental measurements, especially electron density profiles and nuclear magnetic resonance (NMR) lipid order parameters (data not shown; as reported in [12, 13]). Moreover, we are able to reproduce quite accurately the shape of the EPR resistance to permeation curves used to estimate permeability for POPC and POPC/cholesterol (Fig. 2.1b).

The EPR curves were calculated from the spin-lattice relaxation times of nitroxide radical spin labels placed at various depths along the membrane. Membrane permeability coefficients were estimated from the respective areas under the resistance to permeation curves [9, 16]. The EPR permeability estimates are, thus, sensitive to probe positioning within the membrane. The nitroxide spin label group tempocholine (shown in Fig. 2.1d) was used experimentally for the purpose of detecting oxygen in the headgroup region. Tempocholine is structurally similar to the charged POPC headgroup moiety choline. Yet, it is substantially nonpolar, suggesting that the nitroxide spin label may preferentially associate with the nonpolar hydrocarbon portion of the membrane, rather than with the charged headgroups. Figure 2.1c juxtaposes a simplified POPC bilayer image with a simulation free energy curve, showing barriers to oxygen permeation at the headgroups.

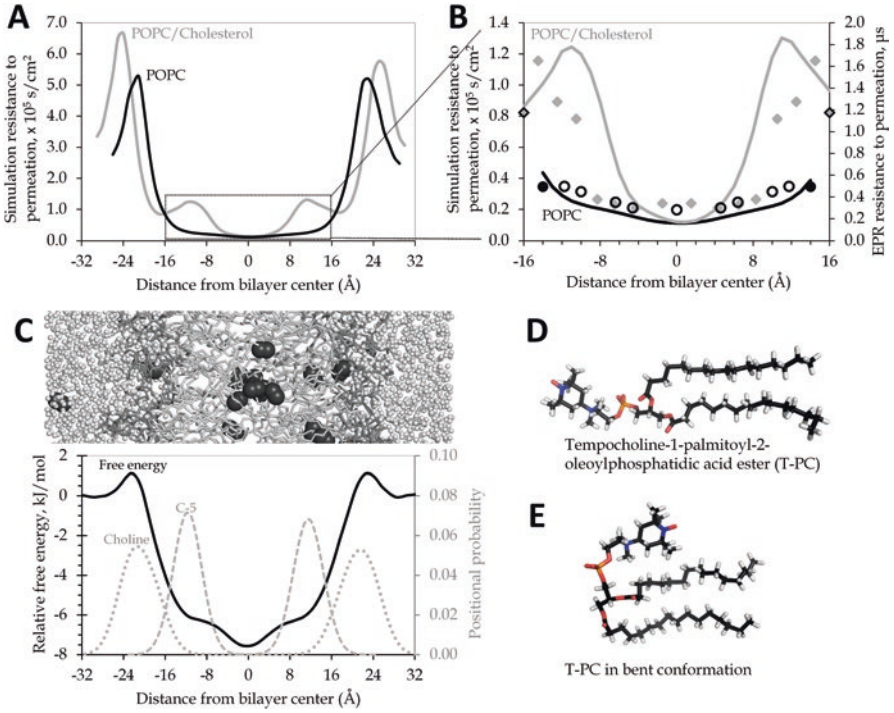

Fig. 2.1 EPR "headgroup" probe may oversample the phospholipid tail region. (**a**) Simulation resistance to permeation gives a similar area under the curve for POPC (*black*) and POPC/cholesterol (*gray*). (**b**) The same simulation resistance to permeation curves (*solid lines*) differ substantially in contour and area under the curve in the region most thoroughly sampled in published EPR measurements. The secondary axis shows the EPR resistance to permeation values [9], placing the probes according to center of the probability distributions observed in our simulations for the corresponding atoms (oleoyl tail carbons 5, 7, 9, 10, 12, 14, and 16 in open *black circles* for POPC or *solid gray diamonds* for POPC/cholesterol; probability distribution data not shown). The T-PC probe positions (*solid black circles* for POPC or *black-outlined diamonds* for POPC/cholesterol) have also been estimated from simulations of POPC with one T-PC molecule in each bilayer leaflet. (**c**) Cropped image of POPC/water/O_2 simulation system, positioned above a relative free energy profile for oxygen across a POPC bilayer system at 37 °C. Relative local free energy for O_2 at 37 °C across a model POPC bilayer shows peaks in the headgroup regions and a free energy minimum in the tail region. Positional probability distributions are shown for the POPC headgroup choline (*dotted line*) and for the fifth carbon of the POPC oleoyl tail (C-5, *dashed line*). (**d**, **e**) Two alternate conformations of the EPR T-PC probe molecule, with the bent conformation favored in preliminary simulations at 25 °C

The simulation positional distributions of the headgroup choline moiety and of the fifth carbon atom (C-5) of the oleoyl tail are also shown.

To better understand the orientational behavior of the EPR headgroup probe, we conducted simulations incorporating a preliminary model of the T-PC probe used experimentally (Fig. 2.1d). In our simulations, the nitroxide spin label dwells predominantly within the hydrophobic phospholipid tail region of the bilayer, near C-5 of the oleoyl tail. As such, we find the T-PC molecule predominantly in a bent conformation

(Fig. 2.1e). This finding requires experimental confirmation, but it suggests that the permeabilities of POPC and POPC/cholesterol may be more similar than expected from the EPR work. Namely, the EPR T-PC probe may substantially underestimate the resistance to permeation for both bilayers *because it may not, in fact, be sampling the headgroup region, where the greatest resistance is seen*. The POPC and POPC/cholesterol resistance to permeation curves differ in contour in the region between −16 and 16 Å (Fig. 2.1b), which we suspect to be the portion of the bilayer most sampled by the EPR spin-label probes, including the intended headgroup probe, T-PC. Considering this region alone, we see about a three-fold difference in the area under the resistance to permeation curve, a result that agrees qualitatively with the EPR permeability estimates.

4 Conclusion

The simulation resistance to permeation curves indicate that pure POPC phospholipid and POPC/cholesterol (1:1 mixing ratio) have fairly similar permeabilities to molecular oxygen. Though we predict a less dramatic permeability difference than expected from published EPR estimates, we do see an increase in the overall resistance to permeation for POPC/cholesterol of roughly 20%, compared with POPC alone. This increased resistance should correspond with a permeability reduction of similar magnitude. While modest on a single-membrane level, the rate-reducing effect may be amplified as oxygen is required to cross or circumvent multiple membranes on its path toward mitochondria buried within tissues [17].

Our simulations further predict that the lipid fraction of biological membranes may be less permeable to oxygen than has generally been assumed, regardless of the cholesterol content. This prediction is based on the substantially greater area under the resistance to permeation curve obtained when resistance in the headgroup region is taken fully into account. It should be noted that the current models neglect inhomogeneities in lipid organization within the plane of the membrane, lipid compositional variation within and across leaflets, as well as the presence of membrane proteins. While such factors may moderate cholesterol's impact in living cells, the models' simplicity is an advantage for distinguishing the direct influence of cholesterol on membrane permeability. Ongoing work will address other membrane compositional factors that may influence oxygen permeability. Additional biological work is needed to test our predictions and to characterize quantitatively the effect of cholesterol on oxygen permeability in intact, functional cells.

Acknowledgments We thank Ross Walker and Benjamin Madej for providing advance access to the cholesterol parameters used in this study. James Ryan Bredin developed the O_2 parameters used in this work. Daniel Lyons contributed valuable computing expertise. The molecular images were generated using PyMOL software [18], and DataThief software [19] was used to infer the experimental values reported in Fig. 2.1b from published plots. SCP thanks James Kindt and Snežna Rogelj for professional mentoring. This work was supported by the NIH under NIGMS grant P20GM103451 and by a gift from the Glendorn Foundation. The content is solely the

responsibility of the authors. We used computing resources of TACC at UT Austin, accessed through XSEDE (funded by NSF grant ACI-1053575), as well as the EXXACT MD SimCluster ("Electra") at New Mexico Tech.

References

1. Mouritsen OG, Zuckermann MJ (2004) What's so special about cholesterol? Lipids 39(11):1101–1113
2. Larsson M, Larsson K, Nylander T, Wollmer P (2003) The bilayer melting transition in lung surfactant bilayers: the role of cholesterol. Eur Biophys J 31(8):633–636
3. Jandl J, Blood H (1996) Textbook of hematology, 2nd edn. Little, Brown and Company, Boston
4. Kawasaki K, Yin JJ, Subczynski WK et al (2001) Pulse EPR detection of lipid exchange between protein-rich raft and bulk domains in the membrane: methodology development and its application to studies of influenza viral membrane. Biophys J 80(2):738–748
5. Raguz M, Mainali L, Widomska J, Subczynski WK (2011) Using spin-label electron paramagnetic resonance (EPR) to discriminate and characterize the cholesterol bilayer domain. Chem Phys Lipids 164(8):819–829
6. Wennberg CL, van der Spoel D, Hub JS (2012) Large influence of cholesterol on solute partitioning into lipid membranes. J Am Chem Soc 134(11):5351–5361
7. Khan N, Shen J, Chang TY et al (2003) Plasma membrane cholesterol: a possible barrier to intracellular oxygen in normal and mutant CHO cells defective in cholesterol metabolism. Biochemistry 42(1):23–29
8. Menchaca HJ, Michalek VN, Rohde TD et al (1998) Decreased blood oxygen diffusion in hypercholesterolemia. Surgery 124(4):692–698
9. Widomska J, Raguz M, Subczynski WK (2007) Oxygen permeability of the lipid bilayer membrane made of calf lens lipids. Biochim Biophys Acta 1768(10):2635–2645
10. Case DA, Berryman JT, Betz RM, et al (2015) AMBER 2015. University of California, San Francisco
11. Salomon-Ferrer R, Götz AW, Poole D et al (2013) Routine microsecond molecular dynamics simulations with AMBER on GPUs. 2. Explicit solvent particle mesh Ewald. J Chem Theory Comput 9(9):3878–3888
12. Dickson CJ, Madej BD, Skjevik ÅA et al (2014) Lipid14: the Amber lipid force field. J Chem Theory Comput 10(2):865–879
13. Madej BD, Gould IR, Walker RC (2015) A parameterization of cholesterol for mixed lipid bilayer simulation within the Amber Lipid14 force field. J Phys Chem B 119(38):12424–12435
14. Jorgensen WL, Jenson C (1998) Temperature dependence of TIP3P, SPC, and TIP4P water from NPT Monte Carlo simulations: seeking temperatures of maximum density. J Comput Chem 19(10):1179–1186
15. Skjevik AA, Madej BD, Walker RC, Teigen K (2012) LIPID11: a modular framework for lipid simulations using Amber. J Phys Chem B 116(36):11124–11136
16. Marrink S-J, Berendsen HJC (1994) Simulation of water transport through a lipid membrane. J Phys Chem 98(15):4155–4168
17. Shea R, Smith C, Pias SC (2016) Magnification of cholesterol-induced membrane resistance on the tissue level: implications for hypoxia. Adv Exp Med Biol 923:43–50
18. Schrödinger LLC (2015) The PyMOL molecular graphics system, Version 1.7.6.5
19. Tummers B (2006) DataThief III

Chapter 3
Chronic Diseases as Barriers to Oxygen Delivery: A Unifying Hypothesis of Tissue Reoxygenation Therapy

G.A. Perdrizet

Abstract Modern medical practice has resulted in the accumulation of a growing number of incurable chronic diseases, many of which are inflammatory in nature. Inflammation establishes a hypoxic microenvironment within tissues, a condition of inflammatory hypoxia (IH). Tissues thus affected become severely compromised, are unable to elicit adaptive responses and eventually develop fibrosis and fixed microvascular deficits. Previous work has demonstrated that tissue hypoxia exits even within the simple human model of self-resolving inflammation, the tuberculin reaction. Failed resolution of IH establishes a vicious cycle within tissues that perpetuates tissue hypoxia and resists standard drug therapies. Diseases such as sepsis, chronic cutaneous wounds, kidney disease, traumatic brain injury, solid tumors, inflammatory bowel disease, and chronic bacterial infections (urinary tract infection, cystic fibrosis) are tissue specific manifestations of chronic IH. Successful reversal of IH, through tissue re-oxygenation therapy (TROT), will break this vicious cycle and restore tissue homeostasis. The examples of solid tumors and inflammatory bowel disease are presented to illustrate a theoretical framework to support this hypothesis. Re-oxygenation of compromised tissues must occur before successful treatment of these diverse chronic diseases can be expected.

Keywords Chronic inflammation • Hypoxia • Hyperbaric oxygen • Oxygen therapy • Chronic disease

G.A. Perdrizet (✉)
Department of Emergency Medicine, Center for Wound Healing and Hyperbaric Medicine, UCSD, San Diego, CA, USA
e-mail: gperdrizet@ucsd.edu

H.J. Halpern et al. (eds.), *Oxygen Transport to Tissue XXXIX*, Advances in Experimental Medicine and Biology 977, DOI 10.1007/978-3-319-55231-6_3

1 Chronic Disease and Inflammatory Hypoxia

The primary objectives of this paper are to: (1) Draw attention to the common finding of inflammatory hypoxia (IH) in many chronic disease states, (2) Relate these diseases to the problem of oxygen delivery as demonstrated by the tuberculin reaction and (3) Highlight the opportunity to reoxygenate chronically diseased tissues to affect cure, alone or in combination with conventional therapies. Two examples of chronic disease will be presented, solid tumors and inflammatory bowel disease, to illustrate a theoretical foundation to support a unifying hypothesis of tissue reoxygenation therapy (TROT). Modern medical practice has cured many acute diseases and significantly extended human life span. This success is associated with the accumulation of a growing number of incurable, chronic diseases, many of which are inflammatory in nature [1]. Inflammation is linked to aging and chronic disease [2]. Inflammation of chronic disease establishes a hypoxic microenvironment within tissues which leads to additional inflammation and hypoxia, a pathologic vicious cycle of IH [3]. Tissues thus affected are severely compromised and unable to elicit adaptive responses and over time develop microvascular deficits and tissue fibrosis. Tissue hypoxia is a fundamental and nonspecific phenomenon found in all injured tissues. Acutely, hypoxia can exert a powerful beneficial effect that is best appreciated during successful, acute wound healing [4]. The nature of oxygen supply and utilization during injury has been previously characterized using the tuberculin reaction, a model of acute, self-resolving IH in man [5]. If IH persists, it can become chronic and maladaptive [6]. Failed resolution of IH establishes a vicious cycle within tissues that perpetuates tissue inflammation and hypoxia and detracts from the effectiveness of current medical therapies. Diseases such as sepsis, chronic cutaneous wounds, kidney disease, traumatic brain injury, solid tumors, inflammatory bowel disease, and chronic bacterial infections (urinary tract infection, cystic fibrosis) are all characterized by the presence of IH. Reversal of IH through TROT may break the vicious cycle of IH and enable normalization of tissue responses and repair.

2 Tuberculin Reaction: An *In Vivo* Human Model of Tissue Oxygen Demand, Diffusion and Deficit

The tuberculin reaction is a well-defined example of IH in humans that resolves spontaneously in all cases. Despite the success of this resolution (96 h), the dermal tissue must first pass through a period of acute inflammation and hypoxia. This process has been elegantly studied by investigators at the University of Dundee, Dundee Scotland and reported in a series of papers that span a decade of work (1984–1994) [7–9]. A standardized tuberculin test was administered to immune individuals and monitored the responses over 5 days. Multiple parameters, including tissue pH, blood flow, transcutaneous oximetry, and fluorescence spectroscopy were measured. Expected and significant findings included an influx of inflammatory cells, reduced pH, increased temperature and elevated blood flow. Tissue oxygenation decreased,

hemoglobin oxygen saturation increased, oxygen extraction decreased and yet oxygen consumption steadily increased. The authors were challenged to understand the apparent discrepancy between the low oxygen-extraction on the one hand and elevated oxygen consumption and hemoglobin saturation on the other, offering explanations such as protective regulation, shunting, or even diffusional resistance. This group further exposed individuals to hyperoxia at 1 ATA (atmosphere absolute) or 2 ATA of HBOT during the tuberculin reaction and then performed similar measurements of oxygen delivery and utilization [10]. Three important observations were made. (1) Under atmospheric conditions transcutaneous oxygen tensions continuously fell over 96 h in all groups. (2) Transcutaneous oxygen tensions were lowest in individuals designated as "strong reactors" and (3) Oxygen consumption increased at 1 ATA oxygen exposure and increased further at 2 ATA of oxygen. It appears that despite the elevated oxyhemoglobin concentration and reduced oxygen extraction observed during this "simple" model of IH, by increasing oxygen delivery an increased oxygen consumption was observed. This suggests that a state of oxygen deficit becomes established very early (within 24 h) in dermal tissues challenged with tuberculin antigen. These data suggest that in the presence of IH, tissues frequently fail to receive adequate oxygen supply to meet metabolic demand. The concept of "protective regulation" bears similarity to other conditions in which there is apparent neglect of oxygen uptake by tissues in which the metabolic demand for oxygen is not being met. See discussions related to oxygen conformance (experimental physiology) and cytopathic hypoxia, dysoxia, or loss of hemodynamic coherence (critical care medicine) [11–15]. The "dysoxia" or lack of uptake of oxygen by compromised tissues can be overcome, at least in part, by the elevation of the partial pressure of oxygen to above atmospheric levels. The barrier to effective oxygen delivery in many chronic diseases is IH and represents a common target for TROT.

3 Tissue Re-oxygenation Therapy (TROT): Chronic Disease, Compromised Tissues and the Potential of Hyperbaric Oxygen Therapy (HBOT)

Based on the findings related to the tuberculin reaction, extension of the re-oxygenation concept to diseases in which tissues have become compromised by established IH seems a logical and prudent therapeutic step that may have large gains for minimal incremental investment and therapeutic risk.

Cancer Therapies The tumor microenvironment (TME) is characterized as a hostile environment with acidic pH, chronic inflammation, and tissue hypoxia. The TME is recognized as a barrier to many potentially effective cancer therapies. The reversal of tumor hypoxia has been periodically tested since 1953, in an effort to enhance tumor cell sensitivity to radiation therapy [16]. Cellular proliferation is dependent upon oxygen availability in tissue culture. Maximal incorporation of nuclear labeling occurs in vitro at an oxygen tension of 3 ATA (2280 mmHg) in both normal and malignant tissues *in vitro* [17]. Many agents have been used as potential

radiation sensitizers, including hyperbaric oxygen therapy (HBOT). HBOT demonstrates improvements in loco-regional control and cancer-free survival rates over other methods [18]. Likewise, hypoxia acts as a barrier to anti-cancer drugs and immunotherapies. Enhancement of drug sensitivity may also be possible. For example, the uptake of radiolabeled 5-FU was increased by >50% following a single exposure of DMBA-induced mammary tumors to HBOT (2.0 ATA × 90 min) [19]. Synergy was reported for experimental hepatoma cell lines exposed to HBOT in vitro (2.0 ATA × 40 min) with either sorafenib or cisplatin [20]. Experimental oxygen therapy (60% oxygen; 456 mmHg), as a physiologic immunoadjuvant, is a simple and elegant approach that has been demonstrated in animal models of melanoma and fibrosarcoma [21, 22]. Tumor reoxygenation is an underutilized and understudied adjunctive anti-cancer therapy.

Inflammatory Bowel Disease (IBD) Chronic IBD, (both ulcerative colitis and Crohn's disease), is characterized by mucosal and submucosal inflammation, tissue hypoxia and bacterial biofilm formation [6]. Animal models, case reports and small series describe clinical responses to HBOT, including in patients with advanced, refractory IBD [23]. Aside from these uncontrolled reports, HBOT has been shown to reduce systemic cytokine levels in patients with IBD and supports a systemic anti-inflammatory effect [24]. To date, no well-controlled randomized studies have been reported that have tested TROT in the setting of IBD or other forms of chronic gastrointestinal inflammation [23, 25]. More recently, a case report describing the successful reversal of chronic IH in the setting of postoperative complications related to the surgical management of IBD has been published [26]. The robust clinical response of refractory "pouchitis" to TROT is compelling and supports the unifying concept of the potential for therapeutic benefit in settings of otherwise untreatable IH.

4 Summary

Chronic diseases are common, costly and their prevalence is increasing. This is, in part, due to the poor effectiveness of current drug therapies. Independent of the specific diagnostic label, there exists a common condition of inflammatory hypoxia in many chronically diseased tissues. Chronically compromised tissues develop severe oxygen deficits that cannot be remediated without increasing oxygen delivered to these tissues. Modern pharmaceuticals elegantly target the inflammatory cascade within these compromised tissues without due consideration for the dominant role played by the coincident hypoxia. Today tissue re-oxygenation therapy is underutilized and understudied. There are many opportunities to revisit conventional treatments and develop new ones, once serious consideration is given to testing tissue re-oxygenation therapy in the setting of chronic disease states.

Acknowledgements Supported, in part, by the Ted and Michelle Gurnee Endowed Chair in Translational Research, Dept. of Emergency Medicine, UCSD, San Diego, CA.

References

1. Ward BW, Schiller JS, Goodman RA (2014) Multiple chronic conditions among US adults: a 2012 update. Prev Chronic Dis 11:E62
2. Pawelec G, Goldeck D, Derhovanessian E (2014) Inflammation, ageing and chronic disease. Curr Opin Immunol 29:23–28
3. Eltzschig HK, Carmeliet P (2011) Hypoxia and inflammation. N Engl J Med 364:656–665
4. Hunt TK, Zederfeldt B, Goldstick TK (1969) Oxygen and healing. Am J Surg 118:521–525
5. Abbot NC, Beck JS, Carnochan FM, Lowe JG, Gibbs JH (1992) Circulatory adaptation to the increased metabolism in the skin at the site of the tuberculin reaction. Int J Microcirc Clin Exp Sponsored Eur Soc Microcirc 11:383–401
6. Biddlestone J, Bandarra D, Rocha S (2015) The role of hypoxia in inflammatory disease (review). Int J Mol Med 35:859–869
7. Newton DJ, Harrison DK, McCollum PT (1996) Oxygen extraction rates in inflamed human skin using the tuberculin reaction as a model. Int J Microcirc Clin Exp Sponsored Eur Soc Microcirc 16:118–123
8. Abbot NC, Beck JS, Harrison DK, Wilson SB (1993) Dynamic thermographic imaging for estimation of regional perfusion in the tuberculin reaction in healthy adults. J Immunol Methods 162:97–107
9. Harrison DK, Abbot NC, Carnochan FM, Beck JS, James PB, McCollum PT (1994) Protective regulation of oxygen uptake as a result of reduced oxygen extraction during chronic inflammation. Adv Exp Med Biol 345:789–796
10. Abbot NC, Beck JS, Carnochan FM, Gibbs JH, Harrison DK et al (1985) 1994. Effect of hyperoxia at 1 and 2 ATA on hypoxia and hypercapnia in human skin during experimental inflammation. J Appl Physiol 77:767–773
11. Ince C (2015) Hemodynamic coherence and the rationale for monitoring the microcirculation. Crit Care 19(Suppl 3):S8
12. Gnaiger E (2003) Oxygen conformance of cellular respiration. A perspective of mitochondrial physiology. Adv Exp Med Biol 543:39–55
13. Fink MP (2015) Cytopathic hypoxia and sepsis: is mitochondrial dysfunction pathophysiologically important or just an epiphenomenon. Pediatr Crit Care Med 16:89–91
14. Pinsky MR (1994) Beyond global oxygen supply-demand relations: in search of measures of dysoxia. Intensive Care Med 20:1–3
15. Haase N, Perner A (2011) Central venous oxygen saturation in septic shock--a marker of cardiac output, microvascular shunting and/or dysoxia? Crit Care 15:184
16. Gray LH, Conger AD, Ebert M, Hornsey S, Scott OC (1953) The concentration of oxygen dissolved in tissues at the time of irradiation as a factor in radiotherapy. Br J Radiol 26:638–648
17. Fabrikant JI, Wisseman CL 3rd, Vitak MJ (1969) The kinetics of cellular proliferation in normal and malignant tissues II. An in vitro method for incorporation of tritiated thymidine in human tissues. Radiology 92:1309–1320
18. Overgaard J (2011) Hypoxic modification of radiotherapy in squamous cell carcinoma of the head and neck--a systematic review and meta-analysis. Radiother Oncol 100:22–32
19. Moen I, Tronstad KJ, Kolmannskog O, Salvesen GS, Reed RK, Stuhr LE (2009) Hyperoxia increases the uptake of 5-fluorouracil in mammary tumors independently of changes in interstitial fluid pressure and tumor stroma. BMC Cancer 9:446
20. Peng HS, Liao MB, Zhang MY, Xie Y, Xu L et al (2014) Synergistic inhibitory effect of hyperbaric oxygen combined with sorafenib on hepatoma cells. PLoS One 9:e100814
21. Hatfield SM, Kjaergaard J, Lukashev D, Schreiber TH, Belikoff B et al (2015) Immunological mechanisms of the antitumor effects of supplemental oxygenation. Sci Transl Med 7:277ra30
22. Hatfield SM, Kjaergaard J, Lukashev D, Belikoff B, Schreiber TH et al (2014) Systemic oxygenation weakens the hypoxia and hypoxia inducible factor 1alpha-dependent and extracellular adenosine-mediated tumor protection. J Mol Med (Berl) 92:1283–1292

23. Dulai PS, Gleeson MW, Taylor D, Holubar SD, Buckey JC, Siegel CA (2014) Systematic review: the safety and efficacy of hyperbaric oxygen therapy for inflammatory bowel disease. Aliment Pharmacol Ther 39:1266–1275
24. Weisz G, Lavy A, Adir Y, Melamed Y, Rubin D et al (1997) Modification of in vivo and in vitro TNF-alpha, IL-1, and IL-6 secretion by circulating monocytes during hyperbaric oxygen treatment in patients with perianal Crohn's disease. J Clin Immunol 17:154–159
25. Rossignol DA (2012) Hyperbaric oxygen treatment for inflammatory bowel disease: a systematic review and analysis. Med Gas Res 2:6
26. Nyabanga CT, Kulkarni G, Shen B (2015) Hyperbaric oxygen therapy for chronic antibiotic-refractory ischemic pouchitis. Gastroenterol Rep (Oxf). doi:10.1093/gastro/gov038

Chapter 4
Dorsiflexor Muscle Oxygenation During Low, Moderate and Submaximal Sustained Isometric Contraction

Adkham Paiziev, Martin Wolf, and Fikrat Kerimov

Abstract Sustained isometric contractions of skeletal muscles produce intramuscular pressures that lead to blood flow restriction. Thus, we have the paradox of rising O_2 demand due to muscle activity and at the same time reduced blood flow. The aim was to assess muscle oxygenation during sustained isometric low (30%), moderate (60%) and submaximal [90% of maximal voluntary contraction (MVC)] contraction of the dorsiflexor muscle. Experiments were conducted on the dominant (right) leg of 8 male students (age 19 ± 2 years, weight 75 ± 6 kg). Tissue oxygen saturation (StO_2) was recorded from the tibialis anterior using near-infrared spectroscopy. StO_2 was higher at 30% compared to both 60% and 90% MVC at all time points after the start of the exercise and higher at 60% than 90%. This indicates that the supply of O_2 did not keep up with its consumption. During arterial occlusion the minimal StO_2 reached 52%, which is significantly higher than StO_2 during 60% and 90% MVC. After each contraction there was a large and immediate hyperemic response, whose resaturation rate continuously increased from 30% to 60% to 90% MVC. The StO_2 resaturation rate was positively correlated with the MVC, indicating a vasodilation depending on the intensity of the exercise.

Keywords Skeletal muscle • exercise • Near Infrared Spectroscopy • Blood occlusion

A. Paiziev (✉) • F. Kerimov
Uzbekistan State Institute of Physical Culture (USIPC), Tashkent, Uzbekistan
e-mail: adkhampaiziev@gmail.com

M. Wolf
Biomedical Optics Research Laboratory (BORL), University of Zurich, Zurich, Switzerland

H.J. Halpern et al. (eds.), *Oxygen Transport to Tissue XXXIX*, Advances in Experimental Medicine and Biology 977, DOI 10.1007/978-3-319-55231-6_4

1 Introduction

Sustained isometric contraction (SIC) of skeletal muscles produces intramuscular pressure (IMP) that restricts muscle blood flow (MBF) and limits O_2 delivery to tissue [1]. MBF plays a key role in regulating the intensity and type of muscle contractions [2]. A limited MBF due to SIC leads to fatigue due lack of O_2 and nutrients. Thus, we have the paradox of rising O_2 demand due to muscle activity and at the same time reduced MBF. To clarify this situation much research has been performed mainly on MBF [3–7]. However, during exercise there are few measurements of MBF by Doppler ultrasound. Previous studies indicate that complete occlusion of MBF occurs at 50–60% of maximal voluntary contractions (MVC) during SIC [3, 4, 6]. MBF was not occluded at the level of the conduit artery during any contraction intensity [3]. Thus, our understanding of the oxygenation of the skeletal muscle in response to different intensities of SIC (low, moderate, submaximal MVC) is still limited.

Despite advantages of fMRI, PET and Doppler ultrasound only one paper has been devoted to measure the hemodynamic response of muscles to SIC [3] by near infrared spectroscopy (NIRS). In the near-infrared (NIR) spectrum (700–900 nm) light penetrates deeply into the tissue and oxyhemoglobin (O_2Hb) and deoxyhemoglobin (HHb) are the strongest absorbers, while myoglobin (Mb) absorbs less. NIRS is an established optical technique to monitor concentration changes of O_2Hb, HHb, total haemoglobin (tHb) and tissue oxygen saturation (StO_2) in a variety of tissues [8, 9]. NIRS instruments are non-invasive, small, and applicable in exercise physiology.

The aim was to assess changes in muscle oxygenation during low, moderate and submaximal SIC of the dorsiflexor muscle.

2 Methods

Eight male students of USIPC were included (age 19 ± 2 years, weight 75 ± 6 kg) and measured on the dominant (right) leg. The foot was placed in an in-house built isometric torso-dynamometer (DC-200, Russia). Tissue O_2 saturation (StO_2) was recorded from the tibialis anterior by NIRS (SenSmart™ Model X-100, NONIN). The sensor was placed over the belly of the tibialis anterior muscle of each individuals with spacing of optodes of 4 cm.

The experiment consisted of pre-exercise (rest) and three successive periods (each ~1 min) of sustained isometric contractions at 30%, 60% and 90% of MVC and separated by rest periods of 3 min (Fig. 4.1). To determine the minimal StO_2 in the dorsiflexors an arterial occlusion was performed at the end of the experiment. The dorsiflexor muscle was selected, because both venous outflow and arterial inflow can be occluded by a proximal cuff. Without blood supply, the muscle metabolism depends on the O_2 in capillaries and muscle cells. Consequently, the O_2Hb

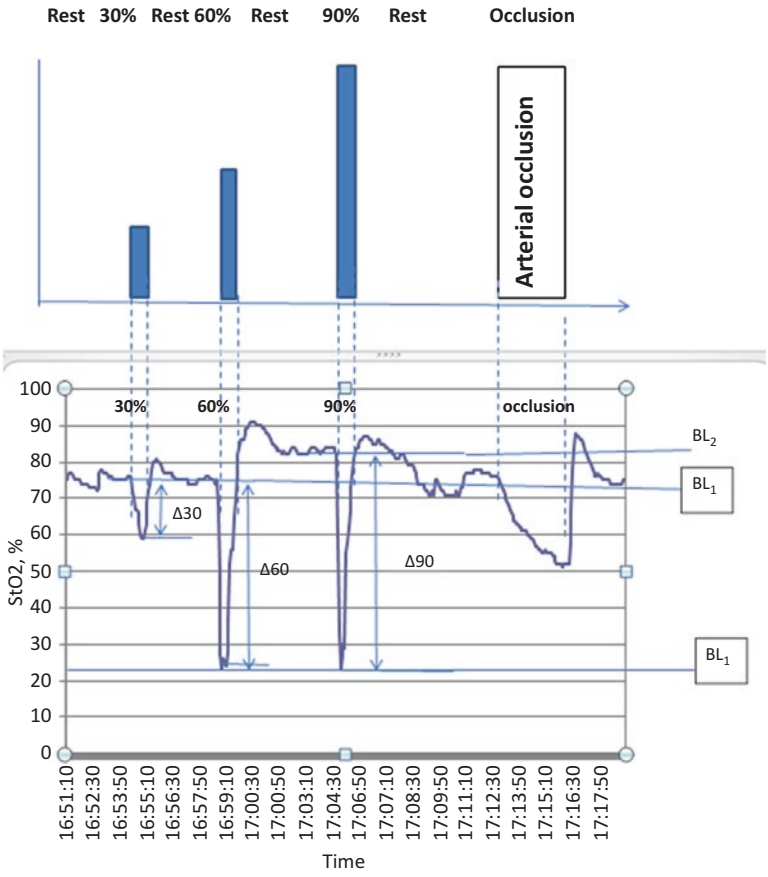

Fig. 4.1 Protocol of experiment (*top*) and example of StO_2 trace (*bottom*). During moderate and submaximal SIC, subjects were not able to perform the exercise for one whole minute

and StO_2 decrease, while HHb increases and tHb remains constant. After the occlusion a hyperemic response occurs, i.e. a rapid increase in O_2Hb, tHb and StO_2, while HHb is washed-out. From this procedure, we calculated O_2 consumption, reoxygenation rate and the half-recovery times of the signals [10].

The recovery baseline (RB) value is the StO_2 value after stabilisation during the rest period following a test period. The performance baseline is the minimum StO2 value reached during SIC. For each individual the NIRS signal was normalized to its maximal value reached during reperfusion after cessation of occlusion. Differences in the StO_2, desaturation rate (De) and resaturation rate (Re) between muscle contraction intensities were analysed by Student's t-test in the statistical software package Statistica for Windows (version 13).

3 Results

Figure 4.1 displays a typical measurement in one subject. The drop in StO_2 increased from low to moderate to submaximal SIC (group values: Table 4.1). Figure 4.2 compares the StO_2 traces for the three different intensities of SIC in one subject. StO_2 was higher at 30% compared with both 60% and 90% MVC and higher at moderate than submaximal MVC ($p < 0.05$). Desaturation rate (De) increased from slow (30%) to moderate (60%) to submaximal contractions ($p < 0.05$) (Table 4.1). Trends of De as a function of MVC are shown in Fig. 4.3. In Fig. 4.3 the deoxygenation rate has an S-like shape and its linear approximation is shown as black line. Similarly the linear approximation of the reoxygenation rate in Fig. 4.3 shown as black line. After each contraction there was a large and immediate hyperemic response (Fig. 4.2). The resaturation rate (Re) of StO_2 after SIC depends on the intensity of the SIC and reflects the integrity and functionality of vascular system. It corresponds to a blood vessel vasodilation in response to the SIC. Re increased from slow to moderate ($p < 0.05$), but remained similar for moderate to submaximal SIC (Table 4.1 and Fig. 4.2).

Table 4.1 Muscle StO_2 parameters during sustained isometric contractions and arterial occlusion (AO)

MVC	30%	60%	90%	AO
F (N)	5.40 ± 1.03	10.90 ± 1.03	16.40 ± 1.03	–
RB (%)	73.16 ± 0.29	73.08 ± 0.87	78.66 ± 3.17	77.75 ± 3.46
De (%/s)	−1.06 ± 0.09	−4.19 ± 0.16	−4.80 ± 0.16	−0.23 ± 0.03
Re (%/s)	0.84 ± 0.19	1.54 ± 0.25	2.65 ± 1.44	2.5 ± 0.08
ΔStO_2 (%)	16.83 ± 4.62	54.5 ± 9.24	59.51 ± 5.14	26.45 ± 1.77

F force, *RB* baseline during rest, *De* desaturation rate during contraction and AO, *Re* resaturation rate after contraction and AO, ΔStO_2 difference between rest and minimum during contraction and AO. Values in mean ± SD

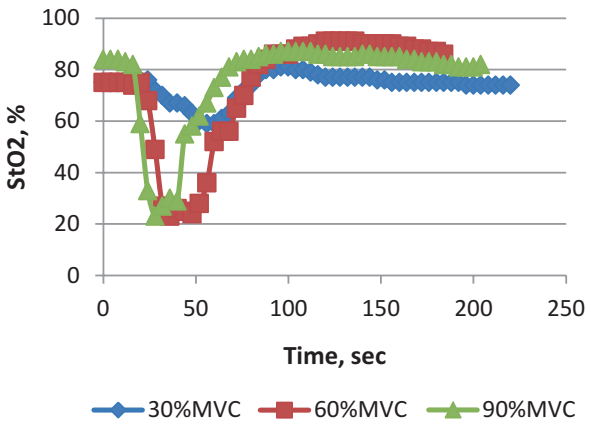

Fig. 4.2 Example of dorsiflexor muscle oxygen saturation (StO_2) during low (30% of MVC), moderate (60%) and submaximal (90%) sustained isometric contractions in one subject

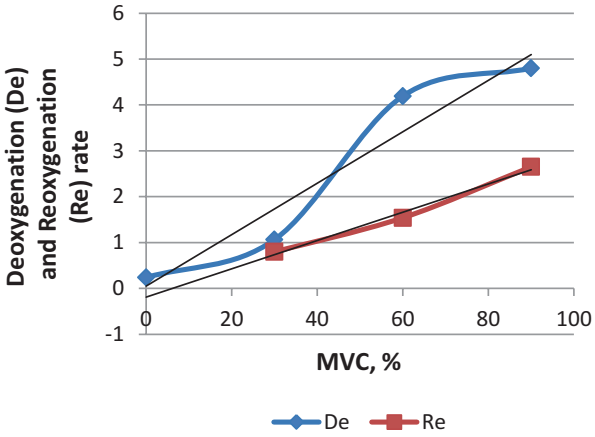

Fig. 4.3 Deoxygenation and reoxygenation rate depend on the intensity of the sustained isometric contraction. MVC = percent of maximal voluntary contraction

During the arterial occlusion the minimal StO2 was 52% (Table 4.1 and Fig. 4.1), which is significantly higher than StO_2 after moderate or submaximal SIC.

4 Discussion

According to the literature [11] an arterial occlusion is applied by inflating the cuff to a pressure of at least 60 mmHg above the systolic pressure. This way, both venous outflow and arterial inflow are blocked. In our case the mean pressure was 88 ± 6 mmHg what correspond to a systolic arterial pressure of about 115–120 mmHg. Blood flow was occluded to the leg by inflating the cuff beyond 180 mmHg. But either this external pressure was not high enough to block blood inflow, or the lower extremity circumference of greater than 75 cm would have required a more efficient tourniquet. Due to these reasons, in dorsiflexor muscle we did have not a full blocking of blood inflow and accordingly we observed during the arterial occlusion a minimal StO_2 which was significantly higher than the StO_2 after moderate or submaximal SIC.

The muscle deoxygenation rate was more enhanced at 90% than 60% MVC because O_2 consumption in exercising muscle is higher at 90% than 60% which we can see as statistically significant increasing of StO_2 from 60% to 90% MVC (Fig. 4.3).

5 Conclusion

The sharp decreases in StO_2 after the start of moderate and submaximal SIC, indicate that the blood vessels are occluded due to intramuscular pressure. This indeed shows that O_2 delivery is impeded and cannot cope with the increased O_2 consumption.

Acknowledgments The authors gratefully acknowledge funding by the Swiss National Science Foundation (Gr. no. 137423).

References

1. Degens H, Salmons S, Jarvis JC (1998) Intramuscular pressure, force and blood flow in rabbit tibialis anterior muscles during single and repetitive contractions. Eur J Appl Physiol Occup Physiol 78:13–19
2. Saltin B, Radegran G, Koskolou MD, Roach RC (1998) Skeletal muscle blood flow in humans and its regulation during exercise. Acta Physiol Scand 162:421–436
3. Chris J, Mcneil CJ, Matti D, Allen MD, Olympico E, Shoemaker JK, Rice CL (2015) Blood flow and muscle oxygenation during low, moderate, and maximal sustained isometric contractions. Am J Physiol Regul Integr Comp Physiol 309:R475–R481
4. Sjogaard G, Savard G, Juel C (1988) Muscle blood flow during isometric activity and its relation to muscle fatigue. Eur J Appl Physiol Occup Physiol 57:327–335
5. Vollestad NK, Wesche J, Sejersted OM (1990) Gradual increase in leg oxygen uptake during repeated submaximal contractions in humans. J Appl Physiol 68:1150–1156
6. Wesche J (1986) The time course and magnitude of blood flow changes in the human quadriceps muscles following isometric contraction. J Physiol 377:445–462
7. Hughson RL, Shoemaker JK, Tschakovsky ME, Kowalchuk JM (1996) Dependence of muscle VO2 on blood flow dynamics at onset of forearm exercise. J Appl Physiol 81:1619–1626
8. Wolf M, Ferrari M, Quaresima V (2007) Progress of near-infrared spectroscopy and topography for brain and muscle clinical applications. J Biomed Opt 12(6):062104
9. Hamaoka T, McCully KK, Quaresima V, Yamamoto K, Chance B (2007) Near-infrared spectroscopy/imaging for monitoring muscle oxygenation and oxidative metabolism in healthy and diseased humans. J Biomed Opt 12(6):062105 1–12
10. Gerovasili V, Dimopoulos S, Tzanis G, Anastasiou-Nana M, Nanas S (2010) Utilizing the vascular occlusion technique with NIRS technology. Int J Ind Ergon 40:218–222
11. Van Beekvelt MCP, Colier WNJM, Wopvers RA, Van Engelen BGM (2001) Performance of infra-red spectroscopy in measuring local O2 consumption and blood flow in skeletal muscle. J Appl Physiol 90(2):511–519

Chapter 5
Factors Determining the Oxygen Permeability of Biological Membranes: Oxygen Transport Across Eye Lens Fiber-Cell Plasma Membranes

Witold Karol Subczynski, Justyna Widomska, and Laxman Mainali

Abstract Electron paramagnetic resonance (EPR) spin-label oximetry allows the oxygen permeability coefficient to be evaluated across homogeneous lipid bilayer membranes and, in some cases, across coexisting membrane domains without their physical separation. The most pronounced effect on oxygen permeability is observed for cholesterol, which additionally induces the formation of membrane domains. In intact biological membranes, integral proteins induce the formation of boundary and trapped lipid domains with a low oxygen permeability. The effective oxygen permeability coefficient across the intact biological membrane is affected not only by the oxygen permeability coefficients evaluated for each lipid domain but also by the surface area occupied by these domains in the membrane. All these factors observed in fiber cell plasma membranes of clear human eye lenses are reviewed here.

Keywords Oxygen • Model membranes • Biological membranes • Permeability • Cholesterol

1 Introduction

The most fundamental function of biological membranes is the creation of barriers between intracellular and extracellular environments as well as between different cellular compartments. This is largely due to the hydrophobicity of the membrane interior. Water soluble components such as ions and sugars can cross biological membranes through channels or transporters. Nonelectrolytes, like molecular oxygen, can cross the lipid bilayer membrane component by passive diffusion,

W.K. Subczynski (✉) • L. Mainali
Department of Biophysics, Medical College of Wisconsin, Milwaukee, WI, USA
e-mail: subczyn@mcw.edu

J. Widomska
Department of Biophysics, Medical University of Lublin, Lublin, Poland

H.J. Halpern et al. (eds.), *Oxygen Transport to Tissue XXXIX*, Advances in Experimental Medicine and Biology 977, DOI 10.1007/978-3-319-55231-6_5

permeating directly through the bilayer. The oxygen flux across the lipid bilayer (J) is proportional to the difference in oxygen concentration in water on either side of the membrane ($C'' - C'$) and the membrane permeability coefficient (P_M):

$$J = -P_M\left(C'' - C'\right) \tag{5.1}$$

Here, P_M describes bulk membrane properties without detailed analysis of mechanisms involved in membrane permeation. This equation implies that P_M can be easily measured using a stop-flow rapid-mixing approach to create an oxygen gradient. These studies have been criticized, however, because the presence of a thick (~2 μm) unmixed water layer prevents immediate contact of oxygenated water with the membrane. It was determined that these methods can be used only for solutes with $P_M < 10^{-2}$ cm/s [1]. Fortunately, Diamond and Katz [2] derived an expression for the permeability coefficient of nonelectrolyte solutes across the lipid bilayer:

$$1/P_M = -\left(C'' - C'\right)/J = r' + \int dx / K\left(x\right) D\left(x\right) + r'' \tag{5.2}$$

The oxygen partition coefficient $K(x)$ and the oxygen diffusion coefficient $D(x)$ are allowed to vary across the bilayer. The integration is taken across the hydrophobic portion of the membrane. Resistances r' and r'' are, conceptually, connected to transport across the head-group region [3]. Thus, the knowledge of profiles of the oxygen diffusion-concentration product across the hydrophobic region of the lipid bilayer allows evaluation the oxygen permeability coefficient across that region.

2 Methods

Electron paramagnetic resonance (EPR) spin-label oximetry approaches allowed the oxygen diffusion-concentration product in any site which can be spin labeled or spin probed by nitroxide spin labels to be obtained. Based on measurements of spin-lattice relaxation time T_1 using the saturation-recovery EPR technique, Kusumi et al. [4] defined an oxygen transport parameter as:

$$W\left(x\right) = T_1^{-1}\left(air,x\right) - T_1^{-1}\left(N_2,x\right) \tag{5.3}$$

Since $W(x)$ is proportional to the collision rate of oxygen with the nitroxide spin label group, it is a function of both the concentration $C(x)$ and the translational diffusion coefficient $D(x)$ of oxygen at depth x in the air-equilibrated membrane,

$$W\left(x\right) = AD\left(x\right)C\left(x\right) \tag{5.4}$$

Using different lipid spin labels, with nitroxide groups located at different depths in membranes, profiles of $W(x)$, and, thus, profiles of $D(x)C(x)$ across membranes,

can be easily obtained (see [5] for an evaluation of A). Combining the theory developed by Diamond and Katz [3] and spin-label oximetry methods, Subczynski et al. [6] developed a procedure to calculate P_M based on the profiles of $W(x)$ across the membrane for samples equilibrated with air. Since the nitroxide moiety of the lipid spin labels can be placed in the headgroup region as well as in the hydrophobic region, r' and r'' in Eq. (5.2) can also be estimated within the integral. For samples equilibrated with air, the local oxygen concentration $C(x)$ and the oxygen concentration in the water phase $C_w(air)$ are related by the equation:

$$K(x) = C(x) / C_w(air) \tag{5.5}$$

and Eq. (5.2) becomes:

$$1 / P_M = AC_w(air) \int dx / W(x) \tag{5.6}$$

Thus, P_M can be evaluated in terms of experimental observable $W(x)$ and $C_w(air)$ can be taken from published tables. Profiles of $W(x)$ are obtained for samples equilibrated with air without the creation of oxygen gradients across the membrane.

3 Results

The EPR spin-labeling method turned out to be very powerful for oximetry measurements, allowing measurements of P_M across homogeneous lipid bilayers and across coexisting membrane domains in model membranes made of commercially available phospholipids and total lipids isolated from biological membranes. It was also successfully applied to evaluate P_Ms across lipid domains induced by membrane integral proteins in intact membranes. Our recent research is focused on the permeability properties of the lipid bilayer portion of fiber cell plasma membranes of eye lenses. These membranes, with their unique lipid composition (extremely high cholesterol (Chol) content) and high load with integral membrane proteins can serve as a good illustration, showing how different factors can affect the oxygen permeability of biological membranes.

3.1 Model Lipid Bilayer Membranes

3.1.1 Effect of Acyl Chains Unsaturation

Incorporation of either a *cis* or *trans* double bond at the C9–C10 position of the acyl chain decreased the oxygen diffusion-concentration product at all locations (depths) in the phospholipid bilayers [5]. We think that the key feature of oxygen transport in the lipid bilayer is the small size of the molecule. Since molecular oxygen is small,

its diffusion in the membrane must be quite different from that of lipids and other molecules of larger sizes. Oxygen transport in the membrane is closely related to the creation and movements of many small, vacant pockets due to rapid *gauche-trans* isomerization of acyl chains and conformational mismatch between lipid molecules. The presence of a rigid double bond would reduce the dynamics of the chain around the double bond. These data indicate that the dynamic *gauche-trans* isomerization of acyl chains plays an important role in oxygen diffusion in the membrane and are in agreement with the arguments advanced by Pace and Chan [7] on the relationship between the diffusion of small molecules in the membrane and kink migration and/or kink formation due to the acyl chain isomerization.

3.1.2 Effect of Cholesterol Intercalation

Based on our observations, we can conclude that the intercalation of Chol in saturated membranes decreases the oxygen diffusion-concentration product in the polar headgroup and hydrocarbon regions (to the depth to which the rigid ring structure of Chol is immersed), but little affects this product in the membrane center [6]. In unsaturated membranes, intercalation of Chol also decreases the oxygen diffusion-concentration product in and near the polar headgroup region but increases this product in the membrane center [5]. Since the major barrier for oxygen permeation is located in and near the polar headgroup region, the presence of Chol decreases total membrane permeability for oxygen despite the increase in the oxygen diffusion-concentration product in the bilayer center. Interestingly, a high cholesterol content is responsible for creating hydrophobic channels for oxygen transport parallel to the membrane surface, concurrently, is responsible for creating the rigidity barrier to oxygen transport across the membrane [8].

3.1.3 Cholesterol-Induced Phases and Domains

When investigating effects of Chol on oxygen transport across lipid bilayer membranes, one must to take into account the membrane phases and domains presented in membranes at different Chol contents. Membranes made of dimyristoylphosphatidylcholine (DMPC) and Chol form one of the simplest paradigms for the study of formation, coexistance, and separation of phases and domains. As shown in the phase diagram presented by Almeida et al. [9] and extended by Mainali et al. [10], at a physiological temperature, the liquid-disordered phase can adopt up to ~10 mol% Chol. This is a homogenous phase with properties (that is, the profile of the oxygen diffusion-concentration product) that change smoothly up to 10 mol% Chol. Above this concentration, a new liquid-ordered phase is formed with a Chol concentration of ~30 mol%. Thus, for Chol contents ranging between 10–30 mol%, these two phases coexist with very different oxygen diffusion-concentration product profiles [11]. The liquid-ordered phase can adopt ~30–50 mol% Chol. Increased Chol concentration drastically changed the profile of the oxygen diffusion-concentration

product, which is bell-shaped at 30 mol% and rectangular-shaped (with abrupt increase of three–four times between C9 and C10) at 50 mol% Chol. Because the liquid-ordered phase of DMPC cannot adopt more than 50 mol% Chol, at higher contents, the excess of Chol forms the pure Chol bilayer domains (CBDs) surrounded by the phospholipid bilayer saturated with Chol [10]. At a Chol content above 66 mol% Chol (which is the Chol solubility threshold for DMPC), these pure CBDs collapse, forming Chol crystals, presumably outside the lipid bilayer. The EPR spin-labeling approach allows estimation of the permeability coefficient for oxygen across the CBD with the use of only two Chol analogue spin labels; thus, based only on approximate profiles of the oxygen diffusion-concentration product [12]. These data indicate that CBDs most strongly affect the total oxygen permeability coefficient. We conclude that oxygen permeation through all these phases and domains should be considered when the total oxygen permeability across lipid bilayer membranes is evaluated.

3.1.4 Lens Lipid Membranes

Lens lipid membranes are formed from the total lipid extracts from different regions of eye lenses. The Chol content in the eye lens fiber-cell plasma membrane is extremely high. Chol saturates the bulk phospholipid bilayer and induces formation of CBDs within the membrane [13]. The saturating Chol content in fiber-cell membranes keeps the bulk physical properties of lens-lipid membranes (including profiles of the oxygen-diffusion concentration product) consistent and independent of changes in phospholipid composition [14]. The phospholipid composition of fiber-cell membranes changes significantly with age and between different regions of the lens. Surprisingly, independent of these differences, profiles of the oxygen diffusion-concentration product across phospholipid domains are very similar in all of the investigated membranes [15]. They have a rectangular shape with an abrupt increase in the oxygen diffusion-concentration product at the C9–C10 position. In the headgroups and hydrocarbon regions to the depth of C9, the product is as low as in gel-phase membranes. At locations deeper than C9, it is as high as in fluid-phase membranes. These profiles are typical for lipid bilayers saturated with Chol and are very different from the bell-shaped profile across membranes without Chol.

3.2 Intact Fiber Cell Plasma Membranes of Eye Lenses

Integral membrane proteins are practically impermeable to oxygen [16]. However, they affect (decrease) the oxygen permeability of the lipid bilayer, creating boundary lipids (around integral proteins) and trapped lipids (in protein-rich domains) for which oxygen transport is significantly lower [17]. In human lens membranes, more than 50% of lipid molecules are in contact with integral proteins.

3.2.1 Lipid Domains

Our most recent studies have focused on intact lens membranes isolated from human lenses [18]. We hypothesized that we should find the presence of the four purported lipid domains that are induced in the lipid bilayer portion because of the presence of integral membrane proteins, namely, bulk, boundary, and trapped lipids, as well as pure CBDs. We were able to confirm the existence of three of them: bulk, boundary, and trapped lipid domains [18].

3.2.2 Oxygen Permeability across Domains in Intact Fiber Cell Membranes

The EPR spin-labeling approach allowed us to evaluate P_M across bulk plus boundary lipid domains, and across trapper lipids in both cortical and nuclear eye lens membranes [18]. Separation of results for bulk lipids and boundary lipids is not possible because the lipids exchange too quickly between these domains. Results obtained for clear lenses from donors from groups age 0–20, 21–40, 41–60, and 61–80 years [18] indicate that for all membrane domains in cortical and nuclear fiber cell membranes, the permeability for oxygen was significantly lower than across water layers of the same thickness as these domains. The lowering effect was mainly due to the presence of membrane proteins and the formation of boundary and trapped lipid domains. For all age groups investigated, the P_M across the bulk plus boundary domain was always smaller (by 30%, on average) in nuclear than in cortical membranes. This difference was even greater for trapped lipids where the P_M across trapped lipids in nuclear membranes, on average, was 45% smaller compared to that in cortical membranes. The permeability of the trapped lipid domain in cortical and nuclear membranes was ~4.7 and ~8.5 times smaller, respectively, then the permeability across water layers of the same thickness as the domain. Thus, the trapped lipid domain forms a major membrane barrier for oxygen transport into the lens center, and this barrier was significantly greater in the lens nucleus. However, for all investigated age groups, the values of the P_M measured for corresponding membrane domains did not change significantly with age.

4 Conclusions

The effective P_M across the lipid bilayer portion of the fiber cell plasma membrane is, in the first approximation, equal to the weighted sum of the P_Ms evaluated for each lipid domain. The weight for each domain is proportional to the surface area occupied by the domain, divided by the total surface occupied by the lipid bilayer portion of the membrane. An EPR spin-labeling method has been developed that allows quantitative evaluation of the amounts of phospholipids and Chol (which determines the surface of the domain) in lipid domains of intact membranes [19].

Application of this method to fiber-cell plasma membranes isolated from cortical and nuclear regions of clear eye lenses indicates that the relative amounts of boundary and trapped phospholipids, and trapped Chol in nuclear membranes increase significantly with donor age. The amount of lipids in those domains in cortical membranes did not change significantly with age. The combination of results for oxygen permeability across lipid domains with those regarding the amount of lipids in domains allowed us to conclude that trapped lipids in the lipid bilayer portion of nuclear fiber cell membranes form a high barrier to oxygen permeation into the lens center, and that this barrier increases with age. In cortical fiber cell membranes, barriers formed by the lipid bilayer domains were significantly lower than in nuclear fiber cells and did not change with age, although these barriers were still considerably greater than across a water layer of the same thickness as domains. Proteins are nearly impermeable to oxygen [16]. Thus, the total effective P_M across the intact membrane is equal to the oxygen permeability coefficient evaluated for the lipid bilayer portion of the membrane, multiplied by the factor proportional to the surface area of the lipid bilayer portion, divided by the surface area of the entire membrane.

Acknowledgments Supported by grants EY015526, EB002052, and EY001931 from the NIH.

References

1. Missner A, Pohl P (2009) 110 years of the meyer–Overton rule: predicting membrane permeability of gases and other small compounds. ChemPhysChem 10:1405–1414
2. Diamond JM, Katz Y (1974) Interpretation of nonelectrolyte partition coefficients between dimyristoyl lecithin and water. J Membr Biol 17:121–154
3. Dix JA, Kivelson D, Diamond JM (1978) Molecular motion of small nonelectrolyte molecules in lecithin bilayers. J Membr Biol 40:315–342
4. Kusumi A, Subczynski WK, Hyde JS (1982) Oxygen transport parameter in membranes as deduced by saturation recovery measurements of spin-lattice relaxation times of spin labels. Proc Natl Acad Sci U S A 79:1854–1858
5. Subczynski WK, Hyde JS, Kusumi A (1991) Effect of alkyl chain unsaturation and cholesterol intercalation on oxygen transport in membranes. Biochemistry 30:8578–8590
6. Subczynski WK, Hyde JS, Kusumi A (1989) Oxygen permeability of phosphatidylcholine-cholesterol membranes. Proc Natl Acad Sci U S A 86:4474–4478
7. Pace RJ, Chan SI (1982) Molecular motions in lipid bilayers. III. Lateral and transverse diffusion in bilayers. J Chem Phys 76:4241–4247
8. Subczynski WK, Wisniewska A (2000) Physical properties of lipid bilayer membranes: relevance to membrane biological functions. Acta Biochim Pol 47:613–625
9. Almeida PF, Vaz WL, Thompson TE (1992) Lateral diffusion in the liquid phases of dimyristoylphosphatidylcholine/cholesterol lipid bilayers: a free volume analysis. Biochemistry 31:6739–6747
10. Mainali L, Raguz M, Subczynski WK (2013) Formation of cholesterol bilayer domains precedes formation of cholesterol crystals in cholesterol/dimyristoylphosphatidylcholine membranes: EPR and DSC studies. J Phys Chem B 117:8994–9003
11. Subczynski WK, Wisniewska A, Hyde JS et al (2007) Three-dimensional dynamic structure of the liquid-ordered domain as examined by a EPR oxygen probing. Biophys J 92:1573–1584

12. Raguz M, Mainali L, Widomska J et al (2011) Using spin-label electron paramagnetic resonance (EPR) to discriminate and characterize the cholesterol bilayer domain. Chem Phys Lipids 164:819–829
13. Mainali L, Raguz M, O'Brien WJ et al (2013) Properties of membranes derived from the total lipids extracted from the human lens cortex and nucleus. Biochim Biophys Acta 1828:1432–1440
14. Subczynski WK, Raguz M, Widomska J et al (2012) Functions of cholesterol and the cholesterol bilayer domain specific to the fiber-cell plasma membrane of the eye lens. J Membr Biol 245:51–68
15. Mainali L, Raguz M, O'Brien WJ et al (2016) Changes in the properties and organization of human lens lipid membranes occurring with age. Curr Eye Res, DOI: 10.1080/02713683.2016.1231325
16. Altenbach C, Greenhalgh DA, Khorana HG et al (1994) A collision gradient method to determine the immersion depth of nitroxides in lipid bilayers: application to spin-labeled mutants of bacteriorhodopsin. Proc Natl Acad Sci U S A 91:1667–1671
17. Ashikawa I, Yin J-J, Subczynski WK et al (1994) Molecular organization and dynamics in bacteriorhodopsin-rich reconstituted membranes: discrimination of lipid environments by the oxygen transport parameter using a pulse ESR spin-labeling technique. Biochemistry 33:4947–4952
18. Raguz M, Mainali L, O'Brien WJ et al (2015) Lipid domains in intact fiber-cell plasma membranes isolated from cortical and nuclear regions of human eye lenses of donors from different age groups. Exp Eye Res 132:78–90
19. Raguz M, Mainali L, O'Brien WJ et al (2015) Amounts of phospholipids and cholesterol in lipid domains formed in intact lens membranes. Exp Eye Res 140:179–186

Chapter 6
Multi-site Measurements of Muscle O_2 Dynamics During Cycling Exercise in Early Post-myocardial Infarction

Shun Takagi, Ryotaro Kime, Norio Murase, Masatsugu Niwayama, Takuya Osada, and Toshihito Katsumura

Abstract The aim of this study was to compare the muscle oxygen dynamics between early post-myocardial infarction (n = 12; MI) and age-matched elderly subjects without MI (n = 12; CON) in several leg muscles during ramp cycling exercise. Muscle oxygen saturation (SmO_2), deoxygenated-hemoglobin concentration (Δdeoxy-Hb), and total-hemoglobin concentration (Δtotal-Hb) were monitored continuously at the distal site of vastus lateralis (VLd), proximal site of the vastus lateralis (VLp), rectus femoris (RF), vastus medialis (VM), gastrocnemius medialis (GM), and tibialis anterior (TA) muscles by near infrared spatial resolved spectroscopy. At given absolute workloads, higher SmO_2 was observed at VLd, VLp, RF, and VM in MI, compared to CON. Simultaneously, in MI, deoxy-Hb was lower at VLd, VLp, and VM than CON. In contrast to the thigh muscles, muscle oxygen dynamics were similar between groups in GM and TA. In total-Hb, no significant differences were found at any measurement sites. These results demonstrated that the absence of muscle deoxygenation was observed in MI muscles, especially in the thigh muscles, but not in the lower leg muscles.

Keywords Cycling exercise • Ischemic heart disease • Muscle O_2 dynamics • Near infrared spectroscopy • Regional difference

S. Takagi (✉)
Faculty of Health and Sports Science, Doshisha University, Kyotanabe, Japan

Faculty of Sport Sciences, Waseda University, Tokorozawa, Japan

Department of Sports Medicine for Health Promotion, Tokyo Medical University, Shinjuku, Japan
e-mail: shtakagi@mail.doshisha.ac.jp

R. Kime • N. Murase • T. Osada • T. Katsumura
Department of Sports Medicine for Health Promotion, Tokyo Medical University, Shinjuku, Japan

M. Niwayama
Department of Electrical and Electronic Engineering, Shizuoka University, Hamamatsu, Japan

H.J. Halpern et al. (eds.), *Oxygen Transport to Tissue XXXIX*, Advances in Experimental Medicine and Biology 977, DOI 10.1007/978-3-319-55231-6_6

1 Introduction

We have reported that an absence of muscle deoxygenation was observed in the distal site of vastus lateralis (VLd) muscle during exercise in early post-myocardial infarction (MI), measured by near infrared spectroscopy (NIRS) [1]. The blunted muscle deoxygenation means that O_2 supply is enhanced and/or that O_2 utilization is impaired in the exercising muscles in MI. Though some previous studies reported that leg blood flow was reduced in heart disease patients [2, 3], there remains a possibility that an absence of muscle deoxygenation in VLd was caused by an enhancement of muscle O_2 supply due to altered blood distribution between leg muscles. If the abnormalities are regional at VLd, muscle deoxygenation may be enhanced in the other sites of leg muscles. The aim of this study was to compare muscle O_2 dynamics in several leg muscles between early post-MI patients and age-matched elderly subjects without MI.

2 Methods

2.1 Subjects

Twelve male patients, 22 ± 8 days after MI (MI group: age 60 ± 9 years; height 168.2 ± 5.4 cm; weight 69.1 ± 7.0 kg, mean ± SD) and 12 age- and body size-matched elderly men without MI (CON group: age 59 ± 10 years; height 167.7 ± 8.0 cm; weight 71.1 ± 10.5 kg) participated in the study. All MI patients had received percutaneous coronary intervention (PCI) before the present study. The study was approved by the Medical Research Ethics Committee of Tokyo Medical University and performed in the cardiac rehabilitation center at Tokyo Medical University Hospital. All subjects were informed of the purpose of the study and written informed consent was obtained.

2.2 Experimental Design

The subjects performed 10 W/min ramp cycling ergometer exercise until exhaustion (Strength Ergo 8, Fukuda-Denshi, Japan). To ensure the safety of the MI patients, electrocardiography was monitored during the experiment. Muscle O_2 saturation (SmO_2, %) and relative changes from rest in oxygenated hemoglobin concentration (Δoxy-Hb, μmol/L), deoxygenated hemoglobin concentration (Δdeoxy-Hb, μmol/L), and total hemoglobin concentration (Δtotal-Hb, μmol/L) were monitored at VLd, the proximal site of the vastus lateralis (VLp), rectus femoris (RF), vastus medialis (VM), gastrocnemius medialis (GM), and tibialis anterior (TA) muscles in the left leg by near infrared spatial resolved spectroscopy (NIR_{SRS}) (Hb12–4, Astem

Co., Japan). The measurement site in VL was defined as 30% of the length between the patella and the greater trochanter, above the patella. VLp was defined at a proximal point of 30% of the length between the patella and the greater trochanter, from the VLd muscle, as defined in a previous study [4]. The NIR_{SRS} device used two wavelengths (770 and 830 nm) for measurement of hemoglobin oxygenation. The probe consisted of one light source and two photodiode detectors, and the distances between the light source and detectors were 20 and 30 mm, respectively. The data sampling rate was 1 Hz. The obtained signals were defined as the values averaged over the last 10 s. Fat layer thickness affects NIR_{SRS} data due to light scattering. Therefore, we measured fat layer thickness at each measurement site by an ultrasound device (LogiQ3, GE-Yokokawa Medical Systems, Japan), then calculated the muscle O_2 dynamics with correction of these effects by normalized measurement sensitivity [5]. The specifications of correction for the influence of fat layer thickness have been fully described [5]. Although an upper limit of fat layer thickness was designated in this study as 10 mm to correct for the effects, fat layer thickness was within ~10 mm at each measurement site in all subjects.

2.3 Statistics

All data are given as means ± standard deviation (SD). To compare changes in muscle O_2 dynamics during exercise between groups, a 2-way repeated-measures analysis of variance was used with group and power output as factors. Where appropriate, the Bonferroni post hoc test was performed to determine specific significant differences. Because one subject could not exercise at more than 91 W, repeated measures between groups were limited to rest, 30, 50, 70, and 90 W compared as a function of power output. Differences in muscle O_2 dynamics at peak exercise, fat layer thickness, and power output at peak exercise were compared between groups using unpaired *t* tests. For all statistical analyses, significance was accepted at $p < 0.05$.

3 Results

Figure 6.1 shows muscle O_2 dynamics at VLd, VLp, and RF, and Fig. 6.2 represents those at VM, GM, and TA in MI and CON. During submaximal exercise, there were significant interactions in SmO_2, Δoxy-Hb, and Δdeoxy-Hb at VLd, VLp and VM, while no significant interactions or main effects of groups were found in Δtotal-Hb at all measurement sites of the thigh muscles. At RF, we also found significant interactions in SmO_2 and Δoxy-Hb, while there were no interactions or main effects of groups in Δdeoxy-Hb. At given absolute workloads, higher SmO_2 and Δoxy-Hb and lower Δdeoxy-Hb were observed in VLd, VLp and VM. Similarly, at RF, SmO_2 and Δoxy-Hb tended to be higher during submaximal exercise. In GM and TA, no significant interactions or main effects of groups were observed at any NIRS parameters.

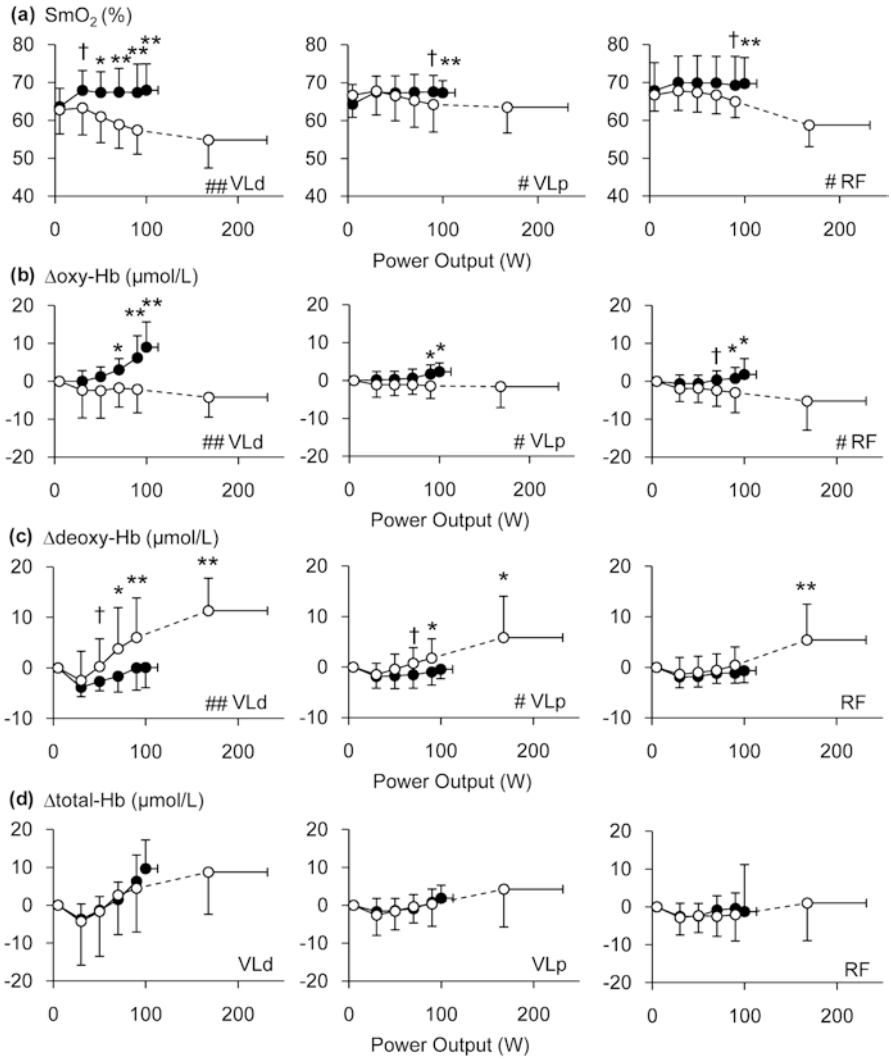

Fig. 6.1 Change in muscle O_2 saturation (SmO_2: **a**), oxygenated hemoglobin (oxy-Hb: **b**), deoxygenated hemoglobin (deoxy-Hb: **c**), and total hemoglobin (total-Hb: **d**) responses in VLd, VLp, and RF muscles during ramp cycling exercise. The *closed circles* show NIRS signals in MI, and the *open circles* show NIRS signals in CON. There was a significant difference between MI and CON (*: $p < 0.05$, **: $p < 0.01$, †: $p < 0.1$), and there was a significant exercise group × power output interaction (#: $p < 0.05$, ##: $p < 0.01$). *Symbols* indicating a significant difference between power output in MI and CON have been omitted for the sake of clarity

At peak exercise, at VLd, VLp, RF, and VM, SmO_2 and Δoxy-Hb were significantly higher, and Δdeoxy-Hb was significantly lower in MI compared to CON. At the lower leg muscles, significantly higher Δdeoxy-Hb was observed, while there were no significant differences in Δoxy-Hb. Moreover, no significant

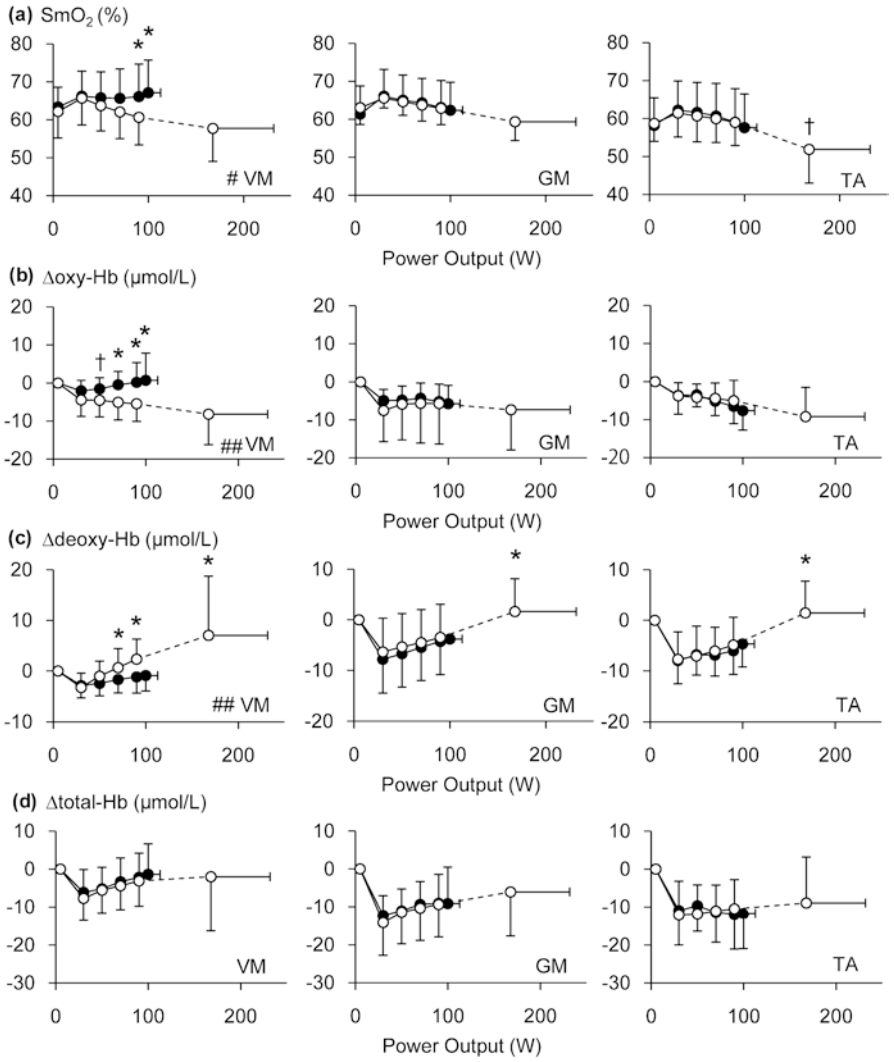

Fig. 6.2 Change in muscle O_2 saturation (SmO_2: **a**), oxygenated hemoglobin (oxy-Hb: **b**), deoxygenated hemoglobin (deoxy-Hb: **c**), and total hemoglobin (total-Hb: **d**) responses in VM, GM, and TA muscles during ramp cycling exercise. The *closed circles* show NIRS signals in MI, and the *open circles* show NIRS signals in CON. There was a significant difference between MI and CON (*: $p < 0.05$, †: $p < 0.1$), and there was a significant exercise group × power output interaction (#: $p < 0.05$, ##: $p < 0.01$). *Symbols* indicating a significant difference between power output in MI and CON have been omitted for the sake of clarity

differences were found in Δtotal-Hb at any measurement sites (Figs. 6.1 and 6.2). Peak power output is lower in MI, compared to CON (MI: 100 ± 13 W, CON: 168 ± 64 W, $p < 0.01$). Fat layer thickness was not different between groups at any measurement sites.

4 Discussion

In the present study, muscle deoxygenation was heterogeneous between leg muscles and also within a single muscle [1]. Therefore, muscle O_2 dynamics were compared between subjects, with and without MI. The results showed that, during submaximal exercise, muscle deoxygenation was blunted in MI, not only at VLd, but also at other thigh muscles, and at a different site of the same VL muscle (VLp), while no significant differences in muscle deoxygenation were observed between MI and CON at the lower leg muscles. Because leg blood flow is generally reduced during exercise in heart disease patients [2, 3], our findings lead us to the possibility that the lower deoxygenation in MI may mainly be caused by impaired muscle O_2 utilization, rather than an enhancement of muscle blood flow due to an alteration in muscle blood flow distribution between muscles. Another possible explanation for diminished muscle deoxygenation at measurement sites may be that circulation is reduced at sites which were not measured in this study (e.g. a deeper area of muscles) in MI. The NIRS data reflects muscle O_2 dynamics in the superficial regions of the muscles, and Okushima et al. have demonstrated that muscle deoxygenation was slightly more enhanced in deep areas than in superficial areas of thigh muscles, especially during high-intensity exercise in healthy young subjects [6]. We would need to directly measure leg blood flow and/or muscle deoxygenation in deep areas of exercising muscle to clarify the mechanism affecting the blunted deoxygenation in the superficial region of the thigh muscles. In addition, it is still unclear why lower deoxygenation was regional at the thigh muscles, but not at the lower leg muscles. Muscle blood flow is greater in thigh muscles than in lower leg muscles during cycling exercise [7]. Therefore, cycling exercise may promote the diminished muscle deoxygenation of thigh muscles in MI patients, in contrast to lower leg muscles. Diminished muscle deoxygenation may be detected in lower leg muscles during walking and running exercise because lower leg muscles largely contribute during the exercise. However, this area warrants further investigation.

In summary, during cycling exercise in MI patients, an absence of muscle deoxygenation was observed in thigh muscles, and muscle deoxygenation was not heightened in lower leg muscles.

Acknowledgments The authors are grateful for revision of this manuscript by Andrea Hope. This study was supported in part by Grant-in-Aid for scientific research from Japan Society for the Promotion of Science (16K16487) to S.T.

References

1. Takagi S, Murase N, Kime R et al (2014) Skeletal muscle deoxygenation abnormalities in early post-myocardial infarction. Med Sci Sports Exerc 46(11):2062–2069
2. Sumimoto T, Kaida M, Yuasa F et al (1996) Skeletal muscle hypoperfusion during recovery from maximal supine bicycle exercise in patients with heart failure. Am J Cardiol 78(7):841–844

3. Wilson JR, Martin JL, Schwartz D et al (1984) Exercise intolerance in patients with chronic heart failure: role of impaired nutritive flow to skeletal muscle. Circulation 69(6):1079–1087
4. Takagi S, Kime R, Murase N et al (2013) Aging affects spatial distribution of leg muscle oxygen saturation during ramp cycling exercise. Adv Exp Med Biol 789:157–162
5. Niwayama M, Suzuki H, Yamashita T et al (2012) Error factors in oxygenation measurement using continuous wave and spatially resolved near-infrared spectroscopy. J Jpn Coll Angiol 52:211–215
6. Okushima D, Poole DC, Rossiter HB et al (2015) Muscle deoxygenation in the quadriceps during ramp incremental cycling: deep vs. superficial heterogeneity. J Appl Physiol 119(11):1313–1319
7. Matsui H, Kitamura K, Miyamura M (1978) Oxygen uptake and blood flow of the lower limb in maximal treadmill and bicycle exercise. Eur J Appl Physiol Occup Physiol 40(1):57–62

Chapter 7
Effects of 8 Weeks' Training on Systemic and Muscle Oxygen Dynamics in University Rugby Players

Shun Takagi, Ryotaro Kime, Masatsugu Niwayama, Kuniaki Hirayama, and Shizuo Sakamoto

Abstract The aim of this study was to investigate the effects of 8 weeks of training on O_2 dynamics in university rugby players. University rugby players (n = 15) participated in 5 strength training sessions and 4 field-based training sessions per week for 8 weeks. Before and after 8-weeks' training, the subjects performed ramp cycling exercise until exhaustion. Muscle O_2 saturation (SmO_2), relative changes from rest in deoxygenated hemoglobin concentration (ΔDeoxy-Hb) and total hemoglobin concentration, cardiac output (CO), and pulmonary O_2 uptake (VO_2) were monitored continuously during exercise. Peak VO_2 and CO were normalized by fat-free mass. Though peak VO_2 tended to be increased after training, there were no significant changes in CO, nor any muscle O_2 dynamic variables at peak exercise between before and after training. However, an increase in peak VO_2 was significantly correlated with diminishment of deoxy-Hb and an increase in SmO_2. Changes in CO caused by training were not related to improved peak VO_2. The improvement of peak VO_2 during 8 weeks of rugby training may have been caused by muscle O_2 supply, rather than increased CO or muscle O_2 extraction.

S. Takagi (✉)
Faculty of Health and Sports Science, Doshisha University, Kyotanabe, Japan

Faculty of Sport Sciences, Waseda University, Tokorozawa, Japan

Department of Sports Medicine for Health Promotion, Tokyo Medical University, Shinjuku, Japan
e-mail: shtakagi@mail.doshisha.ac.jp

R. Kime
Department of Sports Medicine for Health Promotion, Tokyo Medical University, Shinjuku, Japan

M. Niwayama
Department of Electrical and Electronic Engineering, Shizuoka University, Hamamatsu, Japan

K. Hirayama • S. Sakamoto
Faculty of Sport Sciences, Waseda University, Tokorozawa, Japan

H.J. Halpern et al. (eds.), *Oxygen Transport to Tissue XXXIX*, Advances in Experimental Medicine and Biology 977, DOI 10.1007/978-3-319-55231-6_7

Keywords Cardiac output • Muscle oxygenation • Near infrared spectroscopy • Peak aerobic capacity • Strength training

1 Introduction

Rugby union players generally need not only muscle strength, but also high aerobic capacity [1]. To accomplish these, they frequently perform both strength training and field-based training, including aerobic conditioning. However, physiological adaptation of O_2 dynamics, especially peripheral circulation and metabolism during training in rugby players, is unclear.

Near infrared spectroscopy (NIRS) technique is a non-invasive way to measure muscle O_2 dynamics during whole-body exercise, and it is widely used in sports science. As seen in aerobic training [2], long-term [3] or high volume [4] resistance training seems to enhance muscle deoxygenation response during exercise, as measured by NIRS. In contrast, it was also reported that short-term strength training may reduce muscle deoxygenation [5]. To date, it is still unclear whether short-term rugby training, including strength and aerobic training, would improve muscle deoxygenation. The aim of this study is to investigate the effects of strength and aerobic training on O_2 dynamics in rugby union players.

2 Methods

2.1 Subjects

Male university rugby players (n = 15; age 20 ± 1 years; height 176.1 ± 8.3 cm; weight 87.9 ± 13.0 kg, position (forwards/backs): 8/7, mean ± SD) participated in the study. Their playing experience was 11 ± 4 years, and the competitive level of the subjects was high among university teams in Japan. This study protocol was approved by the institutional ethics committee. All subjects were informed of the purpose of the study and written informed consent was obtained.

2.2 Experimental Design

The subjects participated in 5 strength training sessions and 4 field-based training sessions per week for 8 weeks. Strength training was set at 3–5 sets of 6–8 repetitions maximum for 5 days (2 days for lower body; and 3 days for upper body). Field-based training consisted of conditioning and rugby-specific training. Conditioning exercises are designed to improve aerobic and anaerobic function, agility, and speed by endurance running, dash, high interval exercise (cycling,

rowing, boxing), and similar activities for 30-min sets. Examples of rugby-specific training are: defense, attack, team play, and general athletic skills, and these were performed for 60–90 min, as appropriate for the players' positions.

Before and after 8 weeks of training, the subjects performed 30 W/min ramp cycling exercise until exhaustion (Aerobike 75XLII, Combi, Japan). Pulmonary O_2 uptake (VO_2) was monitored continuously during the experiments to determine peak VO_2 using an automated gas analysis system (AE300S, Minato Medical Science, Japan). Cardiac output (CO), stroke volume (SV), and heart rate (HR) were also measured continuously using transthoracic impedance cardiography (PhysioFlow, Manatec Biomedical, France). Muscle O_2 saturation (SmO_2) and relative changes from rest in oxygenated hemoglobin concentration (Δoxy-Hb), deoxygenated hemoglobin concentration (Δdeoxy-Hb), and total hemoglobin concentration (Δtotal-Hb) were monitored at the vastus lateralis (VL) muscle in the left leg by near infrared spatial resolved spectroscopy (NIR_{SRS}) (Astem, Japan). The measurement site in VL was defined as 30% of the length between the patella and the greater trochanter, above the patella [2]. The probe consisted of one light source and two photodiode detectors, and the distances between light source and detectors were 20 and 30 mm, respectively. The data sampling rate was 1 Hz. The obtained signals were defined as the values averaged over the previous 10 s. Fat layer thickness is known to affect NIR_{SRS} data due to light scattering. We therefore measured fat layer thickness at each measurement site with an ultrasound device (LogiQ3, GE-Yokokawa Medical Systems, Japan), then calculated the muscle O_2 dynamics with correction of these effects by normalized measurement sensitivity [6].

Fat-free mass (FFM) was determined by bio-impedance analysis (InBody 720, InBody Japan, Korea) before and after training. VO_2, SV, and CO were subsequently normalized by FFM.

2.3 Statistics

All data are given as means ± standard deviation (SD). To compare changes in O_2 dynamics during exercise between before and after training, a 2-way repeated-measures analysis of variance was used, with training and power output (PO) as factors. Because one subject could not exercise at more than 268 W, repeated measures between groups were limited to rest, 60, 100, 140, 180, 220, and 260 W, compared as a function of PO. Differences in O_2 dynamics variables and PO at peak exercise, fat layer thickness, body weight and FFM were compared between groups using paired *t* tests. For all statistical analyses, significance was accepted at $p < 0.05$.

3 Results

During submaximal exercise, there were no significant interactions in any cardiorespiratory variables or muscle O_2 dynamics, even though higher SV ($p = 0.08$) and lower HR ($p < 0.05$) after training were observed at rest to 260 W. At peak exercise,

there was no significant difference before compared with after training in SV, HR, CO, and muscle O_2 dynamics, while peak VO_2 ($p = 0.09$) and peak PO (319 ± 31 vs. 323 ± 28 W, $p = 0.09$) tended to be increased after training. To clarify the effect of the increase in peak VO_2 on systemic and muscle O_2 dynamics by training, we additionally compared these variables in subjects who had increased peak VO_2 ($n = 9$). Figure 7.1 shows the changes in cardiorespiratory variables (Fig. 7.1a-d) and muscle O_2 dynamics (Fig. 7.1e-h) in subjects who had increased peak VO_2 ($n = 9$). During submaximal exercise, no significant interactions were observed in any systemic or muscle O_2 dynamics, even in subjects who had increased peak VO_2, while we observed higher SV ($p = 0.09$) and lower HR ($p < 0.05$) after training at rest to 260 W. At peak exercise, a significant reduction in Δdeoxy-Hb ($p < 0.05$) and increase in ΔSmO_2 (SmO_2 at peak exercise minus SmO_2 at rest) were observed after training. Peak VO_2 (48.7 ± 5.9 vs. 51.6 ± 5.8 mL/kg FFM/min, $p < 0.01$) and peak PO (317 ± 26 vs. 326 ± 22 W, $p < 0.05$) were significantly increased after training, even though the changes after training were not revealed in the other variables by subgroup analysis.

Change in ΔSmO_2 (ΔSmO_2 after training minus ΔSmO_2 before training) was significantly positively related to change in peak VO_2 ($r = 0.52$, $p < 0.05$, Fig. 7.2a). Similarly, change in Δdeoxy-Hb at peak exercise (Δdeoxy-Hb at peak exercise after training minus Δdeoxy-Hb at peak exercise before training) was negatively associated with change in peak VO_2 ($r = -0.67$, $p < 0.01$) (Fig. 7.2b). An increase in Δoxy-Hb at peak exercise after training compared to before tended to be related to the increase in peak VO_2 ($r = 0.45$, $p = 0.09$). In contrast, change in ΔCO (ΔCO after training minus ΔCO before training; ΔCO equals CO at peak exercise minus CO at rest) was not significantly related to change in peak VO_2 ($r = 0.03$, $p = 0.90$).

Fat layer thickness at VL muscle (4.01 ± 1.68 vs 4.00 ± 1.72 mm, $p = 0.97$), body weight (87.9 ± 13.0 vs 87.6 ± 13.9 kg, $p = 0.53$), and FFM (71.9 ± 9.1 vs 70.6 ± 10.2 kg, $p = 0.37$) were unchanged after compared with before training.

4 Discussion

In this study, neither central nor muscle O_2 dynamics were significantly increased by 8 weeks of rugby training. However, peak VO_2 tended to be improved by training, and the improvement of peak VO_2 was significantly correlated with a diminishment of deoxy-Hb and an increase in oxy-Hb and SmO_2, but not with an increase in CO. A diminishment of deoxy-Hb and an increase in oxy-Hb and SmO_2 partly reflected a decrease in muscle O_2 extraction, and the decreased muscle O_2 extraction can be explained by reduced muscle O_2 use and/or increased muscle O_2 supply.

Fig. 7.1 (continued) responses during ramp cycling exercise before (*closed circles*) and after (*open circles*) training in subjects who had increased peak VO_2. There was a significant difference between before and after training (*: $p < 0.05$). There was a significant main effect of group (†: $p < 0.05$, #: $p < 0.1$). *Symbols* indicating a significant difference between power output before and after training have been omitted for the sake of clarity

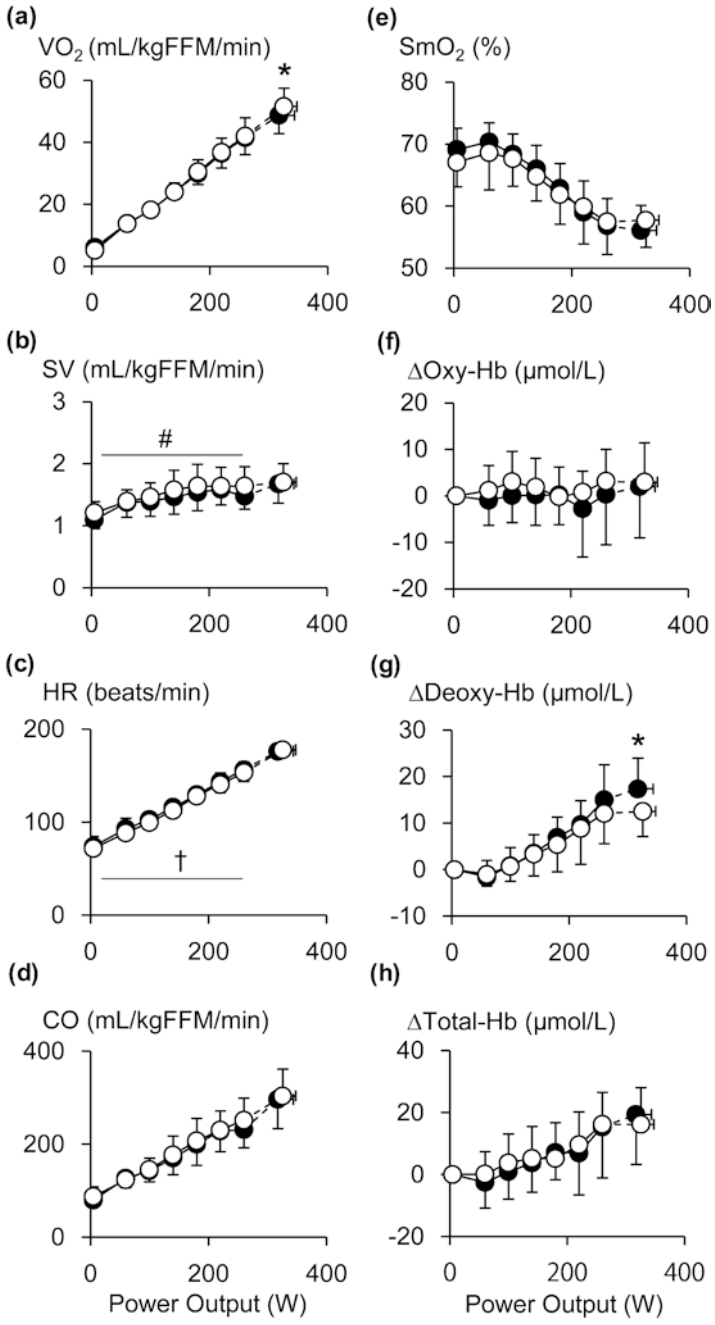

Fig. 7.1 Change in pulmonary O_2 uptake (VO_2: **a**), stroke volume (SV: **b**), heart rate (HR: **c**), cardiac output (CO: **d**), muscle O_2 saturation (SmO_2: **e**), muscle oxygenated hemoglobin (oxy-Hb: **f**), muscle deoxygenated hemoglobin (deoxy-Hb: **g**), and muscle total hemoglobin (total-Hb: **h**)

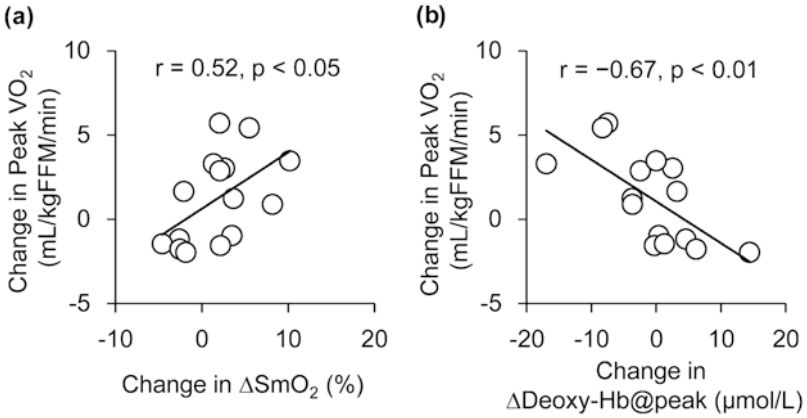

Fig. 7.2 Relationship between change in muscle deoxygenation induced by training and change in aerobic capacity. (**a**), change in ΔSmO_2 (ΔSmO_2 after training minus ΔSmO_2 before training) and change in peak VO_2 (peak VO_2 after training minus peak VO_2 before training). (**b**), change in ΔDeoxy-Hb@peak (ΔDeoxy-Hb@peak after training minus ΔDeoxy-Hb@peak before training) and change in peak VO_2. SmO_2, muscle O_2 saturation. ΔSmO_2, SmO_2 at peak exercise minus SmO_2 at rest. ΔDeoxy-Hb@peak, deoxygenated hemoglobin from rest to peak exercise

Strength training generally increases the cross-sectional area of muscle fibers and, consequently, mitochondrial density may be reduced [7]. However, in our study, the cross-sectional area of VL muscle (confirmed by magnetic resonance imaging, data not shown) did not increase after compared with before training. Therefore, we presume that the decrease in muscle O_2 extraction was mainly caused by increased muscle O_2 supply. Our findings suggest that the improvement of peak VO_2 during short-term rugby training may have been caused by increased muscle O_2 supply, rather than increased CO or increased muscle O_2 extraction, possibly due to an alteration of blood distribution. Future studies are needed to confirm this.

In contrast to the results of previous studies of long-term strength training [3] and traditional aerobic training [2], muscle deoxygenation was not significantly enhanced by 8 weeks of rugby training. The disparities may be partly explained by training volume [5]. In this study, the conditioning sessions did not focus specifically on improving aerobic capacity, and the number of sessions for lower body strength training was low. Hence, training volume in this study may be relatively low, compared to previous studies [3, 4]. Moreover, the subjects in this study had already performed a similar schedule of training before being recruited, therefore, the effects of this round of training may have been particularly small. Furthermore, we observed relatively large inter-individual differences in the effects of training. One possible reason could have been position-specific training; however, we found no significant differences in any variables between the forwards and the backs. Therefore, differences in the players' positions did not fully explain the inter-individual differences in this study. The heterogeneity of the physical and athletic status of rugby players was a major limitation of this study. Our data should be confirmed in a larger, homogeneous group of rugby players.

In summary, our findings suggest that short-term training in rugby players did not enhance muscle deoxygenation. In this study, the improvement of peak VO_2 during short-term rugby training may have been caused by muscle O_2 supply, rather than increased CO or muscle O_2 extraction.

Acknowledgments The authors are grateful for revision of this manuscript by Andrea Hope. We also thank Shoko Takada, Yuka Endo, and Yuka Inoue (Waseda University, Japan) for their helpful technical assistance. This study was supported in part by Research Grant from Mizuno Sports Promotion Foundation to Shun Takagi.

References

1. Reid RM, Williams R (1974) A concept of fitness and its measurement in relation to rugby football. Br J Sports Med 8(2–3):96–99
2. Takagi S, Murase N, Kime R et al (2016) Aerobic training enhances muscle deoxygenation in early post-myocardial infarction. Eur J Appl Physiol 116(4):673–685
3. Lin TY, Lin LL, Ho TC, Chen JJ (2014) Investigating the adaptation of muscle oxygenation to resistance training for elders and young men using near-infrared spectroscopy. Eur J Appl Physiol 114(1):187–196
4. Uchiyama K, Miaki H, Terada S et al (2011) Effect of muscle strength training and muscle endurance training on muscle deoxygenation level and endurance performance. J Phys Ther Sci 23:349–355
5. Usaj A, Jereb B, Robi P et al (2007) The influence of strength-endurance training on the oxygenation of isometrically contracted forearm muscles. Eur J Appl Physiol 100(6):685–692
6. Niwayama M, Suzuki H, Yamashita T et al (2012) Error factors in oxygenation measurement using continuous wave and spatially resolved near-infrared spectroscopy. J Jpn Coll Angiol 52:211–215
7. Chilibeck PD, Syrotuik DG, Bell GJ (1999) The effect of strength training on estimates of mitochondrial density and distribution throughout muscle fibres. Eur J Appl Physiol Occup Physiol 80(6):604–609

Chapter 8
Imaging Redox State in Mouse Muscles of Different Ages

Lily Moon, David W. Frederick, Joseph A. Baur, and Lin Z. Li

Abstract Aging is the greatest risk factor for many diseases. Intracellular concentrations of nicotinamide adenine dinucleotide (NAD^+) and the NAD^+-coupled redox state have been proposed to moderate many aging-related processes, yet the specific mechanisms remain unclear. The concentration of NAD^+ falls with age in skeletal muscle, yet there is no consensus on whether aging will increase or decrease the redox potential of NAD^+/NADH. Oxidized flavin groups (Fp) (e.g. FAD, i.e., flavin adenine dinucleotide, contained in flavoproteins) and NADH are intrinsic fluorescent indicators of oxidation and reduction status of tissue, respectively. The redox ratio, i.e., the ratio of Fp to NADH, may be a surrogate indicator of the NAD^+/NADH redox potential. In this study we used the Chance redox scanner (NADH/Fp fluorescence imaging at low temperature) to investigate the effect of aging on the redox state of mitochondria in skeletal muscles. The results showed that there are borderline significant differences in nominal concentrations of Fp and NADH, but not in the redox ratios when comparing 3.5-month and 13-month old muscles of mice (n = 6). It may be necessary to increase the number of muscle samples and study mice of more advanced age.

Keywords Mitochondria • Muscle • NADH • FAD • Oxidized flavoprotein (Fp) • Redox ratio, aging

L. Moon • L.Z. Li (✉)
Molecular Imaging Laboratory, Department of Radiology, Perelman School of Medicine, University of Pennsylvania, Philadelphia, PA, USA

Britton Chance Laboratory of Redox Imaging, Johnson Research Foundation, Department of Biochemistry and Biophysics, Perelman School of Medicine, University of Pennsylvania, Philadelphia, PA, USA
e-mail: linli@mail.med.upenn.edu

D.W. Frederick • J.A. Baur
Department of Physiology, Perelman School of Medicine, University of Pennsylvania, Philadelphia, PA, USA

Institute for Diabetes, Obesity and Metabolism, Perelman School of Medicine, University of Pennsylvania, Philadelphia, PA, USA

H.J. Halpern et al. (eds.), *Oxygen Transport to Tissue XXXIX*, Advances in Experimental Medicine and Biology 977, DOI 10.1007/978-3-319-55231-6_8

1 Introduction

Imaging tissue redox state can be achieved fluorescently. NADH and FAD are two coenzymes with endogenous fluorescence that play key roles in mitochondrial bioenergetics. NADH and $FADH_2$ pass their electrons to oxygen to generate ATP and water in the electron transport chain. NADH and $FADH_2$ are oxidized to NAD^+ and FAD, respectively. NAD^+ and $FADH_2$ are both non-fluorescent. Britton Chance and colleagues demonstrated that the redox ratio, calculated by the fluorescence intensities of NADH and FAD, which originate primarily from the mitochondria, could be used as a surrogate indicator of the metabolic/redox state of the organelles [1]. The tissue Fp/NADH ratio correlates linearly with measurements of NAD^+/NADH determined biochemically or by mass spectrometry [2, 3]. Note that redox state or potential is the balance between oxidized and reduced forms of specific redox-active molecules and redox state is different from oxidative stress. The redox state of mitochondria may reflect a number of parameters related to aging, including mitochondrial reserve, free radical damage and coupling efficiency.

As aging is the greatest risk factor for a number of diseases, understanding the biological processes underlying aging is important for improving human health and life span. NAD^+ concentration has been shown to decrease with aging in multiple tissues [4, 5] and the regulation of NAD^+ can affect health span and life span in laboratory studies [4, 6]. Moreover, the activation of the NAD^+ salvage pathway enzyme NAMPT (Nicotinamide phosphoribosyltransferase) has been suggested to be neuroprotective [7]. There is not yet a clear consensus on whether the NAD^+-coupled redox potential (NAD^+/NADH) decreases or increases with aging [5, 8]; it is unclear whether this discrepancy is due to differences between organs or technical difficulties with existing methodologies.

Previous work demonstrated that redox indices (NADH, Fp, redox ratio) can provide important information about energy-related biological processes [9, 10]. Here we used the Chance redox scanner (a cryogenic NADH/Fp fluorescence imager) to study the effect of aging on the redox state of mitochondria in skeletal muscles.

2 Materials and Methods

Mice bearing a single Cre-inducible (lox-STOP-lox) allele of *Nampt* under the control of the CAGGS promoter were crossed to mice bearing Cre under the control of the muscle creatine kinase promoter to obtain muscle-specific overexpression of *Nampt* as previously described [11]. Twelve male C57BL6 mice (weight ranging 25–35 g) were divided into four groups: (1) elder *Nampt* transgenic, (2) young *Nampt* transgenic, (3) elder *Nampt* control; (4) young *Nampt* control. Each group contained three mice. The elder age was 13 months, and the young age was 3.5 months. The mice were sacrificed by cervical dislocation. The hind limb

Fig. 8.1 A white-light picture of a mounted mouse quadriceps, showing a flat surface after grinding. The two tubes on the *left side* of the sample were FAD (*above*) and NADH reference standards

muscles were immediately dissected. The whole quadriceps were removed from the anterior surface of the femur bone and cleaned of residual adipose. The quadriceps muscles were then flash frozen in liquid nitrogen and embedded for subsequent redox scanning.

For embedding tissue samples for redox scanning, previously described methods were followed [12–14]. Briefly, a plastic cap (diameter ~ 2.5 cm) filled with 3–4 ml mounting medium (ethanol:glycerol:water = 1:3:6) was immersed in liquid nitrogen for a moment to make the medium half-frozen like a gel. The tissue sample was then placed in the middle of the mounting medium. Frozen tubes (inner diameter ~ 1.5 mm) of 100 μM FAD and NADH solution standards were inserted into the medium in the vicinity of the specimen (Fig. 8.1). More embedding medium was added to cover the whole tissue sample, which was then immersed in liquid nitrogen to freeze completely.

We employed the Chance redox scanner to obtain the fluorescence images of Fp and NADH for all muscle samples, each with 2–3 sections and tissue depth ranging 0.4–1.0 mm. Neutral density filters were added to the emission channels to avoid signal saturation. Image data were post-processed by a customized MATLAB program. The nominal concentrations of Fp and NADH in tissue were interpreted based on reference standards and neutral density filter difference between tissue and standards. They were then used to calculate the Fp redox ratio, i.e., Fp/(NADH + Fp), representing the mitochondrial redox state. Data were expressed as mean ± SD (standard deviation) after first averaging across image sections and then across muscle samples. The comparison between any two groups was analyzed with the t-test, and statistical significance was considered at the level of $p < 0.05$. $0.05 < p < 0.1$ was regarded as borderline significant.

Table 8.1 Mean redox indices for mouse quadriceps (*Nampt* transgenic versus control)

	Mean Fp (μM)	Mean NADH (μM)	Fp redox ratio Fp/(Fp + NADH)
Transgenic elder (n = 3)	10.5 ± 3.6	62 ± 12	0.15 ± 0.04
Control elder (n = 3)	9.9 ± 2.1	66 ± 20	0.14 ± 0.02
p	0.83	0.77	0.79
Transgenic young (n = 3)	14.8 ± 7.2	77 ± 22	0.17 ± 0.02
Control young (n = 3)	16.1 ± 4.9	87 ± 12	0.16 ± 0.02
p	0.81	0.56	0.61

Table 8.2 Mean redox indices of young and elder mouse quadriceps

	Mean Fp (μM)	Mean NADH (μM)	Fp redox ratio Fp/(Fp + NADH)
Young (n = 6)	15.4 ± 5.6	82 ± 17	0.17 ± 0.02
Elder (n = 6)	10.2 ± 2.7	64 ± 15	0.15 ± 0.03
p	0.08	0.07	0.2

3 Results

The redox scanning results showed no significant difference between *Nampt* transgenic groups and control groups for either elder or young mice (Table 8.1). The differences remain insignificant when we pooled the elder and young mice for comparing the transgenic status ($p > 0.1$).

For the aging effects on redox indices, we did not find significant differences between the transgenic young and transgenic elder groups ($p > 0.3$). Neither did we see any redox indices differences between the control young and control elder groups ($p > 0.1$). Since we did not see significant differences in redox indices between the transgenic and control groups, we pooled the muscle samples from transgenic and control groups in order to enhance the power of statistical analysis of the aging effects on redox state. The redox scanning results showed that there are some borderline significant differences in both Fp and NADH between muscles of young and elder mice (Table 8.2). The Fp redox ratio also tended to be higher in young muscle than elder ones, although this did not reach statistical significance. Figure 8.2 shows typical redox images and histograms of the elder and young muscle samples from the *Nampt* control group.

4 Discussion

The redox imaging techniques employed here may have wide-ranging applications in many fields, such as cancer, diabetes, developmental processes, mitochondrial diseases, neurodegenerative diseases, and aging. In this experiment we used the Chance redox scanner to study the redox status of muscle at different ages through imaging.

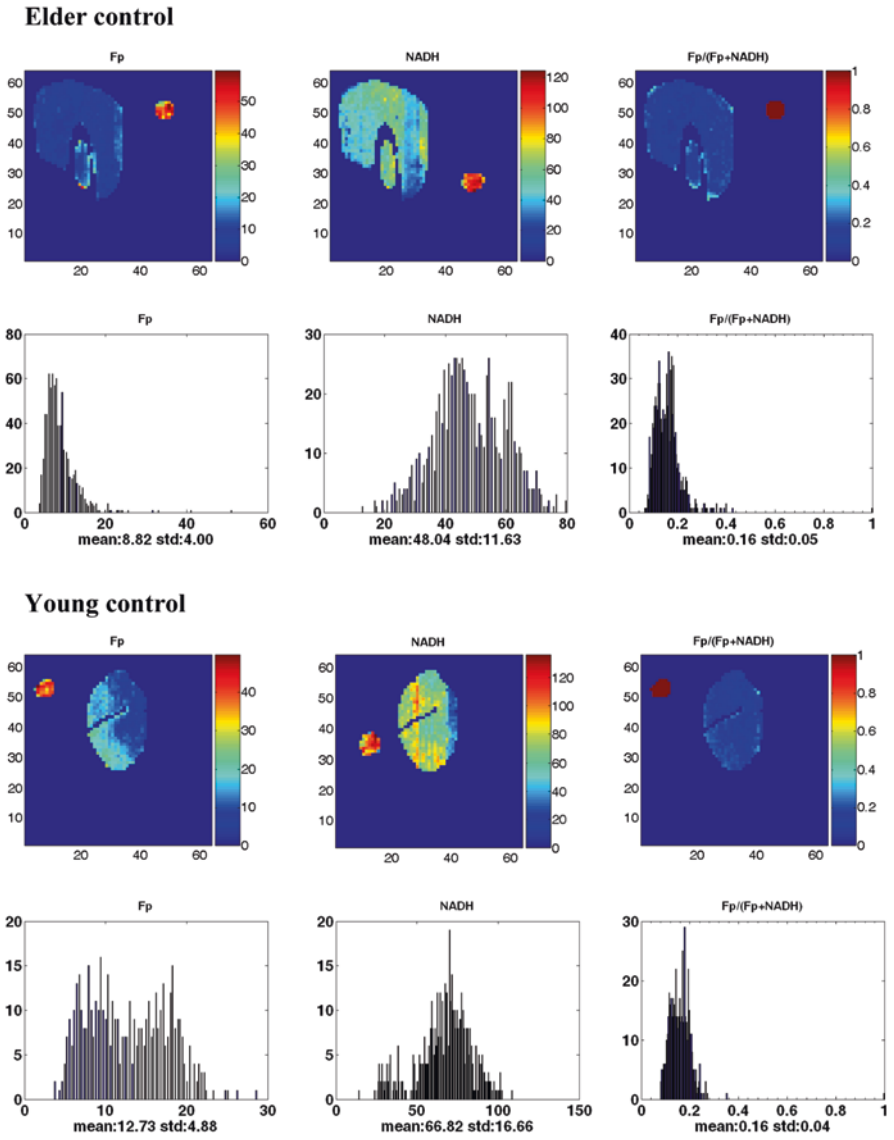

Fig. 8.2 The typical redox images and corresponding histograms of elder age (13 months) and young age (3.5 months) mouse quadriceps samples (*Nampt* control). From *left to right*: Fp, NADH, and Fp redox ratio. As shown by the *color bars* on the *right side* of each image, the Fp or NADH nominal concentrations are in μM; the Fp redox ratio ranges between 0 and 1. The small round spots outside the muscle section are Fp or NADH reference standards. The concentration of reference standard FAD = 46 μM, NADH = 100 μM after the correction of neutral density filters, image matrix 128 × 64 and pixel size 200 μm

Originally we also aimed to observe the effect of *Nampt* overexpression on the redox state of muscles. Since NAD^+ may decrease with aging, previous observation showed that overexpression of *Nampt* preserved muscle NAD^+ levels and exercise capacity in aged mice [15]. Thus, we wondered if *Nampt* overexpression would cause any effect on redox indices (NADH, Fp and redox ratio). However, we found no significant difference between the *Nampt* transgenic group and the control group, consistent with the equilibration of mitochondrial NAD^+/NADH identified in this model using mass spectrometry [11]. Although *Nampt* functions importantly in salvaging NAD^+, other mechanisms likely exist that resist changes in NAD^+ levels, including enhanced activity of NAD-dependent enzymes and feedback inhibition of *Nampt*. Despite the lack of major changes in middle-aged mice, increased capacity for NAD synthesis may help maintain stable NAD levels and redox status at more advanced ages, when NAD normally falls.

When pooling the transgenic and control data, we obtained a borderline significant difference between young and elder groups both in Fp and NADH. Although the Fp redox ratio tended to be lower in elder than the young muscles, we did not observe a significant difference in the Fp redox ratio.

Since Fp and NADH signals are proportional to mitochondrial density and the redox ratio is not, the borderline changes in Fp and NADH but not in redox ratio probably reflect a minor decrease of mitochondrial density with age. We reasoned that the NAD^+ regulating system might be sufficient enough for mice to sustain redox homeostasis up to 13 months of age, potentially explaining why we did not observe significant change in the redox indices. In the future, we can increase the number of mice to improve the statistical power. We can also study mice at a more advanced age of 24–36 months to investigate whether their redox indices might be significantly different from those of young mice.

Acknowledgments We appreciate Dr. Yu Wen and Dr. He N. Xu for their assistance with the paper revision. This work was supported by the NIH grant R01CA155348 and R01CA191207 (PI: L.Z. Li), the Center for Magnetic Resonance and Optical Imaging (CMROI) – an NIH supported research resource (P41EB015893, PI: R. Reddy).

References

1. Chance B, Schoener B, Oshino R et al (1979) Oxidation-reduction ratio studies of mitochondria in freeze-trapped samples. NADH and flavoprotein fluorescence signals. J Biol Chem 254:4764–4771
2. Ozawa K, Chance B, Tanaka A et al (1992) Linear correlation between acetoacetate beta-hydroxybutyrate in arterial blood and oxidized flavoprotein reduced pyridine-nucleotide in freeze-trapped human liver-tissue. Biochim Biophys Acta 1138:350–352
3. Varone A, Xylas J, Quinn KP et al (2014) Endogenous two-photon fluorescence imaging elucidates metabolic changes related to enhanced glycolysis and glutamine consumption in precancerous epithelial tissues. Cancer Res 74:3067–3075
4. Gomes AP, Price Nathan L, Ling Alvin JY et al (2013) Declining NAD+ induces a pseudohypoxic state disrupting nuclear-mitochondrial communication during aging. Cell 155:1624–1638

5. Braidy N, Guillemin GJ, Mansour H et al (2011) Age related changes in NAD+ metabolism oxidative stress and Sirt1 activity in wistar rats. PLoS One 6:e19194
6. Verdin E (2015) NAD(+) in aging, metabolism, and neurodegeneration. Science 350:1208–1213
7. Wang G, Han T, Nijhawan D et al (2014) P7C3 neuroprotective chemicals function by activating the rate-limiting enzyme in NAD salvage. Cell 158:1324–1334
8. Pugh TD, Conklin MW, Evans TD et al (2013) A shift in energy metabolism anticipates the onset of sarcopenia in rhesus monkeys. Aging Cell 12:672–681
9. Xu HN, Li LZ (2014) Quantitative redox imaging biomarkers for studying tissue metabolic state and its heterogeneity. J Innov Opt Health Sci 07:1430002
10. Li LZ (2012) Imaging mitochondrial redox potential and its possible link to tumor metastatic potential. J Bioenerg Biomembr 44:645–653
11. Frederick DW, Davis JG, Davila A Jr et al (2015) Increasing NAD synthesis in muscle via nicotinamide phosphoribosyltransferase is not sufficient to promote oxidative metabolism. J Biol Chem 290:1546–1558
12. Moon L, Sun N, Li LZ (2013) Preliminary investigation on the spatial distribution of the metabolic state in tissue by the chance redox scanner. China Med Devices 28:1–7
13. Xu HN, Nioka S, Glickson J et al (2010) Quantitative mitochondrial redox imaging of breast cancer metastatic potential. J Biomed Opt 15:036010
14. Xu HN, Wu B, Nioka S et al (2009) Quantitative redox scanning of tissue samples using a calibration procedure. J Innov Opt Health Sci 2:375–385
15. Frederick DW, Loro E, Liu L et al (2016) Loss of NAD homeostasis leads to progressive and reversible degeneration of skeletal muscle. Cell Metab 24:269–282

Chapter 9
Amino Acid Hydration Decreases Radiation-Induced Nausea in Mice: A Pica Model

Liangjie Yin, Lauren Vaught, Paul Okunieff, Katherine Casey-Sawicki, and Sadasivan Vidyasagar

Abstract Nausea and diarrhea are common yet inconsistent side effects of abdominal and pelvic irradiation. Their frequency, chronicity, and severity vary greatly, and the reasons for inter-subject variability are unknown. We studied the potential for radiation-induced changes in amino acid absorption and mucosal barrier function to lead to gastrointestinal toxicity. We found profound and prolonged changes in the absorption and secretion of several electrolytes and nutrients, caused by changes in transporter function, after radiation doses as low as 1 to 3 Gy. After identifying absorbed and non-absorbed amino acids, we demonstrated the role of a beneficial amino acid drink to alleviate radiation-related gastrointestinal symptoms in a mouse model.

Keywords Radiation • Nausea • Gastrointestinal toxicity • Pica model • Amino acids

1 Introduction

Radiation-induced gastrointestinal (GI) toxicity is a well-known and common side effect of abdominal and pelvic irradiation. The physiological mechanism causing these symptoms is unknown and has been assumed to be due to cell necrosis, thinning of the mucosa, epithelial apoptosis, or reduced barrier function. However, none of these fully explains the inter-subject variability, chronicity, or severity of the illness [1–4]. For example, nausea is commonly seen in the first days of radiation therapy, sometimes within a few hours, and usually subsides a few hours later. It can be triggered by certain foods and continue or decrease in severity despite continued therapy. Inexplicably, particularly at low radiation doses and delayed time points,

L. Yin • L. Vaught • P. Okunieff (✉) • K. Casey-Sawicki • S. Vidyasagar
Department of Radiation Oncology, University of Florida College of Medicine, Gainesville, FL, USA
e-mail: pokunieff@ufl.edu

H.J. Halpern et al. (eds.), *Oxygen Transport to Tissue XXXIX*, Advances in Experimental Medicine and Biology 977, DOI 10.1007/978-3-319-55231-6_9

there are no observable histological changes in the bowel to explain this phenomenon. Similarly, some patients experience no diarrhea, while others have watery diarrhea. As with nausea, diarrhea can occur at low doses but is more common at higher doses. It can also spontaneously resolve despite daily radiation treatments or continue for a prolonged period after treatment is complete. Thus, neither radiation-induced nausea nor diarrhea have easily understood mechanisms, and both suggest a reversible mechanism related to mucosal cell function not just mucosal cell depopulation.

Current interventions for radiation-induced nausea and diarrhea, though partly effective, are not completely satisfactory. Moving toward an easily adapted intervention, we hypothesized that the small bowel responds to even low radiation doses with changes in the function of electrolyte and nutrient transporters and barrier function. We further hypothesized that providing a nutritional drink with emphasis on amino acids (AAs) that are easily absorbed and improve small bowel barrier function would reduce radiation-induced nausea. We tested this in a mouse model of total-body irradiation (TBI).

2 Methods

Male NIH Swiss mice received TBI doses in the range of 1 to 7 Gy. Although these doses cause no substantial changes in the small bowel mucosa that can be observed histologically, they cause symptoms in humans and mice. Sham irradiation (IR) was used as a control. Specimens were acquired 6 days later, or as indicated in the time course study (Fig. 9.3). Transepithelial transport of electrolytes, glucose, or AAs were measured in Ussing chambers, as described in our previous publications [5, 6]. For the mucosa studies, the ilium was stripped along the submucosal plane to yield pure mucosal sheets devoid of serosal, muscularis, and Auerbach's and Meissner's (submucosal) nerve plexuses. Mucosal segments were bubbled with 95% oxygen and 5% CO_2 and incubated at 37 °C to achieve a system that closely mimicked an *in vivo* system. Isotopes were added either to the mucosal or the serosal side, and transport to the opposite side was measured.

Nausea was measured using the pica assay (i.e., kaolin consumption [7, 8]). The clay was hung outside of the cage within easy reach of the animals, uneaten chips were collected and weighed along with the residual uneaten clay, and this weight was subtracted from the original weight to determine total kaolin consumed. Quantity of water consumed per cage of four animals and body weight were measured. All experiments were approved by the University of Florida Institutional Animal Care and Use Committee.

3 Results

3.1 Radiation Altered Glucose and Amino Acid Absorption

All 20 natural AAs were tested along with several simple sugars. Glucose, glutamine, and many AAs exhibited stable or decreased Na^+-coupled transport, whereas other AAs improved Na^+-coupled absorption following irradiation. For example, glucose absorption was decreased at 1 Gy; it was half of baseline at 3 Gy (Fig. 9.1). Using a range of glucose concentrations, we found that V_{max} decreased (indicating fewer transporters) and K_M increased (indicating the transporters had lower glucose affinity), suggesting a change in the efficiency or type of glucose transporter proteins. The mixture of amino acids (MAAM) that demonstrated improved transport (example AAs in Fig. 9.2) were chosen for the water replacement provided to the animals; they also comprise enterade® (Entrinsic Health Solutions, Norwood, MA), a hydration product that is currently on the market.

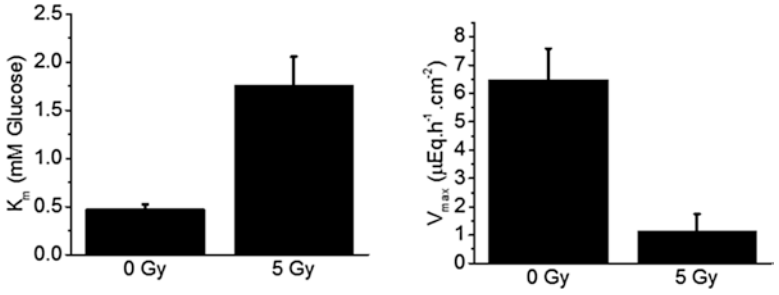

Fig. 9.1 Five Gy increased K_M of glucose absorption ≈4-fold and decreased V_{max} ≈ 5-fold (0 Gy N = 5, 5 Gy N = 3, $p < 0.05$)

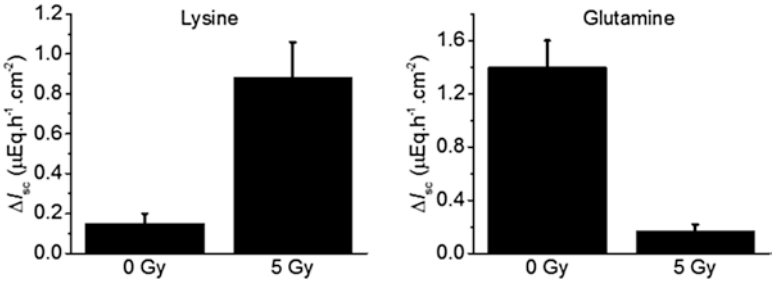

Fig. 9.2 Radiation dose-dependent changes in lysine and glutamine transport (0 Gy and 5 Gy N = 8, $p < 0.05$)

3.2 Radiation Increased Cl^- Secretion, and the Amino Acid Mixture Reduced Radiation-Related Secretion

Anion secretion is a defining characteristic of diarrheal disease. Anion secretion at radiation doses as low as 3 Gy and as early as 24 h after irradiation occur in animals and humans without noticeable changes in histopathology. Radiation led to increased Cl^- secretion over time, which persisted for at least 14 days (Fig. 9.3). As the mucosa was naturally replaced multiple times during that period, the cells exhibiting the abnormal secretion were the progeny of irradiated cells and were not directly irradiated. Replacing the water available to the animals with MAAM substantially reduced Cl^- secretion (Fig. 9.3).

3.3 Radiation Decreased Electrolyte Absorption

Reduced Na^+ absorption is another characteristic of diarrheal disease. Sodium absorption occurs in concert with water absorption. (^{22}Na) flux studies showed a radiation dose-dependent decrease in net Na^+ absorption. For example, basal ileal sodium absorption was 2.8 ± 0.4, compared to irradiation at 1 Gy 1.7 ± 0.3 or 3 Gy 0.5 ± 0.2 μeq h^{-1} cm^{-2}; n = 10, $p < 0.003$. Radiation also similarly decreased Na^+-coupled glucose transport. However, MAAM improved Na^+ absorption toward normal levels.

Pica syndrome: Consumption of kaolin is a commonly used experimental surrogate for nausea, as mice do not have a vomiting reflex. Within 6 days of 2 Gy TBI, mice consumed approximately 150 mg of kaolin, with maximum consumption occurring between days 1 and 3. Ondansetron (2 mg/kg, IP once daily, started within 30 min after irradiation), an antiemetic used to prevent chemotherapy- and radiation-induced nausea and vomiting, and MAAM both partially alleviated kaolin consumption (Fig. 9.4a). Sham-irradiated mice did not consume kaolin.

Water consumption: Weight loss predominantly due to decreased fluid intake is a dominant cause of death in defined pathogen-free animals after TBI or near-TBI. Animals offered MAAM maintained oral hydration and body weight after 3 Gy TBI (Fig. 9.4b). Control animals had substantial weight loss, and water consumption was halved. Ondansetron-treated mice consumed more water than untreated irradiated mice, but they also suffered more weight loss than the MAAM-treated animals.

4 Conclusions

Research of GI distress after irradiation has focused on DNA damage and apoptotic pathway alterations. Little or no work has been done on alterations in the nutrient and electrolyte transporters and other metabolic processes required of the mature epithelium. We have shown that after low doses of irradiation (1– 7 Gy) nutrient and electrolyte transporters experience changes that have substantial metabolic and

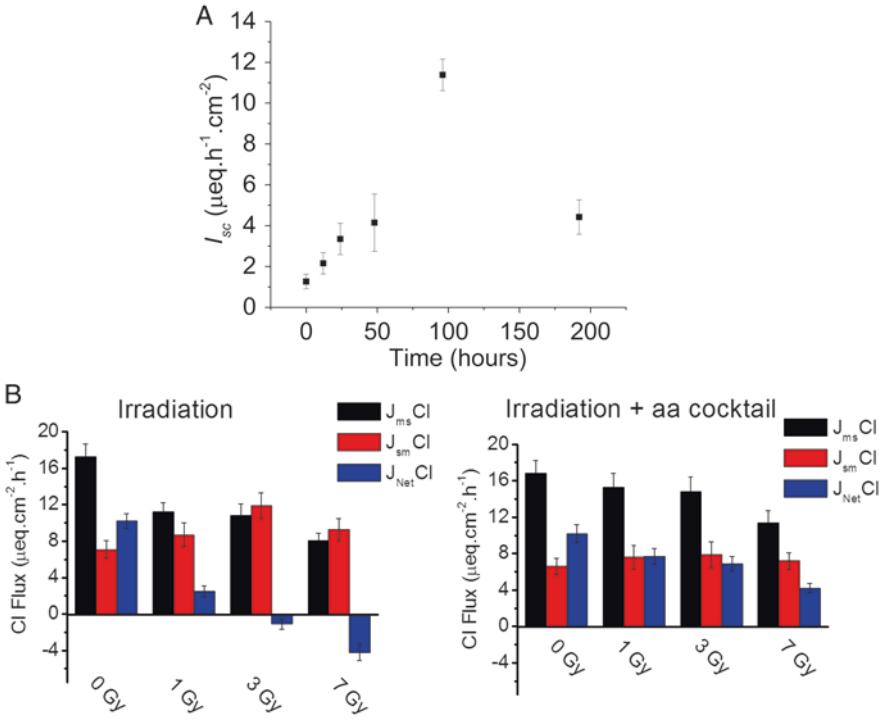

Fig. 9.3 (**a**) Anion secretion with time after 6 Gy whole abdominal radiation exposure. Abnormally high secretion is seen for at least 2 weeks after irradiation. (**b**) The amino acid cocktail returned ileal mucosal to serosal (J_{ms}), serosal to mucosal (J_{sm}), and net chloride transport to near normal at doses up to 7 Gy

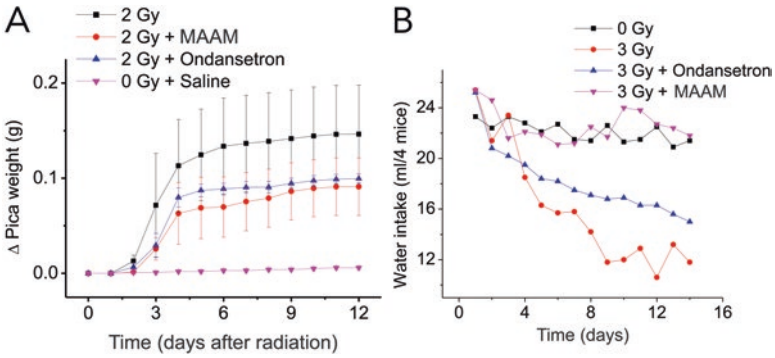

Fig. 9.4 (**a**) The mixture of absorbed amino acid (MAAM) decreased kaolin intake in 2 Gy irradiated mice. (**b**) Fluid intake in mice after 3 Gy irradiation (All groups, N = 5)

physiological consequences. Because these radiation doses may not cause substantial activation of apoptotic pathways, they can lead to near complete DNA repair and can have minimal effect on epithelial thickness or other observable histopathology. Furthermore, we have shown that alterations in the function of nutrient transporters can persist for generations in the progeny of irradiated cells. This inherited phenotypic change is likely due to epigenetic changes and deserves further study, as it may help us understand similar inheritance that occurs when stem cells differentiate or adapt to environmental stress.

The functional changes in AA transporters after irradiation favor absorption of specific AAs. When these AAs were offered to irradiated animals in the form of drinking water or gavage, the animals had decreased pica syndrome, improved oral fluid intake, and reduced weight loss compared to standard acidified water. The benefits to pica match those of pharmacological interventions, but the oral intake and weight preservation exceed that seen with ondansetron; this latter result is likely due to changes in transporter function. Specifically, pathologic GI Cl^- secretion was improved by the MAAM, leading to less GI fluid loss and better water and electrolyte homeostasis.

The mechanism by which radiation affects Cl^- secretion and improves Na^+ and water absorption is unclear. In addition, the mechanism by which MAAM reduces that physiological alteration is also unknown. The murine small bowel mucosa replaces itself every 3–4 days; thus, during the 6 days allowed in most of our studies, many reproductive cycles for the progenitor cells occur, and the progeny mature into absorptive epithelium. The low-stress environment that occurs during the hours in which progeny are bathed in physiologically optimized AAs could facilitate normal and efficient maturation. Lack of that low-stress period could prevent timely epithelial maturation and might help explain the prolonged abnormal phenotype.

A product based on the preferred AAs (enterade®) is under clinical evaluation. It has preliminarily shown a benefit for reduction of diarrhea and weight loss in patients undergoing radiotherapy. Tests are also ongoing with other GI diseases that involve mucosal atrophy.

Acknowledgments This research was supported by the National Space Biomedical Research Institute through NASA NCC 9-58 and Entrinsic Health Solutions (P0018160). Drs. Vidyasagar and Okunieff have shares in Entrinsic Health Solutions and hold scientific advisor positions within the company.

References

1. Taylor S, Demeyin W, Muls A et al (2016) Improving the well-being of men by evaluating and addressing the gastrointestinal late effects (EAGLE) of radical treatment for prostate cancer: study protocol for a mixed-method implementation project. BMJ Open 6:e011773
2. Andreyev J, Ross P, Donnellan C et al (2014) Guidance on the management of diarrhoea during cancer chemotherapy. Lancet Oncol 15:e447–e460
3. Thomas RJ, Holm M, Williams M et al (2013) Lifestyle factors correlate with the risk of late pelvic symptoms after prostatic radiotherapy. Clin Oncol (R Coll Radiol) 25:246–251

4. Andreyev J (2005) Gastrointestinal complications of pelvic radiotherapy: are they of any importance? Gut 54:1051–1054
5. Zhang K, Yin L, Zhang M et al (2011) Radiation decreases murine small intestinal HCO_3-secretion. Int J Radiat Biol 87:878–888
6. Vidyasagar S, MacGregor G (2016) Ussing chamber technique to measure intestinal epithelial permeability. Methods Mol Biol 1422:49–61
7. Goineau S, Castagne V (2016) Comparison of three preclinical models for nausea and vomiting assessment. J Pharmacol Toxicol Methods 82:45–53
8. Machida M, Miyamura Y, Machida T et al (2015) Administration of olanzapine as an anti-emetic agent changes glucose homeostasis in cisplatin-treated rats. Biol Pharm Bull 38:587–593

Chapter 10
Evaluation of Haemoglobin and Cytochrome Responses During Forearm Ischaemia Using Multi-wavelength Time Domain NIRS

Frédéric Lange, Luke Dunne, and Ilias Tachtsidis

Abstract We demonstrate the ability of a 16-wavelength time domain near-infrared spectroscopy system to monitor changes in oxy- and deoxy haemoglobin ([HbO_2] [HHb]) and the oxidation of cytochrome-c-oxidase ([oxCCO]), during forearm ischaemia. We tested two methods to retrieve the concentration changes. The first uses the measured changes in light attenuation and the modified Beer-Lambert law, and the second uses the absorption and scattering estimated by the measured time-point spread function. The system is able to retrieve the concentration changes with both methods, giving similar results. At the end of forearm ischaemia (t = 5 min), we measured an increase in [HHb] of 16.77 ± 2.52 and 16.37 ± 2.33 μMol, and a decrease in [HbO_2] of −6.12 ± 1.62 and −5.57 ± 2.02 μMol for method 1 and 2, respectively. At that same time, the changes in [oxCCO] were −0.36 ± 0.33 and −1.40 ± 1.20 μMol, for method 1 and 2, respectively. These small changes in [oxCCO], despite a huge change in haemoglobin, demonstrate the absence of cross-talk and are comparable to previous measurements using broadband NIRS.

Keywords NIRS • TRS • Cytochrome-c-oxidase • Cuff Occlusion • Haemoglobin

1 Introduction

Near-infrared spectroscopy (NIRS) is now a common tool for monitoring non-invasively the tissue in-vivo changes in oxy- and deoxy haemoglobin ([HbO_2] [HHb]) [1], and has been extensively used to monitor the function and physiology of the brain [2–4].

Most of the NIRS systems monitor changes in [HbO_2], [HHb] using the modified Beer-Lambert law and assume a constant differential pathlength factor to account

F. Lange (✉) • L. Dunne • I. Tachtsidis
Department of Medical Physics and Biomedical Engineering, University College London, London, UK
e-mail: f.lange@ucl.ac.uk

H.J. Halpern et al. (eds.), *Oxygen Transport to Tissue XXXIX*, Advances in Experimental Medicine and Biology 977, DOI 10.1007/978-3-319-55231-6_10

for the effect of the scattering in tissues [5]. These instruments are often referred to as continuous wave (CW) instruments and are highly portable, inexpensive, and easy to use. NIRS CW instruments measure the changes in light attenuation at two or three wavelengths; however, recent upgrades that utilize white light sources and broadband spectrometers for detection allow to measure changes in light attenuation at hundreds of wavelengths [6]. These broadband NIRS instruments can then be used to retrieve information on a third chromophore, the cytochrome-c-oxidase CCO. The CCO is the terminal electron acceptor of the respiratory chain in the mitochondria. NIRS monitors the changes in the redox state of the CCO using the oxidase minus reduced CCO spectra ([oxCCO]): Bale et al. provide a recent review on this topic [7]. Hence, the monitoring of the CCO provides information about metabolism and in particular mitochondrial oxygenation. This extra information, coupled with the classical vascular oxygenation measured by NIRS, enable us to study the link between them, which can be informative of the physiological status of the tissue. While CW NIRS instruments can only measure changes in light attenuation, time domain (TD) systems can quantify absorption and scattering. TD systems can record the arrival time of photons that have traveled through tissue. Then, by fitting the measured arrival of the photon's curve to an analytical model, the absorption and scattering coefficient can be estimated [8]. TD systems are less common because of their higher cost, complexity and size. However, improvement in the quality and decrease in the cost of components, such as fiber lasers and detectors, have increased the use of this technique [9]. One of the current developments of the TD systems is to perform measurements with a considerable number of wavelengths. The main benefit is to be able to retrieve the true optical properties of the tissues over a large bandwidth, which can then be used to estimate the tissue's composition [10]. These systems can also be used to retrieve the CCO chromophore [11].

Towards that goal we have developed a multi-wavelength TD system, described in [12]. Here we demonstrate the ability of our multi-wavelength TD system to retrieve [HbO_2], [HHb] and [oxCCO] responses, by replicating the forearm ischaemia experiment of Matcher et al. [12].

2 Methods

The instrument is based on a supercontinuum laser coupled with an acousto-optical tunable filter that permits the selection of 16 narrow wavelengths, with a full width at half maximum between 2 and 4 nm, in the range of 650–1100 nm. The light is then transmitted on the tissue via a single core optical fibre. The system allows up to two sources points. On the detection side, four optical fibres collect the reflected light to four photon multiplier tubes (PMTs). Then, a router is used to redirect the signal to a single TCSPC card, in order to measure the arrival time of the photons.

Six healthy volunteers (age 24–29 years; 2 females) were recruited from the lab and informed consent was obtained. Measurements were performed on the medial aspect of the left arm. One source and four detectors were used in this experiment.

The emitter and receiver fibres were separated from a relative distance ρ = 3.0 cm by a custom 3D printed probe holder. The 4 detectors were placed close together in a ring arrangement around the sources, and were probing the same area. Measurements were performed in a dark room to decrease the amount of background light. The volunteers positioned their arm in a comfortable resting position on a flat surface. A pneumatic cuff was placed loosely around the left arm. After an initial 5-min period in resting position, the cuff was rapidly inflated to a pressure of 220 mmHg to provide an abrupt venous and arterial occlusion. The cuff occlusion was maintained for 5 min. The cuff was then released and monitoring continued for an additional 5 min. Time-resolved reflectance measurements were simultaneously performed at 16 wavelengths, from 780 to 870 nm, every 6 nm. The acquisition time for every wavelength was 50 ms, resulting in an acquisition frequency of about 1 Hz, including the dead times of the system. We tested two methods in order to retrieve the concentration changes in [HbO_2], [HHb] and [oxCCO]. For method 1 we used the change in attenuation and the modified Beer-Lambert law. This method has the advantage of having a good signal-to-noise ratio (SNR). In order to account for the pathlength, we calculated the true pathlength for every wavelength using the mean arrival time of the photons recorded by the system [12]. Method 2 used the change of the absorption coefficient, obtained by fitting the solution to the diffusion equation for a semi-infinite homogenous medium to the Temporal Point Spread Function (TPSF) [7]. This method suffered from a lower SNR compared with method 1, but has the advantage of being able to distinguish between the change in absorption and scattering. To improve the SNR of method 2, we averaged the data across 10 time points. The data analysed with method 1 were not averaged because of the sufficient SNR with that technic.

Data are presented as mean and the standard error of mean (SEM).

3 Results

Figure 10.1a shows the mean pathlength of the rest period for all participants, including all channels. It should be noted that, since all channels were probing the same area and similar results were found with each of them, we averaged the data across all the channels. The pathlength shows a strong variability among subjects with values (at 810 nm) ranging from 9.04 ± 0.41 cm for subject 3 to 15.76 ± 0.37 cm for subject 1. Figure 10.1b presents the mean scattering coefficient of the rest period for all subjects. The scattering coefficient shows a strong variability (at 810 nm) from 5.26 ± 0.26 cm^{-1} for subject 3 to 7.86 ± 0.22 cm^{-1} for subject 1. This variability might explain the variability of the pathlength. Indeed, the pathlength is dictated by the absorption and scattering coefficient of the tissues. Then, a change in at least one of those properties would have an influence on it [8]. Figure 10.1c presents the grand average across every channel and all subjects (n = 6 subjects × 4 detectors = 24) of the changes in concentration of [HbO_2], [HHb] and [oxCCO] calculated with method 1. Figure 10.1d presents the same grand average with method 2. We see the typical response of haemoglobin to muscle ischaemia with a progressive increase of [HHb]

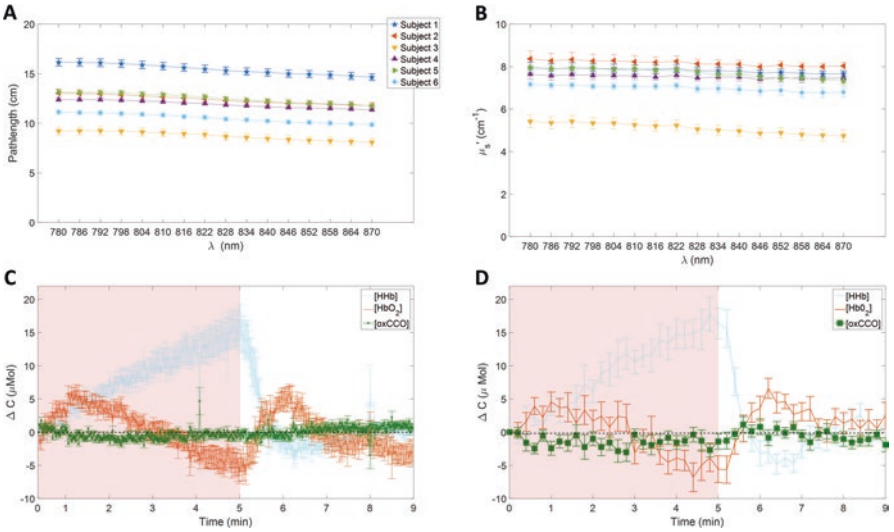

Fig. 10.1 (**a**) Pathlength at rest of every channel for all subjects. (**b**) Scattering coefficient at rest of every channel for all subjects. (**c**) Grand average across all channels and all subjects (n = 24) of the concentration changes for [HHb], [HbO_2] and [oxCCO] from method 1. (**d**) Grand average across all channels and all subjects (n = 24) of the concentration changes for [HHb], [HbO_2] and [oxCCO] from method 2

Table 10.1 Main results of the study: mean values with the standard error of the mean, calculated with both methods, of [HHb], [HbO_2], and [oxCCO] after 2.5 and 5 min of occlusion

	2.5 min after occlusion			5 min after occlusion		
	[HbO_2] (μMol)	[HHb] (μMol)	[oxCCO] (μMol)	[HbO_2] (μMol)	[HHb] (μMol)	[oxCCO] (μMol)
MBLL	1.42 (±0.97)	8.99 (±1.02)	−1.03 (±0.36)	−6.12 (±1.62)	16.77 (±2.52)	−0.36 (±0.33)
$\Delta\mu_a$	0.75 (±1.50)	9.48 (±2.49)	−1.55 (±1.13)	−5.57 (±2.02)	16.37 (±2.33)	−1.40 (±1.20)

MBLL modified Beer-Lambert law

and a progressive decrease of [HbO_2], with the maximum change at the end of occlusion. Indeed, after 2.5 min of occlusion, the changes in [HHb] and [HbO_2] calculated with methods 1 and 2, are 8.99 ± 1.02 and 9.48 ± 2.49 μMol, and 1.42 ± 0.97 and 0.75 ± 1.50 μMol, respectively. After 5 min, at the end of the occlusion, those changes have increased for [HHb] to 16.77 ± 2.52 and 16.37 ± 2.33 μMol, and for [HbO_2] to −6.12 ± 1.62 and −5.57 ± 2.02 μMol, for methods 1 and 2, respectively.

The time course of the [oxCCO] is different to that of the haemoglobins. After 2.5 min of occlusion, the changes calculated with methods 1 and 2 are −1.03 ± 0.36 and −1.55 ± 1.13 μMol, respectively. After 5 min, at the end of the occlusion, those changes are −0.36 ± 0.33 and −1.40 ± 1.20 μMol, respectively. Moreover, both methods of chromophore estimation show a similar qualitative behaviour and a very good agreement in terms of magnitude. These results are summarised in Table 10.1.

4 Discussion

This study shows that, during cuff occlusion, there is an increase in [HHb] and a decrease in [HbO_2], with the maximum change occurring at the end of occlusion. The [oxCCO] showed a different dynamic response compared with the haemoglobins. Matcher et al. [12] postulated that the changes in [oxCCO] during muscle ischaemia should be small. This behaviour was observed in the present study and our results are in good agreement with the literature [12].

We observed that the [HbO_2] response at 2.5 min (middle of the occlusion) was positive. This behaviour is expected since cuff inflation initially occludes the veins, then the arteries. Thus, it causes an augmentation of the [HbO_2] at the beginning of the occlusion before the decrease (Fig. 10.1c, d).

Both methods used for estimation of the chromophore changes showed the same behaviour with similar magnitude changes, especially for [HHb] and [HbO_2]. This agreement might be because we used the true pathlength to calculate the changes of the chromophores with method 1.

The small change of the [oxCCO] is a good indication of the absence of crosstalk between haemoglobin and cytochrome, which is one of the major issues when trying to resolve the [oxCCO] [4]. Indeed, in the presence of crosstalk, the changes in magnitude of the [oxCCO] during a muscular cuff occlusion can be the same as that of the haemoglobins [12].

Both methods qualitatively demonstrate a difference in the dynamic response between [oxCCO] and haemoglobin during a cuff occlusion (Fig. 10.1c, d). In method 1, the average [oxCCO] change, at the end of the occlusion, is very small compared with changes in the hemoglobins. However, in method 2, this difference between haemoglobins and [oxCCO] response was smaller. It is worth noting that we averaged the data in order to extract information with method 2, due to the lower SNR of that method. Despite that fact, Table 10.1 and Fig. 10.1 show that the concentration changes retrieved with method 2 are noisier. This might explain the discrepancy between the two methods for the [oxCCO] quantification. Therefore, we are investigating improvement in methods and instrumentation to overcome this issue.

Method 2 is able to retrieve the concentration changes of the three chromophores with good agreement with method 1. Thus, using our system and method 2, we can investigate the effect of scattering and extract the absolute concentration. The variation of the scattering coefficient could influence the measurement of a small chromophore like CCO; this effect will be investigated in the future.

In conclusion, this multi-wavelength time domain system is able to distinguish between the haemoglobin and cytochrome signal, without crosstalk, during muscle ischemia. It is also shown that our system is able to retrieve the absorption and scattering coefficient of muscle tissue.

Acknowledgements The authors thank The Wellcome Trust (104580/Z/14/Z) for financial support of this work.

References

1. Ferrari M, Quaresima V (2012) A brief review on the history of human functional near-infrared spectroscopy (fNIRS) development and fields of application. NeuroImage 63(2):921–935
2. Wolf M, Ferrari M, Quaresima V (2007) Progress of near-infrared spectroscopy and topography for brain and muscle clinical applications. J Biomed Opt 12:062104
3. Quaresima V, Ferrari M (2016) Functional near-infrared spectroscopy (fNIRS) for assessing cerebral cortex function during human behavior in natural/social situations: a concise review. Organ Res Methods:1–23
4. Scholkmann F, Kleiser S, Metz AJ et al (2014) A review on continuous wave functional near-infrared spectroscopy and imaging instrumentation and methodology. NeuroImage 85:6–27
5. Sassaroli A, Fantini S (2004) Comment on the modified beer–Lambert law for scattering media. Phys Med Biol 49(14):N255–N257
6. Bale G, Elwell CE, Tachtsidis I (2016) From Jöbsis to the present day: a review of clinical near-infrared spectroscopy measurements of cerebral cytochrome-c-oxidase. J Biomed Opt 21(9):091307
7. Patterson MS, Chance B, Wilson BC (1989) Time resolved reflectance and transmittance for the non-invasive measurement of tissue optical properties. Appl Opt 28(12):2331–2336
8. Pifferi A, Contini D, Mora AD et al (2016) New frontiers in time-domain diffuse optics, a review. J Biomed Opt 21(9):091310
9. Konugolu Venkata Sekar S, Farina A, Martinenghi E et al (2015) Broadband time-resolved diffuse optical spectrometer for clinical diagnostics: characterization and in-vivo measurements in the 600-1350 nm spectral range. Proc SPIE 9538:95380R
10. Lange F, Peyrin F, Montcel B (2015) A hyperspectral time resolved DOT system to monitor physiological changes of the human brain activity. Proc SPIE 9536:95360R
11. Dunne L, Hebden J, Tachtsidis I (2014) Development of a near infrared multi- wavelength, multi-channel, time-resolved spectrometer for measuring brain tissue haemodynamics and metabolism. In: Oxygen transport to tissue XXXVI, vol 812. Springer New York, New York
12. Matcher SJ, Elwell CE, Cooper CE et al (1995) Performance comparison of several published tissue near-infrared spectroscopy algorithms. Anal Biochem 227(1):54–68

Chapter 11
Influence of Free Radicals on the Intrinsic MRI Relaxation Properties

Rong-Wen Tain, Alessandro M. Scotti, Weiguo Li, Xiaohong Joe Zhou, and Kejia Cai

Abstract Free radicals are critical contributors in various conditions including normal aging, Alzheimer's disease, cancer, and diabetes. Currently there is no non-invasive approach to image tissue free radicals based on endogenous contrast due to their extremely short lifetimes and low in vivo concentrations. In this study we aim at characterizing the influence of free radicals on the MRI relaxation properties. Phantoms containing free radicals were created by treating egg white with various H_2O_2 concentrations and scanned on a 9.4 T MRI scanner at room temperature. T_1 and T_2 relaxation maps were generated from data acquired with an inversion recovery sequence with varied inversion times and a multi-echo spin echo sequence with varied echo times (TEs), respectively. Results demonstrated that free radicals express a strong shortening effect on T_1, which was proportional to the H_2O_2 concentration, and a relatively small reduction in T_2 (<10%). Furthermore, the sensitivity of this approach in the detection of free radicals was estimated to be in the pM range that is within the physiological range of in vivo free radical expression. In conclusion, the free radicals show a strong paramagnetic effect that may be utilized as an endogenous MRI contrast for its non-invasive in vivo imaging.

Keywords Free radicals • Reactive oxygen species • Proton relaxation properties • MRI

R.-W. Tain
Department of Radiology and Center for MR Research, University of Illinois at Chicago, Chicago, IL, USA

A.M. Scotti • X.J. Zhou • K. Cai (✉)
Department of Radiology and Center for MR Research, University of Illinois at Chicago, Chicago, IL, USA

Department of Bioengineering, University of Illinois at Chicago, Chicago, IL, USA
e-mail: kcai@uic.edu

W. Li
Department of Bioengineering, University of Illinois at Chicago, Chicago, IL, USA

Department of Radiology, Feinberg School of Medicine, Northwestern University, Chicago, IL, USA

H.J. Halpern et al. (eds.), *Oxygen Transport to Tissue XXXIX*, Advances in Experimental Medicine and Biology 977, DOI 10.1007/978-3-319-55231-6_11

1 Introduction

Oxidative stress due to elevated intracellular reactive oxygen species (ROS) is a critical contributor in various conditions including normal aging, Alzheimer's disease, stroke, cardiac arrest, cancer, and diabetes [1]. It is currently accepted that the majority of intracellular ROS production takes place in the mitochondria [2]. The complex I and complex III are the sites of superoxide (O_2^-) production, which results in dismutation to form hydrogen peroxide (H_2O_2) [3], an important intracellular signaling agent. Hydrogen peroxide is freely diffusible, has the highest intracellular concentration compared to other ROS, and can further react to form a strong oxidant, the hydroxyl radical (OH^-) [2]. Fully non-invasive imaging approaches to quantify tissue free radicals are therefore highly demanded and may provide further information on the pathological mechanisms, disease diagnosis and stratification, and treatment response.

Several methods have been developed for studying oxidative stress or ROS such as biochemical analyses [4], the optical redox scanning [5], and exogenous contrast MR-based methods [6–11]. Although those methods advance our understanding of ROS in many pathophysiological conditions, they are either non-direct and/or semi-invasive approaches.

Since free radicals including hydroxyl and superoxide radicals contain unpaired electrons, they may shorten the T_1 relaxation time of nearby water protons excited by RF pulse, resulting in T_1 weighted MRI contrast. To the best of our knowledge, the changes of MRI proton relaxation properties in the presence of free radicals have not yet been studied. This study then created phantoms by treating egg white with and without H_2O_2 to study effects of free radicals, including superoxides and hydroxyl radicals (but not H_2O_2), on proton relaxation times. It is known that ovovtransferrin, accounting for about 12% of total egg white protein pool, contains iron [12] that may trigger the production of free radicals from H_2O_2 through Fenton reaction [13].

2 Methods

The effects of hydroxyl radicals on proton relaxation were evaluated in fresh egg white treated with various concentrations of H_2O_2 (0, 0.025, 0.05, 0.1, and 0.25 v/v%). MRI was performed on a 9.4 T MRI scanner at room temperature. T_1 relaxation time maps were obtained at 1 h post H_2O_2-treatment using an inversion recovery sequence with varied inversion times (0.1, 0.25, 0.75, 1, 1.25, 1.5, 1.75, 2 and 5 s). Other parameters include TE/TR = 5/12000 ms, echo train length = 8, in-plane resolution =0.23 × 0.23 mm^2, and slice thickness = 1.5 mm. For T_2 mapping, a Fast Spin Echo sequence with varied echo times (0.01, 0.025, 0.05, 0.075, 0.1, 0.2, and 0.5 s) was used with 6 s TR and 8 echo train length. In addition, as a control, T_1 and T_2 relaxation times of the aqueous H_2O_2 solution (PBS) were generated using the same MRI protocols.

Another set of egg white samples was dynamically scanned to study the time dependence of T_1 after H_2O_2 treatment (0.25 v/v%) for up to 4 h. The changes of T_1 over time were then fitted into a monoexponential decay function, assuming the overall reaction in egg white follows the pseudo-first-order reaction theory [13]:

$$[ROS] = c_1 e^{-kt}$$

This equation, where $c_1$is the initial concentration of ROS, k is the kinetic coefficient (rate constant of ROS production), and t is time, was used to determine the sensitivity of the proposed approach in the detection of free radicals.

3 Results

Reduction in T_1 was seen in egg white with addition of H_2O_2 (Fig. 11.1a) and was proportional to the added H_2O_2 concentration (Fig. 11.1c). Observed changes in T_2 were within 10% (Fig.11.1b, d). In comparison, there was no H_2O_2 concentration dependent change in T_1 relaxation time of the H_2O_2 aqueous solutions (Fig. 11.2a, c).

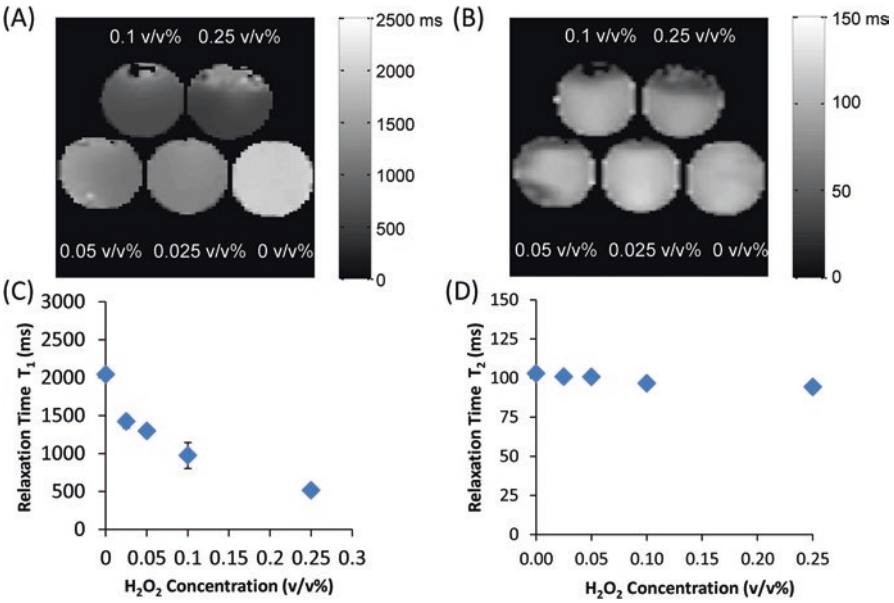

Fig. 11.1 Measurements of relaxation time T_1 and T_2 for egg white treated with various H_2O_2 concentrations. (**a**) and (**b**) are representative T_1 and T_2 time maps of treated egg white, respectively. (**c**) and (**d**) are scatter plots of T_1 and T_2 times measured from multiple experiments (n = 3), respectively. As can be seen, the relaxation time T_1 is associated with H_2O_2 concentration while the changes in T_2 time are negligible

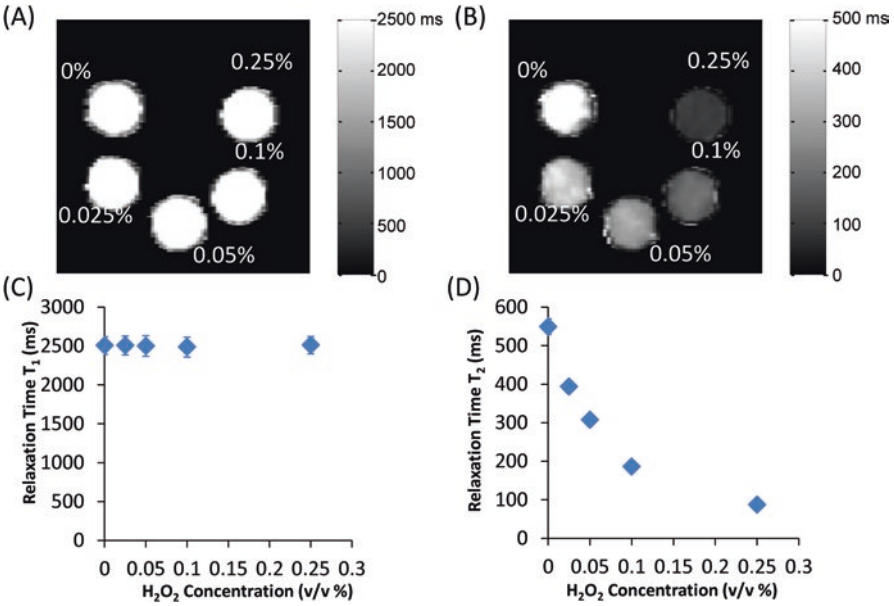

Fig. 11.2 As in Fig. 11.1, but for aqueous H_2O_2 solution. The relaxation time T_1 in diluted H_2O_2 solution has minimal reduction (**a**, **c**); however, the effect from H_2O_2 in T_2 is significant (**b**, **d**)

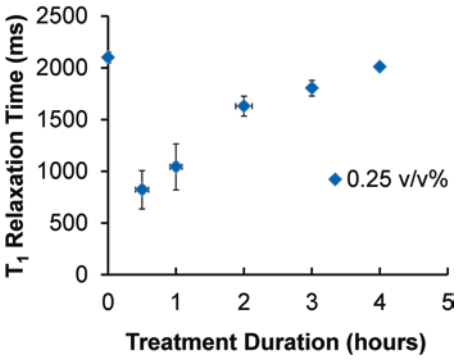

Fig. 11.3 Time dependence of T_1 changes following the addition of H_2O_2 to egg white. Significant reduction in T_1 is observed immediately after the addition of H_2O_2 to egg white. T_1 recovery is associated with ROS concentration generated during the Fenton reaction

Interestingly, reduction of relaxation time T_2 was significant and associated with H_2O_2 concentration (Fig. 11.2b, d). Figure 11.3a shows the time dependence of T_1 changes following the addition of H_2O_2 to egg white solution. After reaching the minimum, T_1 increased back to the pretreatment value. In egg white treated with 0.25 v/v% H_2O_2 at 1 h after treatment, the estimated free radical concentration was 11.6 ± 2.9 pM, assuming a relatively long lifetime (1 μs) for the free radicals [14].

4 Discussion

Non-invasive approachs to detect free radicals using endogenous contrasts are critical for the further understanding of radical-related physiological or pathological conditions. In this study, we studied the intrinsic MRI relaxation properties of free radicals (but not H_2O_2 itself) as the first step towards the development of a non-invasive MRI method in the detection of free radicals. Free radicals were continuously produced through the Fenton reaction by adding H_2O_2 in the iron-rich protein pool of egg white. We observed a significant reduction in T_1 in the treated egg white. This observation supports our hypothesis that free radicals containing unpaired electron are paramagnetic. The influence on relaxation time T_1 from H_2O_2 itself was minimal. T_2 relaxation in egg white with H_2O_2 was reduced only within 10%, but in the H_2O_2 solutions, the T_2 reduction was associated with H_2O_2 concentration. Given that free radicals possess strong paramagnetic effect, we believe T_1-weighted signal may be a potential MR contrast for the detection of in vivo free radicals.

The sensitivity to detect free radicals in egg white using T_1 weighted signal was evaluated based on the time dependent changes of T_1. As can be seen in Fig. 11.3, there was a dip immediately after adding H_2O_2 into egg white. T_1 of the treated samples was recovered to about 85 ± 4% of the baseline at ~3 h after treatment. The recovery of T_1 along with time seems to reflect progress of the Fenton reaction and thus to reflect the concentration of produced free radicals.

The estimated free radical concentration under the assumption of 1 μs lifetime for radicals in egg white treated with H_2O_2 for 1 h was within the known physiological range of radicals. If we consider a much shorter lifetime for hydroxyl radicals (e.g. 1 ns), the sensitivity of this approach based on the estimation of free radical concentration will be much higher, still remaining within reported physiological range values [15–17]. However, detection sensitivity of free radicals in vivo using T_1-weighted technique remains to be confirmed.

The final products of the Fenton reaction are water and molecular oxygen, which is also paramagnetic. We expect mild paramagnetic effect of molecular oxygen on the relaxation time T_1, since previous works have shown that the cerebrospinal fluid fully saturated with oxygen reduces T_1 about less than 10% compared to the controls under room air [18].

Iron oxide may be another confounding factor. However, superparamagnetic iron oxide particles are reported to have a significant shortening effect on T_2 and T_2* relaxation times [19]. We therefore suspect minor effects on relaxation time T_1 from the iron oxide partials.

The observed T_1-shortening effect from H_2O_2 treated egg white may be contributed from multiple free radicals, including hydroxyl radical, superoxide, and hydroperoxyl radicals. Nonetheless, the imaging phantom used in this study mimics the in vivo conditions of oxidative stress due to overproduced H_2O_2 from mitochondria.

A major challenge is the specificity of in vivo free radical detection through T_1 relaxation as this value can be altered by factors such as pathologic processes. For example, hypointense lesions on T_1-weighted image have been used as a surrogate

marker of pathological changes in patients with multiple sclerosis [20]. Given that T_1 relaxation time is intrinsically unspecific for MRI, absolute quantification of ROS using T_1 weighted contrast or T_1 mapping will be challenging. Instead, this technique may be able to detect or quantify the changes in radical production in vivo, particularly under the acute conditions when the contributions from other factors are negligible, such as in the early phase of ischemia or stroke, in the ischemia-reperfusion conditions, or under the conditions when other factors are comparable, such as different grades of the same cancer.

In contrast, relatively no change in T_2 relaxation time was found in treated egg white even though there was a signification reduction in T_2 in the PBS due to H_2O_2 treatment. Several factors may contribute to this observation. To begin with, H_2O_2 concentration in egg white reduced exponentially due to Fenton reaction. The egg white was imaged at about 1 h after H_2O_2 treatment and the remaining H_2O_2 concentration was much less than the baseline. Secondly, there was small reduction of T_2 in egg white for up to 10% (Fig. 11.1d). Finally, proteins and peptides in egg white may serve as buffers that prevent the T_2 dropping.

In conclusion, free radical-induced paramagnetic effect may be utilized as an endogenous MRI contrast for non-invasive imaging of free radicals.

Acknowledgments The authors acknowledge the Department of Radiology and the 3 T Program of the Center of Magnetic Resonance Research at the University of Illinois at Chicago College of Medicine for research support. The authors are also grateful for the valuable discussions with Lin Z. Li and He N. Xu from the Britton Chance redox lab at the University of Pennsylvania.

References

1. Barnham KJ, Masters CL, Bush AI (2004) Neurodegenerative diseases and oxidative stress. Nat Rev Drug Discov 3:205–214
2. Giorgio M, Trinei M, Miqliaccio E et al (2007) Hydrogen peroxide: a metabolic by-product or a common mediator of ageing signals? Nat Rev Mol Cell Biol 8:722–728
3. Murphy MP (2009) How mitochondria produce reactive oxygen species. Biochem J 417:1–13
4. Setsukinai K, Urano Y, Kakinuma K et al (2003) Development of novel fluorescence probes that can reliably detect reactive oxygen species and distinguish specific species. J Biol Chem 278:3170–3175
5. Xu HN, Nioka S, Glickson JD et al (2010) Quantitative mitochondrial redox imaging of breast cancer metastatic potential. J Biomed Opt 15:036010–036010-10
6. Sarracanie M, Armstrong BD, Stockmann J et al (2014) High speed 3D Overhauser-enhanced MRI using combined b-SSFP and compressed sensing. Magn Reson Med 71:735–745
7. Lurie DJ, Li H, Petryakov S, Zweier JL (2002) Development of a PEDRI free-radical imager using a 0.38 T clinical MRI system. Magn Reson Med 47:181–186
8. Emoto MC, Yamato M, Sato-Akaba H et al (2015) Brain imaging in methamphetamine-treated mice using a nitroxide contrast agent for EPR imaging of the redox status and a gadolinium contrast agent for MRI observation of blood–brain barrier function. Free Radic Res 49:1038–1047
9. Tsitovich PB, Burns PJ, McKay AM et al (2014) Redox-activated MRI contrast agents based on lanthanide and transition metal ions. J Inorg Biochem 133:143–154

10. Ratnakar SJ, Viswanathan S, Kovacs Z et al (2012) Europium(III) DOTA-tetraamide complexes as redox-active MRI sensors. J Am Chem Soc 134:5798–5800
11. Ratnakar SJ, Soesbe TC, Lumata LL et al (2013) Modulation of CEST images in vivo by T1 relaxation: a new approach in the design of responsive PARACEST agents. J Am Chem Soc 135:14904–14907
12. Wu J, Acero-Lopez A (2012) Ovotransferrin: structure, bioactivities, and preparation. Food Res Int 46:480–487
13. Lin SS, Gurol MD (1998) Catalytic decomposition of hydrogen peroxide on iron oxide: kinetics, mechanism, and implications. Environ Sci Technol 32:1417–1423
14. Attri P, Kim YH, Park DH et al (2015) Generation mechanism of hydroxyl radical species and its lifetime prediction during the plasma-initiated ultraviolet (UV) photolysis. Sci Rep 5:9332
15. Grill HP, Zweier JL, Kuppusamy P et al (1992) Direct measurement of myocardial free radical generation in an in vivo model: effects of postischemic reperfusion and treatment with human recombinant superoxide dismutase. J Am Coll Cardiol 20:1604–1611
16. Mittal M, Siddiqui MR, Tran K et al (2014) Reactive oxygen species in inflammation and tissue injury. Antioxid Redox Signal 20:1126–1167
17. Gunther MR, Sampath V, Caughey WS (1999) Potential roles of myoglobin autoxidation in myocardial ischemia-reperfusion injury. Free Radic Biol Med 26:1388–1395
18. Zaharchuk G, Busse RF, Rosenthal G et al (2006) Noninvasive oxygen partial pressure measurement of human body fluids in vivo using magnetic resonance imaging. Acad Radiol 13:1016–1024
19. Geraldes CFGC, Laurent S (2009) Classification and basic properties of contrast agents for magnetic resonance imaging. Contrast Media Mol Imaging 4:1–23
20. Parry A, Clare S, Jenkinson M et al (2002) White matter and lesion T1 relaxation times increase in parallel and correlate with disability in multiple sclerosis. J Neurol 249: 1279–1286

Chapter 12
Inter-individual Differences in Exercise-Induced Spatial Working Memory Improvement: A Near-Infrared Spectroscopy Study

Yudai Yamazaki, Daisuke Sato, Koya Yamashiro, Atsuhiro Tsubaki, Yui Yamaguchi, Nana Takehara, and Atsuo Maruyama

Abstract Acute aerobic exercise at a mild intensity improves cognitive function. However, the response to exercise exhibits inter-individual differences, and the mechanisms underlying these differences remain unclear. The objective of this study was to determine potential factors in the brain that underlie differential responses to exercise in terms of cognitive improvement using functional near-infrared spectroscopy. Fourteen healthy subjects participated in these experiments. Participants performed a low intensity cycling exercise at 30% maximal oxygen uptake (VO_{2peak}) for 10 min and performed a spatial memory task before and after exercising (5 and 30 min). The spatial memory task comprised two levels of difficulty (low: 1-dot EXERCISE, high: 3-dot EXERCISE). Cortical oxy-hemoglobin (O_2Hb) levels were recorded using near-infrared spectroscopy during both the exercise and the spatial memory task phases. Regions of interests included the dorsolateral prefrontal cortex (DLPFC), ventrolateral prefrontal cortex (VLPFC), and frontopolar area (FPA). The participants were divided into two groups depending on whether they were responders (improved task reaction time) or non-responders (no improvement). Subsequently, we analyzed the group characteristics and differences in the change in O_2Hb levels during exercise and spatial working memory tasks. Acute mild exercise significantly improved mean reaction times in the 1-dot memory task but not in the 3-dot task across the participants. In the 1-dot EXERCISE, 10 subjects were responders and four subjects were non-responders, whereas in the 3-dot EXERCISE, seven subjects were non-responders. In responders, during exercise, we found higher O_2Hb levels in the right VLPFC response for the 1-dot memory task. Acute mild exercise caused inter-individual differences in spatial memory

Y. Yamazaki (✉) • D. Sato • K. Yamashiro • A. Tsubaki • N. Takehara • A. Maruyama
Institute for Human Movement and Medical Sciences, Niigata University of Health and Welfare, Niigata, Japan
e-mail: wtm15009@nuhw.ac.jp

Y. Yamaguchi
Analytical and Measuring Instruments Division, Shimadzu Corporation, Kyoto, Japan

H.J. Halpern et al. (eds.), *Oxygen Transport to Tissue XXXIX*, Advances in Experimental Medicine and Biology 977, DOI 10.1007/978-3-319-55231-6_12

improvement, which were associated with changes in O_2Hb activity in the prefrontal area during the exercise phase but not during the actual spatial memory task. Therefore, individuals who respond with higher reactivity to mild intensity exercise in the VLPFC might obtain larger spatial working memory improvements following exercise than non-responders.

Keywords Aerobic exercise • Low intensity • Spatial working memory • Inter-individual difference • Functional near-infrared spectroscopy

1 Introduction

Functional near-infrared spectroscopy (fNIRS) is relatively less invasive and easier to administer than other functional imaging techniques. fNIRS measures the concentration changes of oxy-hemoglobin (O_2Hb) and deoxy-hemoglobin (HHb) with a fairly high temporal resolution. Previous studies have used fNIRS to detect cortical activation during daily activity (e.g., talking, walking), cognitive tasks, and aerobic exercise.

Recent studies have reported that even acute low intensity aerobic exercise improves cognitive function similar to that seen with moderate intensity exercise. Byun et al. [1] found that 10 min of low intensity pedaling increased activation in the dorsolateral prefrontal cortex (DLPFC) during the color word Stroop test and improved executive function. However, it is unknown whether acute mild intensity exercise can improve all cognitive functions because of the differential brain activity involved in each cognitive function. For example, executive function requires the activation of the DLPFC and anterior cingulate cortex (ACC) [2], whereas working memory involves not only these areas but also the parietal cortex [3] and hippocampus [4].

In this study, we investigated the effects of mild intensity exercise on a spatial working memory (SWM) task, which declines with aging. The effect of exercise on cognitive function has been found to be highly variable and depends on the subjects. Sibley and Beilock [5] found inter-individual difference in working memory improvement after moderate aerobic exercise. Unfortunately, the mechanisms for these differences remain unclear. Therefore, we aimed to explore the contributing factors by comparing the brain activity of subjects in whom acute mild intensity exercise improves spatial memory function to those who show no improvement. As O_2Hb concentration changes in the prefrontal area increases during aerobic exercise [6] and the prefrontal area plays a role in SWM [7], we hypothesized that the factors underlying individual differences involve activation of the prefrontal cortex during exercise and spatial memory tasks.

2 Methods

Fourteen healthy adults participated in this study (22 ± 0.6 years of age). All participants were right-handed. None had a history of neurological or psychiatric disease, and none were taking any medications. Informed consent was obtained from all participants. The present study was conducted in accordance with the Declaration of Helsinki and with approval granted by the ethics committee of Niigata University of Health and Welfare.

The present study consisted of a maximal graded exercise test and the main experiments. Firstly, maximal oxygen uptake (VO_{2peak}) was measured to determine the appropriate individual intensity for mild exercise, which was defined as 30% of a subject's VO_{2peak} based on the classification of physical activity intensity of the American College of Sports Medicine [8]. Secondly, two main experiments, including a control condition and a mild intensity exercise condition, were conducted with a randomized design on different days. All procedures were performed on a recumbent ergometer (RT2, Monark, Sweden). In the mild exercise condition, participants conducted the SWM task before, 5 and 30 min after exercise. The participants performed 10 min of cycling exercise on a recumbent ergometer with an individual load while maintaining their pedaling rate at 60 rpm. In the control condition, participants rested on a recumbent ergometer instead of performing exercise. A rating of perceived exertion (RPE) was assessed using Borg's scale ranging from 6 (no exertion at all) to 20 (maximal exertion) after each exercise [9].

To assess the effects of acute aerobic exercise on SWM, we used a computerized SWM task [10] on the recumbent ergometer (Fig. 12.1). First, a fixation crosshair appeared for 1000 ms, and participants were instructed to keep their eyes on the crosshair. After the fixation period, one or three black dots appeared at random locations on the screen for 500 ms. The dots were removed from the display for a period of 3000 ms. During this time, participants were instructed to try to remember the location of the previously presented black dots. At the end of the 3000 ms delay, a red dot appeared on the screen in either one of the same locations as the target dots

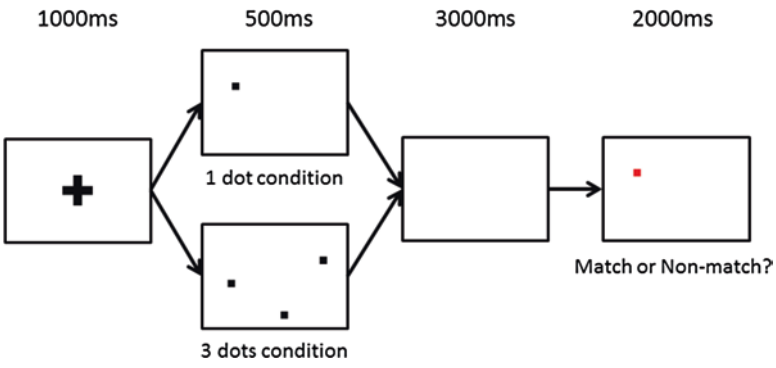

Fig. 12.1 The protocol for the SWM task

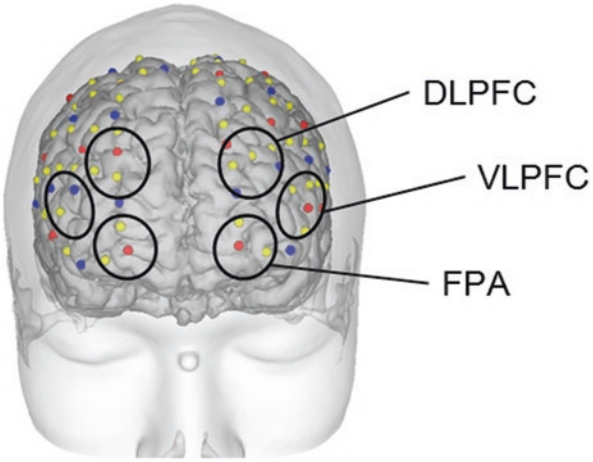

Fig. 12.2 Regions of interests (ROIs) in the present study. *DLPFC* dorsolateral prefrontal cortex, *VLPFC* ventrolateral prefrontal cortex, *FPA* frontopolar area

(the matched condition) or at a different location (the non-matched condition). Participants had 2000 ms to respond to the red dot by pressing one of two buttons on the response pad, the left button for a matched trial and the right button for a non-matched trial. The red dot disappeared after any response from participants or after 2000 ms. In this study, the inter stimulus interval was set at 13.5 s to investigate the cortical response of hemodynamic activity in the prefrontal area. Twenty trials were presented for both set sizes (one or three locations), with 10 trials as matched trials and 10 trials as non-matched trials. Participants were instructed to respond as quickly and accurately as possible. Several practice trials were performed before the baseline task was begun to acquaint the participants with the task instructions and responses. The main outcome measures of interest were task accuracy and reaction time for each session and time point.

fNIRS (LABNIRS, Shimadzu, Japan) was used to measure the concentration changes of O_2Hb and HHb in the regions of interest (ROIs). We used 39 probes (20 sources and 19 detectors), resulting in 52 measurements per channel, and these probes were distributed from the prefrontal area to the sensorimotor area. The inter-probe distance was 3 cm, and the sampling rate was set at 60 ms. Among the 52 channels, we selected those on the left and right DLPFC, ventrolateral prefrontal cortex (VLPFC), and frontopolar area (FPA) as ROIs (Fig. 12.2). Each ROI was defined in each participant by overlay of individual MRI images on the 3D information of probe placement by using fusion software (Shimadzu, Japan). We focused on the changes in O_2Hb as this parameter is considered to be a more robust fNIRS parameter [11]. O_2Hb levels were measured at baseline in the 120 s before starting the exercise, during the 10-min exercise period, for 150 s after finishing the exercise, and during the SWM task. The average levels during the 120 s before the exercise were used as the baseline, and we calculated the O_2Hb concentration changes from baseline by subtracting the average baseline value from each value. The temporal window of analysis in the spatial memory task was from 2 s before

presenting the fixation crosshair to 13.5 s after any response from the participants, and these data were averaged. To explore the factors underlying inter-individual differences in exercise-induced SWM improvement, participants were divided into two groups based on responders and non-responders to the exercise. Responders were defined as the participants who showed improved task performance for each task condition at 5 min after exercise. We compared the peak values of O_2Hb concentrations during exercise and the spatial memory task. Four peak values were selected, including: (1) the minimum peak value during exercise, which is observed immediately after starting exercise; (2) the maximum peak value during exercise; (3) peak to peak value through the intervention (i.e., including the period following exercise); and (4) the peak value during the spatial memory task.

The reaction time (RT) and error rate for the SWM tasks were analyzed using a repeated measures two-way (session × time) analysis of variance (ANOVA) (IBM SPSS Version 18, USA). When main effects were identified, a post hoc test of significant differences was performed. To explore the factors underlying inter-individual differences in spatial memory improvement, each fNIRS peak value was analyzed using independent t-tests (responder × non-responder). The significance level was set at ($p < 0.05$).

3 Results

Figure 12.3 shows the changes in RT for the SWM task on the individual and group basis. Acute mild intensity aerobic exercise significantly improved mean RT in the 1-dot condition across all participants ($p < 0.05$) (Fig. 12.3a). However, no significant main effects or interactions were found in the 3-dot condition across the study population (Fig. 12.3b). However, individual responses in each of the versions of the SWM task showed variability. In the 1-dot condition, there were 10 responders and 4 non-responders. In the 3-dot condition, there were 7

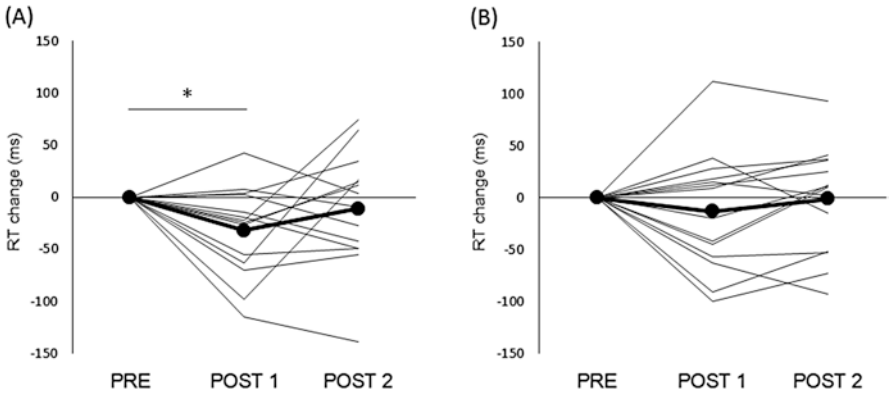

Fig. 12.3 Changes in reaction time during the 1-dot condition (**a**) and the 3-dot condition (**b**) in the SWM task on the individual and group basis

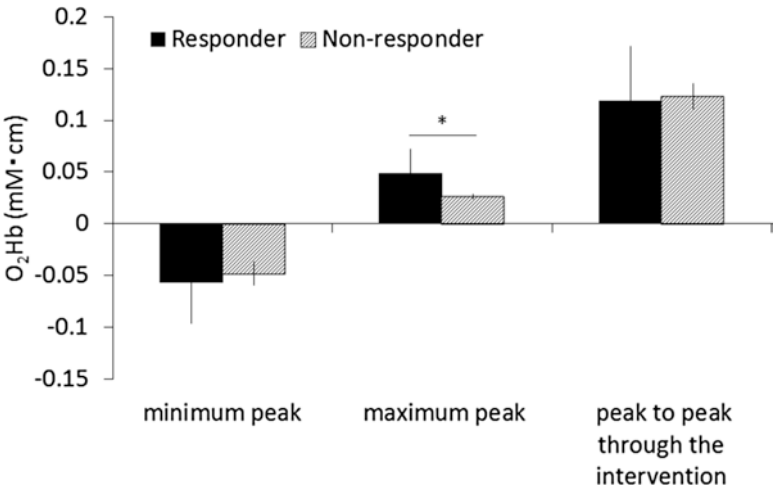

Fig. 12.4 O_2Hb peak values in the right VLPFC during exercise in responders and non-responders

responders and 7 non-responders. The peak value during exercise in the right VLPFC was significantly higher in the responders than in the non-responders identified in the 1-dot condition ($p < 0.05$) (Fig. 12.4). However, there were no significant differences in the other peak values in any ROI during either the exercise period or the SWM task.

4 Discussion

The results of the present study showed that 10 min of mild intensity exercise improved RT in the 1-dot condition in the SWM task although RT did not change for the 3-dot condition. One explanation for this result is that the difficulty of the task influenced the effect of mild intensity exercise on SWM. In the 3-dot condition, participants were required to remember the location of more dots than in the 1-dot condition. Therefore, the memory load of the 3-dot condition may be higher than that of the 1-dot condition. In fact, Nagel et al. [12] demonstrated that increasing the number of dots in a spatial delayed matching task led to a decline in behavioral performance and an increase in the BOLD signal in the DLPFC, premotor cortex, and posterior parietal cortex. The results of the present study suggest that acute mild intensity exercise may have beneficial effects on SWM for easier tasks, whereas this effect is not observed in a more difficult task. Considering that the relationships between the exercise intensity and the improvement in cognitive function follow an inverted U-shape [13], an increase in exercise intensity may benefit the improvement of more complex task performance.

In the present study, we focused on understanding the inter-individual differences in the effects of acute mild intensity exercise on SWM improvement. The results showed higher inter-individual differences in the 3-dot condition than in the 1-dot condition. Furthermore, O_2Hb in the prefrontal area during exercise was different between responders and non-responders. The peak value in the right VLPFC during the exercise phase was at a higher level in the responders identified during the 1-dot condition compared to the non-responders. Previous studies observed that the VLPFC was activated during SWM tasks [14], and activation in the prefrontal area modulated SWM performance [15]. Therefore, the present results would indicate that the participants with higher reactivity to mild intensity exercise in this brain area could obtain larger SWM improvements following exercise.

With regard to O_2Hb activity during the SWM task, we did not find significant differences between responders and non-responders. As described in a recent literature review [16], the relationship between prefrontal activation and cognitive performance is still being discussed. One explanation for the lack of a relationship between brain activation and SWM performance is that other brain areas not examined in the present study were involved in the SWM task. SWM function requires the involvement of the hippocampus, parietal cortex, and medial prefrontal cortex as well as the DLPFC and VLPFC [2–4], unlike executive function (e.g., inhibition), which requires the specific activation of the DLPFC and ACC. Indeed, previous studies reported that SWM performance correlates with various brain activity, even if not related to frontal cortical activity [16]. Unfortunately, fNIRS used in the present study could not detect the activity in the other brain areas, such as the hippocampus and medial prefrontal cortex. Future work is needed to investigate the individual differences using various neuroimaging techniques.

In conclusion, acute mild exercise resulted in individual differences in improvements in spatial working memory, which were associated with changes in O_2Hb activity in the prefrontal area during the exercise but not during the actual spatial memory task. These results suggest that higher activity in the VLPFC in response to mild exercise may contribute to individual differences in the response to exercise-induced cognitive performance.

References

1. Byun K, Hyodo K, Suwabe K, Ochi G, Sakairi Y, Kato M et al (2014) Positive effect of acute mild exercise on executive function via arousal-related prefrontal activations: an fNIRS study. NeuroImage 98:336–345
2. MacDonald AW, Cohen JD, Stenger VA, Carter CS (2000) Dissociating the role of the dorsolateral prefrontal and anterior cingulate cortex in cognitive control. Science 288:1835–1838
3. Bray S, Almas R, Arnold AE, Iaria G, MacQueen G (2015) Intraparietal sulcus activity and functional connectivity supporting spatial working memory manipulation. Cereb Cortex 25:1252–1264
4. Spellman T, Rigotti M, Ahmari SE, Fusi S, Gogos JA, Gordon JA (2015) Hippocampal-prefrontal input supports spatial encoding in working memory. Nature 522:309–314

5. Sibley BA, Beilock SL (2007) Exercise and working memory: an individual differences investigation. J Sport Exerc Psychol 29:783–791
6. Ide K, Horn A, Secher NH (1999) Cerebral metabolic response to submaximal exercise. J Appl Physiol (1985) 87:1604–1608
7. D'Esposito M, Aguirre GK, Zarahn E, Ballard D, Shin RK, Lease J (1998) Functional MRI studies of spatial and nonspatial working memory. Brain Res Cogn Brain Res 7:1–13
8. Thompson PD, Arena R, Riebe D, Pescatello LS, American College of Sports Medicine (2013) ACSM's new preparticipation health screening recommendations from ACSM's guidelines for exercise testing and prescription, ninth edition. Curr Sports Med Rep 12:215–217
9. Borg GA (1982) Psychophysical bases of perceived exertion. Med Sci Sports Exerc 14:377–381
10. Erickson KI, Prakash RS, Voss MW, Chaddock L, Hu L, Morris KS et al (2009) Aerobic fitness is associated with hippocampal volume in elderly humans. Hippocampus 19:1030–1039
11. Plichta MM, Herrmann MJ, Baehne CG, Ehlis AC, Richter MM, Pauli P et al (2006) Event-related functional near-infrared spectroscopy (fNIRS): are the measurements reliable? NeuroImage 31:116–124
12. Nagel IE, Preuschhof C, Li SC, Nyberg L, Bäckman L, Lindenberger U et al (2009) Performance level modulates adult age differences in brain activation during spatial working memory. Proc Natl Acad Sci U S A 106:22552–22557
13. Kamijo K, Nishihira Y, Hatta A, Kaneda T, Wasaka T, Kida T et al (2004) Differential influences of exercise intensity on information processing in the central nervous system. Eur J Appl Physiol 92:305–311
14. Owen AM, Evans AC, Petrides M (1996) Evidence for a two-stage model of spatial working memory processing within the lateral frontal cortex: a positron emission tomography study. Cereb Cortex 6:31–38
15. Wu YJ, Tseng P, Chang CF, Pai MC, Hsu KS, Lin CC et al (2014) Modulating the interference effect on spatial working memory by applying transcranial direct current stimulation over the right dorsolateral prefrontal cortex. Brain Cogn 91:87–94
16. Eyler LT, Sherzai A, Kaup AR, Jeste DV (2011) A review of functional brain imaging correlates of successful cognitive aging. Biol Psychiatry 70:115–122

Part II
Cancer Oxygenation and Metabolism

Chapter 13
Tumor Oxygenation Status: Facts and Fallacies

Peter Vaupel and Arnulf Mayer

Abstract In this chapter we allude to a series of facts and fallacies often encountered in the description of tumor hypoxia, a relevant trait of the tumor microenvironment and a paramount driver of tumor aggressiveness and treatment resistance. The critical role of diffusion distances, terminological inconsistencies considering O_2 partial pressures vs. O_2 concentrations and with it the use of inept units, the impact of O_2 depletion on proliferation and cell viability, the switch in the Warburg dogma, the distribution of hypoxic subvolumes within a tumor, the involvement of O_2 diffusion shunts in the development of chronic hypoxia, and the role of endogenous biomarkers as surrogates for the assessment of hypoxia are discussed in more detail. Special emphasis is put on the clinical relevance of these misconceptions and misinterpretations and their impact on the assessment of hypoxia as well as hypoxia-targeted treatment planning.

Keywords Tumor hypoxia • Oxygen diffusion distances • Hypoxia- inducible factor (HIF) • Hypoxia- inducible biomarkers • Warburg dogma

1 Introduction

In the past two decades, hypoxia has been proposed as a new hallmark of cancer with substantial clinical relevance [1–3] since it exerts a strong impact on gene expression patterns and may lead to the exacerbation of genomic instability and the occurrence of mutations. The majority of the hypoxia-driven changes in gene expression are orchestrated by activation of the hypoxia-inducible factors (HIFs). HIF-1α is the key transcription factor playing a multifaceted role in providing *inter alia* survival advantages for tumor cells, maintenance of cancer cell stemness,

P. Vaupel (✉) • A. Mayer
Department of Radiation Oncology and Radiotherapy, Tumor Pathophysiology Division, University Medical Center, Mainz, Germany
e-mail: vaupel@uni-mainz.de

H.J. Halpern et al. (eds.), *Oxygen Transport to Tissue XXXIX*, Advances in Experimental Medicine and Biology 977, DOI 10.1007/978-3-319-55231-6_13

fostering tumor-promoting responses, resistance to the consequences of oxygen (O_2) and nutrient deprivation, thus leading to a more malignant phenotype [4]. The latter HIF-induced adaptation also includes a metabolic reprogramming and an adenosine-mediated attenuation of antitumor immune responses [5].

Hypoxia also adversely influences the response of tumor cells to standard radiotherapy, some forms of chemotherapy, photodynamic treatments and antitumor immunotherapies. All processes listed above may contribute to malignant progression, i.e., to a more aggressive growth behavior, and an increased propensity for local recurrence and metastasis. For these reasons, hypoxia is strongly correlated with poor patient prognosis [2], and thus should be monitored at diagnosis and during the course of treatment.

Investigations of the role of diffusion-limited hypoxia in the treatment response of tumors stretch back more than 60 years [6]. Following the introduction of exogenous hypoxia-markers and positron-emission tomography (PET, [7]) as well as the pO_2-histography system for direct pO_2 measurements [8], a systematic assessment tumor oxygenation status and the detection of tumor hypoxia became feasible in the clinical setting. The clinical use of these hypoxia-detection techniques was paralleled by the discovery and characterization of HIF [9]. The number of publications on tumor oxygenation and tumor hypoxia has exponentially risen during the last 25 years reaching approx. 4000 reports in 2014/2015 (Fig. 13.1). Despite this enormously increasing body of information and considering the experimental/preclinical and clinical relevance there are still many unsolved problems when describing the development and assessment of tumor hypoxia,

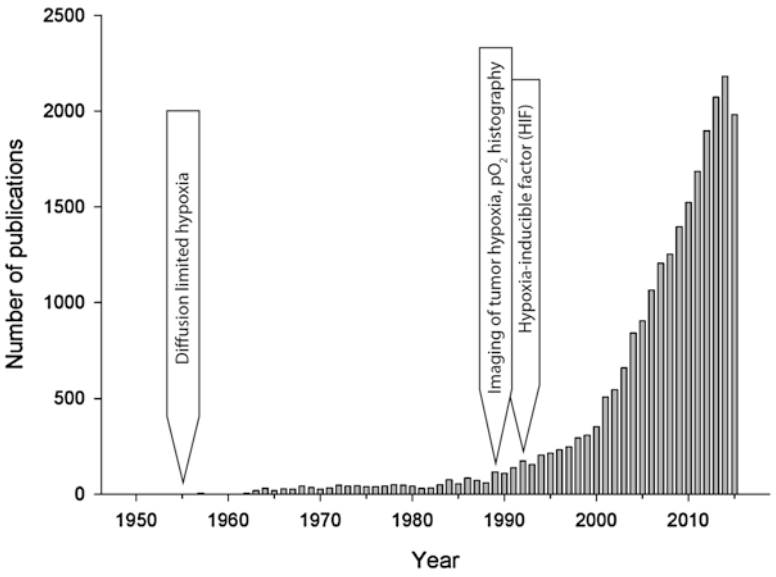

Fig. 13.1 Exponentially increasing number of publications on tumor hypoxia since 1955. *Arrows* indicate "milestone" reports advancing research in the field

partly due to the extreme heterogeneities within and between tumors. Furthermore, many inconsistencies in terminology or use of (inept) units and in the interpretation of data are still prevalent. For this reason, in this article some facts are recalled and fallacies are critically discussed.

2 Facts and Fallacies

In the following sections some of the major misconceptions are highlighted and solutions are suggested.

2.1 Can Typical Diffusion Distances Be Defined in Malignant Tumors?

Considering generally accepted diffusion models for normal and malignant tissues (e.g., Krogh- or Hill-model), both longitudinal (from the arterial to the venous end of microvessels) and radial O_2 diffusion gradients (from microvessels into the surrounding cell layers) exist. The slope of these gradients normally depends on the O_2 availability (i.e., the O_2 transport capacity of the blood × the microvascular flow rate) and the O_2 extraction rate. The latter is primarily determined by the cellular O_2 consumption rate, the O_2 diffusivity and the cell packing density. Taking all variables into account and considering all pathophysiologies (e.g., O_2 shunt diffusion, variability in microvessel lengths, abnormal microvessel architecture) there is clear evidence that singular "typical" diffusion distances cannot exist in malignant tumors. Instead, a broad distribution ("continuum") of O_2 diffusion distances is usually observed (Fig. 13.2). We suggest that statements considering singular "typical" diffusion distances should be avoided because they are misleading due to the extreme heterogeneity of the microvascular density (MVD) within individual tumors. In addition, tortuous, glomeruloid microvasculatures (triggered by VEGF overexpression) can mimic high MVD in 2-dimensional histological sections. These structures should not be regarded as morphological correlates of vascular "hotspots".

2.2 Equivocal Conversion of In Vivo O_2 Partial Pressures into O_2 Concentrations

When reviewing the biological role of hypoxia in malignant tumors, authors often convert – without any need – *in vivo* O_2 partial pressures (pO_2 values) originally measured in tumors, into O_2 concentrations (cO_2) using either Dalton's law (only valid for gas mixtures within the airways!) or Henry's law for gases dissolved in

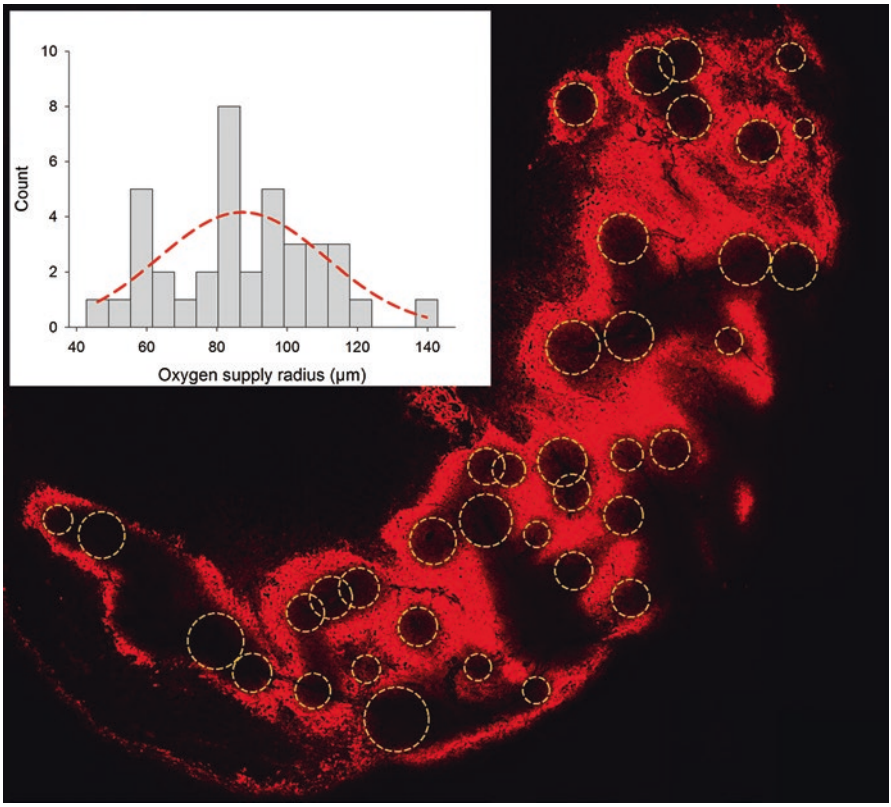

Fig. 13.2 Delineation of oxygen supply radii in a FaDu xenograft using pimonidazole staining (*red*). *Inset*: frequency distribution: median radius: 81 µm, range: 41–142 µm

solutions (e.g., [10–12]), which cannot describe the relationship between partial pressures and concentrations of gases within heterogeneous media such as tissues with lipid-rich membranes, the cytosol and the extracellular space, the latter with a high content of free water. We suggest that the conversion of measured pO_2 values into cO_2 values should be strictly avoided since Bunsen's solubility coefficient is (a) highly dependent on the tissue water content, and (b) not known for heterogeneous tumor tissues. In this context, it has to be mentioned that authors often use "local O_2 concentrations" by mistake, although pO_2 values have been measured in their study (e.g., [10, 13]).

2.3 Oxygen Diffusivity in Normal Tissues Versus Malignant Tumors

Modelling O_2 transport in malignant tumors and simulation of tumor hypoxia in non-invasive molecular imaging modalities requires the computational solution of partial differential equations (PDEs). When using PDEs, the O_2 diffusion coefficient D has to be known. In many instances, for simplification, D values for normal tissues have been used, although D is also highly dependent on the tissue water content [14]. Since malignant tumors have an interstitial water space approx. 3 times larger than normal tissues and on average 10% higher water contents, D in tumors is significantly higher than in normal tissues [15], and thus must be applied when diffusional fluxes in tumors are evaluated. This potential pitfall should be considered in modelling studies.

2.4 O_2 Depletion Merely Limits Proliferation Rather than Causing Tumor Necrosis

In their seminal study on human lung cancers, Thomlinson and Gray [6] have suggested that surpassing critical diffusion distances for O_2 (160–180 μm) may be the primary factor for the development of necrosis. Using more appropriate values for O_2 diffusion coefficients and O_2 consumption rates, we have identified much smaller diffusion distances (<75 μm for breast cancer [15, 16]). In contrast, critical glucose diffusion distances are approx. twofold larger. Based on these data, we conclude that O_2 depletion seems to be the limiting factor for a high proliferation rate of cancer cells (at least for a majority of solid tumors). Additional deprivation of the major nutrient glucose may be the limiting factor for tumor cell viability. This concept is substantially supported by data from Tannock [17] and our own immunohistochemical study showing that all proliferating cells were located within a distance <82 μm from the nearest blood vessel (human FaDu xenografts, Mayer and Vaupel, unpublished results). Therefore, when investigating the impact of tumor hypoxia on cell proliferation and viability, the modulating effect of different glucose concentrations should be taken into account.

2.5 Switching the Warburg Dogma

The original Warburg hypothesis [18] postulating that defective mitochondrial morphology and/or respiratory dysfunction force cancer cells to generate energy with a poor (but much faster) ATP yield through (aerobic) glycolysis appears to be untenable (for a review see [19]). During the last decade, experimental evidence has accumulated that the Warburg effect is not caused by defective

mitochondria (i.e., defective OXPHOS). Instead, it seems to be related to a metabolic reprogramming as part of hypoxia response mechanisms triggered by HIFs, activated oncogenes and mutant tumor suppressors. According to this concept, increased glycolysis allows the diversion of glycolytic intermediates into various biosynthetic pathways (e.g., generation of nucleosides, fatty and amino acids) facilitating the biosynthetic programs that are required for sustained cell proliferation, migration and invasion [20]. Furthermore, aerobic glycolysis provides essential precursors for glutathione-dependent antioxidant capacities to attenuate hypoxic ROS generation. HIF also mediates the adaptation of cancer cells to hypoxia by downregulation of the Krebs cycle and mitochondrial O_2 consumption through inhibition of pyruvate dehydrogenase and facilitation of mitochondrial autophagy [21]. Researchers should exert great caution when anticipating a "cancer-specific metabolism" when what is actually observed may often represent functional plasticity under cellular stress.

Addendum Unnoticed by most of the supporters of his original concept, Warburg himself conceded in 1962 [22] that the respiration of cancer cells is in fact not compromised, thus cutting back on his initial "respiration injury" theory.

2.6 *Hypoxic Subvolumes Are Heterogeneously Distributed Over the Entire Tumor*

Based on experiments using rapidly growing tumors in rodents, a widespread concept claims that malignant tumors usually develop hypoxic and necrotic cores which are surrounded by a viable periphery. Indeed, many human tumors follow this archetypical pattern (e.g., glioblastoma). However, assessment of the viable subvolumes of many different tumor types at the microscopic level has shown the presence of hypoxic microregions which are typically distributed over the entire viable tumor mass [8, 23]. These hypoxic microregions are organized on a submillimeter scale and exhibit steep gradients between well oxygenated and hypoxic parts (Fig. 13.3). They may additionally show temporal variations on a short scale (acute hypoxia). These insights have important clinical implications, e.g., for the concept of dose painting in IMRT techniques, because radiobiologically relevant hypoxia exists at a scale which cannot be selectively irradiated even with the most precise of modern radiotherapy approaches.

2.7 *Oxygen Diffusion Shunt: A Significant Factor in Hypoxia Development*

In malignant tumors, extremely elongated U-shaped microvessels are common. In these hairpin-like vessels O_2 diffusion shunt is a relevant factor contributing to the development of hypoxia on a submillimeter scale prominent around the tip of the

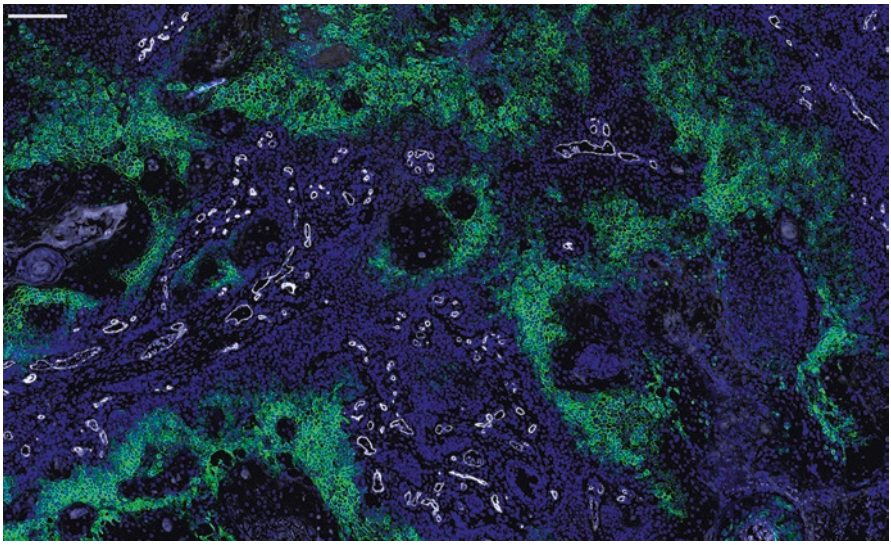

Fig. 13.3 Heterogeneity of hypoxic regions on a submillimeter scale. Steep gradients between well-oxygenated areas (*blue* cell nuclei, DAPI) and hypoxic areas (*green* membrane staining, anti-CA IX) are observed. Microvessels are shown in white (anti-CD 34). Scale bar: 200 µm

vessel loop. This mechanism resembles the O_2 diffusion shunt ("O_2 short circuit") in the renal medulla with high pO_2 values (approx. 40 mmHg) in the outer medulla, and poor oxygenation (8–10 mmHg) around the tip of the loop in the inner medulla, which meets its energy requirements by glycolysis. The mechanism described may significantly contribute to the pathogenesis of chronic hypoxia in tumors with commonly occurring elongated hairpin-like vessels and should not be misinterpreted as evidence for acute hypoxia.

2.8 Role of Hypoxia Markers as Surrogates Describing Tumor Oxygenation

Recently, directly measured tumor pO_2 values using oxygen electrodes, data derived from hypoxia imaging procedures and the expression of hypoxia- inducible biomarkers have been correlated, although these different techniques assess hypoxia on different scales. In imaging studies (a) the spatial resolution is too low with regard to the spatial dimension of microregional heterogeneities and (b) different biologically relevant levels of hypoxia cannot be discriminated, thus excluding correlations

with oxygen electrode measurements. Endogenous biomarkers cannot substitute directly for pO_2 measurements mainly since the HIF- response to O_2 depletion is cell-type dependent and thus precludes quantitative correlations between the expression intensity of the biomarkers and absolute O_2 levels. Additionally, the expression of endogenous hypoxia-associated markers is modulated by non-hypoxic intracellular signalling (e.g., mTOR signalling).

3 Conclusion

In this article we have alluded to a series of experimental facts of cancer research and fundamentals in Respiration Physiology/Pathophysiology occasionally not taken into account by some scientists in the field of oxygen transport to solid tumors and detection/assessment of tumor hypoxia. Possible strategies to avoid these pitfalls have been outlined.

Acknowledgment The authors would like to thank Professor Gabriele Multhoff, Dept. Radiooncology and Radiotherapy, Klinikum rechts der Isar, Technical University Munich, for providing FaDu tumors for hypoxia distance metrics.

References

1. Vaupel P, Mayer A, Höckel M (2004) Tumor hypoxia and malignant progression. Methods Enzymol 381:335–354
2. Vaupel P, Mayer A (2007) Hypoxia in cancer: significance and impact on clinical outcome. Cancer Metastasis Rev 26(2):225–239
3. Ruan K, Song G, Ouyang G (2009) Role of hypoxia in the hallmarks of human cancer. J Cell Biochem 107(6):1053–1062
4. Mayer A, Vaupel P (2013) Hypoxia, lactate accumulation, and acidosis: siblings or accomplices driving tumor progression and resistance to therapy? Adv Exp Med Biol 789:203–209
5. Vaupel P, Mayer A (2016) Hypoxia-driven adenosine accumulation: a crucial microenvironmental factor promoting tumor progression. Adv Exp Med Biol 876:177–183
6. Thomlinson RH, Gray LH (1955) The histological structure of some human lung cancers and the possible implications for radiotherapy. Br J Cancer 9(4):539–549
7. Koh WJ, Rasey JS, Evans ML et al (1992) Imaging of hypoxia in human tumors with [F-18] fluoromisonidazole. Int J Radiat Oncol Biol Phys 22(1):199–212
8. Vaupel P, Schlenger K, Knoop C et al (1991) Oxygenation of human tumors: evaluation of tissue oxygen distribution in breast cancers by computerized O_2 tension measurements. Cancer Res 51(12):3316–3322
9. Wang GL, Semenza GL (1993) Characterization of hypoxia-inducible factor 1 and regulation of DNA binding activity by hypoxia. J Biol Chem 268(29):21513–21518
10. Carreau A, El Hafny-Rahbi B, Matejuk A et al (2011) Why is the partial oxygen pressure of human tissues a crucial parameter? Small molecules and hypoxia. J Cell Mol Med 15(6):1239–1253
11. Muz B, de la Puente P, Azab F et al (2015) The role of hypoxia in cancer progression, angiogenesis, metastasis, and resistance to therapy. Hypoxia (Auckl) 3:83–92

12. Brahimi-Horn MC, Laferrière J, Mazure N et al (2008) Hypoxia and tumour angiogenesis. In: Marmé D, Fusenig N (eds) Tumor angiogenesis: basic mechanisms and cancer therapy. Springer, Berlin\Heidelberg, pp 171–194. doi:10.1007/978-3-540-33177-3_10
13. Spencer JA, Ferraro F, Roussakis E et al (2014) Direct measurement of local oxygen concentration in the bone marrow of live animals. Nature 508(7495):269–273
14. Vaupel P (1976) Effect of percentual water content in tissues and liquids on the diffusion coefficients of O_2, CO_2, N_2, and H_2. Pflügers Arch 361(2):201–204
15. Vaupel P (2004) Tumor microenvironmental physiology and its implications for radiation oncology. Semin Radiat Oncol 14(3):198–206
16. Vaupel P (1990) Oxygenation of human tumors. Strahlenther Onkol 166(6):377–386
17. Tannock IF (1968) The relation between cell proliferation and the vascular system in a transplanted mouse mammary tumour. Br J Cancer 22(2):258–273
18. Warburg O (1956) On respiratory impairment in cancer cells. Science 124(3215):269–270
19. Vaupel P, Mayer A (2012) Availability, not respiratory capacity governs oxygen consumption of solid tumors. Int J Biochem Cell Biol 44(9):1477–1481
20. Gentric G, Mieulet V, Mechta-Grigoriou F (2016) Heterogeneity in cancer metabolism: new concepts in an old field. Antioxid Redox Signal. doi:10.1089/ars.2016.6750
21. Semenza GL (2010) HIF-1: upstream and downstream of cancer metabolism. Curr Opin Genet Dev 20(1):51–56
22. Warburg OH (1962) New methods of cell physiology. Applied to cancer, photosynthesis, and mechanism of X-ray action. Interscience, New York
23. Grosu AL, Souvatzoglou M, Röper B et al (2007) Hypoxia imaging with FAZA-PET and theoretical considerations with regard to dose painting for individualization of radiotherapy in patients with head and neck cancer. Int J Radiat Oncol Biol Phys 69(2):541–551

Chapter 14
Multiparametric Analysis of the Tumor Microenvironment: Hypoxia Markers and Beyond

Arnulf Mayer and Peter Vaupel

Abstract We have established a novel *in situ* protein analysis pipeline, which is built upon highly sensitive, multichannel immunofluorescent staining of paraffin sections of human and xenografted tumor tissue. Specimens are digitized using slide scanners equipped with suitable light sources and fluorescence filter combinations. Resulting digital images are subsequently subjected to quantitative image analysis using a primarily object-based approach, which comprises segmentation of single cells or higher-order structures (e.g., blood vessels), cell shape approximation, measurement of signal intensities in individual fluorescent channels and correlation of these data with positional information for each object. Our approach could be particularly useful for the study of the hypoxic tumor microenvironment as it can be utilized to systematically explore the influence of spatial factors on cell phenotypes, e.g., the distance of a given cell type from the nearest blood vessel on the cellular expression of hypoxia-associated biomarkers and other proteins reflecting their specific state of activation or function. In this report, we outline the basic methodology and provide an outlook on possible use cases.

Keywords Tumor microenvironment • Tumor hypoxia • Multiparametric image analysis • Immunofluorescence • Immunohistochemistry

1 Introduction

A thorough characterization of disease mechanisms (e.g., the relevance of certain driver mutations) is an absolute requirement for the success of targeted strategies in cancer therapy. In a series of publications from the Cancer Genome Atlas Research Network (TCGA, e.g., [1]) this has been achieved using modern genome analysis methods. As an

A. Mayer (✉) • P. Vaupel
Department of Radiation Oncology and Radiotherapy, Tumor Pathophysiology Division, University Medical Center, Mainz, Germany
e-mail: arnmayer@uni-mainz.de; vaupel@uni-mainz.de

H.J. Halpern et al. (eds.), *Oxygen Transport to Tissue XXXIX*, Advances in Experimental Medicine and Biology 977, DOI 10.1007/978-3-319-55231-6_14

additional layer of complexity, however, solid malignant tumors are exceptionally heterogeneous, leading to a situation where a tailored therapeutic approach may be successful in some tumor subvolumes but ineffective in others. An important part of this tumor heterogeneity is caused by the pathological architecture of tumor microvessels and enlarged diffusion distances leading to hypoxia, nutrient deprivation, extracellular acidosis and metabolic waste product accumulation. This characteristic solid tumor microenvironment brings along substantial changes in gene expression, the proteome and a resultant phenotype of tumor cells, which may mediate resistance not only against ionizing irradiation and cytotoxic chemotherapy but also against molecularly targeted and immune-stimulatory approaches. In order to develop successful strategies to overcome this major obstacle against cancer therapy, an *ex vivo* analysis of the microenvironment of human tumors is necessary both to select patients for intensified or de-escalated treatment protocols and to develop specific countermeasures. A method suitable to contribute to the accomplishment of this goal is outlined in this report.

2 Dimensions of Tumor Heterogeneity

Tumor heterogeneity exists at least at three levels: (i) genetic or clonal, (ii) cellular and (iii) architectural. *Clonal heterogeneity*, the result of an evolutionary process originally outlined for tumor cell populations by Peter Nowell [2], has now been unequivocally proven to exist using a combination of whole-exome multiregion spatial sequencing, single nucleotide polymorphism analysis and messenger RNA expression profiling [3]. Diverging genomic constitution of individual manifestations of a tumor within a single patient, i.e., the primary tumor and metastases in different organs, can indeed partially explain incomplete or mixed responses to therapy, which are often observed in the clinic. A prominent example is the development of T790 M resistance mutations against small molecule inhibition of EGFR in lung cancer [4]. Some manifestations of therapeutic resistance are, however, not explained by genomic maladaptation. Instead, they have been shown to arise from functional mechanisms. The term *cellular heterogeneity* refers to the fact that solid malignant tumors are complex tissues composed of many different cell types, which have been demonstrated to actively contribute to tumor growth instead of acting as a passive barrier to cancer cell invasion or as innocent bystanders. Among these cancer promoting cells are activated fibroblasts (“cancer-associated fibroblasts”, [5]), endothelial cells [6], macrophages [7] and regulatory T-cells [8]. Contrary to the depiction of malignant tumors in many textbooks and review articles as rather homogeneous masses of tumor cells (e.g., [9]), the true cellular complexity of solid malignancies is immediately apparent under the microscope and thus well known to the pathologist, but surprisingly less appreciated by many other oncology disciplines. Finally, *architectural heterogeneity* refers to the different degree of abnormalities of higher-order structures. A prominent example of particular relevance to the topic of this communication is the different degree of the abnormality of the tumor blood vessels. It ranges from greatly increased vascular density in isolated

"hotspots" to large, almost avascular areas in which substantial hypoxia develops and from nearly normal configuration of individual tumor microvessels to highly irregular arrangement, orientation and ultrastructure. Many other important aspects also fall in this category, including – but not limited – to the individual hierarchy and localization of the stem cell compartment, patterns of cancer cell invasion (e.g., pushing borders vs. infiltrating single cells) and the degree of immune cell infiltration and activity. Both cellular and architectural heterogeneity can be assessed using morphometric and immunohistochemical methods, e.g., by identifying certain cell types using antibodies against characteristic cell surface markers. In fact, these methods have already experienced broad application in clinically oriented basic oncology research. However, the definition of cellular phenotypes, the identification of activation states and the exploration of spatial patterns of different cell types relative to each other or in relation to higher order structures of the tissue has been severely hampered by the fact that multiplex staining, although certainly possible [10, 11], has always been notoriously difficult to achieve with traditional immunohistochemical methods and even harder to standardize for large research projects. We have thus developed novel approaches to overcome traditional obstacles and enable a truly multiparametric analysis of the tumor microenvironment.

3 Multiparametric Immunohistochemistry in Registered Serial Sections (MIRSS)

High precision microtomes (in the hands of experienced technicians) enable the preparation of very thin (i.e., 3–5 μm) serial paraffin sections as raw material for immunohistochemistry (IHC). When combining this technique with digitization of specimens using high resolution slide scanners and advanced elastic image registration algorithms (e.g., [12]), we have shown that it is possible to follow individual cells through several serial sections and use different IHC markers for each (Fig. 14.1). We have recently demonstrated the feasibility and relevance of this approach in an analysis of the expression of hypoxia-associated markers in squamous cell carcinomas of the vulva, which provided important insights into the pathophysiology of this disease [13]. Although fascinating, this technique has a number of weaknesses, which have to be taken into account. First, the method is quite labor intensive when manual staining is performed. Furthermore, high precision sectioning can be very demanding and sometimes even impossible in "difficult" tissue leading to artefacts which thwart successful image registration. Even though individual sections are thin, a substantial number of sections are needed for multiplex staining, and this can be a problem when only limited amounts of tissue are available. Most importantly, however, segmentation of individual cells, as the prerequisite of single-cell based analyses, turned out to be quite challenging in some types of tissue. Methodological work from our laboratory showed that segmentation of single cells using fluorescence staining of cell nuclei, although far from trivial, provides much more reproducible results.

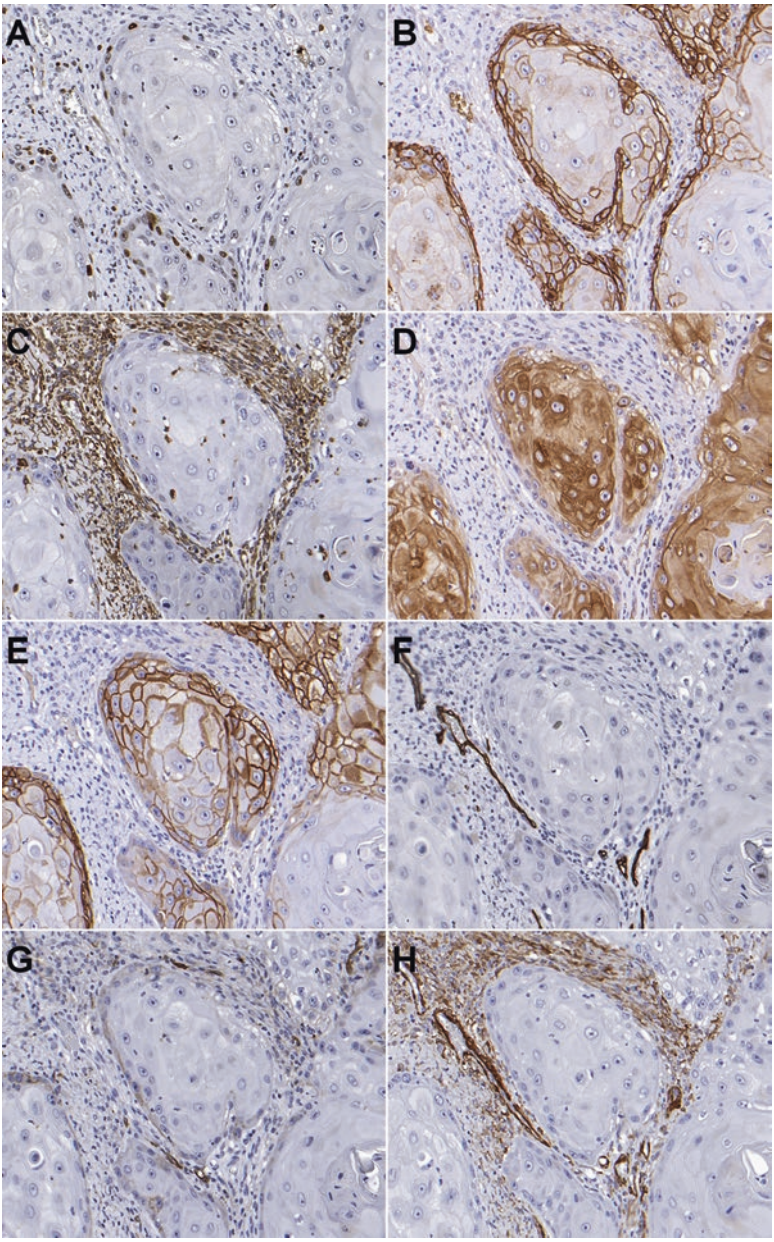

Fig. 14.1 Multiparametric Immunohistochemistry in Registered Serial Sections (MIRSS). Examples from squamous cell carcinoma of the vulva stained for (**a**) Ki67, (**b**) GLUT-1, (**c**) CXCL-12/SDF-1, (**d**) CXCR-4, (**e**) CA IX, (**f**) CD 34, (**g**) podoplanin and (**h**) αSMA. Image registration has been achieved down to the level of individual cells, which can be traced through consecutive slices

4 Multichannel Immunofluorescence Staining Combined with a Quantitative Single-Cell Based Analysis

In 2007, Tóth and Mezey [14] demonstrated the feasibility of multiplex immunofluorescence staining in paraffin sections based on fluorochrome tyramide-mediated signal amplification and repeated cycles of primary antibody denaturation and peroxidase quenching by heat treatment. Among those who embraced this approach were researchers working with the multispectral imaging technology, which employs liquid crystal tuneable filters instead of conventional fluorescence filters. Multispectral imaging enables a high degree of multiplexing through linear unmixing of individual fluorochrome signatures from stacks of images, each representing only a small "window" of the entire wavelength spectrum ("lambda stacks"), albeit at the cost of a certain amount of sensitivity. However, the advantage of high signal strength resulting from tyramide amplification also benefits multichannel fluorescence staining of paraffin sections when using conventional filter technology. Most formalin-fixed and paraffin embedded tissue sections show at least some autofluorescence, which poses much less of a problem when the specific signal is very strong. In 2014, our laboratory started to systematically explore multiplex staining using the fluorochrome tyramide-based approach. The technology turned out to be stable and reproducible, compatible with most antibodies tested (although in our hands strictly limited to monoclonal antibodies) and sensitive [15]. Some drawbacks remain: multichannel immunofluorescence is still labor-intensive when performed as a manual procedure, as a four-plex stain takes two full working days to prepare. Furthermore, conventional fluorochrome tyramide staining sometimes lacks the utmost degree of sensitivity which can be achieved when DAB-based IHC is combined with tyramide-based signal ampflication. It may, however, be possible to overcome the latter problem, since (patented and commercially available) "enhanced tyramide" reagents, according to our preliminary testing, may eventually be as sensitive as the most sensitive conventional brightfield approaches. Cell segmentation, object identification, distance calculations and intensity measurements are carried out in the open source image analysis package CellProfiler [16], while data analysis in a manner similar to flow cytometry is carried out in a specialized commercial software (FCS Express Plus 5, De Novo Software, Glendale, CA, USA).

5 Exploring a New Paradigm of Hypoxia-Mediated Treatment Resistance

Based on published findings of downregulation of EGFR by the hypoxia-inducible PHD-3 [17, 18], we have applied the above-mentioned novel methodology to the study of a possible downregulation of EGFR by hypoxia in cancers of the head and neck region [19]. Indeed, downregulation of EGFR in

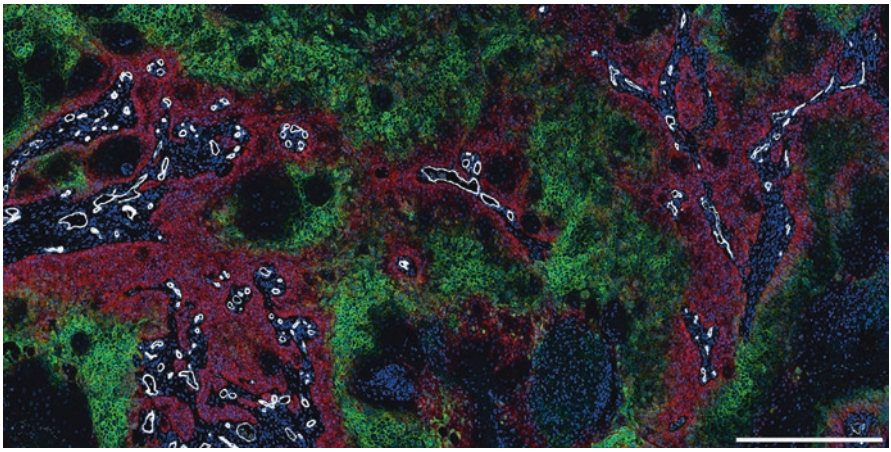

Fig. 14.2 Multichannel immunofluorescence staining of a squamous cell carcinoma of the head and neck region stained for EGFR (*red*, Alexa 647), CA IX (*green*, FITC), CD 34 (*white*, Alexa 546) and cell nuclei (*blue*, DAPI). Preferential clustering of EGFR positive cells is observed in the vicinity of tumor blood vessels, while expression of EGFR is weak or absent in more distant, CA IX-positive tumor areas. Scale bar in the lower right corner, 500 μm

diffusion-limited areas of the tumors, which often expressed the hypoxia-associated marker CA IX, was repeatedly found (Fig. 14.2). These data could form a new paradigm for the regulation of cancer-associated signalling pathways by the tumor microenvironment.

6 Conclusion

Using a newly developed combination of advanced immunofluorescence and image analysis methods, we are currently able to detect up to five different antigens in the same tumor section. These antigens may be utilized to select pivotal intratumoral structures (e.g., blood vessels) and hypoxic cell populations (e.g., tumor cells, stromal cells) by staining for suitable cell surface and hypoxia biomarkers and thus allow us to investigate the spatial relationships between these entities. Our methodology is of broad relevance and we have already successfully employed it to investigate possible mechanisms of resistance mediated by the tumor microenvironment, e.g., against anti-EGFR therapy.

Acknowledgment The authors would like to thank Sysmex GmbH (Norderstedt, Germany) for providing access to slide scanners and scanning services.

References

1. Cancer Genome Atlas Network (2015) Comprehensive genomic characterization of head and neck squamous cell carcinomas. Nature 517(7536):576–582
2. Nowell PC (1976) The clonal evolution of tumor cell populations. Science 194(4260):23–28
3. Gerlinger M, Rowan AJ, Horswell S et al (2012) Intratumor heterogeneity and branched evolution revealed by multiregion sequencing. N Engl J Med 366(10):883–892
4. Chen ZY, Zhong WZ, Zhang XC et al (2012) EGFR mutation heterogeneity and the mixed response to EGFR tyrosine kinase inhibitors of lung adenocarcinomas. Oncologist 17(7):978–985
5. Madar S, Goldstein I, Rotter V (2013) 'Cancer associated fibroblasts' – more than meets the eye. Trends Mol Med 19(8):447–453
6. Carmeliet P, Jain RK (2011) Molecular mechanisms and clinical applications of angiogenesis. Nature 473(7347):298–307
7. Ruffell B, Coussens LM (2015) Macrophages and therapeutic resistance in cancer. Cancer Cell 27(4):462–472
8. Zou W (2006) Regulatory T cells, tumour immunity and immunotherapy. Nat Rev Immunol 6(4):295–307
9. Talmadge JE, Fidler IJ (2010) AACR centennial series: the biology of cancer metastasis: historical perspective. Cancer Res 70(14):5649–5669
10. van der Loos CM (1999) Immunoenzyme multiple staining methods. In: Royal Microscopical Society microscopy handbooks, vol 45. Bios Scientific Publishers, Oxford
11. Mayer A, Höckel M, Schlischewsky N et al (2013) Lacking hypoxia-mediated downregulation of E-cadherin in cancers of the uterine cervix. Br J Cancer 108(2):402–408
12. Arganda-Carreras I, Sorzano COS, Marabini R et al. (2006) Consistent and elastic registration of histological sections using vector-spline regularization. In: Beichel RR, Sonka M (eds) Computer vision approaches to medical image analysis: second international ECCV workshop, CVAMIA 2006 Graz, Austria, May 12, 2006 Revised papers. Springer, Berlin\ Heidelberg, pp 85–95. doi:10.1007/11889762_8
13. Mayer A, Schmidt M, Seeger A et al (2014) GLUT-1 expression is largely unrelated to both hypoxia and the Warburg phenotype in squamous cell carcinomas of the vulva. BMC Cancer 14(1):1–9
14. Toth ZE, Mezey E (2007) Simultaneous visualization of multiple antigens with tyramide signal amplification using antibodies from the same species. J Histochem Cytochem 55(6):545–554
15. Mayer A, Brieger J, Vaupel P et al (2015) Multispectral, multiplexed analysis of the tumor microenvironment in FFPE tissue of head and neck cancer. Strahlenther Onkol 191:S45–S45
16. Lamprecht MR, Sabatini DM, Carpenter AE (2007) CellProfiler: free, versatile software for automated biological image analysis. BioTechniques 42(1):71–75
17. Henze AT, Garvalov BK, Seidel S et al (2014) Loss of PHD3 allows tumours to overcome hypoxic growth inhibition and sustain proliferation through EGFR. Nat Commun 5:5582
18. Garvalov BK, Foss F, Henze AT et al (2014) PHD3 regulates EGFR internalization and signalling in tumours. Nat Commun 5:5577
19. Mayer A, Zahnreich S, Brieger J et al (2016) Downregulation of EGFR in hypoxic, diffusion-limited areas of squamous cell carcinomas of the head and neck. Br J Cancer 115:1351-1358

Chapter 15
Computational Simulation of Tumor Hypoxia Based on In Vivo Microvasculature Assessed in a Dorsal Skin Window Chamber

Lina Xu, Peter Vaupel, Siwei Bai, Bjoern Menze, and Kuangyu Shi

Abstract Malignant growth usually leads to the depletion of oxygen (O_2) supply in most solid tumors. Hypoxia can cause resistance to standard radiotherapy, some chemotherapy and immunotherapy. Furthermore, it can also trigger malignant progression by modulating gene expression and inducing genetic instability. The relationship between microvasculature, perfusion and tumor hypoxia has been intensively studied and many computational simulations have been developed to model tissue O_2 transport. Usually simplified 2D phantoms are used to investigate tumor hypoxia and it is assumed that vessels are perpendicular to the region of interest and randomly distributed across the domain. Such idealistic topology overlooks vascular heterogeneity and is not accurate enough to approximate real scenarios. In addition, experimental verification of the spatial gradient of computational simulations is not directly feasible. Realistic vasculature obtained from fluorescence imaging imported as geometry for partial differential equations solving did not receive necessary attention so far. Therefore, we established a computational simulation of

L. Xu
Department of Informatics, TU München, Munich, Germany

Department of Medical Engineering, TU München, Munich, Germany

Department of Nuclear Medicine, TU München, Munich, Germany

P. Vaupel
Department of Radiation Oncology and Radiotherapy, TU München, Munich, Germany

S. Bai
Department of Medical Engineering, TU München, Munich, Germany

B. Menze
Department of Informatics, TU München, Munich, Germany

Department of Medical Engineering, TU München, Munich, Germany

K. Shi (✉)
Department of Nuclear Medicine, TU München, Munich, Germany
e-mail: k.shi@tum.de

H.J. Halpern et al. (eds.), *Oxygen Transport to Tissue XXXIX*, Advances in Experimental Medicine and Biology 977, DOI 10.1007/978-3-319-55231-6_15

in vivo conditions using experimental data obtained from dorsal skin window chamber tumor preparations in nude rats for the verification of computational results. Tumor microvasculature was assessed by fluorescence microscopy. Since the conventional finite difference method can hardly satisfy the real measurements, we established a finite element method (FEM) for the experimental data in this study. Realistic 2D tumor microvasculature was reconstructed by segmenting fluorescence images and then translated into FEM topology. O_2 distributions and the O_2 gradients were obtained by solving reaction-diffusion equations. The simulation results show that the development of tumor hypoxia is greatly influenced by the irregular architecture and function of microvascular networks.

Keywords Tumor hypoxia • Tumor oxygenation, heterogeneity • Tumor oxygenation, computer simulation • Tumor microvasculature • Oxygen gradients, tumor

1 Introduction

As a consequence of unrestricted malignant growth, O_2 deprivation is a common finding in solid tumors, leading to resistance to standard radiotherapy, chemotherapy and immunotherapy [1–3]. In addition, tumor hypoxia contributes to tumor progression and thus is highly prognostic. Therefore, detection of hypoxia before and during treatment is of great importance in the clinical setting. However, poor blood supply, intrinsic fluctuations of blood flow and irregular or functionally abnormal microvascular networks [4] make it difficult to quantitatively analyze tumor hypoxia on a macroscopic and microscopic level. A multitude of theoretical attempts and clinically used techniques have been adopted in the measurement of tumor oxygenation, among which the direct method using O_2-sensitive microelectrodes is generally considered as minimal invasive but still can cause minor disturbance to the tumor microcirculation. Non-invasive imaging modalities such as magnetic resonance imaging (MRI) or Positron emission tomography (PET) have been applied to assess the tissue oxygenation status. In contrast to many restrictions of experimental designs, computational modelling of O_2 transport provides an alternative way to assist the oxygenation research [5].

The spatio-temporal distribution of O_2 involves getting vessel maps [6] and solving certain partial differential equations (PDEs). The results are usually validated by assessing pimonidazole (PIMO)-staining and are compared to electrode-derived pO_2 measurements using the same cell line [7]. Some recent reports focused on analytic simulations of the tracer distribution or angiogenesis by, respectively, distributing random vessel dots in 2D [8] or generating artificial vessels in 3D [9]. The former assumes vessels perpendicular to the domain and keeps in mind the probability density from a statistic point of view. The latter automatically generates artificial vasculature sprouts, and also concerns a series of vascular morphometric data to ensure that new vessels are morphologically reasonable. Meanwhile, it also considers physiological functions and structures, and adopts special algorithms to

degenerate error-prone vessels. Although both can achieve comparably good results, they are still far from realistic scenarios. In addition, compared to ordinary differential equations (ODEs), reaction-diffusion PDEs are better descriptors in interpreting dynamic tissue O_2 diffusion as it takes into account heterogeneous vascular networks [10]. The PDE model usually solves spatial gradients along and across vessels by the Finite Difference Method (FDM) under prescribed boundary conditions. To our knowledge, only very limited information considers real microvascular geometry and gives the Finite Element Method (FEM) solutions of the PDE model with a finer meshing and better accuracy [11]. In the latter study, frozen tissue microsections from human head and neck xenograft tumor lines were used and immunohistochemically stained for blood vessels *ex vivo* using an antibody against endothelial cells. It only provided a quasi 2D phantom for hypoxia analysis.

Window chambers provide a sophisticated tool in the research of tumor microenvironment, which can obtain high-resolution information of several metabolites such as oxygen [12]. The current study for the first time incorporates the dorsal skin window chamber model in the development of oxygen simulation models. Here we integrate realistic microvasculature of in vivo tumor in observation window measured using fluorescence microscopy for spatial setting of simulation model. The intravital imaging together with the computational model offer a direct insight into visualizing heterogeneous O2 distribution.

2 Methods

2.1 Animal Preparations

A dorsal skin window chamber in a 7-week-old athymic nude (rnu) rat (Charles River Laboratories, Sulzfeld, Germany) was used in this study. This chamber of polyetheretherketone (PEEK) material was designed for the imaging and co-registration of data acquired from a fluorescence microscopy. The human colon adenocarcinoma line HT-29 (G II) was selected for tumor transplantation. Tumor cells were injected into one side of the skin in the center of the window area 3 days after chamber preparation. The skin without tumor was carefully peeled off one week later. Animal studies were approved by the local governmental committee for animal protection (Tierschutzbehörde, Regierung von Oberbayern, license protocol No. 18–13).

2.2 Fluorescence Imaging

Fluorescence imaging was acquired with a microscope after injection of fluorescein isothiocyanate (FITC) dextran in saline (50 mg/ml, 0.8 ml). The tumor vasculature was imaged with a fluorescence microscope (Imager. M2, Zeiss, Germany) equipped with a black/white CCD camera (AxioCam MRm, Zeiss, Germany) and appropriate

image acquisition software (AxioVision, Zeiss, Germany). FITC-dextran with an average molecular weight of 2×10^6 Dalton (Sigma Aldrich, St. Louis, MO, USA) was used as blood flow marker. The rat was anesthetized with midazolam/medetomidine/fentanyl (5/1/0.05 mg/ml). A tail vein catheter was prepared (24 G, BD, Utah, USA) and sealed with a stopper. The window chamber was first fixed to the window chamber adapter, and then fused with a plastic layer on the flat microscopy stage. The body temperature of the rat was maintained at 37 °C using a continuous circulation of water through two sealed gloves surrounding the animal. First, a bright field image and a fluorescence image were recorded. Then, a fluorescence imaging movie was recorded with an exposure time of 50 ms for 6 min, and 3 layers in z-direction of the imaging field of view (FOV) was recorded with 1-mm interval; 0.5 ml of the prepared FITC-dextran solution were injected as a bolus within 5 s into the tail vein 15 s after video recording. Finally, a transparent plastic reference plate was mounted to the window chamber, and a fluorescence image was recorded afterwards. After imaging, 1 ml of Ringer lactate solution was given i.p. Finally, the rat was awakened with atipamezole/flumazenil/naloxone (5/0.1/0.4 mg/ml), and monitored for 3–5 min.

2.3 Reaction-Diffusion PDE Model

The spatial and temporal O_2 distributions are described using PDEs [8, 13]. For the consideration of both chronic and acute hypoxia, the time dependent mathematical reaction-diffusion equation is used as follows:

$$\frac{\partial P}{\partial t} = D_{O_2} \Delta P - \frac{M_0^* P}{P + P_0} \tag{15.1}$$

where D_{O_2} denotes the diffusion coefficient and Δ is the Laplace operator. The second nonlinear term at the right side describes the O_2 consumption rate, considering Michaelis-Menten kinetics [14]. In Eq. (15.1) M_0 is the maximum O_2 uptake rate, P_0 is the value of the O_2 tension for half maximum consumption rate. The consumption part of the model has a great impact on tumor hypoxia [15].

3 Results and Discussion

For simulation of O_2 tensions in the xenografted colon cancer investigated, the related parameters are listed in Table 15.1.

The simulation of O_2 tensions was carried out in a 2D framework. Vessel networks were derived from fluorescence microscopy images. Firstly, we chose the layer which had the best contrast and certain preprocessing methods (denoising and binarization) were used to enhance the features of vascular networks. Obtained

Table 15.1 Parameters for simulation of tumor oxygen supply

Parameter	Parameter description	Value/unit	Reference
P_{RBC}	pO_2 in red blood cells	40 mmHg	[16]
D_{O2}	O_2 diffusion coefficient	2×10^{-5} cm^2/s	[17]
L_{O2}	O_2 mass transfer coefficient	4.1×10^{-4} m/s	[18]
M_0	Maximum "O_2 consumption" rate	15 mmHg/s	[8]
P_0	pO_2 at half maximum consumption rate	2 mmHg	[14]

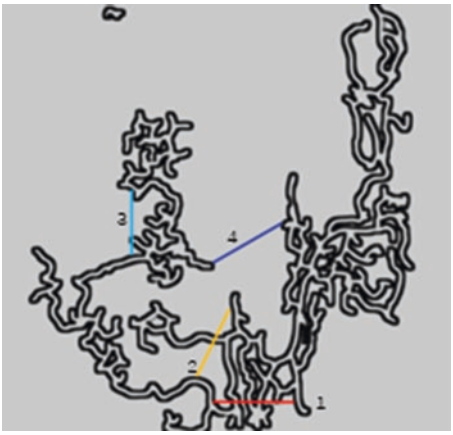

Fig. 15.1 Visualisation of the tumor microvascular network after segmentation of a series of original fluorescence images (image size: 1040 × 1040 μm, selection of 4 different routes for corresponding pO_2 profiles in Fig. 15.3)

images were converted directly to binary ones with reduced noises. Secondly, vessels were manually segmented according to visual inspection. Considering heterogeneous vessel structures and its complexity for meshing, the FEM method using COMSOL 5.2 was adopted to numerically solve PDEs. The segmented vessel map was then imported as geometry for discretizing and meshing in a later stage.

To calculate the O_2 distribution in the tissue, the O_2 outflux $\overrightarrow{j_{O_2}}$ across the vessel wall was defined as the O_2 tension difference across the vessel wall [13]:

$$\overrightarrow{j_{O_2}} = L_{O_2}\left(P - P_{RBC}\right)\vec{n} \tag{15.2}$$

where $\vec{n}$ denotes the normal unit vector whose direction points to the outside of the vessel wall. P_{RBC} refers to the O_2 tension within red blood cells (RBCs), and is assumed to be 40 mmHg for tumor tissue. L_{O_2} is the O_2 mass transfer coefficient.

Figure 15.1 shows the fluorescence image after segmentation and the region of interest (ROI) being 1040 × 1040 μm, with the 2D structure of the realistic in vivo microvessel network of tumor tissue being input as geometry for FEM simulation. The presented structural heterogeneity is visually similar to abnormal tumor microvasculature in [4]. For the purpose of comparisons, we choose 4 lines at different regions marked with numbers to check the varied O_2 distribution.

Figure 15.2 depicts the corresponding O_2 tension distribution based on an average intravascular pO_2 of 40 mmHg. White dashed lines roughly demarcate the anoxic tumor tissue. Presented pO_2 values at increasing distances from the

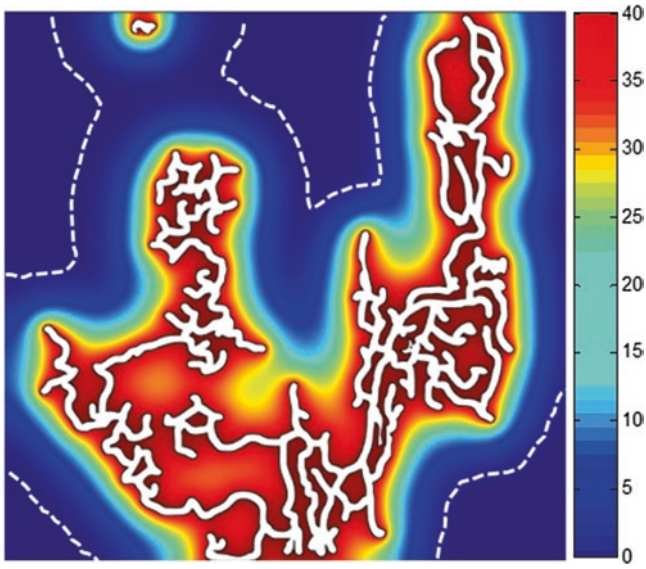

Fig. 15.2 Model simulation of the intratumor O_2 tension distribution based on an average intravascular pO_2 of 40 mmHg. *Color scale*: pO_2 values in mmHg. *White dashed lines* roughly demarcate the anoxic tumor tissue areas

microvasculature under these conditions ranged from approx. 40 mmHg (in the immediate neighborhood of the vessel wall, deep red) to as little as 0–5 mmHg (in the periphery, deep blue). Heterogeneity is visualized via diverse colors. Our simulated O_2 map showed that hypoxia (pO_2 < 10 mmHg) develops at a distance of 65–125 μm from vessel. This is consistent with the empirical data [19, 20] that hypoxia happens at intercapillary distances above 100 μm and anoxia occurs at distances >140 μm.

In Fig. 15.3 selected tissue pO_2 profiles at different locations in the ROI are presented. The individual profiles shown connect perivascular locations of two or more different microvessels with identical intravascular pO_2 values of 40 mmHg as indicated in Fig. 15.1. The computed profiles clearly demonstrate heterogeneous O_2 tension distributions in the intervascular spaces, the results are mostly due to structural and functional irregularities of the microcirculation.

Figure 15.4 shows computed radial pO_2 gradients representing the arterial end of a tumor microvessel (inlet pO_2 = 90 mmHg, upper curve, red gradient), midcapillary position (pO_2 = 40 mmHg, middle curve, yellow gradient) and the capillary outlet position (pO_2 = 10 mmHg, lower curve, blue gradient). The O_2 tensions decrease with increasing distance from the tumor microvessel and reach critical values with subsequent limitations of vivid cell proliferation [21].

This study is limited by assuming a constant pO^2 of 40 mmHg within all vessels, while in fact the heterogeneous vascular network would influence the red blood cell flux over a large distance. At the moment, we focus on studying hypoxia that is reached in a static state in tumor tissue. Detailed behaviors of blood flow like direction and velocity were not considered.

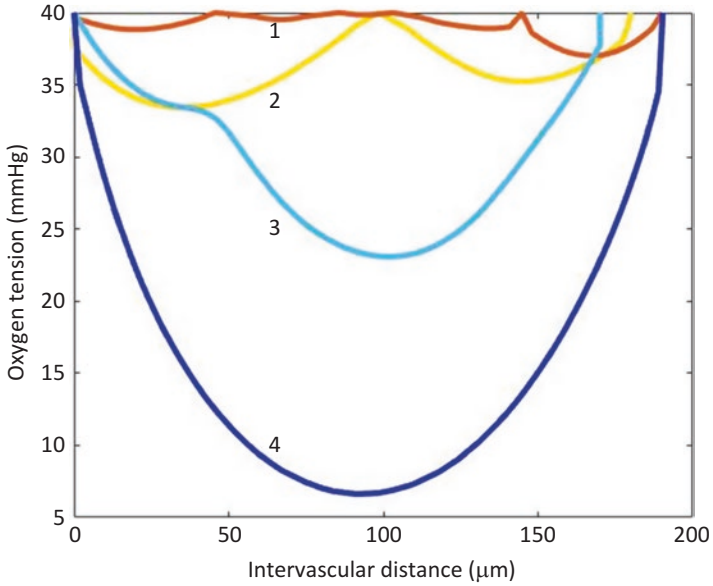

Fig. 15.3 Heterogeneity of extravascular pO_2 profiles at different locations in the tumor tissue (corresponding to 4 different routes marked with *numbers* in Fig. 15.1)

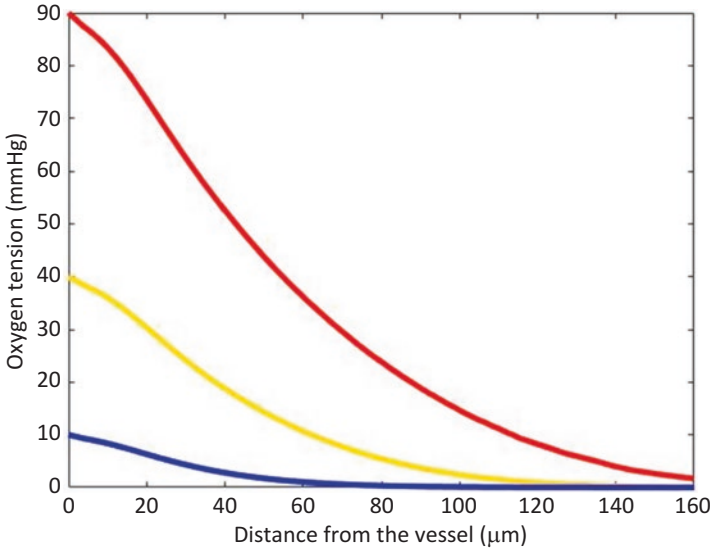

Fig. 15.4 Extravascular (radial) oxygen tension profiles at the arterial end of a tumor microvessel (inlet pO_2 = 90 mmHg, *upper curve, red*), at a midcapillary position (pO_2 = 40 mmHg, *middle curve, yellow*) and at the end of the tumor microvessel (outlet pO_2 = 10 mmHg, *lower curve, blue*)

4 Conclusions

Hypoxia is a crucial trait in tumor progression and thus patients' prognosis. In this paper, oxygen tension (pO_2 value) distribution analyses were carried out by using an established computational model. Since real vasculature obtained from fluorescence imaging imported as geometry for PDEs solving did not receive the necessary attention so far, we aimed to implement a real scenario in vivo as preclinical procedure from a dorsal skin window chamber. The structural and functional irregularities of the tumor microcirculation result in pronounced heterogeneities in the pO_2 distribution, which are consistent with empirical data from the literature. In a following experimental step, these results will be further compared to extracellular oxygen tensions assessed by an O_2 sensor. The problem is that in these preliminary experiments, the field of view of fluorescence and O_2 sensor images do not match very well so far, which hinders direct comparison. Future work will focus on using Raster-Scan Optoacoustic Mesoscopy (RSOM) to measure microvasculature, which can provide a much bigger field of view and higher resolution. Furthermore, the simulation of realistic oxygen transport will benefit from the development of models with heterogeneous perfusion.

References

1. Vaupel P, Kallinowski F, Okunieff P (1989) Blood flow, oxygen and nutrient supply, and metabolic microenvironment of human tumors: a review. Cancer Res 49:6449–6465
2. Vaupel P (2004) The role of hypoxia-induced factors in tumor progression. Oncologia 9:10–17
3. Vaupel P, Multhoff G (2016) Adenosine can thwart antitumor immune responses elicited by radiotherapy. Strahlenther Onkol 192:279–287
4. Vaupel P (2004) Tumor microenvironmental physiology and its implications for radiation oncology. Semin Radiat Oncol 14:198–206
5. Bruley DF (1994) Modeling oxygen transport: development of methods and current state. Adv Exp Med Biol 345:33–42
6. Kelly CJ, Brady M (2006) A model to simulate tumour oxygenation and dynamic [18F]-Fmiso PET data. Phys Med Biol 51:5859–5873
7. Pogue BW et al (2001) Estimation of oxygen distribution in RIF-1 tumors by diffusion model-based interpretation of pimonidazole hypoxia and Eppendorf measurements. Radiat Res 155:15–25
8. Wang Q, Vaupel P, Ziegler SI, Shi K (2015) Exploring the quantitative relationship between metabolism and enzymatic phenotype by physiological modeling of glucose metabolism and lactate oxidation in solid tumors. Phys Med Biol 60:2547–2571
9. Schneider M, Hirsch S, Weber B et al (2014) TGIF: Topological gap in-fill for vascular networks/MACCAI. In : Golland P, Hata N, Barillot C, Hornegger J, Howe R (eds) Medical image computing and computer-assisted intervention – MICCAI 2014: 17th International Conference, Boston, MA, USA, September 14-18, 2014, Proceedings, Part II. Springer International Publishing, Cham, ISBN:978-3-319-10470-6, doi:10.1007/978-3-319-10470-6_12
10. Shi K, Bayer C, Maftei C. et al. (2011) A flow-limited oxygen-dependent diffusion model using heterogeneous perfusion for quantitative analysis of dynamic [18F] FMISO PET. J Nucl Med Meeting Abstracts 52(Suppl1):420

11. Mönnich D et al (2013) Correlation between tumor oxygenation and 18F-fluoromisonidazole PET data simulated based on microvessel images. Acta Oncol 52:1308–1313
12. Helmlinger G, Yuan F, Dellian M, Jain RK (1997) Interstitial pH and pO_2 gradients in solid tumors in vivo: high-resolution measurements reveal a lack of correlation. Nat Med 3:177–182
13. Mönnich D, Troost EGC et al (2011) Modelling and simulation of [18F] fluoromisonidazole dynamics based on histology-derived microvessel maps. Phys Med Biol 56:2045–2057
14. Goldman D (2008) Theoretical models of microvascular oxygen transport to tissue. Microcirculation 15:795–811
15. Secomb TW, Hsu R, Ong ET et al (1995) Analysis of the effects of oxygen supply and demand on hypoxic fraction in tumors. Acta Oncol 34:313–316
16. Secomb TW, Hsu R, Park EYH et al (2004) Green's function methods for analysis of oxygen delivery to tissue by microvascular networks [J]. Ann Biomed Eng 32:1519–1529
17. Tannock IF (1972) Oxygen diffusion and the distribution of cellular radiosensitivity in tumours. Br J Radiol 45:515–524
18. Eggleton CD, Vadapalli A, Roy TK et al (2000) Calculations of intracapillary oxygen tension distributions in muscle. Math Biosci 167:123–143
19. Groebe K, Vaupel P (1988) Evaluation of oxygen diffusion distances in human breast cancer xenografts using tumor-specific in vivo data: role of various mechanisms in the development of tumor hypoxia. Int J Radiat Oncol Biol Phys 15:691–697
20. Vaupel P (1990) Oxygenation of human tumors. Strahlenther Onkol 166:377–386
21. Vaupel P, Mayer A (2007) Hypoxia in cancer: significance and impact on clinical outcome. Cancer Metastasis Rev 26:225–239

Chapter 16
Hypoxia-Related Tumor Acidosis Affects MicroRNA Expression Pattern in Prostate and Breast Tumor Cells

A. Riemann, S. Reime, and O. Thews

Abstract MicroRNAs (miRNAs) are small non-coding RNA sequences which are able to modulate the expression of many functional proteins. The expression level of miRNAs can be modulated by parameters of the tumor microenvironment like hypoxia, nutrient deprivation or oxidative stress. Since miRNAs can act either as oncogenes or tumor suppressors, this may affect malignant progression or therapy resistance. In the present study it was analyzed whether extracellular acidosis can impact on miRNA expression. Therefore, tumor cells (R3327-AT-1 prostate and Walker-256 mammary carcinoma cells) were incubated at pH 6.6 (acidosis) or pH 7.4 (control) for 24 h and changes in miRNA expression were analyzed by PCR array for 84 cancer-associated miRNAs and Next-Generation Sequencing (NGS) with a panel of 765 miRNAs.

In the cancer-related PCR array an acidosis-induced reduction of 5 miRNAs in AT-1 and 6 miRNAs in Walker-256 cells was seen. The miR-203a was consensually down-regulated in both cell lines. Using NGS, 19 miRNAs were found to be upregulated and 14 miRNAS were downregulated in AT-1 prostate cancer cells. In Walker-256 cells the expression of 21 miRNAs was increased and decreased for 17 miRNAs. Eleven miRNAs were regulated by acidosis in both tumor cell lines in the same direction.

Acidosis induced changes in the miRNA expression of prostate and breast carcinoma cells. However, miRNA profiles differed strongly between the tumor cell lines (and between the experimental methods used), indicating that cells can react individually to microenvironmental stress. However, some miRNAs were consensually regulated in both cell lines and thus might represent a general cellular response to an extracellular acidosis.

A. Riemann (✉) • S. Reime • O. Thews
Julius-Bernstein-Institute of Physiology, University of Halle, Halle, Germany
e-mail: anne.riemann@medizin.uni-halle.de

H.J. Halpern et al. (eds.), *Oxygen Transport to Tissue XXXIX*, Advances in Experimental Medicine and Biology 977, DOI 10.1007/978-3-319-55231-6_16

Keywords Acidosis • Tumor • MicroRNA • Next Generation Sequencing (NGS) • Tumor microenvironment

1 Introduction

MicroRNAs (miRNAs) are small, 20–22 nucleotide long, non-coding RNAs which can regulate the gene expression on a post-transcriptional level. Typically, they recognize the complementary sequence at the 3'UTR of the target gene leading to an inhibition of gene expression by hybridization and degradation of the mRNA [1]. It is assumed that approximately 60% of all human genes are regulated by miRNA, resulting in a modulation of many biological processes like differentiation, proliferation and metabolism [2]. Pathologically altered miRNA expression is involved in tumor development, chemosensitivity, invasiveness, EMT and metastasis [3, 4]. In this context they can act either as an oncogene or as a tumor suppressor [2]. Expression of miRNAs can be regulated by oncogenic transcription factors, translocation or epigenetically by promotor methylation [3].

Recently, modulation of miRNA by environmental parameters of the metabolic milieu has been discussed. Since miRNAs enable a rapid regulation of present mRNA, they seem to play an important role in general stress response of cells, for instance during nutrient depletion or oxidative stress by reactive oxygen species [5]. It has been demonstrated that the expression of numerous miRNAs (e.g., miR-210) is altered by hypoxia in the tissue [6]. Interestingly some studies indicate that miRNA expression can not only result from but also cause changes to the tumor microenvironment [7].

The tumor microenvironment differs fundamentally from that of normal tissues and is characterized by an insufficient oxygen supply resulting in forced glycolytic metabolism [8]. For this reason, many tumors show a marked extracellular acidosis which results not only from a forced lactic acid formation by hypoxia-induced anaerobic glycolysis but also from the property of tumor cells to shift to glycolytic metabolism even under sufficient oxygen supply ("Warburg effect"). The extracellular acidification has been shown to influence the malignant behavior of tumors by promoting cell migration or metastasis formation [9, 10]. On the cellular level acidosis can affect the expression or activity of different proteins responsible for tumor progression [11]; however, little is known about the underlying mechanisms.

The aim of the present study was therefore to analyze whether extracellular acidosis can modulate the expression of miRNAs in tumors. For this, two different tumor cell lines were incubated at an acidic pH (6.6) or under control conditions (pH 7.4). These pH values reflect the situation found in normal tissue and solid tumors [8, 12] and it was previously shown that a pH of 6.6 can influence tumor cell phenotype for instance chemoresistance and metastatic potential without inducing apoptosis or necrosis [10, 13]. Changes of miRNA expression were measured by PCR array and by Next-Generation-Sequencing (NGS).

2 Methods

2.1 Cell Culture

The subline AT-1 of the rat R-3327 Dunning prostate carcinoma and the rat mammary carcinoma cell line Walker-256 were used in all experiments. Cells were grown in RPMI medium supplemented with 10% fetal calf serum (FCS). Subsequently they were incubated for 24 h in HEPES- and MES-buffered medium lacking FCS (pH 7.4 or pH 6.6) at 37 °C in a humidified atmosphere with 5% CO_2. After this interval cells were harvested and total RNA was extracted using TRIzol reagent according to the manufacturer's protocol.

2.2 Measurements

MiRNA expression in acidic and control cells was assessed by two different techniques: (1) detection of selected miRNAs by qPCR array and (2) complete analysis of miRNA by NGS.

The PCR array analysis was performed using the miScript miRNA PCR array *Rat Cancer Pathway Finder* (Qiagen, Venlo, Netherlands). This array covers 84 miRNAs associated with a broad spectrum of cancer entities. The array was performed as described by the manufacturer's instructions. For statistical analysis miRNA expression was normalized to a set of controls, and C_q values at pH 6.6 compared to control experiments at pH 7.4. Four independent experiments were performed for each cell line. A consistent effect of acidosis was assumed if all 4 replications of the measurement showed changes in the same direction and the mean was altered at least by a factor of 2.

NGS was performed using Illumina HiScan SQ (Illumina, San Diego, USA). In this approach 765 miRNAs of the rat were detectable. All experiments were performed in triplicate. For the analysis all miRNAs were eliminated which show very low abundance (< 50 counts). For the remaining miRNAs the expression ratio at pH 6.6 to pH 7.4 was calculated. A pH-dependent regulation was assumed if the mean expression changed at least by a factor of 1.5.

3 Results

With the miRNA PCR array several miRNAs were identified that show changes in the expression during extracellular acidosis. The degree of change is described by the $\Delta\Delta C_q$ value in which a value of 2 indicates a 4-fold change in expression. Figure 16.1 shows the acidosis-induced miRNA expression for both cell lines when regulation was twofold or higher. The miRNAs identified by the PCR array were

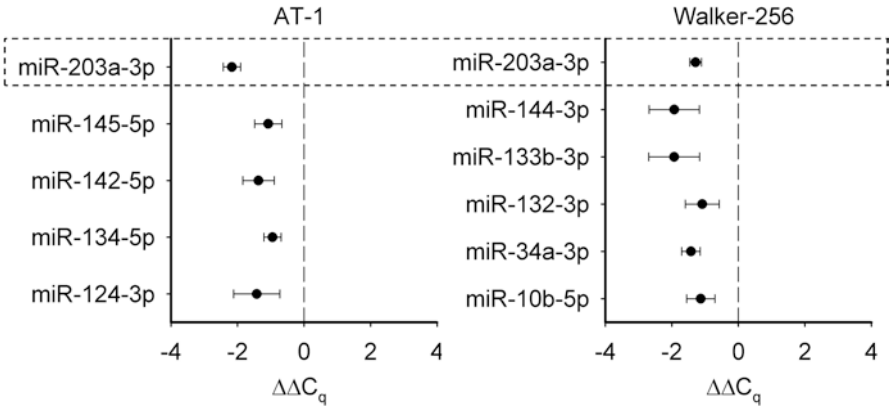

Fig. 16.1 Changes in the expression of acidosis-regulated miRNAs in AT-1 and Walker-256 carcinoma cells detected by miScript miRNA PCR array (Qiagen). These miRNAs showed a consensual change of expression in all measurement replications (n = 4) by a factor of more than 2; miR-203 was uniformly down-regulated in both cell lines. Mean ± SEM; all miRNAs showed a significant reduction of the expression ($p < 0.05$)

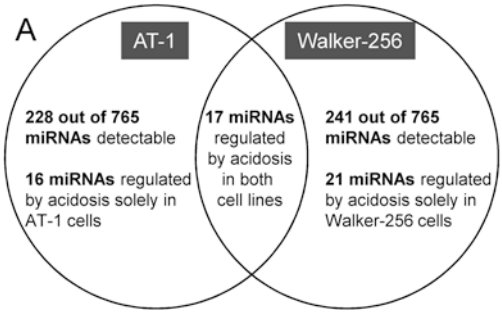

B

consensual regulation		opposing regulation
let-7c	↑	let-7d
miR-7a	↓	miR-9a
miR-17	↓	miR-28
miR-26a	↑	miR-103
miR-27b	↑	miR-125b
miR-30a	↓	miR-3588
miR-34c	↑	
miR-93	↓	
miR-181a	↓	
miR-196a	↑	
miR-196b	↑	

Fig. 16.2 (**a**) Acidosis-regulated miRNAs in AT-1 and Walker-256 carcinoma cells detected by NGS (Next-Generation-Sequencing) (n = 3 for each cell line). (**b**) 11 miRNAs were consensually regulated by low pH in both cell lines (the *arrows* indicate the direction of change) whereas 6 miRNA showed cell line-specific regulation

significantly down-regulated. If a general effect of low pH on cell biology is proposed, acidosis should result in consensual expression changes in different cell lines. However, only miR-203a-3p was down-regulated in both cell lines.

With the PCR array only a limited number of miRNAs could be analyzed. By means of NGS a more comprehensive view is possible. With the system used (Illumina) 765 miRNAs were scanned. In AT-1 cells 228 and in Walker-256 cells 241 miRNAs were detectable (Fig. 16.2a). In AT-1 cells 33 out of these 228 miRNAs showed a systematic regulation by low pH. In Walker-256 cells 38 miRNAs were acidosis-regulated. 17 miRNAs exhibited a pH-dependency in both cell lines (Fig. 16.2b). Eleven of them were regulated in both cell lines consensually indicating a possible general mechanism of acidosis whereas the expression of the remaining 6 miRNAs showed a cell line-specific behavior.

4 Conclusion

The present study clearly reveals that extracellular acidosis (pH 6.6), which is found in many tumors [8], affects the expression of various miRNAs in tumor cells. The expression level as well as the pH-induced changes depended on the cell line used. Since the aim of the study was to elucidate general mechanisms by which the extracellular pH can affect the biological behavior of tumor cells, miRNAs with concurrent regulation in both cell lines were of special interest.

With the miRNA PCR array the miR-203a could be identified to be uniformly down-regulated in two tumor cell lines. All other miRNAs of the array either showed no pH dependency or were regulated in only one cell line. Regulation of miR-203a by acidosis could have a clinical impact since it has been recently described that miR-203 acts as a tumor suppressor and down-regulation of this miRNA is correlated with poor cellular differentiation and patient prognosis [14]. The authors of this study propose that restoration of miR-203 expression may provide therapeutic benefit.

In the NGS analysis additional 11 miRNAs were identified which show a consensual regulation in both cell lines (Fig. 16.2b). The NGS analysis, unlike the PCR array, could not detect miR-203a, since it was below the detection limit. This might be due to the fact that the miR-203a showed only a low abundance in both cell lines. NGS has the advantage to allow complete evaluation of miRNAs, however, compared to qPCR it shows less sensitivity to low abundant miRNAs [15]. The acidosis-dependent miRNAs identified by NGS seem to have also clinical relevance and can affect the patient's prognosis. A decrease of the miRNA let-7c is associated with a reduced chemosensitivity [16], thus the acidosis-induced up-regulation could have a beneficial effect. However, an up-regulation of the miR-196a/b has been described to result in unfavorable prognosis [17].

The present study clearly indicates that the acidic extracellular space of tumors affects the expression of various miRNAs. Since these alterations are associated with changes in the malignant progression of tumors and the patient's prognosis, further studies have to evaluate which targets of these miRNAs may affect the biological behavior of tumors and whether a modulation of the tumor pH affects (via miRNAs) the therapeutic prospects.

Acknowledgments The study was supported by the Wilhelm-Roux program of the medical faculty, University of Halle (FKZ 29/12).

References

1. Eulalio A, Huntzinger E, Izaurralde E (2008) Getting to the root of miRNA-mediated gene silencing. Cell 132:9–14
2. Esquela-Kerscher A, Slack FJ (2006) Oncomirs – microRNAs with a role in cancer. Nat Rev Cancer 6:259–269
3. Lujambio A, Lowe SW (2012) The microcosmos of cancer. Nature 482:347–355

4. Zaravinos A (2015) The regulatory role of microRNAs in EMT and cancer. J Oncol 2015:865–816
5. Leung AK, Sharp PA (2007) microRNAs: a safeguard against turmoil? Cell 130:581–585
6. Gottlieb RA, Pourpirali S (2016) Lost in translation: miRNAs and mRNAs in ischemic preconditioning and ischemia/reperfusion injury. J Mol Cell Cardiol 95:70–77
7. Wentz-Hunter KK, Potashkin JA (2011) The role of miRNAs as key regulators in the neoplastic microenvironment. Mol Biol Int 2011:839–872
8. Vaupel P, Kallinowski F, Okunieff P (1989) Blood flow, oxygen and nutrient supply, and metabolic microenvironment of human tumors: a review. Cancer Res 49:6449–6465
9. Estrella V, Chen T, Lloyd M et al (2013) Acidity generated by the tumor microenvironment drives local invasion. Cancer Res 73:1524–1535
10. Riemann A, Schneider B, Gündel D et al (2014) Acidic priming enhances metastatic potential of cancer cells. Pflugers Arch 466:2127–2138
11. Taylor S, Spugnini EP, Assaraf YG et al (2015) Microenvironment acidity as a major determinant of tumor chemoresistance: proton pump inhibitors (PPIs) as a novel therapeutic approach. Drug Resist Updat 23:69–78
12. Gerweck LE, Seetharaman K (1996) Cellular pH gradient in tumor versus normal tissue: potential exploitation for the treatment of cancer. Cancer Res 56:1194–1198
13. Thews O, Gassner B, Kelleher DK et al (2006) Impact of extracellular acidity on the activity of P-glycoprotein and the cytotoxicity of chemotherapeutic drugs. Neoplasia 8:143–152
14. Lohcharoenkal W, Harada M, Loven J et al (2016) MicroRNA-203 inversely correlates with differentiation grade, targets c-MYC and functions as a tumor suppressor in cSCC. J Invest Dermatol 136:2485–2494
15. Nassirpour R, Mathur S, Gosink MM et al (2014) Identification of tubular injury microRNA biomarkers in urine: comparison of next-generation sequencing and qPCR-based profiling platforms. BMC Genomics 15:485
16. Vinall RL, Tepper CG, Ripoll AA et al (2016) Decreased expression of let-7c is associated with non-response of muscle-invasive bladder cancer patients to neoadjuvant chemotherapy. Genes Cancer 7:86–97
17. Ge J, Chen Z, Li R et al (2014) Upregulation of microRNA-196a and microRNA-196b cooperatively correlate with aggressive progression and unfavorable prognosis in patients with colorectal cancer. Cancer Cell Int 14:128

Part III
Brain Oxygenation and Function

Chapter 17
Cortical and Autonomic Stress Responses in Adults with High Versus Low Levels of Trait Anxiety: A Pilot Study

A. Brugnera, C. Zarbo, R. Adorni, A. Compare, and K. Sakatani

Abstract Stress responses are mediated by complex patterns of cortical and autonomic activity. Earlier studies showed increased recruitment of the right prefrontal cortex (PFC) and parasympathetic withdrawal during a stress task; however, it remains unclear whether these responses change in relation to different levels of psychopathological symptoms, such as trait anxiety. The present study examines the effect of a mathematical task (with a control condition and a stressful/experimental condition) on the PFC and autonomic activity, using a two-channel near infrared spectroscopy (NIRS) and an ECG monitoring system. After a preliminary screening of 65 subjects, a sample of 12 individuals (6 with the highest and 6 with the lowest scores on an anxiety questionnaire, i.e. the STAI trait) was selected. The two groups were similar regarding demographic variables (age, sex, body mass index) and baseline STAI-state scores. Repeated measures ANOVAs were used to compare changes from baseline in oxyhemoglobin (oxy-Hb), heart rate (HR) and root mean square of successive differences (RMSSD) between the two groups. Individuals affected by high levels of trait anxiety showed a reduced bilateral PFC activity during the entire experimental procedure compared to those with low anxiety. No differences in NIRS channels were found between the two groups. During both conditions, RMSSD was lower among individuals affected by high levels of anxious symptoms. Finally, throughout the procedure, changes in HR were higher in the anxious group. Overall, these findings suggest a reduced PFC activity and a larger parasympathetic withdrawal during a stress task in individuals with high levels of trait anxiety compared to those with low anxiety. These results could represent a starting point for future NIRS and ECG studies on the relationship between mental disorders and acute stress responses.

A. Brugnera (✉) • C. Zarbo • R. Adorni • A. Compare
Department of Human & Social Sciences, University of Bergamo, Bergamo, Italy
e-mail: agostino.brugnera@unibg.it

K. Sakatani
NEWCAT Research Institute, Department of Electrical and Electronic Engineering, College of Engineering, Nihon University, Koriyama, Japan

H.J. Halpern et al. (eds.), *Oxygen Transport to Tissue XXXIX*, Advances in Experimental Medicine and Biology 977, DOI 10.1007/978-3-319-55231-6_17

Keywords NIRS • Trait Anxiety • RMSSD • STAI • PFC

1 Introduction

Stress response involves the activation of the central and autonomic systems, that are known to be interconnected by the central autonomic network (CAN) [1]. Through this network, several neuroendocrine, behavioral and visceromotor reactions are controlled by specific brain areas, such as the prefrontal cortex (PFC). During psychosocial stress, the PFC processes emotions and subjective feelings and regulates cardiac reactivity [1, 2].

Earlier NIRS studies in healthy individuals showed activation of the right PFC [3], increased heart rate (HR) and parasympathetic withdrawal [4] in response to stressors. However, few studies have focused on the psychophysiological stress responses of anxious persons. Takizawa et al. [5] reported a positive correlation between higher levels of trait anxiety and a greater decrease in deoxy-Hb in the frontopolar PFC during a stress task. Moreover, high levels of trait anxiety are associated with reduced vagal cardiac function [6], albeit that contradictory results have also been reported [7]. However, to our knowledge, no studies have explored the role of high and low levels of trait anxiety on both PFC and cardiovascular reactivity to acute stressors.

Investigating psychophysiological responses to stress is important as it has been suggested that persons with anxiety disorders have an impairment of the CAN [1]. Indeed, anxious individuals seem unable to manage threat detection, and this reduced cognitive efficiency can lead to endless states of worry and hypervigilance as well as reduced parasympathetic tone [1]. Moreover, anxious individuals experience deficits in working memory and executive functions, as well as a reduced processing and regulation of affective information [8]. This reduced cognitive efficiency is associated with prefrontal hypoactivity [8].

Therefore, this study investigated both prefrontal and cardiological responses to a psychosocial stressor in individuals with low and high levels of trait anxiety, as assessed by the State-Trait Anxiety Inventory (STAI) [9]. We tested the hyphothesis that, during a stress task, individuals with high levels of trait anxiety, compared to those with low levels, will show: (i) reduced vagal activity and increased HR, as proposed by Chalmers et al. [6], and (ii) reduced PFC activity, as suggested by Thayer et al. [8].

2 Methods

A total sample of 65 right-handed and healthy participants underwent extensive psychological testing as part of a larger experiment. All individuals completed the STAI [9], a 40-item self-report measure to assess both the presence and severity of

Table 17.1 Frequencies, means (SD) and their respective *t*-values and *p*-values of demographic and psychological variables by group

	Low anxiety (n = 6)	High anxiety (n = 6)	*t*-value	*p*-value
Sex (frequency)	3 men	3 men	/	0.99
Age (SD)	26.6 (5.6)	22.3 (2.1)	1.78	0.10
BMI (SD)	21.3 (3.3)	23 (4.5)	−0.76	0.54
STAI-Trait (SD)	30 (3.1)	58 (3.1)	−18.3	>0.001
STAI-State (SD)	31.5 (4.8)	37 (4)	−2.16	0.055

the usual propensity to be anxious (Trait scale) and current symptoms of anxiety (State scale). The total score for both scales ranges from 20 to 80, with higher total scores representing higher anxiety severity. Six individuals from the lowest quartile of the distribution of the trait anxiety scores, and six from the highest quartile of the trait anxiety scores, were recruited to participate in the present study, following the procedure suggested by Shapiro et al. [10]. The mean age of the 12 individuals was 24.5 (SD 4.6) years, and six of them were females (i.e. 3 per group). The mean body mass index (BMI) was 22.1 (SD 3.9). All 12 individuals were university students.

Demographic and psychological data of the two groups are reported (separately) in Table 17.1. None of the participants was affected by neurological, psychiatric or other medical (e.g. cardiologic) illnesses as assessed by means of a semi-structured interview.

This study was conducted in accordance with the ethical standards of the American Psychological Association (1992) for the treatment of human experimental volunteers. Each participant provided written consent in compliance with the Declaration of Helsinki (BMJ, 1991; 302:1194).

Participants were seated in a comfortable chair, in a silent room. During the psychophysiological recording they were instructed to avoid any movement of the body and to minimize those of the head. A 5-min rest period (baseline) was followed by completion of a randomized controlled stress task, i.e. the Montreal Imaging Stress Task [11], that is designed to evoke stress responses in the subjects. After a 2-min training phase, participants were randomized to start with a 5-min control condition or with a 5-min experimental (stressful) condition. All participants completed both conditions. Details on the entire procedure can be found in [11].

For measurement of changes in concentrations of oxy-Hb, de-oxy-Hb, and total-Hb in the PFC, a portable Bluetooth® CW-NIRS system was used (PocketNIRS Duo, DynaSense, Japan). This system uses light emitting diodes of three different wavelengths (735, 810, and 850 nm) as light source and one photodiode as a detector, and has two channels (one left and one right). The sampling rate was set to 10.2 Hz. Changes in concentration of hemoglobin are expressed in arbitrary units (a.u.). Optodes were fixed to the individual's forehead using adhesive patches. The NIRS montage replicated the one adopted by Tanida et al. [3]. For the present study, we focused on changes in oxy-Hb only. The signal was post-processed using a freely available MATLAB toolbox (N.A.P., NIRS Analysis Package).

For autonomic measurements we used the Pulse Sensor, a wearable Bluetooth® device (produced by STMicroelectronics and manufactured by MR&D, Italy), that continuously monitors heart activity. The device was positioned on the person's chest by means of an elastic band; the ECG of each individual was visually inspected in order to correct missing beats and artifacts. Time domain (i.e. root mean square of successive differences; RMSSD) analysis of HR variability was performed using a freely available MATLAB toolbox (Kubios HRV). RMSSD is a well-established index to evaluate parasympathetic activity.

Differences between demographic and psychological variables were assessed using independent samples t-tests, or Fisher's exact test. Regarding physiological data, for each task condition we analyzed changes in hemoglobin concentration, HR and RMSSD in relation to differences from the mean baseline value. The mean Δoxy-Hb, mean ΔHR and mean ΔRMSSD were subjected to repeated measures ANOVA. For Δoxy-Hb, the factors were Group (Low and High Trait Anxiety), Condition (Control and Experimental) and Channel (Left and Right). For ΔHR and ΔRMSSD, the factors were Group and Condition. Post-hoc analysis was performed using Tukey's test.

A p-value ≤ 0.05 was considered statistically significant. All analyses were performed with SPSS 23 (IBM, USA) and STATISTICA 12.5 (StatSoft Inc., USA).

3 Results

Preliminary data analysis showed that the RMSSD variables were positively skewed: a log transformation corrected the non-normality. Other variables were normally distributed. Because no differences in behavioral data (i.e. response times to MIST) were found between the two groups, these data are not reported. Table 17.1 shows that the two groups were similar with regard to demographic variables.

ANOVA performed on ΔHR showed an effect of the Group ($F1,10 = 5.92$; $p = 0.003$. Low Anxiety: M = 0.92, SE = 1.92; High Anxiety: M = 7.53, SE = 1.92). Other effects and interactions were not significant.

ANOVA performed on ΔRMSSD showed an effect of the Group ($F1,10 = 7.92$; $p = 0.02$. Low Anxiety: M = 0.11, SE = 0.09; High Anxiety: M = −0.21, SE = 0.09). Other effects and interactions were not significant.

Lastly, ANOVA performed on ΔOxy-Hb (Fig. 17.1) showed an effect of the Group ($F1,10 = 15.02$; $p = 0.003$. Low trait Anxiety: M = 0.051, SE = 0.0008; High trait Anxiety: M = 0.005, SE = 0.008) and an effect of the Condition ($F1,10 = 14.69$; $p = 0.003$. Control: M = 0.002, SE = 0.0006; Experimental: M = 0.004, SE = 0.007). Other effects and interactions were not significant.

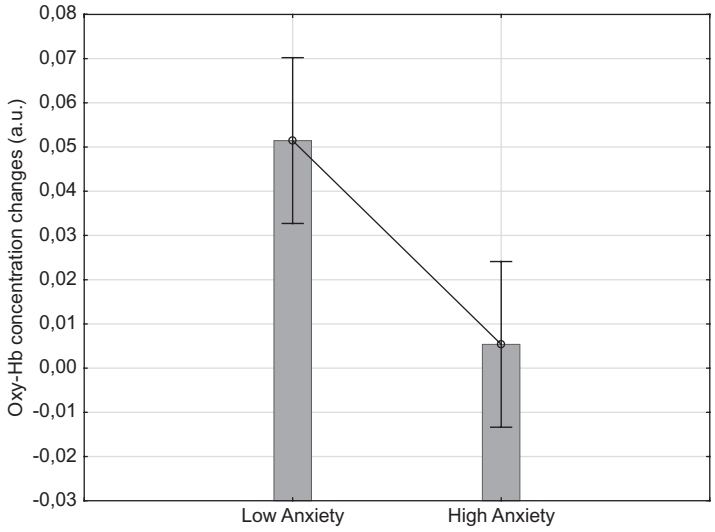

Fig. 17.1 Changes in oxy-Hb concentration in the two groups throughout the procedure. The overall cortical activity in both channels of the High Anxiety group was lower than that of the Low Anxiety group ($p = 0.003$). Vertical bars denote 0.95 confidence intervals

4 Discussion

In summary, these results showed significant cortical and cardiovascular differences between individuals with high and low levels of trait anxiety during the entire procedure (i.e. the cognitive and stressful conditions). Individuals with high trait anxiety compared to individuals with low trait anxiety, showed higher HR as well as reduced PFC activity and parasympathetic withdrawal.

For cortical response, the results show increased PFC activity in the experimental condition compared with the control condition, irrespective of the group; this is attributed to the fact that experimental condition was stressful and more cognitively challenging. The lack of right lateralization during the stressful condition does not allow to confirm earlier findings [3]. Moreover, our results show that individuals with a high level of trait anxiety were characterized by reduced PFC activity throughout the procedure. Probably, as reported by Thayer et al. [8], anxious individuals experience a reduced cognitive efficiency, which could lead to a generalized prefrontal hypoactivity.

Regarding autonomic responses, individuals with high levels of trait anxiety compared to those with low levels, experienced decreased RMSSD and increased HR during the entire procedure; this is partly in accordance with a previous meta-analysis [6].

These specific patterns of autonomic and cortical activity suggest that individuals with high levels of trait anxiety, even without a diagnosis of anxiety disorder, might be affected by a less efficient CAN activity when compared to those with low

levels. According to the CAN model, disrupted CAN activity results in reduced frontal activity that could lead, in turn, to exaggerated sympathetic responses and rigid behaviors (such as hypervigilance, defensiveness, and perseveration), which are typical of anxiety disorders [8]. Indeed, it is known that anxious individuals are characterized by cognitive deficits (i.e. in detecting and managing environmental stimuli) [8].

In conclusion, this is the first NIRS study to investigate both PFC and cardiovascular responses to psychosocial stress in individuals with different levels of trait anxiety but comparable with regard to demographic variables. Despite the limitations of this explorative study (i.e. small sample size, use of a 2-channel NIRS device) some important inferences can be drawn regarding cortical and autonomic changes, in both the cognitive and stressful conditions, in individuals with high anxiety traits. However, additional larger studies are required to further elucidate these findings.

References

1. Thayer JF et al (2009) Heart rate variability, prefrontal neural function, and cognitive performance: the neurovisceral integration perspective on self-regulation, adaptation, and health. Ann Behav Med 37(2):141–153
2. Kogler L et al (2015) Psychosocial versus physiological stress: meta-analyses on deactivations and activations of the neural correlates of stress reactions. NeuroImage 119:235–251
3. Tanida M, Katsuyama M, Sakatani K (2007) Relation between mental stress-induced prefrontal cortex activity and skin conditions: a near-infrared spectroscopy study. Brain Res 1184:210–216
4. Castaldo R et al (2015) Acute mental stress assessment via short term HRV analysis in healthy adults: a systematic review with meta-analysis. Biomed Signal Process Control 18:370–377
5. Takizawa R et al (2014) Anxiety and performance: the disparate roles of prefrontal subregions under maintained psychological stress. Cereb Cortex 24(7):1858–1866
6. Chalmers JA et al (2014) Anxiety disorders are associated with reduced heart rate variability: a meta-analysis. Front Psychiatry 5:80
7. Sanchez-Gonzalez M et al (2015) Trait anxiety mimics age-related cardiovascular autonomic modulation in young adults. J Hum Hypertens 29(4):274–280
8. Thayer JF, Friedman BH (2004) A neurovisceral integration model of health disparities in aging. In: Anderson NB, Bulato RA, Cohen B (eds) Critical perspectives on racial and ethnic differences in health in late life. National Academies Press, Washington, DC, pp 567–603
9. Spielberger CD et al (2000) STAI Y1 and STAI Y2: Italian edition. Organizzazioni Speciali, Firenze
10. Shapiro PA et al (2000) Cerebral activation, hostility, and cardiovascular control during mental stress. J Psychosom Res 48(4–5):485–491
11. Dedovic K et al (2005) The Montreal Imaging Stress Task: using functional imaging to investigate the effects of perceiving and processing psychosocial stress in the human brain. J Psychiatry Neurosci 30(5):319–325

Chapter 18
Relation Between EEG Activity and Brain Oxygenation in Preterm Neonates

Alexander Caicedo, Liesbeth Thewissen, Anne Smits, Gunnar Naulaers, Karel Allegaert, and Sabine Van Huffel

Abstract This study investigates the relationship between brain oxygenation, assessed by means of near infrared spectroscopy (NIRS), and brain function, assessed by means of electroencephalography (EEG). Using NIRS signals measuring the regional cerebral oxygen saturation ($rScO_2$) and computing the fractional tissue oxygen extraction (FTOE), we compared how these variables relate to different features extracted from the EEG, such as the inter-burst interval (IBI) duration and amplitude, the amplitude of the EEG, and the amplitude of the burst. A cohort of 22 neonates undergoing sedation by propofol was studied and a regression of the NIRS-derived values to the different EEG features was made. We found that higher values of FTOE were related to higher values of EEG amplitude. These results might be of used in the monitoring of proper brain function in neonates.

Keywords Propofol • EEG • NIRS • Flow-metabolic coupling

1 Introduction

Coupling between brain blood flow and brain metabolism is well described in both human and animal studies but remains very difficult to measure. Brain activity can be measured by using EEG analysis, reflecting the brain function. However, brain

A. Caicedo (✉) • S. Van Huffel
Department of Electrical Engineering, STADIUS-ESAT, KU Leuven, Leuven, Belgium

imec, Leuven, Belgium
e-mail: acaicedo@esat.kuleuven.be

L. Thewissen • G. Naulaers • K. Allegaert
Department of Development and Regeneration, KU Leuven, Leuven, Belgium

A. Smits
Department of Development and Regeneration, KU Leuven, Leuven, Belgium

Intensive Care and Department of Surgery, Erasmus MC Sophia Children's Hospital, Rotterdam, the Netherlands

H.J. Halpern et al. (eds.), *Oxygen Transport to Tissue XXXIX*, Advances in Experimental Medicine and Biology 977, DOI 10.1007/978-3-319-55231-6_18

metabolic demand is more complicated to assess. Using NIRS we can obtain measurements of cerebral brain oxygenation ($rScO_2$), which can be used to derive the fractional tissue oxygen extraction (FTOE). FTOE reflects the balance between oxygen delivery and oxygen consumption [1]. In a previous study we found that oxygenation changes precede changes in EEG activity in neonates undergoing procedural sedation using propofol. This study used transfer entropy as a measure for the directionality of coupling between changes in EEG and NIRS signals [2]. However, only the directionality between changes in $rScO_2$ and EEG measurements was assessed. Since EEG has proven to be a good predictor for early neonatal outcome, especially in asphyxiated babies [3], quantifying this relation might be of clinical relevance not only for the monitoring of these neonates, but also to understand the physiological processes underlying the regulation of brain metabolism.

Previous studies have shown that the coupling between cerebral metabolic demand and oxygen delivery is disrupted during pathological conditions [4, 5]. However, these studies are descriptive and do not measure in a quantitative way the relation between changes in brain oxygenation and metabolic demand.

In this study we attempt to study the relationship between changes in brain function and brain metabolism, by means of analysis of EEG and NIRS-derived measurements.

2 Methods

Data were obtained as secondary outcome of a study to define the optimal dose of propofol for endotracheal intubation in neonates in the Neonatal Intensive Care Unit at the University Hospitals Leuven (Leuven, Belgium) [6]. To study cerebral flow-pressure autoregulation and flow-metabolism coupling, a subgroup of preterm neonates was defined receiving the INSURE procedure (Intubate, Surfactant, Extubate) after propofol sedation but without concomitant medication, with monitoring of invasively measured arterial blood pressure, NIRS-derived cerebral oxygenation and amplitude-integrated EEG.

NIRS signals were measured using the cerebral neonatal OxyAlert NIRSensor located left frontoparietally (INVOS 5100, Covidien, Mansfield, MA, USA), and EEG measurements were obtained from the channels C3-C4 (Olympic CFM 6000, Natus Medical Inc., Seattle, USA). NIRS signals were recorded using a sampling frequency of 1 Hz, while EEG signals were acquired at 100 Hz. All measurements were obtained before administration of propofol and lasted up to 12 h after propofol administration. For uniformity, we processed the data from the application of propofol up to 10 h afterwards. Artefacts were manually removed from the data. For the EEG measurements, segments of data with an impedance higher than 10KΩ were also removed from further analysis.

For the EEG, we identified the position of bursts and inter-burst intervals (IBI) using an algorithm previously developed by our group [7]. The EEG was decom-

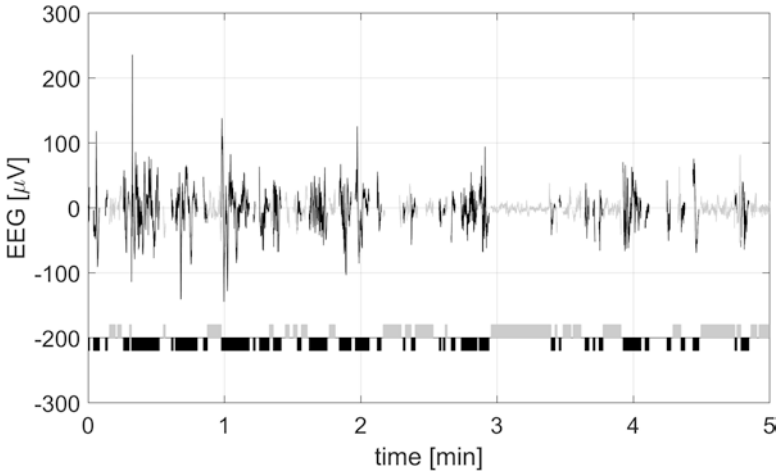

Fig. 18.1 Segmentation of the EEG into bursts (*black solid line*) and IBIs (*grey solid lines*). The *lower boxes* represent the intervals of time for the duration of burst (*black blocks*) and IBIs (*grey blocks*)

posed in two parts, one containing the burst and the other containing the IBIs. The decomposition of one segment of EEG is shown in Fig. 18.1. From these segmented signals, the total time, as well as the root mean square (RMS) value of burst and inter-burst-intervals activity were computed in consecutive overlapping windows of 15 min duration and 14 min of overlap, and they were used as features to represent changes in the EEG. It is important to note that the RMS for the burst was computed using only values within the 15-min window where there were burst, datapoints corresponding to IBIs were not taken into account for this computation. The same procedure was follow for the computation of the RMS value in the IBI. This was repeated until the whole signal was processed. An example of the obtained amplitude features is shown in Fig. 18.2.

Using the NIRS signals, the FTOE = $(SaO_2 - rScO_2)/ SaO_2$ was computed, with SaO_2, the arterial oxygen saturation. For both the $rScO_2$ and the FTOE the running RMS was calculated using consecutive overlapping windows of 15 min of duration and 14 min overlap. In this way for each minute we obtain a series of concomitant features for the EEG and the NIRS signals. The relation between the NIRS and EEG features was quantified by means of linear regression and the amount of explained variance. In order to observe the common trend in the whole population, the median value for each minute from the start of propofol administration up to 600 min thereafter, using data from all patients at that particular time, was computed. This was done for the NIRS and the EEG features, obtaining a median time series for each derived feature. The regression was performed using those final scores.

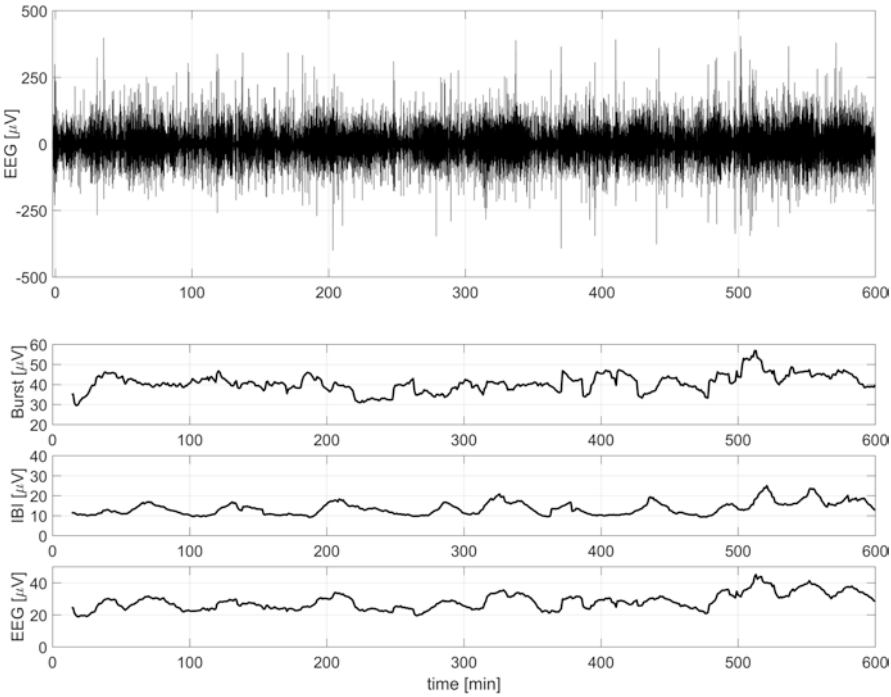

Fig. 18.2 Amplitude features extracted from the EEG signal. In the *upper panel* the raw EEG, in the *lower panels* the running RMS values for the bursts (Burts (μV)), IBIs (IBI (μV)), and the complete EEG signal (EEG (μV)), respectively

3 Results

Data were collected from 22 preterm infants with a median (range) gestational age of 30 (26–35) weeks and median (range) birth weight of 1415 (580–2775) g. The regression between the values of FTOE and the amplitude of the EEG are shown in Fig. 18.3. The regression is represented by the solid line while the 95% confidence intervals are shown as a dashed line. The amount of explained variance in the regression is 48%. In addition, the regression curves between the amplitude and the duration of burst and IBIs with FTOE are shown in Fig. 18.4. It can be seen that the values of FTOE correlate positively with values of burst/IBI amplitude and burst time, and correlate negatively with the duration of the IBIs.

No correlation was found between the EEG features and the $rScO_2$ values ($\rho = 0.1$).

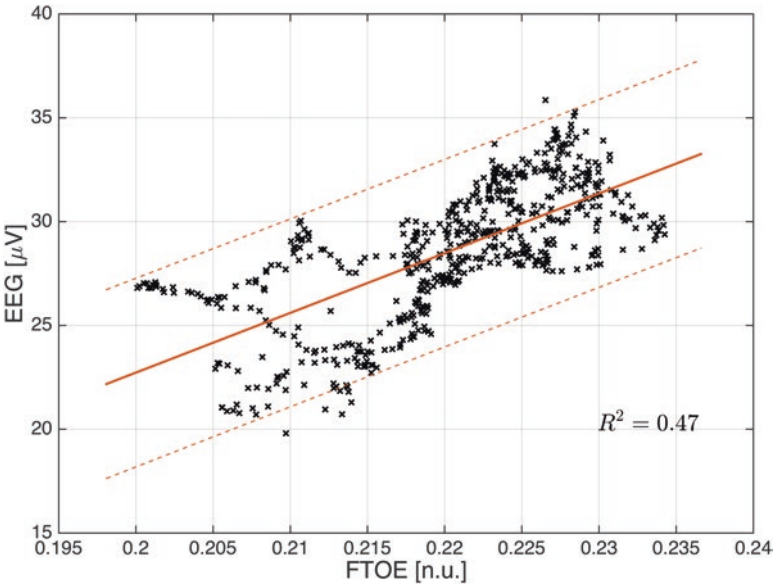

Fig. 18.3 Regression curve between values of FTOE and EEG amplitude. Each *point* represents the median of the EEG feature and FTOE values from all the 22 patients at a given time

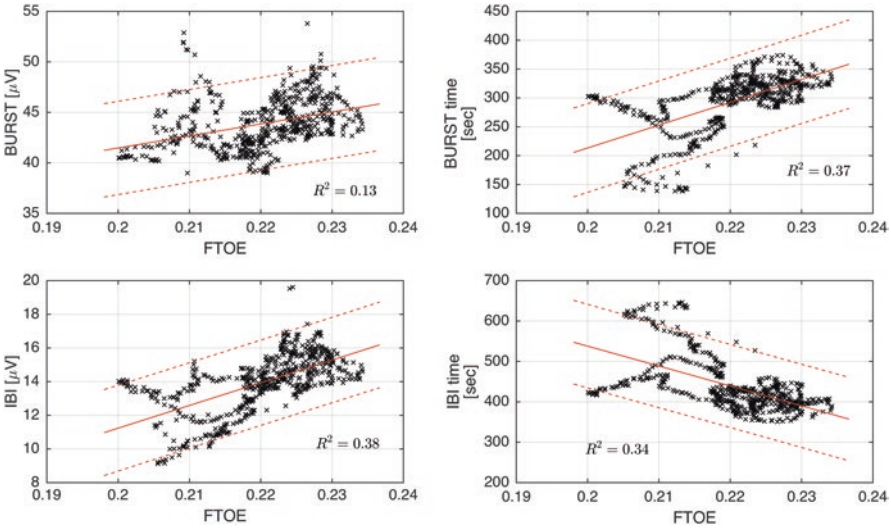

Fig. 18.4 Regression curves between values of FTOE and EEG features, burst and IBI amplitudes and durations. Each *point* represents the median of the EEG feature and FTOE values from all the 22 patients at a given time

4 Discussion and Conclusions

Changes in EEG values were positively correlated to FTOE values, indicating that higher EEG amplitudes lead to larger FTOE values. When decomposing the EEG, the larger values in burst amplitude, IBI amplitude and burst duration were responsible for the larger values of FTOE, while large segments of IBI, i.e. EEG segments that were more suppressed, produced lower FTOE values. This implies that larger values of brain energy levels might be related to larger FTOE values, possibly explained by a higher extraction of oxygen to support brain metabolism. However, it is important to note that a larger EEG amplitude is not always an indication of higher brain energy levels, since it might be caused by a synchronization of the sources that generate the EEG activity. But, the positive/negative relation between FTOE and burst/IBIs duration might indicate that the FTOE is larger when the brain energy levels are higher. Also, it seems that values of FTOE are better explained by the IBI segments in the EEG than the burst.

No correlation was found between the EEG features and $rScO_2$ values. This is explained by the direct relation between $rScO_2$ and peripheral oxygen saturation. FTOE corrects for this relation.

However, the relationship observed by the values of FTOE and EEG amplitude can be attributed to the effect of propofol, which might affect in the same way brain function and metabolism. Since data points up to 10 h after propofol are plotted without any time relation to propofol administration, the effect of propofol might be masked. In addition, a large variability between patients was observed in the variance of the regression curve; this might be explained by the different doses of propofol administered to and the gestational age of the different neonates. Also, no extensive baseline values for $rScO_2$, FTOE and EEG were available, therefore no baseline levels for the FTOE and EEG features could be computed due to the lack of measurements.

There are some limitations to be considered in this study. First, the lack of baseline values does not allow to have a complete overview of the effect of propofol in the relationship between the changes in EEG and FTOE. Second, the results presented in this manuscript show the overall trends among the different patients, but variability due to the dose of propofol administered to the subjects, gestational age, weight, among others, has not been taken into account.

In conclusion, a relation between brain energy levels, assessed by means of EEG measurements and brain metabolism, assessed by FTOE measurements obtained using NIRS, was found in a population of neonates who underwent procedural sedation using propofol. These results can be used as a basis for the development of methodologies to quantitatively compute the relation between brain function and metabolism in neonates. For instance we can continuously monitor the flow-metabolism relation by computing the different EEG features and their relation to FTOE. Whether this relation might be impaired in disease or in neonates under risk, if it is caused by the propofol administration, or if it is due to an underlying regulation mechanisms, is the subject of further study.

Acknowledgments Alexander Caicedo is a postdoctoral fellow of the research foundation Flanders (FWO). Bijzonder Onderzoeksfonds KU Leuven (BOF). This research was also supported by: Center of Excellence (CoE) #: PFV/10/002 (OPTEC). Fonds voor Wetenschappelijk Onderzoek-Vlaanderen (FWO), project #: G.0427.10 N (Integrated EEG-fMRI), G.0108.11 (Compressed Sensing), G.0869.12 N (Tumor imaging), G.0A5513N (Deep brain stimulation). Agentschap voor Innovatie door Wetenschap en Technologie (IWT), project #: TBM 080658-MRI (EEG-fMRI), TBM 110697-NeoGuard. iMinds Medical Information Technologies. Dotatie-Strategisch basis onderzoek (SBO- 2015). ICON: NXT_Sleep. Belgian Federal Science Policy Office. IUAP #P7/19/ (DYSCO, `Dynamical systems, control and optimization', 2012-2017). Belgian Foreign Affairs-Development Cooperation. VLIR UOS programs (2013-2019). EU: European Union's Seventh Framework Programme (FP7/2007-2013): EU MC ITN TRANSACT 2012, #316679, ERASMUS EQR: Community service engineer, #539642-LLP-1-2013. Other EU: INTERREG IVB NWE programme #RECAP 209G. European Research Council: ERC Advanced Grant, #339804 BIOTENSORS This paper reflects only the authors' views and the Union is not liable for any use that may be made of the contained information. The research activities are further facilitated by the agency for innovation by Science and Technology in Flanders (IWT) through the SAFEPEDRUG project (IWT/SBO 130033).

References

1. Naulaers G et al (2007) Use of tissue oxygenation index and fractional tissue oxygen extraction as non-invasive parameters for cerebral oxygenation. Neonatology 92(2):120–126
2. Caicedo A et al (2016) Changes in oxygenation levels precede changes in amplitude of the EEG in premature infants. Adv Exp Med Biol 923:143–149
3. Hallberg B et al (2010) (2010). The prognostic value of early aEEG in asphyxiated infants undergoing systemic hypothermia treatment. Acta Paediatr 99(4):531–536
4. Pichler G et al (2013) aEEG and NIRS during transition and resuscitation after birth: promising additional tools; an observational study. Resuscitation 84(7):973–978
5. Roche-Labarbe N et al (2007) Coupled oxygenation oscillation measured by NIRS and intermittent cerebral activation on EEG in premature infants. NeuroImage 36(3):718–727
6. Smits A (2016) Propofol dose-finding to reach optimal effect for (semi-)elective intubation in neonates. J Pediatr 179:54. doi:10.1016/jpeds.2016.07.049
7. Koolen N et al (2014) Line length as a robust method to detect high-activity events: automated burst detection in premature EEG recordings. Clin Neurophysiol 125(10):1985–1994

Chapter 19
Functional NIRS Measurement of Cytochrome-C-Oxidase Demonstrates a More Brain-Specific Marker of Frontal Lobe Activation Compared to the Haemoglobins

Isabel de Roever, Gemma Bale, Robert J. Cooper, and Ilias Tachtsidis

Abstract Functional near-infrared spectroscopy (fNIRS) is an increasingly common neuromonitoring technique used to observe evoked haemodynamic changes in the brain in response to a stimulus. The measurement is typically in terms of concentration changes of oxy- (ΔHbO_2) and deoxy- (ΔHHb) haemoglobin. However, noise from systemic fluctuations in the concentration of these chromophores can contaminate stimulus-evoked haemodynamic responses, leading to misinterpretation of results. Short-separation channels can be used to regress out extracerebral haemodynamics to better reveal cerebral changes, significantly improving the reliability of fNIRS. Broadband NIRS can be used to additionally monitor concentration changes of the oxidation state of cytochrome-c-oxidase (ΔoxCCO). Recent studies have shown ΔoxCCO to be a depth-dependent and hence brain-specific signal. This study aims to investigate whether ΔoxCCO can produce a more robust marker of functional activation. Continuous frontal lobe NIRS measurements were collected from 17 healthy adult volunteers. Short 1 cm source-detector separation channels were regressed from longer separation channels in order to minimise the extracerebral contribution to standard fNIRS channels. Significant changes in ΔHbO_2 and ΔHHb were seen at 1 cm channels but were not observed in ΔoxCCO. An improvement in the haemodynamic signals was achieved with regression of the 1 cm channel. Broadband NIRS-measured concentration changes of the oxidation state of cytochrome-c-oxidase has the potential to be an alternative and more brain-specific marker of functional activation.

Keywords Near-infrared spectroscopy • Functional activation • Cytochrome-c-oxidase • Haemodynamics • Short-separation regression

I. de Roever (✉) • G. Bale • R.J. Cooper • I. Tachtsidis
Department of Medical Physics and Bioengineering, University College London, London, UK
e-mail: isabel.roever.13@ucl.ac.uk

H.J. Halpern et al. (eds.), *Oxygen Transport to Tissue XXXIX*, Advances in Experimental Medicine and Biology 977, DOI 10.1007/978-3-319-55231-6_19

1 Introduction

Functional near-infrared spectroscopy is commonly used to monitor stimulus-evoked cerebral haemodynamic responses due to neurovascular coupling, via measured regional concentration changes of oxygenated and deoxygenated haemoglobin. A typical functional activation haemodynamic response function consists of an increase in ΔHbO_2 and a concurrent, co-located decrease in ΔHHb. However, one of the main problems with fNIRS is its susceptibility to noise. This can arise from two main sources: task-related systemic activity and systemic-driven changes in the extracerebral layers [1]. The latter is a significant source of interference due to the nature of fNIRS measurements, where light propagates through the superficial layers upon emission and detection in reflectance mode, and hence is highly sensitive to changes in these superficial layers [2].

An increasingly common method to reduce contributions from extracerebral layers is with the use of short source-detector separation NIRS channels to sample only those layers, and use of the resulting signals as regressors in a linear model of the longer fNIRS channels [3]. It has been shown that a short source-detector separation of ~0.8 cm can effectively sample the extracerebral layer [2]. Hence, short channels can facilitate removal of superficial contamination from standard fNIRS channels, significantly improving the reliability of fNIRS measurements.

Using broadband NIRS we can additionally monitor oxidation changes of cytochrome-c-oxidase (CCO). CCO is the terminal electron acceptor in the electron transport chain in the mitochondria and is responsible for more than 95% of oxygen metabolism. Measurements of $\Delta oxCCO$ therefore provides information about oxygen utilisation at a cellular level [4]. The concentration of CCO is less than 10% in vivo than that of haemoglobin, hence a broadband NIRS system is required to accurately separate changes in attenuation due to this chromophore [5].

Recently, it has been shown using a broadband NIRS system with multiple source-detector separations that $\Delta oxCCO$ signals display a depth-dependence not seen in haemodynamic signals during oxygen delivery challenges in the healthy adult head [6]. The $\Delta oxCCO$ response was only seen at longer source-detector separations (3.5 cm) compared to ΔHbO_2 and ΔHHb, which showed a response at all source-detector separations (2, 2.5, 3 and 3.5 cm) interrogating both scalp and brain. This depth-dependence suggests CCO is brain-specific; this is likely due to the higher mitochondrial density in tissue with higher metabolic rates such as the brain compared to tissue with lower metabolic rates [6]. The $\Delta oxCCO$ signal therefore offers an alternative cerebral optical signal to haemodynamic signals.

This study aims to investigate the use of $\Delta oxCCO$ as an alternative and more robust marker of functional activation due to its brain-specificity compared to haemoglobin signals. The extracerebral contribution to the haemodynamic and metabolic signals is investigated with the use of a multi-distance broadband NIRS system, with short separation of 1 cm to probe mostly the skin, scalp and skull.

2 Methods

Healthy adult volunteers were recruited for this study and written informed consent obtained. The study was approved by the University College London (UCL) Ethics Committee. Data were collected from 17 healthy adult volunteers (13 male; age range 22–34 years) during functional activation. A working memory challenge in the form of either a Stroop task or anagram-solving task was used in order to induce a frontal haemodynamic response. Data were collected continuously for a 30 s baseline period, followed by 30 s of activation and 30 s of rest, alternated 4 times. The total acquisition time was therefore 270 s.

Data were collected using a broadband NIRS system called CYRIL (CYtochrome Research Instrument and appLication), previously described [7]. It is an 8-channel system with two light emission fibres; optode holders were placed on the right and left sides of the forehead of each subject as shown in Fig. 19.1. Intensity data from the 4 cm channels displayed poor signal-to-noise ratio so were excluded from further analysis.

CYRIL is comprised of a white light source and a lens-based spectrometer with the capacity to collect light intensity data for 136 wavelengths between 771–906 nm at 1 Hz sampling rate. Measured changes in light attenuation were then converted to concentration changes of ΔHbO_2, ΔHHb and $\Delta oxCCO$ using the UCLn algorithm [5]. As the differential pathlength factor is likely to vary across different source-detector separations, no pathlength was used. Instead, concentration data are presented in terms of μM.cm.

Data analysis was carried out in MATLAB (Mathworks, USA) and using modified versions of functions from the HOMER2 NIRS processing package (http://www.homer-fnirs.org). Concentration data were zero-meaned and bandpass-filtered in the range [0.005 0.3] Hz, using a 5th order Butterworth filter, to remove physiological noise. The haemodynamic response was then extracted using one of two methods: the first was a block-average across all the events for all the subjects to

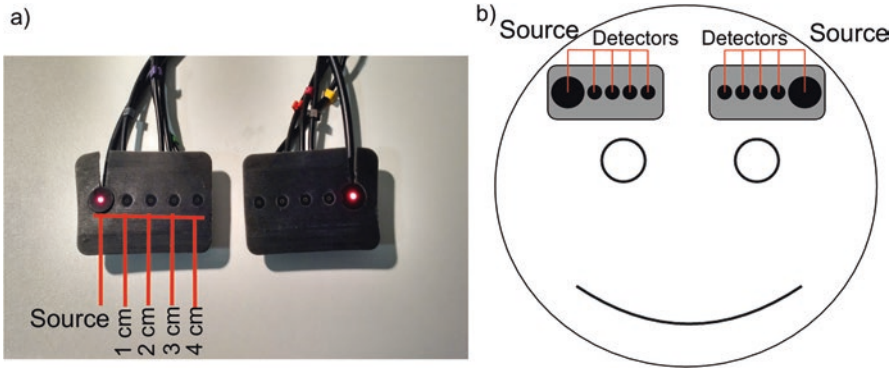

Fig. 19.1 (**a**) Probe holders with source and 4 detectors. (**b**) Diagram showing probe placement

isolate stimulus-related activations from uncorrelated haemodynamic trends ('block average method'); the second involved regression of the 1 cm channel by building a simple general linear model of each chromophore signal from the 2 and 3 cm channels ('short-separation regression method'). This general linear model uses a series of Gaussian basis functions convolved with a vector defining the time of the stimulus presentation to model the haemodynamic response function [8].

All statistical analysis was carried out in SPSS (IBM, USA). A baseline period was defined as the 10 s window immediately prior to the onset of activation, and 10 s activation period was chosen around the maximum change in the middle of the stimulus period. The response for each subject was defined as the difference between activation and baseline. Student's unpaired, one-sided t-test was used to compare the response of the activation compared to zero (i.e. no response) and values of $p < 0.05$ were considered significant. Results are presented as mean ± standard error.

3 Results

The block average and short-separation regressed results for the 1, 2 and 3 cm channels are shown in Fig. 19.2.

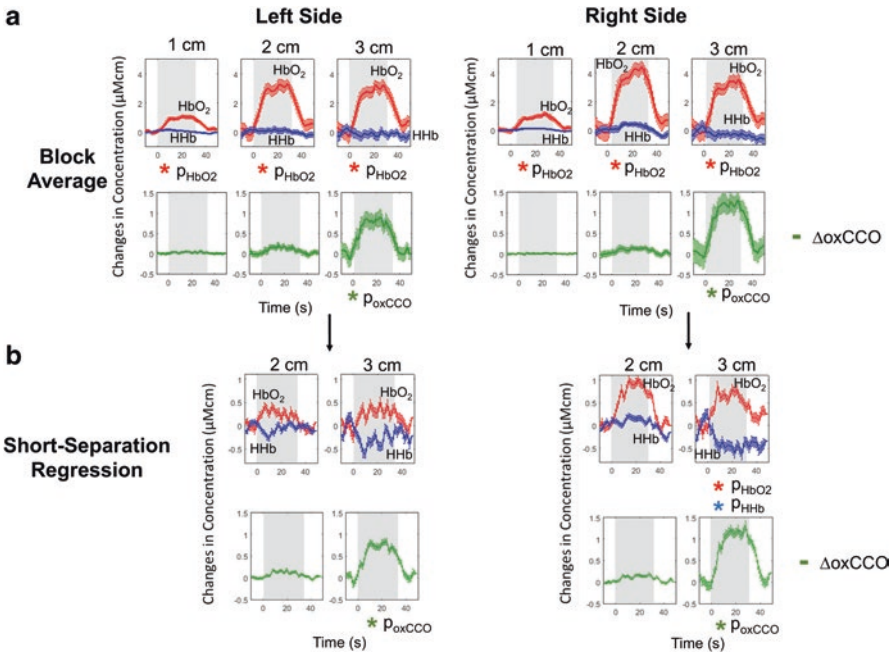

Fig. 19.2 Block-average and standard error of mean for 17 subjects during functional activation for left and right sides (**a**) without regression (**b**) with short-separation regression. Stimulus period indicated by *grey* background

Results of the block-average method for the right side show an increase in ΔHbO_2 at all source-detector separations, with a mean increase of 1.2 ± 0.5 μM.cm at 1 cm, 4.5 ± 1.6 μM.cm at 2 cm and 3.6 ± 1.6 μM.cm at 3 cm. No response is seen in ΔHHb at any of the channels. The ΔoxCCO shows no significant response at 1 cm and 2 cm but a large response is seen at 3 cm of 1.3 ± 0.8 μM.cm. Results for the short-separation regression method show a significant increase in ΔHbO_2 at only 3 cm of 0.9 ± 0.4 μM.cm, whilst ΔHHb now displays a significant decrease at 3 cm of −0.6 ± 0.5 μM.cm. The ΔoxCCO shows similar results as before, with the mean response of 1.3 ± 0.4 μM.cm at 3 cm.

Results for the block-average method for the left side show an increase in ΔHbO_2 at all separations, with mean values of 1.1 ± 0.4 μM.cm at 1 cm, 3.3 ± 1.3 μM.cm at 2 cm and 3.2 ± 1.5 μM.cm at 3 cm. There is no significant change in ΔHHb at any of the separations. ΔoxCCO shows a significant increase at only the 3 cm channel of 0.9 ± 0.8 μM.cm. After short-separation regression, no significant changes are seen in either of the haemodynamic variables. ΔoxCCO displays a similar response as to the block average, with a significant increase of 0.8 ± 0.3 μM.cm at 3 cm.

4 Discussion

We observed a response in ΔoxCCO in only the longer source-detector separation of 3 cm but not in the shorter separations of 1 cm and 2 cm. The regression of the 1 cm channel made no difference to the ΔoxCCO response.

There was a response in ΔHbO_2 at all source-detector separations, whereas ΔHHb showed no significant changes in any of the channels. After short-separation regression, the 2 cm channel did not show any significant response in the ΔHbO_2 and ΔHHb signals for either side, whilst at 3 cm there was a significant increase in ΔHbO_2 and decrease in ΔHHb for the right side and a similar but not significant trend was seen for the left side.

A scalp response was seen in both the right and left sides in the 1 cm channel. Results for the right side block-average at 3 cm show a false negative; no functional activation observed from the haemodynamic signals due to the absence of a significant decrease in ΔHHb. However, ΔoxCCO shows a strong increase that is indicative of functional activation. When the 1 cm short separation is regressed from the longer channels, we see a functional response in the haemoglobins not previously seen, with a significant increase in ΔHbO_2 and now significant decrease in ΔHHb. If only the changes in ΔHbO_2 were reported, then at 1 cm and 2 cm one would observe functional activation; however, taking into account ΔoxCCO and the short-separation regressed ΔHHb signals, we observe no functional activation in these channels. In this case, the ΔoxCCO and regressed ΔHHb signals have the capacity to rule out false positives.

Results for the left hemisphere show no functional activation from the haemoglobin signals at 3 cm even after regression. If we rely on the significant increase in ΔoxCCO as an indicator of functional activation, the haemodynamic result is a false

negative. The 1 cm short-separation regression in this case did not have the capacity to recover the false negative in the haemodynamic signals, which may be due to the scalp response not being fully removed. A false negative could also be caused by systemic changes such as blood pressure producing a significant effect on the brain physiology that masked activation. We did not measure systemic variables so cannot comment on the cause. However, previous studies have found systemic task-related changes to influence NIRS signals [9].

Note that the amplitude of the haemoglobin signals is on a similar scale to that of the ΔoxCCO signals after regression. This could be due to the fundamental characteristics of the regression method. The least-squares static estimator regression approach employed here can result in an underestimation of the haemodynamic response: either because the short-separation measurement has a non-negligible sensitivity to cortical tissue or because the superficial short-separation signal during the functional response mimics the true cerebral response. This effect could likely be improved through the use of a dynamic estimation approach, such as the Kalman filter methodology employed by Gagnon et al. [10].

This study demonstrates that inclusion of the ΔoxCCO signal during functional activation studies with fNIRS can provide an additional robust marker of brain activation allowing better identification of false positives and negatives.

Acknowledgments The authors would like to thank the Centre for Doctoral Training Integrated Photonic and Electronic Systems (EP/L015455/1) and The Wellcome Trust (104580/Z/14/Z) for the financial support of this work. RJC is funded by EPRSC fellowship EP/N025946/1.

References

1. Tachtsidis I, Scholkmann F (2016) False positives and false negatives in functional near-infrared spectroscopy : issues, challenges, and the way forward. Neurophotonics 3:030401–1 – 030401–6
2. Brigadoi S, Cooper RJ (2015) How short is short? Optimum source–detector distance for short-separation channels in functional near-infrared spectroscopy. Neurophotonics 2:025005–1–02005–9
3. Saager RB, Telleri NL, Berger AJ (2011) Two-detector corrected near infrared spectroscopy (C-NIRS) detects hemodynamic activation responses more robustly than single-detector NIRS. NeuroImage 55:1679–1685
4. Bainbridge A, Tachtsidis I, Faulkner SD et al (2013) Brain mitochondrial oxidative metabolism during and after cerebral hypoxia-ischemia studied by simultaneous phosphorus magnetic-resonance and broadband near-infrared spectroscopy. NeuroImage 102:173–183
5. Bale G, Elwell CE, Tachtsidis I (2016) From Jöbsis to the present day: a review of clinical near-infrared spectroscopy measurements of cerebral cytochrome-c-oxidase. J Biomed Opt 21:091307–1–091307–18
6. Kolyva C, Ghosh A, Tachtsidis I et al (2014) Cytochrome c oxidase response to changes in cerebral oxygen delivery in the adult brain shows higher brain-specificity than haemoglobin. NeuroImage 85:234–244

7. Bale G, Mitra S, Meek J et al (2014) A new broadband near-infrared spectroscopy system for in-vivo measurements of cerebral cytochrome-c-oxidase changes in neonatal brain injury. Biomed Opt Express 5:663–676
8. Gagnon L, Cooper RJ, Yücel M et al (2012) Short separation channel location impacts the performance of short channel regression in NIRS. NeuroImage 59:2518–2528
9. Tachtsidis I, Leung TS, Devoto L et al (2008) Measurement of frontal lobe functional activation and related systemic effects: a near infrared spectroscopy investigation. Adv Exp Med Biol 614:397–403
10. Gagnon L, Perdue K, Greve DN et al (2011) Improved recovery of the hemodynamic response in diffuse optical imaging using short optode separations and state-space modeling. NeuroImage 56:1362–1371

Chapter 20
Brain Tissue PO_2 Measurement During Normoxia and Hypoxia Using Two-Photon Phosphorescence Lifetime Microscopy

Kui Xu, David A. Boas, Sava Sakadžić, and Joseph C. LaManna

Abstract Key to the understanding of the principles of physiological and structural acclimatization to changes in the balance between energy supply (represented by substrate and oxygen delivery, and mitochondrial oxidative phosphorylation) and energy demand (initiated by neuronal activity) is to determine the controlling variables, how they are sensed and the mechanisms initiated to maintain the balance. The mammalian brain depends completely on continuous delivery of oxygen to maintain its function. We hypothesized that tissue oxygen is the primary sensed variable. In this study two-photon phosphorescence lifetime microscopy (2PLM) was used to determine and define the tissue oxygen tension field within the cerebral cortex of mice to a cortical depth of between 200–250 μm under normoxia and acute hypoxia (FiO_2 = 0.10). High-resolution images can provide quantitative distributions of oxygen and intercapillary oxygen gradients. The data are best appreciated by quantifying the distribution histogram that can then be used for analysis. For example, in the brain cortex of a mouse, at a depth of 200 μm, tissue oxygen tension was mapped and the distribution histogram was compared under normoxic and mild hypoxic conditions. This powerful method can provide for the first time a description of the delivery and availability of brain oxygen *in vivo*.

Keywords Oxygen partial pressure • 2PLM • Tissue oxygen tension • Distribution histogram • Mouse

K. Xu • J.C. LaManna (✉)
Department of Physiology and Biophysics, Case Western Reserve University, School of Medicine, Robbins Building E611, 10900 Euclid Ave., Cleveland, OH 44106-4970, USA
e-mail: jcl4@case.edu

D.A. Boas • S. Sakadžić
Optics Division, Athinoula A. Martinos Center for Biomedical Imaging, Department of Radiology, Massachusetts General Hospital and Harvard Medical School, Charlestown, MA, USA

H.J. Halpern et al. (eds.), *Oxygen Transport to Tissue XXXIX*, Advances in Experimental Medicine and Biology 977, DOI 10.1007/978-3-319-55231-6_20

1 Introduction

The mammalian brain depends completely on continuous delivery of oxygen to maintain its function. There are numerous intrinsic and extrinsic mechanisms that maintain a suitable level of oxygen availability to the neurons and other cells of the central nervous system. The brain tissue parenchyma exists in a low oxygen environment. For example, the oxygen partial pressure (Po_2) distribution histogram and cumulative occurrence function suggests that 90% of the oxygen levels are below 30 mmHg in rat brain [1]. Hypoxia is any decrease in the availability of oxygen. Under hypoxic condition, decreases in inspired oxygen produce decreases in tissue PO_2. Mammals adapt to prolonged moderate hypoxia by increased ventilation, increased blood hemoglobin and failure to gain weight. Prolonged hypoxia also results in an increase in capillary density, resulting in decreased intercapillary distance achieved through angiogenesis that allows brain tissue oxygen diffusion flux to remain adequate [2]. We have previously demonstrated a right shift and broadening in the distribution of capillary segment lengths in rat brain after 3 weeks of hypoxia [3].

Determining the range of optimal oxygen concentrations in the mammalian brain is important, however, the tools and techniques for quantitative oxygen measurements in the awake, normally functioning brain have been limited, mostly by the need for noninvasiveness. In addition, for any method used, it requires adequate response time and signal localization in both temporal and spatial hetero- geneities at the microregional level. This includes the methods such as polarography, optical, electron paramagnetic resonance (EPR), nuclear magnetic resonance (NMR), positron emission tomography (PET), and mass spectrometric techniques [4]. Two-photon phosphorescence lifetime microscopy (2PLM) of PO_2 can provide detailed distributions of the absolute oxygen concentration in tissue [5–7]. This method enables us to measure PO_2 with high temporal and spatial resolution in three dimensions, and features a measurement depth of up to 250 μm, sub-second temporal resolution. High-resolution images can document the intercapillary oxygen concentration gradients [5]. This method can also be used with intravascular dye administration to provide detailed descriptions of the blood oxygen concentration in arterioles, veinules and capillaries [5, 8].

In this study, 2PLM of PO_2 was used to map the tissue oxygen tension in the mice cerebral cortex down to a cortical depth of 200–250 μm. These data enabled us to determine quantitative distributions of oxygen concentration in the brain tissue.

2 Methods

2.1 Animal Preparation

Animals were prepared under a protocol approved by the Subcommittee on Research and Animal Care at Massachusetts General Hospital. As described previously [5], for imaging of PO_2 in the microvasculature, C57BL/6 mice (male, 25–30 g, 3 months old) were anesthetized by isoflurane (1–2% in a mixture of O_2 and air) under constant temperature. Mice were tracheotomized and a catheter was inserted in the femoral artery to monitor the blood pressure and blood gases and to administer the dyes. A cranial window was opened in the parietal bone with intact dura and sealed with a 150-μm thick microscope coverslip. The concentration of the oxygen-sensitive phosphorescent dye PtP-C343 in the blood immediately after administration was ~16 μM.

2.2 Two-Photon Laser Scanning Microscopy

Partial O_2 pressure in tissue (PtO_2) was measured using *in vivo* two-photon high-resolution PO_2 measurements in mouse cortical microvasculature and tissue, by combining an optimized imaging system with a two-photon–enhanced phosphorescent nanoprobe [5–8]. In brief, the imaging was performed on the brain of anesthetized animals through the sealed cranial windows. The two-photon excitation made it possible to confine the phosphorescence quenching by oxygen to the immediate vicinity of the focal plane, thus minimizing oxygen consumption and/or phototoxicity. During the measurement, isoflurane was discontinued and anesthesia was maintained by first injecting a 50-mg/kg intravenous bolus of α-chloralose followed by continuous intravenous infusion at 40 mg/(kg/h). To reduce possible animal motion during experiments, we administered an intravenous bolus of pancuronium bromide (2 mg/kg) followed by continuous intravenous infusion at 2 mg/(kg/h). Tissue PO_2 values were measured during normoxia with the fraction of inspired oxygen (FiO_2) of 21% and hypoxia (FiO_2 = 10%) [9].

3 Results

Two-photon laser scanning microscopy was used to map the tissue oxygen tension within the mice cerebral cortex of down to a cortical depth of 200–250 μm. Our preliminary data showed that the tissue PO_2 was in the range of 20–60 mmHg and 2–18 mmHg for normoxia and hypoxia, respectively. Figure 20.1 shows an example image from the mouse cortex at a depth of 200 μm, tissue oxygen tension was mapped under normoxic and hypoxic conditions and the tissue PO_2 distribution

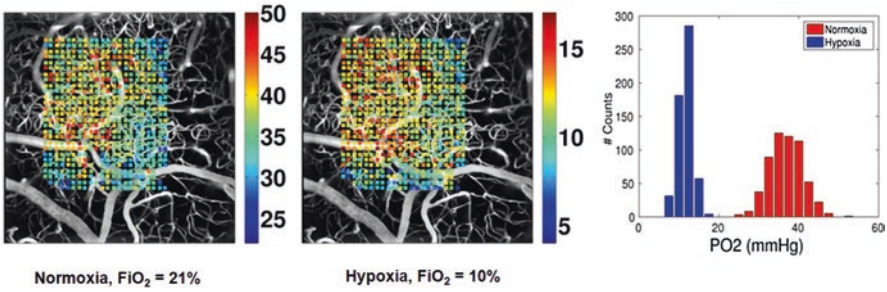

Fig. 20.1 Tissue PO_2 in a mouse brain measured by two-photon phosphorescence lifetime microscopy (2PLM) of PO_2, 200 μm below the cortical surface under normoxic and hypoxic ($FiO_2 = 0.10$) conditions, stack 725 × 725 × 360 μm^3. Tissue oxygen tension was mapped and the tissue PO_2 distribution histograms were compared between normoxia (range 25–50 mmHg) and hypoxia (range 8–18 mmHg). There was no overlap between the PO_2 distributions of the two conditions

histograms were compared. The tissue PO_2 during hypoxia was in the range of 8–18 mmHg, lower than the tissue PO_2 during normoxia (25–50 mmHg). There was no overlap between the PO_2 distributions of the two conditions.

4 Discussion

Key to the understanding of the principles of physiological and structural acclimatization to changes in the balance between energy supply (represented by substrate and oxygen delivery, and mitochondrial oxidative phosphorylation) and energy demand (initiated by neuronal activity), is to determine the controlling variables, how they are sensed, and the mechanisms initiated to maintain the balance. We hypothesized that tissue oxygen is the primary sensed variable during hypoxic acclimatization. In this study, 2PLM of PO_2 allowed us to map the tissue oxygen tension within the mouse cerebral cortex down to a cortical depth of 20–250 μm. The data are best appreciated by quantifying the tissue PO_2 distribution histogram that can then be used for analysis. For example, the images from the cortex of a mouse demonstrated significantly different tissue PO_2 distribution histograms under normoxic and mild hypoxic conditions. We have previously modelled the expected oxygen field changes for the "unit capillary" in rat cerebral cortex and showed the predicted oxygen tension along the length of a "unit capillary" and with respect to tissue depth (distance from the capillary). The model predicts a significant flattening of the distribution curve and tissue oxygen gradients after 3 weeks of mild hypoxia [10]. Global measurements of brain tissue oxygenation generally corroborate these predictions [11]. Two-photon phosphorescence lifetime microscopy of PO_2 will enable us to directly test this model in the mouse studies.

Acknowledgments This study was supported by the NIH grants R01 NS38632, R24 NS092986, R01 NS091230, R01 NS055104, and R01 EB021018.

References

1. LaManna JC (2007) Hypoxia in the central nervous system. Essays Biochem 43:139–151
2. LaManna JC, Vendel LM, Farrell RM (1992) Brain adaptation to chronic hypobaric hypoxia in rats. J Appl Physiol 72:2238–2243
3. LaManna JC, Cordisco BR, Knuese DE et al (1994) Increased capillary segment length in cerebral cortical microvessels of rats exposed to 3 weeks of hypobaric hypoxia. Adv Exp Med Biol 345:627–632
4. Ndubuizu O, LaManna JC (2007) Brain tissue oxygen concentration measurements. Antioxid Redox Signal 9(8):1207–1219
5. Sakadžić S, Roussakis E, Yaseen MA et al (2010) Two-photon high-resolution measurement of partial pressure of oxygen in cerebral vasculature and tissue. Nat Methods 7(9):755–759
6. Finikova OS, Lebedev AY, Aprelev A et al (2008) Oxygen microscopy by two-photon-excited phosphorescence. ChemPhysChem 9(12):1673–1679
7. Lecoq J, Parpaleix A, Roussakis E et al (2011) Simultaneous two-photon imaging of oxygen and blood flow in deep cerebral vessels. Nat Med 17(7):893–898
8. Sakadžić S, Mandeville ET, Gagnon L et al (2014) Large arteriolar component of oxygen delivery implies a safe margin of oxygen supply to cerebral tissue. Nat Commun 5:5734
9. Baraghis E, Devor A, Fang Q et al (2011) Two-photon microscopy of cortical NADH fluorescence intensity changes: correcting contamination from the hemodynamic response. J Biomed Opt 16(10):106003
10. Lauro KL, LaManna JC (1997) Adequacy of cerebral vascular remodeling following three weeks of hypobaric hypoxia. Examined by an integrated composite analytical model. Adv Exp Med Biol 411:369–376
11. Dunn JF, Grinberg O, Roche M et al (2000) Noninvasive assessment of cerebral oxygenation during acclimation to hypobaric hypoxia. J Cereb Blood Flow Metab 20(12):1632–1635

Chapter 21
Age-Related Changes in Physiological Reactivity to a Stress Task: A Near-Infrared Spectroscopy Study

A. Brugnera, C. Zarbo, R. Adorni, A. Gatti, A. Compare, and K. Sakatani

Abstract Aging is associated with changes in biological functions, such as reduced cardiovascular responses to stressful tasks. However, less is known about the influence of age on the reactivity of the prefrontal cortex (PFC) to acute stressors. Therefore, this study aimed to investigate the effects of a computerized-controlled stress task on the PFC and autonomic system activity in a sample of older and younger adults. We recruited a total of 55 healthy, right-handed persons (26 older adults with mean age 69.5, SD 5.8 years; and 29 younger adults with mean age 23.8, SD 3.3 years); groups were balanced for sex. Tasks included a control and an experimental condition: during both tasks individuals had to solve simple mental arithmetic problems. For the experimental condition, all participants were faced with a time limit that induced significant stress. Physiological indexes were collected continuously during the entire procedure using a 2-channel near infrared spectroscopy (NIRS) and an ECG monitoring system. Repeated measures ANOVA were used to assess changes in hemoglobin concentrations, and changes in both heart rate and performance outcomes. NIRS, ECG and performance data showed a significant interaction between the group and condition. Post-hoc analyses evidenced a significant increase in heart rate and Oxy-Hb concentration in the bilateral PFC between the control and experimental condition only in the younger group. Post-hoc analyses of behavioral data showed lower percentages of correct responses and higher response times in the older group. In summary, these results suggested that cardiovascular and cortical reactivity to stress tasks are a function of age. Older individuals seem to be characterized by blunted physiological reactivity, suggestive of

A. Brugnera (✉) • C. Zarbo • R. Adorni • A. Gatti • A. Compare
Department of Human & Social Sciences, University of Bergamo,
Piazzale S. Agostino 2, 24129 Bergamo, Italy
e-mail: agostino.brugnera@unibg.it

K. Sakatani
NEWCAT Research Institute, Department of Electrical and Electronic Engineering,
College of Engineering, Nihon University, Koriyama, Japan

H.J. Halpern et al. (eds.), *Oxygen Transport to Tissue XXXIX*, Advances in Experimental Medicine and Biology 977, DOI 10.1007/978-3-319-55231-6_21

impaired adaptive responses to acute stressors. Therefore, future studies should investigate the underlying physiological mechanisms of prefrontal and cardiovascular changes related to aging.

Keywords Older adults • Younger adults • NIRS • HR • Reactivity

1 Introduction

Aging, or the age-progressive decline in intrinsic physiological function [1], is associated with cognitive impairments as well as functional alterations of the cardiovascular system [2] and prefrontal cortex (PFC) [3]. Literature on elderly suggests that cardiac stress responses may also be impaired [2], while little is known about prefrontal reactivity to stressful tasks.

Regarding the cardiovascular system, aging leads to a reduced reactivity to stressful tasks due to a lowered maximal heart rate (HR) [2, 4]. As suggested by Uchino et al. [2], the lowered maximal HR is probably caused by a decline and compensatory processes in the aging myocardium, such as a decrease in the concentration/sensitivity of myocardial β-adrenergic receptors.

However, to date no studies have investigated prefrontal reactivity to stress in older adults. Indeed, much literature on the aging population has focused on age-related cerebral activity during cognitive tasks, finding a general cognitive decline and an impairment of executive functions [3]. These studies evidenced hypo- or hyper-activation of the PFC during cognitive tasks in older persons compared with younger adults [3, 5]. Specifically, the hyper-activity hypothesis suggests that the aging brain compensates for cognitive decline by hyper-recruiting the frontal cortex or distributing information processing among different areas [3].

Moreover, the cognitive performance of tasks which require information processing is also a function of age [3]. Due to the above-mentioned functional changes at the level of the PFC, older persons are characterized by impaired behavioral responses compared with younger adults [3]. In particular, they show delayed reaction times and a higher number of errors during cognitive tasks.

Therefore, this study aimed to investigate psychophysiological reactivity and behavioral performance during a stress task in a sample of younger and older adults using a 2-channel near infrared spectroscopy (NIRS) and an ECG monitoring system. We tested the hypotheses that during stress response: (i) prefrontal activity would be a function of age, even if we did not specify an a priori direction of the effect due to the lack of literature; (ii) cardiovascular reactivity would be reduced in older compared to younger adults, as suggested in the meta-analysis of Uchino et al. [2]; and (iii) behavioral responses (response times and percentage of correct responses) would be reduced in older compared to younger adults, as shown in earlier studies [3, 4].

2 Methods

A total of 55 healthy, right-handed persons (26 older persons with mean age 69.5, SD 5.8 years; and 29 young adults with mean age 23.8, SD 3.3 years) was recruited for this study. None of the participants was affected by neurological or psychiatric illnesses as assessed by means of a semi-structured interview.

The study was conducted in accordance with the American Psychological Association (1992) ethical standards for the treatment of human experimental volunteers; each participant provided written consent in compliance with the Declaration of Helsinki (BMJ, 1991; 302, 1194).

Participants were seated in a comfortable chair, in a silent room. During psychophysiological recording, they were instructed to avoid any movement of the body and to minimize those of the head. A 5-min rest period (baseline) was followed by completion of a randomized controlled stress task (Montreal Imaging Stress Task, MIST], designed to evoke stress responses in the subjects. After a 2-min training phase, participants were randomized to start with a 5-min control condition or with a 5-min experimental (i.e. stressful) condition. During both tasks, individuals had to solve mental arithmetic problems. In the case of the experimental condition, participants were faced with a time limit that induced significant stress. All participants completed both conditions. Details on the procedure can be found in [6]. Behavioral data of two individuals were not available due to recording problems.

We used a portable Bluetooth® CW-NIRS system (PocketNIRS Duo, DynaSense, Japan) to measure changes in concentration of Oxy-Hb, deOxy-Hb, and total-Hb in the PFC. This system uses light emitting diodes of three different wave-lengths (735, 810, and 850 nm) as light sources and one photo-diode as a detector, and has two channels (one left and one right). The sampling rate was set to 10.2 Hz. The changes in concentration of hemoglobin are expressed in arbitrary units (a.u.). Optodes were fixed to the person's forehead using adhesive patches. The NIRS setup replicated the one adopted by Tanida et al. [7]. this positioning is similar to the midpoint between electrode positions Fp1/Fp3 (left) and Fp2/F4 (right) of the international electroencephalographic 10–20 system [7], with the emitters-detectors located over the dorsolateral and frontopolar areas of the PFC. The signal was post-processed using a freely available MATLAB toolbox (N.A.P., NIRS Analysis Package).

For the autonomic measurements, we used the Pulse Sensor, a wearable Bluetooth® device produced by STMicroelectronics and manufactured by MR&D (Italy). This sensor continuously monitors heart activity. The device was positioned on the person's chest using an adhesive patch or an elastic band. Data were processed using a freely available MATLAB toolbox (Kubios HRV). For the present study, only HR was analyzed. HR data of four individuals were not available due to recording problems. The ECG of each person was visually inspected in order to correct missing beats and artifacts.

Differences in demographic variables were assessed using Fisher exact test (frequencies) or independent sample t-tests. For the latter analyses, independent

variable was the group (Young and Elderly), while the dependent variables were age or years of education. For each task condition, we analyzed changes in hemoglobin concentration and HR in terms of differences from the mean baseline values. Mean Δ Oxy-, deOxy and total-Hb, mean ΔHR values and behavioral data (response times, percentage of correct responses) were subjected to repeated measures ANOVAs. For ΔOxy-Hb, the factors were the group (Young and Elderly), the condition (Control and Experimental) and the channel (Left and Right). For ΔHR and behavioral data, factors were the Group and the Condition. Post-hoc analyses were performed using Tukey's test. A p-value ≤0.05 was considered significant. All analyses were performed with SPSS 23.0 (IBM, USA) and STATISTICA 12.5 (StatSoft Inc., USA).

3 Results

Preliminary data analyses showed that all variables were normally distributed.

Analyses on demographic data were reported in Table 21.1. As evidenced, the two groups were balanced for sex, and were significantly different as regards age. Finally, mean years of education were significantly different between younger and older adults: all the younger participants were university students or attended at least high school, while most of the older ones attended only elementary or middle school. Educational differences between study samples were in line with the census data reported by Italian National Institute of Statistics (ISTAT), suggesting the absence of a selection bias.

ANOVA performed on ΔOxy-Hb showed an effect of the Condition ($F1,53 = 6.43$; $p = 0.01$. Control: $M = 0.0024$ a.u., $SE = 0.0005$; Experimental: $M = 0.003$, $SE = 0.005$). Results suggest an increased bilateral PFC activity between the control and experimental condition, regardless the group. ANOVA also showed a significant interaction between Condition*Group ($F1,53 = 4.82$; $p = 0.03$). Post-hoc analyses showed that only younger adults had a significant increase in ΔOxy-Hb values between the control and experimental condition ($p = 0.0060$). Means and SE are reported in Fig. 21.1 (left panel). All other effects and interactions were non-significant. Analyses performed on ΔdeOxy-Hb showed an effect of the Condition ($F1,53 = 8.14$; $p < 0.01$. Control: $M = -0.0094$ a.u., $SE = 0.0036$; Experimental: $M = 0.014$ a.u., $SE = 0.037$). Results suggest a decrease in deOxy-Hb concentration

Table 21.1 Frequencies, means (SD) and their respective *t*-values of demographic variables by groups

	Younger adults (N = 29)	Older adults (N = 26)	*t*-value	*p* value
Males (percentage)	13 (55.2)	15 (57.7)	/	*ns*
Age (SD)	23.8 (3.31)	69.5 (5.78)	−36.5	< 0.001
Years of education (SD)	15.4 (2.23)	8.73 (3.78)	8.05	< 0.001

ns non-significant

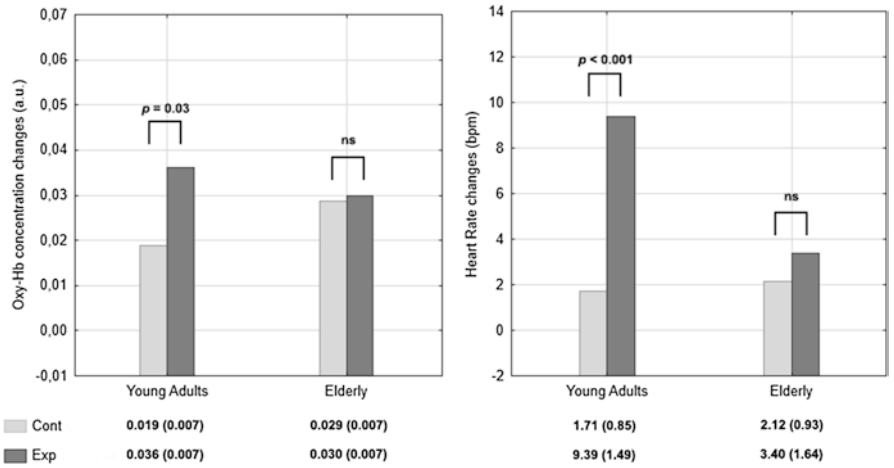

Fig. 21.1 *Left*, changes in Oxy-Hb from baseline (expressed in arbitrary units; a.u.) during the procedure in both groups. *Right*, changes in heart rate from baseline (expressed in beats per minute, BPM) during the procedure in both groups. Means and SE are reported below each group

changes from Control to Experimental condition, regardless the group. All other effects and interactions were non-significant. Finally, the ANOVA performed on total-Hb led to non-significant effects and interactions.

ANOVA performed on ΔHR showed an effect of the Condition ($F_{1,49} = 21.42$; $p < 0.001$. Control: M = 1.92 beats per minute, SE = 0.63; Experimental: M = 6.4, SE = 1.11). Results indicate that the procedure led to an increase in HR between the control and experimental condition. ANOVA also showed a significant interaction between Condition*Group ($F_{1,49} = 10.9$; $p > 0.001$). Post-hoc analyses showed that only the younger adults had a significant increase in ΔHR between the control and experimental condition ($p < 0.001$). Moreover, post-hoc analyses showed that the mean ΔHR of younger adults during the experimental condition was significantly different from the ΔHR of older adults during both conditions ($p < 0.001$). All means and SE are reported in Fig. 21.1 (right panel).

ANOVA performed on Response Times showed an effect of Group ($F_{1,51} = 31.7$; $p < 0.001$. Younger adults: M = 2.97, SE = 0.26 s; Older adults: M = 5.15, SE = 0.28 s) and an effect of Condition ($F_{1,51} = 59.9$; $p < 0.001$. Control: M = 4.8, SE = 0.28; Experimental: M = 3.33, SE = 0.11). The interaction between Group*Condition was also significant ($F_{1,51} = 8.5$; $p = 0.005$). Post-hoc analyses showed that all comparisons were significantly different (all $p < 0.001$), except for the Response Time of younger adults during the control condition compared with the Response Time of older adults during the experimental condition. Finally, ANOVA performed on the percentage of correct responses showed an effect of Condition ($F_{1,51} = 1720$; $p < 0.001$. Control: M = 93.8%, SE = 0.08%; Experimental: M = 52.1%, SE = 0.5%). The interaction between Group*Condition was also significant ($F_{1,51} = 7.46$; $p = 0.008$). Post-hoc analyses showed that all comparisons were significantly different (all p-values <0.05), except for the percentage of correct responses between younger and older adults during the experimental condition.

4 Discussion

In summary, our results suggest that cardiovascular and cortical reactivity to stress tasks are a function of age. Indeed, when compared to younger adults, older individuals seem to be characterized by a blunted cortical and cardiovascular reactivity to a stressful psychosocial task and by behavioral impairments.

Regarding the cortical responses, results showed a bilateral increase in ΔOxy-Hb and a decrease in ΔdeOxy-Hb between the control and experimental condition, irrespective of the group. Therefore, during the experimental condition, participants recruited more cognitive resources in order to solve the mathematical tasks when faced with a time limit. Figure 21.1 shows that, during the control condition, PFC activity in older adults was greater than that of younger adults, even though the difference was not significant. These results are suggestive of PFC hyper-recruitment [3] in older adults when faced with a simple mathematical task. Interestingly, only younger adults experienced a significant bilateral increase in PFC activity between the control and experimental condition. Compared with younger adults, levels of oxygenated hemoglobin in the older adults remained almost identical during the entire procedure. Therefore, our results show reduced cortical reactivity to stress tasks in older adults compared with younger adults. It is worth noticing that the between-group differences in NIRS data were observed only with Oxy-Hb concentration changes.

Regarding cardiological responses, our results confirm previous reports [8]. Indeed, the experimental (i.e. stressful) condition was characterized by increased HR irrespective of the group. However, Fig. 21.1 shows that only younger adults experienced a strong cardiovascular reactivity between the control and experimental (i.e. stressful) condition. Uchino et al. [2] hypothesized that aging leads to a specific decline and compensatory process in the myocardium that, in turn, reduces maximal heart rates.

Finally, during the control condition, compared to younger adults, the response times and percentage of correct responses of older adults were higher and lower, respectively. These results are similar to those reported by others [3]. Older adults seem to suffer from a generalized delay in reaction time and have less attentional resources, due to functional changes in prefrontal activity [3]. Nevertheless, it should be noted that these findings could be (in part) due to the less familiarity of older persons with the use of a PC compared with younger adults. Moreover, the lower educational level among elderly could have potentially influenced our results.

In conclusion, although it is well known that behavioral and cardiac responses are blunted in older adults [2, 3], this is the first NIRS study to investigate cortical reactivity to stressful tasks in older versus younger adults. In these study samples, we found evidence of reduced cortical and cardiovascular reactivity, as well as decreased behavioral performances. However, additional studies are required to confirm these explorative findings and to expand knowledge in this field.

References

1. Flatt T (2012) A new definition of aging? Front Genet 3:148
2. Uchino BN, Birmingham W, Berg CA (2010) Are older adults less or more physiologically reactive? A meta-analysis of age-related differences in cardiovascular reactivity to laboratory tasks. J Gerontol B Psychol Sci Soc Sci 65B(2):154–162
3. Berchicci M et al (2012) Prefrontal hyperactivity in older people during motor planning. NeuroImage 62(3):1750–1760
4. Sakatani K, Tanida M, Katsuyama M (2010) Effects of aging on activity of the prefrontal cortex and autonomic nervous system during mental stress task. Adv Exp Med Biol 662:473–478
5. Herrmann MJ et al (2006) Cerebral oxygenation changes in the prefrontal cortex: effects of age and gender. Neurobiol Aging 27(6):888–894
6. Dedovic K et al (2005) The Montreal imaging stress task: using functional imaging to investigate the effects of perceiving and processing psychosocial stress in the human brain. J Psychiatry Neurosci 30(5):319–325
7. Tanida M, Katsuyama M, Sakatani K (2007) Relation between mental stress-induced prefrontal cortex activity and skin conditions: a near-infrared spectroscopy study. Brain Res 1184:210–216
8. Castaldo R et al (2015) Acute mental stress assessment via short term HRV analysis in healthy adults: a systematic review with meta-analysis. Biomed Signal Process Control 18:370–377

Chapter 22
Development and Validation of a Sensor Prototype for Near-Infrared Imaging of the Newborn Brain

Linda Ahnen, Helene Stachel, Stefan Kleiser, Cornelia Hagmann, Jingjing Jiang, Alexander Kalyanov, Scott Lindner, Martin Wolf, and Salvador Sanchez

Abstract Imaging brain oxygenation is crucial for preventing brain lesions in preterm infants. Our aim is to build and validate a near-infrared optical tomography (NIROT) sensor for the head of neonates. This sensor, combined with an optoacoustic device, will enable quantitative monitoring of the structural and functional information of the brain. Since the head of preterm infants is small and fragile great care must be taken to produce a comfortable and compact device in which a sufficient number of light sources and detectors can be implemented. Here we demonstrate our first prototype. Heterogeneous silicone phantoms were produced to validate the prototype's data acquisition, data processing, and image reconstruction. Reconstructed optical properties agree well with the target values. The mechanical performance of the new NIROT sensor prototype confirms its suitability for the clinical application.

Keywords Near-infrared imaging • Silicone sensor • Reconstruction • Silicone phantoms • 3D print technology

1 Introduction

Cerebral ischemia is one of the key initiating factors for white matter injuries and intraventricular hemorrhage in preterm infants [1]. These pathologies are associated with long-term neurodevelopmental impairments. We are in the design process of a novel multimodal hybrid diagnostic imager to quantitatively monitor brain oxygenation. The novel imager will integrate an optoacoustic (OA) [2] device and a

L. Ahnen (✉) • H. Stachel • S. Kleiser • C. Hagmann • J. Jiang
A. Kalyanov • S. Lindner • M. Wolf • S. Sanchez
Biomedical Optics Research Laboratory, University Hospital Zurich, Zurich, Switzerland
e-mail: linda.ahnen@usz.ch

H.J. Halpern et al. (eds.), *Oxygen Transport to Tissue XXXIX*, Advances in Experimental Medicine and Biology 977, DOI 10.1007/978-3-319-55231-6_22

near-infrared optical tomography (NIROT) [3] sensor in a single system. The OA device includes an US transducer, which obtains structural information of the brain. NIROT will image a more diffuse 3D map of the oxygenation of the preterm baby's brain. Additionally, NIROT provides a 3D fluence (light intensity) estimation of the OA source, which can then be used to obtain quantitative oxygenation values in the OA image. In order to design the prototype NIROT sensor, geometric constraints and medical requirements have to be considered.

For accurate reconstructions of the optical properties in the region of interest, a sufficient number of light sources and detectors need to be implemented. The average head circumference of prematurely born infants varies between 21 and 35 cm for gestational age ranging from 23 to 41 weeks [4]. This severely limits the space available for NIROT measurements. Further spatial constraints result from the combination with the OA probe that necessarily uses the anterior fontanel's aperture for measurements. In order to obtain good quality signals, no light may pass directly between source and detector fibers. Also, the knowledge of the location of the source and detector fibers is crucial for a precise 3D image reconstruction [5]. Additionally, the head's irregular geometry poses difficulties for a good coupling of the light fibers to the skin. The fragile skin of premature infants has to be protected from any injuries. Sensor materials have to be biocompatible and need to be easy to clean and disinfect. Our aim is to build a prototype NIROT sensor that fulfils these requirements and is suitable for clinical application.

2 Methods

2.1 NIROT Sensor Overview

The NIROT sensor geometry is a ring structure, leaving space in its center for the OA device, which consists of a handheld ultrasound probe and a light source. The NIROT sensor includes 16 source and 4 detector microfiber bundles (Loptek GmbH & Co. KG, Berlin, Germany), fixed to a rigid ring (diameter 4.6 cm), which is embedded into soft silicone. The source and detector microfibers bundles consist of about 470 and 570 microfibers, with a diameter of 30 and 70 μm, respectively. The source and detector bundles have a bending radius of 4 and 7 mm, respectively. They are highly flexible and thus provide space for the OA device. Measurements are performed using the commercially available Imagent (ISS Inc., Champaign, IL, USA). It consists of 2 × 16 laser diodes that emit near-infrared light at 760 and 834 nm with an output power of 10 mW. Four photomultiplier tubes serve as light detectors. The Imagent is a frequency domain (110 MHz) near-infrared spectroscopy device, which measures the phase, amplitude, and mean of the sinusoidally modulated light intensity.

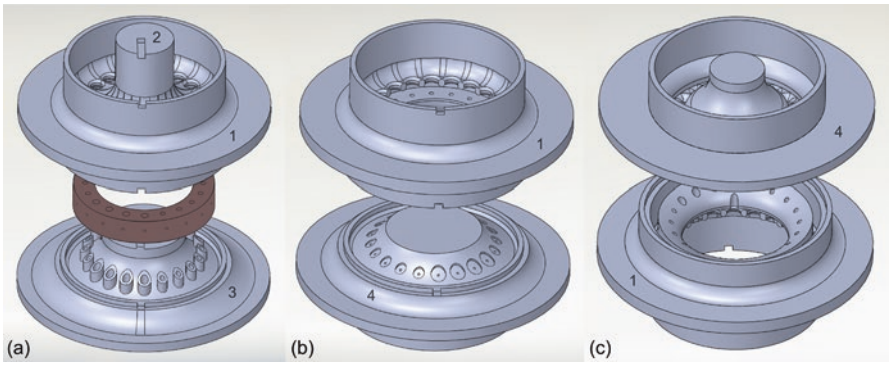

Fig. 22.1 (**a**) Shows the mold employed to cast the black silicone casing. It consists of parts *1*, *2*, and *3*. The rigid ring to which the fibers will be fixed is shown in *dark grey*. (**b**, **c**) Show two views of the mold (parts *1* and *4*) used to fill the optical windows with transparent silicone

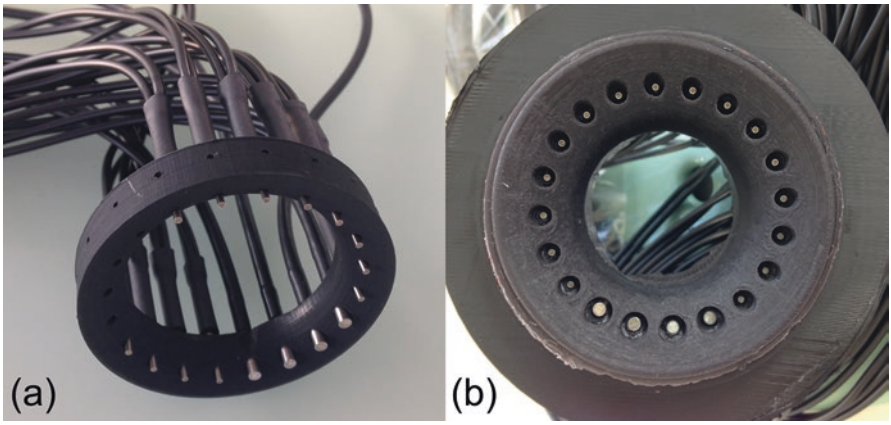

Fig. 22.2 (**a**) Shows the 3D printed rigid inner ring. Some source and detector fibers are fixed to it with the help of screws that are inserted perpendicular to the fibers. (**b**) Shows the fiber/ring structure embedded into black biocompatible silicone casing. The space around the fiber ends will later be filled with transparent silicone in order to create optical windows

2.2 Development of NIROT Sensor

In a first step, the light fibers are inserted into the 3D printed rigid ring (Fig. 22.1a, ring in dark grey) and fixed with M 1.2 screws (Fig. 22.2a). This ensures a fixed relative position of the sensor's source and detector fibers during the measurement. This ring, together with the fibers, is then placed into the mold (Fig. 22.1a) to cast a black silicone casing (Fig. 22.2b).

The inner ring and the mold of the NIROT sensor are produced using an Ultimaker 2 (Ultimaker B.V., Geldermalsen, the Netherlands) fused deposition modelling 3D printer. Acrylonitrile butadiene styrene (ABS) is heated up and deposited in small

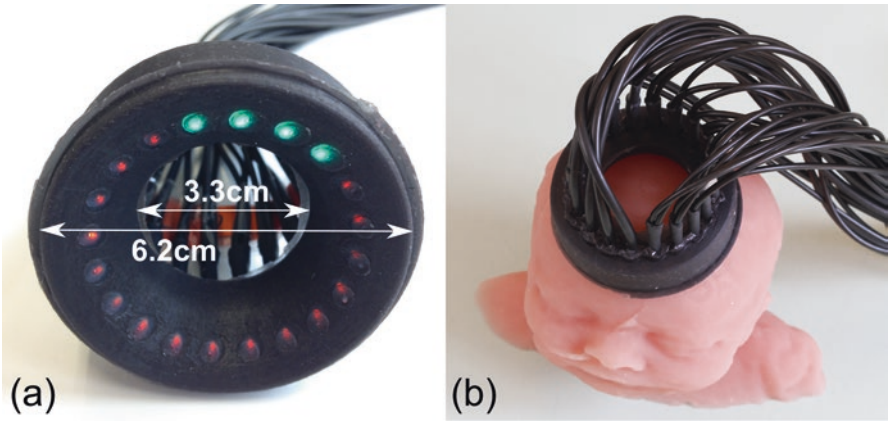

Fig. 22.3 (**a**) Finished NIROT sensor prototype with 16 sources and 4 detectors. (**b**) Shows the NIROT sensor placed on a silicone baby head phantom. The fibers are spread apart to provide space in the middle for the OA measurement

layers following the computer model of the different parts (Fig. 22.1). The nozzle size was 0.4 mm. For the 3D prints a layer height of 0.07 mm, a shell thickness of 1.4 mm, a fill density of 35% and a print speed of 50 mm/s is chosen. The outer shell printing speed is reduced to 35 mm/s to ensure an accurate printing. All 3D printed parts are sandpapered thoroughly to remove any directionality of the printing material. This is important to avoid any surface structures in the silicone, which might cause light piping. The black silicone casing surrounds the entire ring-fiber structure with silicone, except the fiber ends (Fig. 22.2b). This prevents light piping from source to detector fibers. In a second casting step, the mold shown in Fig. 22.1b, c was employed to fill transparent silicone into the hollow space around the fiber ends to create optical windows. To ensure a good light coupling into tissue, the optical windows were designed to be slightly elevated from the black silicone structure as can be seen in Fig. 22.1b (part 4). The soft silicone casing (Silpuran 2400/25 and Elastosil black RAL9011, WACKER Silicones, Burghausen, Nünchritz, Germany) is biocompatible and easy to disinfect. It allows the sensor to slightly adapt to the geometry of the head and prevents skin lesions. The finished NIROT sensor is shown in Fig. 22.3. In the NIROT sensor ring, the source-detector distance covers a range from 0.7 cm up to 4.6 cm. This results in a light intensity variation in the order of 10^3 [6], which exceeds the Imagent dynamic range. In order to address this problem, the emitted light intensity is attenuated with neutral density filters of varying optical density. The optical density of the filters is inversely correlated with source and detector distance to maintain an approximately constant light intensity at the detectors for a homogeneous medium.

2.3 Validation with Phantoms

Two heterogeneous silicone head phantoms with optical properties similar to the target application in preterm infants [7] were produced to validate the NIROT sensor (Fig. 22.3b). For this a 3D surface structure was extracted from MRI data and printed. From this 3D printed head a silicone mold was made to produce realistic head phantoms. Differently sized inclusions may be inserted into the head phantom's silicone mold. Here, spherical inclusions were employed to simulate localized lesions in the brain with a step change in optical properties. The head circumference of the phantoms was 28 cm. The phantoms consisted of a bulk material with an absorption coefficient of $\mu_a \approx 0.005$ mm^{-1} and a reduced scattering coefficient of $\mu_s' \approx 0.5$ mm^{-1}. The spherical inclusions (diameter 1.5 cm) in the head phantom were chosen to have larger absorption than the bulk material ($\mu_a \approx 0.05$ mm^{-1} and $\mu_a \approx 0.02$ mm^{-1}). The μ_s' of the inclusions was the same as the background. Image reconstructions of optical properties were performed with the software Nirfast [8, 9] based on data measured with the Imagent. Nirfast is a finite element software to simulate light propagation in tissue. For the reconstruction, a spherical shape was implemented in Nirfast to model the phantom head. During the 3D image reconstruction μ_s' was assumed to be constant.

3 Results, Discussion and Conclusion

The new NIROT sensor prototype is compact and light. The ease of handling makes it very suitable for the clinical application at the bedside, where space is limited. The elevated optical windows of the sensor enable moderate adaption to the head's surface, ensuring good light coupling. No light piping between the source and detector fibers was detected during the measurements on the silicone head phantoms. Figure 22.4 shows two center cross-sections of the 3D reconstructed image

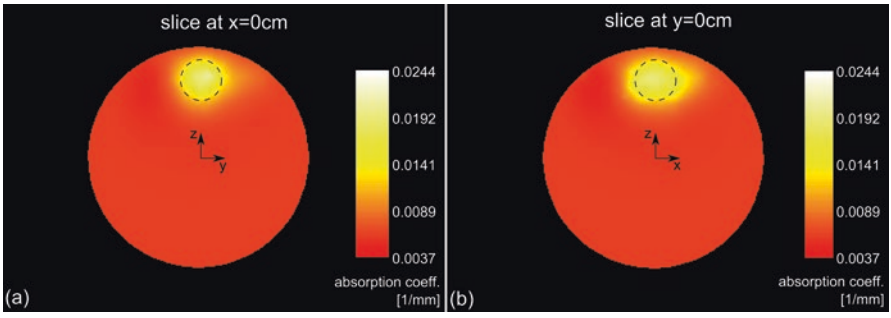

Fig. 22.4 Two center cross-sections of the 3D image reconstruction of the absorption coefficient are shown. (**a**) Shows the z-y plane, and (**b**) shows the z-x plane. The bulk absorption coefficient is 0.005 and 0.05 mm^{-1} of the spherical inclusion. The spherical inclusion's actual size and location is shown in *dashed lines*

for the phantom with the spherical inclusion with $\mu_a \approx 0.05\ mm^{-1}$. The shape and location of the inclusion was accurately reconstructed. Although the reconstruction model assumes a spherical head shape, it is applied onto a non-spherical head phantom. This results in a slight distortion of the inclusion shape as is visible in Fig. 22.4. The reconstructed μ_a of the spherical inclusions are lower than the target values (see Sect. 22.2.3). This is a well-known effect and mainly results from the smearing of the original spherical inclusion.

Here, we have presented a first prototype NIROT sensor that fulfils all the requirements for its clinical application (together with the OA device). The sensor has been validated with phantoms and in the near future the NIROT sensor will be tested in a dedicated clinical trial. For this the NIROT sensor design will be slightly changed to fit an egg-like shape, corresponding closer to the head than the current spherical shape to enable measurements in patients.

Acknowledgments This work was supported by the SwissTransMed project ONIRIUS, Swiss Cancer Research project KFS-3732-08-2015, KFSP Tumor Oxygenation and KFSP Molecular Imaging Network Zurich of the University Zurich, Swiss National Science Foundation (Grant number 139238 and 159490) and by the National Competence Center for Biomedical Imaging.

References

1. Khwaja O, Volpe JJ (2008) Pathogenesis of cerebral white matter injury of prematurity. Arch Dis Child Fetal Neonatal Ed 93(2):F153–F161
2. Beard P (2011) Biomedical photoacoustic imaging. Interface focus 1(4):602–631. doi:10.1098/rsfs20110028
3. Hebden JC, Austin T (2007) Optical tomography of the neonatal brain. Eur Radiol 17(11):2926–2933
4. Barbier A, Boivin A, Yoon W et al (2013) New reference curves for head circumference at birth, by gastational age. Pediatrics 131(4):e1158. doi:10.1542/peds.2011-3846
5. Ahnen L, Wolf M, Hagmann C et al (2016) Near-infrared image reconstruction of newborns' brains: robustness to perturbations of the source/detector location. In: Oxygen transport to tissue XXXVII. Springer, New York, pp 377–382
6. Hueber DM, Fantini S, Cerussi AE, et al (1999) New optical probe designs for absolute (self-calibrating) NIR tissue hemoglobin measurements. In: BiOS'99 international biomedical optics symposium. International Society for Optics and Photonics, pp 618–631
7. Arri SJ, Muehlemann T, Biallas et al (2011) Precision of cerebral oxygenation and he-moglobin concentration measurements in neonates measured by near-infrared spectroscopy. J Biomed Opt 16(4):047005
8. Jermyn M, Ghadyani H, Mastanduno MA et al (2013) Fast segmentation and high-quality three-dimensional volume mesh creation from medical images for diffuse optical tomography. J Biomed Opt 18(8):086007. doi:10.1117/1.JBO.18.8.086007
9. Dehghani H, Eames ME, Yalavarthy PK et al (2009) Near infrared optical tomography using NIRFAST: algorithm for numerical model and image reconstruction. Commun Numer Methods Eng 25:711–732

Chapter 23
Directional Migration of MDA-MB-231 Cells Under O_2/pH Gradients

Y. Enokida, Y. Tsuruno, K. Okubo, Y. Yamaoka, and E. Takahashi

Abstract We hypothesized that cancer cells actively migrate toward intratumor microvessels, guided by tissue gradients of metabolic substrates (such as O_2) and/or metabolites (such as CO_2/H^+). To test this hypothesis, we developed an in vitro model in which cellular energy metabolism establishes gradients of O_2/nutrient/metabolite in monolayer cells cultured in a conventional culture dish. When gradients of O_2 ranging from 3% to ~0% were produced, MDA-MB-231 cells located at 300, 500 and 1500 μm downstream in the gradient demonstrated significant directional migrations (Rayleigh *z* test). We also found a similar directionality in cell migration at the same location even when the initial O_2 level in the O_2 gradient was raised from 3% to 21%. Interestingly, such directionalities were no longer demonstrated when the cell density was lowered from 1.8×10^6 to 0.9×10^6 cells/ml. In the former, the magnitude of the extracellular pH gradient in regions 300 and 500 μm downstream in the gradient was significantly larger. Thus, the direction of cell migrations appeared to depend on the gradient of extracellular pH rather than on O_2.

Keywords Migration • Oxygen gradients • pH gradients • Cancer metastasis • MDA-MB-231 cell

1 Introduction

Locally proliferating cancer cells finally reach the intra-tumor microvessels and enter the vasculature (intravasation). To elucidate the mechanism for intravasation, we hypothesized that some cancer cells actively migrate towards the microvessels utilizing the gradients in the tissue as the cue for the direction [1]. These gradients include O_2, pH and CO_2, energy substrates, metabolites, energy state, and cytokines.

Y. Enokida • Y. Tsuruno • K. Okubo • Y. Yamaoka • E. Takahashi (✉)
Advanced Technology Fusion, Graduate School of Science and Engineering, Saga University, Saga, Japan
e-mail: eiji@cc.saga-u.ac.jp

H.J. Halpern et al. (eds.), *Oxygen Transport to Tissue XXXIX*, Advances in Experimental Medicine and Biology 977, DOI 10.1007/978-3-319-55231-6_23

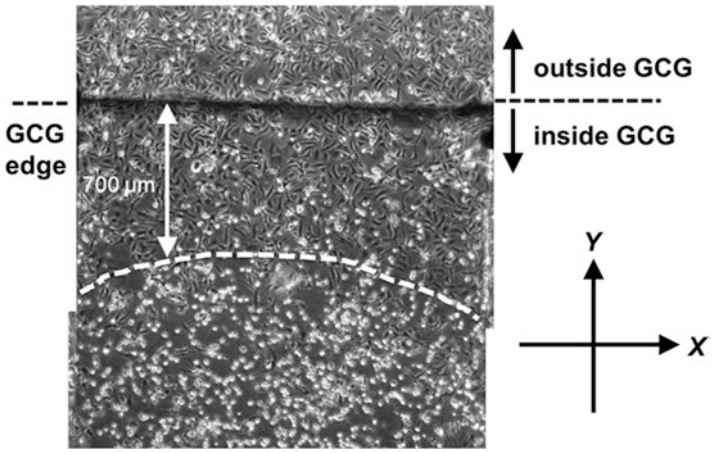

Fig. 23.1 MDA-MB-231 cells under the GCG. Cells >700 μm from the GCG edge (O_2 entrance) had rounded shapes suggesting severe hypoxic stress whereas cells were still viable (LIVE/DEAD Cell Viability Assays®). O_2 outside of the GCG was 3%

Our initial hypothesis was that the gradients of tissue O_2 concentration may direct cell migrations [2].

To examine this hypothesis in vitro, we devised the gap cover glass (GCG) that allows us to produce consistent O_2 gradients in monolayer cells cultured in a conventional collagen (type I) coated culture dish [2]. In the GCG, continuous reductions in O_2 concentration are produced starting from the edge of the GCG (O_2 entrance) towards the inside of the GCG. Thus, when the O_2 concentration outside the GCG was set at 3%, cells were supposed to be exposed to 3% to ~0% O_2 along the O_2 diffusion path. In fact, MDA-MB-231 cells locating approximately >700 μm from the edge appear to undergo severe hypoxic stress (Fig. 23.1). In this condition, cells located at 300, 500, and 1500 μm from the edge of the GCG demonstrated directional migrations toward the edge of the GCG (O_2 source) [2].

In the present study, we first examined whether the O_2 gradient, among varieties of tissue gradient, is the primary cue for the cell migration in our experimental model. Then, we examined the possibility that the gradients of extracellular pH might also determine cell movement.

2 Methods and Results

To examine whether the gradient of O_2 is the primary cue for the directional cell migration that we demonstrated in a previous study [2], we repeated the same experiment but the O_2 concentration outside of the GCG was increased to 21%, rather than the 3% in the previous study. In this condition, the cell in the GCG is supposed to be exposed to a gradient of O_2 ranging from 21% at the edge to ~18% at 500 μm

Table 23.1 *P*-values for the Rayleigh *z* test for directionality. $P < 0.05$ indicates a unidirectional migration

	3% O_2 high density	21% O_2 high density	21% O_2 low density
Outside	(0.68)	(0.28)	(0.47)
100 μm	(0.51)	(0.15)	(0.52)
300 μm	< 0.00003	0.011	(0.98)
500 μm	0.025	< 0.0002	(0.42)
700 μm	(0.052)	(0.13)	(0.31)
900 μm	(0.055)	0.019	< 0.0007
1500 μm	0.047	0.005	(0.88)

Left column indicates the distance from the O_2 entrance (GCG edge). High density and low density represent 1.8×10^6 and 0.9×10^6 cells/ml, respectively

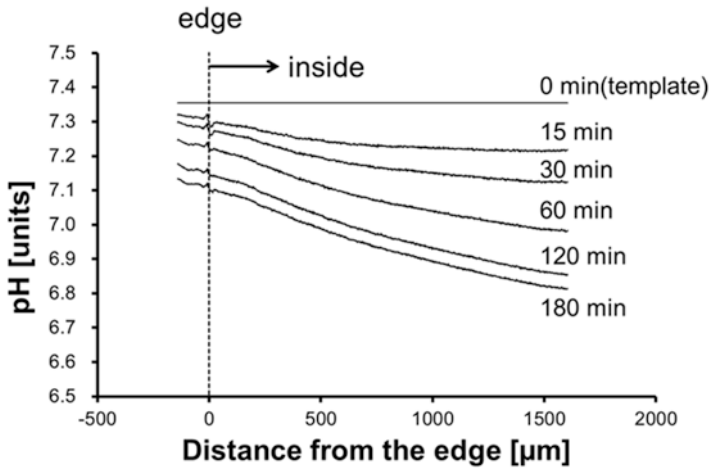

Fig. 23.2 Gradients of extracellular pH in the GCG

inside the GCG. We assume that these O_2 levels are too high for the intracellular O_2 sensing mechanism, if any, to respond.

Table 23.1 indicates the Rayleigh *z* test of directionality. Surprisingly, at this high O_2 concentration, significant directional migrations were demonstrated in the cell located at 300, 500, and 1500 μm from the edge of the GCG, that were similar to the previous experiment at 3% O_2.

Then, we focused on gradients of extracellular pH in the GCG. Because the GCG hinders release of metabolically produced CO_2 to air, extracellular pH should decrease in the GCG. In addition, Leibovitz's L-15 medium that we used in the measurement does not contain a strong buffer such as HCO_3^- and the pH gradients in the GCG should be exaggerated. We measured the medium pH under the GCG by fluorometry using BCECF (3′-O-Acetyl-2′,7′-bis(carboxyethyl)-4 or 5-carboxyfluorescein). Figure 23.2 shows the gradients of pH under the GCG. To exclude the influence of the

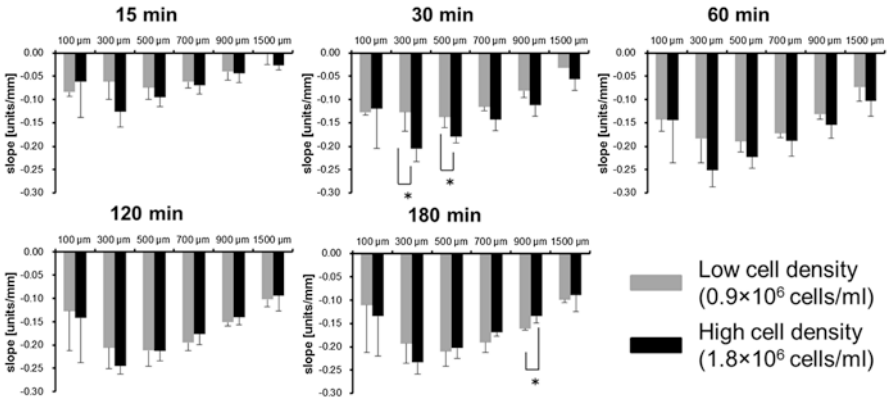

Fig. 23.3 Gradients of extracellular pH in low cell density (0.9×10^6 cells/ml) and high cell density (1.8×10^6 cells/ml) experiments. Time after the GCG placement is also indicated. *, $p < 0.05$

O_2 gradient, all the experiments were conducted at 21% O_2. To further elucidate the effect of pH gradients on cell migration, the experiment was conducted with the cell density halved (0.9×10^6 cells/ml) in order to alter the pH gradient. As indicated in Table 23.1, the directional cell movement at 300, 500, and 1500 μm was not demonstrated in this condition.

If extracellular pH is the cue for the directional migration observed in the previous high cell density experiment at 21% O_2, there should be a difference in the pH gradient between the high cell density experiment and the low cell density experiment. Figure 23.3 shows the gradients of pH at 100, 300, 500, 700, 900 and 1500 μm inside from the edge of the GCG. While pH gradients in these locations varied dynamically, we found a significant difference in pH gradients between the two groups at 300 and 500 μm at 30 min after GCG placement, and at 900 μm at 180 min after GCG placement.

3 Discussion

Intravasation of cancer cells is the initial step for hematogenous metastasis, whereas its mechanism remains unclear. Cancer cell intravasation is believed to depend on passive mechanisms including those arising from elevated interstitial pressure. In addition, recent studies have indicated active mechanisms for intravasation [1]. We are particularly interested in the hypothesis that cancer cells actively migrate toward intra-tumor microvessels along metabolic gradients in the tissue [2]. Initially, we focused on tissue gradients of O_2 concentration as the cue for cell migration, because hypoxia may promote motility of tumor cells through the HIF-1α pathway [3].

The newly devised GCG produced consistent gradients of O_2 in monolayer MDA-MB-231 cells cultured in a conventional culture dish. Based on the Rayleigh *z* test, we found directionalities in cell migration at a physiological O_2 range (i.e., 0–3%) whereas a similar directionality in cell movement was also demonstrated at a very high O_2 environment (i.e., 21%). It is unlikely that the intracellular O_2 sensor, such as HIF-1α, was activated at such a high O_2 range [4]. Thus, we were prompted to search for other gradients formed in the GCG as a cue for cell migration.

The GCG not only blocks O_2 supply to the cell, but also blocks release of metabolically produced CO_2 to air. Retention of CO_2 decreases pH in the medium. In addition, cancer cells including MDA-MB-231 cell used in the present study may vigorously excrete lactate to the extracellular medium. Consequently, large pH gradients should be produced in the extracellular medium. Therefore, we focused here on gradients of extracellular pH as a cue for cell migrations.

Acidic extracellular pH promotes binding of transmembrane integrin receptors with extracellular matrix ligands. Thus, gradients of extracellular pH over a cell may affect its migration. Using the Dunn chamber, Paradise et al. demonstrated that $\alpha_v\beta_3$ CHO-B2 and bovine retinal microvascular endothelial cells showed preferential migration toward acid in extracellular pH gradients [5]. Also, Jagielska et al. demonstrated in vitro that oligodendrocyte precursor cells exhibit a directional migration along pH gradients toward acidic pH despite that this movement appeared disadvantageous to overall survival of the cell [6].

In the present experiment, if the pH gradient would have guided the cell, the direction would be toward less acidic pH, which might confer not only a benefit for survival but also promote intravasation. While the magnitude of the pH gradient in the GCG changed dynamically, the pH gradient was always steeper at 300 and 500 μm along the diffusion path. We were able to manipulate the pH gradient at these locations by changing the cell density from 1.8×10^6 cells/ml to 0.9×10^6 cells/ml in which the pH gradients were significantly reduced (Fig. 23.3). Such differences in the pH gradient coincided with the directionality in cell migration; cells originally located at 300 and 500 μm demonstrated migration toward the GCG edge in the high cell density experiment whereas the migration was random in direction in the low cell density experiment.

Using a novel in vitro model, we examined a question whether O_2 gradients can be a major cue for directional migration of MDA-MB-231 cells. Results of the present experiment appear to discount the role of the O_2 gradient as a cue for cell migration and rather favor the extracellular pH gradients. We are planning to significantly reduce the pH gradient in the GCG by using hepes buffered medium instead of the present L-15 medium, with the aim to definitely define the role of extracellular pH in directional migration of MDA-MB-231 cells.

Acknowledgments This study was supported by JSPS KAKENHI Grant Number 26430117 to ET.

References

1. Bockhorn M, Jain RK, Munn LL (2007) Active versus passive mechanisms in metastasis: do cancer cells crawl into vessels, or are they pushed? Lancet Oncol 8:444–448
2. Yahara D, Yoshida T, Enokida Y et al (2016) Directional migration of MDA-MB-231 cells under oxygen concentration gradients. Adv Exp Med Biol 923:129–134
3. Gilkes DM, Xiang L, Lee SJ et al (2014) Hypoxia-inducible factors mediate coordinated RhoA-ROCK1 expression and signaling in breast cancer cells. Proc Natl Acad Sci U S A 111:E384–E393
4. Jiang BH, Semenza GL, Bauer C et al (1996) Hypoxia-inducible factor 1 levels vary exponentially over a physiologically relevant range of O_2 tension. Am J Phys 271:C1172–C1180
5. Paradise RK, Whitfield MJ, Lauffenburger DA et al (2013) Directional cell migration in an extracellular pH gradient: a model study with an engineered cell line and primary microvascular endothelial cells. Exp Cell Res 319:487–497
6. Jagielska A, Wilhite KD, Van Vliet KJ (2013) Extracellular acidic pH inhibits oligodendrocyte precursor viability, migration, and differentiation. PLoS One 8:e76048

Chapter 24
Environmental Enrichment Induces Increased Cerebral Capillary Density and Improved Cognitive Function in Mice

Chuan He, Constantinos P. Tsipis, Joseph C. LaManna, and Kui Xu

Abstract Enrichment provides an environment that fosters increased physical activity and sensory stimulation as compared to standard housing. Promoting and sustaining stimulation increases neuronal activity and, consequently, brain oxygen demand. The mammalian brain modulates its microvascular network to accommodate tissue energy demand in a process referred to as angioplasticity. In this study we investigated the effect of an environmental enrichment on cerebral capillary density and cognitive performance in mice. Microvascular density (N/mm^2) was determined by GLUT-1 immunohistochemistry in mice (3 months old) after 3 weeks of placement in a non-enriched or an enriched environment. The Y-maze test and a novel object recognition test were used to evaluate cognitive function in the aged mice (18 months old) after 4 weeks of environmental enrichment. Compared to the non-enriched control mice, the mice with environmental enrichment had significantly higher (~30%) capillary density in cortical brain. The enriched aged mice (n = 12) showed improved cognitive function, presented as a significantly higher alternation rate in the Y-Maze test compared to the non-enriched controls (n = 8). Our data suggest that environmental enrichment may result in increased brain capillary density and improved cognitive performance.

Keywords Angiogenesis • Preconditioning • Cognitive performance • Angioplasicity • Aged mouse

C. He
Department of Neurology, Jiangsu-Shengze Hospital of Nanjing Medical University, Suzhou 215228, China

C.P. Tsipis • J.C. LaManna • K. Xu (✉)
Department of Physiology and Biophysics, Case Western Reserve University, School of Medicine, Cleveland, OH, USA
e-mail: kxx@case.edu

H.J. Halpern et al. (eds.), *Oxygen Transport to Tissue XXXIX*, Advances in Experimental Medicine and Biology 977, DOI 10.1007/978-3-319-55231-6_24

1 Introduction

Environmental enrichment is an experimental setting in which animals experience more sensory stimulation and exploring activities. Increasing numbers of studies have shown that long-time housing in an enriched environment can enhance neurogenesis in the dentate gyrus of hippocampus and, thus, improve learning and memory [1]. It has been shown that environmental enrichment stimulated endothelial cell proliferation both in the hippocampus and in the prefrontal cortex in rats [2]. Up to now, the effect of environmental enrichment on brain plasticity and cognitive function were mostly studied in immature or young animals [3–5]. However, neurodegenerative and brain vascular disease mainly involve aged persons. Aging is a physiological process associated with cognitive decline [1]. In addition, the aging population is at risk for increased morbidity and mortality following ischemic or hypoxic events, such as those related to stroke or other neurodegenerative conditions. The mammalian brain modulates its microvascular network to accommodate tissue energy demand in a process referred to as angioplasticity. Brain angioplasticity, including angiogenesis, may play an important role in cognitive and neurological rehabilitation from age-related neurodegenerative and neurovascular diseases.

In this study we investigated the effect of 3 weeks of environmental enrichment on cerebral capillary density in mice. We also evaluated the change of cognitive performance in aged mice (18 months old) after 4 weeks of environmental enrichment.

2 Methods

2.1 Environmental Enrichment

The experimental protocol was approved by the Animal Care and Use Committee at Case Western Reserve University. Three-month-old mice and 18-month-old mice were randomly placed into the environmental enrichment and non-enriched control groups, respectively. Enrichment cages were supplied with various toys of different size, shape, and texture to promote visual/sensory stimulation and physical activity through climbing, burrowing, and exploration [6]. Toys were cycled between enrichment cages approximately every 3 days throughout the time course. Groups of three mice were housed in each enrichment cage to prevent overcrowding/competition and monitored on a daily basis. The non-enriched control mice were maintained in standard housing devoid of enrichment and monitored on a regular schedule. After 3 weeks of placement in the enrichment cage or non-enrichment cage, the capillary density was determined in the 3-month-old mice. Cognitive function was evaluated in the 18-month-old mice before and after 4 weeks of enrichment.

2.2 Determination of Cerebral Capillary Density

After 3 weeks of placement in the enrichment cage or non-enrichment cage, the capillary density was determined in the 3-month old mice. Brain microvascular density was determined by immunohistochemical staining for glucose transporter-1 (GLUT-1) and by counting the number of GLUT-1 positive capillaries per unit area (N/mm^2), as described previously [7–9]. Perfusion, paraffin-embedded sectioning and capillary density determination of the mouse cerebral cortex is detailed by Tsipis et al. and strictly adhered to for the purposes of this study [9]. Coronal serial sections (5 μm) of frontal cortex (levels of Bregma 0.98 to 0.38 mm, [10]) were made on a microtome and stained for GLUT-1 [9]. For each brain, at least four different GLUT-1 stained sections were averaged for quantification. Each quantified section was at least 50 μm apart from the subsequent quantified section.

2.3 Measurement of Cognitive Function

The Y-maze test and a novel object recognition test were used to evaluate cognitive function in the aged mice (18 months old). The test is based on the innate preference of animals' spontaneous alternations. A high alternation rate is indicative of sustained cognition as the animals must remember which arm was entered last, so as not to re-enter it [11]. Testing occurred in a Y-shaped maze with three silver-colored metal arms at a 120° angle from each other. After introduction to the center of the maze, the animal was allowed to freely explore the three arms for 6 min. The sequencing and number of arm entries were recorded, and the alternation rate (%) was calculated. Novel objects recognition test: this test is based on the natural tendency of rodents to investigate a novel object instead of a familiar one [12, 13]. Each animal was allowed a 10-min training session with exposure to two identical toy bricks placed in the back left and right corners of the arena. After the training session, the animal was returned to its home cage for a 30-min retention interval. For testing, each animal was lowered into the testing arena in which one familiar object was replaced with differently shaped toy bricks. Each session was video-recorded and the animal was given 10 min to explore. The frequency and duration of inspecting the objects were recorded. The novel object exploration rate (%) was calculated as the time spent with the novel object divided by the total time spent exploring either object.

2.4 Statistical Analysis

All values are presented as mean ± SD. Statistical analyses were performed using SPSS version 20.0 for Windows. Comparison between any two groups was analysed with a t-test for paired sample, two-tailed. Significance was considered at the level of $p < 0.05$.

3 Results

3.1 *Effect of Environmental Enrichment on Cerebral Capillary Density*

After 3 weeks of placement in the enrichment cage or non-enrichment cage, the capillary density was determined in the 3-month-old mice. As shown in Fig. 24.1, microvascular density (N/mm^2) was determined by GLUT-1 positive capillary profiles identified in the cerebral cortex. Environmentally enriched mice exhibited a 29% increase in capillary density as compared to the non-enriched controls (N/mm^2, 514 ± 48 vs 400 ± 48, n = 7 and n = 6, respectively). The Y-maze test and the novel object recognition test were used to evaluate cognitive function in the18-month-old mice before and after 4 weeks of placement in the enrichment or non-enrichment cages. For the Y-maze test, the non-enriched control group and the enriched group had similar alternation rates before the placement (%, 57 ± 12 vs. 55 ± 6, n = 8 and n = 12, respectively). As shown in Fig. 24.2, after 4 weeks of enrichment, the enriched mice showed improved a significantly higher alternation rate in the Y-Maze test compared to the non-enriched controls (%, 63 ± 110 vs. 49 ± 10). The non-enriched control mice and the enriched mice had a similar novel object exploration rate (~60%) before and after the 4 weeks of placement.

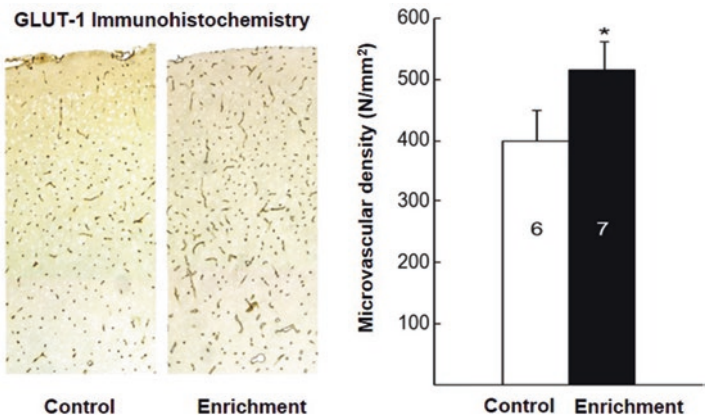

Fig. 24.1 GLUT-1 immunohistochemistry (*left panel*) and microvascular density (N/mm^2) as identified by GLUT-1 positive endothelial cells (*right panel*) in the cerebral cortex in the non-enriched control and environmental enrichment groups. Values are mean ± SD, *significance vs. control group (t-test, $p < 0.05$), n of each group was indicated on bar

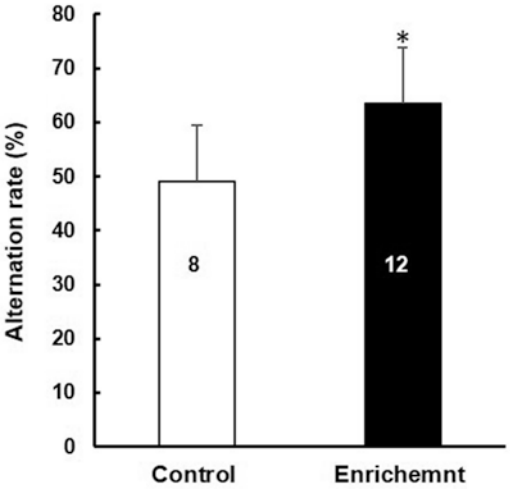

Fig. 24.2 Alternation rate (%) in the Y-maze test in the cerebral cortex in the non-enriched control and environmental enrichment groups. Values are mean ± SD, *significance vs. control group (t-test, $p < 0.05$), n indicated on each bar

3.2 Effect of Environmental Enrichment on Cognitive Function in Aged Mice

The Y-maze test and the novel object recognition test were used to evaluate cognitive function in the18-month-old mice before and after 4 weeks of placement in the enrichment or non-enrichment cages. For the Y-maze test, the non-enriched control group and the enriched group had similar alternation rates before the placement (%, 57 ± 12 vs. 55 ± 6, n = 8 and n = 12, respectively). As shown in Fig. 24.2, after 4 weeks of enrichment, the enriched mice showed improved significantly higher alternation rate in the Y-Maze test compared to the non-enriched controls (%, 63 ± 110 vs. 49 ± 10). The non-enriched control mice and the enriched mice had a similar novel object exploration rate (~60%) before and after the 4 weeks of placement.

4 Discussion

Enrichment provides an environment that fosters increased physical activity and sensory stimulation as compared to standard housing. Promoting and sustaining stimulation increases neuronal activity and, consequently, brain oxygen demand. In this study we investigated the effect of an environmental enrichment on cerebral capillary density and cognitive performance in mice. We found that 3–4 weeks of environmental enrichment induced cerebral angiogenesis in adult mice, and, especially, improved cognitive performance in the aged mice (18 months old). In an enrichment environment, mice spent more time exploring toys and doing more

exercise, such as aerobic movement on running wheels [3]. At the same time, during exploration, the mice's brain receives more sensory stimulation leading to enhanced brain plasticity and cognitive function. It has been shown that standardized environmental enrichment enhanced brain plasticity in healthy rats and prevents cognitive impairment in epileptic rats [14]. Studies have indicated that brain derived neurotrophic factor (BDNF) plays a major role in environmental enrichment mediated neuroprotection [15]. It has also been shown that fibroblast growth factor-2 induced by enriched environment enhances angiogenesis and neurobehavioral functions in chronic hypoxic-ischemic brain injury [16].

In summary, our data show that environmental enrichment induced increased brain capillary density and improved cognitive performance, especially in the aged mice, suggesting that environmental enrichment may induce structural and function changes in the brain, and indicate treatment potential for age-related neurodegenerative and neurovascular diseases.

Acknowledgments This study was supported by NIH grant NIH R01 NS 38632.

References

1. Mora F (2013) Successful brain aging: plasticity, environmental enrichment, and lifestyle. Dialogues Clin Neurosci 15(1):45–52
2. Ekstrand J, Hellsten J, Tingstrom A (2008) Environmental enrichment, exercise and corticosterone affect endothelial cell proliferation in adult rat hippocampus and prefrontal cortex. Neurosci Lett 442(3):203–207
3. Mustroph ML, Chen S, Desai SC et al (2012) Aerobic exercise is the critical variable in an enriched environment that increases hippocampal neurogenesis and water maze learning in male C57BL/6J mice. Neuroscience 219:62–71
4. Hosseiny S, Pietri M, Petit-Paitel A et al (2015) Differential neuronal plasticity in mouse hippocampus associated with various periods of enriched environment during postnatal development. Brain Struct Funct 220(6):3435–3448
5. Pang TY, Hannan AJ (2013) Enhancement of cognitive function in models of brain disease through environmental enrichment and physical activity. Neuropharmacology 64:515–528
6. Barak B, Shvarts-Serebro I, Modai S et al (2013) Opposing actions of environmental enrichment and Alzheimer's disease on the expression of hippocampal microRNAs in mouse models. Transl Psychiatry 3(9):e304
7. Benderro GF, LaManna JC (2012) Hypoxia-induced angiogenesis is delayed in aging mouse brain. Brain Res 1389:50–60
8. Benderro GF, LaManna JC (2014) HIF-1α/COX-2 expression and mouse brain capillary remodeling during prolonged moderate hypoxia and subsequent re-oxygenation. Brain Res 1569:41–47
9. Tsipis CP et al (2014) Hypoxia-induced angiogenesis and capillary density determination. Methods MolBiol 1135:69–80
10. Paxinos G, Franklin KBJ (2003) The mouse brain in stereotaxic coordinates, 2nd edn. Academic Press, San Diego
11. Dellu F, Mayo W, Cherkaoui J (1992) A two-trial memory task with automated recording: study in young and aged rats. Brain Res 588(1):132–139

12. Messier C (1997) Object recognition in mice: improvement of memory by glucose. Neurobiol Learn Mem 67(2):172–175
13. Antunes M, Biala G (2012) The novel object recognition memory: neurobiology, test procedure, and its modifications. Cogn Process 13:93–110
14. Fares RP, Belmeguenai A, Sanchez PE et al (2013) Standardized environmental enrichment supports enhanced brain plasticity in healthy rats and prevents cognitive impairment in epileptic rats. PLoS One 8(1):e53888
15. Jain V, Baitharu I, Prasad D et al (2013) Enriched environment prevents hypobaric hypoxia induced memory impairment and neurodegeneration: role of BDNF/PI3K/GSK3 pathway coupled with CREB activation. PLoS One 8(5):e62235
16. Seo JH, Yu JH, Suh H et al (2013) Fibroblast growth factor-2 induced by enriched environment enhances angiogenesis and motor function in chronic hypoxic-ischemic brain injury. PLoS One 8(9):e74405

Chapter 25
Improving Retinal Image Quality Using Registration with an SIFT Algorithm in Quasi-Confocal Line Scanning Ophthalmoscope

Yi He*, Yuanyuan Wang*, Ling Wei, Xiqi Li, Jinsheng Yang, and Yudong Zhang

Abstract When high-magnification images are taken with a quasi-confocal line scanning ophthalmoscope (LSO), the quality of images always suffers from Gaussian noise, and the signal to noise ratio (SNR) is very low for a safer laser illumination. In addition, motions of the retina severely affect the stabilization of the real-time video resulting in significant distortions or warped images. We describe a scale-invariant feature transform (SIFT) algorithm to automatically abstract corner points with subpixel resolution and match these points in sequential images using an affine transformation. Once n images are aligned and averaged, the noise level drops by a factor of $\sqrt{n}$ and the image quality is improved. The improvement of image quality is independent of the acquisition method as long as the image is not warped, particularly severely during confocal scanning. Consequently, even better results can be expected by implementing this image processing technique on higher resolution images.

Keywords Confocal microscopy • Feature extraction • Image matching • SIFT

*Yi He and Yuanyuan Wang contributed equally to this work.

Y. He (✉) • L. Wei • X. Li • J. Yang • Y. Zhang
The Key Laboratory on Adaptive Optics, Chinese Academy of Sciences, Chengdu 610209, China
e-mail: heyi_job@126.com

Y. Wang
The Key Laboratory on Adaptive Optics, Chinese Academy of Sciences, Chengdu 610209, China

Graduate School of Chinese Academy of Sciences, Beijing 100039, China

Wenzhou Medical University, Wenzhou 325035, China

H.J. Halpern et al. (eds.), *Oxygen Transport to Tissue XXXIX*, Advances in Experimental Medicine and Biology 977, DOI 10.1007/978-3-319-55231-6_25

1 Introduction

The scanning laser ophthalmoscope (SLO) is a confocal imaging technique that produces real-time, contrast enhancement en-face retinal images by 2-D raster scanning illumination and detecting backscattered light through a confocal arranged pinhole [1, 2]. A simplified quasi-confocal line scanning ophthalmoscope (LSO) has the same basic principles of operation as the SLO's, the only difference being that, in the LSO, the image is generated over time by recording the scattered light from a focused line spot as it is scanned in one dimension across the region to be illuminated [3], and a slit aperture is placed in front of the detector in conjugate of the retina plane to produce a 'quasi-confocal' image.

Usually, the quality of images suffers from Gaussian noise, and the signal-to-noise ratio (SNR) of LSO images is very low for a safer laser illumination for the human retina. To improve image quality, sequences of images are averaged to reduce noise and make visible the spatial structure present in the image [4]. However, the LSO images vary due to variations in blurring caused by retinal motions. These motions introduce significant distortions, and also warp images during eye fundus imaging [4]. Thus, this requires each image in the sequence to be aligned or registered with the others to compensate for eye movements. O'Connor et al. applied a frame-to-frame cross-correlation to determine retinal movements in SLO images [5]. Vogel et al. applied a map-seeking circuit (MSC) algorithm to compute correlations to account for more general motions [6]. Recently, the use of a second-order polynomial to model the field that maps two SLO images has been proposed [7].

In this article, a novel computational technique, known as the scale-invariant feature transform (SIFT), is applied to extract distinctive invariant features. With matched features, an affine transformation is used to remove eye motions, and 20 images in sequence are aligned and averaged to improve the image quality. Implemented on this quasi-confocal LSO system, the SIFT-based image registration can be used as a medical early detection tool, since it enables a simple, noninvasive, measurement at relatively low illumination power and, most importantly, as well as improving the quality of images with low cost.

2 Method

A schematic diagram of our LSO system is shown in Fig. 25.1 and a detailed description of the LSO system can be found in Yi He et al. [8, 9]. The cylindrical lens and the galvanometer, as shown in Fig. 25.1, were used as a line beam scanner.

SIFT is an image registration algorithm, which can automatically abstract corner points with subpixel resolution from two sequence images [10]. The flow chart of the SIFT algorithm is shown in Fig. 25.2. There are four principal computation steps in the SIFT algorithm: Building Gaussian Scale space using a difference-of-Gaussian (DoG) function; Key point detection; Orientation assignment; and Descriptor generation.

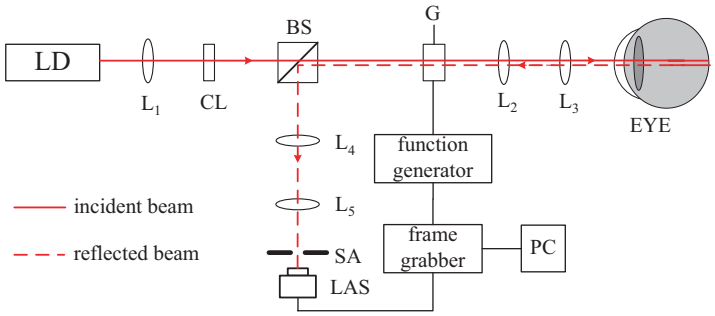

Fig. 25.1 Schematic of the LSO system. *LD* laser diode, *BS* beam splitter, *CL* cylindrical lens, *L1 ~ L5* lenses, *SA* slit aperture, *G* galvanometer-driven scanner, *LAS* linear array sensor

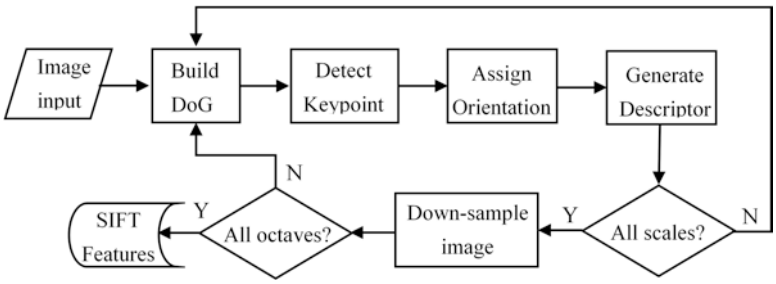

Fig. 25.2 Flow chart of the SIFT algorithm

In order to reduce calculation time and maintain more robust performance, an improved SIFT method in software architecture for matching sequences of images is presented. The method generates the Gaussian Scale-space pyramid in frequency domain to complete the SIFT feature detector more quickly. Specifically, the inputting image is first executed by the Fast Fourier Transform (FFT), and the various operations are performed in the frequency domain before the DoG pyramid is generated using the inverse FFT.

Actually, retinal motions can produce translate distortions most of the time, with a few rotational distortions. Consequently, with point features matched by SIFT, the affine transformation is sufficient to stitch sequence images together by mapping them into the same coordinate system.

The affine transformation of an image point $[x\ y]^T$ to the corrected image point $[x'\ y']^T$ can be written in the following form:

$$\begin{bmatrix} x' \\ y' \end{bmatrix} = \begin{bmatrix} m_1 & m_2 \\ m_3 & m_4 \end{bmatrix} \begin{bmatrix} x \\ y \end{bmatrix} + \begin{bmatrix} t_x \\ t_x \end{bmatrix}, \tag{25.1}$$

Where the model translation is $[t_x\ t_y]^T$ and the affine rotation, scale, and stretch are represented by the m_i parameters. Eq. (25.1) can be rewritten as follows:

$$Xt = b, with\ X = \begin{bmatrix} x & y & 0 & 0 & 1 & 0 \\ 0 & 0 & x & y & 0 & 1 \\ \cdot & \cdot & \cdot & \cdot & \cdot & \cdot \\ \cdot & \cdot & \cdot & \cdot & \cdot & \cdot \end{bmatrix}, t = \begin{bmatrix} m_1 \\ m_2 \\ m_3 \\ m_4 \\ t_x \\ t_y \end{bmatrix}, b = \begin{bmatrix} x' \\ y' \\ . \\ . \end{bmatrix}, \tag{25.2}$$

Matrices X and b can be determined by the matched points from the SIFT abstracting, and column vector t includes the transformation parameters to be solved. This equation shows a single matched point, but any number of further matched points can be added, with each match contributing two more rows to the matrices A and b. As a result, the least-squares solution for the vector t can be estimated by the corresponding normal equation, which is given by:

$$t = \left[X^T X\right]^{-1} X^T b, \tag{25.3}$$

To implement the affine transformation at least three corresponding points from the SIFT extraction are needed. The parameters in vector t can be used to map retinal images into the same coordinate for image registrations.

3 Result and Experiment

The SIFT algorithm was then used to extract and match point features of two sequential images, and the matched features are shown in Fig. 25.3a. With the matched point pairs, the affine transformation was used to register these images, and the result is shown in Fig. 25.3b.

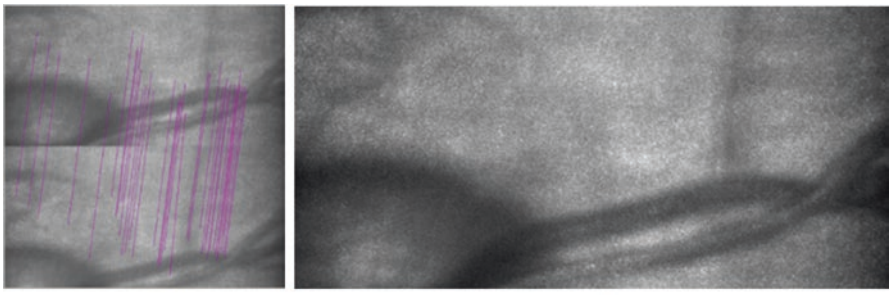

Fig. 25.3 Registration of retinal images. (**a**) Point features matched by SIFT, and (**b**) co-added image by the affine transformation

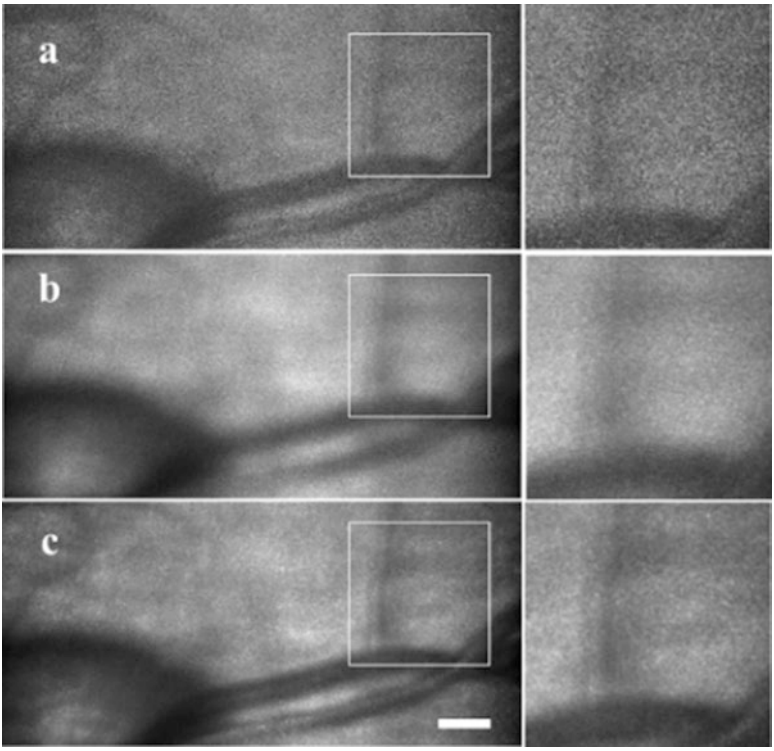

Fig. 25.4 (**a**) Single retinal frame compared to (**b**) the averaged image without registration, (**c**) averaged image with SIFT registration. The image is 10° across, with its *left side* at the optic nerve head. Scale bar, 100 μm. The rectangles are the magnified ROIs in the *right side*

With the SIFT and affine transformation for image aligned, 20 images were registered to produce an improved image; comparisons between a single retinal image and the improved one are shown in Fig. 25.4. While in Fig. 25.4a, it is almost impossible to identify fine structures in this frame except for vessels; in Fig. 25.4c, the dynamic range is much better and some fine structures in the image are much clearer. In Fig. 25.4b, the averaged image without registration is plotted, in which blurred motions made the image quality much worse.

The right side of Fig. 25.4 is a magnified ROI taken from the rectangles in the retinal images. Once again, the fine structure is much clearer after averaging the image with registration, mostly due to eliminating the distortions caused by saccades between frames. The SNR has also improved owing to image registration and coaddition. A comparison of an ROI of the averaged image without registration is shown in this figure; many more distortions occurred due to image processing without registration. As a result, small features of blood vessels are visible after averaging images with registration, improving the image contrast.

The power spectrum describes the amplitude of the spectral power in the images that is distributed across spatial frequency, and the power spectra of images in Fig. 25.4 is shown in Fig. 25.5. The spectral power of one single image is almost

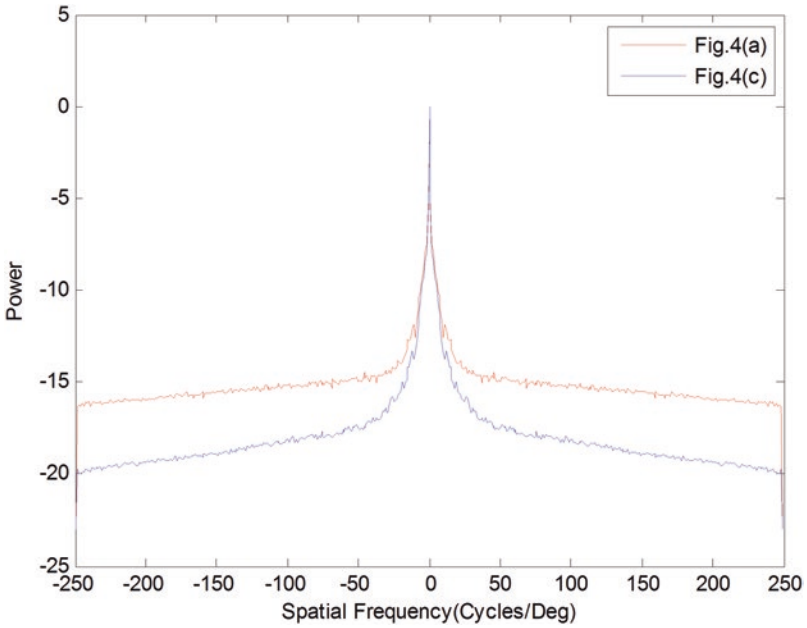

Fig. 25.5 Averaged power spectrum for one frame (*red curve*) and for the registered image (*blue curve*)

constant after certain frequencies, which means that the signal and the noise are almost inseparable in each image. However, the power spectra of the registered image are decreased at the high frequencies; this indicates that the noise is effectively suppressed and the image quality is improved after image processing.

With the SIFT registration and affine transformation, many more successive frames could be registered and averaged to improve the image quality. In order to verify the image registration, we registered 100 frames of retinal images to determine retinal motions, and the maximum and minimum absolute values of parameter t in Eq. (25.3) are listed in Table 25.1. It can be seen that there are almost no large amplitudes of rotation, scale and stretch motions, while the primary motions are translation motions with maximum values of about 40 and 85 pixels in the 100 frames.

4 Conclusion

In this work, we presented an image registration method that enables quality enhancement of retinal images. First, the SIFT algorithm is used to automatically abstract point features with subpixel resolution and match these points in sequential images. In addition, the affine transformation uses the matched points to register the

Table 25.1 Maximum and minimum absolute values of the parameter *t*

	m_1	m_2	m_3	m_4	t_x	t_y
Max(pixel)	1.038932	0.039538	0.009962	1.001082	40.374892	84.577253
Min(pixel)	0.972748	0	0.005458	0.939837	0.0027293	0.0048301

frames to eliminate image distortions caused by saccade motions. Consequently, this image processing produces an averaged image with registration, a better contrast, as well as a relatively high SNR, improving the image quality.

The efficiency of this approach has been demonstrated on a rather simple optical setup, quasi-confocal LSO system on subjects with healthy eyes. By registering and averaging 20 successive frames, a much better image was gained, to a point that some fine structures can be distinguished. By examining the power spectrum at high frequencies, we can verify that noise was considerably suppressed, and the noise level dropped by a factor of $\sqrt{n}$ once n images were aligned and averaged.

Even when implemented on this quasi-confocal LSO system, the SIFT based image registration can also be used as a medical early detection tool, since it enables a simple, noninvasive measurement at a relatively low illumination power. Moreover, as the acquisition of the retinal images is independent of the optical system, this approach can be performed on higher resolution images (fundus camera, SLO or OCT with aberration compensation) to further improve image quality.

Acknowledgements This work is supported by the National Science Foundation of China (Grant NO. 61605210), the National Instrumentation Program (NIP, Grant No. 2012YQ120080), the Jiangsu Province Science Fund for Distinguished Young Scholars (Grant NO. BK20060010), the Frontier Science research project of the Chinese Academy of Sciences (Grant NO. QYZDB-SSW-JSC03), the Strategic Priority Research Program of the Chinese Academy of Sciences (Grant NO. XDB02060000), the National Key Research and Development Program of China (2016YFC0102500), and the Zhejiang Province Technology Program (Grant No. 2013C33170).

Reference

1. Roorda A, Romero-Borja F et al (2002) Adaptive optics scanning laser ophthalmoscopy. Opt Express 10:405–412
2. Wang ZB, Wei D, Wei L et al (2014) Aberration correction during real time in vivo imaging of bone marrow with sensorless adaptive optics confocal microscope. J Biomed Opt 19(8):086009
3. Hammer DX, Ferguson RD et al (2006) Line-scanning laser ophthalmoscope. J Biomed Opt 11:041126
4. Sheehy CK, Yang Q et al (2012) High-speed, image-based eye tracking with a scanning laser ophthalmoscope. Biomed Opt Express 3(10):2611–2622
5. O'Connor NJ et al (1998) Fluorescent infrared scanning-laser ophthalmoscope for three-dimensional visualization: automatic random-eye-motion correction and deconvolution. Appl Opt 37:2021–2033
6. Hammer DX, Ferguson RD et al (2006) Adaptive optics scanning laser ophthalmoscope for stabilized retinal imaging. Opt Express 14:3354–3367

7. Li H, Lu J et al (2010) Tracking features in retinal images of adaptive optics confocal scanning laser ophthalmoscope using KLT-SIFT algorithm. Biomed Opt Express 1(1):31–40
8. He Y, Wei L, Wang Z, Yang J, Li X, Shi G, Zhang Y (2015) Extraction of ultra-high frequency retinal motions with a line scanning quasi-confocal ophthalmoscope. J Optics 17(1):015301
9. Yi H, Wei L, Wang Z, Yang J, Li X, Shi G, Zhang Y (2015) Precision targeting for retinal motion extraction using cross-correlation with a high speed line scanning ophthalmoscope. J. Optics 17(12):125303
10. Lowe DG (1999) Object recognition from local scale-invariant feature. In: Proceedings of the international conference on computer vision, Corfu, pp 1150–1157

Chapter 26
A New Method Based on Graphics Processing Units for Fast Near-Infrared Optical Tomography

Jingjing Jiang, Linda Ahnen, Alexander Kalyanov, Scott Lindner, Martin Wolf, and Salvador Sanchez Majos

Abstract The accuracy of images obtained by Diffuse Optical Tomography (DOT) could be substantially increased by the newly developed time resolved (TR) cameras. These devices result in unprecedented data volumes, which present a challenge to conventional image reconstruction techniques. In addition, many clinical applications require taking photons in air regions like the trachea into account, where the diffusion model fails. Image reconstruction techniques based on photon tracking are mandatory in those cases but have not been implemented so far due to computing demands. We aimed at designing an inversion algorithm which could be implemented on commercial graphics processing units (GPUs) by making use of information obtained with other imaging modalities. The method requires a segmented volume and an approximately uniform value for the reduced scattering coefficient in the volume under study. The complex photon path is reduced to a small number of partial path lengths within each segment resulting in drastically reduced memory usage and computation time. Our approach takes advantage of wavelength normalized data which renders it robust against instrumental biases and skin irregularities which is critical for realistic clinical applications. The accuracy of this method has been assessed with both simulated and experimental inhomogeneous phantoms showing good agreement with target values. The simulation study analyzed a phantom containing a tumor next to an air region. For the experimental test, a segmented cuboid phantom was illuminated by a supercontinuum laser and data were gathered by a state of the art TR camera. Reconstructions were obtained on a GPU-installed computer in less than 2 h. To our knowledge, it is the first time Monte Carlo methods have been successfully used for DOT based on TR cameras. This opens the door to applications such as accurate measurements of oxygenation in neck tumors where the presence of air regions is a problem for conventional approaches.

J. Jiang • L. Ahnen • A. Kalyanov • S. Lindner • M. Wolf • S.S. Majos (✉)
Biomedical Optics Research Laboratory (BORL), Department of Neonatology, University Hospital Zurich (USZ), Zurich, Switzerland
e-mail: Salvador.SanchezMajos@usz.ch

H.J. Halpern et al. (eds.), *Oxygen Transport to Tissue XXXIX*, Advances in Experimental Medicine and Biology 977, DOI 10.1007/978-3-319-55231-6_26

Keywords Diffuse optical imaging • Monte Carlo methods • Graphics processing unit • Air segments • Time-resolved measurement

1 Introduction

Diffuse Optical Tomography (DOT) is a promising technique to reveal the spatial distribution of absorption (μ_a) and scattering (μ_s) coefficients in tissue. These quantities are directly related to oxygenation levels, providing functional information for diagnosis and medical research. Unfortunately, DOT techniques are limited by their relatively low spatial resolution. Image reconstruction for small objects is extremely challenging, especially when they are deeply embedded in tissue due to the diffusive nature of light propagation.

DOT performance can be substantially improved if prior information concerning the spatial distribution of tissue types is integrated in the image reconstruction algorithms [1]. In this approach, the aim of DOT is no longer to reconstruct the spatial distribution of optical properties, but to recover segmented functional images (see an example in Fig. 26.1a). In real clinical scenarios, prior information can be obtained from other imaging methods, such as CT or MRI. Even in this more favorable scenario a major obstacle for the successful application of DOT to realistic clinical cases is the limited validity of the diffusion approximation for modelling light propagation in tissue. Areas with low scattering and absorption coefficients give rise to significant departures from the diffusion model. Especially important is the case of air-filled regions, like the trachea, where photon propagation is ballistic.

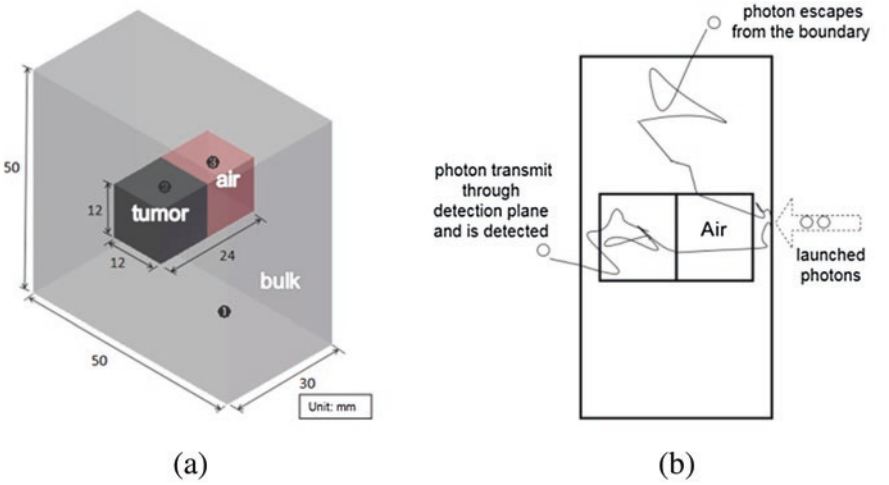

Fig. 26.1 (**a**) Segmented virtual phantom used in this study. (**b**) Photon propagation through the segmented tissue model. Note straight tracks in the air segment

Problems also arise in the case of small source-detector distances and in regions close to the tissue boundary [2]. These scenarios can be handled by Monte Carlo (MC) methods where photons are tracked individually and no approximation is needed. Each photon undergoes thousands of scattering events where the scattering angle is given by the Henyey-Greenstein function and the survival rate is calculated based on the Beer-Lambert Law. Consequently, MC methods are slow, especially for TR DOT, which has precluded their use in clinical settings. Although significant progress has been made recently by taking advantage of advanced parallel computing techniques [3], the number of forward problem simulations needed in standard reconstructions is still too large for this approach to be practical.

Our aim was to employ prior geometrical information not only to boost the performance of DOT systems but to significantly accelerate TR reconstructions based on MC methods and to test this technique on a computer model and experimentally on a segmented silicone phantom using a supercontinuum laser and a TR camera.

2 Methods

2.1 MC Based fast Reconstruction Algorithm

Photon propagation is parallelized using the Monte Carlo eXtreme (MCX) code [3], running on a dual-GPU computer (Geforce gtx960, Nvidia Corp.) which results in acceleration factors for the forward problem roughly proportional to the number of GPU cores.

In order to reduce the typically large number of calls to the MC simulator during image reconstruction, a scaling method is applied where trajectories of photons are stored only when changes in μ_s happen. The survival photon probability can be scaled by the attenuation factor corresponding to the μ_a values in each segment to create a new arrival time distribution since the path shape is fully determined by μ_s [4, 5]. This scaling method can significantly speed up MC reconstructions and is much less memory intensive than a fully voxelized approach, since only the path length within each segment is stored.

To apply this method to realistic clinical problems we propose the use of wavelength normalized data. This data type is defined by the ratio of the Fourier transforms of the arrival time histograms at different wavelengths. It is especially suitable for TR measurements since it performs an automatic deconvolution of the response function of the detectors and removes off focal plane variable time delays since they both appear as multiplicative factors in the Fourier data. Off-focal plane variable time delays due to photon path lengths naturally appear in irregular tissue shapes and are unavoidable when imaging body parts. Another major advantage of this data is that it has the potential of significantly reducing the detrimental effect of hair and melanin in the quality of the reconstructed images.

2.2 Simulation Study on a Tissue Model Containing Air

To validate the suitability of this method for volumes containing air regions, image reconstructions were performed on a slab model (50 × 50 × 30 mm) consisting of three segments mimicking normal tissue, tumor, and air, respectively (Fig. 26.1a). The tumor and air regions are cubes with a length of 12 mm and are located in the center of the bulk region. The optical properties in the air segment are set to $\mu_a = 0$ and $\mu_s = 0$ so that neither scattering nor absorbing events happen and, consequently, photons propagate in straight lines (Fig. 26.1b).

We selected wavelengths $\lambda_1 = 780$ nm and $\lambda_2 = 650$ nm to conduct the reconstructions based on a study of optimum contrast that took both the phase and the amplitude into consideration. Although penetration depth for 650 nm is relatively low, phase contrast is large for this wavelength pair and the small phantom thickness suggests its use for this case study. For general clinical cases, signal strength has to be integrated into the wavelength selection algorithm. Physiologically meaningful optical properties were selected for the actual parameters of bulk ($\mu_a^{B,\lambda_1} = 0.0254$ mm^{-1} and $\mu_a^{B,\lambda_2} = 0.0267$ mm^{-1}) and tumor ($\mu_a^{T,\lambda_1} = 0.0544$ mm^{-1} and $\mu_a^{T,\lambda_2} = 0.1574$ mm^{-1}). μ_s were assumed identical in tumor and bulk with the values $\mu_s^{\lambda_1} = 0.8667$ mm^{-1} and $\mu_s^{\lambda_2} = 0.9028$ mm^{-1}.

The reference data were obtained by launching 2×10^{10} photons to generate the TR signals in transmission mode in a simulation where 100 detectors covered the whole right profile plane of the phantom, and a source with perpendicular launch direction was placed slightly off the center on the left profile so that enough photons could travel through both the bulk region and the tumor. Reconstructions were performed by tracking 1.2×10^9 photons in each call to the MC simulator.

2.3 Phantom Measurements

The fast reconstruction algorithm was also validated in a dedicated experimental test. The setup (Fig. 26.2a) consisted of a supercontinuum laser SuperK Extreme EXR-15 (NKT, Denmark) to generate picosecond pulses of white light covering a wide optical spectrum from 400 nm up to 2000 nm with a total optical power of 6 W, an acousto-optic tunable filter (AOTF) to select independent narrow bands, a set of galvo-mirrors (Thorlabs, Inc., US) for laser beam control and a complementary metal–oxide–semiconductor (CMOS) TR camera with an embedded array of single photon avalanche diodes [6]. The phantom used in this experiment containing three homogeneous segments (Fig. 26.2b) was made from silicone (PDMS) and was fabricated with a 3D printed mold. Phantoms with air regions are being developed as well and will be used in future experiments.

Two wavelengths in the red area $\lambda_1 = 680$ nm and $\lambda_2 = 640$ nm were selected for the measurement and reconstruction. The scattering coefficient of the whole volume was tuned by adding TiO_2 to the value $\mu_s^{\lambda_1} = \mu_s^{\lambda_2} = 0.5556$ mm^{-1} as measured

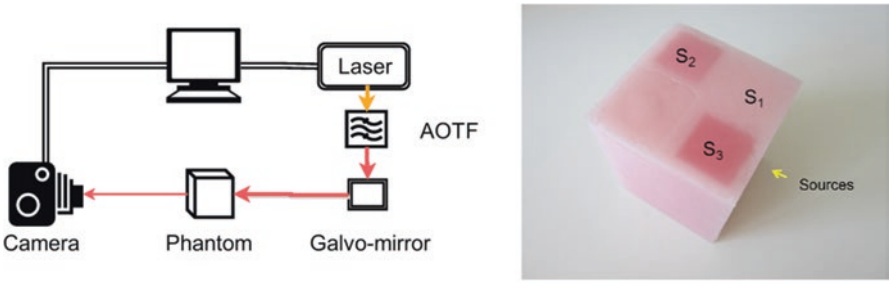

Fig. 26.2 (**a**) Schematic of the experimental setup, where AOTF stands for acousto-optic tunable filter. (**b**) A three-segment (s_1, s_2 and s_3) silicone phantom with three different μ_a values tuned by increasing concentrations of a *red* dye

independently by a calibrated in-house frequency domain instrument. The μ_a for the three segments were $\mu_a^{s_1,\lambda_1} = 0.001\ \text{mm}^{-1}$, $\mu_a^{s_2,\lambda_1} = 0.006\ \text{mm}^{-1}$, $\mu_a^{s_3,\lambda_1} = 0.011\ \text{mm}^{-1}$ for λ_1 and $\mu_a^{s_1,\lambda_2} = 0.003\ \text{mm}^{-1}$, $\mu_a^{s_2,\lambda_2} = 0.012\ \text{mm}^{-1}$, $\mu_a^{s_3,\lambda_2} = 0.021\ \text{mm}^{-1}$ for λ_2 , and were controlled by adding a red dye at different volumetric concentrations. In the experiment, four sources were projected by the galvo-mirrors on the right visible profile of the phantom and a sample of pixels of the camera consisting of 100 detectors covering an area of $40 \times 40\ \text{mm}^2$ on the opposite side were selected as data sources for the image reconstruction algorithm.

3 Results and Discussion

3.1 Simulation Results

To assess the performance of the reconstruction for the air-segment model, the recovered optical parameters were compared with the original and 'guess' values (Fig. 26.3a). A nearly perfect fit with ~1% error was achieved after an iterative fitting process of 1 h 44 min. These results are representative for a wide range of tumor and bulk properties.

3.2 Experimental Results

The reconstructed values, initial guesses and reference parameters are shown in Fig. 26.3b. The deviation from the true value in the reconstructed μ_s was <1% (not shown in the figures). The fitted μ_a showed an average error of 30%. At this point, we do not have an explanation for the different accuracies in the reconstructions of the three segments. Possible factors affecting this first measurement are: reflections in the optical system and the support structure, small time drifts of the TDCs from

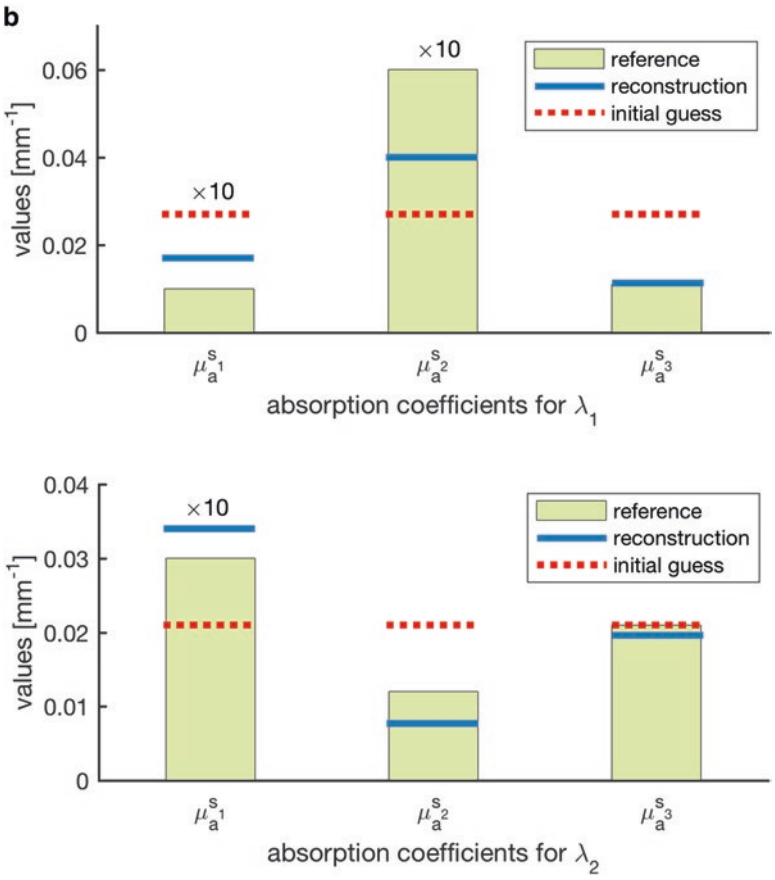

Fig. 26.3 (**a**) Reconstructed results for the computer model containing an air region. (**b**) Reconstructed absorption coefficients of segments s_1, s_2 and s_3 for measurement on the silicone phantom shown in Fig. 26.2b

temperature variations in the chip, variations in the dark count rate, and calibration failures of sources and detectors. The accuracy of this technique can be further improved by including a larger number of wavelengths in the dataset and use a spectral approach in which chromophore concentrations are reconstructed instead of absorption values.

4 Conclusions

In this paper, we described and validated a reconstruction technique based on MC methods for TR DOT in segmented volumes using wavelength normalized data. The method relies on the assumption that the variations in μ_s can be considered smaller

than those of μ_a and, consequently, a unique value for μ_s can be fitted for the entire volume. An approach based on segmented tissue types is appropriate for a technique with low intrinsic spatial resolution and has the key beneficial effect of drastically reducing the memory required for the scaling method used here for the MC-based reconstructions. In addition, the significant reduction in the number of variables results in a well-defined problem where precise values of optical properties within each segment can be unambiguously found. The performance of this method for imaging volumes with air regions has been studied in the simulated case presented above and experiments with real phantoms are planned for the future. The self-calibrating method based on wavelength-normalized data avoids the detrimental effect of skin pigmentation, the detector's response and optical transfer function in image reconstruction, giving rise to a much more robust approach to clinical problems.

Acknowledgments This work was supported by the SwissTransMed project ONIRIUS, Swiss Cancer Research project KFS-3732-08-2015, KFSP Tumor Oxygenation and KFSP Molecular Imaging Network Zurich of the University of Zurich, and by the National Competence Center for Biomedical Imaging.

References

1. Zhu C, Liu Q (2013) Review of Monte Carlo modeling of light transport in tissues. J Biomed Opt 18(5):050902
2. Andreas HH, Raymond EA, Randall LB (1998) Comparison of finite-difference transport and diffusion calculations for photon migration in homogeneous and heterogeneous tissues. Phys Med Biol 43(5):1285
3. Fang Q, Boas DA (2009) Monte Carlo simulation of photon migration in 3D turbid media accelerated by graphics processing units. Opt Express 17(22):20178–20190
4. Alerstam E, Andersson-Engels S, Svensson T (2008) White Monte Carlo for time-resolved photon migration. J Biomed Opt 13(4):041304. -041304-10
5. Liu Q, Ramanujam N (2007) Scaling method for fast Monte Carlo simulation of diffuse reflectance spectra from multilayered turbid media. J Opt Soc Am A 24(4):1011–1025
6. Niclass C et al (2008) A 128×128 single-photon image sensor with column-level 10-bit time-to-digital converter array. IEEE J Solid State Circuits 43(12):2977–2989

Chapter 27
PFC Blood Oxygenation Changes in Four Different Cognitive Tasks

Tomotaka Takeda, Yoshiaki Kawakami, Michiyo Konno, Yoshiaki Matsuda, Masayasu Nishino, Yoshihiro Suzuki, Yoshiaki Kawano, Kazunori Nakajima, Toshimitsu Ozawa, Yoshihiro Kondo, and Kaoru Sakatani

Abstract Aging often results in a decline in cognitive function, related to alterations in the prefrontal cortex (PFC) activation. Maintenance of this function in an aging society is an important issue. Some practices/drills, moderate exercise, mastication, and a cognitive task itself could enhance cognitive function. In this validation study, before evaluating the effects of some drills on the elderly, we examined the neural substrate of blood oxygenation changes by the use of four cognitive tasks and fNIRS. Seven healthy volunteers (mean age 25.3 years) participated in this study. Each task session was designed in a block manner; 4 periods of rests (30 s) and 3 blocks of four tasks (30 s). The tasks used were: a computerized Stroop test, a Wisconsin Card Sorting Test, a Sternberg working memory paradigm, and a semantic verbal fluency task. The findings of the study are that all four tasks activated PFC to some extent, without laterality except for the verbal fluency task. The results confirm that NIRS is suitable for measurement of blood oxygenation changes in frontal brain areas that are associated with all four cognitive tasks.

Keywords Cognitive function • NIRS • PFC • Stroop test • Wisconsin Card Sorting Test

T. Takeda (✉) • Y. Kawakami • M. Konno • Y. Matsuda • M. Nishino
Y. Suzuki • Y. Kawano • K. Nakajima • T. Ozawa
Department of Oral Health and Clinical Science, Division of Sports Dentistry, Tokyo Dental College, Tokyo, Japan
e-mail: ttakeda@tdc.ac.jp

Y. Kondo
Department of General Dentistry, Tokyo Dental College Chiba Hospital, Tokyo, Japan

K. Sakatani
NEWCAT Research, Institute, Department of Electrical and Electronics Engineering, College of Engineering, Nihon University, Tokyo, Japan

H.J. Halpern et al. (eds.), *Oxygen Transport to Tissue XXXIX*, Advances in Experimental Medicine and Biology 977, DOI 10.1007/978-3-319-55231-6_27

1 Introduction

Japan is rapidly becoming a super-aging society. As indicated in previous re-search, aging is associated with a decline in cognitive function, related to alterations in prefrontal cortex (PFC) activation [1, 2]. Maintenance of this function in an aging society is an important issue. Many cognitive tasks, such as the Stroop task (ST) [3, 4], the Wisconsin Card Sorting Test (WCST) [5, 6], the Sternberg working memory paradigm (SWMP) [7], and the verbal fluency task (VFT) [8–10], are widely used for evaluating and improving cognitive function using near-infrared spectroscopy (NIRS) [3, 5, 8, 9] or functional MRI [4, 6, 7, 10]. Unique studies concerning the cognitive function and gum chewing have been conducted and suggested the relation in it [11, 12]. Some practices/drills, moderate exercise, mastication, and cognitive tasks themselves could enhance cognitive function in older adults.

PFC plays an important role in the process of the cognitive function. Many functional neuroimaging techniques, including positron emission tomography, functional MRI, magnetoencephalography, and NIRS are thought to objectively evaluate human cranial nerve activity. NIRS measures the concentration changes of oxygenated hemoglobin (oxy-Hb), deoxygenated hemoglobin (deoxy-Hb), and total hemoglobin (total hemoglobin = oxy-Hb + deoxy-Hb) [13, 14]. Signal changes represent changes in local cerebral blood flow and oxygen expenditure, and the oxy-Hb concentration changes represents brain activity [15]. Functional NIRS is a powerful, non-invasive imaging technique that offers many advantages, including compact size, no need for specially equipped facilities, and the potential for real-time measurement [16, 17]. Thus, fNIRS could evaluate the effects of the practices/drills on cognitive tasks [3, 5, 8, 9].

In this validation study, before evaluating the effects of the drills, we examined the neural substrate of blood oxygenation changes due to the cognitive tasks. The study design was approved by the Ethics Committee of Tokyo Dental College, Japan (No.436).

2 Methods

Seven healthy volunteers (mean age 25.3 years) participated in this study after written informed consent was obtained. Participants had no personal or family history of neuropsychiatric illness, were free of medication, and all were right-handed. Activity in the PFC was measured by a multi-channel NIRS (OEG-16, Spectratech, Japan). The set of measurement probes (inter-optode distance 30 mm) were affixed to the participant's forehead. The recording channels resided in the brain between the nearest pairs of emitter and detection probes. A 2 × 6 probe configuration, involving 6 light emitters (wavelength 840 and 770 nm) and 6 detector probes, was used, which resulted in a total of 16 channels. The array of the light emitter and detector probes covered an area of the forehead, with the most inferior channel

located at Fp1 and Fp2 according to the International 10–20 system of electrode placement [18]. Each task session was designed in a block manner, i.e. 4 periods of rest (30 s) and 3 blocks of four tasks (30 s). The tasks used were: a computerized ST [3, 4] (including both congruent and incongruent Stroop tasks), the WCST [5, 6], the SWMP [7], and a semantic VFT [8–10].

To obtain the hemodynamic response, concentration changes in oxy-Hb, deoxy-Hb and total hemoglobin (tHb = [oxy-Hb] + [deoxy-Hb]) were calculated. BRain Suite (BRSystems, Japan) software was used for analysis. A bandpass filter (0.02–0.5 Hz) and a moving average (7 samples) with a 1.53 Hz sampling frequency were used. A linear fitting function for baseline correction was employed. The pre-task baseline was determined as the mean across 7 s just before the active task period; the post-task baseline was determined as the mean across the last 8 s of the resting period; then, linear fitting was performed on the task data between these two baselines. Following this correction, the four tasks were performed; data were averaged in each channel for each subject. For subsequent analyses, only oxy-Hb concentration changes registered during each task were considered; this is because this NIRS parameter usually shows the clearest pattern of activation and is proposed to be the most sensitive indicator of changes in regional cerebral blood flow [15]. Since the neural activity did not increase immediately after beginning the tasks, the oxy-Hb values between 10 and 30 s in each task were used for analysis. To investigate the involvement of a laterality of the PFC in each task, we divided the measured points into seven right and seven left channels (two central channels were not involved in laterality comparison). Also, to examine the influence of the task difference on total PFC activity, averaged oxy-Hb concentration changes in each channel were totaled in each task and compared. Statistical evaluations of the laterality in each task were performed using a one-sided paired Student's t-test, and one-way analyses of variance for repeated measurements were calculated for total PFC activity in each task using Excel Statistics (Microsoft Japan). A p-value of <0.05 was considered significant.

3 Results

Figure 27.1 shows a representative subject's curves during the WCST. Figure 27.2 shows the average curves of the changes in oxy-Hb concentration over time in the four tasks. Laterality and total comparison results for each task are summarized with statistical results in Table 27.1.

The findings of the study are that all four tasks activated bilateral PFC to some extent, with no significant differences in task comparison and in laterality except for the verbal fluency task.

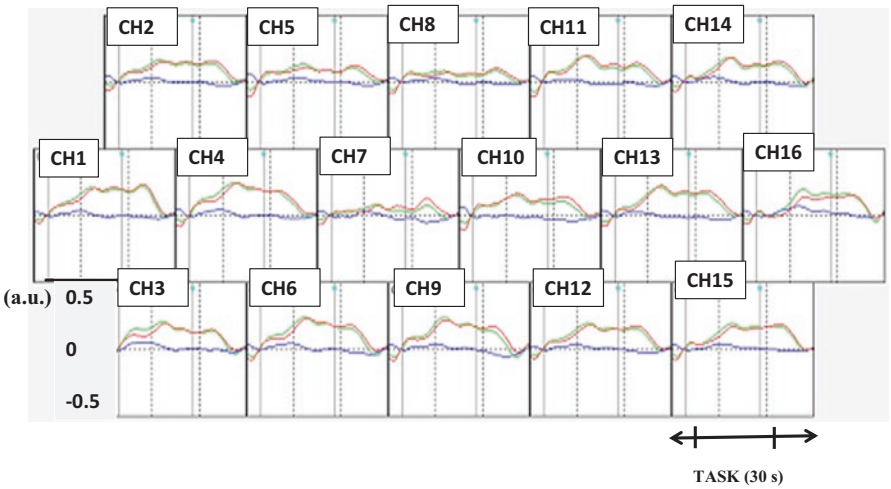

Fig. 27.1 Representative NIRS waves in the WCST

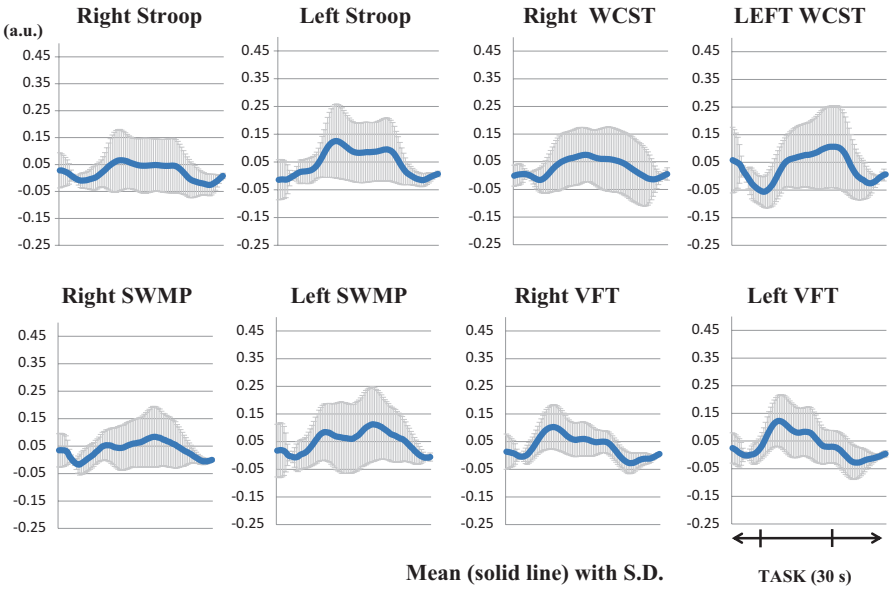

Fig. 27.2 Average curves of changes in oxy-Hb concentration over time

4 Discussion

The findings in this study are in line with previous studies. Activation for the ST was found in the bilateral prefrontal area [4]. A bilateral increase in oxygenated hemoglobin (oxy-Hb) was observed in the PFC in the majority of subjects during the

Table 27.1 Data on the comparison of laterality and the total results for each of the four tasks

	Left (M ± S.D.)	Statistics	Right (M ± S.D.)	Total (M ± S.D.)	ANOVA: P-Value
ST	0.083 ± 0.026	n.s.	0.079 ± 0.030	0.082 ± 0.026	0.41
WCST	0.079 ± 0.026	n.s.	0.098 ± 0.038	0.085 ± 0.033	
SWMP	0.078 ± 0.005	n.s.	0.079 ± 0.060	0.076 ± 0.039	
VFT	0.080 ± 0.016	[a]	0.060 ± 0.023	0.069 ± 0.024	

Unit: (a.u.) *M* mean, *S.D.* standard deviation
[a]$p < 0.05$ *n.s* non-significant

WCST [5, 6]. In an fMRI study, SWMP involved the anterior portions of the lateral PFC, bilaterally [7]. Some studies have mentioned laterality of the left hemisphere is thought to be dominant in VFT [9, 10]. However, a study has mentioned laterality in the ST [3] and a significant increase of oxy-Hb in both hemispheres during a VFT [8]. We plan to examine these issues in future studies on the elderly.

The NIRS method has some shortcomings, e.g. NIRS mainly detect in surface areas of the cerebral cortex; NIRS measurement is associated with possible confounders such as skin blood flow [19], respiration and blood pressure; and NIRS has a relatively low spatial resolution. Despite these shortcomings, NIRS is becoming increasingly useful in neuroscience.

In summary, within the limitations of this study, the findings are that all four tasks activated PFC to some extent, without laterality except for the verbal fluency task. The results confirm that NIRS is suitable for the measurement of blood oxygenation changes in frontal brain areas that are associated with all four cognitive tasks.

Acknowledgments This research was partly supported by Japan Science and Technology Agency, under Strategic Promotion of Innovative Research and Development Program, and a Grant-in-Aid from the Ministry of Education, Culture, Sports, Sciences and Technology of Japan (23300247, 25463025, and 25463024).

References

1. Jimura K, Braver TS (2010) Age-related shifts in brain activity dynamics during task switching. Cereb Cortex 20:1420–1431
2. Paxton JL, Barch DM, Racine CA et al (2008) Cognitive control, goal maintenance, and prefrontal function in healthy aging. Cereb Cortex 18:1010–1028
3. Ehlis AC, Herrmann MJ, Wagener A et al (2005) Multi-channel near-infrared spectroscopy detects specific inferior-frontal activation during incongruent Stroop trials. Biol Psychol 69:315–331
4. Langenecker SA, Nielson KA, Rao SM (2004) fMRI of healthy older adults during Stroop interference. NeuroImage 21:192–200
5. Sumitani S, Tanaka T, Tayoshi S et al (2006) Activation of the prefrontal cortex during the Wisconsin card sorting test as measured by multichannel near-infrared spectroscopy. Neuropsychobiology 53:70–76

6. Nyhus E, Barcelo F (2009) The Wisconsin card sorting test and the cognitive assessment of prefrontal executive functions: a critical update. Brain Cogn 71:437–451
7. Heinzel S, Lorenz RC, Pelz P et al (2016) Neural correlates of training and transfer effects in working memory in older adults. NeuroImage 134:236–249
8. Herrmann MJ, Ehlis AC, Fallgatter AJ (2003) Frontal activation during a verbal-fluency task as measured by near-infrared spectroscopy. Brain Res Bull 61:51–56
9. Yeung MK, Sze SL, Woo J et al (2016) Altered frontal lateralization underlies the category fluency deficits in older adults with mild cognitive impairment: a near-infrared spectroscopy study. Front Aging Neurosci 8:59
10. Schlosser R, Hutchinson M, Joseffer S et al (1998) Functional magnetic resonance imaging of human brain activity in a verbal fluency task. J Neurol Neurosurg Psychiatry 64:492–498
11. Tucha L, Simpson W (2011) The role of time on task performance in modifying the effects of gum chewing on attention. Appetite 56:299–301
12. Hirano Y, Obata T, Takahashi H et al (2013) Effects of chewing on cognitive processing speed. Brain Cogn 81:376–381
13. Hoshi Y (2003) Functional near-infrared optical imaging: utility and limitations in human brain mapping. Psychophysiology 40:511–520
14. Jobsis FF (1977) Noninvasive, infrared monitoring of cerebral and myocardial oxygen sufficiency and circulatory parameters. Science 198:1264–1267
15. Hoshi Y, Kobayashi N, Tamura M (2001) Interpretation of near-infrared spectroscopy signals: a study with a newly developed perfused rat brain model. J Appl Physiol 90:1657–1662
16. Shibusawa M, Takeda T, Nakajima K et al (2009) Functional near-infrared spectroscopy study on primary motor and sensory cortex response to clenching. Neurosci Lett 449:98–102
17. Tanida M, Sakatani K, Takano R et al (2004) Relation between asymmetry of prefrontal cortex activities and the autonomic nervous system during a mental arithmetic task: near infrared spectroscopy study. Neurosci Lett 369:69–74
18. Konno M, Takeda T, Kawakami Y et al (2016) Relationships between gum-chewing and stress. Adv Exp Med Biol 876:343–349
19. Tachtsidis I, Scholkmann F (2016) Erratum: Publisher's note: false positives and false negatives in functional near-infrared spectroscopy: issues, challenges, and the way forward. Neurophotonics 3:039801

Chapter 28
Diet-Induced Ketosis Protects Against Focal Cerebral Ischemia in Mouse

Kui Xu, Lena Ye, Katyayini Sharma, Yongming Jin, Matthew M. Harrison, Tylor Caldwell, Jessica M. Berthiaume, Yu Luo, Joseph C. LaManna, and Michelle A. Puchowicz

Abstract Over the past decade we have consistently shown that ketosis is neuroprotective against ischemic insults in rats. We reported that diet-induced ketotic rats had a significant reduction in infarct volume when subjected to middle cerebral artery occlusion (MCAO), and improved survival and recovery after cardiac arrest and resuscitation. The neuroprotective mechanisms of ketosis (via ketogenic diet; KG) include (i) ketones are alternate energy substrates that can restore energy balance when glucose metabolism is deficient and (ii) ketones modulate cell-signalling pathways that are cytoprotective. We investigated the effects of diet-induced ketosis following transient focal cerebral ischemia in mice. The correlation between levels of ketosis and hypoxic inducible factor-1alpha (HIF-1α), AKT (also known as protein kinase B or PKB) and 5′ AMP-activated protein kinase (AMPK) were determined. Mice were fed with KG diet or standard lab-chow (STD) diet for 4 weeks. For the MCAO group, mice underwent 60 min of MCAO and total brain infarct volumes were evaluated 48 h after reperfusion. In a separate group of mice, brain tissue metabolites, levels of HIF-1α, phosphorylated AKT (pAKT), and AMPK were measured. After feeding a KG diet, levels of blood ketone bodies (beta-hydroxyburyrate, BHB) were increased. There was a proportional decrease in infarct volumes with increased blood BHB levels (KG vs STD; 4.2 ± 0.6 vs 7.8 ± 2.2 mm^3, mean ± SEM). A positive correlation was also observed with HIF-1α and pAKT relative to blood BHB levels. Our results showed that chronic ketosis can be induced in mice by KG diet and was neuroprotective

K. Xu • L. Ye • K. Sharma • M.M. Harrison • T. Caldwell • J.M. Berthiaume • J.C. LaManna
Departments of Physiology and Biophysics, Case Western Reserve University, School of Medicine, Cleveland, OH, USA

Y. Jin • Y. Luo
Neurosugery and Nutrition, Case Western Reserve University, School of Medicine, Cleveland, OH, USA

M.A. Puchowicz (✉)
Nutrition, Case Western Reserve University, School of Medicine, Cleveland, OH, USA
e-mail: map10@case.edu

H.J. Halpern et al. (eds.), *Oxygen Transport to Tissue XXXIX*, Advances in Experimental Medicine and Biology 977, DOI 10.1007/978-3-319-55231-6_28

against focal cerebral ischemia in a concentration dependent manner. Potential mechanisms include upregulation of cytoprotective pathways such as those associated with HIF-1α, pAKT and AMPK.

Keywords Ketogenic diet • Ischemia-reperfusion injury • HIF-1α, AKT • Neuroprotection.

1 Introduction

The ketogenic diet (KG) is a high-fat, very low-carbohydrate diet which results in hepatic production of ketone bodies due to elevated beta-oxidation of fats by the liver [1]. Ketone bodies (beta-hydroxybutyrate and acetoacetate; BHB, AcAc) are well utilized by brain as an energy substrate, especially during glucose sparing conditions, such as with long-term fasting or chronic feeding of a KG diet [2, 3]. Ketosis results in elevated blood ketone bodies which are alternate energy substrates to glucose and are known to be well utilized by brain. The KG diet is a well-established, non-pharmacological approach to treating drug-resistant epilepsy in children [4] and has shown promise in treating other neurological conditions such as Alzheimer and stroke. Ketones are also beneficial substrates during metabolic derangements of glucose metabolism such as with ischemia reperfusion injury induced oxidative stress [5]. The metabolic adaptation to chronic ketosis, as well as the mechanistic actions of ketosis in brain (globally and cellular) are multifactorial and not well understood. This study focused on investigating the potential mechanisms associated with hypoxic inducible factor-1alpha (HIF-1α) and neuroprotection in diet-induced ketotic mice. In mice pre-conditioned with a KG diet for 4 weeks, the effect of ketosis on brain focal cerebral ischemia (via reversible middle cerebral artery occlusion; MCAO) was investigated. Additionally, metabolic analysis of concentrations of energy metabolites and levels of HIF-1α, AKT, and 5′ AMP-activated protein kinase (AMPK) were also determined using mass-spectrometry and Western Blot methods.

2 Methods

2.1 Animals

Experimental protocols were approved by the Institutional Animal Care and Use Committee (IACUC) at Case Western Reserve University (CWRU). Male Blk6 Mice (11 weeks old) were fed either KG (high fat, carbohydrate restricted) or standard lab-chow (STD) diets for 4 weeks before ischemia experiments or tissue collections [6]. Mice were maintained on a 12:12 light-dark cycle with their diets and water available ad libitum. Diet Protocols: ketogenic (KG; 89.5 fat %, 10.4 protein %, 0.1

CHO %; Research Diets, New Brunswick, NJ, USA, diet) and standard (STD; 27.5 fat %, 20.0 protein%, 52.6, provided by the CWRU animal facility). Weekly blood ketone body (BHB) concentrations were analysed using a keto-meter (Precision Xtra, Abbott, Alameda, CA, USA) from a small blood sample taken from the tail and their body weights were monitored pre- and post-diet treatment.

2.2 Middle Cerebral Artery Occlusion (MCAO)

Transient focal ischemia using a mouse MCAO model [7]: MCA mice underwent 60 min of MCAO and reperfusion. To ensure consistent and successful blockage of MCA, we monitored ischemia in all of our animals by Laser Doppler flowmetry (PeriFlux System 5000). Mice were perfused transcardially and the total infarct volumes were evaluated by Giemsa staining 48 h after reperfusion. The infarct areas are quantified using the NIH ImageJ software.

2.3 Western Blot Analysis

The analysis of HIF-1α, and related cell signalling targets such as AKT and AMPK, were measured by Western Blot analysis. Proteins (20 μg) from homogenized whole brain tissues were separated on a 12% gel, then transferred to a polyvinylidene difluoride (PVDF) membrane, blocked with 5% bovine serum albumin (BSA), and incubated with primary antibody overnight. Antibodies: HIF-1α (R&D, [1:2000]), AKTtot (CST, [1:2000]), pAKTser473 (CST, [1:2000]), pAKTthr308 (CST, [1:500]), and HSC70 (loading control, Santa Cruz, [1:5000]). Following incubation with secondary antibodies (1:15,000), proteins were detected by chemiluminescence, and densitometry was performed using Image J software [8].

2.4 Metabolic Panels: GCMS-Based Analysis

Targeted metabolic profiling by GCMS (gas chromatography-MS) analysis included measurements of citric acid cycle intermediates (CAC; absolute concentrations; μmol/g tissue) collected from fresh frozen brain tissue homogenates of mice fed either KG or STD diets [9]; the GC-MS analysis of CAC intermediates were analysed as their trimethylsilyl (TBDMS; Regis) derivatives on an Agilent 5973 N-MSD equipped with an Agilent 6890 GC system coupled to a DB-17MS capillary column (30 m × 0.25 mm × 0.25 μm) and operated in electron impact ionization mode [10].

2.5 Statistical Analysis

All values were presented as mean ± SEM. Statistical analyses were performed using SPSS v 20.0 for Windows. The comparison between any two groups was analysed with a t-test for paired sample, two-tailed. Significance was considered at the level of $p < 0.05$.

3 Results

3.1 Diet-Induced Ketosis on Infarct Volume Following MCAO in Mice

After 4 weeks of the KG diet, plasma ketone bodies (beta-hydroxyburyrate, BHB; mM) were increased (range 1.1–2.6) in the KG mice. The infarct volumes were decreased in the KG group (n = 7) compared to the STD group (n = 4), (4.2 ± 0.6 vs 7.8 ± 2.2 mm^3, mean ± SEM, p = 0.16) in a concentration-dependent manner, as there was a proportional decrease in infarct volume with increased blood BHB levels (Fig. 28.1).

3.2 Diet Induced Ketosis on HIF-1α Accumulation, AKT Activation, AMPK and Metabolites

HIF-1α levels were measured in cortical brain homogenates of KG (n = 5) and STD (n = 5) diet mice by Western Blot analysis. The HIF-1α levels increased significantly in the KG diet group (Fig. 28.2) compared to baseline levels of the STD diet group. In Fig. 28.3, the levels of the blood BHB was graphed against the abundance of protein targets detected. There was a positive correlation between the protein targets of HIF-1α and AKT (phosphorylation of ser473, thr308), and the circulating BHB concentrations (mM) in mice fed a KG diet for 4 weeks. AKT_{total} was not significantly different between the two groups. There was an insignificant positive correlation between HIF-1α and blood BHB (Fig. 28.3a). While the phosphorylation of both the serine and threonine sites of AKT showed a strong positive correlation to the level of blood BHB, the serine site showed a statistically significant correlation (Fig. 28.3b). Protein levels of AMPK (phosphorylation and total) were also

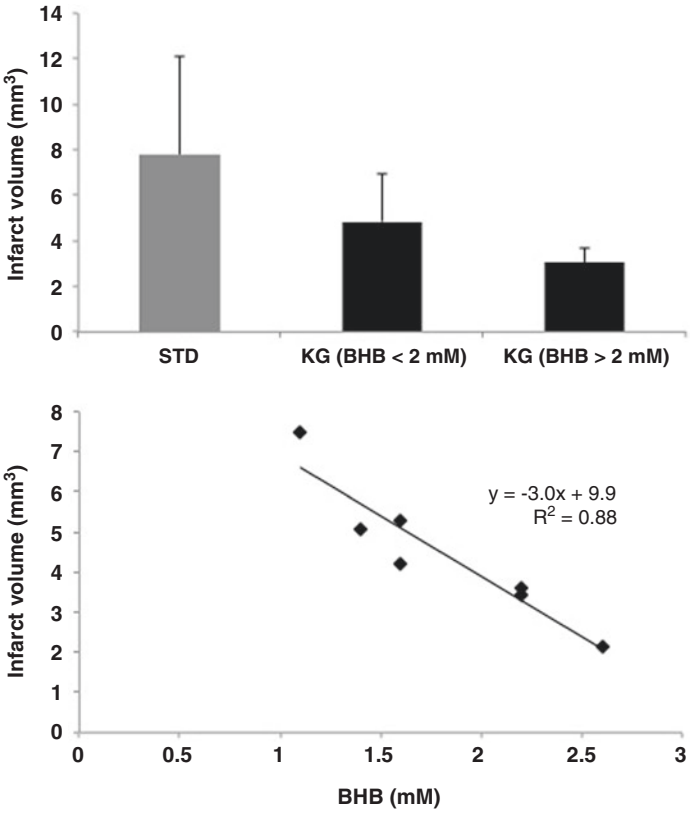

Fig. 28.1 *Upper panel*: infarct volume (mm^3) in the STD and KG groups at 48 h reperfusion following 60 min middle cerebral artery occlusion (MCAO). *Lower panel*: correlation of infarct volume with blood BHB levels, there was a decreased infarct volume with increased blood BHB levels (STD group: n = 4; KG group; n = 7)

significantly increased in the KG diet group compared to the STD group (Fig. 28.3c, d). Additionally, there was a significant correlation of the $pAKT_{thr}$ and the CAC intermediates (fumarate and malate) and BHB (tissue and plasma), Fig. 28.4. Although there were no significant findings with the other metabolites measured (succinate, citrate, aspartate, 2-hydroxyglutarate, GABA), their concentrations trended higher in the KG diet group compared to STD group (data not shown).

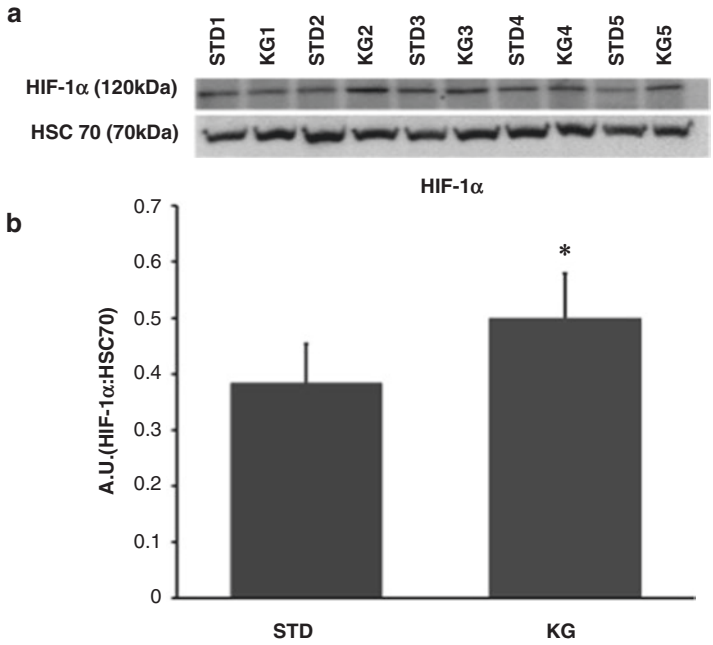

Fig. 28.2 KG diet upregulates HIF-1α protein. (**a**) Western Blot analysis of HIF-1α. (**b**) HIF-1α protein levels were normalized to HSC 70 loading control. HIF-1α was significantly higher in KG mice. The values presented are the mean ± S.E.M (n = 5). *Denotes statistical significance ($p < 0.05$)

4 Discussion

The mechanism through which KG confers neuroprotection is still largely unknown, but has been thought to be through the fact that ketones are alternate energy substrates to glucose [2–6], especially under conditions when glucose metabolism is impaired such as with ischemia reperfusion injury [5]. More recent studies have implicated KG in modulating cell-signaling pathways that are cytoprotective. The primary signaling pathways associated with cyto-protection include HIF-1α, AKT, and AMPK and these pathways are known to have overlapping signaling targets. Neuroprotective properties of ketosis may be through HIF-1α, a primary constituent associated with hypoxic angiogenesis and a regulator of neuroprotective responses [11, 12]. Our results demonstrate that the diet-induced ketotic mice exhibited significant upregulation in HIF-1α and AMPK phosphorylation, as well as neuroprotection in KG mice exposed to MCAO. These changes correlated strongly with blood BHB levels. Circulating BHB levels correlated with pAKT protein targets, suggesting a dose-dependent effect on the activity of signalling targets that are both localized and systemic. The association between pAKT and metabolites (e.g. fumarate and malate) also suggested that the neuroprotective properties of ketosis may be

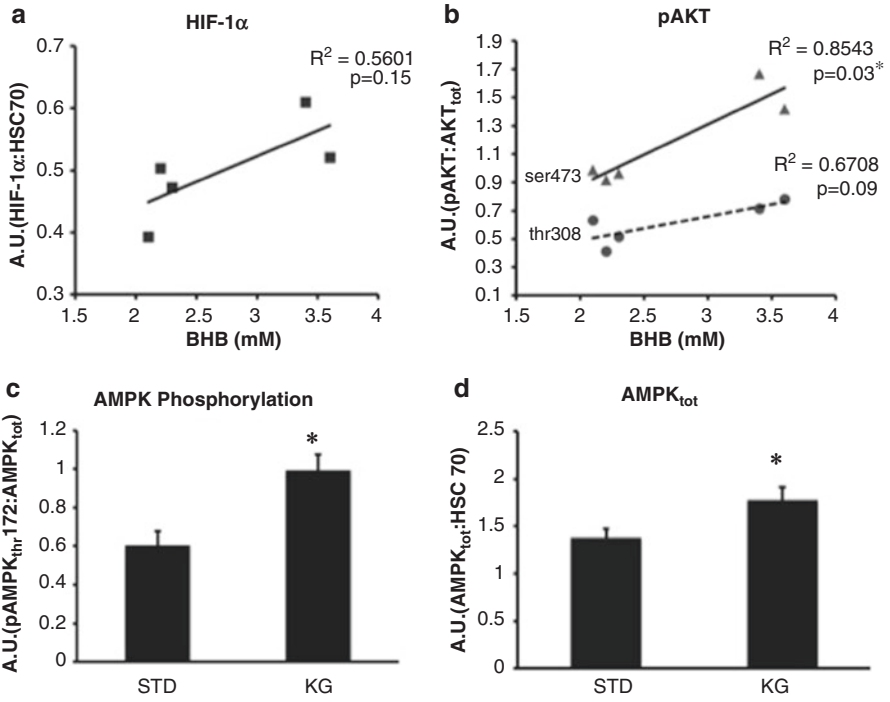

Fig. 28.3 Correlation between protein targets and circulating BHB concentrations in mice fed a ketogenic diet for 4 weeks. (**a**) Positive correlation between HIF-1α and plasma BHB. (**b**) Phosphorylation of both the serine and threonine sites of AKT showed positive correlation to blood BHB levels. (**c**) AMPK phosphorylation was significantly increased in KG group. (**d**) AMPK total. *indicates significance ($p < 0.05$; $n = 5$ per group)

through the modulation of energetics or redox state of the cell. Our work represents a novel finding with respect to post-translational regulation of a family of cytoprotective proteins that are regulated in concentration manner related to the degree of ketosis. Such an adaptive response to ketosis implies a greater sensitivity of cellular signalling pathways to alterations in circulating ketone bodies than previously reported.

In summary, our results showed that ketosis can be induced in mice by a KG diet and is neuroprotective against focal cerebral ischemia in a concentration-dependent

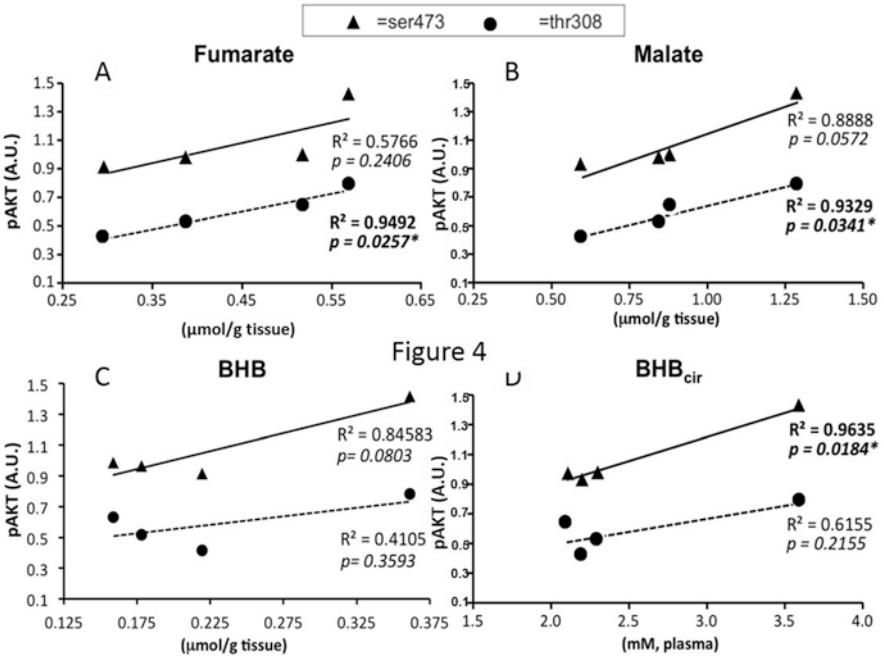

Fig. 28.4 Diet-induced activation of pAKT correlates with metabolic response and level of ketosis. *Upper panels*: citric acid cycle intermediates, fumarate and malate, showed a positive correlation with protein levels of pAKT (ser473 and thr308). *Lower panels*: positive correlation between pAKT and BHB levels as measured in both blood and brain tissue. *indicates significance ($p < 0.05$), n = 5 per group

manner. Potential mechanisms include upregulation of cellular salvation pathways, such as those associated with HIF-1α, AKT and AMPK.

Acknowledgments This study was supported by NIH grant R01 HL 092933-01A1.

References

1. Cahill GF Jr, Owen OE (1968) Starvation and survival. Trans Am Clin Climatol Assoc 79:13–20
2. Owen OE, Morgan AP, Kemp HG et al (1967) Brain metabolism during fasting. J Clin Invest 46:1589–1595
3. DeVivo DC, Leckie MP, Ferrendelli JS et al (1978) Chronic ketosis and cerebral metabolism. Ann Neurol 3:331–337
4. Freeman JM, Vining EP, Pillas DJ et al (1998) The efficacy of the ketogenic diet-1998: a prospective evaluation of intervention in 150 children. Pediatrics 102:1358–1363
5. Maalouf M, Rho JM, Mattson MP (2009) The neuroprotective properties of calorie restriction, the ketogenic diet, and ketone bodies. Brain Res Rev 59:293–315
6. Puchowicz MA, Xu K, Sun X et al (2007) Diet-induced ketosis increases capillary density without altered blood flow in rat brain. Am J Physiol Endocrinol Metab 292:E1607–E1615

7. Luo Y, Shen H, Liu HS et al (2013) CART peptide induces neuroregeneration in stroke rats. J Cereb Blood Flow Metab 33:300–310
8. Benderro GF, Sun X, Kuang Y et al (2012) Decreased VEGF expression and microvascular density, but increased HIF-1 and 2alpha accumulation and EPO expression in chronic moderate hyperoxia in the mouse brain. Brain Res 1471:46–55
9. Zhang Y, Kuang Y, LaManna JC et al (2013) Contribution of brain glucose and ketone bodies to oxidative metabolism. Adv Exp Med Biol 765:365–370
10. Kombu RS, Brunengraber H, Puchowicz MA (2011) Analysis of the citric acid cycle intermediates using gas chromatography-mass spectrometry. Methods MolBiol 708:147–157
11. Semenza GL (2001) Hypoxia-inducible factor 1: oxygen homeostasis and disease pathophysiology. Trends Mol Med 7:345–350
12. Baranova O, Miranda LF, Pichiule P et al (2007) Neuron-specific inactivation of the hypoxia inducible factor 1 alpha increases brain injury in a mouse model of transient focal cerebral ischemia. J Neurosci 27:6320–6332

Chapter 29
Evaluation of Pleasure-Displeasure Induced by Use of Lipsticks with Near-Infrared Spectroscopy (NIRS): Usefulness of 2-Channel NIRS in Neuromarketing

M. Tanida, M. Okabe, K. Tagai, and K. Sakatani

Abstract In order to examine whether near-infrared spectroscopy (NIRS) would be a useful neuromarketing tool, we employed NIRS to evaluate the difference of pleasure-displeasure in women, induced by the use of different types of lipsticks. The subjects used lipsticks A and B; A is softer than B. Concentration changes of oxy-Hb were measured in the bilateral prefrontal cortex (PFC) during use of lipsticks A and B. We evaluated the right and left dominancy of PFC activity by calculating the Laterality Index (LI) (LI = leftΔoxy-Hb - rightΔoxy-Hb); positive LI indicates left-dominant activity while negative LI indicate right-dominant activity. We found a significant interaction between the use of lipsticks A and B, using a two-way factorial analysis of variance [$F(1,13) = 9.63$, $p < 0.01$]; Δoxy-Hb in the left PFC was larger than that in the right PFC during the use of lipstick A, while Δoxy-Hb in the right PFC tended to be larger than that in the left PFC during the use of lipstick B ($p < 0.1$). The LI of lipstick A was larger than that of lipstick B (paired T-test, $p = 0.0083$). We suggest that lipstick A caused a more positive emotional response than lipstick B, since greater left than right frontal cortical activity is associated with positive affect. These results suggest that 2-channel NIRS may be a useful neuromarketing tool, since it allows objective assessment of pleasure-unpleasure.

Keywords Prefrontal asymmetry • TRS-NIRS • Lipstick • Comfort

M. Tanida • M. Okabe • K. Tagai
Shiseido Global Innovation Center, Yokohama, Japan

K. Sakatani (✉)
NEWCAT Research Institute, Department of Electrical and Electronics Engineering, College of Engineering, 1 Nakagawara, Tokusada, Tamuramachi, Koriyama, Fukushima 963-8642, Japan

Department of Neurological Surgery, School of Medicine, Nihon University, Tokyo, Japan
e-mail: sakatani.kaoru@nihon-u.ac.jp

H.J. Halpern et al. (eds.), *Oxygen Transport to Tissue XXXIX*, Advances in Experimental Medicine and Biology 977, DOI 10.1007/978-3-319-55231-6_29

1 Introduction

Neuromarketing is a field of study that involves application of neuroscientific methods, such as neuroimaging techniques, to analyze and understand human behavior related to markets and marketing exchanges [1]. Magneto-encephalography (MEG), functional magnetic resonance imaging (fMRI) and electroencephalography (EEG) have been used as neuroimaging techniques in neuromarketing research [2]. However, these techniques are not suitable for over-the-counter use.

Near-infrared spectroscopy (NIRS) appears to be an attractive alternative method, since NIRS is compact and less stressful during measurements. Although 2-channel NIRS provides limited information about brain function, we can evaluate emotional responses based on the prefrontal cortex (PFC) activity measured by 2-channel NIRS [3–7]. In the present study, we investigate whether 2-channel NIRS allows us to objectively evaluate customer preferences for lipsticks.

2 Methods

2.1 Subjects

We studied 14 women (aged 22.7 ± 1.6 years), all of whom were deemed right-handed according to the laterality quotient questionnaire of the Edinburgh Handedness Inventory. All subjects provided written informed consent as required by the Human Subjects Committee of the Shiseido Life Science Institute, Japan.

2.2 Experimental Protocol

The subjects used two kinds of lipsticks (i.e. lipsticks A and B); lipstick A is softer than lipstick B, but there is no difference in color or flavor between them.

We evaluated the feeling associated with use of the lipsticks using our original Visual Analog Scale (VAS) with four items, i.e., softness, comfort, liking, and melting texture; each item was scored from 0 to 100). In order to avoid possible effects of the VAS feeling evaluation on the PFC activity measured by NIRS, we evaluated the VAS after the NIRS measurement. In addition, the subject was not allowed to obtain any prior information about which lipstick they are using before the NIRS measurement. During the experiment, a photoelectric sensor (Tsuyama Mfg Co., Tokyo, Japan) was used to continuously monitor heart rate (HR).

We employed quantitative, near-infrared time-resolved spectroscopy (TRS: Hamamatsu Photonics K.K, Hamamatsu, Japan) for measurement of the PFC activity evoked by the use of lipsticks A and B. Details of this system have been described previously [8–11]. Briefly, it consists of three pulsed laser diodes with different

wavelengths (761, 791, and 836 nm) having a pulse duration of 100 ps at a repetition frequency of 5 MHz, a photomultiplier tube, and a circuit for time-resolved measurement based on the time-correlated single photon counting method. The observed temporal profiles were fitted to the photon diffusion TRSequation using the nonlinear least-squares fitting method. The reduced scattering and absorption coefficients for the three wavelengths were calculated. The concentrations of oxy-Hb, deoxy-Hb, and total Hb (=oxy-Hb + deoxy-Hb; t-Hb) were then calculated using the least-squares method. The concentrations of Hb were expressed in μM.

2.3 Data Analysis

The evoked CBO changes in the bilateral PFC were continuously monitored by TRS and were averaged every second during: (1) baseline conditions for 30 s; (2) use of lipstick A or B for 30 s; and (3) recovery for 30 s. To analyze PFC activity in response to the use of lipsticks, we calculated changes in oxy-Hb concentration during lipstick use. The mean baseline values (measured during 30 s) were subtracted from the mean activation values (measured during the first 30 s of lipstick use).

We evaluated the right and left dominancy of the PFC activity by calculating the Laterality Index (LI) (i.e., LI = leftΔoxy-Hb – rightΔoxy-Hb); a positive LI indicates left-dominant activity while a negative LI indicates right-dominant activity. .

3 Results

The VAS score of the melting texture for lipstick A was significantly higher than that for lipstick B (Fig. 29.1a). There was no significant difference in heart rate changes between lipstick A and B (Fig. 29.1b).

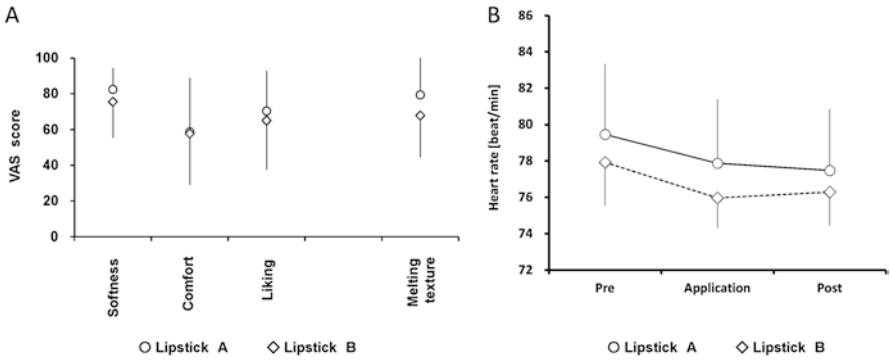

Fig. 29.1 (**a**) Differences of VAS score between lipstick A (*circles*) and lipstick B (*diamonds*) (**b**) Changes of heart rate during the course of experiment (symbols as in (*A*))

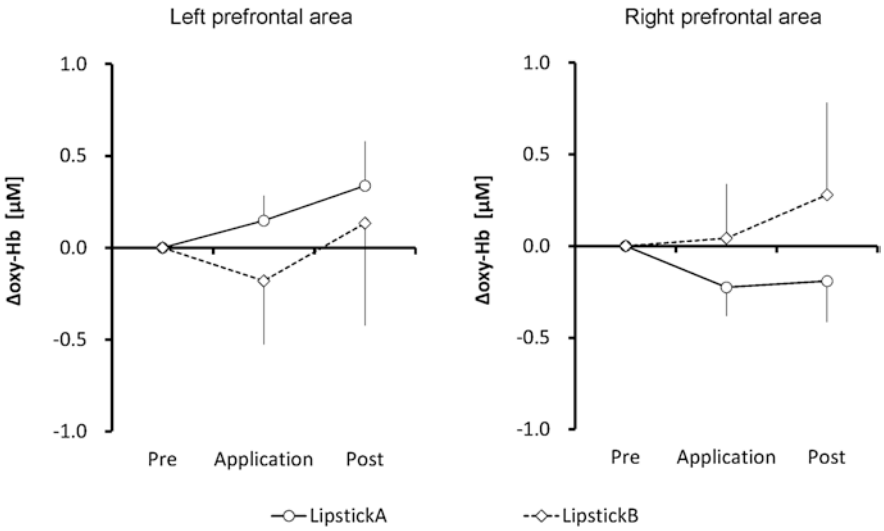

Fig. 29.2 Changes of oxy-Hb in the *right* and *left* prefrontal cortex during use of lipsticks A and B

TRS demonstrated different patterns of oxy-Hb changes between lipsticks A and B (Fig. 29.2). That is, lipstick A induced an increase of oxy-Hb in the left PFC associated with a decrease in the right PFC (LeftΔoxy-Hb = 0.15 ± 0.14, RightΔoxy-Hb = −0.22 ± 0.16), resulting in a left-dominant pattern. In contrast, lipstick B induced only small changes of oxy-Hb (LeftΔoxy-Hb = −0.18 ± 0.35, RightΔoxy-Hb = 0.043 ± 0.30).

We found a significant interaction between the use of lipsticks A and B, using a two-way factorial analysis of variance [$F(1,13) = 9.63$, $p < 0.01$]; Δoxy-Hb in the left PFC was larger than that in the right PFC during the use of lipstick A, while Δoxy-Hb in the right PFC tended to be larger than that in the left PFC during the use of lipstick B ($p < 0.1$) (Fig. 29.3a). In addition, the LI of lipstick A was larger than that of lipstick B (paired t-test, $p = 0.0083$) (Fig. 29.3b).

4 Discussion

The present results indicate that use of lipstick A induced more left-dominant PFC activity than use of lipstick B. In addition, lipstick A showed a significantly higher score for melting texture than lipstick B. These findings are consistent with the valence-asymmetry hypothesis, which asserts that the left/right asymmetry of PFC activity is correlated with specific emotional responses to mental stress and personality traits [12–14]. More precisely, Davidson reported that the asymmetry of prefrontal electrical signals recorded from the surface of the scalp

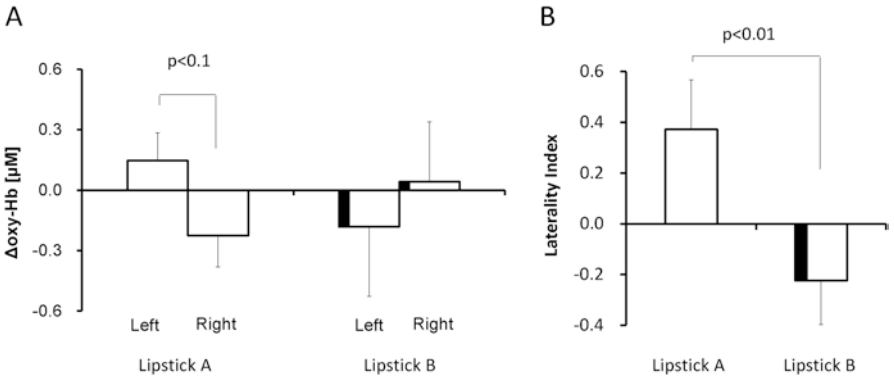

Fig. 29.3 (**a**) Changes of oxy-Hb during use of lipsticks A and B in the *right* and *left* PFC (**b**) Laterality index of lipsticks A and B

were related to emotional processes, insofar as there is relatively more left-frontal activity associated with positive emotion, whereas there is relatively more right-frontal activity associated with negative emotion [12]. This hypothesis has been confirmed in several studies using a variety of methods, including EEG, fMRI, PET, and NIRS.

In contrast to neuroimaging techniques such as fMRI, PET, and multi-channel NIRS (so-called Optical Topography), 2-channel NIRS provides limited information about brain function. However, 2-channel NIRS allows us to evaluate positive and negative emotions induced by sensory stimulations based on the left/right asymmetry of PFC (i.e. the valence-asymmetry hypothesis). Thus, our present results indicate that 2-channel NIRS may be useful in neuromarketing, particularly in evaluation of customer preferences in the over-the-counter situation.

Finally, it should be noted that we used time-resolved NIRS for measurements of PFC activity in the present study. In contrast to continuous-wave NIRS, time-resolved NIRS allows quantitative measurements of Hb concentration changes [8, 10, 11]. Thus, we could perform statistical analysis using the absolute values of Hb concentration changes induced by lipsticks A and B in the subjects, who might have had different values of optical pathlength [9].

Acknowledgments This research was supported in part by a Grant-in-Aid from the Ministry of Education, Culture, Sports, Sciences and Technology of Japan (Grant-in-Aid for Exploratory Research 25560356), and grants from Southern Tohoku Hospital (Fukushima, Japan) and Iing Co., Ltd. (Tokyo, Japan).

References

1. Lee N, Broderick AJ, Chamberlain L (2007) What is “neuromarketing”? A discussion and agenda for future research. Int J Psychophysiol 63:199–204
2. Vecchiato G, Astolfi L, De Vico FF et al (2011) On the use of EEG or MEG brain imaging tools in neuromarketing research. Comput Intell Neurosci 2011:643489
3. Tanida M, Sakatani K, Takano R et al (2004) Relation between asymmetry of prefrontal cortex activities and the autonomic nervous system during a mental arithmetic task: Near infrared spectroscopy study. Neurosci Lett 369:69–74
4. Tanida M, Katsuyama M, Sakatani K (2007) Relation between mental stress-induced prefrontal cortex activity and skin conditions: a near infrared spectroscopy study. Brain Res 1184:210–216
5. Tanida M, Katsuyama M, Sakatani K (2008) Effects of fragrance administration on stress-induced prefrontal cortex activity and sebum secretion in the facial skin. Neurosci Lett 432:157–161
6. Sakatani K (2012) Optical diagnosis of mental stress: review. Adv Exp Med Biol 737:89–95
7. Ishikawa W, Sato M, Fukuda Y, Matsumoto T, Takemura N, Sakatani K (2014) Correlation between asymmetry of spontaneous oscillation of hemodynamic changes in the prefrontal cortex and anxiety levels: a near-infrared spectroscopy study. J Biomed Opt 19:027005
8. Yokose N, Sakatani K, Murata Y et al (2010) Bedside monitoring of cerebral blood oxygenation and hemodynamics after aneurysmal subarachnoid hemorrhage by quantitative time-resolved near-infrared spectroscopy. World Neurosurg 73:508–513
9. Katagiri A, Dan I, Tuzuki D et al (2010) Mapping of optical pathlength of human adult head at multi-wavelengths in near infrared spectroscopy. Adv Exp Med Biol 662:205–212
10. Tanida M, Sakatani K, Tsujii T (2012) Relation between working memory performance and evoked cerebral blood oxygenation changes in the prefrontal cortex evaluated by quantitative time-resolved near-infrared spectroscopy. Neurol Res 34:114–119
11. Machida A, Shirato M, Tanida M et al (2016) Effects of cosmetic therapy on cognitive function in elderly women evaluated by time-resolved spectroscopy study. Adv Exp Med Biol 876:289–295
12. Davidson RJ (1993) Cerebral asymmetry and emotion: conceptual and methodological conundrums. Cognit Emot 7:115–138
13. Davidson RJ, Irwin W (1999) The functional neuroanatomy of emotion and affective style. Trends Cogn Sci 3:11–21
14. Davidson RJ, Jackson DC, Kalin NH (2000) Emotion, plasticity, cortex, and regulation: perspectives from affective neuroscience. Psychol Bull 126:890–909

Chapter 30
Relationships Between Gum Chewing and Stroop Test: A Pilot Study

Y. Kawakami, T. Takeda, M. Konno, Y. Suzuki, Y. Kawano, T. Ozawa, Y. Kondo, and K. Sakatani

Abstract Cognitive function tends to decrease with aging, therefore maintenance of this function in an aging society is an important issue. The role of chewing in nutrition is important. Although several studies indicate that gum chewing is thought to improve cognitive function, it remains debatable whether gum-chewing does in fact improve cognitive function. The Stroop test is a psychological tool used to measure cognition. A shorter reaction time indicates a mean higher behavioral performance and higher levels of oxy-Hb concentration. fNIRS is a powerful, non-invasive imaging technique offering many advantages, including compact size, no need for specially equipped facilities, and the potential for real-time measurement. The left dorsolateral prefrontal cortex (DLPFC) seems to be mainly involved in the Stroop task.

The aim of the present study was to investigate the hypothesis that gum-chewing changes cerebral blood flow in the left DLPFC during the Stroop test, and also changes the reaction time. Fourteen healthy volunteers (mean age 26.9 years) participated in this study after providing written informed consent. A piece of tasteless gum weighing 1.0 g was used. Each session was designed in a block manner, i.e. 4 rests (30 s) and 3 blocks of task (30 s). A computerized Stroop test was used (including both congruent and incongruent Stroop tasks) which calculates a response time automatically. The Binominal test was used for comparisons ($p < 0.05$). The results show activation of the left DLPFC during the Stroop task and that gum chewing significantly increases responses/oxy-Hb concentration and significantly shortens the reaction time.

Y. Kawakami (✉) • T. Takeda • M. Konno • Y. Suzuki • Y. Kawano • T. Ozawa
Department of Sports Dentistry, Tokyo Dental College, Chiba, Japan
e-mail: kawakamiyoshiaki@tdc.ac.jp

Y. Kondo
Department of General Dentistry, Tokyo Dental College Chiba Hospital, Chiba, Japan

K. Sakatani
NEWCAT Research, Institute, Department of Electrical and Electronics Engineering, College of Engineering, Nihon University, Chiyoda, Tokyo, Japan

H.J. Halpern et al. (eds.), *Oxygen Transport to Tissue XXXIX*, Advances in Experimental Medicine and Biology 977, DOI 10.1007/978-3-319-55231-6_30

Keywords Stroop test • Gum- chewing • Near-infrared spectroscopy • The left dorsolateral prefrontal cortex • Cognitive function

1 Introduction

Cognitive function tends to decrease with aging [1]. Maintenance of this function in aging society is an important issue [2]. The role of chewing in nutrition is important and studies have shown the relationship between chewing and cognitive performance including memory, attention, and executive function. Several studies have indicated that gum-chewing is considered to improve cognitive function [3–7]. Mastication has been shown on magnetic resonance imaging (MRI) to increase prefrontal cortex (PFC) blood flow [8, 9]. Increased blood flow to the brain may, in part, be the reason for increased cognition. However, it remains debatable whether or not chewing gum does improve cognitive function.

The Stroop test [10, 11] is a psychological tool that measures cognition and the ability to focus attention on a task. Stroop Interference is the well-known increased response time (RT) for naming font colors of incongruent color words compared to font colors of congruent color words.

NIRS can investigate the changes in cerebral hemodynamics and metabolism measures [12, 13]. Signal changes represent changes in local cerebral blood flow and oxygen expenditure, and the oxy-Hb level represents brain activity [14]. Functional NIRS is a powerful, non-invasive imaging technique offering many advantages, including compact size, no need for specially equipped facilities, and the potential for real-time measurement [15, 16].

Mean concentration levels of oxy-Hb were correlated with behavioral performance in the cognitive task. A shorter reaction time in the Stroop test showed higher levels of oxy-Hb concentration [17] in the left dorsolateral PFC (DLPFC) [10].

Therefore, the aim of the present study was to investigate the hypothesis that gum-chewing changes cerebral blood flow in the left DLPFC during the Stroop test and also changes the reaction time.

2 Methods

The study design was approved by the Ethics Committee of Tokyo Dental College (No. 436). Fourteen healthy volunteers (7 females, 7 males; mean age 26.9 ± 2.98 years) participated in this study after providing written informed consent. Participants had no personal or family history of neuropsychiatric illness, were free of medication, and all were right-handed. A piece of tasteless gum weighing 1.0 g (Lotte, Saitama, Japan) was used as a chewing sample. The hardness of the gum base was 6.4×10^3 Pa s (medium type). Chewing rate and force were

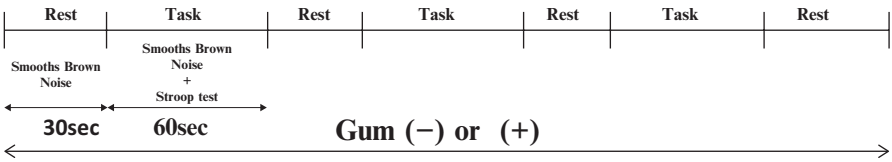

Fig. 30.1 Each task session was designed in a block manner: 4 rests (30 s) and 3 tasks (Stroop test) (30 s)

determined by the participants themselves. Under the gum chewing condition, chewing was done throughout the measurement. NIRS measurements were conducted during resting periods and trials of the Stroop test. Each session was designed in a block manner, i.e. 4 periods of rest (30 s) and 3 blocks of tasks (30 s). During the rest periods, participants were instructed to sit still with their eyes open. During the test periods, the participants conducted a computerized Stroop Test, including both congruent and incongruent Stroop trials (Don't Be Confused! Version 2.10, Japan) (Fig. 30.1). The response time was calculated automatically.

Activity in the PFC was measured by a multi-channel NIRS; (OEG-16, Spectratech, Japan) operated by an OEG-16. Exe V 3.0 [18]. The measurement probes (inter-optode distance 30 mm) were affixed to the participant's forehead. The recording channels resided in the optical path in the brain between the nearest pairs of emitter and detection probes. A 2 × 6 probe configuration involving 6 light emitters (wave-length 840 and 770 nm) and 6 detector probes was used, which resulted in a total of 16 channels. The array of the light emitter and detector probes covered an area of the forehead, with the most inferior channel located at Fp1 and Fp2 according to the International 10–20 system of electrode placement. The region of interest was placed at the left DLPFC [10]. Data from three channels were averaged for analysis.

To obtain the hemodynamic response, changes in the concentration of oxy-Hb, deoxy-Hb and total hemoglobin were calculated. BRain Suite (BRSystems, Japan) software was used for the analysis. A bandpass filter and a moving average were used. A linear fitting function for baseline correction was employed. The pre-task baseline was determined as the mean across 7 s just before the active-task period; the post-task baseline was determined as the mean across the last 8 s of the resting period; then linear fitting was performed on the task data between these two baselines. Following this correction, the 3 task repetitions, data were averaged in 3 channels of the left DRPFC and subject. For subsequent analyses, only changes in the oxy-Hb concentration registered during each task were considered. This is because the NIRS parameter usually shows the clearest pattern of activation and is proposed to be the most sensitive indicator of changes in regional cerebral blood flow [14]. The neural activity did not increase immediately after the start of the tasks; therefore, the oxy-Hb values between 10 and 30 s in each task were used for the analysis. The Binominal test was used for the comparisons ($p < 0.05$).

3 Results

Gum chewing significantly increased responses/oxy-Hb concentration in the left DLPFC of the region of interest (Fig. 30.2). Also, gum chewing significantly shortens the reaction time (Fig. 30.3).

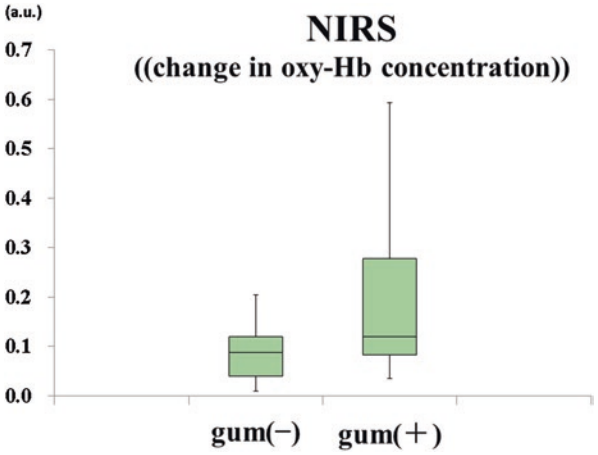

Fig. 30.2 oxy-Hb concentration changes in Gum (−) and Gum (+)

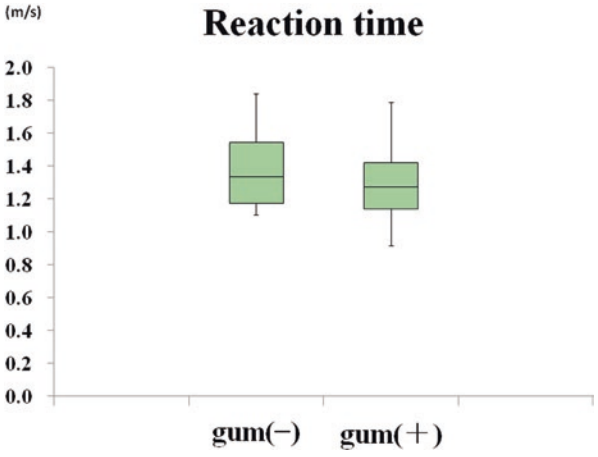

Fig. 30.3 Changes in reaction time in Gum (−) and Gum (+)

4 Discussion

The main findings of the present NIRS study are that gum-chewing significantly increases responses/oxy-Hb concentration and significantly shortened the reaction time of the Stroop test. Following these Stroop trials, this suggests that cerebral activation is specifically related to cognitive interference in this part of the brain. This result is largely in line with previous findings [3–7]. It is thought that the increase in cognition while chewing gum might be due to an increase in cerebral blood flow, a specific aspect of attention, increases the amount of glucose released, or creates a context-dependent effect [3, 5, 19] .

Cognitive training has shown the potential to slow down or even restore some aspects of age-related decline in working memory function [20–22]. The effects of acute gum-chewing in cognitive function showed the same kind of result [3–7]. Thus, daily gum-chewing might improve cognitive function in an elderly group.

For that, a proper occlusion and a mastication function in each person should be maintained. Erbay et al. [23] showed that chewing gum may not be directly effective on depressed mood; however, it may reduce the symptoms originating from depression such as the gastrointestinal symptoms, including, for example, loss of appetite, and flatulence. Narita et al. [24] concluded that a partial dental prosthesis significantly stimulates both masticatory muscle and dorsal PFC activities, which might contribute to the prevention of cognitive impairment in elderly individuals. Hosoi et al. [25] showed that brain function activity was enhanced by improvement of complete dentures and by wearing of partial dentures.

In summary, the finding of this study is that gum-chewing significantly increased responses/oxy-Hb concentration of the DLPFC and shortened the reaction time during the Stroop task.

Acknowledgments This research was partly supported by the Japan Science and Technology Agency, under the Strategic Promotion of Innovative Research and Development Program, and a Grant-in-Aid from the Ministry of Education, Culture, Sports, Sciences and Technology of Japan (23300247, 25463025, and 25463024).

References

1. Carp J, Gmeindl L, Reuter-Lorenz PA (2010) Age differences in the neural representation of working memory revealed by multi-voxel pattern analysis. Front Hum Neurosci 4:217
2. Onozuka M, Watanabe K, Fujita M et al (2002) Evidence for involvement of glucocorticoid response in the hippocampal changes in aged molarless SAMP8 mice. Behav Brain Res 131:125–129
3. Baker JR, Bezance JB, Zellaby E et al (2004) Chewing gum can produce context-dependent effects upon memory. Appetite 43:207–210
4. Tucha L, Simpson W, Evans L et al (2010) Detrimental effects of gum chewing on vigilance in children with attention deficit hyperactivity disorder. Appetite 55:679–684

5. Tucha L, Simpson W (2011) The role of time on task performance in modifying the effects of gum chewing on attention. Appetite 56:299–301
6. Onyper SV, Carr TL, Farrar JS et al (2011) Cognitive advantages of chewing gum. Now you see them, now you don't. Appetite 57:321–328
7. Hirano Y, Obata T, Kashikura K et al (2008) Effects of chewing in working memory processing. Neurosci Lett 436:189–192
8. Takada T, Miyamoto T (2004) A fronto-parietal network for chewing of gum: a study on human subjects with functional magnetic resonance imaging. Neurosci Lett 360:137–140
9. Momose I, Nishikawa J, Watanabe T et al (1997) Effect of mastication on regional cerebral blood flow in humans examined by positron-emission tomography with 15O-labelled water and magnetic resonance imaging. Arch Oral Biol 42:57–61
10. Ehlis AC, Herrmann MJ, Wagener A et al (2005) Multi-channel near-infrared spectroscopy detects specific inferior-frontal activation during incongruent Stroop trials. Biol Psychol 69:315–331
11. Hyodo K, Dan I, Suwabe K et al (2012) Acute moderate exercise enhances compensatory brain activation in older adults. Neurobiol Aging 33:2621–2632
12. Hoshi Y (2003) Functional near-infrared optical imaging: utility and limitations in human brain mapping. Psychophysiology 40:511–520
13. Jobsis FF (1977) Noninvasive, infrared monitoring of cerebral and myocardial oxygen sufficiency and circulatory parameters. Science 198:1264–1267
14. Hoshi Y, Kobayashi N, Tamura M (2001) Interpretation of near-infrared spectroscopy signals: a study with a newly developed perfused rat brain model. J Appl Physiol 90:1657–1662
15. Shibusawa M, Takeda T, Nakajima K et al (2009) Functional near-infrared spectroscopy study on primary motor and sensory cortex response to clenching. Neurosci Lett 449:98–102
16. Tanida M, Sakatani K, Takano R et al (2004) Relation between asymmetry of prefrontal cortex activities and the autonomic nervous system during a mental arithmetic task: near infrared spectroscopy study. Neurosci Lett 369:69–74
17. Leon-Carrion J, Damas-Lopez J, Martin-Rodriguez JF et al (2008) The hemodynamics of cognitive control: the level of concentration of oxygenated hemoglobin in the superior prefrontal cortex varies as a function of performance in a modified Stroop task. Behav Brain Res 193:248–256
18. Yamada T, Umeyama S, Matsuda K (2012) Separation of fNIRS signals into functional and systemic components based on differences in hemodynamic modalities. PLoS One 7:e50271
19. Stephens R, Tunney RJ (2004) Role of glucose in chewing gum-related facilitation of cognitive function. Appetite 43:211–213
20. Brehmer Y, Rieckmann A, Bellander M et al (2011) Neural correlates of training-related working-memory gains in old age. NeuroImage 58:1110–1120
21. Klingberg T (2010) Training and plasticity of working memory. Trends Cogn Sci 14:317–324
22. Backman L, Nyberg L (2013) Dopamine and training-related working-memory improvement. Neurosci Biobehav Rev 37:2209–2219
23. Erbay FM, Aydın N, Satı-Kırkan T (2013) Chewing gum may be an effective complementary therapy in patients with mild to moderate depression. Appetite 65:31–34
24. Narita N, Kamiya K, Yamamura K et al (2009) Chewing-related prefrontal cortex activation while wearing partial denture prosthesis: pilot study. J Prosthodont Res 53:126–135
25. Hosoi T, Morokuma M, Shibuya N et al (2011) Influence of denture treatment on brain function activity. JpnDent Sci Rev 47:56–66

Chapter 31
Effects of Motor Imagery on Cognitive Function and Prefrontal Cortex Activity in Normal Adults Evaluated by NIRS

M. Moriya and K. Sakatani

Abstract Recent near-infrared spectroscopy (NIRS) studies demonstrated that physical exercise enhances working memory (WM) performance and prefrontal cortex (PFC) activity during WM tasks in normal adults. Interestingly, the effects of rehabilitation (i.e. physiotherapy) on post-stroke patients could be enhanced by motor imagery (MI), an active process during which the specified action is reproduced within WM without any actual physical movement. However, it is not known whether MI can enhance cognitive function and associated brain activity. To clarify these issues, we evaluated the effect of MI on WM performance and PFC activity during WM tasks in normal adults, employing NIRS. We studied 10 healthy adults. The present study was a crossover comparison test; the MI training and control condition (rest) were applied to the subjects at random. The Time Up and Go method was used for MI training: the subject sat on a chair and conducted MI for 3 min, three times. Neuronal activity (oxyhemoglobin concentration) in the bilateral PFC was measured using 2-CH NIRS during WM tasks. We found that MI improved the behavioral performance of WM compared with the control ($p < 0.01$). NIRS revealed that MI enhanced PFC activity induced by the WM task compared with the control task ($p < 0.01$). These results suggest that MI can improve cognitive function and increase associated PFC activity in normal adults.

Keywords NIRS • Rehabilitation • Working memory • Prefrontal cortex • Motor imagery

M. Moriya
Department of Rehabilitation, Nihon University Itabashi Hospital, Tokyo, Japan

K. Sakatani (✉)
NEWCAT Research Institute, Department of Electrical and Electronics Engineering, College of Engineering, Fukushima, Japan
e-mail: sakatani.kaoru@nihon-u.ac.jp

H.J. Halpern et al. (eds.), *Oxygen Transport to Tissue XXXIX*, Advances in Experimental Medicine and Biology 977, DOI 10.1007/978-3-319-55231-6_31

1 Introduction

Motor imagery (MI) involves reproduction of an action within working memory (WM) without any actual physical movement. It has been used in rehabilitation [1], for example to improve recovery of motor function following stroke, and also has a number of exciting potential applications, for example to provide brain-machine interfacing [2]. Reproduction of the motor image by the working memory is associated with activation of the prefrontal cortex (PFC) [3], and PFC activation can be measured by means of near-infrared spectroscopy (NIRS) in terms of oxyhemoglobin concentration changes.

The purpose of this study is to examine the neuro-physiological effects of MI training. Specifically, we used NIRS to examine the effect of MI on PFC activity and we evaluated the influence of MI-induced PFC activity changes on WM task performance in normal adults.

2 Methods

We studied 10 healthy adults (6 males and 4 females, age 25.5 ± 1.2 years). All participants provided written informed consent as required by the Human Subjects Committee of the Nihon University Hospital (Japan).

The subject performed the imagined Time Up and Go for motor imagery (MI) [4] and the control task with the resting condition at random. The motor image task being used in previous studied had Time Up and Go (TUG-i). To recall for 10 min sitting at a chair, Time Up and Go (TUG-real: TUG-r) has conventionally been measured in the same environment in which it has been set. TUG is composed of a plurality of operation of standing, walking, direction-changing and sitting.

The modified Sternberg Test (ST) was used as a working memory (WM) task [5–7]. In ST, subjects were asked to remember one digit and six digits successively. There were eight 1-digit trials and eight 6-digit trials. Each trial began with the presentation of one digit or a set of six digits to be encoded for 1 s on a display. Then a blank display was shown for 2 s, followed by the test digit until a response was obtained within 2 s. Subjects held a small box with two buttons side by side. They were required to press the right button if they thought the test digit was contained within the encoded stimulus and to press the left one if not, as quickly and accurately as possible. Similar tasks have been used in NIRS experiments and demonstrated that they activated the PFC [5–7].

We measured concentration changes of oxyhemoglobin (oxy-Hb), deoxyhemoglobin (deoxy-Hb) and total Hb (t-Hb) in the bilateral PFC during the WM task using a two-channel NIRS (PNIRS-10, Hamamatsu Photonics K.K., Hamamatsu, Japan). The NIRS probes were set symmetrically on the forehead; the positioning is similar to the midpoint between electrode positions Fp1/F3 (left) and Fp2/F4 (right) of the international 10–20 system [8]. The sensor part (weighing approximately

100 g, which imposes a minimal burden on the subject) communicated with a PC via Bluetooth™ (class 2).

We analyzed the changes in oxy-Hb concentration by subtracting the mean control values from the mean activation values induced by ST. We evaluated behavioral performance (response time and accuracy) of the WM task. The oxy-Hb concentration changes and behavioral performance before and after the exercise were compared using a paired student's t-test.

3 Results

Figure 31.1 shows a typical example of NIRS parameter changes in the PFC during MI and ST. MI increased oxy-Hb and t-Hb associated with a decrease of deoxy-Hb. ST caused similar NIRS parameter changes before and after MI. It should be noted that the ST-induced changes of oxy-Hb after MI were larger than those before MI.

Table 31.1 compares changes of oxy-Hb concentrations induced by ST before and after MI. The mean changes of oxy-Hb concentrations in the PFC induced by ST after MI were significantly higher than those before MI ($p < 0.05$). In contrast, there were no significant effects of the control task on ST-induced oxy-Hb changes.

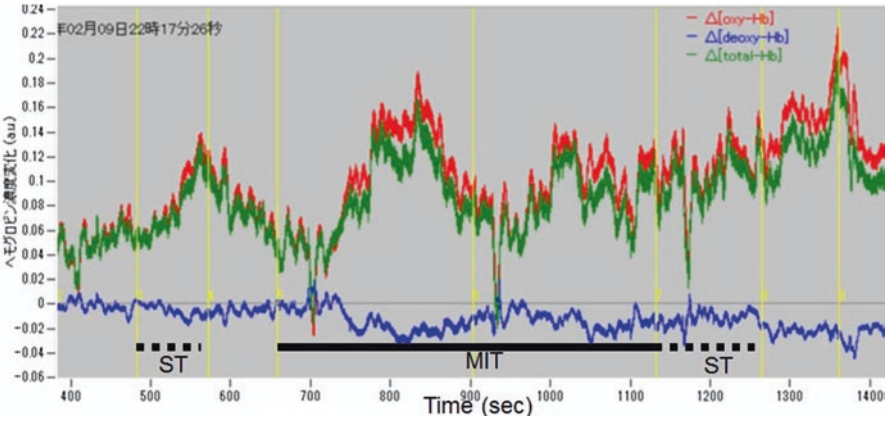

Fig. 31.1 A typical example of NIRS parameter changes during motor imagery (MI) and the Sternberg Test (ST)

Table 31.1 Effects of motor imagery and control task on changes of oxy-Hb induced by the Sternberg Test

	Control		Image	
	Right PFC	Left PFC	Right PFC	Left PFC
Before	0.022 ± 0.02	0.013 ± 0.03	0.007 ± 0.03	0.007 ± 0.04
After	0.019 ± 0.02	0.012 ± 0.03	0.041 ± 0.03*	0.049 ± 0.04*

*$p < 0.05$

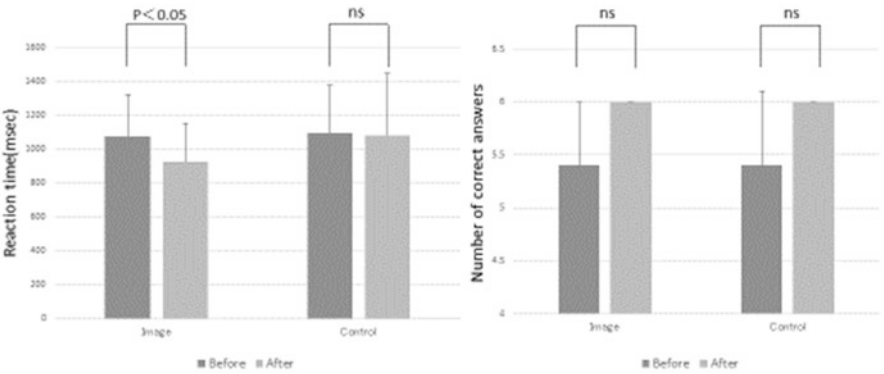

Fig. 31.2 (**a**) Effect of MI on reaction time; and (**b**) Number of correct answers on the Sternberg Test

Figure 31.2 shows the effect of MI on the performance of ST. The response time of ST after MI was significantly shorter than that before MI; there was no effect of the control task on the response time. In contrast, MI had no significant effect on the accuracy of ST (i.e. number of correct answers).

4 Discussion

This is the first study to examine the acute effects of motor imagery on cognitive function in normal adults using NIRS. We measured Δoxy-Hb change at the PFC during the working memory task (i.e. the Sternberg Test) after motor imagery. Behavioral analysis shows that motor imagery improved behavioral performance of the working memory task compared with the control sessions; the subjects responded more quickly after motor imagery. In contrast, there were no significant effects on the PFC activity and behavioral performance after the control sessions. These findings suggest that motor imagery could enhance the PFC activity associated with working memory performance.

Studies have demonstrated that physical exercise enhances cognitive function associated with an increase of brain activity [9, 10]. Employing a similar NIRS and working memory task in the present study, we examined the acute effect of physical exercise (moderate intensity exercise with an ergometer) on PFC activity in older adults using NIRS [5]. We observed that the physical exercise improved the behavioral performance and enhanced the PFC activity, similar to earlier findings.

Some animal studies have proposed physiological mechanisms for the effect of physical exercise on cognitive functions, such as brain-derived neurotrophic factor [11]. However, the physiological mechanism of motor imagery on cognitive function is not yet clear. It is reported that motor imagery activates various cortical areas, including the PFC [3]. Conditioning of the PFC activity induced by motor

imagery may enhance PFC activity and the related cognitive function, such as the working memory.

In conclusion, the present study has successfully demonstrated, for the first time, the acute motor imagery effect on cognitive function and PFC activity in normal adults using NIRS.

Acknowledgments This research was supported in part by a Grant-in-Aid from the Ministry of Education, Culture, Sports, Sciences and Technology of Japan (Grant-in-Aid for Exploratory Research 25560356), and grants from Alpha Electron Co., Ltd. (Fukushima, Japan) and Iing Co., Ltd. (Tokyo, Japan).

References

1. Harris JE, Hebert A (2015) Utilization of motor imagery in upper limb rehabilitation: a systematic scoping review. Clin Rehabil 29:1092–1107
2. Alonso-Valerdi LM, Salido-Ruiz RA, Ramirez-Mendoza RA (2015) Motor imagery based brain-computer interfaces: an emerging technology to rehabilitate motor deficits. Neuropsychologia 79:354–363
3. Hétu S, Grégoire M, Saimpont A et al (2013) The neural network of motor imagery: an ALE meta-analysis. Neurosci Biobehav Rev 37:930–949
4. Beauchet O, Annweiler C, Assal F et al (2010) Imagined Timed Up & Go test: a new tool to assess higher-level gait and balance disorders in older adults? J Neurol Sci 294:102–106
5. Tsujii T, Komatsu K, Sakatani K (2013) Acute effects of physical exercise on prefrontal cortex activity in older adults: a functional near-infrared spectroscopy study. Adv Exp Med Biol 765:293–298
6. Sakatani K, Tanida M, Hirao N et al (2014) Ginko biloba extract improves working memory performance in middle-aged women: role of asymmetry of prefrontal cortex activity during a working memory task. Adv Exp Med Biol 812:295–301
7. Tanida M, Sakatani K, Tsujii T (2012) Relation between working memory performance and evoked cerebral blood oxygenation changes in the prefrontal cortex evaluated by quantitative time-resolved near-infrared spectroscopy. Neurol Res 34:114–119
8. Tanida M, Katsuyama M, Sakatani K (2007) Relation between mental stress-induced prefrontal cortex activity and skin conditions: a near-infrared spectroscopy study. Brain Res 1184:210–216
9. Colcombe S, Kramer AF (2003) Fitness effects on the cognitive function of older adults: a meta-analytic study. Psychol Sci 14:125–130
10. Colcombe SJ, Kramer AF, McAuley E et al (2004) Neurocognitive aging and cardiovascular fitness: recent findings and future directions. J Mol Neurosci 24:9–14
11. Zoladz JA, Pilc A (2010) The effect of physical activity on the brain derived neurotrophic factor: from animal to human studies. J Physiol Pharmacol 61:533–541. Review.

Chapter 32
Site Specificity of Changes in Cortical Oxyhaemoglobin Concentration Induced by Water Immersion

D. Sato, K. Yamashiro, Y. Yamazaki, A. Tsubaki, H. Onishi, N. Takehara, and A. Maruyama

Abstract Our previous studies have shown that water immersion (WI) changes sensorimotor processing and cortical excitability in the sensorimotor regions of the brain. The present study examined the site specificity of the brain activation during WI using functional near infrared spectroscopy (fNIRS). Cortical oxyhaemoglobin (O_2Hb) levels in the anterior and posterior parts of the supplementary motor area (pre-SMA and SMA), primary motor cortex (M1), primary somatosensory cortex (S1), and posterior parietal cortex (PPC) were recorded using fNIRS (OMM-3000; Shimadzu Co.) before, during, and after WI in nine healthy participants. The cortical O_2Hb levels in SMA, M1, S1, and PPC significantly increased during the WI and increased gradually along with the filling of the WI tank. These changes were not seen in the pre-SMA. The results show that WI-induced increases in cortical O_2Hb levels are at least somewhat site specific: there was little brain activation in response to somatosensory input in the pre-SMA, but robust activation in other areas.

Keywords Water immersion • Oxyhaemoglobin concentration • Site specificity • Sensorimotor • fNIRS

D. Sato (✉) • K. Yamashiro • A. Maruyama
Institute for Human Movement and Medical Sciences, Niigata University of Health and Welfare, Niigata, Japan

Department of Health and Sports, Niigata University of Health and Welfare, Niigata, Japan
e-mail: daisuke@nuhw.ac.jp

Y. Yamazaki • A. Tsubaki • H. Onishi • N. Takehara
Institute for Human Movement and Medical Sciences, Niigata University of Health and Welfare, Niigata, Japan

H.J. Halpern et al. (eds.), *Oxygen Transport to Tissue XXXIX*, Advances in Experimental Medicine and Biology 977, DOI 10.1007/978-3-319-55231-6_32

1 Introduction

Water immersion (WI) induces a variety of physiological responses depending on physical parameters such as temperature and hydrostatic pressure. The induced physiological changes can have therapeutic benefits, and indeed WI is used as part of rehabilitation regimens for orthopaedic, cardiovascular, and respiratory disorders. Additionally, recent studies have reported that exercise in water has beneficial effects on cognitive function [1], though cortical activity during WI remains incompletely understood. Our previous studies have revealed that WI changes cortical activation in sensory and motor related areas via hydrostatic pressure [2, 3]. However, the site-specificity of WI-induced cortical activities has yet to be investigated.

Functional near-infrared spectroscopy (fNIRS) measures the concentrations of oxyhaemoglobin (O_2Hb) and deoxyhaemoglobin (HHb) in tissue based on their differential absorption at multiple wavelengths, using the modified Beer-Lambert law [4]. Thus, fNIRS is widely used to monitor real-time haemodynamic changes related to cortical neural activation in several situations, such as during WI, exercise, and task performances.

In the present study, we used fNIRS to investigate the activation of the sensory, motor, and higher order motor-related areas during WI. We hypothesized that WI would induce cortical activity, and that the activity might be site specific because of the distribution of neurons activated by somatosensory stimulation [5].

2 Methods

2.1 Participants

Nine healthy males were recruited from the Niigata University of Health and Welfare (mean age: 21.8 years, range: 20–26 years). All subjects were right-handed. None of the participants had a history of neurological, major medical, or psychiatric disorders. This study was approved by the local ethics committee of the Niigata University of Health and Welfare, and was performed in accordance with the Declaration of Helsinki. Written informed consent was obtained from all subjects after providing a complete description of the study's methods, risks, and research goals.

2.2 Experimental Procedure

Participants wore only swimwear during the experimental sessions. Participants sat in a water immersion tank (BB-300G; Sakaimed Co.) and remained seated throughout the 32 min experiment (Fig. 32.1). The experimental session consisted

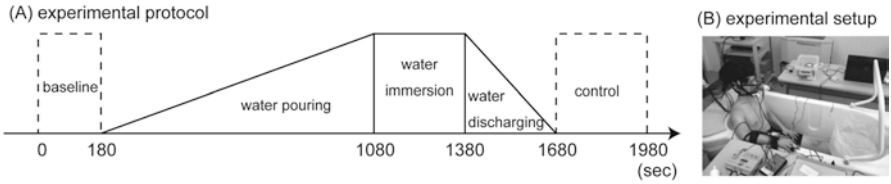

Fig. 32.1 Experimental protocol (**a**) and experimental setup (**b**) in the present study

of a non-immersed control condition for baseline recording (3 min), a water pouring condition (tank filling; 15 min), a water immersion condition (15 min), a water discharging condition (5 min), and another non-immersed control condition (5 min). To minimize the effect of body temperature changes on cortical activity, the ambient and water temperatures were maintained at 30 °C and 34 °C, respectively.

2.3 fNIRS Measurements

The fNIRS system used in this study (OMM-3000; Shimadzu, Kyoto, Japan) consists of 12 light source fibres and 12 detectors, totalling 36 source-detector pairs (labelled channels 1–36). The interoptode distance was 3.0 cm. Each light source has three laser diodes with wavelengths of 780, 805, and 830 nm to detected changes in O_2Hb, HHb, and total haemoglobin (totalHb). Signals were converted to concentrations (in mmol mm) by applying the modified Beer-Lambert law online at a sampling rate of 190 ms. We selected O_2Hb concentration as a marker of cortical activity because it is the most sensitive indicator of sensory- and motor-related changes in regional cerebral blood flow [6, 7]. Signals acquired during baseline were subtracted from signals acquired during WI to yield the specific cortical fNIRS response to somatosensory stimulation. Signals were then averaged over 10-s epochs. For fNIRS probe placement, the Cz position of the international 10–20 system was used to ensure consistent optode placement between subjects. Since we aimed to examine cortical activity in sensory- and motor-related area, the fNIRS array map covered the central and parietal areas of the scalp. The area was divided into four regions of interest based on the functional anatomy of the central and parietal scalp region [6, 8, 9]. The primary somatosensory cortex (S1) was covered by channels 17 and 23, the posterior parietal cortex (PPC) by channels 18 and 24, the supplementary motor area (SMA) by channels 15 and 21, pre-SMA by channels 14 and 20 and the primary motor area (M1) by channels 16 and 22 (demarcated by circles in Fig. 32.2).

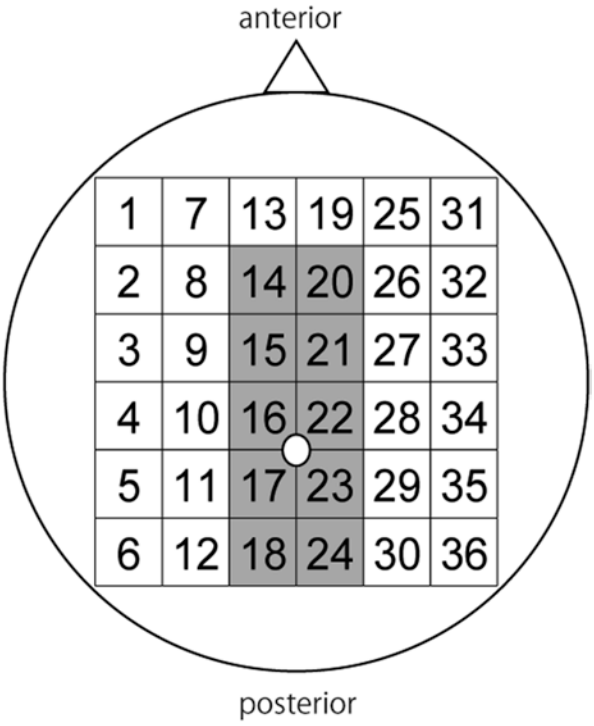

Fig. 32.2 Channel layout of fNIRS The open circle represents the Cz position. Grey squares represent the regions of interest (ROI)

2.4 Blood Pressure, Heart Rate, Skin Blood Flow, Quadriceps Muscle Oxygenation and Oxygen Uptake (VO_2) Measurement

Systolic blood pressure (SBP), diastolic blood pressure (DBP), heart rate (HR), and skin blood flow were monitored continuously and averaged over 10-s epochs. Blood pressure and HR were measured (beat to beat) using a fingertip photoplethysmograph (Finometer MIDI; Monte System Corporation) on the right hand. Surface blood flow (SBF) at the forehead was measured using laser Doppler flowmetry (FLO-C1; OMEGAWAVE Inc.). Voltage outputs from the laser Doppler measurements were normalized to baseline levels because laser Doppler flow signals are unable to provide absolute blood flow values. To measure quadriceps muscle oxygenation (O_2Hb@VL), one set of NIRS optodes were placed on the skin over the left vastus lateralis muscle 10–12 cm above the knee; the optodes were secured using double sided adhesive tape. The optode separation distance was 4 cm, corresponding to a penetration depth of ~2 cm. Optodes were connected to a laser Doppler flowmeter (BOM-L1TR SF, OMEGAWAVE Inc.). Expired respiratory gas

was analysed using an automated metabolic analyser (MG-360; Minato, Tokyo, Japan), which had been calibrated with known concentrations of O_2 and CO_2 for fractional concentrations of both gases. VO_2 was calculated every 10 s during the experiment.

2.5 Statistical Analysis

All data are presented as the mean ± standard error of the mean (SEM). Data were analysed using the computer software SPSS (v.18; SPSS Inc.). The O_2Hb in each brain region, MAP, HR, SBF, O_2Hb@VL, and VO_2 were subjected to a one-factor repeated ANOVA by time (each 10-s period), and Dunnett's *post hoc* test was used. If the assumption of sphericity was violated in Mauchly's sphericity test, the degree of freedom was corrected using Greenhouse-Geisser correction coefficient epsilon, and then the F-values and P-values were recalculated. The significance level was set at 5%.

3 Results

The results of the one-way ANOVA showed increasing O_2Hb concentrations in S1, PPC, SMA, and M1, but not in pre-SMA (Fig. 32.3). Post-hoc testing revealed that these changes were initially seen in S1 and PPC (7 min and 40 s after starting the pouring to fill the tank), followed by in SMA and M1 (1 min after pouring had ceased, and true WI had begun), compared to baseline.

MAP, SBF, and VO_2 showed no significant differences compared to baseline throughout the experiment (Fig. 32.4). On the other hand, the results of the one-way

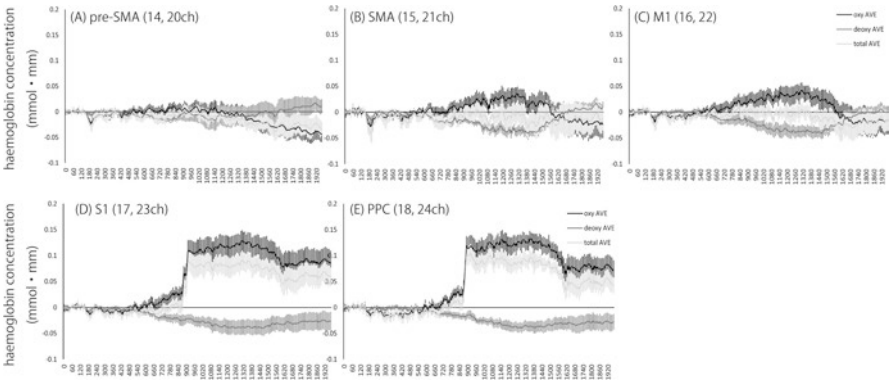

Fig. 32.3 Changes of haemoglobin concentration in pre-SMA (**a**), SMA (**b**), M1 (**c**), S1 (**d**) and PPC (**e**)

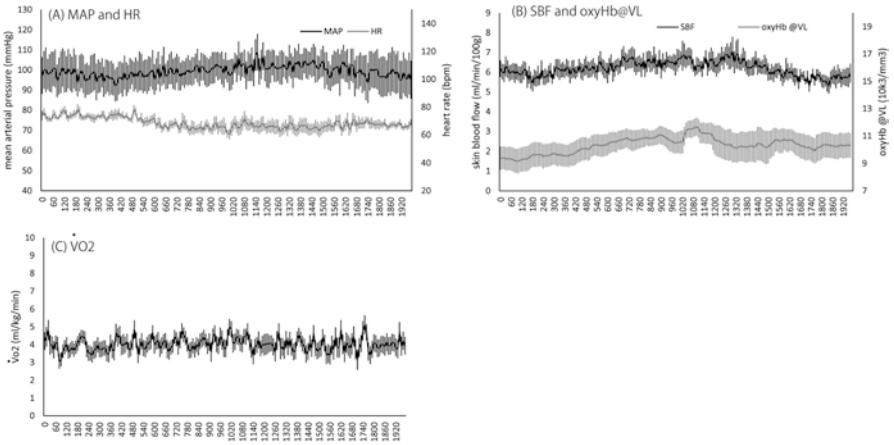

Fig. 32.4 Changes of MAP and HR (**a**), SBF and oxyHb@VL (**b**), and VO2 (**c**)

ANOVA showed deceasing HR and increasing O_2Hb@VL (Fig. 32.4). Post-hoc testing revealed that HR significantly decreased 7 min after starting the pouring condition compared to baseline, and O_2Hb@VL dramatically increased 3 min and 40 s after starting the pouring.

4 Discussion

The present study found site specificity in the WI-induced increasing O_2Hb concentration in the, motor and higher-order motor areas without changes in SBF, blood pressure, or VO_2. These results support our hypothesis; they indicate that WI increases cortical activities in sensory and motor areas are due to somatosensory input by hydrostatic pressure, and also that these WI-induced cortical activities were site specific.

Somatosensory input activates several cortical areas, which has been consistently found in previous magnetoencephalography (MEG) [10] and functional magnetic resonance imaging (fMRI) [11] studies. Inputs to the skin are transmitted to S1, and thereafter are projected to other sensory- and motor-related areas. In fact, several studies have reported that in addition to S1, PPC, SMA, and M1 are activated by somatosensory inputs, such as with vibration [12], balloon diaphragms [13], and a spring press [14]. Bodegard et al. [14] showed that pressure stimuli from a spring to the index finger increases S1 activation, as well as activation in the PPC, SMA, and M1; these activations were reflected in hand posture, such as an extended index finger, and were due to sensory information arriving in the PPC, SMA, and M1. Therefore, WI-induced cortical activities in the same areas can possibly be attributed to somatosensory input by hydrostatic pressure. So far, the possibility that these activities might simply reflect increasing oxygen transportation accompanied

by increasing venous return had not been eliminated. However, given the present results, where not only increases in O_2Hb without SBF and VO_2 changes were found, but these activities were also site specific, it is safe to assume that whole-body circulation has little-to-no effect.

Interestingly, changes in O_2Hb have never been seen only in the pre-SMA, unlike in other brain areas. This phenomenon might be explained by the distribution of neurons responsive to somatosensory input among the pre-SMA and other areas. Anatomical studies have shown that the SMA can be regarded as including two separate areas. The caudal part, which is now simply termed SMA, receives neural input by somatosensory stimulation whereas the rostral part, the pre-SMA, receives projections from the prefrontal cortex and the cingulate motor areas [15]. Also, the SMA receives projections from the superior parietal associative area, whereas the pre-SMA receives input from the inferior parietal associative area [15]. Therefore, the cortical activities induced by somatosensory input from WI would have to have site-specific activation patterns because of the differences in demand of each neural function.

The present study may not completely dispel the important concern that autonomic nervous system (ANS) activity might affect brain O_2Hb concentrations. Indeed, a decreasing HR was seen at almost the same time as the increasing cortical and muscle O_2Hb concentration. Previous research has shown that WI at a thermoneutral temperature similar to the present study was reported to alter ANS activity. Particularly, short-duration (5–30 min) WI increases heart rate variability, particularly its high-frequency component, indicating a shift toward enhanced parasympathetic nervous activity [16–18]. A previous study using fMRI showed a positive correlation between sympathetic nervous activity and the blood oxygenation level dependent signal [19]. Additionally, the parasympathetic reflex vasodilation is involved in the regulation of cerebral haemodynamics via trigeminal afferent inputs [20]. Based on these results, the site specificity of changes in cortical O_2Hb concentrations would be explained by different vascular distribution (i.e. middle and anterior cerebral artery) which might have a different innervation of the vascular bed. Therefore, further research is required to completely clarify the relationship between the ANS and O_2Hb concentrations in the brain.

The present study has several limitations that should be considered. Firstly, O_2Hb concentration is an indirect parameter to evaluate neural activity based on the theory for activity/flow coupling. Therefore, we need further study examining the cortical response to water immersion using electrophysiological methods which can evaluate neural activity directly. Additionally, we did not measure body temperature in the present study. It may affect the O_2Hb concentration in S1 and PPC which did not return to the baseline after water discharge.

In conclusion, WI-induced increases in cortical O_2Hb levels are site specific because there was little brain activation in response to somatosensory input in the pre-SMA, but robust activation in other brain areas.

Acknowledgments This study was supported by JSPS KAKENHI 15 K12712 and a Grant-in-Aid for Exploratory Research from Niigata University of Health and Welfare.

References

1. Sato D, Seko C, Hashitomi T et al (2015) Differential effects of water-based exercise on the cognitive function in independent elderly adults. Aging Clin Exp Res 27(2):149–159
2. Sato D, Onishi H, Yamashiro K et al (2012) Water immersion to the femur level affects cerebral cortical activity in humans: functional near-infrared spectroscopy study. Brain Topogr 25(2):220–227
3. Sato D, Yamashiro K, Onishi H et al (2012) The effect of water immersion on short-latency somatosensory evoked potentials in human. BMC Neurosci 13:13
4. Boas DA, Gaudette T, Strangman G et al (2001) The accuracy of near infrared spectroscopy and imaging during focal changes in cerebral hemodynamics. NeuroImage 13(1):76–90
5. Tanji J (1985) Comparison of neuronal activities in the monkey supplementary and precentral motor areas. Behav Brain Res 18(2):137–142
6. Miyai I, Tanabe HC, Sase I et al (2001) Cortical mapping of gait in humans: a near-infrared spectroscopic topography study. NeuroImage 14(5):1186–1192
7. Niederhauser BD, Rosenbaum BP, Gore JC et al (2008) A functional near-infrared spectroscopy study to detect activation of somatosensory cortex by peripheral nerve stimulation. Neurocrit Care 9(1):31–36
8. Suzuki M, Miyai I, Ono T et al (2008) Activities in the frontal cortex and gait performance are modulated by preparation. An fNIRS study. NeuroImage 39(2):600–607
9. Suzuki M, Miyai I, Ono T et al (2004) Prefrontal and premotor cortices are involved in adapting walking and running speed on the treadmill: an optical imaging study. NeuroImage 23(3):1020–1026
10. Hari R, Forss N (1999) Magnetoencephalography in the study of human somatosensory cortical processing. Philos Trans R Soc Lond Ser B Biol Sci 354(1387):1145–1154
11. Deuchert M, Ruben J, Schwiemann J et al (2002) Event-related fMRI of the somatosensory system using electrical finger stimulation. Neuroreport 13(3):365–369
12. Fox PT, Burton H, Raichle ME (1987) Mapping human somatosensory cortex with positron emission tomography. J Neurosurg 67(1):34–43
13. Numminen J, Schurmann M, Hiltunen J et al (2004) Cortical activation during a spatiotemporal tactile comparison task. NeuroImage 22(2):815–821
14. Bodegard A, Geyer S, Herath P et al (2003) Somatosensory areas engaged during discrimination of steady pressure, spring strength, and kinesthesia. Hum Brain Mapp 20(2):103–115
15. Tanji J (1994) The supplementary motor area in the cerebral cortex. Neurosci Res 19(3):251–268
16. Rowell LB, O'Leary DS (1990) Reflex control of the circulation during exercise: chemoreflexes and mechanoreflexes. J Appl Physiol (1985) 69(2):407–418
17. Saiki H, Nakaya M, Sudoh M et al (1981) Effect of physical fitness and training on physiological responses to hypogravity. Acta Astronaut 8(9–10):959–969
18. Schipke JD, Pelzer M (2001) Effect of immersion, submersion, and scuba diving on heart rate variability. Br J Sports Med 35(3):174–180
19. Fan J, Xu P, Van Dam NT et al (2012) Spontaneous brain activity relates to autonomic arousal. J Neurosci 32(33):11176–11186
20. Ishii H, Sato T, Izumi H (2014) Parasympathetic reflex vasodilation in the cerebral hemodynamics of rats. J Comp Physiol B 184(3):385–399

Chapter 33
Changes in Oxyhemoglobin Concentration in the Prefrontal Cortex and Primary Motor Cortex During Low- and Moderate-Intensity Exercise on a Cycle Ergometer

Nana Takehara, Atsuhiro Tsubaki, Yudai Yamazaki, Chiaki Kanaya, Daisuke Sato, Shinichiro Morishita, and Hideaki Onishi

Abstract The present study investigated whether changes in oxyhemoglobin (O_2Hb) concentration over time differed across brain regions according to differences in gross movement intensity. Thirteen healthy adults (21.2 ± 1.0 years, 8 women) participated in this study. After 180 s of rest, the participants performed 600 s of exercise on a cycle ergometer. Exercise intensity was set at 30%VO_2peak and 50%VO_2peak. The prefrontal cortex (PFC) and primary motor cortex (M1) were chosen as regions of interest. In addition, mean arterial pressure (MAP) and scalp blood flow (SBF) were measured simultaneously. O_2Hb concentration in PFC and M1 was significantly decreased in initial phase of the exercise, while it was significantly increased from the mid to final phase for both intensities compared with resting state values ($p < 0.01$). The O_2Hb concentrations in the PFC and M1 were significantly decreased in the initial exercise phase. However, the MAP and SBF values did not exhibit a similar pattern. The main findings of our study were the follows: (1) During cycle ergometer exercise at the 30% and 50% O_2Hb peak, the after O_2Hb concentrations were transiently decreased in the initial exercise phase, and the concentrations then steadily increased in both the PFC and M1; and (2) the duration of the transient decreases in the O_2Hb concentrations varied according to the brain region and exercise intensity.

N. Takehara (✉) • Y. Yamazaki • C. Kanaya
Graduate School, Niigata University of Health and Welfare,
1398 Shimami-cho, Kita-ku, Niigata-shi, Niigata 950-3198, Japan

Institute for Human Movement and Medical Sciences, Niigata University of Health and Welfare, 1398 Shimami-cho, Kita-ku, Niigata-shi, Niigata 950-3198, Japan
e-mail: hpm15005@nuhw.ac.jp

A. Tsubaki • D. Sato • S. Morishita • H. Onishi
Institute for Human Movement and Medical Sciences, Niigata University of Health and Welfare, 1398 Shimami-cho, Kita-ku, Niigata-shi, Niigata 950-3198, Japan

H.J. Halpern et al. (eds.), *Oxygen Transport to Tissue XXXIX*, Advances in Experimental Medicine and Biology 977, DOI 10.1007/978-3-319-55231-6_33

Keywords Cortical oxyhaemoglobin • Low- and moderate-intensity exercise • Near-infrared spectroscopy

1 Introduction

Near-infrared spectroscopy (NIRS) is used to measure neuronal activity-dependent changes in hemoglobin dynamics utilizing varying amounts of light transmitted through the cerebral cortex [1]. One advantage of this method is that it is both non-invasive and non-restrictive, thus allowing measurements to be obtained during gross movements [2–6].

Previous studies have used NIRS to measure changes in oxyhemoglobin (O_2Hb) concentration in the prefrontal cortex (PFC) during exercise of different intensities on a cycle ergometer. Such studies have reported that, regardless of exercise intensity, reductions in O_2Hb concentration are observed in the initial stages of exercise, though these levels increase incrementally until the end of exercise [2]. Additionally, several studies have reported that increases in O_2Hb levels during exercise are dependent on exercise intensity [2–4]. Furthermore, differential changes in O_2Hb levels over time have been observed in the PFC, motor cortex, and somatosensory cortex during a finger-tapping task [7]. Consequently, some researchers have suggested that changes in O_2Hb over time may differ across brain regions and according to the intensity of gross movements. Thus, the present study investigated changes in O_2Hb levels over time in the PFC and primary motor cortex (M1) in participants engaging in low- and moderate-intensity exercise using a cycle ergometer.

2 Methods

Thirteen healthy adults (average ± standard deviation; age: 21.2 ± 0.6 years; eight women, five men) participated in the present study. No participants had any history of cardiovascular disease. After a thorough explanation of the experiment, both written and verbal informed consent was obtained from all participants. This research was conducted in accordance with the Declaration of Helsinki and upon obtaining approval from the ethics committee of the Niigata University of Health and Welfare.

Participants were asked to pedal on a cycle ergometer (75XLII, Combi Wellness). Exercise intensities were established at 30% and 50% of maximum oxygen uptake (VO_2peak), as determined by an exercise stress test. Following a rest period of 180 s participants performed 600 s of continuous exercise using a cycle ergometer. The pedaling speed was set at 55 rpm.

Levels of O_2Hb in the cerebral cortex were measured using an NIRS imaging system (OMM/3000, Shimadzu Corp.). Ten light emitter probes and ten detector

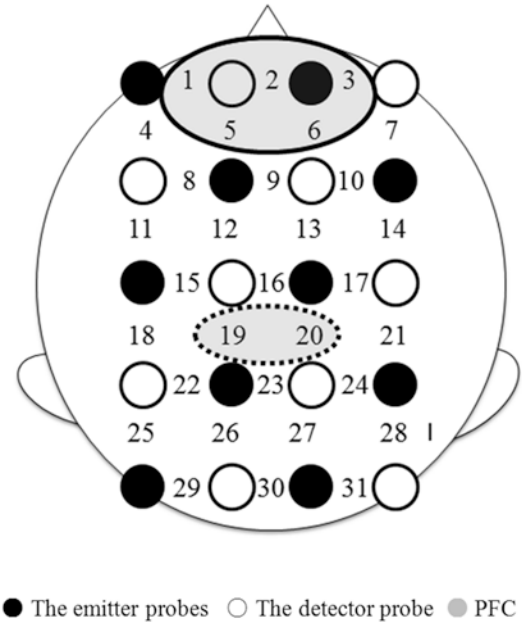

Fig. 33.1 Probe placement and regions of interest. The solid line represents the PFC. The dotted line represents the M1. The black dots represent the emitter probes, and the white dots represent the detector probe. PFC: prefrontal cortex; M1: primary motor cortex

probes provided 23-channel simultaneous recording and were arranged in a 4 × 5 array. A 30-mm interoptode distance was used to measure the O_2Hb levels. The Cz position of the International 10–20 System was used to ensure consistent optode placement among all participants. The areas of interest were the PFC (Chaps. 1, 2, 3, 5, and 6) and M1 (Chaps. 19 and 20) (Figs. 33.1, 33.2 and 33.3).

Mean arterial pressure (MAP) was measured with a cuff on the third finger of the left hand, using a beat-to-beat blood pressure monitor (Finometer, Finepress Medical Systems). Skin blood flow (SBF) was measured at the forehead using a laser tissue blood flowmeter (OMEGAFLOW FLO-C1, OMEGAWAVE, Inc.). The data were acquired at 1000 Hz via an A/D converter (Power Lab 8/30, AD instruments, Australia).

Statistical analysis was conducted using the free statistical software R 3.3.1 (R Core Team). To measure changes in O_2Hb levels in the PFC and M1, the amount of change from the average value during the 180 s of rest to the 600 s of exercise was calculated and averaged every 30 s. The Friedman test was conducted for the two factors of exercise intensity and time. When a main effect was observed, *post hoc* comparisons of exercise intensity were conducted using the Mann-Whitney U-test, while comparisons of time were conducted Steel's method. The significance level for both analyses was set at $p < 0.05$.

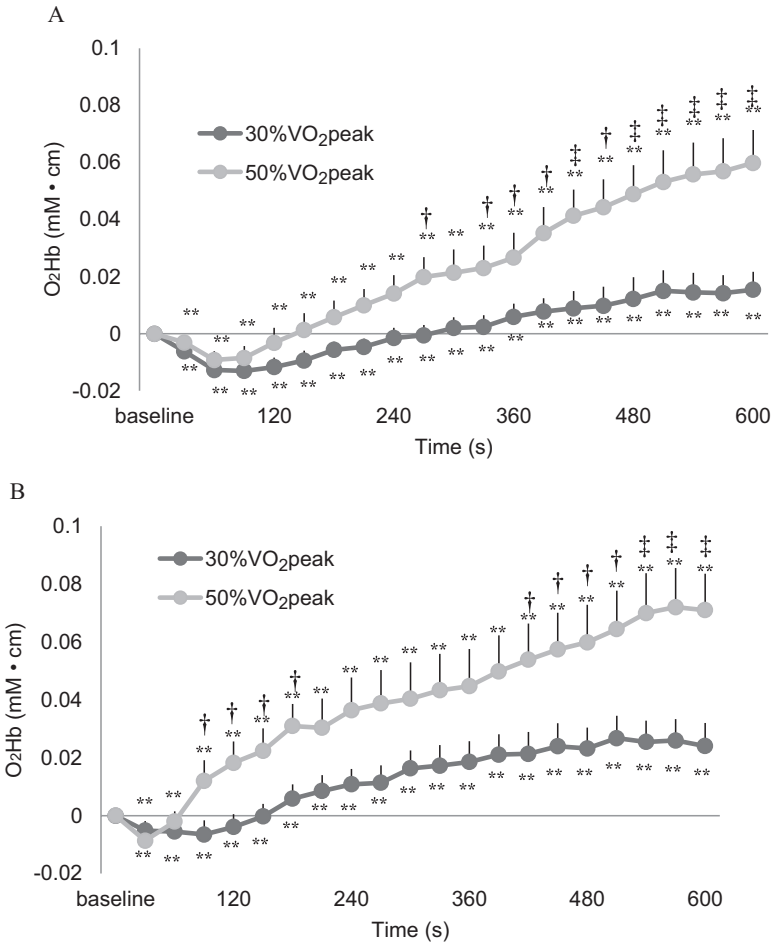

Fig. 33.2 Changes in the oxyhemoglobin response in the PFC (**a**) and M1 (**b**) over time. Values are expressed as the average ± SE. *p < 0.05, **p < 0.01; significantly different from baseline. †p < 0.05, ‡p < 0.01; significantly different from the other exercise intensity. PFC: prefrontal cortex; M1: primary motor cortex

3 Results

In the PFC, main effects of exercise intensity (p = 0.00) and time (p = 0.00) were determined by the Friedman test. *Post hoc* analyses revealed that relative to resting state values, significant reductions in O_2Hb concentration were observed in the 30%VO_2peak condition from 30 to 270 s, while significantly higher values were observed from 300 to 600 s (respectively, p < 0.01). Furthermore, significantly lower O_2Hb values were observed in the 50%VO_2peak condition from 30 to 120 s, while significantly higher values were observed from 150 to 600 s (respectively,

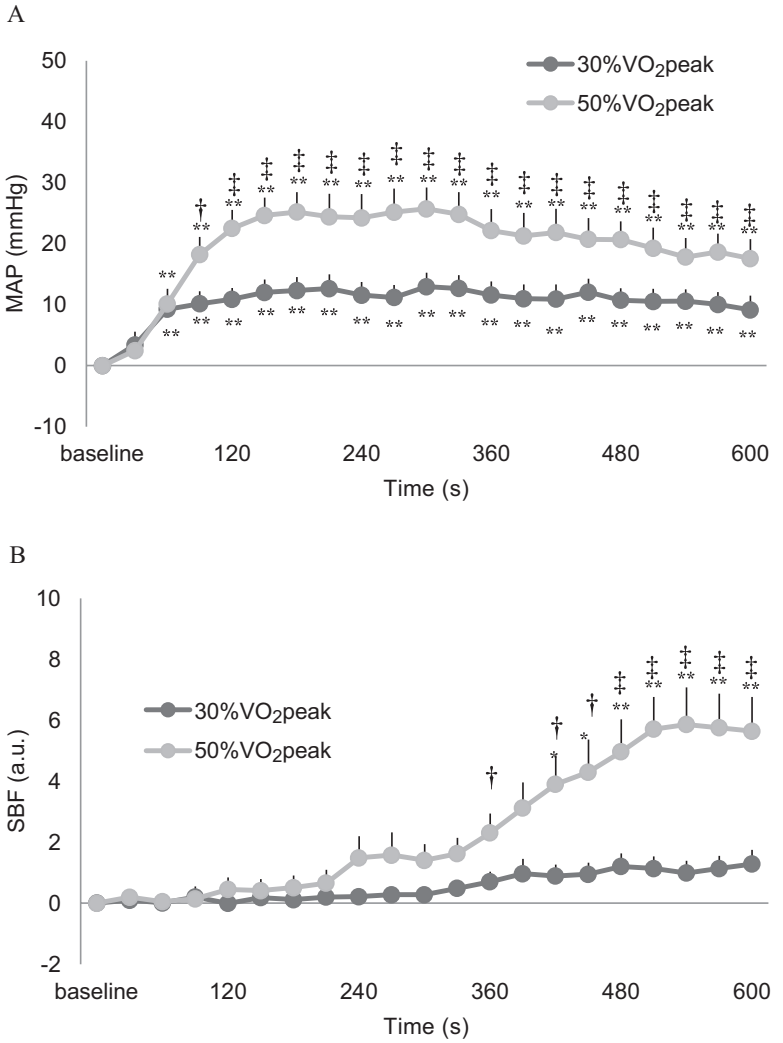

Fig. 33.3 Changes in MAP (**a**) and SBF (**b**) responses over time. Values are expressed as the average ± SE. *p < 0.05, **p < 0.01; significantly different from baseline. †p < 0.05, ‡p < 0.01; significantly different from the other exercise intensity. MAP mean arterial pressure; SBP scalp blood flow

p < 0.01). Main effects of exercise intensity (p = 0.00) and time (p = 0.00) were also observed in M1. Compared to resting state values, significant reductions in O_2Hb concentration were observed in the 30%VO_2peak condition from 30 to 150 s, while significantly higher values were observed from 180 to 600 s (respectively, p < 0.01). In addition, significantly lower O_2Hb values were observed in the 50%VO_2peak condition from 30 to 60 s, while significantly higher values were observed from 90 to 600 s (respectively, p < 0.01).

Main effects of exercise intensity ($p = 0.00$) and time ($p = 0.00$) on MAP and SBF were determined. *S*ignificantly higher MAP values were observed in both the 30%VO_2peak and 50%VO_2peak conditions from 60 to 600 s ($p < 0.05$), relative to resting state values. SBF values were significantly higher in the 30%VO_2peak condition from 480 to 510 s ($p < 0.05$), while significantly higher values for the 50%VO_2peak condition were observed at 240 s and from 330 to 600 s($p < 0.05$), relative to the resting state.

4 Discussion

The present study investigated changes in O_2Hb levels in the PFC and M1 over time during 30% and 50% VO_2peak exercise on a cycle ergometer. The main findings of our study were the follows: (1) During cycle ergometer exercise at the 30% and 50% O_2Hb peak, the after O_2Hb concentrations were transiently decreased in the initial exercise phase, and the concentrations then steadily increased in both the PFC and M1; and (2) the duration of the transient decreases in the O_2Hb concentrations varied according to the brain region and exercise intensity.

Previous studies have reported that data obtained via NIRS are easily affected by blood pressure and SBF [8–10]. However, the results of the present study suggest that the effects of MAP and SBF on transient decreases in O_2Hb concentration during the initial period of exercise are small. Consequently, we believe that the O_2Hb data obtained via NIRS in the present study accurately captured changes in O_2Hb levels in the regions of interest.

The results of the present study indicate that, when exercise was performed at 30% or 50%VO_2peak, transient reductions in O_2Hb concentration were observed during the initial periods of exercise in both the PFC and M1. According to previous studies, when neural activity in the brain is enhanced in response to increased tissue oxygen consumption and glucose metabolism, blood flow to the brain increases [11]. These increases in cerebral blood flow can be observed approximately 3 s after increases in neural activity in the brain [12], following which changes are observed in approximately 6-s intervals, until sufficient increases have occurred [13]. During this time, a temporary reduction in brain levels of O_2Hb can be observed. Additionally, according to research by Endo et al., O_2Hb concentration in the PFC during gross movement decreases during the first 5 min after the start of activity [2]. Therefore, the initial period of gross movement may be a period during which the oxygen supply is insufficient for the oxygen demands of the brain.

Following the transient reductions in O_2Hb concentration in the initial stages of exercise, we observed increases in O_2Hb concentration in the M1 earlier than in the PFC. A previous study reported that the manner of O_2Hb change over time during a task is reflective of the differing roles of each brain region [7]. Consequently, in the initial stages of exercise, it is necessary to give preferential oxygen supply to the M1 over the PFC, and this might explain why the O_2Hb levels began to increase earlier in the M1 than in the PFC. We further confirmed that O_2Hb levels began to increase

earlier in the 50%VO_2peak condition than in the 30%VO_2peak condition. Indeed, previous reports have noted that, as exercise intensity increases from 30%VO_2peak to 50%VO_2peak, O_2Hb concentration [2–4] and cerebral blood flow increase [14].

In conclusion, the results of the present study suggest that, due to gross movement, O_2Hb levels in the cerebral cortex transiently decrease in the initial stages of exercise; thereafter, the time at which these levels begin to increase differs based on the brain region and exercise intensity.

References

1. Jobsis FF (1977) Noninvasive, infrared monitoring of cerebral and myocardial oxygen sufficiency and circulatory parameters. Science 23:1264–1267
2. Endo K, Matsukawa K, Liang N et al (2013) Dynamic exercise improves cognitive function in association with increased prefrontal oxygenation. J Physiol Sci 63(4):287–298
3. Giles GE, Brunyé TT, Eddy MD et al (2014) Acute exercise increases oxygenated and deoxygenated hemoglobin in the prefrontal cortex. Neuroreport 25:1320–1325
4. Timinkul A, Kato M, Omori T et al (2008) Enhancing effect of cerebral blood volume by mild exercise in healthy young men: A near-infrared spectroscopy study. Neurosci Res 61:242–248
5. Bediz CS, Oniz A, Guducu C et al (2016) Acute supramaximal exercise increases the brain oxygenation in relation to cognitive workload. Front Hum Neurosci 10:174
6. Suzuki M, Miyai I, Ono T et al (2004) Prefrontal and premotor cortices are involved in adapting walking and running speed on the treadmill: an optical imaging study. NeuroImage 23:1020–1026
7. Sato T, Ito M, Suto T et al (2007) Time courses of brain activation and their implications for function: a multichannel near-infrared spectroscopy study during finger tapping. Neurosci Res 58:297–304
8. Minati L, Kress IU, Visani E et al (2011) Intra- and extra-cranial effects of transient blood pressure changes on brain near-infrared spectroscopy (NIRS) measurements. J Neurosci Methods 197:283–288
9. Miyazawa T, Horiuchi M, Komine H et al (2013) Skin blood flow influences cerebral oxygenation measured by near-infrared spectroscopy during dynamic exercise. Eur J Appl Physiol 113:2841–2848
10. Hirasawa A, Yanagisawa S, Tanaka N et al (2015) Influence of skin blood flow and source-detector distance on near-infrared spectroscopy-determined cerebral oxygenation in humans. Clin Physiol Funct Imaging 35:237–244
11. Fox PT, Raichle ME, Mintun MA et al (1988) Nonoxidative glucose consumption during focal physiologic neural activity. Science 241:462–464
12. Bandettini P, Wong EC, Hinks RS et al (1992) Time course EPI of human brain function during task activation. Magn Reson Med 25:390–397
13. Taoka T, Iwasaki S, Uchida H et al (1998) Age correlation of the time lag in signal change on EPI-fMRI. J Comput Assist Tomogr 22:514–517
14. Sato K, Ogoh S, Hirasawa A et al (2011) The distribution of blood flow in the carotid and vertebral arteries during dynamic exercise in humans. J Physiol 589:2847–2856

Chapter 34
Tissue Blood Volume Parameters Measured by Continuous-Wave and Spatially Resolved NIRS Show Different Changes During Prolonged Cycling Exercise

Takuya Osawa, Keisuke Shiose, and Hideyuki Takahashi

Abstract Near-infrared spectroscopy (NIRS) shows two types of tissue blood volume (BV) parameters: the total hemoglobin concentration (cHb; assessed by continuous-wave NIRS) and the normalized tissue hemoglobin index (nTHI; evaluated by spatially resolved NIRS). This study was performed to investigate the differences between cHb and nTHI, estimated by calibration using acute reduction of BV at the onset of exercise. Seven active male volunteers (age: 22 ± 4 years) performed a prolonged (60-min) cycling exercise test at 65% or 70% of the peak oxygen uptake. During the tests, cHb and nTHI from the vastus lateralis muscle were monitored. The two parameters were expressed relative to the resting value of 100% and the minimum value of 0% at the onset of exercise. The value of cHb started to increase after arriving at the minimum value and continued until the end of exercise. Similar to cHb, nTHI increased acutely from the lowest level, but the parameter remained almost unchanged from ~5 min throughout the test. Therefore, the two parameters interacted significantly. Moreover, in comparison with the same exercise duration, cHb was significantly higher than nTHI from the 28th min to the end of the test. These results suggest that cHb and nTHI in working muscle are not synchronized during prolonged exercise, especially after ~30 min. The differences between the two BV parameters are likely partly attributable to other factors, such as the increase in skin blood flow.

Keywords Tissue blood volume • Muscle • Prolonged cycling • Spatially resolved near infrared spectroscopy • Cutaneous blood flow

T. Osawa (✉)
COI Project Center, Juntendo University, Chiba, Japan
e-mail: takuya.osawa.jp@gmail.com

K. Shiose • H. Takahashi
Department of Sports Science, Japan Institute of Sports Sciences, Tokyo, Japan

H.J. Halpern et al. (eds.), *Oxygen Transport to Tissue XXXIX*, Advances in Experimental Medicine and Biology 977, DOI 10.1007/978-3-319-55231-6_34

1 Introduction

Near infrared spectroscopy (NIRS) can non-invasively and continuously monitor the changes of oxygenated and deoxygenated hemoglobin and myoglobin (oxy-Hb/Mb and deoxy-Hb/MB, respectively). These parameters show the changes obtained from the measurement area. It is essential to evaluate the changes in tissue blood volume (BV) to understand the other NIRS parameters [1].

One of the parameters of BV change is the total hemoglobin concentration (cHb) assessed by continuous-wave NIRS (NIR-CWS), and another is the normalized total hemoglobin index (nTHI) assessed by spatially resolved NIRS (NIR-SRS). In previous studies, although oxygenation parameters monitored by both NIR-CWS and NIR-SRS were investigated concurrently, there have been few studies of cHb and nTHI [2]. We reported previously that the two BV parameters from the working muscles changed differently during an incremental running exercise [3]. However, this previous study was insufficient to determine the cause of the differences between cHb and nTHI, because these values were calibrated from the maximal to minimum values throughout the test, the running was a relatively complex exercise, and the intensity was changed throughout the test. Therefore, this study was performed to compare the two BV parameters, cHb and nTHI, from working muscle during a constant-load prolonged cycling exercise.

2 Methods

2.1 Participants

Seven active young male volunteers participated in this study (age 22 ± 4 years; height 1.68 ± 0.07 m; body mass 58.7 ± 7.8 kg; peak oxygen uptake (VO_{2peak}) 54.8 ± 5.9 mL/kg/min, mean ± S.D.). Before participating in the experiment, subjects received an explanation of the study procedures and potential risks, and then signed an informed consent document. This study was approved by the local ethics committee and all work was performed in accordance with the Declaration of Helsinki.

2.2 Experimental Design

This study was organized on two separate days. On the first occasion, after the subjects were familiarized with the experiments, they performed an incremental exercise test using a cycle ergometer (Excalibur Sport; Lode, Groningen, the Netherlands) to determine both the work rate–oxygen uptake (VO_2) relationship and the peak VO_2 (VO_{2peak}). On the second day, following sitting rest for 1 min, the subjects performed constant-load cycle exercise at 65% or 70% of VO_{2peak} for 60 min. The subjects pedaled in the upright position at a pedaling rate of 60 rpm.

2.3 Measurements

Minute ventilation (V_E) and VO_2 were obtained using a computerized metabolic cart (AE300; Minato, Osaka, Japan) and heart rate (HR) was measured using a heart rate monitor (Polar RS800CX; Polar Electro, Kempele, Finland) at rest and at the 5th, 30th and 60th min.

The two BV parameters, cHb and nTHI, were monitored simultaneously throughout the test from the belly of the vastus lateralis muscle (VL) using the NIRS system (NIRO-200NX; Hamamatsu Photonics, Shizuoka, Japan). The principle, validity, and limitations of the measurements have been reported in previous review articles [4, 5]. Two fiber optic bundles transmitted the NIR light to the tissues of interest. The NIR light source consisted of three laser diodes that emitted light at different wavelengths (775, 810, and 850 nm), the intensity of which was measured continuously at 2 Hz. The source-detector distances were 2.5 and 3 cm. The probes were housed in a plastic holder and fixed with tape and bandages. The differential path length factor was omitted from the measurements in this study because this factor is unknown for VL. The data of cHb and nTHI were normalized to percentages with the resting value at the lowest pedaling position before exercise and the minimum value at the onset of exercise defined as 100% and 0%, respectively (Fig. 34.1).

2.4 Statistical Analyses

The data are presented as means ± S.E. Statistical analyses were performed using the statistical package SPSS for Windows (version 22.0; SPSS, Chicago, IL). For comparison between cHb and nTHI, two-way repeated ANOVA was used to determine the significance of differences, and the paired *t* test was performed when significant effects were found. In all analyses, $P < 0.05$ was taken to indicate statistical significance.

3 Results

VO_2, V_E, and HR were significantly higher during exercise than at rest. Hence, VO_2 was similar at the 5th, 30th and 60th min, and the same was true for V_E. On the other hand, HR increased continuously throughout the test.

Both cHb and nTHI dropped at the onset of exercise and increased rapidly for a few minutes. After ~5th min, nTHI was almost unchanged, but cHb increased gradually. There was a significant interaction between the two BV parameters. In addition, cHb was significantly higher than nTHI after the 28th min (Fig. 34.2).

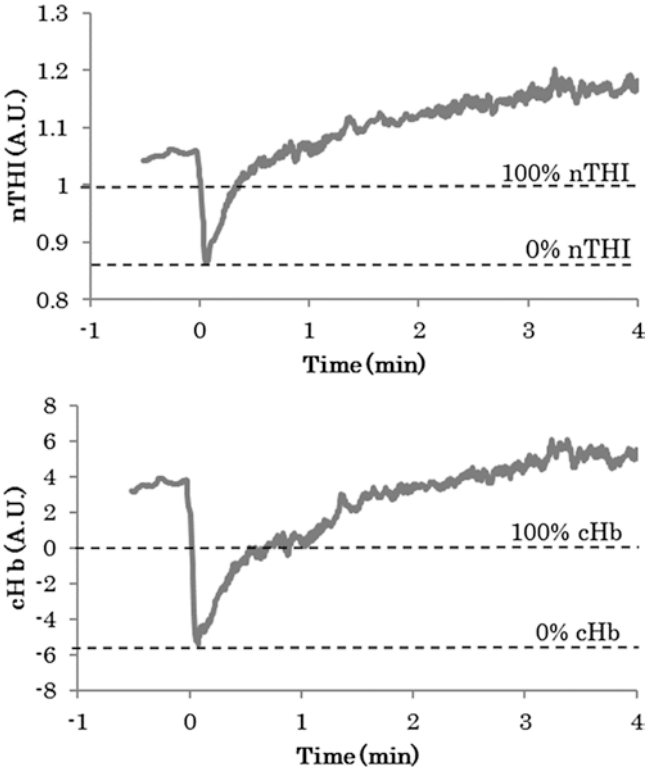

Fig. 34.1 A representative example for the calibration of cHb (upper) and nTHI (bottom). The resting value at the lowest pedal position before exercise were taken as 100% of cHb (the value showed 0) and nTHI (the value showed 1). The minimum value after the onset of exercise was defined as 0% of cHb and nTHI

4 Discussion

We examined the two BV parameters assessed using two NIRS methodologies, NIR-CWS and NIR-SRS, from one system in working muscles (VL) during a constant-load, prolonged (60-min) cycling exercise. To compare the two BV parameters, the baselines of tissue blood volume were established using both the resting value before exercise and the minimum value at the onset of exercise.

The two BV parameters, cHb and nTHI, interacted significantly, and were different after the 28th min. Our previous study [3] indicated that the two parameters in working muscles changed differently during incremental running exercise, but the factors involved could not be determined as the exercise protocol was complex (i.e., running, and changing exercise intensity) and these BV parameters were calibrated using the maximal and minimum values throughout the test. In the present study, performed during constant-load prolonged cycling exercise, cHb from VL increased continuously along with the increase of exercise duration, suggesting that cHb was partly affected by cutaneous blood flow (CBF), although CBF could not

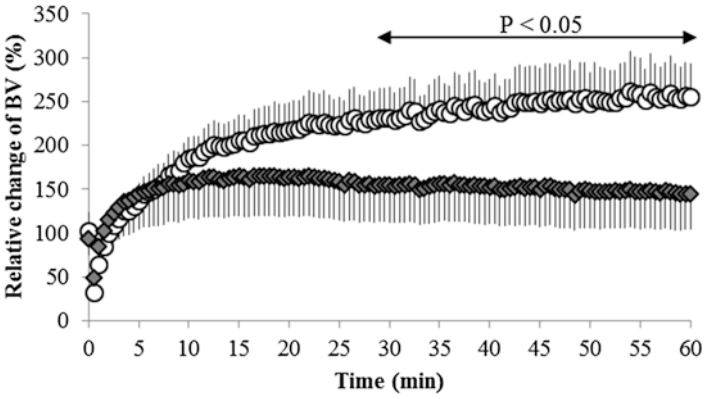

Fig. 34.2 Relative changes (%) in cHb (open circles) and nTHI (solid squares) during constant-load cycling exercise for 60 min. Values are means ± S.E. There was a significant interaction between cHb and nTHI. Hence, cHb were higher than nTHI from the 28th min until the end of exercise

be evaluated in this study. CBF is altered by both hyperthermia and non-hyperthermia [6]. However, the increased CBF with high body temperature in the latter half of the test may influence the change of cHb, but not nTHI. In a previous study using a short distance detector between the emitter and receiver, the oxy-Hb/Mb monitored by NIR-CWS was reported to increase in parallel with CBF during heat stress [7]. Similar to oxy-Hb/Mb, cHb would be partly influenced by CBF. On the other hand, the oxygenation parameter of NIR-SRS (tissue oxygen index: TOI) was little affected by the change of cHb and heat stress [8]. Therefore, nTHI assessed by NIR-SRS would be little affected by CBF, in contrast to cHb.

In this study, the resting value before exercise was taken as 100% and the minimum value at the onset of exercise was defined as 0%. The drop seen after the onset of exercise was thought to be derived from the mechanical stress of muscle contraction and sympathetic nerve activity-induced vasoconstriction [9]. According to our tentative hypothesis that cHb was affected by CBF, the possibility that cHb was affected by CBF 'at the onset of exercise' as well as the latter half of the test could not be excluded, which was related to the correctness of the calibration method in this study. At the onset of exercise, the body temperature would be unchanged, whereas vasomotor activity is altered non-thermally. However, the vessels within non-glabrous skin, such as the thigh (VL), measured in this study show little constriction [10, 11]. Therefore, CBF between the resting value and the minimum value at the onset of exercise would be similar and would have little effect on the calibration method.

In summary, the BV parameter assessed by NIR-SRS (nTHI) was unchanged from the 5th min until the end of exercise, but the BV parameters assessed by NIR-CWS (cHb) increased gradually during constant-load prolonged cycling exercise, and the two parameters showed a significant difference. The difference would be derived from the increase of CBF although this study could not clearly determine the underlying mechanisms. NIRS could provide further insight if the difference between the two parameters could be elucidated in future studies.

References

1. Osawa T, Kime R, Hamaoka T et al (2011) Attenuation of muscle deoxygenation precedes EMG threshold in normoxia and hypoxia. Med Sci Sports Exerc 43:1406–1413
2. Robbins D, Elwell C, Jimenez A et al (2012) Localised muscle tissue oxygenation during dynamic exercise with whole body vibration. J Sports Sci Med 11:346–351
3. Osawa T, Arimitsu T, Takahashi H (2016) Do two tissue blood volume parameters measured by different near-infrared spectroscopy methods show the same dynamics during incremental running? Adv Exp Med Biol 876:27–33
4. Hamaoka T, McCully KK, Quaresima V et al (2007) Near-infrared spectroscopy/imaging for monitoring muscle oxygenation and oxidative metabolism in healthy and diseased humans. J Biomed Opt 12:062105
5. Grassi B, Quaresima V (2016) Near-infrared spectroscopy and skeletal muscle oxidative function in vivo in health and disease: a review from an exercise physiology perspective. J Biomed Opt 21:091313
6. Charkoudian N (2010) Mechanisms and modifiers of reflex induced cutaneous vasodilation and vasoconstriction in humans. J Appl Physiol 109:1221–1228
7. Davis SL, Fadel PJ, Cui J et al (2006) Skin blood flow influences near-infrared spectroscopy-derived measurements of tissue oxygenation during heat stress. J Appl Physiol 100:221–224
8. Tew GA, Ruddock AD, Saxton JM (2010) Skin blood flow differentially affects near-infrared spectroscopy-derived measures of muscle oxygen saturation and blood volume at rest and during dynamic leg exercise. Eur J Appl Physiol 110:1083–1089
9. Mense S, Stahnke M (1983) Responses in muscle afferent fibres of slow conduction velocity to contractions and ischaemia in the cat. J Physiol 342:383–397
10. Yamazaki F (2002) Vasomotor responses in glabrous and nonglabrous skin during sinusoidal exercise. Med Sci Sports Exerc 34:767–772
11. Yanagimoto S, Kuwahara T, Zhang Y et al (2003) Intensity-dependent thermoregulatory responses at the onset of dynamic exercise in mildly heated humans. Am J Physiol Regul Integr Comp Physiol 285:R200–R207

Chapter 35
Delayed Onset of Reoxygenation in Inactive Muscles After High-Intensity Exercise

Takuya Osawa, Keisuke Shiose, and Hideyuki Takahashi

Abstract Oxygenation, measured by near-infrared spectroscopy (NIRS), in inactive muscles decreases during high-intensity exercise because of the decrease of oxygen supply. However, there have been few reports regarding recovery of inactive muscle oxygenation after exercise. This study was performed to examine reoxygenation in the biceps brachii muscle (BB) after supramaximal cycling exercise. Six active young male volunteers (age: 22 ± 3 years, peak oxygen uptake (VO_{2peak}): 53.8 ± 5.4 mL/kg/min, mean ± S.D.) performed warm-up exercise, followed by cycling exercise at 140% of VO_{2peak} for 30 s and then at 0 watt for 4 min (recovery exercise). Tissue oxygen saturation (StO_2) in the vastus lateralis muscle (VL) and BB was monitored by spatially resolved NIRS throughout the test. The decrease rate of StO_2 during exercise was 24.7 ± 7.5 p.p. in VL and 15.1 ± 8.2 p.p. in BB (N.S.). StO_2 in VL increased immediately after the end of exercise, but StO_2 in BB decreased continuously for 12.7 ± 7.8 s after exercise. Moreover, the time of half-recovery from the minimum to peak values after exercise was significantly ($P < 0.05$) longer at StO_2 in BB (39.5 ± 12.2 s) than VL (25.2 ± 6.0 s). These results suggest that the recovery of microvascular oxygen supply and blood flow in inactive muscles does not start immediately after exercise.

Keywords Inactive muscle • Recovery • Near infrared spectroscopy • Supramaximal exercise • Sympathetic nerve activity

T. Osawa (✉)
COI Project Center, Juntendo University, Chiba, Japan
e-mail: takuya.osawa.jp@gmail.com

K. Shiose • H. Takahashi
Department of Sports Science, Japan Institute of Sports Sciences, Tokyo, Japan

H.J. Halpern et al. (eds.), *Oxygen Transport to Tissue XXXIX*, Advances in Experimental Medicine and Biology 977, DOI 10.1007/978-3-319-55231-6_35

1 Introduction

Near infrared spectroscopy (NIRS) can non-invasively and continuously assess the tissue oxygen status from various parts of the body [1], and the values reflect the balance between tissue oxygen supply and consumption. Thus, deoxygenation is brought about not only by the increase of oxygen consumption, but also the decrease of oxygen supply. For example, tissue deoxygenation is aggravated by arterial occlusion which stops blood flow to the tissue [2, 3], and under conditions of hypoxia, which decreases arterial oxygen content, despite similar muscle oxygen consumption under normoxia [4, 5].

Sympathetic nerve activity (SNA), which has a strong vasoconstrictor effect, is increased during exercise and related to exercise intensity. In active muscles, oxygen supply to the tissue does not decrease but rather increases, as the local blood flow is compensated by the increase of shear stress-induced vasodilation. However, in inactive (non-contracting, non-exercising) muscles, the increase of SNA would bring about a reduction of blood flow and oxygen supply to tissue despite the increase of bulk blood flow in the inactive limbs [6, 7]. In previous studies, inactive muscle deoxygenation assessed by NIRS was suggested to be induced by SNA during high-intensity exercise compared to moderate-intensity exercise [6, 8].

As mentioned above, the increase of SNA-induced tissue deoxygenation in inactive muscle occurs during high-intensity exercise, but the decrease of SNA and the recovery of tissue oxygenation after exercise have not been clarified. This study was performed to investigate inactive muscle oxygenation after high-intensity exercise. We hypothesized that vasoconstriction in the inactive muscle would last and the tissue would be further deoxygenated after high-intensity exercise, as the increase of SNA does not occur immediately after the onset of exercise [9] and the effects of hormones on the tissue are generally slower than those of the nervous systems.

2 Methods

2.1 Subjects

Six active young male volunteers participated in this study (age 22 ± 3 years; height 1.69 ± 0.06 m; body mass 59.3 ± 5.0 kg; peak oxygen uptake (VO_{2peak}): 53.8 ± 5.4 mL/kg/min, mean ± S.D.). Before participating in the experiment, subjects received an explanation of the study procedures and potential risks, and they then signed an informed consent document. This study was approved by the local ethics committee and all work was performed in accordance with the Declaration of Helsinki.

2.2 Experimental Design

The study was composed of two separated days. On the first day, the subjects performed an incremental exercise test using a cycle ergometer (Excalibur Sport; Lode, Groningen, the Netherlands) in the upright position to determine both the work rate–oxygen uptake (VO_2) relationship and the peak VO_2 (VO_{2peak}). On the second day, following sitting rest for 1 min, 35% of VO_{2peak} exercise for 5 min, and no-load (0 watt) cycle exercise for 3 min, the subjects performed supramaximal cycle (SMC) exercise at 140% of VO_{2peak} for 30 s, and then no-load cycle exercise for 4 min. The pedaling rate was maintained at 70 rpm and the subject was instructed to maintain their upper body and arm positions.

2.3 Measurements

The tissue oxygen saturation (StO_2) from the bellies of the biceps brachii (BB) and vastus lateralis muscles (VL) were monitored throughout the test using a spatially resolved NIRS system (NIRO-200NX; Hamamatsu Photonics, Shizuoka, Japan). Two fiber optic bundles transmitted the NIR light produced by the laser diodes to the tissues of interest. Three different-wavelength laser diodes (775, 810, and 850 nm) were provided as light sources, and the intensity of transmitted light was measured continuously at 2 Hz. The source–detector distances were 2.5 and 3 cm. The probes were housed in a plastic holder and fixed with tape and bandages.

To analyze the recovery of tissue oxygenation in active (VL) and inactive (BB) muscles, the time of half-recovery of tissue oxygenation from the minimum value at or after SMC exercise to the peak value after SMC exercise was calculated [10].

2.4 Statistical Analyses

The data are presented as means ± S.D. The paired *t* test was used for comparison of StO_2 between VL and BB. In all analyses, $P < 0.05$ was taken to indicate statistical significance.

3 Results

The StO_2 dynamics of both VL and BB in a representative subject are shown in Fig. 35.1. StO_2 of both VL and BB decreased significantly during SMC exercise. The StO_2 in VL rose immediately after SMC exercise, and the peak value during recovery exercise was higher than that before SMC exercise ($P < 0.05$). On the

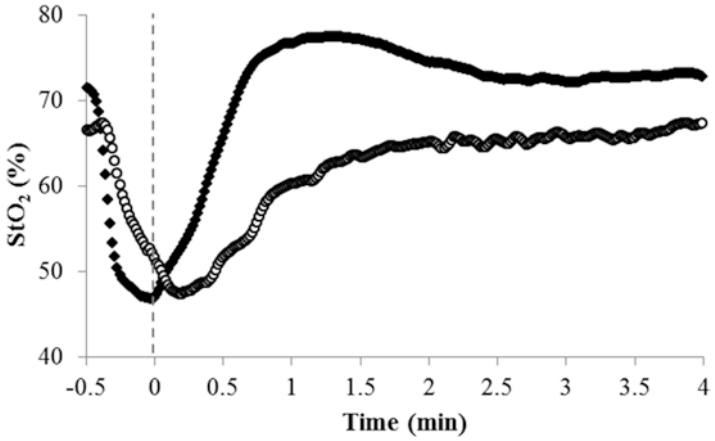

Fig. 35.1 Changes of StO_2 in VL (closed squares) and BB (open circles) in a representative subject from the pre-SMC exercise (−0.5 min) until the end of recovery exercise (4 min). The dotted line indicates the end of the SMC exercise

Table 35.1 Mean StO_2 values and timing of VL and BB in each phase

Variables		VL	BB
Immediately before SMC exercise	Value (%)	71.7 ± 3.1	66.7 ± 2.6*
	Time (s)	–30.0 ± 0.0	–30.0 ± 0.0
End of SMC exercise	Value (%)	47.0 ± 6.6	51.7 ± 10.3
	Time (s)	0.0 ± 0.0	0.0 ± 0.0
Difference between pre- and post-SMC exercise	Value (p.p.)	24.7 ± 7.5	15.1 ± 8.2
Minimum StO_2 during recovery	Value (%)	47.0 ± 6.6	46.1 ± 10.2
	Time (s)	0.0 ± 0.0	12.7 ± 7.8*
Peak StO_2 during recovery	Value (%)	78.0 ± 4.1	68.8 ± 2.1*
	Time (s)	76.3 ± 13.9	200.2 ± 39.8 *
Difference between the minimum and peak StO_2	Value (p.p.)	31.0 ± 7.3	22.8 ± 9.9
Half-recovery of StO_2	Value (%)	62.5 ± 4.1	57.4 ± 5.5
	Net time (s)	25.2 ± 6.0	26.8 ± 7.1
	Gross time (s)	25.2 ± 6.0	39.5 ± 12.2*

Values are means ± S.D. Significant difference between VL and BB in the same variables
*$P < 0.05$

other hand, the StO_2 in BB dropped continuously after SMC exercise in all subjects. Moreover, the peak value during recovery exercise was not significantly changed compared to the resting value. Although the net time for half-recovery of tissue oxygenation from the lowest value was similar between VL and BB, the gross time from the end of SMC exercise (i.e. the sum of the time of minimum StO_2 during recovery plus the net time) was longer in BB than VL ($P < 0.05$) (Table 35.1).

4 Discussion

We examined the recovery of tissue oxygenation from the active (VL) and inactive (BB) muscle after SMC exercise. The main findings of this study were that the recovery of tissue oxygenation in BB did not begin immediately after exercise and deoxygenation continued for several seconds. These results would be due to the slow response of the disappearance of vasoconstriction action.

Deoxygenation in BB occurred during SMC exercise although the muscle did not contract and the tissue oxygen consumption increased little, similar to the results of previous studies [6, 8]. This is due to the decrease of oxygen supply to the tissue, which was derived from the increase of SNA and sympathetic nervous hormones, such as noradrenaline, constricting the vascular smooth muscles. Then, the decreases of blood flow and oxygen supply to tissue in the inactive muscles would induce muscle deoxygenation. On the other hand, the deoxygenation in VL during SMC exercise would be provoked by the increase of muscle oxygen consumption. SNA affects the vascular smooth muscles in not only the inactive muscles but also the active muscles, but the strong action of vasodilation induced by endothelium-derived relaxing factors, such as nitric oxide, occurs locally [11]. These responses, i.e. blood flow redistribution, are reasonable for performing high-intensity systemic exercise, which has high oxygen demand in the whole body.

The deoxygenation in BB continued for several seconds after the end of SMC exercise. This would be because vasoconstriction action also lasted and because neither tissue blood flow nor oxygen supply began to recover. It was reported that the response of group III and IV afferents was delayed for several seconds after the onset of exercise [9]. Therefore, it is likely that the onset of SNA attenuation from the end of exercise would be delayed, although it was unclear whether the increase and decrease response speeds of SNA were similar. Moreover, the residual effects of vasodilation induced by the action of alpha-1 adrenergic receptors would delay the recovery of inactive muscle oxygenation after SMC exercise.

In this study, the electromyographic (EMG) activity in BB was not assessed, but it was thought to be very small because elbow flexion and contraction were not performed in the upright position. Although Nagasawa reported that inactive muscle oxygen consumption increased during high-intensity cycling [12], the degree of increase was very small compared to working muscles, and the inactive muscle deoxygenation would be little affected. Sample size was very small (six subjects), but all subjects showed similar oxygenation and the results were statistically significant. The delayed recovery of tissue oxygenation in inactive muscle after exercise has not been reported previously, and these results could provide insight to understand the microcirculation and metabolism. Previous studies revealed the relationship between recovery of working muscle oxygenation after exercise and aerobic capacity [10]. In future studies, it will be necessary to evaluate the relationship between the recovery of inactive muscle oxygenation after exercise and other physiological parameters in a larger sample.

References

1. Hamaoka T, McCully KK, Quaresima V et al (2007) Near-infrared spectroscopy/imaging for monitoring muscle oxygenation and oxidative metabolism in healthy and diseased humans. J Biomed Opt 12:062105
2. Broxterman RM, Ade CJ, Craig JC et al (2015) Influence of blood flow occlusion on muscle oxygenation characteristics and the parameters of the power-duration relationship. J Appl Physiol 118:880–889
3. Hansen J, Thomas GD, Harris SA et al (1996) Differential sympathetic neural control of oxygenation in resting and exercising human skeletal muscle. J Clin Invest 98:584–596
4. Osawa T, Kime R, Katsumura T et al (2010) Effects of acute hypoxia on the inflection point of muscle oxygenation. Adv Exp Med Biol 662:385–390
5. Osawa T, Kime R, Hamaoka T et al (2011) Attenuation of muscle deoxygenation precedes EMG threshold in normoxia and hypoxia. Med Sci Sports Exerc 43:1406–1413
6. Shiroishi K, Kime R, Osada T et al (2010) Decreased muscle oxygenation and increased arterial blood flow in the non-exercising limb during leg exercise. Adv Exp Med Biol 662:379–384
7. Tanaka H, Shimizu S, Ohmori F et al (2006) Increases in blood flow and shear stress to nonworking limbs during incremental exercise. Med Sci Sports Exerc 38:81–85
8. Ogata H, Arimitsu T, Matsuura R et al (2007) Relationship between oxygenation in inactive biceps brachii muscle and hyperventilation during leg cycling. Physiol Res 56:57–65
9. Mense S, Stahnke M (1983) Responses in muscle afferent fibres of slow conduction velocity to contractions and ischaemia in the cat. J Physiol 342:383–397
10. Ichimura S, Murase N, Osada T et al (2006) Age and activity status affect muscle reoxygenation time after maximal cycling exercise. Med Sci Sports Exerc 38:1277–1281
11. Maeda S, Miyauchi T, Sakane M et al (1997) Does endothelin-1 participate in the exercise-induced changes of blood flow distribution of muscles in humans? J Appl Physiol 82:1107–1111
12. Nagasawa T (2008) Oxygen consumption in nonexercising muscle after exercise. Int J Sports Med 29:624–629

Chapter 36
Cortical Oxyhemoglobin Elevation Persists After Moderate-Intensity Cycling Exercise: A Near-Infrared Spectroscopy Study

Atsuhiro Tsubaki, Nana Takehara, Daisuke Sato, Shinichiro Morishita, Yuta Tokunaga, Kazuhiro Sugawara, Sho Kojima, Hiroyuki Tamaki, Yudai Yamazaki, and Hideaki Onishi

Abstract Near-infrared spectroscopy (NIRS) can measure cortical activity during gross motor tasks based on the cerebral hemodynamic response. Although some reports suggest that cycling exercise improves cortical oxygenation, its after-effects are unknown. We examined the after-effects of low- and moderate-intensity cycling exercise on cortical oxygenation. Ten healthy volunteers (mean age 21.3 ± 0.7 years; 4 women) underwent cycle ergometer exercise at 30% or 50% of VO_2peak for 20 min, followed by an 8-min post-exercise rest (PER). O_2Hb levels of the supplementary motor area (SMA) and sensorimotor cortex (SMC) were recorded using a near-infrared spectroscopy system. Skin blood flow (SBF) and mean arterial pressure (MAP) were continuously measured. The peak values of O_2Hb between exercise and PER were compared. The O_2Hb, SBF, and MAP increased in the exercise phase. SBF degraded over time, and MAP decreased immediately after exercise. The O_2Hb decreased immediately and increased again in the PER. There were no significant differences between exercise and PER in the SMC in the 30% VO_2peak experiment or in the SMA and SMC in the 50% VO_2peak experiment. The O_2Hb in the motor-related area was elevated during both exercise and PER especially in the 50% VO_2peak experiment.

Keywords Cortical oxyhemoglobin • Cycling exercise • Moderate-intensity • Motor-related area • After-effects

A. Tsubaki (✉) • N. Takehara • D. Sato • S. Morishita • K. Sugawara • S. Kojima • H. Tamaki
Y. Yamazaki • H. Onishi
Institute for Human Movement and Medical Sciences, Niigata University of Health and Welfare, 1398 Shimami-cho, Kita-ku, Niigata-city, Niigata 950-3198, Japan
e-mail: tsubaki@nuhw.ac.jp

Y. Tokunaga
Niigata Rehabilitation Hospital, 761, Kizaki, Kita-ku, Niigata-shi, Niigata 950-3304, Japan

H.J. Halpern et al. (eds.), *Oxygen Transport to Tissue XXXIX*, Advances in Experimental Medicine and Biology 977, DOI 10.1007/978-3-319-55231-6_36

1 Introduction

Near-infrared spectroscopy (NIRS) measures the concentration of oxyhemoglobin (O_2Hb) and deoxyhemoglobin (HHb) in tissues, using the modified Beer-Lambert law [1], and is suitable for investigating cortical oxygenation during human gait [2] and cycling exercise [3, 4] based on its non-invasiveness. It is well known that aerobic training leads to an increase in grey matter volume in motor-related areas [5]. Additionally, the effect of a single bout of aerobic exercise on cortical oxygenation has been measured during exercise [4, 6]. However, the after-effects of a single bout of aerobic exercise and the effect of exercise intensity are currently unknown.

Our study determined the after-effects of constant-load cycle ergometer exercise performed at low- and moderate-intensity in terms of O_2Hb changes in motor-related cortical areas.

2 Methods

2.1 Participants

Ten healthy volunteers (mean age 21.3 years, SD 0.7 years; 4 women) participated in this study. The subjects did not exhibit symptoms of neurological, medical, or cardiovascular disease and were not taking any medications. Each subject provided written consent after receiving information regarding the potential risks, study objectives, measurement techniques, and benefits associated with the study. This study was approved by the Ethics Committee of Niigata University of Health and Welfare and conformed to the standards of the Declaration of Helsinki.

2.2 Experimental Procedure

To determine individual exercise workload, peak oxygen consumption (VO_2peak) was obtained by an automated metabolic analyzer (AE-310, Minato Medical Science, Osaka, Japan) using an incremental protocol on a cycle ergometer (Aerobike 75XLII; Combi, Tokyo, Japan) before the main experiments. Exhaustion was defined as described previously [4].

In the main experiment, subjects performed constant work-rate exercise corresponding to 30% or 50% of VO_2peak on a cycle ergometer for 20 min, following a 4-min rest and a 4-min warm-up period. An 8-min post-exercise rest (PER) followed the main exercise. During this experiment, the NIRS signals, skin blood flow (SBF), and mean arterial pressure (MAP) were measured continuously.

2.3 NIRS Measurements

A multichannel NIRS imaging system (OMM-3000; Shimadzu Co., Kyoto, Japan) with continuous multiple wavelengths (780, 805, and 830 nm) was used to detect changes in oxyhemoglobin (O_2Hb) and deoxyhemoglobin (HHb) using the modified Beer-Lambert law [4] at a sampling rate of 190 ms. NIRS optodes, consisting of 12 light-source fibers and 12 detectors providing 34-channel simultaneous recording, were set in a 3 × 8 multichannel probe holder. A 30-mm interoptode distance was used to measure cortical tissue oxygenation. We used a double-density probe holder, consisting of 2 sets, one of which was shifted to half the optode distance from the origin. The Cz position of the international 10–20 system was used to ensure consistent optode placement among all subjects [6]. The NIRS array map covered the right central, left central, and parietal areas of the scalp to measure cortical tissue-oxygenation in motor-related areas. Regions of interest (ROI) were the supplementary motor area (SMA) and sensorimotor cortex (SMC) (Fig. 36.1).

2.4 Blood Pressure and Skin Blood-Flow Measurements

Beat-to-beat MAP was recorded by volume clamping the finger pulse with a finger photoplethysmograph (Finometer; Finapres Medical Systems, Amsterdam, the Netherlands) on the left middle finger. Changes in SBF were measured at the forehead using a laser Doppler blood flow meter (Omegaflow FLO-CI; Omegawave Inc., Osaka, Japan). Analogue data were converted to digital data using an A/D converter (PowerLab; AD Instruments, Australia) at a 1000-Hz sampling rate.

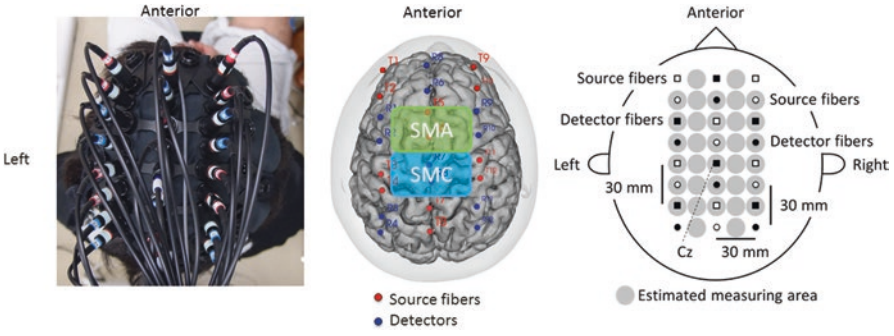

Fig. 36.1 Location of the 12 light-source fibers and 12 detectors, and regions of interest (ROI). White squares and white circles are light-source fibers and black squares and black circles are detector fibers. Each set (squares and circles) consisted of six light-source fibers and six detector fibers, with an interoptode distance of 30 mm, and were spaced evenly

Table 36.1 Comparison of oxyhemoglobin (O_2Hb) between exercise and post-exercise rest (PER) for each region of interest (ROI) (mM.cm)

	ROI	Exercise	PER	*p*-value
30% VO_2peak	SMA	0.038 ± 0.013	0.024 ± 0.009	< 0.05
	SMC	0.044 ± 0.016	0.032 ± 0.011	0.09
50% VO_2peak	SMA	0.084 ± 0.015	0.072 ± 0.009	0.23
	SMC	0.099 ± 0.042	0.097 ± 0.036	0.83

Values are presented as mean ± standard error of the mean (SEM). Paired *t*-test was used to obtain *p*-values

2.5 Statistical Analysis

SBF and MAP were down-sampled by adopting the sampling rate for NIRS monitoring. To obtain temporal changes, the averages of the O_2Hb and HHb for each ROI, SBF, and MAP were expressed as the change from the average rest phase value and were calculated every 1 min. The peak values of O_2Hb during exercise and PER were compared by a paired t-test with the significance level set at $p < 0.05$. The relationship between O_2Hb and SBF was assessed using Pearson's correlation coefficients, with significance set at $p < 0.05$ during the main exercise period and PER period.

3 Results

O_2Hb moderately elevated through the main experiment in SMA and SMC at 30% of VO_2peak. HHb drifted below the rest phase in both ROI. During 50% VO_2peak exercise, O_2Hb increased during the initial 7 min of the 20-min main exercise, and then maintained its value in both regions until the end of exercise. The SBF and MAP increased in the exercise phase.

After the exercise, O_2Hb decreased immediately and subsequently increased again in the PER for 30% VO_2peak and 50% VO_2peak conditions. The elevated O_2Hb persisted throughout the PER in both ROIs. SBF degraded over time, and MAP decreased immediately after the exercise. For the 30% VO_2peak experiment, O_2Hb during exercise was significantly larger than during PER in the SMA. There were no significant differences between exercise and PER in the SMC in the 30% VO_2peak experiment or in the SMA and SMC in the 50% VO_2peak experiment (Table 36.1) (Figs. 36.2 and 36.3).

The correlation coefficients between SBF and O_2Hb differed between the exercise phase and PER (Table 36.2). There were significant positive correlations between O_2Hb and SBF in both ROIs and for both intensities during the exercise phase. However, in the PER there were no significant correlations between O_2Hb and SBF for either ROI or intensity level.

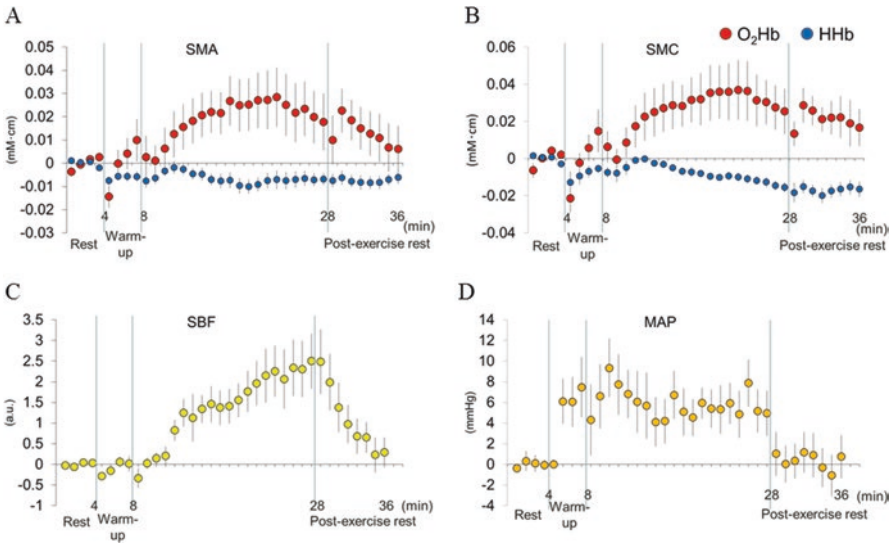

Fig. 36.2 Temporal changes in oxyhemoglobin (O_2Hb, red circle) and deoxyhemoglobin (HHb, blue circle) values in the supplemental motor area (SMA, A), in the sensorimotor cortex (SMC, B), and skin blood flow (SBF, C) and mean arterial pressure (MAP, D) for exercise at 30% of VO_2peak. Values are presented as mean ± standard error of the mean (SEM)

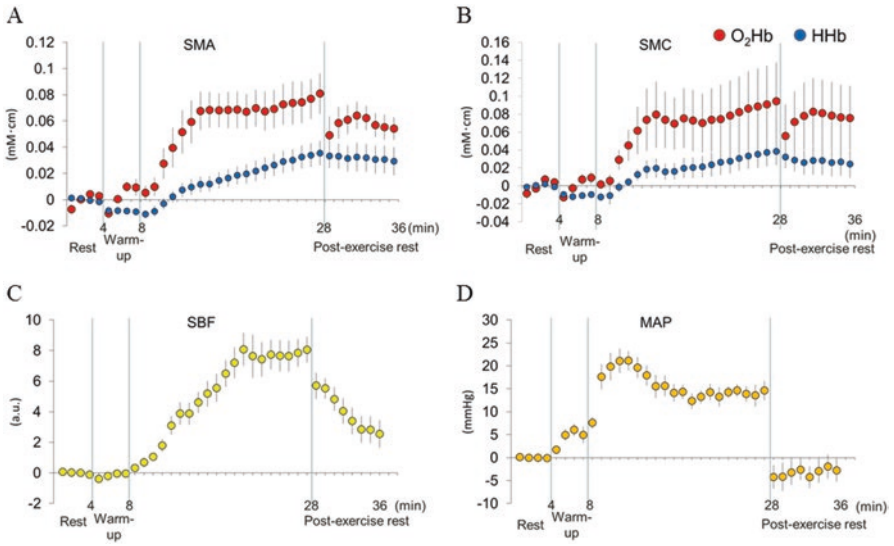

Fig. 36.3 Temporal changes in oxyhemoglobin (O_2Hb, red circle) and deoxyhemoglobin (HHb, blue circle) values in the supplemental motor area (SMA, A), in the sensorimotor cortex (SMC, B), and skin blood flow (SBF, C) and mean arterial pressure (MAP, D) for exercise at 50% of VO_2peak. Values are presented as mean ± standard error of the mean (SEM)

Table 36.2 Relationship between oxyhemoglobin (O_2Hb) and skin blood flow (SBF) during exercise and post-exercise rest (PER) for each intensity and each region of interest (ROI)

	ROI	Exercise	*p*-value	PER	*p*-value
30% VO_2peak	SMA	0.807	< 0.01	0.546	0.162
	SMC	0.831	< 0.01	0.070	0.870
50% VO_2peak	SMA	0.896	< 0.01	– 0.100	0.813
	SMC	0.869	< 0.01	– 0.620	0.101

Pearson's correlation coefficients

4 Discussion

In the present study, we measured cerebral oxygenation in motor-related areas during and after low- and moderate-intensity cycling exercise. O_2Hb increased during exercise, and then increased again after participants stopped the exercise; O_2Hb values following exercise did not differ from the values obtained during exercise, most notably for moderate-intensity exercise.

NIRS can be used to measure changes in the cerebral hemodynamic response and metabolism, thus allowing for the use of multichannel NIRS recording for functional optical imaging of human brain activity [7]. Although many studies have reported cerebral oxygenation levels during incremental [3, 4, 8] or constant work-rate [6, 9] exercise, the after-effects of the exercise were unknown. Our study clarifies the after-effects of a gross motor task, and thus provides fundamental data regarding neural plasticity induced by exercise.

It is necessary to consider the effect of systemic changes on initial O_2Hb levels. In this study, SBF, MAP, and O_2Hb all increased during 20-min of exercise at 30% of VO_2peak and 50% of VO_2peak. In contrast, we observed that O_2Hb, SBF, and MAP exhibited different changes in the PER in this study. The correlation coefficients between SBF and O_2Hb were 0.807 to 0.896 during exercise. Meanwhile, the correlation coefficients between SBF and O_2Hb were −0.620 to 0.546 in the PER. These results indicate that, although O_2Hb might be affected by SBF and/or MAP during 20-min cycling exercise, the effects of systemic changes on O_2Hb were very weak in the PER. Several studies have indicated that SBF influences O_2Hb changes as measured by NIRS [10, 11]. In addition, MAP influences O_2Hb [12]. We have previously described that, although SBF, MAP, and O_2Hb were moderately to strongly correlated during 5-min of exercise at 30% of VO_2peak or 50% of VO_2peak [13], correlation coefficients between SBF, MAP, and O_2Hb fluctuated during 20-min of exercise at 30% of VO_2peak [6]. Our previous study showed correlation coefficients between SBF, MAP, and O_2Hb that were negative or very weak after the exercise (r = −0.798 in SBF; r = 0.253 in MAP) [13].

The O_2Hb values increased again in SMA and SMC in the PER following both exercise intensities. In particular, O_2Hb values in the PER after 50%VO_2peak exercise did not differ significantly from the values obtained during the exercise. These results suggest that cerebral oxygenation in the PER in motor-related areas was similar to that during the exercise, even though the participants had stopped their

movements. We consider that the exercise-induced blood flow increase might be based on vasodilation of the capillaries in the motor-related area. Moderate intensity aerobic exercise increases cerebral blood flow [14]. Increased blood flow produces nitric oxide (NO), which is a vasodilator in neurovascular coupling [15, 16]. NO-induced vasodilation may cause elevated O_2Hb to persist after moderate-intensitycycling exercise. In contrast, O_2Hb reflects changes in cortical neural activation [2, 17, 18]. Based on this phenomenon, neural activation in motor-related areas may remain after exercise. We need to ascertain that neural activation persists after exercise using other modalities.

This study had some limitations. First, we only measured oxygenation of the motor-related cerebrum, due to methodological limitations. Our study did not consider the distribution of cerebral blood flow within other cortical regions during and after exercise. Second, the measurement locations differed for SBF and O_2Hb. SBF was recorded at the forehead to prevent interference from the near-infrared and laser light emitted from the laser Doppler flow meter.

In conclusion, we found that elevated O_2Hb values in motor-related areas persist after exercise, and indeed remain as high as during exercise. This result suggests that neuroplasticity may be facilitated by aerobic exercise training.

Acknowledgments This study was supported by a Grant-in-Aid for Scientific Research (C) from the Japan Society for the Promotion of Science and a Grant-in-Aid for Exploratory Research from the Niigata University of Health and Welfare.

References

1. Boas DA, Gaudette T, Strangman G et al (2001) The accuracy of near infrared spectroscopy and imaging during focal changes in cerebral hemodynamics. NeuroImage 13:76–90
2. Miyai I, Tanabe HC, Sase I et al (2001) Cortical mapping of gait in humans: A near-infrared spectroscopic topography study. NeuroImage 14:1186–1192
3. Bhambhani Y, Malik R, Mookerjee S (2007) Cerebral oxygenation declines at exercise intensities above the respiratory compensation threshold. Respir Physiol Neurobiol 156:196–202
4. Rupp T, Perrey S (2008) Prefrontal cortex oxygenation and neuromuscular responses to exhaustive exercise. Eur J Appl Physiol 102:153–163
5. Anazodo UC, Shoemaker JK, Suskin N et al (2013) An investigation of changes in regional gray matter volume in cardiovascular disease patients, pre and post cardiovascular rehabilitation. Neuroimage Clin 3:388–395
6. Tsubaki A, Takai H, Kojima S et al (2016) Changes in cortical oxyhaemoglobin signal during low-intensity cycle ergometer activity: a near-infrared spectroscopy study. Adv Exp Med Biol 876:79–85
7. Tamura M, Hoshi Y, Okada F (1997) Localized near-infrared spectroscopy and functional optical imaging of brain activity. Philos Trans R Soc Lond Ser B Biol Sci 352:737–742
8. Peltonen JE, Paterson DH, Shoemaker JK et al (2009) Cerebral and muscle deoxygenation, hypoxic ventilatory chemosensitivity and cerebrovascular responsiveness during incremental exercise. Respir Physiol Neurobiol 169:24–35
9. Higashimoto Y, Honda N, Yamagata T et al (2011) Activation of the prefrontal cortex is associated with exertional dyspnea in chronic obstructive pulmonary disease. Respiration 82:492–500

10. Takahashi T, Takikawa Y, Kawagoe R et al (2011) Influence of skin blood flow on near-infrared spectroscopy signals measured on the forehead during a verbal fluency task. NeuroImage 57:991–1002
11. Kirilina E, Jelzow A, Heine A et al (2012) The physiological origin of task-evoked systemic artefacts in functional near infrared spectroscopy. NeuroImage 61:70–81
12. Minati L, Kress IU, Visani E et al (2011) Intra- and extra-cranial effects of transient blood pressure changes on brain near-infrared spectroscopy (NIRS) measurements. J Neurosci Methods 197:283–288
13. Tsubaki A, Takai H, Oyanagi K et al (2016) Correlation between the cerebral oxyhaemoglobin signal and physiological signals during cycling exercise: A near-infrared spectroscopy study. Adv Exp Med Biol 923:159–166
14. Sato K, Ogoh S, Hirasawa A et al (2011) The distribution of blood flow in the carotid and vertebral arteries during dynamic exercise in humans. J Physiol 589:2847–2856
15. Frangos JA, Eskin SG, Mcintire LV et al (1985) Flow effects on prostacyclin production by cultured human endothelial cells. Science 227:1477–1479
16. Dimmeler S, Fleming I, Fisslthaler B et al (1999) Activation of nitric oxide synthase in endothelial cells by Akt-dependent phosphorylation. Nature 399:601–605
17. Obrig H, Wolf T, Doge C et al (1996) Cerebral oxygenation changes during motor and somatosensory stimulation in humans, as measured by near-infrared spectroscopy. Adv Exp Med Biol 388:219–224
18. Niederhauser BD, Rosenbaum BP, Gore JC et al (2008) A functional near-infrared spectroscopy study to detect activation of somatosensory cortex by peripheral nerve stimulation. Neurocrit Care 9:31–36

Chapter 37
Relation Between Cognitive Function and Baseline Concentrations of Hemoglobin in Prefrontal Cortex of Elderly People Measured by Time-Resolved Near-Infrared Spectroscopy

Y. Murayama, Y. Sato, L. Hu, A. Brugnera, A. Compare, and Kaoru Sakatani

Abstract We evaluated relationship between cognitive function and cerebral blood oxygenation (CBO) of the prefrontal cortex (PFC) at rest in 113 adults (age 72.3 ± 12.0 years). We employed a two channel time-resolved near-infrared spectroscopy (TRS), which allows non-invasive measurements of baseline concentrations of oxyhemoglobin (oxy-Hb), deoxyhemoglobin (deoxy-Hb), total-hemoglobin (t-Hb) (μM) and oxygen saturation (SO_2, %) of the bilateral PFC without any tasks. We examined cognitive functions using the Mini-Mental State Examination (MMSE) (range from 0 to 30) and the Touch M which evaluates working memory function semi-automatically on a touchscreen (range from 0 to 100); the mean MMSE and Touch M scores of all subjects were 24.8 ± 4.6 (mean ± SD; range 11–30) and 41.3 ± 22.1 (range 1–100), respectively. Employing Pearson's correlation analysis, we evaluated correlation between the TRS parameters and cognitive function. We found a significant positive correlation between the MMSE scores and SO_2 ($r = 0.24$, $p < 0.02$). In addition, we observed significant positive correlations between Touch M scores and baseline concentrations of oxy-Hb ($r = 0.26$, $p < 0.02$), total-Hb ($r = 0.23$, $p < 0.05$), and SO_2 ($r = 0.23$, $p < 0.05$). TRS allowed us to evaluate the relation between CBO in the PFC at rest and cognitive function.

Keywords TRS • NIRS • Dementia • Alzheimer's disease • Cognitive function

Y. Murayama • Y. Sato • L. Hu • A. Brugnera • A. Compare • K. Sakatani (✉)
NEWCAT Research Institute, Department of Electrical and Electronics Engineering, College of Engineering, 1 Nakagawara, Tokusada, Tamuramachi, Koriyama, Fukushima Prefecture, Koriyama, Japan, 963-8642

Department of Human & Social Science, University of Bergamo, Bergamo, Italy
e-mail: sakatani.kaoru@nihon-u.ac.jp

H.J. Halpern et al. (eds.), *Oxygen Transport to Tissue XXXIX*, Advances in Experimental Medicine and Biology 977, DOI 10.1007/978-3-319-55231-6_37

1 Introduction

As the world's population is rapidly aging, dementia has become an important public health problem. In order to prevent the onset and deterioration of cognitive function, it is important to develop techniques for objective assessment of cognitive function. Positron Emission Tomography (PET) and Magnetic Resonance Imaging (MRI) have been used for the diagnosis of dementia [1]; PET evaluates changes of cerebral blood flow and oxygen metabolism while MRI evaluates changes of volumes such as cortexes and hippocampus. These techniques, however, require large facilities and have high costs for examination and maintenance. A simple and less costly method to assess cognitive function is necessary for screening test of dementia.

Near infrared spectroscopy (NIRS) appears to be an attractive alternative method since it is compact and less costly than MRI or PET. NIRS, which employ continuous wave light, allows to measure relative changes of hemoglobin (Hb) concentration in cerebral blood vessels [2]. In contrast, time-resolved near infrared spectroscopy (TRS), which employs picosecond light pulses, permits quantitative measurements of Hb concentrations at rest [3]. TRS has been applied to monitoring of cognitive function in normal adults [4, 5] and cerebral blood flow in patients with cerebrovascular diseases [6].

In the present study, employing TRS, we evaluated relationship between cognitive function and Hb concentrations at rest of the prefrontal cortex (PFC) in middle and old-aged subjects.

2 Methods

2.1 Subjects

We studied 113 subjects (60 males, 53 females; age 72.3 ± 12.0 years (mean ± SD); range 45–91 years; 82 cases ≧65 years, 31 cases <65 years) who exhibited a variety of cognitive function between normal and dementia (see Sect. 2.2 Assessment of Cognitive Function). All subjects visited Southern Touhoku Kasuga Rehabilitation Hospital (Sukagawa city, Japan) due to various symptoms including forgetfulness. The subjects provided written informed consent as required by the Human Subjects Committee of the Rehabilitation Hospital; when the subject had difficult to understand the informed consent due to cognitive dysfunction, their family provided.

2.2 Assessment of Cognitive Function

Initially, we evaluated cognitive function of the subjects using the Mini Mental State Examination (MMSE), which is effective as a screening tool that can be used to systematically assess mental status [7]: no cognitive impairment = 24–30; mild

cognitive impairment = 18–23; severe cognitive impairment = 0–17. The mean MMSE scores were 24.8 ± 4.6 (range 11–30); 80 cases for normal, 23 cases for mild, 10 cases for sever cognitive impairment. In addition, we evaluated cognitive function using the Touch M (HUMAN Co. Ltd., Japan) which examines working memory function semi-automatically on a touchscreen [8]. The maximum scores of the Touch M is 100; the scores of 70–100, 40–69 and 0–39 indicate normal, mild impairment and impairment of working memory, respectively [8]. The mean Touch M scores were 41.3 ± 22.1 (range 1–100); 8 cases for normal, 37 cases for mild, 33 cases for sever cognitive impairment (total 78 cases).

2.3 TRS Measurement

We measured the baseline concentrations of Hb in the bilateral PFC at resting condition employing TRS (TRS-21, Hamamatsu Photonics K.K., Hamamatsu, Japan) [9], which was used in our previous studies [4–6]. Details of this system have been described by us previously [4–6]. Briefly, it consists of three pulsed laser diodes with different wavelengths (761, 791, and 836 nm) having a duration of 100 ps at a repetition frequency of 5 MHz, a photomultiplier tube, and a circuit for time-resolved measurement based on the time-correlated single photon counting method. The observed temporal profiles were fitted into the photon diffusion equation [3, 9] using the non-linear least-squares fitting method. The concentrations of oxy-Hb, deoxy-Hb, t-Hb (=oxy-Hb + deoxy-Hb) and SO_2 were calculated using the least-squares method. The concentrations of Hb were expressed in μM.

The TRS probes were set symmetrically on the forehead with a flexible fixation pad so that the midpoint between the emission and detection probes was 3 cm above the centers of the upper edges of the bilateral orbital sockets (Fig. 37.1a); this positioning is similar to the midpoint between electrode positions Fp1/Fp3 (left) and Fp2/Fp4 (right) of the international electroencephalographic 10–20 system. MRI confirmed that the emitter-detector was located over the dorsolateral and frontopolar areas of the bilateral PFC (Fig. 37.1b). The distance between the emitter and detector was set at 3 cm.

It was reported that the contribution ratio of the cerebral tissue to optical signals (i.e. ratio of partial optical pathlength to total optical pathlength) at the probe distances of 2, 3 and 4 cm as 33%, 55% and 69%, respectively [10]. Based on this result, we suggest the contribution rate of the PFC was about 55% in the present study.

2.4 Data Analysis

Employing Pearson's correlation analysis, we evaluated correlations between TRS parameters and cognitive function evaluated by the MMSE and Touch M scores. In addition, we compared TRS parameters between normal subjects (MMSE≧24) and subjects with cognitive impairment (MMSE≦23) using t-test.

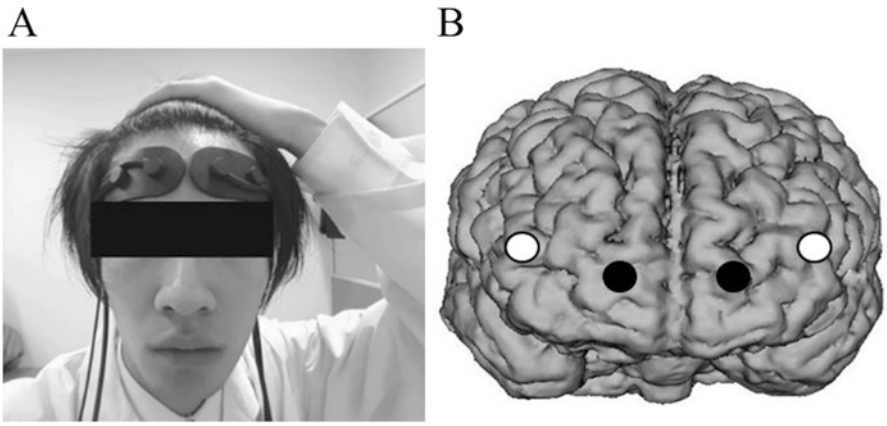

Fig. 37.1 (**a**), Location and (**b**), Position of the TRS probes (*The black dot* Emitter, *The white dot* Detector)

3 Results

There was a significant negative correlation between the age of the subjects and MMSE scores ($r = -0.43$, $p < 0.01$) (Fig. 37.2a) and Touch M scores ($r = -0.40$, $p < 0.01$) (Fig. 37.2b). In addition, there was a significant positive correlation between MMSE scores and Touch M scores ($r = 0.44$, $p < 0.01$) (Fig. 37.2c).

The SO_2 in the PFC measured by TRS varied between the subjects; however, there was a significant positive correlation between MMSE and SO_2 in the left PFC ($r = 0.24$, $p < 0.02$) and the right PFC ($r = 0.24$, $p < 0.02$) (Fig. 37.3).

There was a significant positive correlation between Touch M scores and SO_2 in the left PFC ($r = 0.25$, $p < 0.05$) and the right PFC ($r = 0.23$, $p < 0.05$) (Fig. 37.4a). In addition, Touch M scores showed a significant positive correlation with oxy-Hb concentrations at rest in the left PFC ($r = 0.27$, $p < 0.02$) and the right PFC ($r = 0.26$, $p < 0.02$) (Fig. 37.4b). In contrast, MMSE scores showed no correlation with oxy-Hb concentrations at rest.

Finally, we observed significant larger SO_2 in the bilateral PFC of normal subjects than those of impaired subjects (Table 37.1).

4 Discussion

The present study demonstrates that SO_2 in the bilateral PFC at rest showed a significant positive correlation with both the MMSE and Touch M scores. In addition, the baseline concentrations of oxy-Hb at rest also showed a significant positive correlation with Touch M scores. It should be emphasize that the correlation coefficient (r) was relatively low, but statistically significant. These results are consistent with our recent TRS study, which showed that elderly women with normal or

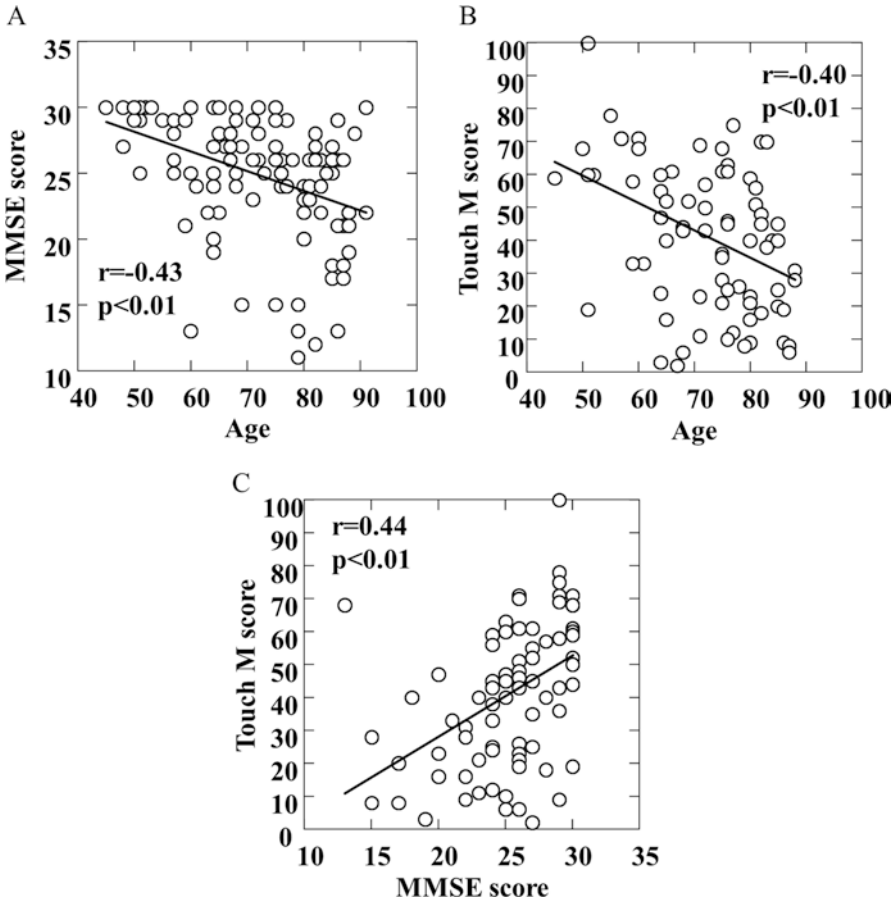

Fig. 37.2 Relationships between ages and cognitive function. (**a**) ages vs MMSE scores, (**b**) ages vs Touch M score, (**c**) MMSE scores vs Touch M score

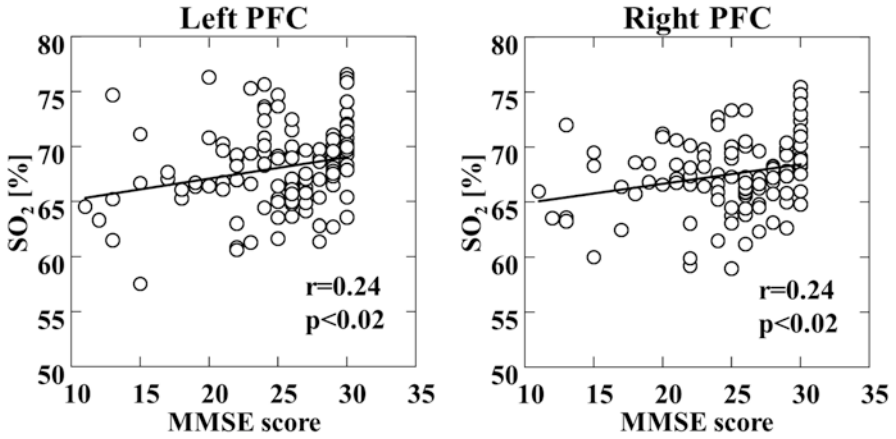

Fig. 37.3 Relationships between MMSE score and SO_2 in the left and right PFC

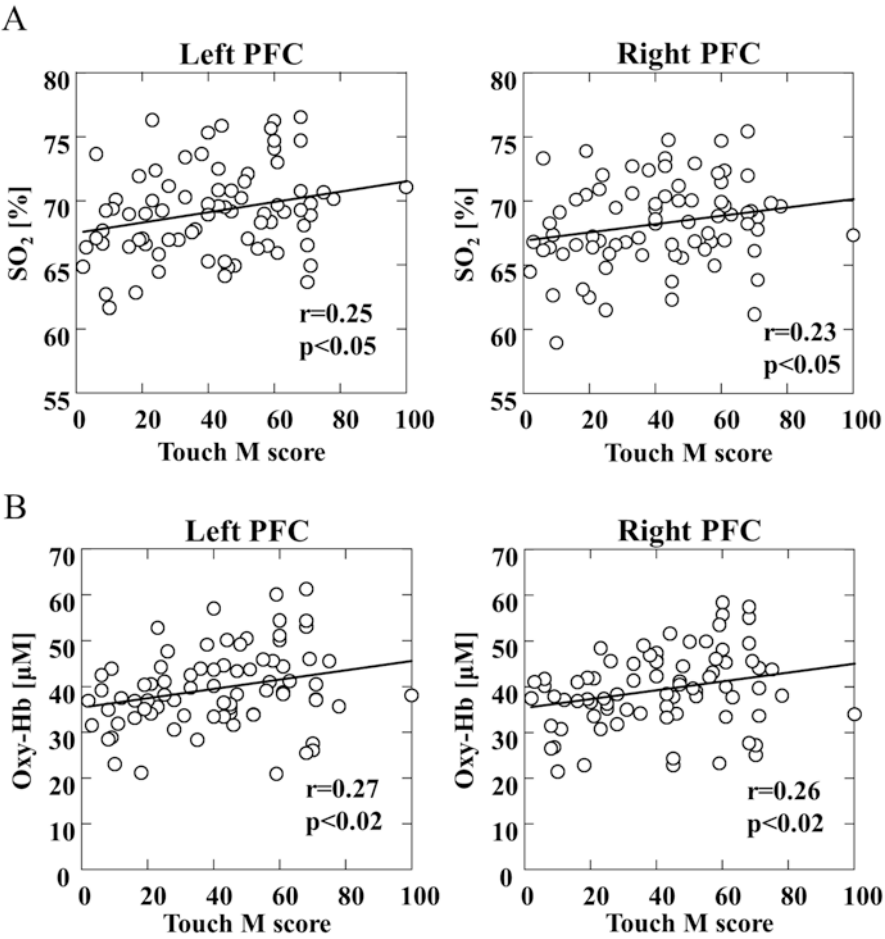

Fig. 37.4 Relationships between working memory function evaluated by Touch M and TRS parameters: (**a**) Touch M scores vs SO_2 in the left and right PFC. (**b**) Touch M scores vs oxy-Hb concentrations at rest in the left and right PFC

Table 37.1 Comparison of TRS parameters between normal subjects and subjects with impaired cognitive function

		Normal (MMSE ≥ 24)	Impaired (MMSE ≤ 23)	p value
Left	oxy-Hb	38.72	38.30	>0.1
	deoxy-Hb	18.15	18.90	>0.1
	total-Hb	56.86	57.20	>0.1
	SO_2	67.89	66.69	<0.05*
Right	oxy-Hb	38.70	37.05	>0.1
	deoxy-Hb	17.57	18.04	>0.1
	total-Hb	56.27	55.09	>0.1
	SO_2	68.50	66.91	<0.05*

* $p<0.05$

mild cognitive impairment (MMSE score 24.1 ± 3.8) exhibited higher baseline concentrations of oxy-Hb and t-Hb in the PFC than those with moderate cognitive impairment (MMSE score 10.3 ± 5.8) [5].

In order to elucidate the physiological basis of the relation between TRS measurements and cognitive function, the following observations should be considered. Simultaneous measurements of TRS and PET in normal adults demonstrated that SO_2 and t-Hb measured by TRS significantly increased, associated with an increase of regional cerebral blood flow (rCBF) and volume (rCBV) induced by acetazolamide [11]. In addition, dementia showed decreased rCBF or glucose metabolism in various brain regions including the frontal cortex, particularly in patients with frontal dysfunction, such as apathy [12, 13]. Based on these observations, we suggest that the concentrations of Hb in the PFC at rest measured by TRS correlate with the rCBF and rCBV in the PFC at rest, which reflect cognitive functions related with the PFC, such as working memory.

Finally, the advantages of TRS should be discussed. First, TRS allows us to measure Hb concentrations at rest; therefore, it allows us to assess cognitive function without any task. Second, TRS is compact and less expensive than PET and MRI. In addition, TRS has less stress on subjects at the time of measurement than PET and MRI. Further studies are necessary to apply TRS to screening test of cognitive dysfunction.

Acknowledgments This research was supported in part by the Strategic Research Foundation Grant-aided Project for Private Universities (S1411017) and a Grant-in-Aid for Exploratory Research (25560356) from the Ministry of Education, Culture, Sports, Sciences, and Technology of Japan. Furthermore, this research was supported through grants from Iing Co., Ltd. (Tokyo, Japan) and Southern Tohoku Hospital (Fukushima, Japan).

References

1. Scheltens P, Blennow K, Breteler MM et al (2016) Alzheimer's disease. Lancet 388(10043):505–517. doi:10.1016/S0140-6736(15)01124-1
2. Wolf M, Ferrari M, Quaresima V (2007) Progress of near-infrared spectroscopy and topography for brain and muscle clinical applications. J Biomed Opt 12:062104
3. Patterson MS, Chance B, Wilson C (1986) Time resolved reflectance and transmittance for the non-invasive measurement of tissue optical properties. Appl Opt 28:2331–2336
4. Tanida M, Sakatani K, Tsujii T (2012) Relation between working memory performance and evoked cerebral blood oxygenation changes in the prefrontal cortex evaluated by quantitative time-resolved near-infrared spectroscopy. Neurol Res 34:114–119
5. Yokose N, Sakatani K, Murata Y et al (2010) Bedside assessment of cerebral vasospasms after subarachnoid hemorrhage by near infrared time-resolved spectroscopy. Adv Exp Med Biol 662:505–511
6. Machida A, Shirato M, Tanida M et al (2016) Effects of Cosmetic Therapy on Cognitive Function in Elderly Women Evaluated by Time-Resolved Spectroscopy Study. Adv Exp Med Biol 876:289–295
7. Tombaugh TN, McIntyre NJ (1992) The mini-mental state examination: a comprehensive review. J Am Geriatr Soc 40(9):922–935

8. Hayashi Y, Kijima T, Satou K et al (2011) Examination of the evaluation method of visual-spatial cognitive function using the touch screen device. Jpn J Geriatr Psychiat 22: 439–447 (Japanese)
9. Oda M, Nakano T, Suzuki A et al (2000) Near infrared time-resolved spectroscopy system for tissue oxygenation monitor. SPIE 4160:204–210
10. Kohri S, Hoshi Y et al (2002) Quantitative evaluation of the relative contribution ratio of cerebral tissue to near-infrared signals in the adult human head: a preliminary study. Physiol Meas 23(2):301–312
11. Ohmae E, Ouchi Y, Oda M et al (2006) Cerebral hemodynamics evaluation by near-infrared time-resolved spectroscopy: correlation with simultaneous positron emission tomography measurements. NeuroImage 29:697–705
12. Marshall GA, Monserratt L, Harwood D et al (2007) Positron emission tomography metabolic correlates of apathy in Alzheimer disease. Arch Neurol 64:1015–1020
13. Waragai M, Yamada T, Matsuda H (2007) Evaluation of brain perfusion SPECT using an easy Z-score imaging system (eZIS) as an adjunct to early-diagnosis of neurodegenerative diseases. J Neurol Sci 260:57–64

Chapter 38
Physiological Effects of Continuous Colored Light Exposure on Mayer Wave Activity in Cerebral Hemodynamics: A Functional Near-Infrared Spectroscopy (fNIRS) Study

A.J. Metz, S.D. Klein, F. Scholkmann, and U. Wolf

Abstract We are increasingly exposed to colored light, but its impact on human physiology is not yet extensively investigated. In the present study we aimed to determine the effects of colored light on human cerebral Mayer wave activity (MWA). We measured oxy- ([O_2Hb]), deoxy- ([HHb]), total hemoglobin ([tHb]) concentrations and tissue oxygen saturation (StO_2) by functional near-infrared spectroscopy (fNIRS) in the left and right pre-frontal cortex (L-PFC, R-PFC) of 17 subjects (median age: 29 years, 6 women). In a randomized crossover design subjects were exposed to blue, red, green, and yellow LED light for 10 min. Pre-light (8 min, baseline) and post-light (15 min, recovery) conditions were darkness. MWA was calculated from band-pass filtered fNIRS signals (~0.08–0.12 Hz). The medians from the last 3 min of each period (baseline, light exposure, recovery) were statistically analyzed. MWA was increased during red and green light vs. baseline and after blue light exposure in recovery in the L-PFC. MWA differed depending on the chosen frequency range, filter design, and type of signals to analyze (raw intensity, hemoglobin signal from multi-distance method or modified Beer-Lambert law, or within hemoglobin signals).

Keywords Functional near-infrared spectroscopy • Brain • Mayer wave activity • Colored light exposure

A.J. Metz • S.D. Klein • U. Wolf (✉)
University of Bern, Institute of Complementary Medicine,
Fabrikstrasse 8 CH-3012, Bern, Switzerland
e-mail: ursula.wolf@ikom.unibe.ch

F. Scholkmann
University of Bern, Institute of Complementary Medicine,
Fabrikstrasse 8 CH-3012, Bern, Switzerland

University of Zurich, University Hospital Zurich, Biomedical Optics Research Laboratory,
Department of Neonatology, Zurich, Switzerland

H.J. Halpern et al. (eds.), *Oxygen Transport to Tissue XXXIX*, Advances in Experimental Medicine and Biology 977, DOI 10.1007/978-3-319-55231-6_38

1 Introduction

Color and colored light are of great importance in daily life. While a number of interactions between colored light and the human physiology are known, many other potential physiological effects of colored light are yet unexplored. There are many therapeutic applications of light, outlining the importance of the interaction between colored light and physiology. For example, blue light is employed in the treatment of neonatal jaundice [1]. Several studies investigated colored light and physiology in association with the circadian system, e.g. suppression of melatonin secretion in the late evening [2]. A few studies measured the interaction of light with human physiology during the day. Colored light had no effect on heart rate [3, 4], but blue light exposure led to increased cerebral tissue oxygenation (StO_2) during and after exposure [5], assessed by fNIRS. The effect of colored light exposure on the Mayer wave activity (MWA) has not yet been investigated. Mayer waves are known as global spontaneous hemodynamic oscillations at ~0.1 Hz, and can be detected by several methods (e.g. NIRS) and were first described in blood pressure measurements [6, 7].

Our aim was to study the effects of colored light exposure on human cerebral MWA measured by fNIRS in adults. We were also interested how the MWA power measure is affected by band-pass filter parameters, by the methods to calculate the power, and by the time range included. We hypothesized that blue would affect the MWA differently than *green*, *red*, and possibly *yellow*.

2 Methods

Subjects We measured 17 subjects (6 female; median age 29 years, range 25–65 years). Data from one subject were excluded due to red-green color blindness. The remaining subjects were right-handed and non-smokers (except one). The study was approved by the Ethics Committee of the Canton of Zurich and subjects gave informed consent prior to the study participation.

Protocol The subjects were exposed to colored lights (red, green, blue, yellow) on different days between 8:30 h and 18:00 h in a randomized cross-over protocol. The 10 min light exposure was preceded by a baseline of 8 min and followed by a recovery period of 15 min, both of which were in darkness. The subjects were seated upright and faced a white wall (distance open eyes-wall ~110 cm) which was illuminated by 30 lux LED light (yellow was mixed from red and green), confirmed by a DT-1308 light meter (ATP Instrumentation Ltd., UK). The LED spectra were peaks with maxima at 450 nm (blue), 515 nm (green), and 630 nm (red) and half maximum bandwidths between 20–35 nm. Four subjects were not exposed to yellow light because their agenda did not allow for an additional measurement.

Near-Infrared Spectroscopy Absorption and scattering were measured by a multi-distance (MD) frequency domain NIRS system (ISS Imagent, ISS Inc.,

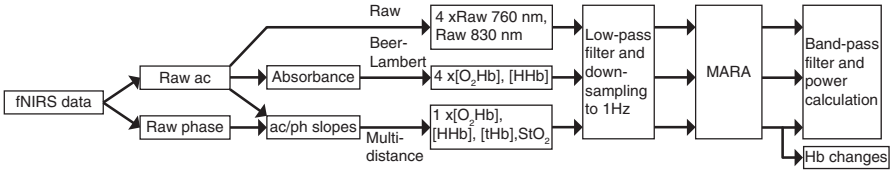

Fig. 38.1 fNIRS data processing stream to determine MWA. The low-pass filter was a least-squares filter ($N = 935$) at 0.3 Hz. MARA denotes the "movement artefact removal algorithm" [11] and was applied independently to each fNIRS signal

Illinois, USA) at two wavelengths (760 and 830 nm) at 25 Hz. Each sensor included four different distances in a line geometry (~ 2, 2.5, 3, 3.5 cm) which permit the calculation of the light intensity loss over distance [8, 9]. For each sensor we obtained oxy- and deoxyhemoglobin ([O_2Hb], [HHb]), total hemoglobin [tHb] = [O_2Hb] + [HHb] and tissue oxygen saturation StO_2 = [O_2Hb]/[tHb] by molar absorption coefficients from [10]. The sensors were placed over the left and right prefrontal (L-PFC, R-PFC) and visual cortices, respectively. Only data from the L-PFC and R-PFC were analyzed here.

Data Analysis Prior to the analysis, the data were investigated manually in order to remove too noisy signals. Figure 38.1 depicts the data processing stream. All data were low-pass filtered (cut-off at 0.3 Hz) and down-sampled to 1 Hz. To remove movement-related artifacts, we employed the "movement artefact removal algorithm" (MARA) [11] with a slightly different reconstruction method. Instead of the spline interpolation we fitted a 2nd degree polynomial model with a window length p to the artefact segments (Matlab function 'smooth', option 'loess'), and then subtracted the fit from the artefact. Hence, the parameter p can be any positive integer value. The necessary parameters (p, length of moving window L, and the threshold T) were found individually for each time series. Most commonly, L was set to represent 3 s and p to represent 1 or 40 s of the data. The amount of artefacts in the data is shown in Table 38.1. After MARA, hemoglobin (Hb) concentration changes (Hb changes in Fig. 38.1) were computed from the MD data (a) or data were band-pass filtered and the power calculated (b). Concerning (a), data were further smoothed (window length: 2 min). Median values were calculated from time windows of interest (i.e. the last 3 min of baseline, colored light exposure, or recovery) to obtain the concentration changes. Concerning (b), the signals were band-pass filtered by a window-based finite-impulse-response (FIR) filter (order: 101) with an flat-top window and the power was calculated from the 3 min signals according to $P = \frac{1}{N}\sum_{N}^{i=1} x_i^2$

We obtained a power value from each Hb time series. A sensitivity analysis was computed for the MWA values determined based on the applied method we employed different filters (window based FIR or least square FIR), band-widths (0.095–0.105, 0.075–0.125, 0.05–0.15 Hz), lengths (3 min or whole period), or power calculation methods (as above or from the summed frequency spectra).

Table 38.1 Amount of artefact for the different signals based on the MARA corrections

	% Clean	Median	75th pc.	95th pc.	max. (%)	*N*	median *L*/*p*
Raw signals	38.3	0.6%	2.5%	7.8%	15.6	230	3/40
Beer-Lambert	57	0%	1.2%	7.3%	20.9	920	3/40
Multi-distance	55.2	0%	0.3%	9.8%	33.4	460	3/1

N number of signals, *L*, *p* MARA parameters, *pc* percentile, *max* maximum

Statistics Values of different variables were compared between the baseline and the colored light exposure (*col-base*) and between the recovery and the colored light exposure (*recov-col*) by Wilcoxon signed rank tests ($\alpha = 0.05$, two-sided). We tested color differences by Friedman tests ($\alpha = 0.05$). We excluded the yellow light condition due to the lower number of subjects in this condition. We did not correct for multiple comparisons since this was an explorative study.

3 Results

L-PFC results for the initial parameters are shown in Fig. 38.2 and the first row of Table 38.2. Table 38.2 also presents the changes obtained when employing different filter /power calculation /time period parameter sets. The last row also shows the changes obtained from the long distance (3.5 cm) raw intensity channels or from the Beer-Lambert calculated Hb variables. We obtained one difference within the color conditions for StO_2 at the color-baseline comparison. For the R-PFC, MWA was not dependent on the color condition or time point. Significant changes occurred when varying filter parameters or when using the Beer-Lambert law, similar to the L-PFC results (data not shown).

4 Discussion and Conclusion

Light of different colors affected Mayer wave activity. Our results indicate an increased power in the recovery after blue light exposure and during red and green light exposure in the L-PFC. The left-right difference is consistent throughout the different parameter sets applied to calculate the power. Mayer waves are considered to be a global phenomenon [7, 12, 13], thus the left-right difference may indicate an influence of vasomotion, which has been more localized in the microvasculature [13–15]. However, one study reported that the MWA amplitude differed between head regions [16].

We observed a higher MWA in the raw intensity signals compared to the MD Hb concentration signals. For this reason we also calculated the results from the raw intensity channels and from the Beer-Lambert law based Hb variables. As seen in Table 38.2, especially the Beer-Lambert results differ considerably. These differences

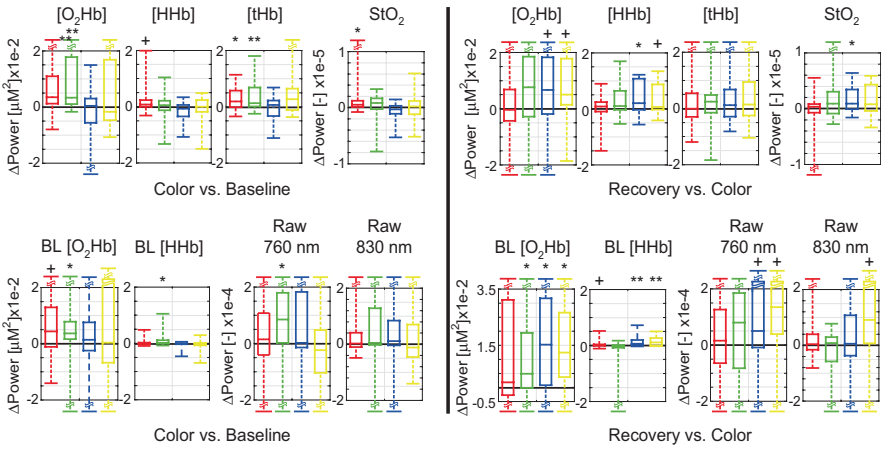

Fig. 38.2 MWA changes from NIRS data evoked by colored light in the L-PFC. *Top row*: MWA calculated from the multi-distance approach. Bottom row: MWA calculated from Beer-Lambert law data (*BL*) or raw intensity data (*Raw*). Power differences are calculated for the different variables from the last 3 min of either color exposure ("Color"), "Baseline", or "Recovery". The boxplots represent differences between the time points (whiskers: 2.5 and 97.5% percentile). Box colors represent the color conditions, *red*, *green*, *blue*, or *yellow*, always presented from *left* to *right* in this order. Significances: * $p < 0.05$, ** $p < 0.01$, and trends + $p < 0.1$

Table 38.2 Sensitivity of the MWA to the calculation parameters for the L-PFC

L-PFC	Color-Baseline				Recovery-Color			
	MD	MD	MD	MD	MD	MD	MD	MD
Calculation parameters	[O_2Hb]	[HHb]	[tHb]	StO_2	[O_2Hb]	[HHb]	[tHb]	StO_2
F1, $N = 101$, R1, PowT, 3 min	R↑↑, G↑↑	-	R↑, G↑↑	R↑	-	B↑	-	B↑
F1, $N = 101$, R1, PowT, all min	R↑, G↑↑	-	R↑, G↑	-	-	-	-	-
F2, $N = 300$, R1, PowT, 3 min	R↑, G↑↑	R↑	G↑	R↑	-	-	-	-
F2, $N = 300$, R2, PowT, 3 min	G↑↑	-	R↑, G↑	-	-	B↑	-	B↑
F2, $N = 300$, R3, PowT, 3 min	R↑	R↑	G↑	R↑	-	G↑	-	G↑
F1, $N = 101$, R1, PowP, 3 min	-	-	-	-	G↑↑	B↑↑	-	B↑
F1, $N = 101$, R1, PowAR, 3 min	R↑↑	-	-	-	B↑	B↑↑	-	B↑
	BL [O_2Hb]	BL [HHb]	Raw 760 nm	Raw 830 nm	BL [O_2Hb]	BL [HHb]	Raw 760 nm	Raw 830 nm
F1, $N = 101$, R1, PowT, 3 min	G↑	G↑	G↑	-	G↑, B↑, Y↑	B↑↑ Y↑↑	-	-

The different variables were either calculated from multi-distance (MD) or the Beer-Lambert law (BL) or directly from the RAW intensity channels. *F1* FIR filter with flat-top window, *F2* least-squares FIR filter, *3 min* power was calculated from the last 3 min of each period, *All min* power was calculated from whole period, *PowT* power was calculated from time series, *PowP, PowAR* power was calculated from Fourier transform (Matlab function periodogram) or auto-regressive model (order 100, Matlab function pyulear) as sum of spectrum times frequency resolution. Passbands: R1: 0.095–0.105 Hz. R2: 0.075–0.125 Hz. R3: 0.05–0.15 Hz. *R* red, *G* green, *B* blue, *Y* yellow. ↑ $p < 0.05$, ↑↑ $p < 0.01$

may be explained by either the artefact correction performed separately for all signals or the penetration depth. The MD approach extracts cerebral changes better than single distance approaches [17]. Few power changes were seen in the [HHb], which is pre-dominantly located in the venous compartment and indicate less MWA in this compartment. However, the increase in recovery after blue light exposure was observed in [HHb] and StO_2 and may indicate a MWA change in the venous compartment.

A MWA increase in recovery after blue light was mostly found applying filters with a passband around 0.075–0.125 Hz, but not for wider or narrower passbands or when including the whole period instead of the last 3 min. MWA increase during red or green light was seen for all passbands, but not when calculating the MWA from the frequency domain. It is possible that the signal noise was high enough to induce considerable variability in the approximate frequency domain transforms due to windowing (hamming windows were used). We observed a significant difference within the color conditions only for StO_2. A higher number of subjects would be necessary to observe significant differences between the colors also for the other variables.

Our fixed center passband frequency (0.1 Hz) may have reduced sensitivity, since not all subjects showed clear peaks at 0.1 Hz. Furthermore, we did not exclude non-responders, which further decreased sensitivity. Yellow light was a mixture from red and green, but no MWA was seen for yellow even though red and green showed MWA. Reasons may be the lower number of subjects contributing to the yellow light condition or that the actual green and red illuminances were lower as result of the superposition, compared to pure red or green illumination.

Altogether, we studied the effect of colored light on MWA. Our results indicate that MWA was, in accordance with our hypothesis, influenced differently by colored light, especially red, green and blue. The results vary depending on the calculation performed (filter, power calculation, signal and distance used). This raises the need for improved understanding of these differences and for a standardized MWA calculation procedure, e.g. by standardizing filter kind, range, order, and used signal for the MWA calculation.

References

1. Maisels MJ, McDonagh AF (2008) Phototherapy for neonatal jaundice. N Engl J Med 358(9):920–928
2. Chellappa SL, Gordijn MC, Cajochen C (2011) Can light make us bright? Effects of light on cognition and sleep. Prog Brain Res 190:119–133
3. Jacobs KW, Hustmyer FE Jr (1974) Effects of four psychological primary colors on GSR, heart rate and respiration rate. Percept Mot Skills 38(3):763–766
4. Schäfer A, Kratky KW (2006) The effect of colored illumination on heart rate variability. Forsch Komplementmed 13(3):167–173
5. Weinzirl J, Wolf M, Nelle M et al (2012) Colored light and brain and muscle oxygenation. Adv Exp Med Biol 737:33–36

6. Mayer S (1876) Studien zur Physiologie des Herzens und der Blutgefässe 6. Abhandlung: Über spontane Blutdruckschwankungen. Sitzungsberichte Akademie der Wissenschaften in Wien. Mathematisch-naturwissenschaftliche Classe. Anatomie 74:281–307
7. Julien C (2006) The enigma of Mayer waves: Facts and models. Cardiovasc Res 70(1):12–21
8. Fantini S, Franceschini MA, Gratton E (1994) Semi-Infinite-Geometry Boundary-Problem for Light Migration in Highly Scattering Media - a Frequency-Domain Study in the Diffusion-Approximation. J Opt Soc Am B 11(10):2128–2138
9. Hueber DM, Fantini S, Cerussi AE et al (1999) New optical probe designs for absolute (self-calibrating) NIR tissue hemoglobin measurements. Proc SPIE III 3597:618–631
10. Wray S, Cope M, Delpy DT et al (1988) Characterization of the near infrared absorption spectra of cytochrome aa3 and haemoglobin for the non-invasive monitoring of cerebral oxygenation. Biochim Biophys Acta 933(1):184–192
11. Scholkmann F, Spichtig S, Muehlemann T et al (2010) How to detect and reduce movement artifacts in near-infrared imaging using moving standard deviation and spline interpolation. Physiol Meas 31(5):649–662
12. Bumstead JR, Bauer AQ, Wright PW et al (2016) Cerebral functional connectivity and Mayer waves in mice: Phenomena and separability. J Cereb Blood Flow Metab 37:471–484. 0271678X16629977
13. Nilsson H, Aalkjaer C (2003) Vasomotion: mechanisms and physiological importance. Mol Interv 3(2):79–89. 51
14. Pradhan RK, Chakravarthy VS (2011) Informational dynamics of vasomotion in microvascular networks: a review. Acta Physiol 201(2):193–218
15. Rivadulla C, de Labra C, Grieve KL et al (2011) Vasomotion and neurovascular coupling in the visual thalamus in vivo. PLoS One 6(12):e28746
16. Yücel MA, Selb J, Aasted CM et al (2016) Mayer waves reduce the accuracy of estimated hemodynamic response functions in functional near-infrared spectroscopy. Biomed Opt Express 7(8):3078–3088
17. Tachtsidis I, Scholkmann F (2016) False positives and false negatives in functional near-infrared spectroscopy: issues, challenges, and the way forward. Neurophotonics 3(3):030401

Part IV
EPR Oximetry and Imaging

Chapter 39
Electron Paramagnetic Resonance pO_2 Image Tumor Oxygen-Guided Radiation Therapy Optimization

Boris Epel, Matt Maggio, Charles Pelizzari, and Howard J. Halpern

Abstract Modern standards for radiation treatment do not take into account tumor oxygenation for radiation treatment planning. Strong correlation between tumor oxygenation and radiation treatment success suggests that oxygen-guided radiation therapy (OGRT) may be a promising enhancement of cancer radiation treatment. We have developed an OGRT protocol for rodents. Electron paramagnetic resonance (EPR) imaging is used for recording oxygen maps with high spatial resolution and excellent accuracy better than 1 torr. Radiation is delivered with an animal intensity modulated radiation therapy (IMRT) XRAD225Cx micro-CT/ therapy system. The radiation plan is delivered in two steps. First, a uniform 15% tumor control dose (TCD_{15}) is delivered to the whole tumor. In the second step, an additional booster dose amounting to the difference between TCD_{98} and TCD_{15} is delivered to radio-resistant, hypoxic tumor regions. Delivery of the booster dose is performed using a multiport conformal beam protocol. For radiation beam shaping we used individual radiation blocks 3D-printed from tungsten infused ABS polymer. Calculation of beam geometry and the production of blocks is performed next to the EPR imager, immediately after oxygen imaging. Preliminary results demonstrate the sub-millimeter precision of the radiation delivery and high dose accuracy. The efficacy of the radiation treatment is currently being tested on syngeneic FSa fibrosarcoma tumors grown in the legs of C3H mice.

Keywords Electron paramagnetic resonance • Oxygen imaging • Radiation delivery • Cancer treatment • Image guided radiotherapy

B. Epel • M. Maggio • C. Pelizzari • H.J. Halpern (✉)
Center for EPR Imaging In Vivo Physiology; Department of Radiation and Cellular Oncology, University of Chicago, Chicago, IL, USA
e-mail: bepel@uchicago.edu; mmaggio@uchicago.edu; c-pelizzari@uchicago.edu; hhalpern@uchicago.edu

H.J. Halpern et al. (eds.), *Oxygen Transport to Tissue XXXIX*, Advances in Experimental Medicine and Biology 977, DOI 10.1007/978-3-319-55231-6_39

1 Introduction

Radiation therapy is a major mode of cancer treatment. It uses high-energy photons to destroy or damage cancer cell DNA, leading to cell death. Modern intensity modulated radiation therapy (IMRT) [1, 2] systems can deliver radiation beams with sharp spatial gradients over fractions of a cm in human patients. This is especially important for normal tissues that must be spared to ensure good post- treatment quality of life. Radiation oncologists have clear dose/volume thresholds above which normal organ function is compromised. These 'avoidance structures' provide clear instructions to the oncologist planning a radiation treatment, directing where the dose must be lowered.

Reduction of the dose delivered to normal tissues remains a challenging problem. Because delivery of the treatment involves propagation of radiation beams through the whole body, some radiation dose is delivered to normal tissues. Therefore, reduction of the treatment dose to the entire tumor will necessarily reduce normal tissue damage. Modern clinical practice strives to deliver a homogeneous dose distribution to the whole tumor. This does not take into account different cellular or regional radiation resistance and may be optimized.

Hypoxia (or abnormally low oxygenation) is a characteristic feature of solid tumors. Tumor hypoxia is both a result of abnormal tumor vasculature development [3] and a stimulus for the development of an aggressive cancer phenotype [4]. It is known that hypoxia creates radiation resistance [5]. Clinical studies of tumor hypoxia have indicated worse disease-free survival outcomes of patients with hypoxic head, neck and uterine cervix cancers [6]. Similar results were observed in mouse models [7].

Cell studies confirm that cells exposed to different oxygen levels demonstrate a different response to radiation treatment (Fig. 39.1a). When exposed to a low oxygen atmosphere the cells are three times more resistant to irradiation compared with oxygenated cells [5]. The relationship between the radiation sensitivity of the cells on treatment outcome can be modeled using the animal survival fraction vs the

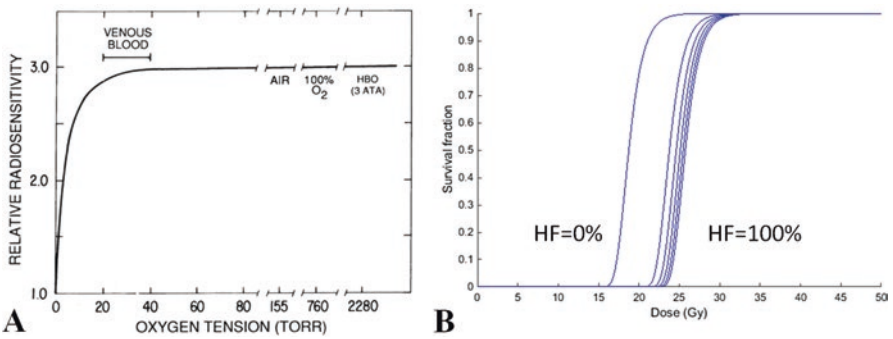

Fig. 39.1 (**a**) Radiation sensitivity of the cells to radiation as a function of their oxygenation, from [5]. (**b**) Expectation of animal survival as a function of radiation dose. Multiple curves for different tumor hypoxic fractions are shown

applied dose curve (Fig. 39.1b). The fraction of animals cured by a dose of radiation is calculated as the chance of the last cancer clonogen surviving the radiation dose. The dose that has a 50% of chance of destroying the last clonogen (surviving fraction 0.5) is called the tumor control dose, TCD_{50}. Figure 39.1b demonstrates modeled surviving fractions for intermixtures of oxygenated and deoxygenated cells. In a clinical setting, the homogeneous therapeutic dose (the dose exceeding TCD_{95}) for a fully hypoxic tumor is given. Figure 39.1b clearly shows that in well-oxygenated areas this dose can be reduced significantly, while in hypoxic areas a TCD_{98} and higher doses are necessary.

This establishes quantitative oxygen imaging as a basis for the determination of the dose to the regions of tumor hypoxia. Oxygen-guided radiation therapy (OGRT) may be a promising enhancement of cancer radiation treatment.

We are validating OGRT using mice tumors whose volumes are on average 380 microliters, a factor of 10–100 smaller than tumors in human subjects. This required the development of unprecedented sub-millimeter precision of radiation delivery. As a method for non-invasive pO_2 in vivo measurements, we used electron paramagnetic resonance (EPR) imaging [8, 9]. For radiation delivery we used the XRAD225Cx micro-CT/ therapy system. The radiation beams were shaped using blocks fabricated using 3D printing from GMASS tungsten infused polymer at the time of the experiment. This paper presents details on the instrumental aspects and validation of the OGRT protocol.

2 Methods

2.1 Oxygen-Guided Radiation Treatment

An overall scheme of the OGRT experiment if presented in Fig. 39.2. The experiment is started by obtaining MRI and oxygen EPR images. Anatomic MRI images were obtained using a Bruker 9.4 T imaging system. Ten-min partial oxygen pressure, pO_2 images were obtained using a 250 MHz pulse EPR imager [10] and injectable partially deuterated trityl OX63 (OX71) spin probe synthesized by the Novosibirsk Institute of Organic Chemistry. A spin-lattice relaxation-based oxygen imaging protocol was used [8].

In the second step, the MRI image is segmented based on tissue T_2 contrast to determine the tumor location. The MRI image is then registered with the EPR image and the tumor mask is transferred into the EPR image coordinate system. For the radiation target we used tumor areas with a $pO_2 \leq 10$ torr.

In the third step the CT image was obtained and registered with the pO_2 EPR image to locate the radiation target volume in the CT coordinate space. Then, the shapes of the radiation beams were calculated and radiation blocks were fabricated. Finally, radiation blocks were installed into the irradiator and the treatment plan was administered.

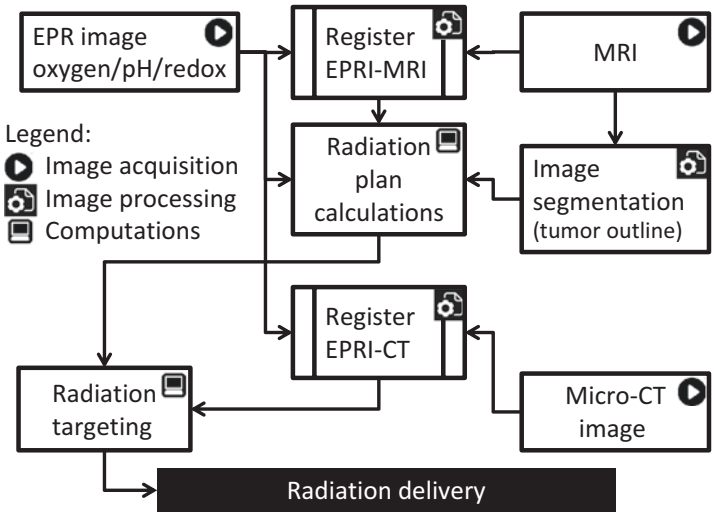

Fig. 39.2 Flowchart of the radiation treatment protocol

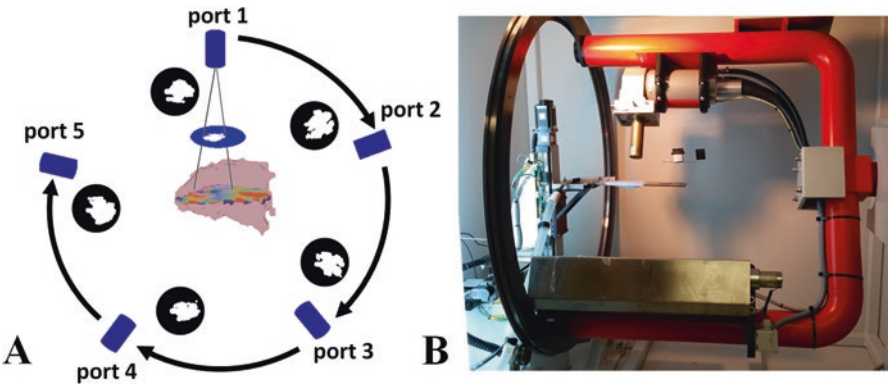

Fig. 39.3 (**a**) Formation of the conformal radiation beam shapes using the beam's eye view method. (**b**) Gantry and object table of the small animal CT/irradiator

2.2 Radiation Targeting

For administration of radiation treatment an XRAD225Cx micro-CT with a 225 kVp delivery system (Fig. 39.3b) was used. For the first treatment step, uniform irradiation was given to the whole tumor to a 15% tumor control dose (TCD_{15}) of 22.5 Gy. This dose was delivered using two opposed beams that covered the whole tumor in anterior-posterior, and posterior-anterior alignments. Then, a booster dose corresponding to the difference between TCD_{95} and TCD_{15} was delivered to hypoxic areas (see Sects. 2.3 and 2.4).

The booster dose was delivered using a five-port protocol (Fig. 39.3a). Five ports were chosen as a compromise between the dose delivery precision and the treatment duration. For each port the radiation head was oriented (as show in Fig. 39.3a) with 360/5 = 72 degree step, and 1/5 of the complete dose was delivered.

For beam shape calculation we used a conformal beam's eye view (BEV) approach. BEVs were calculated by projecting a line from the X-ray source through the radiation block and radiation target. As radiation target we used pO_2 image areas below 10 torr. For these calculations we created a grid in the plane of the radiation block with a pixel size of 0.025 mm × 0.025 mm. Those lines that were passing through the grid pixel and were intersecting any hypoxic area in the pO_2 image volume, resulted in a transparency mask for the radiation block.

For the animal protocol, to accommodate errors resulting in positioning of the object, image registration and tumor location, BEV were dilated by 1.2 mm.

2.3 Radiation Block Fabrication

3D printing is the only technology capable of fabricating radiation attenuation blocks for conformal beams in a short time on site. For block fabrication we used GMASS Tungsten Metal ABS (Turner MedTech, USA). This material contains ABS plastic infused with tungsten particles to a density of 4 g/ml. The blocks had radiation attenuation spectral properties of tungsten with overall attenuation of about one fourth of the lead block of identical thickness. Blocks were fabricated using fused deposition modelling (FDM) M2 3D printer (MakerGear, Beachwood, OH, USA) equipped with a 0.35-mm nozzle. For block manufacture the FDM printer melts the filament and extrudes it through the nozzle. The nozzle follows a tool path controlled by a computer-aided manufacturing software package, and the part is built from the bottom up, one layer at a time.

The radiation block transparency masks were exported as planar contour coordinates from the radiation planning software. These contours were then extruded and subtracted from the 3D model of radiation block creating the beam opening. The out-of-plane thickness of the blocks of 10 mm was chosen to provide 100-fold beam attenuation. OpenScad (http://www.openscad.org/) software was used to render the final radiation block 3D STL model. Simplify 3D software (https://www.simplify3d.com/) was used to prepare the STL model for 3D printing. The modest beam divergence was incorporated into the block design. The radiation block collimator holder (Fig. 39.4c) was 3D printed using the same material.

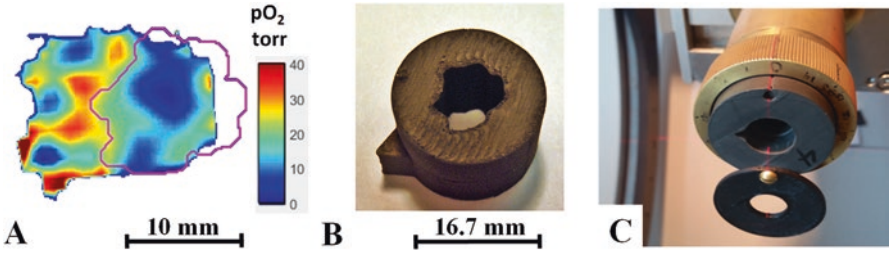

Fig. 39.4 (**a**) EPR oxygen image. The beam's eye view is shown with the magenta-colored contour. (**b**) Radiation block fabricated for this beam's eye view. (**c**) Radiation block holder

2.4 Radiator Calibration

Delivery of the radiation involves rotation of the gantry with the radiation source and collimator about the isocenter. Physical stress on the machine results in minor deviations of the radiation beam center from the isocenter, differing for each gantry angle. These deviations are reproducible and can be corrected for during radiation block fabrication. For geometrical calibration we used a circular beam targeted at a small lead sphere located at the isocenter of the machine. The beams were detected using the CT-detector of the irradiator. By offsetting the aperture position in the radiation block we ensured the location of the lead sphere shadow in the exact center of the radiation beam.

2.5 Radiation Delivery Validation

The delivered dose was validated using radiation sensitive Gafchromic™ EBT3 medical dosimetry film (Ashland, Fiskeville, RI, USA). The film itself was calibrated using an ion chamber. Based on our experience we assumed uniform film sensitivity within a single film batch.

For 3D spatial delivery validation, we constructed 3D phantoms from five to seven 22x22 mm radiation films of ~0.4 mm thickness spaced by 1-mm plastic spacers, overall 8–10.8 mm thick (Fig. 39.5a). The phantom had tubes passing through it for registration and treatment center definition, which was assigned to the center of the middle spacer identified by a hole in the spacer.

After the radiation protocol, using blocks as applied in animal treatment, the films were scanned and a digital phantom was formed. Spatial locations of the films were determined based on the CT image. The results were registered to a theoretical dose map using radiation planning software. The theoretical model included propagation of beams through the space without scattering or attenuation.

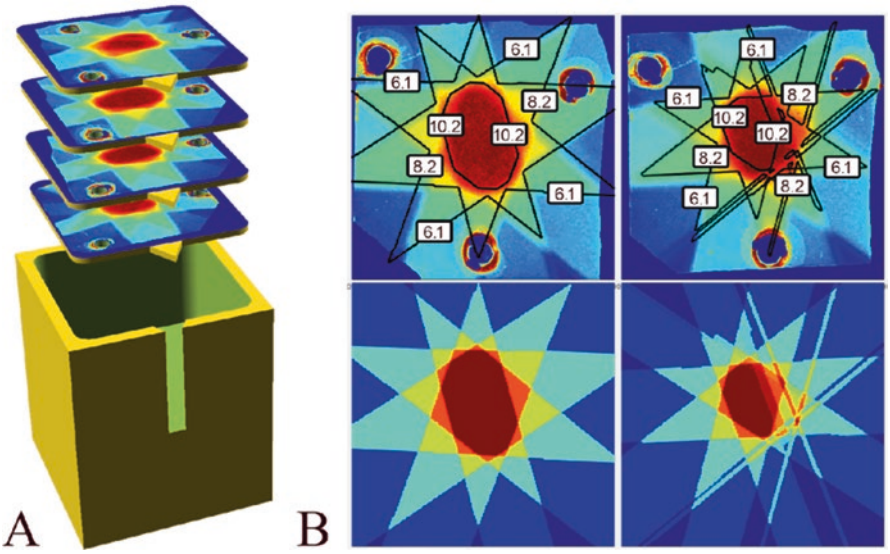

Fig. 39.5 (**a**) 3D rendering of the phantom used for radiation delivery validation. Four dosimetry films and spacers are shown. (**b**) Radiation doses obtained from dosimetry films (*top row*) overlapped with dose isolines from theoretical beam calculations (*bottom row*). The color maps of all plots are identical

2.6 Image Registration

EPR and MRI images were registered with the help of 3–4 fiducials embedded into a vinyl polysiloxane dental mold [11]. For MRI, tubes filled with water were used. EPRI fiducials had 2 mM of narrow line FINLAND spin probe. Empty tubes were used for CT imaging. The ArbuzGUI MATLAB toolbox, developed by the Center for EPR Imaging in vivo Physiology at the University of Chicago, was used for image registration [http://epri.uchicago.edu].

2.7 Animal Model

FSa fibrosarcoma tumors grown in the gastrocnemius of the legs of C3H mice were used. Animal experiments followed USPHS policy, and were approved by the Institutional Animal Care and Use Committee.

3 Results and Discussion

3.1 Validation of Spatial Radiation Distribution

The 3D rendering of the radiation validation phantom is shown in Fig. 39.5a. For validation we used radiation films interleaved with spacers to achieve the overall phantom length of about 8–10.8 mm. Although the fiducial tubes penetrating the phantom are not shown in the figure, the holes for fiducial tubes are visible. We applied the radiation protocol designed for one of the animals to this phantom. The top row of Fig. 39.5b shows the radiation doses as determined from the films. The traces of five beams are visible. Due to beam attenuation the dose on the enter side of the phantom is slightly higher than the dose at the exit side. The bottom row of Fig. 39.5b shows the results of beam propagation calculations. The dose isolines from theoretical calculations are overlaid with the experimental dose results to facilitate the comparison. Differences between the predicted radiation beam edges and the evident location of the edges in the film, were due to rapid tumor leg contour in the longitudinal direction and an estimated 0.5–0.7 mm setup location error.

For precise evaluation of the spatial errors, a 3D reconstruction of the delivered dose from the radiation films is required. At this point we restricted our evaluation to in-plane beam deviation only. This analysis can overestimate the errors, especially for beams administered at small angles to the film plane.

3.2 Conformal Versus Spherical Radiation Delivery

We compared a 5-port conformal radiation delivery protocol (Figs. 39.5a and 39.6a) used in this work, with a much more commonly used spherical delivery protocol. For a spherical protocol, a circular aperture is used and radiation is delivered while the radiation source is moving along a circular trajectory around the target (Fig. 39.6d).

Radiation volume histograms provide an assessment of radiation delivery to target and non-target volumes. Ideally, 100% of the target (for this study, hypoxic tumor areas) should receive a full dose and 0% of non-target (for this study, the well-oxygenated part of tumor) should receive no radiation. In practice, the last condition is never satisfied. The radiation beams propagating through the object will necessarily deliver some radiation to non-target areas; however, the overall dose can be minimized.

For the comparison, we have chosen a spherical delivery protocol with the best discrimination between target and non-target areas. This protocol delivers a full (100%) dose to only ~80% of target. By increasing the beam diameter this number can be increased to 100%. However, in this case, the hypoxic and most of the well-oxygenated areas might receive similar doses. The delivery of a full radiation dose to non-target area exceeds 35% (Fig. 39.6b). The histogram for conformal beams

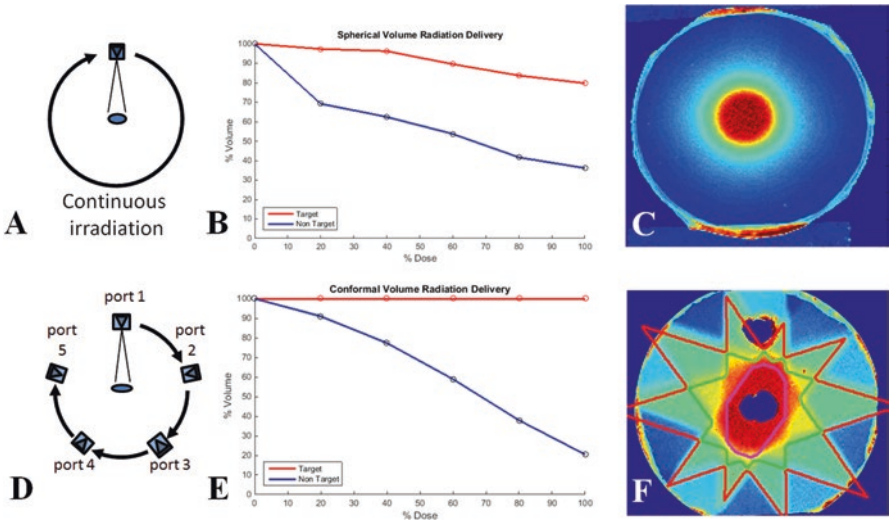

Fig. 39.6 (**a**–**c**) Spherical radiation delivery protocol. (**d**–**f**) 5-port conformal radiation protocol. (**b**) and (**e**), corresponding radiation volume histograms. (**c**) and (**f**), dose distribution in the central plane as detected by the radiation film

(Fig. 39.6e) is considerably closer to our expectations for precise radiation treatment: 100% of the target volume receives a complete dose and only 20% of the non-target area receives a complete dose.

3.3 Overall Radiation Delivery Precision and Outlook

The OGRT described here has to take into account a number of uncertainties and errors that have accumulated during the procedure. In our estimation, the largest uncertainty is introduced by EPR oxygen image spatial resolution. The numeric resolution of the image was taken as 2 voxels of the image matrix, or $0.66 \times 2 = 1.32$ mm. Studies that evaluated image resolution from the image representation of an object edge reported a similar value [9, 10]. Image registration uncertainty can be evaluated in a similar way, only in this case EPR fiducial images had a twice higher resolution, or 0.66 mm. Adding to these uncertainties the 0.4 mm error of radiation delivery and 0.4 mm 3D printing accuracy, one can estimate the overall precision of approximately 1.2 mm. To ensure guaranteed radiation delivery, the treatment protocol should incorporate at least a 1.2 mm margin. For our experiments we resorted to the safer 1.2 mm margins. The apertures of the radiation blocks for animal experiments are dilated by this margin.

Although it is impossible to predict how successful the application of OGRT will be for cancer treatment, this work is an important step in the development of targeted radiation treatment for small animals. This long awaited validation of the new technology will allow for targeted radiation delivery on affordable animal tumor models.

4 Conclusions

We have demonstrated that radiation delivery to rodents with sub-millimeter precision is possible. We are looking forward to the results of oxygen-guided radiation therapy in animals.

Acknowledgments This study was supported by NIH grants P41 EB002034 and R01 CA98575.

References

1. Leibel SA, Fuks Z, Zelefsky MJ, Hunt M, Burman CM, Mageras GS, Chui CS, Jackson A, Amols HI, Ling CC (2003) Technological advances in external-beam radiation therapy for the treatment of localized prostate cancer. Semin Oncol 30:596–615
2. Mundt A, Roeske J (2005) Intensity modulated radiation therapy. B.C.Decker, Hamilton
3. Vaupel P, Mayer A (2007) Hypoxia in cancer: significance and impact on clinical outcome. Cancer Metast Rev 26:225–239
4. Graeber TG, Osmanian C, Jacks T, Housman DE, Koch CJ, Lowe SW, Giaccia AJ (1996) Hypoxia-mediated selection of cells with diminished apoptotic potential in solid tumours. Nature 379:88–91
5. Rockwell S, Dobrucki IT, Kim EY, Marrison ST, Vu VT (2009) Hypoxia and radiation therapy: past history, ongoing research, and future promise. Curr Mol Med 9:442–458
6. Hockel M, Schlenger K, Aral B, Mitze M, Schaffer U, Vaupel P (1996) Association between tumor hypoxia and malignant progression in advanced cancer of the uterine cervix. Cancer Res 56:4509–4515
7. Elas M, Magwood JM, Butler B, Li C, Wardak R, Barth ED, Epel B, Rubinstein S, Pelizzari CA, Weichselbaum RR, Halpern HJ (2013) EPR oxygen images predict tumor control by a 50% tumor control radiation dose. Cancer Res 73:5328–5335
8. Epel B, Bowman MK, Mailer C, Halpern HJ (2014) Absolute oxygen R1e imaging in vivo with pulse electron paramagnetic resonance. Magnet Reson Med 72:362–368
9. Epel B, Halpern H (2013) Electron paramagnetic resonance oxygen imaging in vivo. Electron Paramag Res 23:180–208
10. Epel B, Sundramoorthy SV, Mailer C, Halpern HJ (2008) A versatile high speed 250-MHz pulse imager for biomedical applications. Conc Magn Reson B 33B:163–176
11. Haney CR, Fan X, Parasca AD, Karczmar GS, Halpern HJ, Pelizzari CA (2008) Immobilization using dental material casts facilitates accurate serial and multimodality small animal imaging. Conc Magn Reson B 33B:138–144

Chapter 40
Using India Ink as a Sensor for Oximetry: Evidence of its Safety as a Medical Device

Ann Barry Flood, Victoria A. Wood, and Harold M. Swartz

Abstract Clinical EPR spectroscopy is emerging as an important modality, with the potential to be used in standard clinical practice to determine the extent of hypoxia in tissues and whether hypoxic tissues respond to breathing enriched oxygen during therapy. Oximetry can provide important information useful for prognosis and to improve patient outcomes. EPR oximetry has many potential advantages over other ways to measure oxygen in tissues, including directly measuring oxygen in tissues and being particularly sensitive to low oxygen, repeatable, and non-invasive after an initial injection of the EPR-sensing material is placed in the tumor. The most immediately available oxygen sensor is India ink, where two classes of carbon (carbon black and charcoal) have been identified as having acceptable paramagnetic properties for oximetry. While India ink has a long history of safe use in tattoos, a systematic research search regarding its safety for marking tissues for medical uses and an examination of the evidence that differentiates between ink based on charcoal or carbon black has not been conducted. Methods. Using systematic literature search techniques, we searched the PubMed and Food and Drug Administration databases, finding ~1000 publications reporting on adverse events associated with India/carbon based inks. The detailed review of outcomes was based on studies involving >16 patients, where the ink was identifiable as carbon black or charcoal. Results. Fifty-six studies met these criteria. There were few reports of complications other than transient and usually mild discomfort and bleeding at injection, and there was no difference in charcoal vs. carbon black India ink. Conclusions. India ink was generally well tolerated by patients and physicians reported that it was easy to use in practice and used few resources. The risk is low enough to justify its use as an oxygen sensor in clinical practice.

Keywords Carbon particles • EPR sensot • India ink • Structured literature review • Adverse Events

A.B. Flood (✉) • V.A. Wood • H.M. Swartz
EPR Center for the Study of Viable Systems at Dartmouth, Geisel School of Medicine at Dartmouth College, Hanover, NH, USA
e-mail: Ann.B.Flood@Dartmouth.edu

H.J. Halpern et al. (eds.), *Oxygen Transport to Tissue XXXIX*, Advances in Experimental Medicine and Biology 977, DOI 10.1007/978-3-319-55231-6_40

The clinical value of repeated measurements of oxygen in tissues rests fundamentally on the central roles that oxygen levels play in a large array of physiological and pathophysiological processes. Despite this importance, oxygen in tissues is seldom measured directly. If measured at all, oxygen level is assessed in the vascular system, while the greater need for many clinical applications is to know the oxygen level in tissues. Diseases whose treatment strategies would benefit from taking tissue oxygen into account include tumors, peripheral vascular disease, and wound healing. For example, in radiation treatment of cancers, the level of oxygen in the tumor is the single most important variable that affects the treatment outcomes [1]. Developing treatment plans taking this into account, especially if the oxygen in the patient's tissues can be successfully manipulated to improve the therapeutic ratio, is a key motive for identifying oximetry methods than can provide this information to clinicians while being readily and noninvasively integrated into clinical care for these patient groups.

Several unique features of EPR oximetry have the potential to address these needs, i.e., after a paramagnetic sensor is initially injected or implanted into a tissue of interest, EPR oximetry can make repeated and noninvasive measurements that directly assess tissue oxygen. These EPR measurements can be made repetitively in two clinically important ways: (1) Because scans can be taken virtually continuously for several minutes while patients rest comfortably, minute by minute changes can be assessed, including evaluating whether the tissue is responsive to the patient's breathing enriched oxygen. (2) The patient can also be measured again at any time, over a period of up to many months if appropriate. This allows evaluating the tissue's response to therapy and monitoring progression of disease. Another clinically important advantage of EPR is that it is particularly sensitive to measuring very low levels of oxygen in tissues, i.e., at the hypoxic levels that are prognostic of a tumor being potentially more resistant to therapy and/or of its greater likelihood of being aggressive. In order to take advantage of these features of EPR, a paramagnetic sensor needs to be initially injected into tissue. India ink (reported here) is one such sensor.

India ink as a paramagnetic sensor has several advantages. For patients, by way of being similar to cosmetic tattoos, a mark made by superficially injecting paramagnetic India ink can be easily understood. Also, because of its similarity to cosmetic tattoos and medical ink markers already in use, the regulatory path to marketing it is relatively straightforward. The disadvantage for patients is its permanent cosmetic appearance, even when small or not publicly visible (such as on the bottom of the foot or inside the mouth, cervix or colon). For the currently available clinical applications using L-band EPR in vivo oximetry, the principal technical disadvantage is its capability to place and measure sensors in tissues only only within ~5–35 mm from body surfaces. In particular, because of the relatively broad line of India ink, the working depth is less than 10 mm; moreover, in order to get a representative depth in the tumor, we usually restrict the measurements to tumors that are within 5 mm of the surface. (In contrast, the working depth of L-Band for

very narrow-lined oximetric materials such as sensors made from lithium phthalocyanine can be 30 mm; in this case, we restrict the measurements to tumors within 25 mm. Under advanced preclinical development and preparations for initiating clinical trials is an implantable resonator that would remove any restriction on depth [5, 6]).

For India ink to be successful as a sensor for EPR oximetry, it is necessary to ensure that its carbon particles have strong EPR signals that are sufficiently sensitive to the presence of oxygen. To that end, Bernard Gallez et al. [2] have investigated many candidate inks using *carbon black* [3] and *charcoal* [4]. Swartz et al. [5, 6] have successfully used two inks with the necessary EPR properties to measure tissue oxygen in vivo in 27 humans with 36 ink injections using L-band EPR. Spurred by the importance of conducting clinical studies of oxygen in tumors, this paper reports on a systematic review of the medical literature conducted to determine whether there are any safety concerns in using India ink for oximetry and whether there is evidence of any differences in inks based on charcoal or carbon black.

India ink is composed of carbon particles combined with a suspending agent (i.e., water and potentially other ingredients) to form an aqueous suspension. Carbon particles are a large class of compounds that may have chemisorbed oxygen complexes such as carboxylic and phenolic groups on their surfaces to varying degrees, depending on the conditions of their manufacture.

When carbon particles are used in humans, three attributes about carbon are most significant: its purity, whether it is activated, and how it was made:

Factor 1: *Purity* is relevant because, while carbon is basically inert with a several-thousand-year-long history of its safe use in humans, impurities associated with incomplete combustion during its production can have more, or more serious, side effects. For example, polycyclic aromatic hydrocarbons (PAHs) that come from incompletely combusted fuels may be carcinogenic.

Factor 2: *Activation* of carbon particles refers to being reheated and oxidized after their initial production, with the outcome that particles become highly porous. When carbon is prescribed to be ingested for people following consumption of a toxic substance, this property is desirable because it enhances carbon particle's adsorptive properties, making it more effective as a detoxifier. For this reason, *activated* forms of carbon are more likely to be available in pharmacies for human use. However, there is no evidence that this property impacts its safety or effectiveness when used for tattooing/medical marking or as a sensor for oximetry.

Factor 3: How it is made (and from what). In part because there are numerous variations of carbon, numerous synonyms of each variant, and an inconsistent use of these synonyms [7], the safety data sheets typically use a name and the unique numerical identifier of chemical substances assigned by Chemical Abstracts Service (CAS). This review refers to the two main classes of carbon particles used in India ink as *carbon black* (CAS 1333-86-4 [or −3 or −5]) or *charcoal* (CAS 7440-44-0).

While there is no evidence that one class of carbon is safer than the other when used in medical or cosmetic marking, there is a long history of cosmetic tattoo inks being more likely to be made from *carbon black*. In addition, US brands of inks used in medical marking usually use *carbon black*, while European, Asian and Australian brands for medical marking typically use *charcoal*. Therefore, this review has deliberately distinguished these two classes of carbon in reports of adverse events and will evaluate whether there is any evidence of differences between them.

As noted above, India inks also have a suspending component. There is only one ingredient common to all cosmetic tattoo inks and all medical marking inks found in our review: water. While charcoal based inks tend to not add anything else, most cosmetic tattoo inks and carbon black inks have other ingredients added for purposes of improving preservation, viscosity, pH, etc. (See Table 40.1 for details.) While most of these ingredients are food grade and listed as generally regarded as safe (GRAS), these additional ingredients have the potential to be the source of any side effects and so need to be considered when evaluating the safety of India ink for markers in oximetry.

Beyond the ingredients of the 'India ink' per se, other factors may impact whether any problems are reported in each study, e.g., the sterility of the manufacturing process, the hygienic practices of the tattooist or the tattoo facilities, the training and qualifications of the injector, or any problems encountered during its administration (like unintentionally perforating an anatomical border during injection of a polyp in the colon). Similarly, medical use studies may report on the efficacy of the marker for its intended use, e.g., if the intent is to mark areas for future resection, the authors may focus on how visible the marker was during surgery. These problems may not have any bearing on the marker as used in oximetry. Consequently, we will consider these additional factors as important contexts in evaluating the evidence of the safety of India ink for oximetry.

India inks deliberately injected as permanent tattoos have a long history of usage in humans dating back at least several thousand years [8, 9]. The ~5300-year-old mummified 'iceman' whose tattooed remains were recovered in 1991 from a glacier provides evidence of the long use of carbon markings in Europe, also suggesting their likely association with medical treatment [10, 11]. More importantly, there is an extensive body of evidence, based on millions of people from all races many of whom have had their tattoos for a lifetime, that carbon tattoos are generally very safe and not life-threatening.

The object of carbon marking of the skin, whether for cosmetic, punitive or medical reasons, is to leave a permanent and visible marking that is otherwise relatively inert. Because it is administered using needles to push or inject the particles below the epidermal layer, acute biological side effects such as superficial pain and bleeding may occur, which should resolve within ~2 days [12].

The intended uptake and long-term storage of ink particles by the dermal and sub-cutaneous fibroblasts are based on a specific non-inflammatory defense mechanism that protects the living body against injuries and invasions by non-toxic

Table 40.1 Black dye and other ingredients in brand name India inks, by reviewed use in cosmetic tattooing, medical marking or both

Use for ink (brands)	Dye (CI & CAS codes)	Other ingredients[a]
Cosmetic Tattoo Only (Demco Black, Makkuro Sumi Blackout Tattoo, True Black, Kabuki Outlining Ink, Wilson's Black Tattoo Ink)	Carbon Black CI#77266 CAS# 1333-86-4 Black Pigment 7 CI#77266	Water Ethyl alcohol Isopropyl alcohol Shellac Propylene glycol Hamamelis virginiana (Witch Hazel) Glycerin (glycerol) PEG-200 glyceryl stearate PVP (polyvinylpyrrodone) Rheology modifier acrylic mionormer
Medical Marking and Non-Medical Uses (Kor-i-Noor, Pelikan, Higgins Black Magic, Defco/BD India Ink)	Carbon Black CAS# 1333-86-3	Water Ammonia hydroxide Phenol Ethylene glycol Shellac Natural resins Undisclosed nonhazardous ingredients
Medical Marking Only (*carbon black*: Accu-Tatt, Steritatt, Endomark, Spot, Black Eye, Printex) (*charcoal*: Sterimark, Carbo- Rep, Charcotrace, Carlo Erba)	Carbon Black CI#77266 CAS# 1333-86-5 Charcoal CAS# 7440-44-0 Activated Charcoal CAS# 7440-44-0	*Both:* Water, Sodium chloride *Carbon black inks only*: Hamamelis virginiana/Witch Hazel Glycerin/Glycerol Isopropyl alcohol polysorbate Benzyl alcohol Simethicone Carboxymethylcellulose sodium salt *Charcoal inks only:* Gum Arabic [b]Sodium hydroxide [b]Hydrochloric acid

[a]Other ingredients include any used for suspension, preservatives, improved viscosity, medical preventive uses, etc. Most MSDS indicate, or use CAS indicating, ingredients are food safe or cosmetic safe and some add 'sterile' or 'medical grade'
[b]Listed as being used for pH only as needed (only for Charcotrace)

foreign bodies without necessarily involving immune reactions. Studies of the basic pathology of tattoos done in animals [13] and humans [14] substantiate the body's response to carbon as an inert foreign object. These studies show that, within 24 h after injection, carbon particles are endocytosed by fibroblasts as well as macrophages in the dermis and subcutis. Biopsies of human tattoos at 1 month showed no sign of inflammation, scarring or necrosis. Biopsies at 1, 3, 40 years all found stable carbon particles within cell membranes. Macrophages, present in the epidermis, were observed to take up larger particles and were at least partially responsible for initial removal of some of the ink from the epidermis With the reformation of the basement membrane as recovery from the trauma from the needle

is completed, there is no further removal by macrocytes**.** Because the fibroblasts tend to remain in place and live a long time, the carbon particles they contain remain permanently embedded in the body and in their original location.

Of particular relevance for this review are medical uses of carbon particles, particularly as used for marking, which parallel the intended use for oximetry. Seven uses of inks for medical marking have been reported in the literature: (1) marking the gastro-intestinal tract for future surgical biopsy or removal, e.g., marking polyps or tumor sites in the colon for rectal and sigmoid resection [15–24]; (2) marking nonpalpable tumors in the head and neck, e.g., marking recurrences, detectable only by imaging methods after prior thyroidectomy, for surgical resection [25–27]; (3) marking nonpalpable breast tumors for surgical removal [28–31] or for stereotactic marking of the track during needle biopsy to guide anticipated future surgery [32–35]; (4) marking the field of radiation for radiotherapy delivered in multiple fractions [36]; (5) marking the periphery of breast cancer tumors for future surgery following neoadjuvant chemotherapy which might change the original margins [37]; (6) identifying the sentinel lymph node of primary tumors where the route of lymphatic drainage is ambiguous such as head and neck, breast cancers in the medial third of the breast, or periclitoral vulvar tumors, which may have unilateral or bilateral lymphatic drainage [38]; and (7) marking superficial tissues to use as a paramagnetic sensor for EPR oximetry [5, 6, 39].

There are four primary ways that medical uses differ from cosmetic tattooing (in addition to being more likely to use inks manufactured or prepared in-house under more controlled circumstances that adhere to pharmacopeia standards). First, medical marking uses a hollow needle for injecting the ink rather than a tattoo machine, with the intent to place the ink superficially but below the dermis or mucosal surface. Second, medical uses may target tissues not used in cosmetic tattoos, e.g., the submucosa of the colon or oral cavity or deeper tissues including tumors. Third, although pigments other than carbon-particle-based may be used in medical marking, the purposes are not cosmetic and so a more restricted set of pigments (green, blue or carbon particles) are used. Fourth, injections of pigment at a single site may be larger (e.g., the volume of pigment injected deep into the submucosa and transmural regions prior to colorectal neoplasm resections [40]).

One very pertinent result of the very lengthy and widespread use of India ink in human subjects was that the Food and Drug Administration (FDA) does not claim regulatory jurisdiction over its manufacture and use. (Note: worldwide, in the EU, Asian countries, and New Zealand/Australia among others, governments have also opted not to regulate the inks injected into humans.) Instead, the FDA has chosen to designate all such inks (whether used for cosmetic or medical marking) as 'cosmetics' [41] which do not require FDA approval based on evidence of its safety and efficacy before being marketed. Manufacturers may optionally choose to apply for a 510(k) premarketing notification, e.g., two US carbon black inks (Spot® and Endomark™) are marketed as an approved 'medical device' for marking.

While the peer-reviewed literature and marketing brochures often contain claims about the safety of using India ink as a medical marker, the contents are not based

on a systematic review of the available evidence and may be oriented toward enhancing sales or demonstrating its use. Therefore, we undertook a systematic search of the published literature and other key databases to examine available evidence about the safety of India ink used in medical marking and to obtain data about the inks that would allow differentiating between carbon black and charcoal.

The databases used in the systematic search were PubMed (for peer-reviewed articles) and the FDA's database for reporting post-marketing events and ClinicalTrials.gov (for other official but non-peer-reviewed sources). A keyword and title search resulted in 975 articles, dating from 1893 through July 2016, that reported clinical studies of adverse events. ABF and VAW independently reviewed the titles and abstracts of all 975, eliminating those reporting only on tattoo *removal*, nonmedical or chemical analyses, medical uses other than for marking (e.g., detoxification), nanoparticles, or animal studies. All studies cited in the manufacturer's website for brand name medical marking inks were included. Among the remaining 178 articles reviewed in detail, 46 were dropped after reading of the article revealed that they were not pertinent. In addition, where articles did not specify the type of carbon used, the safety data sheets for named manufacturers were consulted to distinguish charcoal and carbon black. Nonetheless, the majority of articles about cosmetic tattoos and 42% of those reporting medical uses did not provide enough information to distinguish carbon black from charcoal ink.

Indeed, among cosmetic articles, most pigments were unidentified beyond their color: 63.4% reporting on 'black' pigment were case studies involving one or two people with tattoos, and 24.4% were broad overviews about tattooing and its general potential for side effects (i.e., were not systematic reviews). Among the remaining 12.2%, three were surveys about the experience of people with cosmetic tattoos and two were studies of cadaver tissue containing cosmetic tattoos.

As reported in the three surveys and the overviews of cosmetic tattoos, the overall rate of experiencing a problem associated with black ink is very low (~2%). Although there are rare serious complications [42], the overwhelming majority of problems, if any, were not serious, i.e., would not be reportable adverse events in a clinical study. (Of note, the most common 'problems' associated with cosmetic tattoos, infection due to poor hygienic practices during or following the tattooing, 'regret' and desire to remove the tattoo, are not associated with a pigment type per se. Likewise, transient bleeding and soreness are associated with the tattooing process, not the pigment.)

Potential problems associated with black ink in cosmetic articles included:

(a) Acute reactions (i.e., usually resolving in a few hours or days): local reactions, bleeding, pain and local inflammation (lasting longer with infection). Local reactions reported include local itchiness, redness, swelling, stinging.
(b) Chronic reactions (i.e., late onset and/or lasting for several weeks or longer): continuing or late onset local reactions, color fading, granulomas (i.e., non-painful raised protuberances at the edge or on the surface of the tattoo), scar formation, excessive reaction to foreign bodies, and sensitivity to light.

Of particular interest here are the 53 articles that discussed any type of medical use for marking *and* identified the pigment as either carbon black (62.3%) or charcoal (37.7%). For the details reported in this summary, we also excluded the case studies, studies with <16 patients, and the overviews from this group, leaving (a) 11 studies involving a total of 547 patients with ≥1 injections of carbon black ink (Table 40.2) and (b) 12 studies, totaling 3850 patients with ≥1 injections using charcoal ink (Table 40.3). All 23 of these larger studies involved using carbon-based inks for pre-surgical marking, albeit used in a variety of organs, e.g., colon, breast, esophagus, stomach. Each study was carried out in a different medical center located in 11 different countries.

This final, most pertinent group of 23 large studies reported either no or only a few minor problems attributable to either carbon black or charcoal ink. No acute symptoms related to hypersensitivity or granulomas were reported for either type of ink.

There were some apparent differences between charcoal and carbon black inks: The charcoal studies were more likely to mention acute pain or bleeding, but the rate of experiencing any pain was well under 1% and usually described as well tolerated or mild and transient, i.e., associated with the injection. One patient's lesion was temporarily enlarged. For carbon black inks, three studies reported local dispersion of the ink. One study using ink to mark sentinel lymph nodes reported that one *non*-sentinel node was marked. However, these few differences in reporting outcomes do not appear to be attributable to the ink so much as to the medical use and the absence of any standards for clinical studies to report outcomes for procedures that are adjuvant to other therapies. Because the ink was only ancillary, authors if discussing the ink at all tended to focus on whether the ink performed adequately as a marker to correctly and readily identify lesions, whether patients tolerated the injections well, and the advantages for clinicians, i.e., how easily the injection was performed and how little time or few financial resources it necessitated.

Because many medical uses involved surgical resection, postsurgical specimens could be examined. For such studies, for both charcoal and carbon black ink, the reported histology was generally consistent with the expected low-grade biological response to ink as an inert foreign object, i.e., most were mild and consistent with the ink being labeled as 'well tolerated'. The typical time between injection and obtaining the specimen was ~14 days when used for pre-surgical marking. However, for other uses, or when the lesion was not resected, the follow-up period reported was up to 14 months for carbon black and 7 years for charcoal, although no long-term problems were reported.

In summary, the overwhelming body of evidence suggests that both carbon black and charcoal inks used in medical marking are well tolerated by patients and easily performed with minimal resources of time or supplies in a clinical setting. Based on this systematic search of studies over several decades of worldwide experience, we conclude that the evidence based using charcoal and carbon black inks for medical marking supports the safety of its use as a paramagnetic sensor for oximetry.

Table 40.2 Review of 11 studies with >16 subjects, using carbon black based inks for medical marking

Author (ref #) Year country	Ink brand or homemade in pharmacy	Medical use	# of study participants and areas injected	Adverse events/ reactions	Other problems/comments?
Sun [24] 2009 China	Pelikan	Long-term localization of atrophic gastritis	53 patients	None	None
Fennerty [17] 1992 USA	Pelikan,	localization of colonic lesions	26 patients with 32 india ink tattoos in colonic mucosa	Biopsies showed carbon particles in the mucosa, but no inflammatory reactions.	The mean follow-up time was 14 months. All follow-up visits showed the mucosa still darkly tattooed
Shaffer [22] 1999 USA	Difco India Ink (now BD)	localization of Barrett's mucosa in esophagus	19 patients	None	None
Shatz [23] 1991 USA	Higgins	Localization of colonic lesions	64 patients	None	One patient had ink injected through the wall of the sigmoid into the peritoneal cavity, but was asymptomatic. Leakage may occur and obscure the polypectomy site.
Choy [38] 2015 USA	Spot	Localization of axillary lymph nodes (breast cancer)	28 patients	Inadvertent staining of lymphatic channels proximal to the node, migration of ink between nodes causing inadvertent staining of additional nodes.	One tattoo wasn't visualized. Authors believe that may be due to the injection being a small volume. For 3 patients the pigment was detected during surgery, but not during histology. Staining of a lymph node that was not a sentinel node occurred in one patient.

(continued)

Table 40.2 (continued)

Author (ref #) Year country	Ink brand or homemade in pharmacy	Medical use	# of study participants and areas injected	Adverse events/ reactions	Other problems/comments?
Hwang [18] 2010 Korea	Spot	Localization of colonic lesions	20 patients	Local leakage was seen with one patient (without peritonitis or abdominal pain). No other adverse events.	India ink does not diffuse through the mesentery and is thus permanent.
Park [20] 2008 Korea	Spot	Localization of colorectal tumors	63 patients	1 patient had ink diffused extensively. 6 patients had localized diffusion of ink; 1 patient had chills.	Patient with extensive diffusion made lesion hard to see.
Cipe [16] 2016 Turkey	Spot	Localization of distal surgical margin for rectal cancer	40 patients received marking; 25 patients were controls.	None	None
Aboosy [15] 2005 Netherlands	Rotring	Localization of soft colorectal lesions	19 patients with small lesions	None	5 patients had India ink particles present in lymph nodes
McArthur [19] 1999 USA	Koh-I-Noor,	Localization of colonic lesions	195 patients: 50 marked before surgery and 145 marked for future localization	No patients reported any incidence of fever or persistent abdominal pain and no examinations revealed evidence of abdominal tenderness.	Ink was injected through the bowel wall in a few cases.
Salomon [21] 1993 USA	Koh-I-Noor (& homemade)	Localization of colonic lesions	20 patients; 12 had undergone resection.	2 patients had pigmented histiocytes and mild chronic inflammation. Others had superficial mucosal ulceration, granulation of tissue containing ink stained histiocytes, ink staining of macrophages in local lymph nodes.	They were unable to keep the homemade ink in suspension so only Koh-I-Noor was used.

Table 40.3 Review of 12 studies with >16 subjects, using charcoal India inks for medical marking

Author (ref #) Year country	Brand name or 'Homemade' in pharmacy	Medical use	# of study participants and areas injected	Adverse events/ reactions	Problems not related to pigment/ comments
Mathieu [37] 2007 France	Sterimark	Localization of breast carcinoma	109 total patients:	Pain from injection in 6 pts. No other pain, inflammation, or redness observed	none
Chami [25] 2005 France	Sterimark	Ultrasound guided localization of recurrent thyroid lesions	101 lesions from 53 patients	3 patients had marked pain without other complications (one revealed neuroma).	Thirteen lesions had been injected but were not found intraoperatively. Carotid artery was injured in two cases. Histological analysis was difficult for one granuloma . Ink sometimes blocked in needle.
Cavalcanti [33] 2012 Brazil	Homemade	localization of breast lesions using ultrasound or mammography	135 specimens from 109 patients	No symptoms reported. In all specimens, foreign body granulomas: Acute inflam: 57 mild, 15 mod, 5 severe with abscess. Chronic inflam: 111 mild, 17 mod. 12 fat necrosis. 1 displacement artifacts	Comfortable for the patient and easy to perform. No impairment to histological analysis from injection.
Kang [26] 2009 Korea	Homemade	Ultrasound guided localization of recurrent thyroid lesions	83 lesions in 55 patients	No clinically important complications. No intolerable pain or bleeding.	Two pts. had visible dots. 3 lesions could not be injected due nearness to major vessels. 2 lesions could not be detected by surgeons due to fibrosis.

(continued)

Table 40.3 (continued)

Author (ref #) Year country	Brand name or 'Homemade' in pharmacy	Medical use	# of study participants and areas injected	Adverse events/ reactions	Problems not related to pigment/ comments
Ko [28] 2007 Korea	Homemade	Ultrasound guided localization of breast lesions	164 lesions in 134 patients	No adverse events noted other than initial pain and bleeding. Histopathology showed only low-grade foreign body reactions.	Large excision had to be made in one case where needle was blocked and not enough ink was injected. Two patients had a visible mark from the injection. Blockage of needle in 8 cases, but strong pressure allowed ink to be injected. Assistant continually agitated solution.
Langlois [29] 1991 Australia	Homemade	Localization of breast lesions using stereoscopic images	56 lesions (53 patients)	None	None
Mazy [34] 2001 Belgium	Homemade	Localization of breast lesions using stereoscopic images or ultrasound	221 lesions in 153 patients	Ink was 'well tolerated' by patients; In 79% of specimens no significant histological modification . Deposits were isolated in fat tissue or in the neoplasic proliferations without dissemination of the product. Local inflammatory reaction was noted in 21%, primarily consisting of a lymphoplasma-cytic infiltration, a hystiocytic and giant cell response or a neutrophilic infiltration.	Some discomfort from injections. The histological reactions when present did not prevent microscopic analysis, except in one small lesion (4 mm) that was partially masked by the charcoal

Mullen [35] 2001 USA	Homemade	Localization of breast lesions using stereoscopic images	376 patients (237 lesions marked, 200 followed for study)	None	Injected ink spread to chest wall; discharge of black liquid from biopsy tract several days after. Followed for up to 7 yrs with no additional problems
Svane [31] 1983 Sweden	Homemade	Localization of breast lesions using stereoscopic images	56 lesions (31 removed at other hospitals)	None	Injection displaced one fibroadenoma (~5mm) and it was not marked as a result
Tirelli [27] 2016 Italy	Homemade	localization of parotid masses	23 patients 219 patients with carbon marking	2 cases had transient increase in lesion size,	In 4 cases the charcoal was above the lesion rather than in it, believed due to the density of the tissue.
Rose [30] 2003 Australia	Charco-trace	Localization of breast lesions	vs 292 with hookwire marking	None	Carbon tracks resist slicing and carbon can distort or obscure the lesion
Azavedo [32] 1989 Sweden	Homemade	Localization of breast lesions	2510 women	None	none

Acknowledgements This work was supported by the National Institutes of Health (National Cancer Institute grant P01 CA190193).

Disclosures ABF and HMS are owners of Clin-EPR, LLC, which manufacturers EPR devices for investigational clinical applications.

References

1. Vaupel P, Mayer A (2015) The clinical importance of assessing tumor hypoxia: relationship of tumor hypoxia to prognosis and therapeutic opportunities. Antioxid Redox Signal 10:878–879. doi:10.1089/ars.2014.6155
2. Gallez B (2003) Packaging of paramagnetic materials in oximetry and other applications. In: Berliner LJ (ed) *In Vivo* EPR (ESR): theory and application. Springer, New York, pp 259–283. doi:10.1007/978-1-4615-0061-2
3. Charlier N, Beghein N, Gallez B (2004) Development and evaluation of biocompatible inks for the local measurement of oxygen using in vivo EPR. NMR Biomed 17:303–310. doi:10.1002/nbm.902
4. Jordan BF, Baudelet C, Gallez B (1998) Carbon-centered radicals as oxygen sensors for in vivo electron paramagnetic resonance: screening for an optimal probe among commercially available charcoals magnetic resonance materials in physics. Biol Med 7:121–129
5. Swartz HM, Williams BB, Hou H, Khan N, Jarvis LA, Chen EY, Schaner P, Ali AN, Gallez B, Kuppusamy P, Flood AB (2016) Direct and repeated clinical measurements of p02 for enhancing cancer therapy and other applications. Adv Exp Med Biol 923:95–104
6. Swartz HM, Williams BB, Zaki BI, Hartford AC, Jarvis LA, Chen E, Comi RJ, Ernstoff MS, Hou H, Khan N, Swarts SG, Flood AB, Kuppusamy P (2014) Clinical EPR: unique opportunities and some challenges. Acad Radiol 21(2):197–206
7. Long CM, Nascarella MA, Valberg PA (2013) Carbon black vs. black carbon and other airborne materials containing elemental carbon: physical and chemical distinctions. Environ Pollut 181:271–286
8. Dorfer L, Moser M, Spindler K, Bahr F, Egarter-Vigl E, Dohr G (1998) 5200-year-old acupuncture in central Europe? Science 282:242–243
9. Dorfer L, Moser M, Bahr F, Spindler K, Egarter-Vigl E, Giullén S, Dohr G, Kenner T (1999) A medical report from the stone age? Lancet 354:1023–1025
10. Kean WF, Tocchio S, Kean M, Rainsford KD (2013) The musculoskeletal abnormalities of the similaun iceman ("Ötzi"): clues to chronic pain and possible treatments. Inflammopharmacology 21(1):11–20
11. Pabst MA, Letofsky-Pabst I, Bock E, Moser M, Dorfer L, Egarter–Vigl E, Hofer E (2009) The tattoos of the tyrolean iceman: a light microscopical, ultrastructural and element analytical study. J Archaeol Sci 36:2335–2341
12. Sperry K (1992) Tattoos and tattooing. Part II: gross pathology, histopathology, medical complications, and applications. Am J Forensic Med Pathol 13(1):7–17
13. Fujita H, Nishil Y, Yamashita K, Kawamata A, Yoshikawa K (1988) The uptake and long-term storage of India ink particles and latex beads by fibroblasts in the dermis and subcutis of mice, with special regard to the non-inflammatory defense reaction by fibroblasts. Arch Histol Cytol 51(3):285–294
14. Lea PJ, Pawlowski A (1987) Human tattoo. Electron microscopic assessment of epidermis, epidermal-dermal junction, and dermis. Int J Dermatol 26:453–458
15. Aboosy N, Mulder CJ, Berends FJ, Meijer JW, Sorge AA (2005) Endoscopic tattoo of the colon might be standardized to locate tumors intraoperatively. Rom J Gastroenterol 14(3):245–248

16. Cipe G, Cengiz MB, Idiz UO et al (2016) The effects of preoperative endoscopic tattooing on distal surgical margin and ileostomy rates in laparoscopic rectal cancer surgery: a prospective randomized study. Surg Laparosc Endosc Percutan Tech 26(4):301–303
17. Fennerty MB, Sampliner RE, Hixson LJ, Garewal HS (1992) Effectiveness of India ink as a long-term colonic mucosal marker. Am J Gastroenterol 87(1):79–81
18. Hwang MR, Sohn DK, Park JW et al (2010) Small-dose India ink tattooing for preoperative localization of colorectal tumor. J Laparoendosc Adv Surg Tech. Part A 20(9):731–734
19. McArthur CS, Roayaie S, Waye JD (1999) Safety of preoperation endoscopic tattoo with india ink for identification of colonic lesions. Surg Endosc 13(4):397–400
20. Park JW, Sohn DK, Hong CW et al (2008) The usefulness of preoperative colonoscopic tattooing using a saline test injection method with prepackaged sterile India ink for localization in laparoscopic colorectal surgery. Surg Endosc 22(2):501–505
21. Salomon P, Berner JS, Waye JD (1993) Endoscopic India ink injection: a method for preparation, sterilization, and administration. Gastrointest Endosc 39(6):803–805
22. Shaffer RT, Francis JM, Carrougher JG et al (1998) India ink tattooing in the esophagus. Gastrointest Endosc 47(3):257–260
23. Shatz BA, Thavorides V (1991) Colonic tattoo for follow-up of endoscopic sessile polypectomy. Gastrointest Endosc 37(1):59–60
24. Sun L, Si J, Chen S, Liu W, Zhao L, Wang L (2009) The establishment and clinical appliance of technique of mucosa marking targeting biopsy. Hepatogastroenterology 56(89):59–62
25. Chami L, Hartl D, Leboulleux S et al (2015) Preoperative localization of neck recurrences from thyroid cancer: charcoal tattooing under ultrasound guidance. Thyroid : Off J Am Thyroid Assoc 25(3):341–346
26. Kang TW, Shin JH, Han BK et al (2009) Preoperative ultrasound-guided tattooing localization of recurrences after thyroidectomy: safety and effectiveness. Ann Surg Oncol 16(6):1655–1659
27. Tirelli G, Cova MA, Boscolo-Rizzo P, Da Mosto MC, Makuc E, Gardenal N (2016) Charcoal suspension tattoo: a new technique for intraoperative detection of small tumors of the parotid gland. Ann Otol Rhinol Laryngol 125(7):529–535
28. Ko K, Han BK, Jang KM et al (2007) The value of ultrasound-guided tattooing localization of nonpalpable breast lesions. Korean J Radiol 8(4):295–301
29. Langlois SL, Carter ML (1991) Carbon localisation of impalpable mammographic abnormalities. Australas Radiol 35(3):237–241
30. Rose A, Collins JP, Neerhut P, Bishop CV, Mann GB (2003) Carbon localisation of impalpable breast lesions. Breast (Edinburgh/Scotland) 12(4):264–269
31. Svane G (1983) A stereotaxic technique for preoperative marking of non-palpable breast lesions. Acta Radiol Diagn 24(2):145–151
32. Azavedo ESG, Auer G (1989) Stereotactic fine-needle biopsy in 2594 mammographically detected non-palpable lesions. Lancet 1(8646):1033–1036
33. Cavalcanti TC, Malafaia O, Nassif PA et al (2012) Non-palpable breast lesions marked with coal suspension: evaluation of anatomopathological aspects, viability of interpretation and inflammatory response. Revista do Colegio Brasileiro de Cirurgioes 39(6):469–475
34. Mazy S, Galant C, Berliere M, Mazy G (2001) Localization of non-palpable breast lesions with black carbon powder (experience of the Catholic University of Louvain). J Radiol 82(2):161–164
35. Mullen DJ, Eisen RN, Newman RD, Perrone PM, Wilsey JC (2001) The use of carbon marking after stereotactic large-core-needle breast biopsy. Radiology 218(1):255–260
36. Rathod S, Munshi A, Agarwal J (2012) Skin markings methods and guidelines: a reality in image guidance radiotherapy era. South Asian J Cancer 1(1):27–29
37. Mathieu MC, Bonhomme-Faivre L, Rouzier R, Seiller M, Barreau-Pouhaer L, Travagli JP (2007) Tattooing breast cancers treated with neoadjuvant chemotherapy. Ann Surg Oncol 14(8):2233–2238

38. Choy N, Lipson J, Porter C et al (2015) Initial results with preoperative tattooing of biopsied axillary lymph nodes and correlation to sentinel lymph nodes in breast cancer patients. Ann Surg Oncol 22(2):377–382
39. Khan N, Hou H, Hein P et al (2005) Black magic and EPR oximetry: from lab to initial clinical trials. Adv Exp Med Biol 566:119–125
40. Kirchoff DD, Hang JH, Cekic V et al (2014) Endoscopic tattooing to mark distal margin for low anterior rectal and select sigmoid resections. Surg Innov 21:376–380
41. Food and Drug Administration (2012). Tattoos & permanent makeup: fact sheet http://www.fda.gov/ Cosmetics/ProductsIngredients/Products/ucm108530.htm. Accessed 20 Aug 2016
42. Islam PS, Chang C, Selmi C, Generali E, Huntley A, Teuber SS, Gershwin E (2016) Medical complications of tattoos: a comprehensive review. Clin Rev Allergy Immunol 50(2):273–286

Chapter 41
Measurement of pO_2 in a Pre-clinical Model of Rabbit Tumor Using OxyChip, a Paramagnetic Oxygen Sensor

H. Hou, N. Khan, and P. Kuppusamy

Abstract The objective of this work was to establish a novel and robust technology, based on electron paramagnetic resonance (EPR) oximetry, as a practical tool for measurement of tumor oxygen. Previously, we have reported on the development of oxygen-sensing paramagnetic crystals (LiNc-BuO) encapsulated in a biocompatible polymer, called OxyChip. In this report we present our recent data on the use of OxyChip for pO_2 measurements in the tumor of a pre-clinical, large-animal rabbit model. The results establish that OxyChip is capable of noninvasive and repeated measurement of pO_2 in a large animal model.

Keywords Electron paramagnetic resonance (EPR) • Oximetry • OxyChip • Partial pressure of oxygen (pO_2) • Rabbit • VX2 tumor

1 Introduction

Despite the clinical significance and importance of tissue oxygen levels in the diagnosis, prognosis, and treatment of several pathologies [1], there is clearly an unmet need for devices to measure oxygen levels with a reasonable degree of accuracy, reliability, and robustness. Our laboratory is interested in bringing the accuracy and reliability of electron paramagnetic resonance (EPR)oximetry [2] to the clinical realm for useful measurements in cardiovascular, cancer, and cutaneous applications. Previously, we have discovered unique solid-state implants (probes) and procedures that enable unsurpassed accuracy and repeated interrogation of tissue oxygen level at specific sites over a period of time, extending to months or longer [3]. However, these developments are limited primarily to laboratory research involving cells and small animals. Therefore, we plan to translate this promising technology to

H. Hou • N. Khan • P. Kuppusamy (✉)
Department of Radiology, Geisel School of Medicine at Dartmouth College, Rubin 601, 1 Medical Center Drive, Lebanon, NH 03756, USA
e-mail: kuppu@dartmouth.edu

H.J. Halpern et al. (eds.), *Oxygen Transport to Tissue XXXIX*, Advances in Experimental Medicine and Biology 977, DOI 10.1007/978-3-319-55231-6_41

the clinical realm, by developing probes and procedures specifically intended for pO_2 measurements in transcutaneous, subcutaneous, and deep tissue/organs and validate them in pre-clinical animal models. Here we report our first studies in the tumor of a large animal model, namely rabbit. The results demonstrate the feasibility and reliability of making repeated measurements of pO_2 in a pre-clinical model.

2 Methods

2.1 Fabrication and Calibration of OxyChips

Microcrystals of LiNc-BuO were prepared as described previously [4]. Medical grade polydimethylsiloxane (PDMS) base, namely MED-4210 Platinum Silicone Elastomer, was obtained from Factor II, Inc. (Lakeside, AZ). OxyChips containing 40% LiNc-BuO (w/w) in PDMS were prepared in the form of a wire (diameter, 0.6 mm; length 5 cm) using a modification of a previously reported procedure [5]. Briefly, the PDMS base and catalyst/crosslinker (supplied with the PDMS elastomer) were mixed in a 10:1 ratio, after which the LiNc-BuO crystals were added. The heterogeneous dispersion/mixture was outgassed using a vacuum desiccator. One end of a 20-G PTFE (polytetrafluoroethylene) tube was dipped into the PDMS mixture and negative pressure was applied from the other end with a 10-ml syringe to draw the mixture into the tubing to about 5 cm. The PTFE tubing with PDMS mixture was cured in an oven for at least 8 h at 70 °C, followed by withdrawing (by gentle pulling) of the cured PDMS chip out from the tubing. The chip (wire) was further cured at 70 °C overnight. The cured chip (referred to as OxyChip) was in the form of a wire (0.6-mm diameter) that is cut into small segments of 1.0–5.0-mm length for use. In order to verify that mechanical stress or tearing of PDMS coating does not occur resulting in leaching of LiNc-BuO crystals, the OxyChips were suspended in water and subjected to continuous stirring for 72 h at room temperature, after which the chips were removed and dried. Prior to implantation, the chips were sterilized by autoclaving at 121 °C for 30 min. The present study used OxyChips of 5.0-mm length and 0.6-mm diameter. This OxyChip provides an average pO_2 in a volume of about 1.4 mm^3, and therefore samples a region that may include many capillary segments at the implant site. There are several advantages in using OxyChip than other raw (un-encapsulated) paramagnetic crystals. Encapsulation in PDMS effectively shields the LiNc-BuO crystals from interaction with the biological milieu and thus limits the probability of local and/or systemic toxicity from interactions with the tissue. Further, the encapsulation will hold the crystals together and prevent any migration of them from the site of implant. The OxyChip can be left in the tissue or removed when no longer needed using biopsy procedures. Simultaneous measurements of pO_2 from multiple sites can be made by implanting 2–4 OxyChips. We have obtained an Investigational Device Exemption from FDA to test the safety and feasibility of oximetry using OxyChips (5.0 mm × 0.6 mm) in cancer patients.

Linewidth *versus* pO_2 calibration and oxygen response-time curves of OxyChip were constructed by measuring EPR linewidth while the equilibrating gas content was changed from 0–21% oxygen. The EPR measurements were carried out using a custom-built L-band (1.2 GHz) spectrometer with a surface-loop resonator. Gases with known compositions of oxygen (0%, 5% and 21%; balance nitrogen) equilibrated at 37 °C, were flushed over the OxyChip, while the spectra were recorded every minute until a steady linewidth, indicative of equilibration, was achieved.

2.2 Animal Preparation

All the animal procedures were approved by the Institutional Animal Care and Use Committee of Geisel School of Medicine at Dartmouth College (USA). Three New Zealand female rabbits (2.0–2.5 kg body weight) obtained from Charles River Laboratories (Wilmington, MA) were used for all experiments. The animals were separately maintained in a clean 12-h light-dark cycle with free access to food and water. For all experimental procedures, 3.0–3.5% isoflurane mixed with 30% O_2 was used for anesthesia induction, 2.5–3.0% isoflurane in 30% O_2 for surgery procedure including the implantation of tumor and OxyChips, and 2.0–2.5% in 30% O_2 for maintenance of anesthesia during EPR measurements. The core temperature of the animal was measured using a rectal probe and maintained at 37 ± 1 °C using a heating pad.

2.3 Propagation and Inoculation of VX2 Carcinoma in Rabbit, OxyChip Placement, and pO_2 Measurements

Small (4 × 10 mm) pieces of VX2 carcinoma, which were originally obtained from Dr. Hoopes (Geisel School of Medicine, Dartmouth College), were used for inoculation in rabbit mammary pad as described previously [6, 7]. Briefly, under isoflurane anesthesia, pieces of 2 × 2 mm VX2 carcinoma were implanted and grown subcutaneously in the posterior flank of a rabbit. When the tumors reached a size of 20–30 mm, in approximately 12–14 days after implantation, they were surgically removed and sliced into 2 × 2-mm pieces and then implanted subcutaneously in the left mammary pad in the other rabbits. When the tumor in the mammary pad reached a size of 6–10 mm, a single piece of OxyChip was implanted in the center of the tumor at a depth of 3–5 mm from the surface of the tumor. A second piece of OxyChip was implanted in the right mammary pad at a depth of 1 mm from the surface. Measurements of normal (mammary pad) and tumor pO_2 values were performed under 30% O_2 breathing for 20 min (baseline) and hyperoxia challenge induced by 100% oxygen inhalation for 15–18 min every 2 days for up to 3 weeks after OxyChip implantation.

3 Results and Discussion

The stability of OxyChip calibration in VX2 tumor and mammary fat pad (normal tissue) in rabbits was evaluated. Figure 41.1 shows a comparison of EPR linewidth *versus* pO_2 calibration of an OxyChip before implantation and after removal from the tumor 3 weeks later. The data showed a linear variation of EPR linewidth with pO_2 in the measured range of 0–21% oxygen. Further, there was no change in the linearity or oxygen sensitivity of the chip after 3 weeks of residency in the tumor establishing the stability of calibration. Calibration of chips implanted in the mammary fat pad also showed similar stability (data not shown). The results agree with the calibration data of OxyChip and LiNc-BuO crystals measured in mice and rats [4, 8].

We next evaluated changes in tumor and normal tissue pO_2 values as a function of tumor growth. Figure 41.2 shows the pO_2 values measured in a VX2 tumor and mammary fat pad of a rabbit over 3 weeks of tumor growth. The pO_2 in the tumor remained hypoxic throughout the period while the mammary pad showed substantially higher values (3.9 ± 1.0 mmHg vs. 25.5 ± 2.4 mmHg). The values, in general, appeared to be lower and increasing during the first 7–10 days, apparently due to surgical trauma and inflammation associated with the implantation of OxyChip [4, 8]. The pO_2 value in the VX2 tumor measured by OxyChip EPR oximetry appears to be more reliable when compared to values reported by other methods, for example 16.0 ± 14.8 mmHg [9] or 52.4 ± 18.3 mmHg [10] using fiber optic fluorescence method.

Figure 41.3 shows the effect of hyperoxygenation on VX2 tumor and mammary pad tissue. The baseline pO_2 measured during the first 20-min administration of 30% O_2 with 2–2.5% isoflurane via nose-cone breathing was 6.5 ± 0.5 mmHg. When the oxygen composition in the breathing mask was switched to 100%, the pO_2 showed a rapid increase reaching a maximum of 21.2 ± 0.4 mmHg in about 10 min. The corresponding values for mammary pad was 23.9 ± 0.8 mmHg and 49.0 ± 1.3 mmHg, respectively.

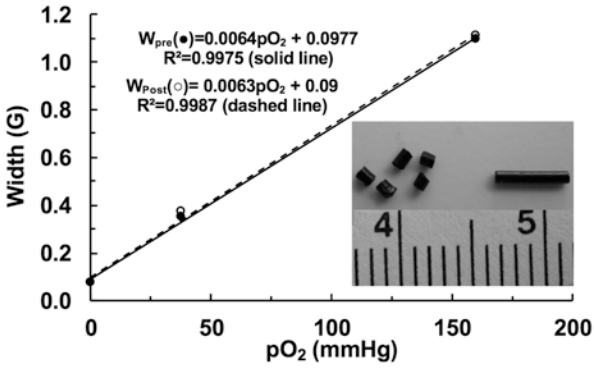

Fig. 41.1 Calibration curve of OxyChip used for pO_2 measurement in rabbit VX2 tumor. OxyChips of dimension 0.6-mm diameter and 5.0-mm length (shown in the inset) were calibrated before implantation (pre) and after explanation (post) from the tumor 3 weeks later. The data show a stable and linear calibration of OxyChip

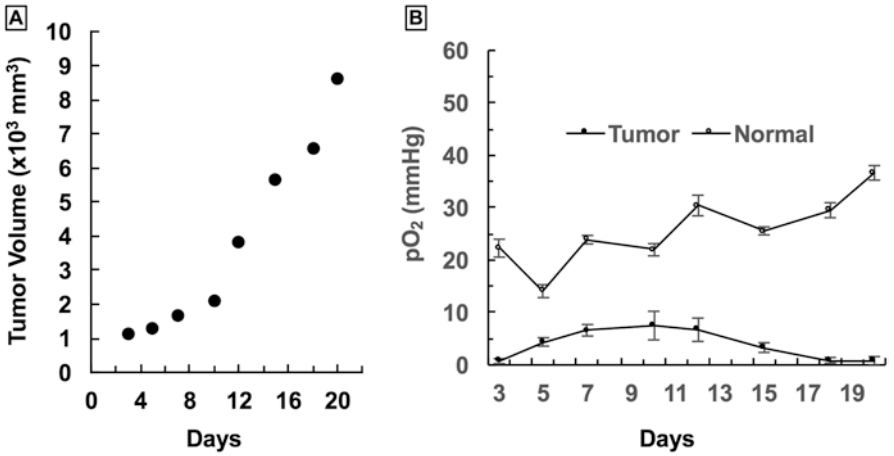

Fig. 41.2 Representative data showing the growth of an ectopic VX2 tumor and changes in pO_2 values measured in rabbit mammary pad over 3 weeks. The pO_2 values were measured in the tumor and normal mammary fat pad using implanted OxyChip. (**A**) Tumor growth curve. (**B**) pO_2 values measured in the tumor and normal tissue over 3 weeks. The pO_2 data shown are Mean ± SEM representing the measurement error. Mean ± SEM values over the 3-week period for tumor and mammary pad were 3.9 ± 1.0 mmHg and 25.5 ± 2.4 mmHg, respectively

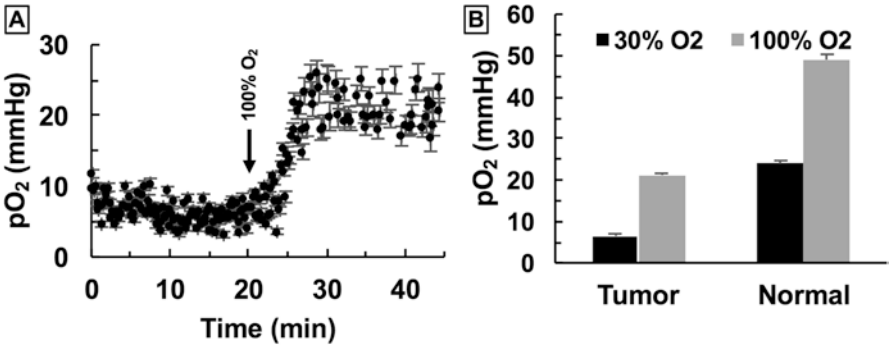

Fig. 41.3 Effect of hyperoxygenation on tumor pO_2. (**A**) Changes in tumor pO_2 during 30% and 100% oxygen breathing. (**B**) Changes in tumor and normal mammary fat pad pO_2 up on 100% O_2 breathing. Data represent Mean ± SEM (N = 10 scans)

4 Conclusion

The study demonstrated for the first time that OxyChip was capable of monitoring pO_2 values in a large animal model of tumor as a function of tumor growth and hyperoxic intervention. The VX2 tumor in the mammary pad was hypoxic and responsive to hyperoxygenation intervention.

Acknowledgment This work was supported by National Institutes of Health grant EB004031.

References

1. Kulkarni A, Kuppusamy P, Parinandi NL (2007) Oxygen, the lead actor in the pathophysiologic drama: enactment of the trinity of normoxia, hypoxia, and hyperoxia in disease and therapy. Antiox Redox Signal 9:1717–1730
2. Ahmad R, Kuppusamy P (2010) Theory, instrumentation, and applications of electron paramagnetic resonance oximetry. Chem Rev 110:3212–3236
3. Swartz HM, Hou H, Khan N et al (2014) Advances in probes and methods for clinical EPR oximetry. Adv Exp Med Biol 812:73–79
4. Pandian RP, Parinandi NL, Ilangovan G et al (2003) Novel particulate spin probe for targeted determination of oxygen in cells and tissues. Free Radic Biol Med 35:1138–1148
5. Meenakshisundaram G, Eteshola E, Pandian RP et al (2009) Fabrication and physical evaluation of a polymer-encapsulated paramagnetic probe for biomedical oximetry. Biomed Microdevices 11:773–782
6. Chen JH, Chen JH, Lin YC et al (2004) Induction of VX2 carcinoma in rabbit liver: comparison of two inoculation methods. Lab Anim 38:79–84
7. Zhu M, Lin XA, Zha XM et al (2015) Evaluation of the therapeutic efficacy of sequential therapy involving percutaneous microwave ablation in combination with ^{131}I-Hypericin using the VX2 rabbit breast solid tumor model. PLoS One 10:1–16
8. Hou H, Khan N, Nagane M et al (2016) Skeletal muscle oxygenation measured by EPR oximetry using a highly sensitive polymer-encapsulated paramagnetic sensor. Adv Exp Med Biol 923:351–357
9. Sun CJ, Li C, Lv HB et al (2014) Comparing CT perfusion with oxygen partial pressure in a rabbit VX2 soft-tissue tumor model. J Radiat Res 55:183–190
10. Levy EB, Johnson CG, Jacobs G et al (2015) Direct quantification and comparison of intratumoral hypoxia following transcatheter arterial embolization of VX2 liver tumors with different diameter microspheres. J Vasc Interv Radiol 26:1567–1573

Chapter 42
Correlation Between Hypoxia Proteins and EPR-Detected Hypoxia in Tumors

Martyna Krzykawska-Serda, Richard C. Miller, Martyna Elas, Boris Epel, Eugene D. Barth, Mathew Maggio, and Howard J. Halpern

Abstract Rapid expansion of tumor cells that outpace existing vasculature essential for nutrient and oxygen support as well as waste removal, correlates with profound changes in the microenvironment including angiogenesis, vasodilation, glucose metabolism, and cell cycle perturbations. Since hypoxic cells are up to three times more radioresistant than normoxic cells, identification of hypoxic populations to predict radiotherapeutic outcome is important. The consequences of hypoxia and activated proteins contribute to radioresistant tumors and radiotherapeutic failure. Stereotactic MCa4 tumor tissue biopsies from mouse tumors that were guided by electron paramagnetic resonance (EPR) O_2 imaging were examined for hypoxia-induced proteins. The oxygen broadening of narrow EPR spectral lines or, equivalently, the increase in relaxation rates of electron magnetization, report pO_2 with 1–2 torr resolution in image voxels less than 1 mm^3. The pO_2 reporter molecule OX063d64 (trityl) was used to acquire the data described here. Trityl appears to be selectively retained in tumors with a half-life of ~30 min. We used an inversion recovery electron spin echo (IRESE) to measure the T1 rate of the trityl inside the tumor bearing leg. We estimate our uncertainty in pO_2 measurement to be 1–3 torr per voxel. Three hypoxic cell biomarkers, hypoxic-induced factor 1-alpha (HIF-1α), vascular endothelial growth factor (VEGF), and carbonic anhydrase IX (CA9), were examined using the ELISA assay. Quantification of these proteins based on results from the ELISA immunoassay kits indicate a strong correlation between EPR pO_2-identified hypoxic fractions (<10 torr) and HIF-1α, VEGF, and CA9. We clearly demonstrate that hypoxic regions in tumors generate substantial amounts of HIF-1α, VEGF, and CA9 protein.

M. Krzykawska-Serda (✉) • M. Elas
Department of Biophysics Faculty of Biochemistry, Biophysics and Biotechnology, Jagiellonian University, ul. Gronostajowa 7, 30-387, Krakow, Poland
e-mail: martyna.krzykawska@uj.edu.pl

R.C. Miller • B. Epel • E.D. Barth • M. Maggio • H.J. Halpern
Department of Radiation and Cellular Oncology, The University of Chicago, Chicago, IL, USA

Center for EPR Imaging In Vivo Physiology, The University of Chicago, Chicago, IL, USA

H.J. Halpern et al. (eds.), *Oxygen Transport to Tissue XXXIX*, Advances in Experimental Medicine and Biology 977, DOI 10.1007/978-3-319-55231-6_42

Keywords Hypoxia • pO2 • Ca9 • HIF1 • VEGF

1 Introduction

For more than 60 years, the importance of oxygen (O_2) in the response of tumors to therapeutic radiotherapy has been known [1]. In addition, several but not all chemotherapy agents show decreased efficacy in a low oxygen environment [2, 3]. Rapid proliferation of tumor cells places a stress on the existing vascular bed supplying nutrients and oxygen while at the same time limiting the removal of waste products.

The microenvironmental state of hypoxia often induces the expression of a wide variety of proteins. A hypoxic microenvironment may be created due to diffusion difficulties when a tumor expands beyond its blood supply, or because of perfusion problems caused by structural deformities of blood vessels, or by anemia induced by hormonal changes, or lack of exercise, or heavy smoking. Reduced O_2 levels below 10 torr produce a hostile microenvironment for tumor cells and their response may include the activation of hypoxia-induced proteins that activates angiogenesis, vasodilation, glucose metabolism, cell cycle perturbations, apoptosis, increased mutations, genomic instability, and malignant progression [4–9]. In particular, hypoxia inhibits prolyl hydroxylase (PHD) which leads to HIF-1α accumulation and translocation to the nucleus, dimerization with HIF-1β and activation of the hypoxic response element (HRE). HRE activates gene transcription to up-regulate carbonic anhydrase IX (CA9), vascular endothelial growth factor (VEGF) and other hypoxia-activated proteins. CA9 proteins are involved in the catalytic hydration of carbon dioxide to carbonic acid which facilitates glucose metabolism and regulation of micro environmental acidity.

Using CA9 as a marker of hypoxic cells in cervical cancer has been proposed during radiotherapy treatment plans [6]. VEGF is an endothelial mitogen which stimulates angiogenesis while other activated proteins regulate vasodilation or the inhibition of cell cycle progression. Cell-cycle arrest at the G_1/S check point is triggered by a HIF-1α-mediated activation of the cyclin-dependent kinase inhibitors p21 and p27. Increased levels of p53 by hypoxia may lead to activation of apoptosis but, at the same time, hypoxia is capable of inducing the BCL-2 anti-apoptotic pathway [9–11], which can have a strong influence of therapy efficiency and tumor progression. EPR imaging allows us to predict not only the hypoxic portion of the tumor but, generally, the part of the tumor with totally different metabolism while in a hypoxic state. In other words, the hypoxic fraction is not only about pO_2 levels but includes the altered pathophysiology of tumor cells in hypoxic regions [12, 13].

EPR oxygen imaging is a reliable technique to identify hypoxic areas within tumors [12]. Images are obtained using injected narrow line, low relaxation rate trityl spin probes that enable pulse radiofrequency EPR O_2 images of tumors. Low relaxation rates of trityl have enabled novel T1, rather than T2, based oxymetry, which provides pO_2 imaging. Voxels with less than 10 torr (HF10) O_2 assist with obtaining biopsy samples from MCa4 tumors.

The aim of this study was to provide the validation that these pO_2 images provide a quantitative basis for measuring tumor and normal tissue response to abnormally low pO_2 levels. As an example of molecular relevance of provided pO_2 information the HIF-1α, VEGF, and CA9 concentrations were determined. Quantification of hypoxic biomarkers may be diagnostic of tumor control while elucidating the development of malignancy.

2 Methods

2.1 Ethics Statement

This study was carried out in accordance with the recommendations in the Guide for the Care and Use of Laboratory Animals of the National Institutes of Health. All animal work was approved by the University of Chicago Institutional Animal Care and Use Committee (IACUC), protocol number 71697. All efforts were made to minimize any suffering and, at the end of each experiment, mice were humanely euthanized.

2.2 pO_2 Imaging Technique

Electron paramagnetic resonance (EPR) O_2 imaging (EPROI) gives quantitative localized pO_2 images of hypoxic regions in tumors [14]. The oxygen broadening of narrow EPR spectral lines or, equivalently, the increase in relaxation rates of electron magnetization, report the pO_2 with 1–2 torr resolution in image voxels as small as 1 mm^3 [13]. Trityl is extracellular in its distribution and is rapidly cleared from the body through renal excretion with a half-life of ~5 min. It appears to be selectively retained in tumors with a half-life of ~30 min. OXO63 and the partially deuterated O_2 reporter OXO63d24, also known as OXO71, have very limited dependence on viscosity. By using pulse sequences that image the longitudinal relaxation rate, R1 (R1 = 1/T1, where T1 is the longitudinal relaxation time), self-relaxation of the trityl spin probe is reduced to well within the 1 torr uncertainties of our image voxel pO_2 values.

2.3 Biopsy procedure

Electron paramagnetic resonance O_2 imaging (EPROI) was used to guide biopsies of tumors in C3H mice by selection of biopsy tracks in pO_2 images. After that, tissue was collected by a biopsy needle (5 mm of diameter) attached to a stereotactic device (uniform XYZ coordinates for whole procedure with 0.1 mm resolution).

Figure 42.1 shows a core biopsy sample being taken while guided by an EPR image displaying hypoxic voxels. Based on the EPR image, each core biopsy sample was segmented corresponding to their pO_2 concentration, as shown, e.g. in Fig. 42.2 for samples 39, 40, and 41. Each segment was measured and frozen separately in liquid nitrogen until tissue homogenization. Tissue lysates were stored at −80 °C.

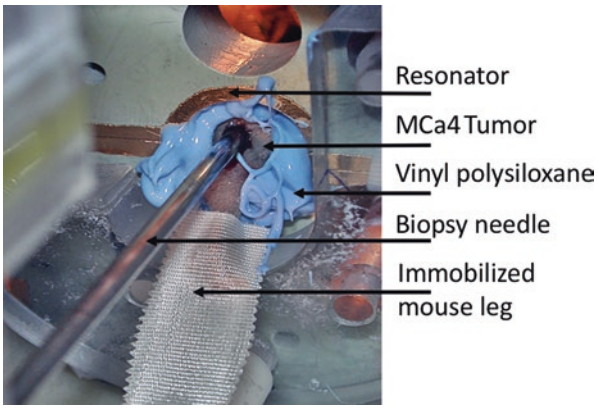

Fig. 42.1 Typical tumor tissue sampling technique inside the EPR resonator. The tumor position is fixed by vinyl polysiloxane and mouse leg is immobilized. Core biopsy samples were guided by EPR imaging and stereotactic device (in XYZ coordinates). The special care was taken to minimalize total time of imaging-biopsy procedure. Mouse condition was established and monitored during the time of experiment

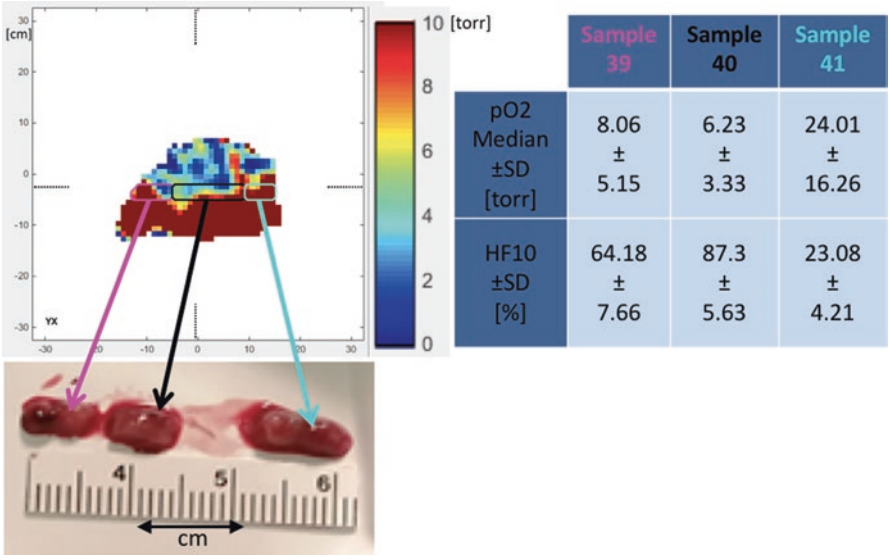

	Sample 39	Sample 40	Sample 41
pO2 Median ±SD [torr]	8.06 ± 5.15	6.23 ± 3.33	24.01 ± 16.26
HF10 ±SD [%]	64.18 ± 7.66	87.3 ± 5.63	23.08 ± 4.21

Fig. 42.2 Image-guided biopsy and segmentation of core biopsy sample. Biopsy samples were freeze in liquid nitrogen around 1 min after sample collection. The EPR YZ image represent the pO_2 map cross-section through the selected biopsy track. The scale of the pO_2 image was adjusted to 10 torr to visualized HF10 inside the tumor (*maroon* color represent normoxic tissue)

2.4 ELISA

Biopsy samples were thawed and sonicated while on ice to release cellular proteins. After high-speed centrifugation at 14,500 rpm for 5 min at 4 °C, supernatants were collected and total proteins/μL determined for each sample using the Bradford Assay. Enzyme-linked immunosorbent assay (ELISA) kits from US Biologicals, Salem, MA were used to determine protein quantities for HIF-1α, VEGF, and CA9 protein in accordance with the manufacturer's instructions. After the addition of 50 μl of stop solution, color development was determined immediately at 450 nm using a 96-well microtiter plate reader. Each sample was assayed in triplicate.

2.5 Data Analysis and Statistics

The standard deviation (SD) of estimated protein concentration [pg/ml] was calculated per sample based on the variation between sample replicates during ELISA. The HF10 measurement uncertainty was calculated as described elsewhere [12]. The linear fits were performed in Origin 9.0 software with direct error bars weighted method and proper statistics were calculated (r, r^2). ANOVA assay was used to determined p values.

3 Results

Applied methodology indicates that our EPROI technique provides information about tumor pO_2 with high precision and biological consequences at the molecular level. Quantification of HIF-1α, VEGF, and CA9 protein levels from ELISA are seen in Fig. 42.3 (as a function of HF10 oxygen concentration) and suggest a strong direct correlation with EPR pO_2-identified hypoxic fractions especially for HIF-1α and CA9. The VEGF is related to H10 but we can observe some extreme data points not close to the fit (as described by r, r^2 statistics).

4 Conclusions

For several years the molecular signaling pathways have been the focus of cancer therapists. Recently, the role of HIF, a master regulator of cells deprived of adequate oxygen, nutritional support, and waste removal, has been shown to play a pivotal role in the adaptive response of cells distant from the vascular bed. The

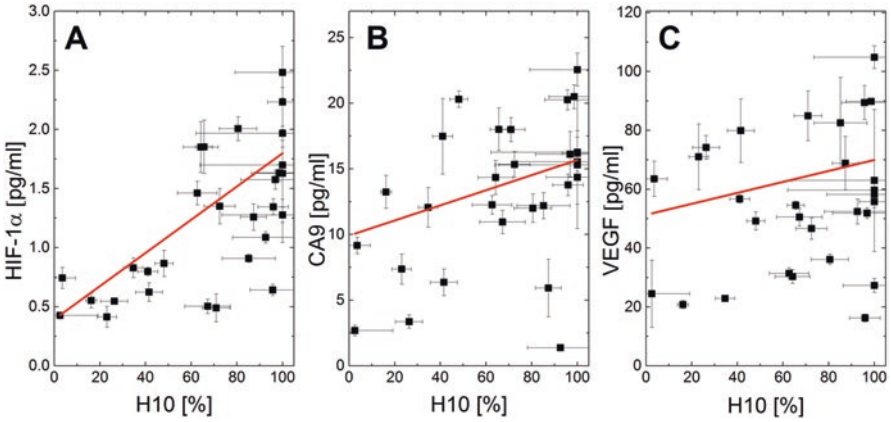

Fig. 42.3 Correlation between HF10 (pO_2 =< 10 torr) calculated in percentage of tumor volume and (**a**) HIF-1α, (**b**) CA9 and (**c**) VEGF proteins levels [pg/ml] estimated based on the ELISA assays (after normalization to protein concentration in biopsy samples lysates). The linear fits were performed and proper statistics were calculated: (**a**) r = 0.67, r^2 = 0.43, p < 0.0001; (**b**) r = 0.38, r^2 = 0.11, p = 0.041; (**c**) r = 0.32, r^2 = 0.07, p = 0.095

proteomic shift of cells in hypoxic zones to overcome nutritional deprivation, stimulate angiogenesis, reduce apoptotic propensity, and adapt cells to an acidic environment demonstrates the resilience of cells in vivo to survive a harsh environment. Tumor pO_2, shown in EPR O_2 images [12, 13] can provide relevant information about tissue biology on molecular level, especially after registration with MRI images to provide detailed anatomical information. Additionally, application of stereotactic device correlated with EPR-MRI coordinates allow us to high presided biopsy sample collection. By concentrating on the relationship between hypoxia and HIF-1α, VEGF, and CA9 response in vivo, we can approximate such a response as a simple linear function. In this way, we have demonstrated that HIF-1α, VEGF, and CA9 protein levels increase linearly as pO_2 levels diminish.

Acknowledgements Grant Support This work was supported by grants from the NIH including R01 CA98575 and P41 EB002034.

References

1. Gray LH, Conger AD, Ebert M et al (1953) The concentration of oxygen dissolved in tissues at the time of irradiation as a factor in radiotherapy. Br J Radiol 26:638–648
2. Teicher BA, Holden SA, al-Achi A et al (1990) Classification of antineoplastic treatments by their differential toxicity toward putative oxygenated and hypoxic tumor subpopulations in vivo in the FSaIIC murine fibrosarcoma. Cancer Res 50:3339–3344

3. Moulder JE, Rockwell S (1987) Tumor hypoxia: its impact on cancer therapy. Cancer Metastasis Rev 5:313–341
4. Graeber TG, Osmanian C, Jacks T et al (1996) Hypoxia-mediated selection of cells with diminished apoptotic potential in solid tumours. Nature 379:88–91
5. Giaccia AJ (1996) Hypoxic stress proteins: survival of the fittest. Semin Radiat Oncol 6:46–58
6. Goda N, Ryan HE, Khadivi B et al (2003) Hypoxia-inducible factor 1 alpha is essential for cell cycle arrest during hypoxia. Mol Cell Biol 23:359–369
7. Olive PL, Aquinos-Parsons C, MacPhail SH et al (2001) Carbonic Anhydrase 9 as an endogenase marker for hypoxic cells in cervical cancer. Cancer Res 61:8924–8929
8. Koumenis C, Alarcon R, Hammond E et al (2001) Regulation of p53 by hypoxia: dissociation of transcriptional repression and apoptosis from p53-dependent transactivation. Mol Cell Biol 21:1297–1310
9. Soengas MS, Alarcon RM, Yoshida H et al (1999) Apaf-1 and caspase-9 in p53-dependent apoptosis and tumor inhibition. Science 284:156–159
10. Hockel M, Vaupel P (2001) Tumor hypoxia: definitions and current clinical, biologic, and molecular aspects. J Natl Cancer Inst 93:266–276
11. Vaupel P (2004) The role of hypoxia-induced factors in tumor progression. Oncologist 9(suppl 5):10–17
12. Elas M, Hleihel D, Barth ED et al (2011) Where it's at really matters: in situ in vivo vascular endothelial growth factor spatially correlates with electron paramagnetic resonance pO2 images in tumors of living mice. Mol Imaging Biol 13:1107–1113
13. Elas M, Magwood JM, Butler B et al (2013) EPR oxygen images predict tumor control by a 50% tumor control radiation dose. Cancer Res 73:5328–5335
14. Elas M, Williams BB, Parasca A, Mailer C, Pelizzari CA, Lewis MA, River JN, Karczmar GS, Barth ED, Halpern HJ (2003) Quantitative tumor oxymetric images from 4D electron paramagnetic resonance imaging (EPRI): methodology and comparison with blood oxygen level-dependent (BOLD) MRI. Magn Reson Med 49(4):682–691

Chapter 43
Triarylmethyl Radical OX063d24 Oximetry: Electron Spin Relaxation at 250 MHz and RF Frequency Dependence of Relaxation and Signal-to-Noise

Yilin Shi, Richard W. Quine, George A. Rinard, Laura Buchanan, Sandra S. Eaton, Gareth R. Eaton, Boris Epel, Simone Wanless Seagle, and Howard J. Halpern

Abstract The triarylmethyl radical OX063d24 is currently used for pulsed electron paramagnetic resonance oximetry at 250 MHz. Both $1/T_1$ and $1/T_2$ increase with increasing oxygen concentration. The dependence of $1/T_1$ on probe concentration is smaller than for $1/T_2$. To inform the selection of the optimum frequency for *in vivo* oximetry $1/T_1$, $1/T_2$ and signal-to-noise were measured as a function of frequency between 400 and 1000 MHz on a variable-frequency spectrometer with an adjustable-frequency cross-loop resonator. $1/T_1$ and $1/T_2$ decrease with increasing frequency and signal-to-noise increases with increasing frequency, which are all favourable for imaging at higher frequencies. However, depth of penetration of the radio frequency (RF) into an animal decreases with increasing frequency. Assuming that the RF loss in the animal to be studied determines the resonator Q, our results indicate that the optimum frequency for *in vivo* imaging will be determined by the desired depth of penetration in the tissue.

Keywords Electron spin relaxation • Oximetry • Signal-to-noise ratio • Variable frequency • Triarylmethyl radical

Y. Shi • L. Buchanan • S.S. Eaton • G.R. Eaton (✉)
Department of Chemistry and Biochemistry and Center for EPR Imaging In Vivo Physiology, University of Denver, Denver, CO 80210, USA
e-mail: geaton@du.edu

R.W. Quine • G.A. Rinard
School of Engineering and Computer Science and Center for EPR Imaging In Vivo Physiology, University of Denver, Denver, CO 80210, USA

B. Epel • S.W. Seagle • H.J. Halpern
Department of Radiation and Cellular Oncology and Center for EPR Imaging In Vivo Physiology, University of Chicago, Chicago, IL 60637, USA

H.J. Halpern et al. (eds.), *Oxygen Transport to Tissue XXXIX*, Advances in Experimental Medicine and Biology 977, DOI 10.1007/978-3-319-55231-6_43

1 Introduction

Electron paramagnetic resonance (EPR) is the method of choice for imaging oxygen concentration in tissues, using either injectable [1] or implantable probes [2]. A widely-used injectable trityl probe is designated as OX063 and its partially deuterated form is OX063d24. These trityls have narrow-line EPR spectra. Deuteration reduces the peak-to-peak linewidth for aqueous solutions from 16 μT to 8 μT [3], which increases signal amplitude. In this chapter we report the dependence of relaxation rates for OX063d24 on spin probe and oxygen concentration at 250 MHz, which is the frequency at which it is currently used.

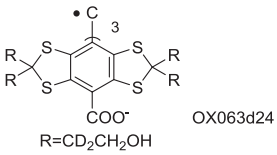

OX063d24

A major question for the further development of *in vivo* EPR imaging is selection of the optimum resonance frequency, and corresponding field, for oximetry in small animals such as mice. The selection depends on multiple factors including the frequency dependence of signal-to-noise (*S/N*) and of $1/T_1$ and $1/T_2$ for the spin probe, in addition to the depth of penetration of the radio frequency (RF) into the animal. The experiments in this study were designed to address this question and to compare results for OX063 and OX063d24.

2 Methods

The synthesis of OX063d24, methyl-tris[8-carboxy-2,2,6,6 tetrakis[2-(1-hydroxyethyl-d_2)]-benzo(1,2-d:4,5-d')bis [1, 3]dithiol-4-yl] (GE Healthcare, Little Chalfont, Buckinghamshire, UK) has been reported elsewhere [4]. Solutions were prepared in 10 mM HEPES buffer containing 0.9% wgt/vol of NaCl (154 mM) or in phosphate buffered saline (PBS) solution (137 mM NaCl, 2.7 mM KCl, 10 mM Na_2HPO_4 and 1.8 mM KH_2PO_4). Unless otherwise noted, samples were contained in quartz tubes that were de-oxygenated by bubbling with N_2 and flame sealed.

Electron spin relaxation rates at 250 MHz were measured at the University of Chicago on the previously-described spectrometer [5]. Experiments at 400–1000 MHz were performed at the University of Denver using the variable frequency UHF spectrometer described in [6]. This spectrometer was used previously for analogous measurement for OX063 with normal isotopic abundance [7]. The cross-loop resonator that was used for the multifrequency measurements was designed such that the frequency can be adjusted between about 400–1000 MHz with the same 16-mm OD sample and the same filling factor, thus maintaining all resonator characteristics,

except resonance frequency and resonator Q, constant throughout the series of relaxation and *S/N* measurements. Resonator Q was measured using an HP 8719D network analyzer, which has an operating range of 50 MHz to 13.5 GHz. Measurements of relaxation times at 1.5 GHz were performed on the previously described spectrometer at the University of Denver and a cross-loop resonator with a narrow range of frequency adjustments [8]. T_2 was measured by two-pulse electron spin echo and T_1 was measured by three-pulse inversion recovery [7]. Reported values are averages of three measurements and the error bars shown in the figures are standard deviations. *S/N* was calculated by three methods for the same sample [7]: from the amplitude of field-swept 2-pulse echo-detected spectra, from the amplitude of echo decays, and from the amplitude of the inversion recovery signal. Each of these methods produces a signal that is proportional to spin concentration, so the average *S/N* reflects the results achievable by several spectroscopic approaches. The averages obtained by the three methods are reported and error bars are standard deviations.

3 Results and Discussion

At 250 MHz the dependence of $1/T_1$ for OX063d24 on radical concentration is much smaller than for $1/T_2$ (Fig. 43.1). The dependence on oxygen partial pressure is similar for $1/T_1$ and $1/T_2$ (Fig. 43.2). The relaxation mechanisms that are the bases for these dependencies are independent of frequency [3, 9].

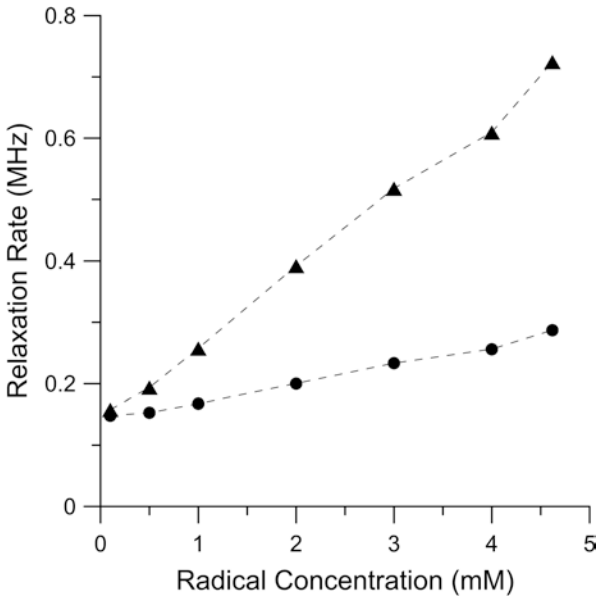

Fig. 43.1 Dependence of relaxation rates on radical concentration for OX063d24 at 250 MHz and 37 °C in deoxygenated saline solution; (●) $1/T_1$, (▲) $1/T_2$

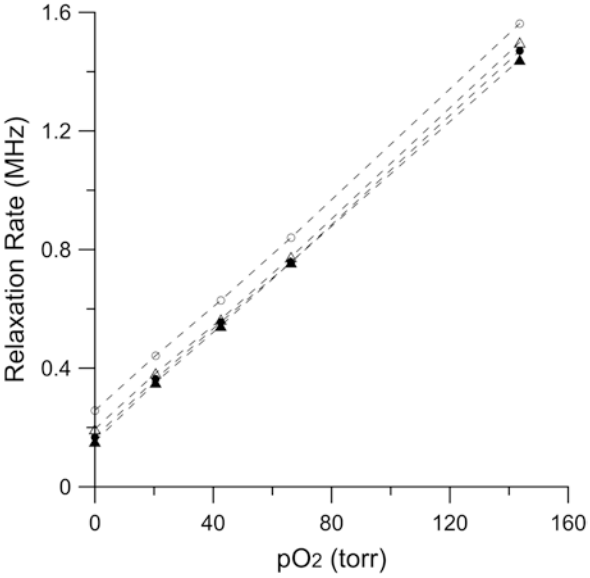

Fig. 43.2 Dependence of relaxation rates for OX063d24 on oxygen partial pressure at 250 MHz in saline solution at 37 °C; 1 mM solution (●) $1/T_1$, (○)$1/T_2$ and 0.5 mM solution (▲)$1/T_1$ (Δ) $1/T_2$

For both OX063d24 and OX063, $1/T_1$ decreases with increasing frequency between 400 and 1500 MHz (Fig. 43.3). Between 400 and 1000 MHz $1/T_1$ is consistently smaller for OX063d24 than for OX063. At 250 MHz the dominant contribution to $1/T_1$ for trityls is modulation of electron-proton dipolar coupling by molecular tumbling which is proportional to $\tau_R/(1 + \omega^2\tau_R^2)$ where τ_R is the molecular tumbling correlation time and ω is the RF frequency in angular units, $2\pi\nu$ [10]. When frequency is varied, this term is maximum for $\tau_R = 1/\omega$. Based on the viscosity dependence of the tumbling-dependent contribution to $1/T_1$ for OX063 at 250 MHz, the molecular tumbling correlation time, τ_R, in water solution is about 0.42 ns. For 250 MHz $1/\omega = 0.64$ ns and for 1500 MHz $1/\omega = 0.11$ ns. Thus, this contribution to spin lattice relaxation is close to maximum at 250 MHz and decreases with increasing frequency above about 250 MHz. This is why the contribution to $1/T_1$ due to modulation of electron-proton dipolar interaction decreases with increasing frequency for both OX063d24 and OX063 in the frequency range studied (Fig. 43.3). Deuteration of OX063d24 decreases the number of protons in close proximity to the unpaired spin, which is why modulation of electron-nuclear dipolar interaction makes a smaller contribution to $1/T_1$ for OX063d24 than for OX063 at frequencies up to 1000 MHz and therefore $1/T_1$ is smaller for OX063d24 than for OX063. At 1500 MHz the spin-lattice relaxation is dominated by a local mode which is not impacted by deuteration of the trityl, so relaxation rates for OX063d24 and OX063 are the same within experimental uncertainty at 1500 MHz.

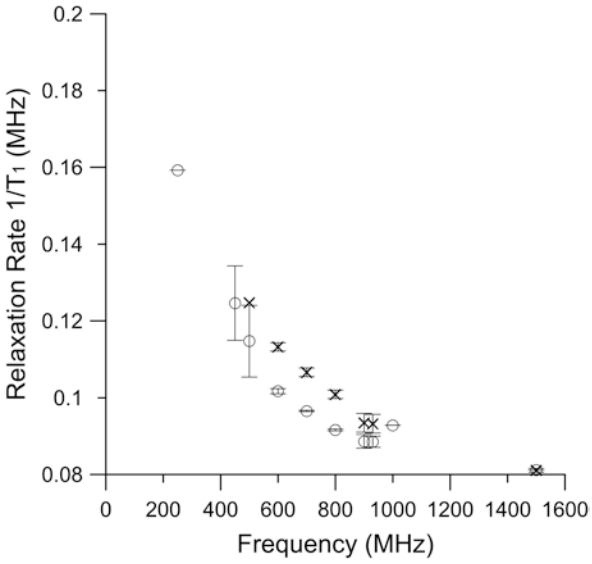

Fig. 43.3 Microwave frequency dependence of $1/T_1$ in pH = 7.4 HEPES (10 mM) + 154 mM NaCl at ambient temperature (19 °C): (○) 0.2 mM OX063d24, (x) 0.2 mM OX063 (Data for OX063 are reproduced from Ref. [7])

The spin-spin relaxation rates $1/T_2$ for both OX063d24 and OX063 also decrease with increasing frequency (Fig. 43.4). $1/T_2$ for OX063d24 is consistently smaller than for OX063, and the differences between $1/T_2$ for the two radicals is larger than for $1/T_1$. Both radicals are near the rapid tumbling regime were $1/T_2 = 1/T_1$, so the decrease in $1/T_1$ with increasing frequency contributes to the decrease in $1/T_2$ and the smaller $1/T_1$ for OX063d24 contributes to smaller $1/T_2$. The larger values of $1/T_2$ than of $1/T_1$ for both trityls reflect contributions from radical-radical collisions and incomplete motional averaging of *g*- and hyperfine anisotropy [7]. Deuteration reduces the hyperfine couplings to the unpaired electron so there is less anisotropy to be averaged, which enhances the difference between $1/T_1$ and $1/T_2$ for OX063d24 relative to that for OX063.

If one assumes that the EPR resonator has been optimized for the animal to be studied, the resonator Q will be largely determined by the lossy tissue of the animal. Consequently, our signal-to-noise results are normalized by the square root of Q [7]. For OX063 the normalized *S/N* increased significantly as the frequency was increased from about 450 to 905 MHz [7] (Fig. 43.5). The uncertainty in measurements of *S/N* are substantially greater for OX063d24 than for OX063 (Fig. 43.5). The frequency dependence of *S/N* is less well-defined for OX063d24, but appears to follow a similar trend. The decrease in Q with increasing frequency in the resonator used for these experiments [7] is larger than would be likely for an animal, because the dominant impact on Q seems to be the eddy currents in the homogeneous salt solutions. Eddy currents will be less important for the heterogeneous structure of animal tissue.

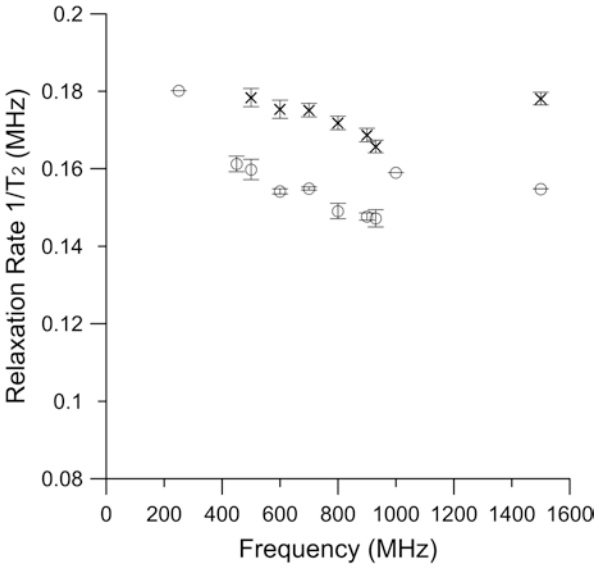

Fig. 43.4 Microwave frequency dependence of $1/T_2$ in pH = 7.4 HEPES (10 mM) + 154 mM NaCl at ambient temperature (19 °C): (◯) 0.2 mM OX063d24, (x) 0.2 mM OX063 (Data for OX063 are reproduced from Ref. [7])

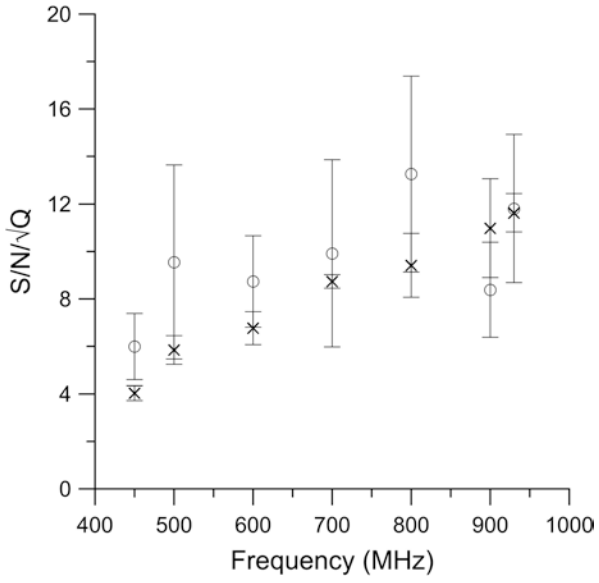

Fig. 43.5 Microwave frequency dependence of S/N (normalized by $\sqrt{Q}$) for OX063 in pH = 7.4 HEPES (10 mm) + 154 mM NaCl at ambient temperature (19 °C). (◯) 0.2 mM OX063d24, (x) 0.2 mM OX063 (Data for OX063 are reproduced from Ref. [7])

4 Conclusions

The smaller values of $1/T_1$ and $1/T_2$ for OX063d24 than for OX063 are advantageous for oximetry. Slower relaxation rates mean that collisions of O_2 with the trityl probe result in larger fractional changes in relaxation rates at higher Zeeman frequencies, thereby enhancing oximetric imaging. Increasing *S/N* with increasing frequency also is advantageous. These advantages of operating at higher frequency need to be weighed against the potential disadvantage that the depth of penetration of RF into tissue decreases with increasing frequency. Penetration decreases with increase in RF frequency differently for different tissues. Approximations based on literature values are published in [11] and summarized up to 500 MHz [12] or 1000 MHz [13]. At 1000 MHz penetration was about 3 cm in muscle to about 20 cm in fat. Thus, for mouse imaging, use of up to about 1000 MHz appears to be feasible from the perspective of both the properties of the OX63d24 probe and RF penetration in tissue. There may be some limitation due to practical aspects of construction of an imager, such as whether it is desired to have a small bench-top unit.

Acknowledgments This research was funded in part by NIH P41 EB002034 (HJH, PI), R01 CA098575 (HJH, PI) and R01CA177744 (GRE, PI).

References

1. Epel B, Halpern HJ (2015) Comparison of pulse sequences for R_1-based electron paramagnetic resonance oxygen imaging. J Magn Reson 254:56–61
2. Khan N, Hou H, Swartz HM, Kuppusamy P (2015) Direct and repeated measurement of heart and brain oxygenation using in vivo EPR oximetry. Methods Enzymol 564:529–552
3. Epel B, Bowman MK, Mailer C, Halpern HJ (2014) Absolute oxygen R1e imaging *in vivo* with pulse electron paramagnetic resonance. Magn Reson Med 72:362–368
4. Kuzhelev A, Trukhin D, Krumkacheva O, Strizhakov R, Rogozhnikova O, Troitskaya T, Fedin M, Tormyshev V, Bagryanskaya E (2015) Room-temperature electron spin relaxation of triarylmethyl radicals at the X- and Q-Bands. J Phys Chem B 119:13630–13640
5. Halpern HJ, Spencer DP, van Polen J, Bowman MK, Nelson AC, Dowey EM, Teicher BA (1989) Imaging radio frequency electron-spin-resonance spectrometer with high resolution and sensitivity for in vivo measurements. Rev Sci Instrum 60: 1040–1050 Epel E, Bowman MK, Mailer C, Halpern HJ (2014) Absolute oxygen R1e imaging in vivo with pulse electron paramagnetic resonance. Magn Reson Med 27:362–368
6. Quine RW, Rinard GA, Shi Y, Buchanan LA, Biller JR, Eaton SS, Eaton GR (2016) UHF EPR spectrometer operating at frequencies between 400 MHz and 1 GHz. Conc Magn Reson B, Magn Reson Eng. doi:10.1002/cmr.b.21328
7. Shi Y, Quine RW, Rinard GA, Buchanan L, Eaton SS, Eaton GR, Epel B, Seagle SW, Halpern HJ (2017) Triarylmethyl radical: EPR signal to noise at frequencies between 250 MHz and 1.5 GHz and dependence of relaxation on radical and salt concentration and on frequency. Z Physik Chem 231:923–937
8. Quine RW, Rinard GA, Ghim BT, Eaton SS, Eaton GR (1996) A 1-2 GHz pulsed and continuous wave electron paramagnetic resonance spectrometer. Rev Sci Instrum 67:2514–2527

9. Molin YN, Salikhov KM, Zamaraev KI (1980) Spin exchange: principles and applications in chemistry and biology. Springer-Verlag, Berlin
10. Owenius R, Eaton GR, Eaton SS (2005) Frequency (250 MHz to 9.2 GHz) and viscosity dependence of electron spin relaxation of triarylmethyl radicals at room temperature. J Magn Reson 172:168–175
11. Halpern HJ, Bowman MK (1991) Low-frequency EPR spectrometers: MHz range. In: Eaton GR, Eaton SS, Ohno K (eds) EPR imaging and in vivo EPR. CRC Press, Boca Raton, p Ch. 6
12. Robataille P-ML, Kangarlu A, Abduljalil AM (1999) RF penetration in ultra high field MRI: challenges in visualizing details within the center of the human brain. Comput Assist Tomography 23:845–849
13. Collins CM (2006) Radiofrequency field calculations for high field MRI. Biol Magn Reson 26:209–248

Chapter 44
In Vivo EPR Resolution Enhancement Using Techniques Known from Quantum Computing Spin Technology

Robabeh Rahimi, Howard J. Halpern, and Takeji Takui

Abstract A crucial issue with in vivo biological/medical EPR is its low signal-to-noise ratio, giving rise to the low spectroscopic resolution. We propose quantum hyperpolarization techniques based on 'Heat Bath Algorithmic Cooling', allowing possible approaches for improving the resolution in magnetic resonance spectroscopy and imaging.

Keywords In vivo EPR • Quantum computing • Heat bath algorithmic cooling

1 Introduction

Magnetic Resonance Imaging (MRI) and Magnetic Resonance Spectroscopy (MRS) rely on Magnetic Resonance (MR) signals originating from the transverse magnetization of nuclear spins, typically proton spins of water, within biological or target entities. Magnetic field gradients are used for spatial encoding of the MR signals. Therefore, the MRI resolution is very dependent on the MR signals. The goal is to enhance the MRI and MRS resolution; one of the approaches to achieve this is to increase the MR signals. There is a linear proportionality between the MR signal and spin polarization. Thus, the spin polarization needs to be enhanced in order to improve MRI resolution. If the applied static magnetic field in the MRI

R. Rahimi (✉)
Department of Radiation Oncology, University of Miami Miller School of Medicine, Miami, USA

Department of Radiation and Cellular Oncology, University of Chicago, Chicago, IL, USA
e-mail: rrahimid@uchicago.edu

H.J. Halpern
Department of Radiation and Cellular Oncology, University of Chicago, Chicago, IL, USA

T. Takui
Department of Chemistry and Molecular Materials Science, Graduate School of Science, Osaka City University, Osaka, Japan

H.J. Halpern et al. (eds.), *Oxygen Transport to Tissue XXXIX*, Advances in Experimental Medicine and Biology 977, DOI 10.1007/978-3-319-55231-6_44

and MRS processes is increased, then the MR signal due to the population difference between relevant magnetic sublevels is increased and, thus, the MRI and MRS resolution can be enhanced.

Currently, the majority of the operating clinical MRI devices use 1.5 tesla magnets which yield the proton spin polarization of about 10^{-5} that is very small. Using a 3 Tesla magnet for MRI slightly increases the polarization of spins, but still never gives even an order of magnitude enhancement.

If we were not aiming for an ultimately in vivo practice, we would propose running MRI at a very low sample temperature. While a colder sample, in principle, gives larger signals, this technique is not always applicable for in vivo practice.

Dynamic Nuclear Polarization (DNP) is an approach that polarizes spins to higher levels than the equilibrium polarization provided by a static magnetic field. DNP typically enhances the spin polarization for up to several orders of magnitude, therefore it is a well-appreciated technique compared to other approaches used for similar purposes. DNP for clinical applications relies on using specific nuclear spins as contrast agents. These spins are very long-lived spins, determined by their spin-lattice relaxation time. DNP cannot, by any means, produce polarization enhancement larger than γ_m/γ_n, whereγ_m is the gyromagnetic of the spin with the higher polarization (the donor) and γ_n is the gyromagnetic of the spin with the lower spin polarization (the acceptor).

In this paper we introduce a technique new to clinical MRI users, albeit familiar to the quantum information community, for enhancing the image resolution of clinical modalities. The technique is close to DNP in the sense that it relies on conceptually similar physics, but is superior to DNP since it surpasses the DNP threshold for polarization enhancement.

Quantum information science is an emerging field which is underlain by new aspects of quantum mechanical concepts in physics. During the last two decades, quantum information science has made significant progress, covering many topics of quantum information processing, quantum computing and relevant nanotechnology.

Despite the fact that, from the theoretical side, quantum information science has continuously resulted in interesting and important outcomes, in an empirical scenario the story is not very favorable and far from being complete. Several physical systems have been proposed for physical realizations of quantum information science. Some of them have been tested and been used for implementing simple quantum protocols, but still this area is in the cradle except for quantum communication technology.

For any application related to quantum information science, spin systems are supposed to possess well-defined spins that give high-resolution spectra [1]. Spin systems such as the ones treated in Nuclear Magnetic Resonance (NMR) and Electron Paramagnetic Resonance (EPR) are known so far to be among the most promising candidates for exploiting quantum effects and implementing quantum algorithms.

Better resolution in quantum practices is only achieved by employing highly pure spin states. Also, for quantum error correction, which is a fundamental requirement for any scalable quantum processors such as fault-tolerant quantum computers, it is inevitable to have access to spins with high polarization. The reason is that most quantum algorithms require the initialization of the qubit system and the error correction during any gate operations is efficiently empowered by freshly prepared qubits in their pure states. Special techniques in terms of sophisticated quantum spin technology should be employed to achieve high spin polarization for quantum information science practices. Quantum information processing proposes several clever approaches to prepare pure spin polarizations, for example DNP followed by Heat Bath Algorithmic Cooling (HBAC), to increase spin polarizations beyond the Shannon entropy bound.

We aim to bring these findings from quantum information science to clinical studies where high resolution MRI/EPR is in demand. Brassard and colleagues [2] have already shown that Algorithmic Cooling may supply the same quality of measurements as methods currently being used, but with significantly lower amounts of RF applied to the patient. However, not all quantum hyperpolarization techniques can be useful for in vivo practices. For example, parahydrogen-induced polarization requires special equipment and chemistry-oriented tactics to operate in vivo systems. Thus, it is important to consider the special needs of in vivo use when applying these ideas. We next illustrate an appropriate application using HBAC.

2 Heat Bath Algorithmic Cooling and Hyperfine-Coupled Spin Systems

HBAC [3–8] is a technique for extracting entropy from a principal system as one subsystem and depositing the entropy into the environment, the so-called bath as another subsystem. The important point here is that the entropy is carried out by dynamic processes and with HBAC, basically, it is possible to cool down the spin system to a temperature below the environment temperature. The dynamic process can be achieved by quantum logic operations. During the process of HBAC, the principal system is frequently brought to interaction with the environment, and therefore the system is not a closed system and the Shannon entropy bound is not observed. Here, we give a brief explanation of the HBAC with simulation results that prove the practicality of the proposal of this work. An extended discussion on HBAC and the preliminary experimental data, in addition to complete simulation results based on realistic conditions, can be found in literature, including [8, 9].

Let us assume a principal system that contains n spins. This system is in contact with a heat bath that has polarization ε_b. The goal is to polarize a single spin in the principal system to the extent of the polarization larger than the bath. This is done using HBAC. Among different implementations of HBAC, the Partner Pairing Algorithm [4] is the optimal method for HBAC. There are two main steps; the step

for refreshing the spins, and a compression step. There is one spin which is in thermal contact with a bath polarization, therefore reduces the entropy of the principal system. This spin thermally contacting to the heat bath can relax faster than the other n-1 spins in the principal system. The step of the thermal contact is followed by the compression step. The main and distinct operationality of HBAC compared to other DNP techniques comes because of the step of compression operations, which enable to raise the entropy of one subsystem and to lower the counterpart of the other system. In this process (box), a numbers of 'quantum gates' (unitary and reversible operations) are applied for rearranging the symmetry of the spin system. In a simplified picture, the compression box is an operator, which rearranges the diagonal elements of the density matrix of the system in descending order. The whole procedure is repeated until the target spin reaches a threshold, as proven to be $\varepsilon_b 2^{n-2}$ if $\varepsilon_b < < 2^{-n}$. The polarization of the target spin can arbitrarily get close to unity, if $\varepsilon_b > > 2^{-n}$ [9, 10].

HBAC has been experimentally demonstrated with solid state NMR systems. The final polarization achieved in the experiment exceeded the bath thermal polarization [11, 12]. While NMR is a good physical system for realizing HBAC, due to its very good controllability of nuclear spins by applying RF pulses, the issue with NMR is that a highly polarized spin for intermediate environment is not readily available. In this context, electron-nuclear, hyperfine-coupled spin systems are advantageous since the characteristic short relaxation time of electrons in molecular frames can uptake the entropy from the principal system and expose it to the bath environment.

For proof of the methodology, malonic acid as a molecular spin system was tested for realizing HBAC in hyperfine-coupled spin systems. Particularly, carbon atoms of malonic acid have been labeled to ^{13}C. Then, malonic acid was irradiated by x- or gamma rays, generating malonyl radical by breaking one of the α-hydrogen bonds. All the g- and hyperfine tensors necessary to find the anisotropic conditions and simulate HBAC processes have experimentally been determined. It has turned out that this molecular system is an excellent candidate for being used for the simulations and practices.

Simulation was performed under the conditions derived from the experiments at ambient temperature. Relaxation times and dephasing times of the spins, in addition to the system temperature were used as realistic parameters, as derived from pulse-based EPR experiments. As a result, it is shown that even by having some reasonable sources of errors, it is indeed possible to achieve a polarization on a single carbon spin which amounts to 1.22 times of the electron spin polarization [9]. This is indeed a few orders of magnitude enhancement over the carbon original spin polarization.

3 Conclusions

In this work, we have proposed the use of the techniques available from quantum information science to pre-clinical, and hopefully in the future, clinical applications of in vivo EPR. We aim for HBAC since it is typically close to the DNP process.

DNP has been used for a few years for pre-clinical and clinical applications. HBAC is superior to DNP techniques because HBAC can surpass the Shannon entropy, therefore a polarization larger than the environment polarization can be achieved.

Solid state NMR experiments demonstrated that the polarization of a spin system could be larger than that of the environment. We have discussed here that NMR still suffers from the lack of accessibility to a spin with short relaxation time, which plays the role of the pumping spin, and fast interaction with the environment of the heat bath. Therefore, the conclusion was to use an electron-nuclear hyperfine coupled spin system, in which the electron spin is a mediator accelerating the fast thermal contact. The simulation based on realistic parameters has show that the idea is workable and more sophisticated pulse-based microwave spin technology should be implemented, controlling all the gate operation steps including the compression ones. From the experimental side, HBAC is challenging for in vivo EPR situation as well as model materials as molecular spins in ensemble which show more pronounces HBAC. The experimental efforts are still in progress.

Acknowledgments RR would like to thank Guanru Feng, the Institute for Quantum Computing, University of Waterloo, ON, for helpful discussions and drawing attention to the simulation results of the previous joint works. Supported by NIH grants P41 EB002034 and R01 CA98575.

References

1. Rahimi R, Sato K, Carl P, Hofer P, Laflamme R, Takui T (2016) Exploiting quantum effects in electron-nuclear coupled molecular spin systems. In: Chapter 2, biological magnetic resonance, vol 31. Springer Science & Business Media, New York
2. Brassard G, Elias Y, Mor T, Weinstein Y (2014) Prospects and limitations of algorithmic cooling. Eur Phys J 129:258
3. Boykin PO, Mor T, Roychowdhury V, Vatan F, Vrijen R (2002) Proc Natl Acad Sci U S A 99:3388
4. Fernandez JM, Lloyd S, Mor T, Roychowdhury V (2004) Intl J Quantum Inf 2(4):461
5. Schulman LJ, Mor T, Weinstein Y (2005) Phys Rev Lett 94:120501
6. Rempp F, Michel M, Mahler G (2007) Phys Rev A 76:032325
7. Kaye P (2007) Quantum Inf Proc 6(4):295
8. Park DK, Feng GR, Rahimi R, Labruyene S, Shibata T, Nakazawa S, Sato K, Takui T, Laflamme R, Baugh J (2015) Quantum Inf Proc 14(7):2435–2461
9. Park D, Rodrigues-Briones NA, Feng G, Rahimi R, Baugh J, Laflamme R (2016) Spin based heat bath algorithmic cooling: reviews and prospects. In: Chapter 8, biological magnetic resonance, vol 31. Springer Science & Business Media, New York
10. Rodríguez-Briones NA, Laflamme R (2016) Phys Rev Lett 116:170501
11. Baugh J, Moussa O, Ryan CA, Nayak A, Laflamme R (2005) Nature 438(7067):470
12. Ryan CA, Moussa O, Baugh J, Laflamme R (2008) Phys Rev Lett 100:140501

Part V
Blood Products and Substitutes

Chapter 45
Hemoglobin-Based Oxygen Carrier (HBOC) Development in Trauma: Previous Regulatory Challenges, Lessons Learned, and a Path Forward

Peter E. Keipert

Abstract Historically, hemoglobin-based oxygen carriers (HBOCs) were being developed as "blood substitutes," despite their transient circulatory half-life (~ 24 h) vs. transfused red blood cells (RBCs). More recently, HBOC commercial development focused on "oxygen therapeutic" indications to provide a temporary oxygenation bridge until medical or surgical interventions (including RBC transfusion, if required) can be initiated. This included the early trauma trials with *HemAssist*® (Baxter), *Hemopure*® (Biopure) and *PolyHeme*® (Northfield) for resuscitating hypotensive shock. These trials all failed due to safety concerns (e.g., cardiac events, mortality) and certain protocol design limitations. In 2008 the Food and Drug Administration (FDA) put all HBOC trials in the US on clinical hold due to the unfavorable benefit:risk profile demonstrated by various HBOCs in different clinical studies in a meta-analysis published by Natanson et al. (2008). During standard resuscitation in trauma, organ dysfunction and failure can occur due to ischemia in critical tissues, which can be detected by the degree of lactic acidosis. Sangart's Phase 2 trauma program with MP4OX therefore added lactate >5 mmol/L as an inclusion criterion to enroll patients who had lost sufficient blood to cause a tissue oxygen debt. This was key to the successful conduct of their Phase 2 program (ex-US, from 2009 to 2012) to evaluate MP4OX as an adjunct to standard fluid resuscitation and transfusion of RBCs. In 2013, Sangart shared their Phase 2b results with the FDA, and succeeded in getting the FDA to agree that a planned Phase 2c higher dose comparison study of MP4OX in trauma could include clinical sites in the US. Unfortunately, Sangart failed to secure new funding and was forced to terminate development and operations in Dec 2013, even though a regulatory path forward with FDA approval to proceed in trauma had been achieved.

Keywords HBOC • MP4OX • Hemoglobin solutions • Trauma • Hemorrhagic shock

P.E. Keipert, PhD (✉)
Keipert Corp. Life Sciences Consulting, San Diego, CA, USA, 92130
e-mail: keipertcorpconsulting@gmail.com

H.J. Halpern et al. (eds.), *Oxygen Transport to Tissue XXXIX*, Advances in Experimental Medicine and Biology 977, DOI 10.1007/978-3-319-55231-6_45

1 Introduction

Hemoglobin-based oxygen carriers (HBOCs) have historically been referred to as "blood substitutes," which is a misnomer considering their transient circulatory half-life (i.e., typically ~24 h) versus transfused red blood cells (RBCs) that remain in circulation for weeks. As a result, there have been significant regulatory challenges to develop an HBOC as an alternative to RBC transfusion in clinical settings where blood transfusion is typically part of the standard of care. The risk of viral disease transmission from donor RBCs is always a concern to patients, even though the blood banking industry has implemented numerous strategies and new tests to reduce these risks to exceedingly low levels [1]. To market an HBOC for reduction or avoidance of RBC transfusion, regulators demanded compelling clinical data to demonstrate equivalent safety versus allogeneic donor RBCs. This would have required unrealistically large numbers of patients, and an unreasonable cost and time commitment. Commercial development therefore re-focused on alternative clinical scenarios where the physicochemical properties of the HBOC are used to enhance oxygen delivery to hypoxic tissues in ischemic organs. By acting as an "oxygen therapeutic" agent, the HBOC can be used as a "bridge" to transfusion, or as an alternative to RBCs in situations where transfusion is not an established therapy or may be contraindicated [2]. This provides a greater opportunity to prevent or treat ischemia-related morbidity and to potentially reduce mortality, and thereby demonstrate sufficiently compelling efficacy to satisfy the regulatory requirement for clinical benefit to gain marketing approval of an HBOC.

2 Medical Need in Trauma and Rationale for HBOCs

Mortality following blunt or penetrating injuries in trauma patients is typically caused by acute hemorrhagic shock resulting from severe and uncontrolled blood loss, and hemorrhage accounts for 30–40% of all deaths after trauma [3]. Shock is characterized by inadequate perfusion (ischemia) that leads to a shortage of cellular substrates, and insufficient oxygenation of vital organs (tissue hypoxia). Most tissues initially maintain adequate energy generation to support cellular metabolism by anaerobic glycolysis, resulting in lactic acid production in proportion to the overall oxygen debt. It is hypothesized that following severe shock, damage to the microcirculation delays restoration of normal perfusion, which is a significant contributor to worse outcome due to delayed resolution of the lactic acidosis.

Studies have shown that the severity of lactic acidosis in trauma is closely associated with worse outcomes [4, 5]. Moreover, the time needed to resolve lactic acidosis may be more important than the peak value reached, and prolonged elevation of lactate levels has been correlated with increased risk of organ failure and higher mortality [6]. Currently there is no approved medication or therapy to specifically address the altered state of the microcirculation during hemorrhagic shock. In order

for an HBOC to perform as an "ischemic rescue" therapeutic agent, it must augment oxygen transport in the microcirculation, improve homogeneity of oxygen flux in capillaries, and facilitate diffusion of oxygen from RBCs to the endothelial cells lining vessels in hypoxic tissues.

The average mortality rate in modern trauma centers has reached low levels (~ 12–15%), which makes a pure mortality-based primary outcome for an HBOC trial a difficult hurdle to achieve. For those trauma patients in severe hemorrhagic shock who also exhibit higher levels of blood lactate (> 5 mmol/L) due to critical tissue ischemia, a recent analysis by Lefering et al. (2013) showed that mortality rates are about two-fold higher (~ 25–30%) [7]. This higher-risk patient population therefore represents an opportunity for HBOC treatment, given as an adjunct to standard-of-care resuscitation, to improve survival as part of a composite clinical efficacy endpoint to demonstrate patient benefit in late-stage clinical trials.

3 Clinical Experience: Lessons Learned with HBOCs in Trauma

Several different HBOC formulations that demonstrated efficacy in preclinical animal models of hemorrhagic shock resuscitation, have also been tested in clinical trials in trauma: Baxter's α-α diaspirin crosslinked human Hb (*HemAssist®*), Biopure's glutaraldehyde-polymerized bovine Hb (*Hemopure®*), Northfield's glutaraldehyde-polymerized human Hb (*PolyHeme®*), and Sangart's maleimide-pegylated human Hb (MP4OX). The important lesson that has been learned in the past 10–15 years from these studies is that the physicochemical properties of each HBOC (e.g., lower P50, higher COP, degree of pegylation, type of chemical modification, molecular size, lower Hb concentration, physiological viscosity) play a role in determining both its safety profile, and whether a particular HBOC will enhance microvascular perfusion in critical organs and restore oxygenation of ischemic tissues sufficiently to reverse any accumulated oxygen debt. Despite success in preclinical animal models, several early-generation HBOC formulations (Baxter, Biopure, and Northfield) with higher P50 and lower COP were unable to translate their preclinical efficacy into patient benefit in late-stage human trauma trials [8].

One of the frequently observed adverse events (AEs) associated with earlier generation HBOCs was hypertension, caused by vasoconstriction secondary to scavenging of nitric oxide. This vasoconstriction effect had the unfortunate consequence of compromising the intended benefit of administering an HBOC to treat tissue ischemia in trauma. Perhaps more importantly, trial design issues played a role in limiting the ability of earlier HBOC trauma studies to demonstrate compelling clinical efficacy. By defining inclusion criteria that were overly broad, these studies allowed for inclusion of patients at both ends of the injury spectrum, i.e., those severely injured and likely to die no matter what intervention was given, and those with non

life-threatening injuries who survive regardless of treatment. Using the degree of hypotension based on a patient's systolic blood pressure (SBP) < 90 mmHg as a criterion for inclusion may have limited proper evaluation of the severity of hemorrhagic shock, resulting in poor patient selection, potential under-resuscitation, and possibly inappropriate dosing. The NORTHFIELD study also withheld potentially life-saving RBC transfusions for 12 h post-injury. These protocol design issues represent shortcomings of the BAXTER and NORTHFIELD trauma studies that may be partly to blame for their inability to demonstrate sufficient efficacy. When combined with the observations that the incidence of some serious adverse event (SAE) rates (including MI, hypertension, coagulopathy) and mortality were higher in HBOC-treated patients, it became impossible to achieve a favorable demonstration of clinical benefit and produced negative opinions and rejections from regulatory authorities. After their Phase 3 programs failed, both BAXTER and NORTHFIELD decided to terminate their HBOC development due to insufficient funding to pursue new studies and based on other commercial and business considerations.

SANGART's recent Phase 2 trauma program with MP4OX added an important design feature missing from previous protocols, i.e., an elevated blood lactate ≥5 mmol/L as a physiological biomarker for inclusion at randomization to prospectively select patients who had suffered sufficient blood loss to reach a critical level of tissue ischemia [9]. SANGART completed a 51-patient pilot Phase 2a feasibility study in 2010 to compare two doses, and a 329-patient multi-center, randomized, single-dose Phase 2b study in 2012. Both of these studies were double blinded, and demonstrated the safety and potential efficacy of a low dose of MP4OX given as an adjunct to standard fluid resuscitation and blood product therapy (i.e., RBCs, FFP, platelets, as needed) in severely injured trauma patients. The Phase 2a study demonstrated more rapid reversal of lactic acidosis and a correlation with better outcomes when lactate levels normalized (≤ 2.2 mmol/L) within 8 h or when lactate decreased by ≥20% in 2 h [10]. In the Phase 2b study, a numerically higher percentage of patients treated with MP4OX were alive and discharged from hospital at Day 28 (primary efficacy endpoint) versus controls (57% vs. 50%; $p = 0.18$). Overall mortality in the MP4OX-treated patients was slightly lower compared to controls (11.6% vs. 13.9%; $p = 0.73$), which represents the first and only trauma study to demonstrate fewer deaths in HBOC-treated patients. There were no differences in the frequency of SAEs or AEs between the two groups. Multiple secondary endpoints also showed promising trends in the MP4OX group (i.e., fewer days on ventilator, in the ICU and in the hospital, as well as faster times to complete resolution of organ failure) [11].

In hindsight, the Phase 2b study was underpowered to confirm the efficacy of the 250-mL MP4OX treatment. One shortcoming of the SANGART Phase 2 program was the premature selection of a single low dose for the Phase 2b study, based on insufficient dose escalation to evaluate higher doses in the Phase 2a feasibility study, which resulted in the need for an additional follow-up study to complete a proper dose comparison. As a result, a 570-patient double-blind, controlled, Phase 2c dose-comparison protocol was designed to determine whether treatment with a 500-mL or 750-mL dose of MP4OX versus standard-of-care might improve patient outcomes and demonstrate compelling efficacy in severely injured trauma patients with evidence of lactic acidosis due to hemorrhagic shock.

4 Regulatory Challenges, Safety, and a Pathway Forward

Previous regulatory guidance from the Food and Drug Administration (FDA) had suggested sponsors demonstrate safety of HBOCs in clinically stable elective surgery patients before moving to high-risk trauma patients [12]. Ironically, it is precisely in trauma patients where an HBOC with appropriate properties may have the greatest opportunity to show clinical benefit, as these patients present with a significant burden of morbidity and risk of death from severe hemorrhagic shock and the adverse ischemic consequences of tissue hypoperfusion. In April 2008, a conference sponsored by the FDA, the Dept. of Defense, and the National Institutes of Health (NIH) was convened to review the current status and safety of various HBOCs in development. The FDA's position and premise for holding this conference at that time was that similar SAE profiles amongst several HBOC products were raising questions regarding the possibility of common underlying mechanism(s) of toxicity despite differences between these HBOC formulations. A variety of opinions were expressed regarding these safety concerns; however, most experts suggested that the biggest challenge for the field was to identify appropriate clinical situations where there would be a more favorable balance of benefit to risk for HBOCs, and finding appropriate methods to evaluate the efficacy and safety of HBOCs in these settings [13].

Coincident with the FDA workshop, was the release of a publication by Natanson *et al*. reporting a meta-analysis to evaluate the relative risk of MI and death in patients enrolled in various HBOC trials [14]. Despite significant methodological issues and questionable statistical validity of a statistical analysis that aggregated disparate trials from a variety of patient populations (i.e., elective surgery vs. emergency or trauma), with different controls (patients receiving crystalloids vs. colloids vs. blood products), and HBOC preparations with diverse physicochemical properties, Natanson concluded that HBOCs were associated with an increased relative risk of death and MI. Due to concerns raised by this meta-analysis, the FDA imposed an immediate clinical hold on all HBOC trials that were either ongoing or planned in the USA at that time. Not surprisingly, several scientific experts and commercial HBOC developers challenged the validity of the methodology and conclusion(s) of this meta-analysis and the FDA's reaction to it [15].

Fortunately, regulatory authorities within the European Union (EU) and in multiple countries worldwide disagreed with the FDA-imposed moratorium, and decided to allow clinical studies to continue after performing their own internal safety review of all relevant clinical and preclinical data provided to them. At that time, Sangart decided to re-focus their clinical development from elective orthopedic surgery to a high-risk trauma indication where MP4OX would have a greater opportunity to demonstrate patient benefit, using Sangart's clinical data from two previous Phase 3 trials in hip arthroplasty [16, 17] as a supporting safety database. Regulators in South Africa, France, Germany, and the UK approved the Phase 2a pilot trauma study in 2009. Subsequently, from 2011 to 2012, Sangart also completed a larger Phase 2b trauma trial after successfully obtaining regulatory approvals in 14 countries worldwide (not including the USA).

While the FDA was intrigued by the success of the Phase 2a trial and the safety profile for MP4OX in that study, they were still unwilling to allow US sites to participate in the Phase 2b trauma trial. However, the FDA was eager for Sangart to show them the results from the Phase 2b study. To help the FDA understand that their pegylated and high affinity MP4OX formulation was different from most early-generation HBOCs, Sangart agreed with the FDA's request for a new submission to summarize all relevant biophysical characterization data, preclinical hemodynamic pharmacology and oxygenation findings, and any new clinical results available from the trauma program. A follow-up pre-IND submission for a new Phase 2c trauma study to compare two higher doses of MP4OX was submitted to the FDA in 2013, and the FDA agreed that Sangart could include US sites in this international trial.

Unfortunately, this positive opinion from the FDA came too late for Sangart to initiate patient enrollment in the Phase 2c study, because a failure to secure new funding forced Sangart to terminate development and cease operations in December 2013. Nevertheless, efforts are still underway to secure new funding to re-establish clinical development of MP4OX and other HBOC formulations for potential future applications in trauma and other ischemia-related clinical settings.

5 Future Directions and Indications for HBOC Development

There have been many potential clinical indications proposed for using HBOCs to prevent or treat acute ischemic conditions [18]. These cover a range of potential applications: [i] protection/maintenance of the functional integrity of vital organs at risk from various medical conditions and/or surgical procedures, e.g., brain (stroke, TBI), spinal chord (vascular surgery), heart (MI, cardiac arrest, angioplasty, CPR, bypass surgery), kidney (transplant surgery), and gut (surgery, shock); [ii] oncology applications to enhance oxygenation of solid tumors (during radiation and/or chemotherapy); [iii] organ transplantation (*ex vivo* perfusion to prolong storage hold-time for heart, lung, kidney, or liver), [iv] drug delivery (targeting oncology drugs conjugated to Hb to the liver); [v] ischemic limbs (peripheral vascular disease, diabetes); [vi] wound healing; [vii] Sickle Cell Disease (acute vaso-occlusive crisis); [viii] sepsis (refractory hypotensive shock); [ix] acute hemolytic anemia (oxygenation bridge); [x] veterinary use (due to limited availability of species-specific animal blood); and [xi] compassionate use (as a temporary blood substitute) for life-threatening anemia when RBCs are not available.

A number of ischemia-related indications are being pursued by Prolong Pharmaceuticals (South Plains, NJ) in early-stage clinical trials using their pegylated bovine carboxyHb (*Sanguinate*™). By correcting oxygenation levels and down-regulating inflammation, *Sanguinate* may have the potential to effectively treat many of the debilitating comorbidities of Sickle Cell disease (SCD) and other disorders caused by anemia and/or hypoxia/ischemia [19]. These include preventing delayed graft function following kidney transplantation, treating painful vaso-

occlusive crises in adult patients with SCD and beta-Thalassemia, and reducing or preventing delayed cerebral ischemia following subarachnoid hemorrhage.

Recent research in the field has focused on the oxidative properties of Hb and how they can be modified to reduce the potential intrinsic toxicity of exogenously added iron and heme when HBOCs are infused. One such approach, developed by SynZyme Technologies (Sioux Falls, SD) [20] involves polynitroxylation of a pegylated Hb to create PNPH (aka *SanFlow*, or nanoRBC) as a nanomedicine for use in critical care and resuscitation following hemorrhagic shock [21]. Polynitroxylation adds superoxide dismutation activities to the Hb, which when infused create a superoxide-free vascular space. This helps to conserve endogenous nitric oxide levels within the vasculature, thereby preventing vasoconstriction and maintaining microcirculatory blood flow. PNPH has been evaluated in preclinical animal studies in stroke [22] and traumatic brain injury (TBI) [23], and has demonstrated both safety and neuroprotective properties (i.e., prevent neuronal death, restore MAP, reduce brain edema and increase cerebral perfusion pressure) following resuscitation in a murine model of combined TBI plus hemorrhagic shock [24].

Traumatic hemorrhage from penetrating and/or blunt injury offers a huge potential market for an HBOC as an adjunct to early resuscitation in both military and civilian settings. Similarly, non-traumatic hemorrhagic shock represents a potential expansion of the trauma indication, by using HBOC treatment following cerebral bleeding, ruptured aortic aneurysms, iatrogenic hemorrhage during vascular surgery, or obstetric bleeding from a ruptured placenta. TBI represents a subset of trauma with perhaps the highest mortality and longest hospital and ICU stays. Any HBOC that can treat oxidative stress from superoxide, down-regulate inflammation, and deliver oxygen to ischemic tissue holds great promise as a potential therapeutic agent in trauma, TBI, SCD, and possibly in stroke.

Acknowledgments PEK was formerly employed by Sangart Inc. (San Diego, CA) as VP, Clinical Development, during the conduct of the MP4OX clinical trials in trauma.

References

1. Epstein JS, Jaffe HW, Alter HJ et al (2013) Blood system changes since recognition of transfusion-associated AIDS. Transfusion 53:2365–2374
2. Mitchell P, Weiskopf R, Zapol WM (2013) NIH/FDA/DOD interagency working group on oxygen therapeutics. In: Kim HW, Greenburg AG (eds) Hemoglobin-based oxygen carriers as red cell substitutes and oxygen therapeutics. Springer, Berlin, pp 141–147
3. Kauvar DS, Wade CE (2005) The epidemiology and modern management of traumatic hemorrhage: US and international perspective. Crit Care 9:S1–S9
4. Abramson D, Scalea TM, Hitchcock R et al (1993) Lactate clearance and survival following injury. J Trauma 35:584–589
5. Manikis P, Jankowski S, Zhang H et al (1995) Correlation of serial blood lactate levels to organ failure and mortality after trauma. Am J Emerg Med 13:619–622
6. Regnier MA, Raux M, Le Manach Y et al (2012) Prognostic significance of blood lactate and lactate clearance in trauma patients. Anesthesiology 117:1276–1288

7. Lefering R, Zielske D, Bouillon B et al (2013) Lactic acidosis is associated with multiple organ failure and need for ventilator support in patients with severe hemorrhage from trauma. Eur J Trauma Emerg Surg 39(5):487–493. doi:10.1007/s00068-013-0285-3
8. Jahr JS, Akha AS, Holtby RJ (2012) Crosslinked, polymerized, and PEG-conjugated hemoglobin-based oxygen carriers: clinical safety and efficacy of recent and current products. Curr Drug Discov Technol 9:158–165
9. Brohi K, Plani F, Moeng M et al (2010) Multicenter randomized controlled trial TRA-204 to evaluate the safety and efficacy of MP4OX in lactate clearance following trauma hemorrhage. Crit Care Med 38:749
10. Brohi K, Levy H, Keipert PE et al (2011) Normalization of lactate within 8 hours or ≥20% clearance in initial 2 hours correlate with outcomes from traumatic hemorrhage. Crit Care Med 39:643
11. Brohi K, Boffard K, Zielske D et al (2013) Effects of MP4OX, an oxygen therapeutic, on clinical outcomes in trauma patients with hemorrhagic shock: a Phase IIb multi-center randomized placebo-controlled trial. Poster presentation: American Association for the Surgery of Trauma (AAST) meeting, San Francisco
12. US Food and Drug Administration (2004) Draft guidance for industry: criteria for safety and efficacy evaluation of oxygen therapeutics as red blood cell substitutes. Issued Oct 2004 (www.rsihata.com/updateguidance/usfda2/bio1/ucm080290)
13. Silverman TA, Weiskopf RB (2009) Hemoglobin-based oxygen carriers: current status and future directions. Anesthesiology 111:946–963
14. Natanson C, Kerns SJ, Lurie P et al (2008) Cell-free hemoglobin-based blood substitutes and risk of myocardial infarction and death. A meta-analysis. JAMA 299:2304–2312
15. Letters to the Editor (2008) Hemoglobin-based blood substitutes and risk of myocardial infarction and death. JAMA 300:1295–1300
16. Olofsson CI, Górecki AZ, Dirksen R et al (2011) Evaluation of MP4OX for prevention of perioperative hypotension in patients undergoing primary hip arthroplasty with spinal anesthesia: a randomized, double-blind, multicenter study. Anesthesiology 114:1048–1063
17. Van der Linden P, Gazdzik TS, Jahoda D et al (2011) A double-blind, randomized, multicenter study of MP4OX for treatment of perioperative hypotension in patients undergoing primary hip arthroplasty under spinal anesthesia. Anesth Analg 112:759–773
18. Winslow RM (2006) Clinical indications for blood substitutes and optimal properties. In: Winslow RM (ed) Blood substitutes. Elsevier, London, pp 115–125
19. Misra H, Lickliter J, Kazo F et al (2014) Pegylated carboxyhemoglobin bovine (*Sanguinate*): results of a Phase I clinical trial. Artif Organs 38:702–707
20. Hsia JC, Ma L (2012) Compositions and methods of use of neurovascular protective multifunctional polynitroxylated pegylated carboxy hemoglobins for transfusion and critical care medicine. US Patent 8273857B2 (https://patents.google.com/patent/US8273857B2/en)
21. Hsia CJC, Ma L (2012) A hemoglobin-based multifunctional therapeutic: polynitroxylated pegylated hemoglobin. Artif Organs 36:215–220
22. Zhang J, Cao S, Ma L et al (2013) Protection from transient focal cerebral ischemia by transfusion of polynitroxylated pegylated hemoglobin. Stroke 44:A154
23. Shellington DK, Du L, Wu X et al (2011) Polynitroxylated pegylated hemoglobin: a novel neuroprotective hemoglobin for acute volume-limited fluid resuscitation after combined traumatic brain injury and hemorrhagic hypotension in mice. Crit Care Med 39:494–505
24. Brockman EC, Bayir H, Blasiole B et al (2012) Polynitroxylated-pegylated hemoglobin attenuates fluid requirements and brain edema in combined traumatic brain injury plus hemorrhagic shock in mice. J Cereb Blood Flow Metab 33:1457–1464

Chapter 46
The Penultimate Tyrosine Residues are Critical for the Genotoxic Effect of Human Hemoglobin

Sandeep Chakane, Vijay Markad, Kisan Kodam, and Leif Bülow

Abstract Hemoglobin (Hb) is a potent oxidant outside the erythrocyte. The tyrosines α140 and β145 play an important role in the structure and function of Hb by forming switch and hinge contacts. These carboxy-terminal residues of the alpha and beta chains, respectively, were replaced to phenylalanine and several different methods were used to characterize the obtained mutants including a comet and plasmid DNA cleavage assay. It was observed that the genotoxic effect was 40% higher for αY140F compared with the wildtype, the βY145F and the double (αY140/β145F) mutants as determined by the comet assay. Cleavage of purified plasmid DNA after Hb application also revealed that the αY140F mutant showed 2-fold higher activity, while the βY145F and αY140/β145F mutants reduced the activity compared to wildtype Hb. This study clearly indicates that the penultimate tyrosines are involved in the genotoxicity of Hb.

Keywords Hemoglobin • Genotoxicity • Comet assay • Plasmid DNA • Supercoiled DNA

1 Introduction

Free or acellular Hb in the circulatory system is responsible for several serious and potentially life threatening conditions [1]. The protein is involved in a plethora of different reactions, e.g. various redox reactions and binding of nitric oxide (NO).

S. Chakane • L. Bülow (✉)
Pure and Applied Biochemistry, Department of Chemistry, Lund University, 223 62 Lund, Sweden
e-mail: leif.bulow@tbiokem.lth.se

V. Markad • K. Kodam
Department of Chemistry, Savitribai Phule Pune University, 411 007 Pune, India

H.J. Halpern et al. (eds.), *Oxygen Transport to Tissue XXXIX*, Advances in Experimental Medicine and Biology 977, DOI 10.1007/978-3-319-55231-6_46

Particularly its oxidative reactions together with hydrogen peroxide have been dissected in detail [2]. Cooper et al. have demonstrated that βY145F is one of the critical radical formation sites in Hb [3].

The tyrosines adjacent to the C-terminals of the alpha and beta chains of Hb play important roles in stabilizing the T state. The residues αY140 and βY145 thus form hydrogen bonds with the carbonyls groups of αV93 and βV98, respectively [4, 5]. The replacement of these penultimate Tyr residues with aromatic amino acids such as Phe has been shown to have a major impact on the oxygen affinity of Hb, especially for the αY140F mutant [5]. Earlier studies have largely focused on the influence of Hb reactivity on lipid and protein modifications. Here, we demonstrate that simple assays can also be utilized to characterize toxicity effects on nucleic acids caused by Hb. In the present study, we have employed the comet and a plasmid DNA (pDNA) cleavage assay for characterizing the genotoxic effects of wildtype (wt) and mutant Hb proteins. It was observed that αY140F escalated DNA cleavage activity of Hb, while the hydrolytic effects were much less pronounced for β145F.

2 Methods

The wt and mutant Hbs were constructed, expressed and purified as described earlier [6]. Primers were purchased from MWG Biotec (Ebersberg, Germany). Enzyme Phusion (Finnzymes Oy, Espoo, Finland) was used for site-directed mutagenesis. The methylated DNA was digested by *Dpn*I (Fermentas, Helsingborg, Sweden) and mutated plasmids were transformed into *E. coli* strain BL21 DE3. The expressed protein was purified by CM Sepharose followed by Q Sepharose chromatography [7]. To prevent oxidative side reactions during handling, the protein samples were kept in their CO forms by bubbling with carbon monoxide (CO) at every step of expression and purification. The protein concentration was calculated on the basis of molar heme equivalent. To prepare metHb, the CO forms were incubated with potassium ferricyanide (10 mM) at 4 °C in presence of strong light. The excess ferri/ferrocyanide was removed from the ferric proteins by filtration through a size exclusion Sephadex G-25 column (approx. 5 × 0.5 cm). The concentration of Hb was determined by reduction of an aliquot of the ferric protein to the deoxy form using sodium dithionite, and using the extinction coefficient of 133 mM^{-1} cm^{-1} at 430 nm.

Single cell gel electrophoresis or comet assay was carried out to investigate the ability of the Hb samples to induce DNA strand breaks. Lymphocytes were isolated from peripheral blood (collected from healthy male volunteers) using lymphocyte separation medium (HiSepTM LSM 1077, Himedia, India). Cells were washed with phosphate buffered saline (PBS) and finally resuspended in RPMI 1640 medium (Hyclone, Thermo Scientific). Lymphocytes (1 × 104 cells/ml) were incubated with various concentrations of mutant metHb (2.5, 5 and 10 μM, 30 min, 37 °C). Hemin (10 μM), the reactive ferric protoporphyrin-IX group released from a cell-free Hb, was used as control. Cells incu-

bated in RPMI 1640 (30 min, 37 °C) and H_2O_2 (100 μM, 5 min, 4 °C) were used as the negative and positive control, respectively. After each treatment, the cells were washed with cold PBS and processed for the comet assay.

The alkaline comet assay was carried out as described by Singh et al. [8]. The cells (10 μl) were mixed with 90 μL of 0.55% low-melting agarose, and layered on slides (precoated with 1.0% normal-melting agarose) and kept on ice for 5 min. After solidification of the agarose, slides were covered with another layer of 90 μL of low-melting agarose (0.50%) and then immersed in lysis solution (2.5 M NaCl, 100 mM EDTA, 10 mM Tris, 1% Triton X-100, and 10% DMSO) for 2 h at 4 °C. After lysis, DNA was allowed to unwind in alkaline buffer (300 mM NaOH, 10 mM Na_2EDTA, pH > 13.0) for 25 min before electrophoresis at 25 V and 300 mA for 25 min at 4 °C. To neutralize the excess alkali, slides were washed thrice with neutralizing buffer (0.4 M Tris, pH 7.5) for 5 min at 4 °C. Slides were then stained with 75 μL of ethidium bromide and observed under the fluorescence microscope (Olympus CX41, Japan) equipped with a CCD camera. Comet images (50 cells from each of two replicated slides, three independent experiments and 300 images per sample) were analyzed by a computer-assisted image analysis system (CASP software). Percent tail DNA (% tail DNA) was determined for quantification of DNA damage.

The DNA cleavage assay was also carried out by incubating each ferric Hb (metHb) variant with purified pUC18 plasmid (25 ng/μl) at 37 °C. DNA degradation was monitored by analyzing samples every 2 h. The percentage of remaining supercoiled plasmid DNA (sc DNA) was determined by agarose gel electrophoresis as estimated by densitometry analysis with the help of the 'Quantity one' software from Bio-Rad. Calculations of statistical significance were made by one way Anova followed by Tukey's multiple comparison test.

3 Results

Lymphocytes were incubated with several concentrations (2.5–10 μM) of each mutant metHb. Any possible interference from intrinsic haptoglobin [9] in the assay was minimized by avoiding the use of calf serum in this assay. These experiments demonstrated that Hb induced severe DNA damage in lymphocytes already after 30 min incubation at 37 °C. The mutant αY140F induced significantly more (40%) DNA damage ($P < 0.05$) compared with wt Hb. In the range tested, DNA damage effects were proportionally dependent on the Hb concentration used. The βY145F and double (αY140/β145F) mutants showed the same DNA damages as wt Hb (Fig. 46.1, Table 46.1). Hemin was used as a control to examine if the molecular mechanisms behind the DNA cleavage observed could be directly linked to the heme groups or associated with radicals on the globin chains. It resulted in similar cleavage results as control cells, indicating that formation of radicals on the globin polypeptide chains is involved in the reaction. Generally, the Tyr residues are the

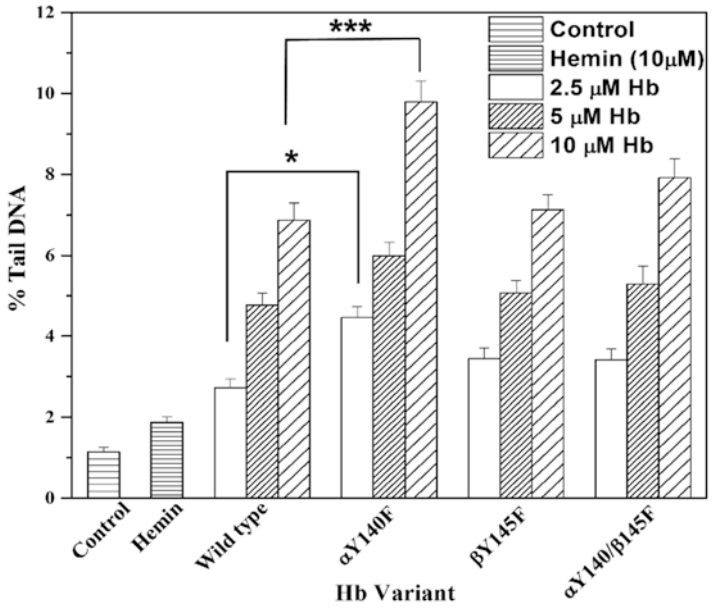

Fig. 46.1 DNA damage by different Hb variants as determined by the comet assay. αY140F showed significantly more DNA damage than wildtype Hb. Comet images from three independent experiments were performed and 50 comet images were analyzed for each experiment in duplicate. Data were analyzed by one-way ANOVA followed by Tukey's multiple comparison test (* $P < 0.05$; *** $P < 0.001$)

Table 46.1 Comet assay of different Hb samples

	% tail DNA		
Sample	2.5 μM Hb	5 μM Hb	10 μM Hb
Wild type	2.72	4.77	6.89
αY140F	4.46*	5.99^{ns}	9.80***
βY145F	3.45^{ns}	5.07	7.29^{ns}
αY140/β145F	3.41 ^{ns}	5.28	8.00^{ns}

The % tail DNA at different protein concentrations were determined
Control sample and hemin did not cause DNA damage. An average of 300 images/sample were analyzed and statistical calculations were performed by one-way ANOVA followed by Tukey's multiple comparison test (*$P < 0.05$; ***$P < 0.001$; *ns* not significant)

primary radical formation sites within the Hb molecule, under the oxidative stress [10]. Therefore, another Phe mutant was examined, αY24F, but it showed identical damage patterns as wt Hb further strengthening the proposed roles of αY140 and βY145 in modulating DNA damage effects.

To further characterize the DNA cleavage activity of Hb, the protein samples were incubated together with purified supercoiled plasmid DNA (scDNA). The

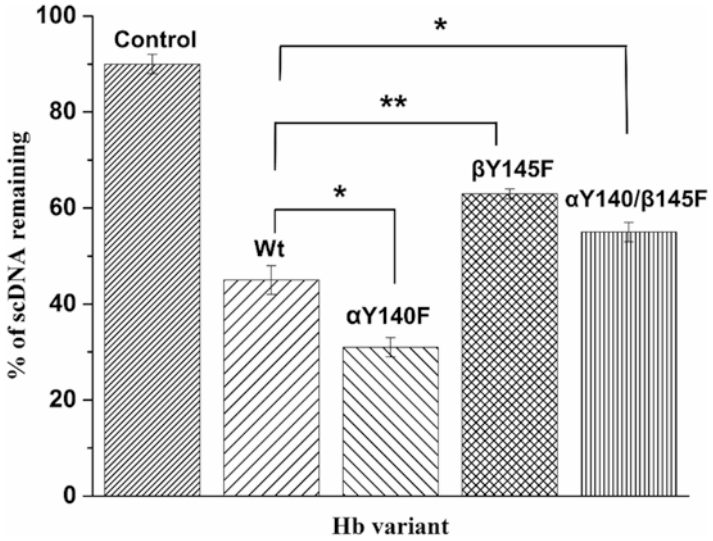

Fig. 46.2 Effects of different Hb variants on plasmid DNA cleavage as analyzed by the reduced level of supercoiled DNA after incubation at 30 min at 37 °C (n = 6, * $P < 0.05$; ** $P < 0.01$)

cleavage activity proved to be directly related to the concentration of Hb applied. Under the conditions used, wt showed 40% of remaining sc DNA, whereas only 30% remained after 12 h of incubation using the αY140 mutant. However, when examining the βY145F and the αY140/β145F mutants, 63% and 55% scDNA remained, respectively (Fig. 46.2).

4 Discussion

Many enzymes use Tyr residues in catalysis or long-range electron transfer. This study focused on the penultimate Tyr residues of Hb. There are several natural mutants at these position: Hb Osler (Tyr β145Asp), Hb Bethesda (Tyr β145His), Hb Rainier (Tyrβ145Cys) and Hb McKees Rocks (Tyr β145terminated) with a high oxygen affinity and lack of T state conformation. However, only one natural mutant for αY140 has been reported where the Tyr has been replaced with His (HbVar database) [11].

Hb is a redox active protein that easily can modify proteins, lipids and nucleic acids. Two different assays were developed to characterize the damaging effects of Hb on DNA. In the comet assay, lymphocytes were used to characterize the genotoxic effects of different Hb mutants. In this approach, Hb molecules penetrate the cell membranes and are then allowed to react with available nucleic acids. The effects of Hb on cells are rapid, within minutes, and take place even at very low concentrations, in the μM range. Both the oxy and met forms of Hb generate similar

DNA cleavages. Glei et al. have shown that cell-free Hb can cause DNA damage in primary colon cells as well in a colon cancer cell line. Moreover, hemin proved to be more cytotoxic than genotoxic by interacting strongly with cell membranes [12].

The comet assay was complemented with a more direct plasmid DNA-based assay. Two levels of DNA degradation caused by Hb were monitored, the conversion of sc to open circular (oc) DNA, which requires a single nick on the DNA molecules, as well as the more extensive cuts needed for formation of linear DNA. Both the comet and plasmid assays generated similar results. It was observed that αY140F showed higher DNA cleavage activity than the βY145F and αY140/β145F. Recent studies by Zhao et al. [13] and Deshpande et al. [14] using myoglobin have also confirmed the role of reactive oxygen species in pDNA cleavage as well as the involvement of catalytically active amino acids for DNA cleavage. Lipid peroxidation was examined for comparative purposes and it was observed that αY140F produced higher levels of conjugated diene than wt (unpublished data). Thus, similar data were obtained from the lipid peroxidation and comet assay, but this is not absolute since they occur with different mechanisms. In comet assay, DNA damage can occur due to the mitochondrial or membrane damage [15]. However, peroxyl and alkoxyl radicals are produced from lipid hydroperoxides by the redox active heme [16]. Interestingly, βY145F and αY140/β145F generated less marked DNA cleavage compared with wt, indicates the penultimate Tyr of the beta chain is a leading radical formation site and is consistent with previous findings [3]. This can be valuable for the further development of hemoglobin-based oxygen carriers (HBOCs) with reduced genotoxicities.

Acknowledgments The Swedish Research Council, Swedish Fund for Strategic Research and Erasmus Mundus Lot 13 to SC are all gratefully acknowledged.

References

1. Olsson MG, Allhorn M, Bülow L et al (2012) Pathological conditions involving extracellular hemoglobin: molecular mechanisms, clinical significance, and novel therapeutic opportunities for α(1)-microglobulin. Antioxid Redox Signal 17:813–846
2. Mollan TL, Alayash AI (2013) Redox reactions of hemoglobin: mechanisms of toxicity and control. Antioxid Redox Signal 18:2251–2253
3. Cooper CE, Schaer DJ, Buehler PW et al (2012) Haptoglobin binding stabilizes hemoglobin ferryl iron and the globin radical on tyrosine beta145. Antioxid Redox Signal 18:2264–2273
4. Huang S, Peterson ES, Ho C et al (1997) Quaternary structure sensitive tyrosine interactions in hemoglobin: a UV resonance Raman study of the double mutant rHb (beta99Asp-->Asn, alpha42Tyr-->Asp). Biochemistry 36:6197–6206
5. Kneipp J, Balakrishnan G, Chen R et al (2006) Dynamics of allostery in hemoglobin: roles of the penultimate tyrosine H bonds. J Mol Biol 356:335–353
6. Reeder BJ, Grey M, Silaghi-Dumitrescu RL et al (2008) Tyrosine residues as redox cofactors in human hemoglobin: implications for engineering nontoxic blood substitutes. J Biol Chem 283:30780–30787

7. Ratanasopa K, Cedervall T, Bülow L (2016) Possibilities of using fetal hemoglobin as a platform for producing Hemoglobin-Based Oxygen Carriers (HBOCs). Adv Exp Med Biol 876:445–453
8. Singh NP, McCoy MT, Tice RR et al (1988) A simple technique for quantitation of low levels of DNA damage in individual cells. Exp Cell Res 175:184–191
9. Ratanasopa K, Chakane S, Ilyas M et al (2013) Trapping of human hemoglobin by haptoglobin: molecular mechanisms and clinical applications. Antioxid Redox Signal 18:2364–2374
10. Deterding LJ, Ramirez CD, Dubin RJ et al (2004) Identification of free radicals on hemoglobin from its self-peroxidation using mass spectrometry and immuno-spin trapping: observation of a histidinyl radical. J Biol Chem 279:11600–11607
11. Giardine B, Borg J, Viennas E et al (2014) Updates of the HbVar database of human hemoglobin variants and thalassemia mutations. Nucleic Acids Res 42:D1063–D1069
12. Glei M, Klenow S, Sauer J et al (2006) Hemoglobin and hemin induce DNA damage in human colon tumor cells HT29 clone 19A and in primary human colonocytes. Mutat Res Fund Mol Mech Mutagen 594:162–171
13. Zhao Y, Du KJ, Gao SQ et al (2016) Distinct mechanisms for DNA cleavage by myoglobin with a designed heme active center. J Inorg Biochem 156:113–121
14. Deshpande MS, Junedi S, Prakash H et al (2014) DNA cleavage by oxymyoglobin and cysteine-introduced metmyoglobin. Chem Commun 50:15034–15036
15. Olive LP, Banáth PJ (2006) The comet assay: a method to measure DNA damage in individual cells. Nat Protoc 1:23–29
16. Moore KP, Holt SG, Patel RP et al (1998) A causative role for redox cycling of myoglobin and its iby alkalinization in the pathogenesis and treatment of rhabdomyolysis-induced renal failure. J Biol Chem 273:31731–31737

Chapter 47
Methemoglobin: A New Way to Distinguish Burn Depth

Guennadi Saiko

Abstract In this work, we present a model of dynamics of methemoglobin (MetHb) in burn injuries and show that measuring levels of MetHb can distinguish thickness in burn injuries. *Methods*: The model of dynamics of MetHb levels in blood of subjects with burn injuries has been developed based on the vascular morphology of the skin. The model contains burn-specific and non-specific components. *Results*: The model predicts three distinct outcomes: (a) superficial burn, where the superficial plexus is mainly intact, (b) partial thickness burn, where the superficial plexus lies within the zone of coagulation, but the deep plexus is mainly intact, and (c) full depth burn, where the deep plexus lies in the zone of coagulation. The use of MetHb as a marker of burn injury has not just anatomical, but also physiological justification. The model is in qualitative agreement with a clinical study and an animal model (Yorkshire swine), which used Near Infrared Spectroscopy to assess MetHb levels in burns. *Conclusions*: MetHb level in burn injuries is a physiological variable that can be used to classify burn injuries.

Keywords Burn injury • Burn injury assessment • Methemoglobin • Tissue viability • Burn depth

1 Introduction

Burn injury is one of the most common injuries associated with trauma, with more than 1.25 million patients seeking medical attention each year in the U.S. alone [1]. Treatment of burns depends substantially on classification by their depth: superficial or first-degree burns (epidermal injury), partial thickness or second-degree burns (dermal injury), full thickness or third-degree burns (destruction of the subcutaneous layer), and fourth-degree burns (destruction of the underlying tissues and muscles). Burn depth assessments are performed visually and rely heavily on the

G. Saiko (✉)
Department of Physics, Ryerson University, Toronto, ON, Canada
e-mail: gsaiko@ryerson.ca

H.J. Halpern et al. (eds.), *Oxygen Transport to Tissue XXXIX*, Advances in Experimental Medicine and Biology 977, DOI 10.1007/978-3-319-55231-6_47

experience of the physician. As a result, the burn depth is routinely underestimated during the initial examination [2]. Non-viable tissue may appear viable for some time after injury. In addition to that, some degree of progressive microvascular thrombosis is often observed on the wound periphery. The inaccuracies associated with diagnosis affect treatment. Thus, the correct determination of burn depth and tissue viability is of great importance.

A wide range of diagnostic tools for diagnosis of burn injury has recently been reported [3]: laser Doppler, various dyes, ultrasonography, thermography, nuclear magnetic resonance and optical coherence tomography. However, to date, none of these technologies have achieved widespread clinical acceptance or utilization.

In a report by Cross [4], the author proposed to use spectroscopy of methemoglobin (MetHb) to assess burn depth and tissue viability in burn injuries. Methemoglobin is an important biomolecule with a substantial presence in tissues, which can be characterized using optical reflectance measurements due to its absorption maximum at 630 nm. However, the idea has not received yet a wide clinical adoption in part due to the lack of theoretical justification.

The purpose of this work is to develop a realistic model of MetHb dynamics in burns, which will justify using MetHb spectroscopy/imaging as a noninvasive tool to assess burn depth and tissue viability.

2 Model

We developed a model of the burn, which depicts the dynamics of the methemoglobin in the burn. The goal is to build a physiological model, however, it should be based on anatomy and morphology of the skin.

Skin Vasculature The skin vasculature consists of two plexuses: a superficial and a deep plexus of arterioles and venules. The deep plexus is located in the lower part of the reticular dermis close to the dermal-hypodermal junction. The superficial plexus (or subpapillary plexus) is situated in the upper part of the reticular dermis, just beneath the papillary dermis. Those two plexuses lie parallel to the skin surface. They are connected to one another by communicating vessels (ascending arterioles and descending venules) and lead eventually to veins residing within septa of the subcutaneous fat. Arterioles and venules of the deep dermis and hypodermis are larger than the corresponding vessels of the superficial plexus (diameter 50–100 versus 25 μm). From the superficial plexus, a network of capillaries loops into each dermal papilla.

Burn Injury Model The primary mechanism of tissue damage in thermal burns is protein unfolding [5] or denaturation. This can occur at temperatures as low at 40–44 °C, but the process is substantially accelerated above 70 °C. In particular, a 10 s exposure caused endothelial necrosis within the first 30% of the dermis versus a 30 s injury where the physical levels of necrosis were measured at 85% of the dermis [6].

Methemoglobin Methemoglobin is an important biomolecule and is formed when the iron of the hemoglobin is oxidized to its ferric state. In healthy individuals only 1% of circulating hemoglobin is MetHb, and anything greater is considered to be methemoglobinemia. Oxyhemoglobin can undergo spontaneous oxidation at the heme iron centerin the process, which is called auto-oxidation [7]. Only 24% of MetHb formation occurs from the auto-oxidation process and the remainder occurs from reactive oxygen species (ROS) and reactive nitrogen species (RNS). In normal situations, the red blood cell functions as an efficient antioxidant and contains many reductive systems within the cell [8]. The NADH cytochrome b5/cytochrome b5 reductase system accounts for 99% of daily MetHb reduction. The reconversion rate of MetHb in normal individuals is 15% per hour.

Due to denaturation of most enzymes in burn injury, all enzymatic pathways of MetHb formation and reduction are grossly impaired. Thus, within the burn site MetHb is formed mostly in the process of auto-oxidation and its reduction is substantially impaired, which leads to MetHb accumulation in the injured blood vessels within the wound.

Burn-Specific Methemoglobin Dynamics If the extent of burn injury goes beyond the epidermal layer, some (if not all) vessels of the superficial plexus and the deep plexus (for partial thickness burn and above) are occluded and hemoglobin is trapped within them. Hemoglobin trapped in damaged vessels undergoes auto-oxidization. In burn injury, within the zone of coagulation and stasis, enzymes are mostly unfolded (denaturated) and therefore the ability to reduce MetHb is grossly diminished.

Accelerated creation and diminished reduction of the MetHb lead to accumulation of MetHb in burn wounds. We can describe this process by the first-order kinetic equation with γ as a rate of auto-oxidation, which can be estimated as 3% per day [9].

If the immune system is capable of delivering leucocytes to the burn site, then the neutrophils will scavenge dead cells and cellular debris from the injury site, including trapped hemoglobin. We can emulate this process by introducing a multiplier *(1-N)*, where *N* is the percentage of cell debris engulfed by neutrophils.

Thus, the burn-specific dynamics will be governed by three processes: (a) heat-induced conversion of ferrous to ferric hemoglobin [10], which is responsible for immediate increase in MetHb concentration post-burn (we will denote this ratio by β, which using [4] can be evaluated as 0.003), (b) auto-oxidation of trapped Hb, and (c) the phagocytosis and metabolic degradation of Hb by neutrophils.

The extent of the process is conditioned by the degree of the injury: the deeper the zone of coagulation, the more hemoglobin being trapped.

Burn-Non-Specific Methemoglobin Dynamics In the case of burn injury, there is an extensive damage to the tissue, including denaturation of multiple enzymes responsible for ROS reduction. Thus, the overall ROS concentration in the vicinity of burn injury growths substantially, which results in an increase of MetHb concentration locally. If the size of the burn site is large, then it will manifest itself in significant changes to systemic MetHb concentration as well. We can assess the impact

of the burn size on the systemic and local MetHb concentrations. The local component of the MetHb concentration will depend on the overall time RBCs will spend in the zone of the injury. Thus, the local MetHb concentration will depend linearly on the diameter of the burn. Circulating red blood cells will be diluted by the body. Hence, the systemic MetHb concentration increase will be determined mostly by the area of the burn site.

We should point out that this mechanism of MetHb concentration increase is not specific to the burn injury and will be applicable to any type of acute wound. The magnitude of this effect can be larger in burn injury due to denaturation of enzymes that reduce ROS, and can lead to higher ROS concentrations.Thus, taking into account burn-specific and non-specific mechanisms we can write the expression for the MetHb concentration in the burn site

$$c_{MetHb} = c_{circ}\left(\alpha_b + \Delta\alpha_s + \Delta\alpha_l\right) + c_{trap}\left(\alpha_b + \beta + \gamma t\right)\left(1 - N\left(t\right)\right) \tag{47.1}$$

Here c_{circ} and c_{trap} correspond to the volume concentration of circulated and trapped hemoglobin. α_b, $\Delta\alpha_s$, and $\Delta\alpha_l$ denote baseline MetHb concentration in the blood and its systemic and local increase over the baseline post-injury. *N(t)* is the percentage of engulfed debris. We also ignored all terms higher than linear in the expansion of the solution for the trapped MetHb concentration.

3 Results

The model predicts different dynamics of MetHb accumulation in burn injury in three different scenarios: (a) superficial burn, where the superficial plexus is mainly intact, (b) partial thickness burn, where the superficial plexus lies within the zone of coagulation, but the deep plexus is mainly intact, and (c) full depth burn, where the deep plexus lies in the zone of coagulation.

For a superficial burn (superficial thickness, ST), the superficial plexus is mainly intact and functioning. Arterioles of the superficial plexus are dilated and blood flow (i.e., perfusion) in the affected area is increased. Enhanced perfusion combined with decreased ROS reduction activity (due to denaturation of some enzymes, e.g. SOD) leads to elevated ROS concentrations. In addition, some capillary loops are occluded and hemoglobin is trapped within them. Hemoglobin trapped in damaged vessels undergoes auto-oxidation, while its reduction in damaged vessels is impaired. Thus, overall MetHb presence in the burn injury is gradually increasing (build-up in damaged vessels and increased concentration in intact vessels due to increased systemic and local ROS activity).

However, with mainly intact superficial plexus, the response of the innate immune system is fast and efficient. The influx of neutrophils, which scavenge cell debris, is the first line of an innate immune defense. Phagocytosis by human neutrophils takes on average 9 min [11]. During this scavenging phase, which takes place

for approximately 24 h, the wound still has increased ROS concentration, which will manifest itself in elevated MetHb levels. After 24–48 h, all cellular debris including trapped hemoglobin gets scavenged and MetHb levels start returning to a physiological norm.

For partial thickness burn (both superficial (SPT) and deep (DPT) partial thickness), where the superficial plexus lies within the zone of coagulation, but the deep plexus is mainly intact, the superficial plexus is no longer functioning properly. Some (if not all) vessels of the superficial plexus are occluded and hemoglobin is trapped within them. Hemoglobin molecules are mostly denaturated. Hemoglobin trapped in damaged vessels undergoes auto-oxidation and MetHb concentration is gradually increasing. Neutrophils cannot access the burn site from the superficial plexus. Their influx comes from the deep plexus; however, migration and scavenging take a longer time, thus the inflammation stage is longer. The MetHb presence increases during the first 48 (for SPT) or 72 (for DPT) h, after that it starts declining.

Finally, for the full thickness burn (FT), where the deep plexus lies in the zone of coagulation, neither superficial nor deep plexuses are functioning properly. All blood vessels are occluded and hemoglobin is trapped within them. Hemoglobin molecules are denatured. Hemoglobin trapped in damaged vessels undergoes auto-oxidation and MetHb concentration gradually increases. However, diffusion of oxygen to the tissue is limited, thus the tissue is hypoxic and the auto-oxidation rate is lower than for superficial and partial thickness burns. Neutrophils cannot access the burn site. Their influx comes from far away intact zones and the immune system is overwhelmed. This results in necrosis and the non-viable tissue becomes the most probable outcome.

We assessed predictions of the model for up to 72 h post-burn numerically (see Fig. 47.1). Based on [12], volumes of capillaries, upper and lower plexuses were estimated as equal. Auto-oxidation rate γ was set to 0.015 a day, with further reduction for full depth burn by 60%.

4 Discussion and Conclusions

The proposed model is consistent with existing burn injury classification: superficial (epidermal damage only), partial thickness (dermal injury), and full thickness (destruction of the subcutaneous layer) burns. However, the use of MetHb as a marker of burn injury has not just anatomical, but also physiological justification.

Our model predictions are in qualitative agreement with experiments using spatially resolved NIRS. In particular, in the animal model (Yorkshire swine) [4] it was found that MetHb levels were significantly increased in deep partial thickness burn sites relative to superficial burn and control sites. Deep partial thickness injury MetHb levels were 29% greater than superficial injuries and 50% greater than control at 24 h post-burn. By 72 h post-burn injury, in deep injuries, MetHb levels were 66% greater than superficial burns and showed a 72% increase above control levels.

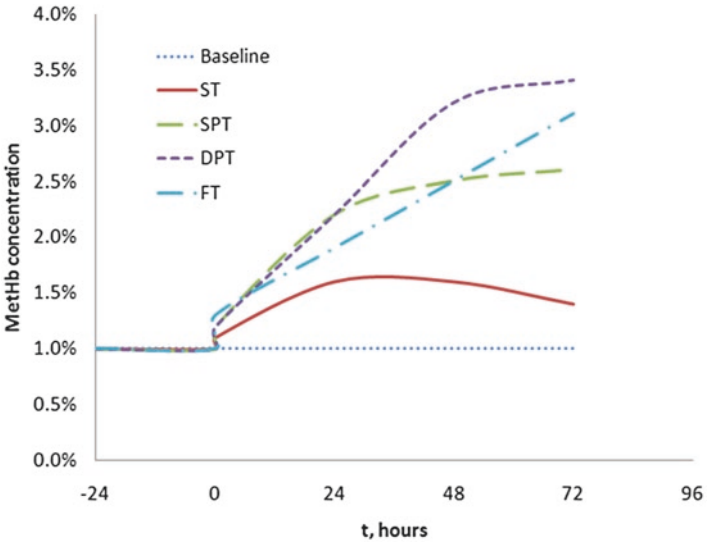

Fig. 47.1 MetHb dynamics in superficial (ST-*solid line*), superficial partial thickness (SPT-*long dash*), deep partial thickness (DPT-*dash*), and full thickness (FT-*dot dash*) burn injury vs. pre-injury baseline (*dotted*)

In a clinical study by Cross et al. (2016; unpublished data) (Cross KM, private communication), a total of 297 burn sites from 26 patients was assessed 24, 48, and 72 h post-burn injury. At 24 h, MetHb levels increased by 25% in non-viable injuries compared to viable ones, and was 44% greater than that of control. At 48 h, MetHb in non-viable injuries increased to 46% above the viable injury and 73% greater than control. By 72 h post-burn, non-viable burns had a MetHb level 80% greater than control.

In both human and swine experimental models the difference between various burn degrees became more pronounced over time, allowing the differentiation of burn depth and tissue viability as early as 24 h post-burn injury: PT has substantially more MetHb than ST or FT. After that, according to experiments and consistent with the model: (a) for superficial burns MetHb content will reach the maximum and start receding, (b) for partial thickness burn it will keep increasing for another 24 h (SPT) or 48 h (DPT) and then start receding, (c) finally, for full thickness burn MetHb concentration will keep increasing past the 48 h and 72 h timepoints, but with a smaller slope than in partial thickness burns.

In future, the predictions of the model (including MetHb concentrations and spatial distribution) can be verified in MRI experiments, which allow direct MetHb distribution measurements.

In summary, we developed a model of preferred accumulation of MetHb in burn injury, which supports the notion of the use of methemoglobin as a marker of burn depth and tissue viability in burn wounds. The proposed model can be used to better understand burn injury healing and to optimize infection prevention, wound dressings, and adjuvant wound healing therapies.

References

1. Grout P, Horsley M, Touquet R (1993) Epidemiology of burns presenting to an accident and emergency department. Arch Emerg Med 10(2):100–107
2. Papini R (2004) Management of burn injuries of various depths. BMJ 329(7458):158–160
3. Monstrey S, Hoeksema H, Verbelen J et al (2008) Assessment of burn depth and burn wound healing potential. Burns 34(6):761–769
4. Cross KM (2010) Assessment of tissue viability in acute thermal injuries using near infrared point spectroscopy. PhD thesis, U of Toronto, Toronto, Canada
5. Despa F, Orgill DP, Neuwalder J et al (2005) The relative thermal stability of tissue macromolecules and cellular structure in burn injury. Burns 31:568–577
6. Singer AJ, Berruti L, Thode HC et al (2000) Standardized burn model using a multiparametric histologic analysis of burn depth. Acad Emerg Med 7:1–6
7. Mansouri A, Lurie AA (1993) Concise review: methemoglobinemia. Am J Hematol 42:7–12
8. Minetti M, Malorni W (2006) Redox control of red blood cell biology: the red blood cell as a target and source of prooxidant species. Antioxid Redox Signal 8:1165–1169
9. Umbreit J (2006) Methemoglobin—it's not just blue: a concise review. Am J Hematol 82:134–144
10. Farahani K, Saxton RE, Yoon HC et al (1999) MRI of thermally denatured blood: methemoglobin formation and relaxation effects. Magn Reson Imaging 17:1489–1494
11. Hampton MB, Vissers MC, Winterbourn CC (1994) A single assay for measuring the rates of phagocytosis and bacterial killing by neutrophils. J Leukoc Biol 55(2):147–152
12. West JB (ed) (1991) Best and Taylor's physiological basis of medical practice, 12th edn. Williams and Wilkins, Baltimore, p 1170

Chapter 48
Characterization of Protein-Protein Interactions in Recombinant Hemoglobin Producing *Escherichia coli* Cells Using Molecularly Imprinted Polymers

Ka Zhang, Tongchang Zhou, Lei Ye, and Leif Bülow

Abstract The worldwide blood shortage has generated demands for alternatives to transfusible human blood. One such important option is based on recombinant hemoglobin-based oxygen carriers (rHBOCs). Most efforts have been focused on various *E. coli* based production systems. One of the key challenges in these systems is to devise an efficient and economical protein production strategy involving selection of suitable host cell and Hb variant, growth conditions and media engineering. Hb also influences the heterologous host cell metabolism and therefore the identification of modified protein-protein interactions is critical for optimizing Hb production. In this study, molecularly imprinted polymers (MIPs) directed against Hb were used to identify the human Hb protein interaction network in *E. coli*. One *E. coli* host protein, glyceraldehyde 3-phosphate dehydrogenase (GAPDH), interacted strongly with Hb, especially fetal Hb (HbF).

Keywords Recombinant hemoglobin • Molecularly imprinted polymer • Glyceraldehyde 3-phosphate dehydrogenase • Protein-protein interaction • Escherichia coli

K. Zhang • T. Zhou • L. Ye
Division of Pure and Applied Biochemistry, Department of Chemistry, Lund University, Box 124, 22100 Lund, Sweden

L. Bülow (✉)
Division of Pure and Applied Biochemistry, Department of Chemistry, Lund University, Box 124, 22100 Lund, Sweden

PlantLink, Division of Pure and Applied Biochemistry, Department of Chemistry, Lund University, Box 124, 22100 Lund, Sweden
e-mail: leif.bulow@tbiokem.lth.se

H.J. Halpern et al. (eds.), *Oxygen Transport to Tissue XXXIX*, Advances in Experimental Medicine and Biology 977, DOI 10.1007/978-3-319-55231-6_48

1 Introduction

The proteome of the erythrocyte embraces 2289 proteins [1]. Protein-protein interactions are essential for maintaining its proper function. The characterization of these interactions is not trivial and most of these studies have been elucidated using various mathematical and computational tools [2, 3]. This work has generated a complex map, an interactome, which has been instrumental for generating a better understanding of some specific hematological disorders, particularly sickle cell disease (SCD). Hemoglobin (Hb) is the most abundant protein in the erythrocyte. Several internal proteins have been found to form complexes with Hb, both as transient and/or stable complexes [4, 5]. Such interactions have several different consequences in terms of controlling cell metabolism and oxygen binding and transport.

With the advent of heterologous Hb production in a range of different host cells, knowledge of protein-protein interactions in these new cellular settings between Hb and host cell proteins (HCP) is needed. Such protein complexes are cumbersome to isolate and frequently difficult to fully characterize. 2D electrophoresis followed by advanced mass spectroscopic approaches is often the major path to identify interacting protein partners.

In this study, an alternative strategy, based on molecularly imprinted polymers (MIPs), has been utilized to identify host cell proteins that bind to human Hb. MIP can be viewed as artificial plastic receptors with the ability to specifically recognize target molecules [6, 7]. Such designed polymer particles offer a valuable alternative for binding and capture of Hb molecules, in free or complexed forms. In this work, we developed new Hb-specific polymer beads by surface molecular imprinting in Pickering emulsion [8, 9]. Hb-MIP selectively recognizes various Hb variants and complexes directly from *E. coli* crude extracts in one step. Interacting HCPs could be co-purified with Hb and the obtained complexes could subsequently be characterized by mass spectroscopy.

2 Methods

Recombinant *E. coli* cells producing adult and fetal hemoglobin (HbA and HbF), respectively, were cultivated according Ratanasopa et al. [10] After harvesting by centrifugation, the cells were suspended in 20 mM sodium phosphate buffer pH 6.0 and sonicated. Cell debris was removed by centrifugation for 40 min at 12,000 rpm and the supernatant was filtrated using a 0.45-μm Minisart filter (Sartorius). The obtained crude extracts of HbA and HbF, respectively, were then used as starting materials for protein-protein interaction analyses.

Hb-imprinted polymer beads were synthesized by Pickering emulsion polymerization which has been described earlier [9] (Fig. 48.1). To synthesize the beads, about 3 mg purified HbA was adsorbed on 10 mg silica nanoparticles and the protein-coated silica particles were then used to stabilize an oil-in-water emulsion

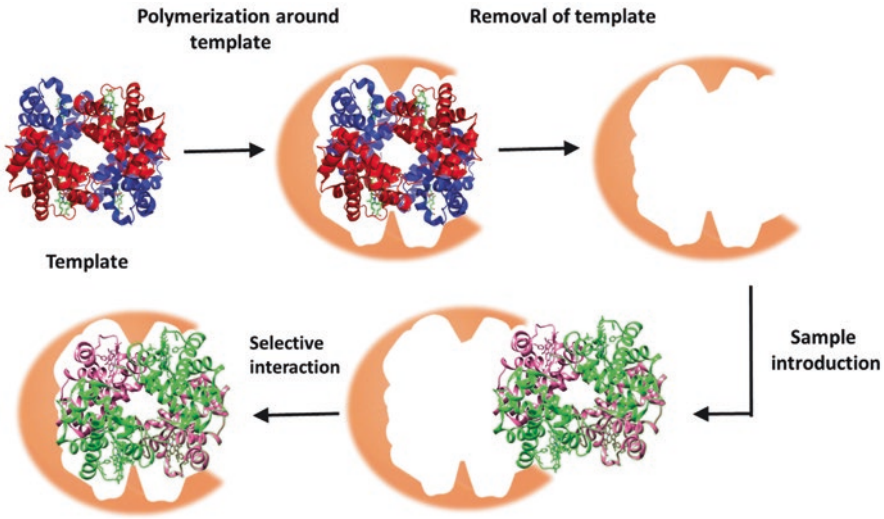

Fig. 48.1 Schematic illustration of the molecular imprinting process

(Pickering emulsion). In the first step, methacrylic acid and acrylamide were allowed to self-assemble around the Hb molecules based on physical interactions between functional groups on the protein and the monomers. After free radical polymerization around the template Hb molecules, the protein-silica particles were finally removed, leaving behind an Hb imprinted matrix with the binding sites on the polymer surface. The prepared Hb imprinted particles were packed into a volume of 1 ml in a HR 5/5 column (GE Healthcare, Uppsala, Sweden) for chromatographic characterization. All chromatographic experiments were performed on an ÄKTA Explorer system (GE Healthcare, Uppsala, Sweden) and peak absorbance was monitored at 280 nm and 420 nm. After equilibration the MIP column with 20 mM sodium phosphate buffer pH 6.0, the *E. coli* crude extracts were directly injected in the same buffer with a flow rate 0.2 ml/ min. All solutions were bubbled with CO to maintain the Hb in its stable carboxy form. Bound proteins were subsequently eluted by a linear gradient from 6.0 to a final pH 8.0 at a flow rate of 1 ml/ min. The Hb containing fractions were collected and concentrated using a Vivaspin column with 30,000 MWCO (Sartorius). The efficiency of the Hb purification was visualized by SDS-PAGE on precast 4–20% Mini-Protean TGX gels (BioRad) using Coomassie brilliant blue for staining. Meanwhile, by SDS-PAGE all the components can be separated for more identification.

Selected spots from SDS-PAGE were then manually cut out, destained and digested with modified porcine trypsin (Promega) according to the protocol supplied by Amersham Bioscience. Sequence information was acquired by electrospray ionization (ESI) on a TermoFinnigan LCQ DECA XP Plus Ion Trap Mass Spectrometer (ThermoFinnigan, Stockholm, Sweden) coupled to an Agilent 1100 series LC system (Agilent, Stockholm, Sweden). MS/MS database searches were

performed using Mascot Daemon (Matrix Science, www.matrixscience.com). Up to one missed cleavage was allowed and searches were carried out with fixed carbamidomethylation of cysteines and variable oxidation of methionine residues.

PatchDock was used to model the protein-protein interactions. PatchDock performs docking based on molecular shape representation and surface patch matching. Approximately 1000 predictions were generated using PatchDock and all the predictions were submitted to FireDock to refine 10 best solutions. The FireDock is based on optimisation of side-chain conformations and rigid-body orientation and gives a high-throughput refinement.

3 Results

Figure 48.2 shows the elution profile of HbA and HbF from MIP column by a linear pH gradient to a final pH 8.0. It demonstrates that both HbA and HbF could be effectively separated from the *E.coli* crude extracts in one-step. Fractions were collected and immediately concentrated and analyzed by SDS-PAGE. From SDS-PAGE, it was evident that another protein of molecular size ~35 kDa co-eluted with Hb. This was especially pronounced for HbF. To identify this additional polypeptide, the protein band was isolated from the SDS-PAGE gel and subjected to an in-gel digestion followed by LC-MS/MS analysis. The MS/MS results (Table 48.1)

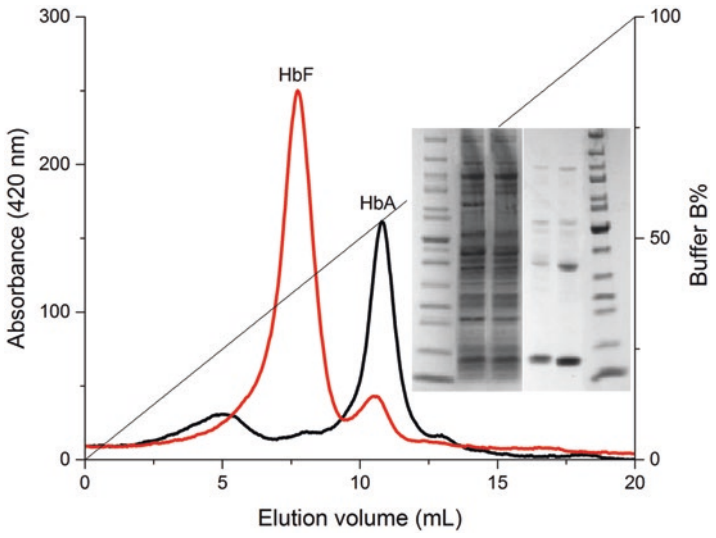

Fig. 48.2 Elution profiles of HbA and HbF *E.coli* crude cell extracts injected onto the MIP column, flow rate 1 ml/min, and using a linear pH gradient from 6.0 to 8.0. The collected fractions were analyzed by SDS-PAGE as presented in the figure. Spot a was selected for subsequent analysis by mass spectrometry

Table 48.1 Mass Spectrometry of spot as determined by SDS-PAGE

	Accession no.	Protein name	Species matched	Nominal Mass	MASCOT score
Spot a	P0A9B2	Glyceraldehyde-3-phosphate dehydrogenase A	*Escherichia coli*	35,681	1760

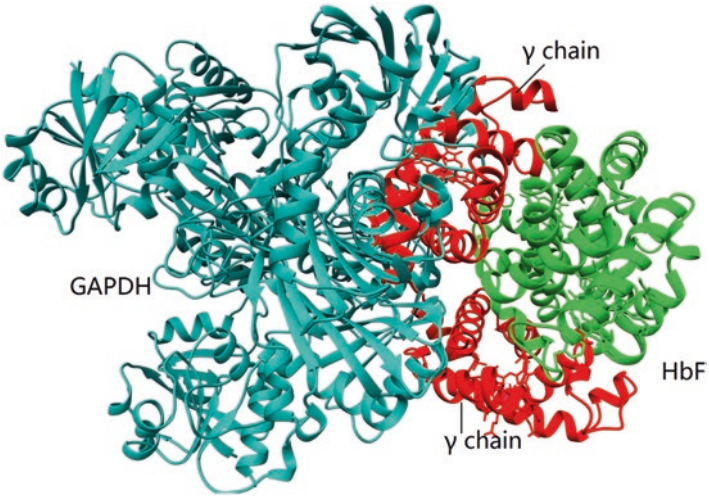

Fig. 48.3 Docking model for HbF (PDB: 1FDH) and GAPDH (PDB: 1GAD) complex. The gamma chains of HbF are shown in *red* and the alpha chains are shown in *green*. Those of GAPDH are shown in *light blue*

showed that the ~35 kDa protein was the host protein glyceraldehyde-3-phosphate dehydrogenase (GAPDH), which is a key enzyme in the glycolytic pathway of the host cell *E. coli*.

In order to further characterize the Hb-GAPDH complex, a model was developed using PatchDock and FireDock. The PatchDock provides rigid body docking while FireDock provides flexible refinement of protein-protein docking. Figure 48.3 shows the best structure from FireDock refinement. It was seen that the gamma chain of HbF is directly involved in the binding with GAPDH.

4 Discussion

Recombinant hemoglobin (Hb) is often an excellent choice as starting material in the production of hemoglobin based oxygen carriers (HBOC), especially when access to natural Hb sources is limited [11, 12]. Human Hb can thus be expressed and produced in a range of different hosts including bacteria, yeast, mice and plants. Besides providing a sustainable production of Hb, the protein can be modified to

better fit HBOC applications. Rational mutagenesis has thus been used to improve and optimize the properties of Hb such as reducing its reactivity with NO, diminishing autoxidation rate, and minimizing heme loss [13]. Modulating radical transfer reactions via tyrosine residues on the Hb molecule is another example of the advantage of using recombinant Hb [14]. In addition, mutagenesis can be used to improve the stability and expression yields thereby facilitating Hb production in a larger scale [15–17]. Modifications that enhance plasma half-life (hence mimicking PEGylation) can also be introduced at the genetic level thereby eliminating the need for subsequent chemical modification steps in HBOC production.

Previously the highest Hb yields have been obtained in *E. coli* and yeast (*Saccharomyces cerevisiae)*. Due to its simplicity most efforts have been focused on the *E. coli* production system. However, *E. coli* also involves several challenges especially in the cultivation of different Hb variants. For instance, cultivation of *E. coli* cells producing HbA and HbF, respectively, differs substantially in terms of growth rates, need of oxygen supply and use of carbon source. In this study it was demonstrated that especially the gamma chains of HbF interact strongly with GAPDH, one of the key enzymes in the glycolytic pathway of *E. coli*. The observed interactions between Hb and GAPDH will interfere with the regular *E. coli* metabolism. By mutating specific residues on the Hb molecules that mediate such interactions, production of recombinant proteins will be facilitated. This clearly indicates that cell metabolism needs to be carefully controlled to optimize Hb production in heterologous systems.

Acknowledgments Swedish Research Council, the Swedish Fund for Strategic Research and China Scholarship Council are gratefully acknowledged for financial support.

References

1. Goodman SR, Daescu O, Kakhniashvili DG et al (2013) The proteomics and interactomics of human erythrocytes. Exp Biol Med 238:509–518
2. Rao VS, Srinivas K, Sujini GN et al (2014) Protein-protein interaction detection: methods and analysis. Int J Proteomics 2014:147648
3. Zahiri J, Bozorgmehr JH, Masoudi-Nejad A (2013) Computational prediction of protein–protein interaction networks: algo-rithms and resources. Curr Genomics 14:397–414
4. Basu A, Chakrabarti A (2015) Hemoglobin interacting proteins and implications of spectrin hemoglobin interaction. J Proteome 128:469–475
5. Cooper CE, Schaer DJ, Buehler PW et al (2013) Haptoglobin binding stabilizes hemoglobin ferryl iron and the globin radical on tyrosine β145. Antioxid Redox Signal 18:2264–2273
6. Whitcombe MJ, Rodriguez ME, Villar P et al (1995) A new method for the introduction of recognition site functionality into polymers prepared by molecular imprinting – synthesis and characterization of polymeric receptors for cholesterol. J Am Chem Soc 117:7105–7111
7. Ye L, Mosbach K (2008) Molecular imprinting: synthetic materials as substitutes for biological antibodies and receptors†. Chem Mater 20:859–868
8. Shen X, Zhou T, Ye L (2012) Molecular imprinting of protein in Pickering emulsion. Chem Commun (Camb) 48:8198–8200

9. Zhou T, Zhang K, Kamra T et al (2015) Preparation of protein imprinted polymer beads by Pickering emulsion polymerization. J Mater Chem B 3:1254–1260
10. Ratanasopa K, Cedervall T, Bülow L (2016) Possibilities of using fetal hemoglobin as a platform for producing hemoglobin-based oxygen carriers (HBOCs). In: Elwell EC, Leung ST, Harrison KD (eds) Oxygen transport to tissue XXXVII. Springer, New York, New York, pp 445–453
11. Natarajan C, Jiang X, Fago A et al (2011) Expression and purification of recombinant hemoglobin in escherichia coli. PLoS One 6:e20176
12. Varnado CL, Mollan TL, Birukou I et al (2012) Development of recombinant hemoglobin-based oxygen carriers. Antioxid Redox Signal 18:2314–2328
13. Olson JS, Eich RF, Smith LP et al (1997) Protein engineering strategies for designing more stable hemoglobin-based blood substitutes. Artif Cells Blood Substit Immobil Biotechnol 25:227–241
14. Reeder BJ, Grey M, Silaghi-Dumitrescu RL et al (2008) Tyrosine residues as redox cofactors in human hemoglobin: implications for engineering nontoxic blood substitutes. J Biol Chem 283:30780–30787
15. Smith BJZ, Gutierrez P, Guerrero E et al (2011) Development of a method to produce hemoglobin in a bioreactor culture of escherichia coli BL21(DE3) transformed with a plasmid containing plesiomonas shigelloides heme transport genes and modified human hemoglobin genes. Appl Environ Microbiol 77:6703–6705
16. Makino T, Skretas G, Georgiou G (2011) Strain engineering for improved expression of recombinant proteins in bacteria. Microb Cell Factories 10:1–10
17. Graves PE, Henderson DP, Horstman MJ et al (2008) Enhancing stability and expression of recombinant human hemoglobin in *E. coli*: progress in the development of a recombinant HBOC source. Biochim Biophys Acta 1784:1471–1479

Part VI
Other

Chapter 49
Tissue-Integrating Oxygen Sensors: Continuous Tracking of Tissue Hypoxia

Natalie A. Wisniewski, Scott P. Nichols, Soya J. Gamsey, Steve Pullins, Kit Y. Au-Yeung, Bruce Klitzman, and Kristen L. Helton

Abstract We describe a simple method of tracking oxygen in real-time with injectable, tissue-integrating microsensors. The sensors are small (500 μm × 500 μm × 5 mm), soft, flexible, tissue-like, biocompatible hydrogels that have been shown to overcome the foreign body response for long-term sensing. The sensors are engineered to change luminescence in the presence of oxygen or other analytes and function for months to years in the body. A single injection followed by non-invasive monitoring with a hand-held or wearable Bluetooth optical reader enables intermittent or continuous measurements. Proof of concept for applications in high altitude, exercise physiology, vascular disease, stroke, tumors, and other disease states have been shown in mouse, rat and porcine models. Over 90 sensors have been studied to date in humans. These novel tissue-integrating sensors yield real-time insights in tissue oxygen fluctuations for research and clinical applications.

Keywords Biosensor • Fluorescence • Luminescence • Hydrogel • Metabolism

1 Introduction

Poor tissue oxygenation is linked to microvascular disease, critical limb ischemia, poor outcomes in cancer therapies, compartment syndrome, sepsis, wound healing, and a variety of other disease states and tissue malfunctions [1–4]. Few techniques exist for continuously monitoring tissue oxygen levels (e.g. electrochemical probes, microdialysis, MRI, EPR), and they are time intensive, require costly large

N.A. Wisniewski (✉) • S.J. Gamsey • S. Pullins • K.Y. Au-Yeung • K.L. Helton
Profusa, Inc., South San Francisco, CA, USA
e-mail: natwis@alumni.duke.edu

S.P. Nichols
Profusa, Inc., South San Francisco, CA, USA

Plastic Surgery Lab, Duke University, Durham, NC, USA

B. Klitzman
Plastic Surgery Lab, Duke University, Durham, NC, USA

H.J. Halpern et al. (eds.), *Oxygen Transport to Tissue XXXIX*, Advances in Experimental Medicine and Biology 977, DOI 10.1007/978-3-319-55231-6_49

equipment, lack accuracy, and/or typically require anesthesia or restraint, thereby excluding the possibility for real-time monitoring during daily life [5]. This report summarizes ongoing NIH and DARPA funded research on the development of novel, low-cost, tissue-integrating sensors that enable real-time continuous measurement of tissue oxygen for months to years, with special focus on continuous hypoxia monitoring for localized tissue ischemia and systemic oxygenation inferred from local measurements in healthy tissue.

The foreign body response (FBR) has long been known as the major culprit in developing long-term accurate in vivo biosensors [6–8]. To overcome the FBR in designing long-term oxygen sensors, we begin with soft, tissue-like, hydrogel scaffold materials [9, 10], originally developed for tissue engineering applications. Within this hydrogel, nano/molecular sensors are engineered to optically report oxygen levels (or other analyte levels of interest depending on the recognition element selected). Dyes are synthetically engineered to emit in the near infra-red (optical window of the skin), covalently link to the hydrogel backbone, and be stable under in vivo conditions. The specially designed micro-architecture of the hydrogel sensor contains over 60% void space and encourages tissue and capillary growth into and throughout the entire sensor (Fig. 49.1). Unlike other implantable sensors,

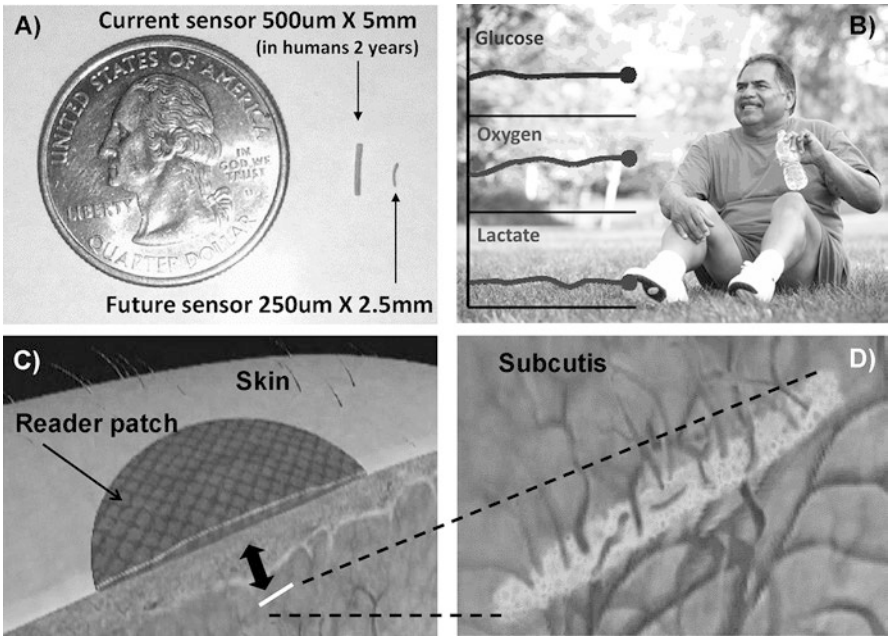

Fig. 49.1 Overview of tissue-integrating sensing system. (**a**) Miniature fluorescent hydrogel sensor. (**b**) Mobile health platform vision for continuous metabolic monitoring with a multi-analyte sensor. (**c**) Optical reader patch (*black arrow*) sits on the surface of skin and non-invasively interrogates the hydrogel sensor (white fiber) and sends data wirelessly to a computer interface or cell phone. (**d**) Tissue-integration without fibrous encapsulation of the soft, porous hydrogel sensor enables long term continuous monitoring of body analytes

the porous hydrogel has a large surface area for analyte diffusion. In addition, the use of soft, tissue-like materials reduces the likelihood of biomechanical factors affecting the long-term sensor acceptance in tissue [11, 12].

2 Methods

2.1 Tissue-Integrating Sensor

The particular injectable microsensors reported here are composed of a biocompatible hydrogel, poly (2-hydroxyethyl methacrylate) (pHEMA) and a near infrared (NIR) oxygen-sensitive palladium-benzoporphyrin molecule (Pd-MABP) [13]. The microsensor measures oxygen in the body based on the principle of phosphorescence quenching of metalloporphyrins, a well-established technique with excellent sensitivity and specificity to physiologic oxygen [14–17]. The pHEMA hydrogel is biocompatible, has good oxygen permeability, excellent mechanical properties, and a long history of use in medical devices [18]. The Pd-MABP molecules are covalently attached to the pHEMA hydrogel, ensuring that the sensing chemistry is retained in the hydrogel structure. To create the tissue-integrating properties, pre-polymer solution is filled into tubes of various sizes into which quality-controlled, monodisperse templating beads have been close-packed and sintered. Pre-polymer solution is crosslinked, and tubes and sintering beads are removed through solvent dissolution [9, 10]. The miniature sensors (0.5 mm × 0.5 mm × 5 mm) are designed to remain in the body permanently; they are soft and tissue-like to minimize stress at the material-tissue interface caused by motion and pressure, which can damage or stimulate adjacent immune cells and prolong the inflammatory phase [11, 19].

2.2 Non-invasive Optical Reader

A non-invasive optical reader for use on animals and humans was designed to read the signals from injected tissue-integrating sensors (Concept in Fig. 49.1c and prototype shown in 49.2d). A reader is manually positioned over a sensor and taped into place. A thermometer built into the surface of the reader continuously allows for temperature correction. An LED pulses illumination light into the skin above the sensors, and a photodetector collects emission light emanating from the sensor.

The phosphorescent lifetime, a property of the oxygen sensitive dye, is measured, thereby providing a signal unaffected by optical path permutations such as blood flow fluctuations, tissue ingrowth, oxy/deoxyhemoglobin ratio, melanin content and hydration [20].

The current oxygen sensing system can measure lifetime to within 2 μs or better, which equates to ~1 μM O_2, allowing good resolution within the observable range to date (2–70 μM).

2.3 In Vivo Application

In the work presented here sensors are injected with a 16 or 18-gauge needle in the subcutaneous tissue or other soft tissue of interest (brain, muscle, tumor). Sensors are visualized with the Perkins Elmer IVIS Imager in small animal models. Fluorescence from serial IVIS images is plotted to show changes in relative oxygen over time in response to challenges such as cycling fraction of inspired oxygen (fiO_2) from 1.00 down to 0.12 in anesthetized mice, rats, and pigs. For quantitative O_2 measurements derived from phosphorescent lifetime decay, the prototype optical reader described above and pictured in Fig. 49.2d is placed over the sensors. For the purpose of this manuscript, O_2 is reported in relative units to clearly visualize fluctuation in response to oxygen challenges. Several hundred sensors have been optimized in mice, rats, and pigs. Over 90 sensors have been tested in humans including 50 in healthy volunteers and 40 in critical limb ischemia patients [21].

3 Results

Figure 49.2 summarizes data from pre-clinical models and human studies showing sensor response up to 2.5 years after injection. Sensors have been histologically verified to reside between 2 and 8 mm under the skin and to avoid the foreign body response. Sensors respond to changes in O_2 concentration within a few seconds in response to breathable (fiO_2) or physical (pressure) oxygen challenges in mice, rats, pigs, and humans.

The benefits of such O_2 sensing technology is the ability to non-invasively monitor status of tissue in a continuous, mobile format. The cost of instrumentation is orders of magnitude cheaper than MRI or EPR, however with lower spatial resolution. Repeated insertions and perturbations of tissue that are required by percutaneous fiber optics or Clark electrodes are eliminated. Furthermore, the luminescent lifetime measurement technique is immune to errors from movement, injection depth (<1 cm), or other optical artifacts (e.g., blood flow, oxy/deoxyhemoglobin ratio) [20].

Some challenges of the luminescent tissue-integrating technology include temperature sensitivity and depth. Current surface temperature correction may be improved in the future by incorporation of temperature sensitive luminophores into the hydrogel. Current injectable sensors are limited to ~1 cm depth due to sensor brightness, which could be enhanced by creating larger sensors, though must be balanced with trade-offs (e.g., patient inconvenience). Sensors may be engineered through formulation optimization to enhance brightness for monitoring deeper tissues.

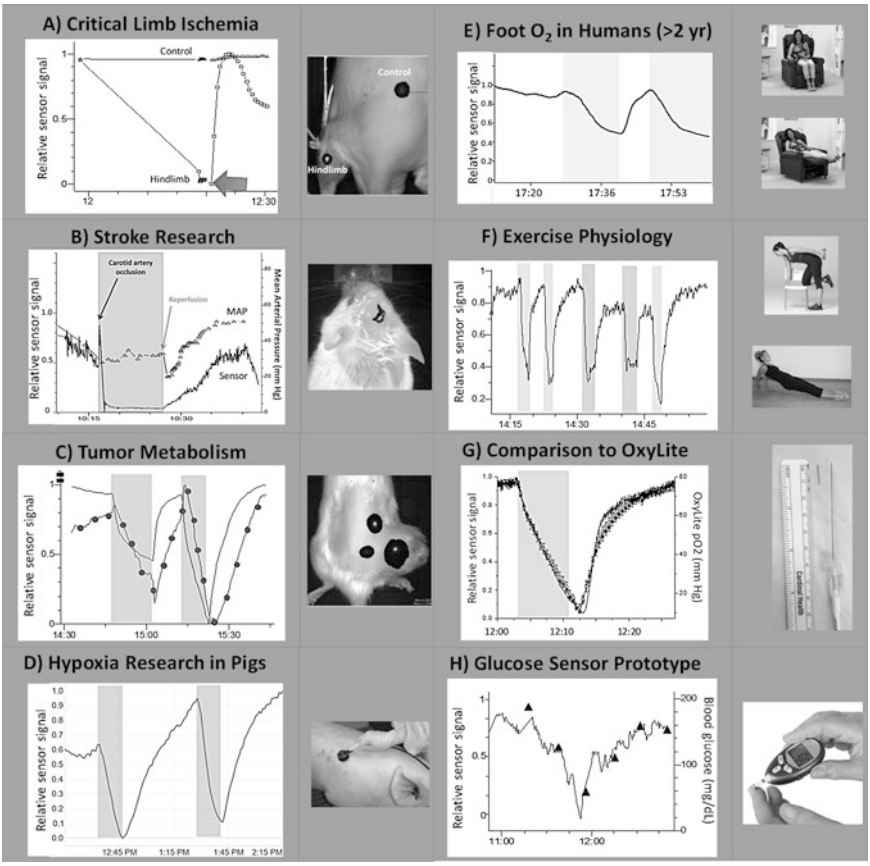

Fig. 49.2 Sensor performance in vivo. *Color shading* in C, D, and G indicate periods at 1.00, 0.21 (1st grey bar) and <0.2 fiO_2 (2nd grey bar). (**a**) Critical Limb Ischemia: Hindlimb sensor measured sudden changes in O_2 upon application and release of a tourniquet (*arrow*). (**b**) Stroke Research: Sensor in mouse brain shows reduced tissue O_2 due to induced stroke (carotid artery occlusion) and subsequent recovery after resolving the occlusion. (**c**) Tumor Metabolism: Sensors in a tumor (*circles*) and control tissue (*line*) measure oxygenation during hypoxia. Sensors can be utilized to measure the real-time action of oncological drugs on tumor metabolism and physiology. (**d**) Hypoxia Research in Pigs: Sensor in pig subcutis measures tissue O_2 during acute hypoxia episodes with prototype handheld reader (described in 2.3). (**e**) Foot O2 in Humans (>2 years): Elevating (*white area*) and lowering (*grey area*) of foot causes change in tissue O_2 monitored by sensors 2.5 years post-injection. Foot O_2 is important to healing chronic wounds. (**f**) Exercise Physiology: Tissue deoxygenation from isotonic exercise is observed in sensors placed near tricep. (**g**) Comparison to OxyLite: O_2 Sensors (*open circle* and *filled square*) respond similarly to a percutaneously inserted fiber optic sensor (Oxylite, Oxford Optronics) (*solid line*). (**h**) Glucose Sensor Prototype: Presented is the same O_2-sensitive platform with the addition of glucose oxidase to measure glucose concentrations in a rat. The sensors were monitored 3 weeks post-injection. Capillary blood glucose is indicated with triangles. These preliminary data demonstrate the proof-of-concept application of the luminescent hydrogel sensor to extend beyond continuous measurement of oxygen

4 Conclusions

Tissue-integrating hydrogel microsensors enable continuous *in vivo* monitoring to provide powerful insights into tissue-level physiology with the potential to help make more informed therapeutic, real-time decisions about various disease states. The methods discussed present potential cost- and time-effective methods to monitor tissue oxygenation long-term in pre-clinical and clinical situations.

Acknowledgments This work was funded in part by R01EB016414, R43DK093139 and R43DK09115 from the National Institutes of Health, W911NF-11-1-0119 and W31P4Q-12-C-0205 from the Defense Advanced Research Projects Agency and the U.S. Army Research Office and sponsored research projects from Profusa, Inc. with Duke University.

References

1. Kara A, Akin S, Ince C (2016) Monitoring microcirculation in critical illness. Curr Opin Crit Care 22:413–512
2. Giatromanolaki A, Harris AL (2001) Tumour hypoxia, hypoxia signaling pathways and hypoxia inducible factor expression in human cancer. Anticancer Res 21:4317–4324
3. Guo S, DiPietro LA (2010) Factors affecting wound healing. J Dent Res 89:221–229
4. Weick JW, Kang H, Lee L et al (2016) Direct measurement of tissue oxygenation as a method of diagnosis of acute compartment syndrome. J Orthop Trauma 30:585–591
5. Paul DW, Stenken JA (2015) A review of flux considerations for in vivo neurochemical measurements. Analyst 40:3709–3730
6. Anderson JM, Rodriguez A, Chang DT (2008) Foreign body reaction to biomaterials. Semin Immunol 20:86–100
7. Nichols SP, Koh A, Storm WL et al (2013) Biocompatible materials for continuous glucose monitoring devices. Chem Rev 113:2528–2549
8. Wisniewski N, Moussy F, Reichert WM (2000) Characterization of implantable biosensor membrane biofouling. Fresen J Anal Chem 366:611–621
9. Kotov NA, Liu Y, Wang S et al (2004) Inverted colloidal crystals as three-dimensional cell scaffolds. Langmuir 20:7887–7892
10. Marshall AJ, Irvin CA, Barker T et al (2004) Biomaterials with tightly controlled pore size that promote vascular in-growth. ACS Polym Prepr 45:100–101
11. Helton KL, Ratner BD, Wisniewski NA (2011a) Biomechanics of the sensor-tissue interface-effects of motion, pressure, and design on sensor performance and the foreign body response-part I: theoretical framework. J Diabetes Sci Technol 5:632–646
12. Helton KL, Ratner BD, Wisniewski NA (2011b) Biomechanics of the sensor-tissue interface-effects of motion, pressure, and design on sensor performance and foreign body response-part II: examples and application. J Diabetes Sci Technol 5:647–656
13. Gamsey S, Wisniewski N, Helton K et al (2016) Oxygen sensors. US Patent 9375494, 28 Jun 2016
14. Rumsey WL, Vanderkooi JM, Wilson DF (1988) Imaging of phosphorescence: a novel method for measuring oxygen distribution in perfused tissue. Science 241:1649–1651
15. Lo LW, Koch CJ, Wilson DF (1996) Calibration of oxygen-dependent quenching of the phosphorescence of pd-meso-tetra (4-carboxyphenyl) porphine: a phosphor with general application for measuring oxygen concentration in biological systems. Anal Biochem 236:153–160

16. Vinogradov SA, Grosul P, Rozhkov V et al (2003) Oxygen distributions in tissue measured by phosphorescence quenching. Adv Exp Med Biol 510:181–185
17. Wilson DF, Vinogradov SA, Grosul P et al (2006) Imaging oxygen pressure in the rodent retina by phosphorescence lifetime. Adv Exp Med Biol 578:119–124
18. Montheard JP, Chatzopoulos M, Chappard D (1992) 2-hydroxyethyl methacrylate (HEMA): chemical properties and applications in biomedical fields. J Macromol Sci Rev Macromol Chem Phys 32:1–34
19. Klueh U, Liu Z, Feldman B et al (2011) Metabolic biofouling of glucose sensors in vivo: role of tissue microhemorrhages. J Diabetes Sci Technol 5:583–595
20. Nagl S, Stich MI, Schaeferling M, Wolfbeis OS (2009) Method for simultaneous sensing of two species using optical probes of different decay time, and its application to an enzymatic reaction at varying temperature. Anal Bioanal Chem 393:1199–1207
21. Montero-Baker M, Au-Yeung KY, Wisniewski NA et al (2015) The use of micro-oxygen sensors (MOXYs) to determine dynamic relative oxygen indices in the feet of patients with limb-threatening ischemia during endovascular therapy: the first-in-man “Si Se Puede” study. J Vasc Surg 61:1501–1509

Chapter 50
Optical Design of Adaptive Optics Confocal Scanning Laser Ophthalmoscope with Two Deformable Mirrors

Jinsheng Yang, Yuanyuan Wang, Xuejun Rao, Ling Wei, Xiqi Li, and Yi He

Abstract We describe the optical design of a confocal scanning laser ophthalmoscope with two deformable mirrors. Spherical mirrors are used for pupil relay. Defocus aberration of the human eye is corrected by a Badal focusing structure and astigmatism aberration is corrected by a deformable mirror. The main optical system achieves a diffraction-limited performance through the entire scanning field (6 mm pupil, 3 degrees on pupil plane). The performance of the optical system, with correction of defocus and astigmatism, is also evaluated.

Keywords Adaptive optics • Confocal scanning laser ophthalmoscopy • Optical design • Deformable mirror

1 Introduction

Confocal scanning laser ophthalmoscopy (CSLO) is widely used in retinal tomography, hemodynamic, etc. [1, 2]. However, due to the limitation of dynamic aberrations of the human eye, the horizontal resolution of the image (being about 30

J. Yang (✉) • X. Rao • L. Wei • X. Li • Y. He
The Key Laboratory on Adaptive Optics, Chinese Academy of Sciences, Chengdu 610209, China

The Laboratory on Adaptive Optics, Institute of Optics and Electronics, Chinese Academy of Sciences, Chengdu 610209, China
e-mail: jinsyang@126.com

Y. Wang
Graduate School of Chinese Academy of Sciences, Beijing 100039, China

Wenzhou Medical University, Wenzhou 325035, China

The Key Laboratory on Adaptive Optics, Chinese Academy of Sciences, Chengdu 610209, China

The Laboratory on Adaptive Optics, Institute of Optics and Electronics, Chinese Academy of Sciences, Chengdu 610209, China

H.J. Halpern et al. (eds.), *Oxygen Transport to Tissue XXXIX*, Advances in Experimental Medicine and Biology 977, DOI 10.1007/978-3-319-55231-6_50

microns) is unable to reach eye cells of resolution [3]. With the adaptive optics techniques introduced to CSLO by Roorda in 2002, the horizontal resolution of CSLO reached the level of about 2.5 microns, and has successfully captured a photoreceptor cell and blood flow in in-vivo real-time images [4–6]. Subsequently, Berkley University, Indiana University, the Institute of Optics and Electronics, the Chinese Academy of Sciences, as well as other institutes, also have access to the adaptive optics confocal scanning laser ophthalmoscopy (AOCSLO) fundus images [7, 8].

Due to the deformable mirror stroke, volume limitations in the existing AOCSLO systems, as well as aberrations of the AOCSLO optical system and the eye (including high-order and low-order aberrations), cannot be fully corrected. Therefore, these systems use optical devices, such as glasses, to correct low-order aberrations of the human eye and optical systems, in advance. In order to overcome these shortcomings, an AOCSLO optical system with a double deformable mirror has been designed, which is aimed at achieving the diffraction limit performance through the entire field ($3° \times 3°$ on pupil plane with 6 mm pupil). The performance of the design in the correction of defocus and astigmatic aberrations of the human eye and optical systems is also analysed here.

2 Methods

In this design, in order to eliminate the influence of back reflection and chromatic aberrations, spherical mirrors are used for pupil relay (Fig. 50.1). The light path is a double pass system, including a light source, three scanners, a wavefront sensor, two deformable mirrors and a detector. Parallel light passes through a series of optical elements and finally focuses on the retina of the human eye, and light scattered by the retina returned along the original path is collected by the detector. In order to obtain the fundus imaging, scanners are used to change the directions of the beams relevant to the eye.

The design using two scan scanners on a horizontal direction is aimed at increasing scanning vision, the optical system scan range can be extended to $5° \times 5°$. Two deformable mirrors are used to correct higher-order aberrations of optical systems and the human eye, and astigmatic aberrations. A Badal focusing structure consists of mirrors FM3 and FM4 for the correction of defocus aberration of the eye.

Because the wavefront sensor and detector are modularized and on-axis optics are relatively free from aberrations, they are not included in our design part. The design focuses on the main optical path.

In the main lightpath of the AOSLO, there are 6 pupil conjugate planes: DM1 pupil, horizontal scanners XS1 and XS2, vertical scanner YS, DM2 pupil, and the actual pupil of the human eye (Fig. 50.2). It can be thought of as a series of telescopes that relay the pupil to the various conjugate elements. Spherical mirrors, which have to be used off-axis, are used for pupil relay on the main optical plane. The off-axis aberrations (e.g. astigmatism and coma) are generated in this structure.

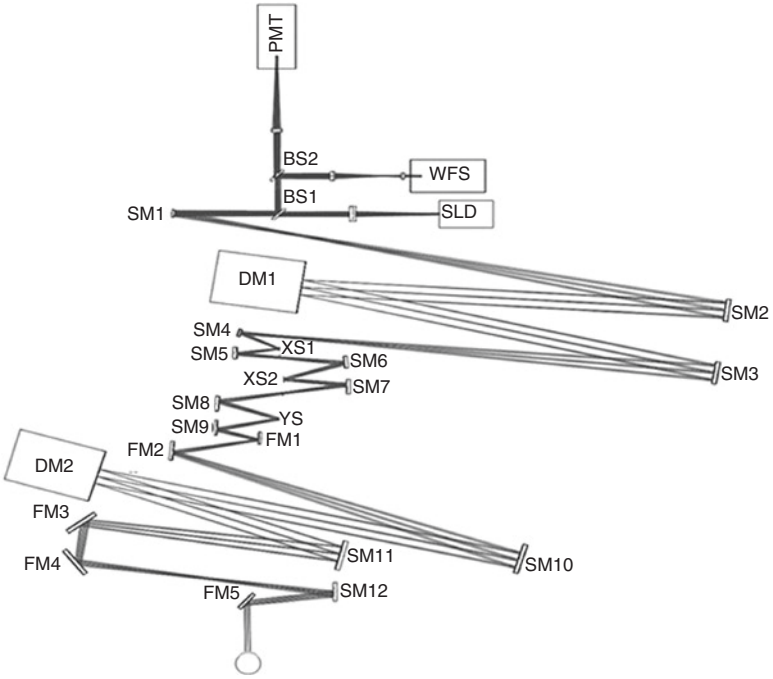

Fig. 50.1 Overview of the AOCSLO system. SM1-SM12 are spherical mirrors; FM1-FM5 are flat mirrors; XS1-XS2 are horizontal scanners; YS is a vertical scanner; WFS is wavefront sensor, and PMT is a detector

The human eye is modeled as a perfect lens to allow Zemax focusing on the optical system's performance without human influence. However, taking into account retinal curvature, we give the imaging plane a radius of −12 mm, which is the same as the curvature of the retina (Fig. 50.2).

Based on the primary aberration theory, a spherical mirror used off-axis should generate astigmatism, coma and other off-axis aberrations; optical systems need to be optimized. However, spherical mirrors placed on the main optical plate cannot eliminate the astigmatic aberration. The rule for this design is to optimize the tilt angle of the mirrors to minimize the aberrations, except for astigmatism aberrations. The astigmatic aberrations can eventually be eliminated through the DM2.

When the system is working, three scanning mirrors change the field angle on the pupil plane and produce a raster pattern on the retina [9]. At each position of the sweep, there is a new system configuration. We selected some configurations to represent the system performance. This can be simulated by Multi-Configuration Editor in Zemax software. In our design, we set three multi-configuration surfaces (2 scanning mirrors) and 17 configuration points expanding a 3° × 3° field on the pupil, which projects an approximate 900 × 900 μm square on the retina (Fig. 50.3). The 17 configuration points and the angles of the scan mirrors are presented in Table 50.1.

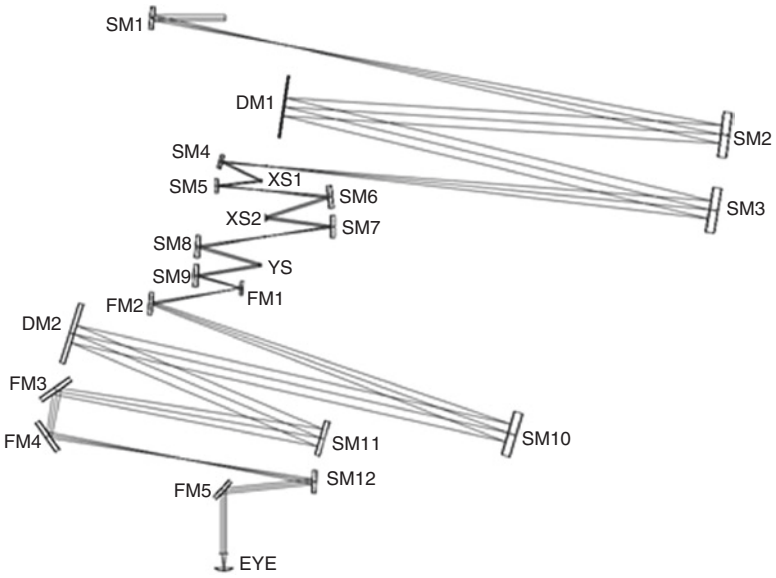

Fig. 50.2 The light delivery path. SM1-SM12 are spherical mirrors; FM1-FM5 are flat mirrors; XS1-XS2 are horizontal scanners; YS is a vertical scanner; WFS is wavefront sensor, and PMT is a detector

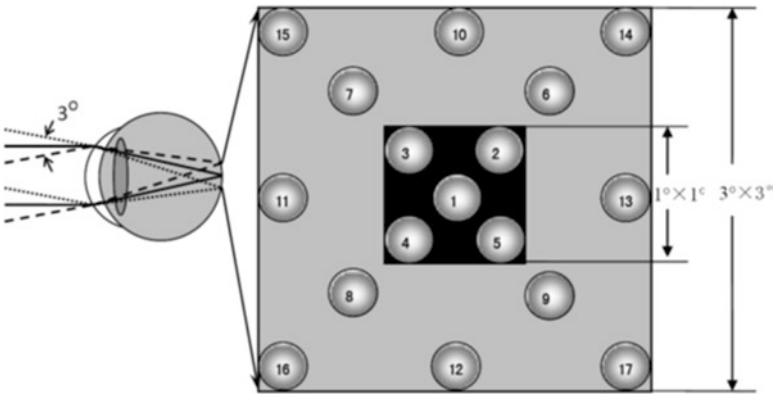

Fig. 50.3 Raster scanning and multi-configuration on image plane

Optimization was performed through all the configurations to yield an acceptable root mean square (RMS) wavefront error for each point. Operands' weight in Merit Function Editor was adjusted to balance the contribution of each configuration. For example, the central field was compromised to help the corner field performance.

Table 50.1 Scan angles corresponding to the configurations

Configuration	Human eye (°)		XS1 (°)	XS2 (°)	YS1 (°)
1	0	0	0	0	0
2	0.5	0.5	0.75	0	0.5
3	−0.5	0.5	−0.75	0	0.5
4	−0.5	−0.5	−0.75	0	−0.5
5	0.5	−0.5	0.75	0	−0.5
6	1	1	0.75	0.5	1
7	−1	1	−0.75	−0.5	1
8	−1	−1	−0.75	−0.5	−1
9	1	−1	0.75	0.5	−1
10	1.5	0	0.75	1	0
11	0	1.5	0	0	1.5
12	−1.5	0	−0.75	−1	0
13	0	−1.5	0	0	−1.5
14	1.5	1.5	0.75	1	1.5
15	−1.5	1.5	−0.75	−1	1.5
16	−1.5	−1.5	−0.75	−1	−1.5
17	1.5	−1.5	0.75	1	−1.5

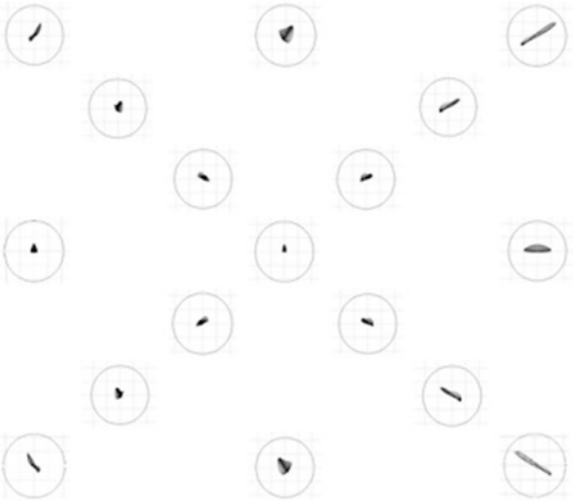

Fig. 50.4 Spot diagram of the whole scanning field. Airy disks are shown as *black circles*

3 Results

The spot diagram of the whole scanning field is shown in Fig. 50.4. The square from inside to outside represents a 1° × 1°, 2° × 2° and 3° × 3° field. It is symmetrical horizontally but asymmetrical vertically. Performances on the central field were degraded to balance the different configurations, but are still in Airy disk. Together with the increasing scanning field, astigmatism was dramatically increased. Because

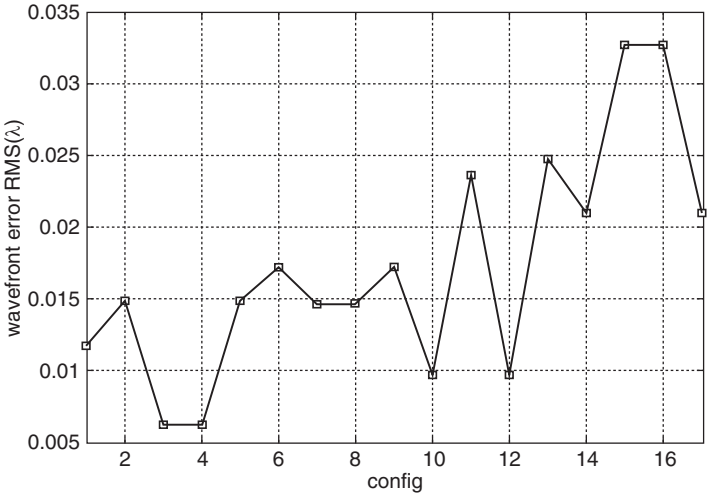

Fig. 50.5 RMS value of wavefront error of the whole scanning field

we set the RMS wavefront error as optimizing target, the spot size may not be minimized at the best focus plane.

According to Marachel's criterion, an optical system with RMS wavefront error $< 1/14\lambda$ is diffraction limited. Figure 50.5 shows the through-focus RMS wavefront error for all the scanning positions. Each line represents a scanning position, and the line with asterisks is the diffraction limit ($1/14\lambda$). The $1° \times 1°$ and $2° \times 2°$ fields are well below the diffraction limit, and one corner of the $3° \times 3°$ field is barely under the diffraction limited line to satisfy the criterion.

After analysis of the original aberrations of the system, the low-order aberration correction of the system was analyzed. Figure 50.6 shows the spot diagram after correction of -2D defocus by a Badal focusing structure, and correction of -1.5D astigmatism by DM2. Figure 50.7 shows the wavefront aberration RMS values of different imaging fields. Results show that, image resolution is better than that from diffraction-limited system.

4 Conclusions

We have described the optical design of an AOCSLO system. It achieves a diffraction-limited criterion through all the scanning fields (6 mm pupil, $3° \times 3°$ on pupil plane). In our design, we use spherical mirrors for pupil relay. An additional deformable mirror (DM2) is introduced to correct the astigmatism of the optical system and the human eye, and a reflective Badal focusing structure corrects defocus of the human eye. The optical system could be used in multi-wavelength applications.

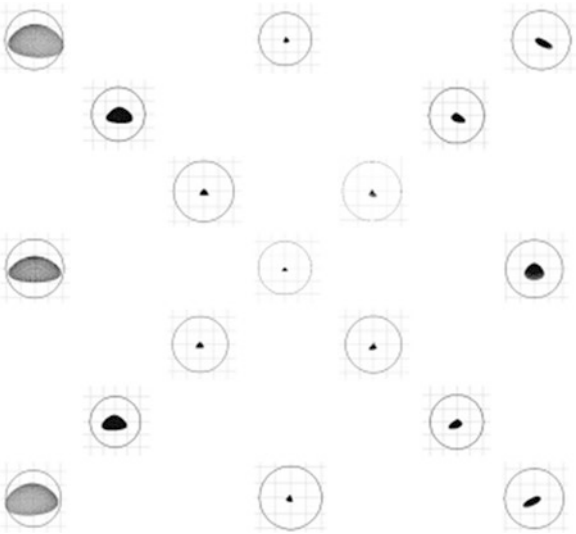

Fig. 50.6 Spot diagram of the whole scanning field. Airy disks are shown as *black circles*

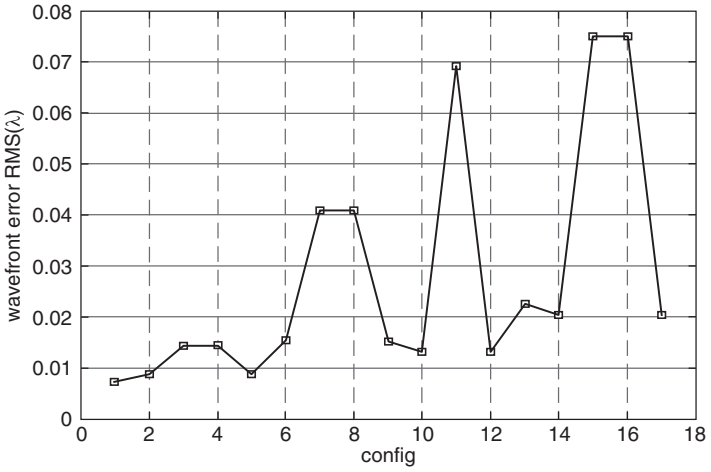

Fig. 50.7 RMS value of wavefront error of the whole scanning field

Acknowledgements This work is supported by the National Science Foundation of China (Grant NO. 61605210), the National Instrumentation Program (NIP, Grant No. 2012YQ120080), the Jiangsu Province Science Fund for Distinguished Young Scholars (Grant NO. BK20060010), the Frontier Science research project of the Chinese Academy of Sciences (Grant NO. QYZDB-SSW-JSC03), the Strategic Priority Research Program of the Chinese Academy of Sciences (Grant NO. XDB02060000), the National Key Research and Development Program of China (2016YFC0102500), and the Zhejiang Province Technology Program (Grant No. 2013C33170), CAS "Light of West China" program.

References

1. Webb RH, Hughes GW, Pomerantzeff O (1980) Flying spot TV ophthalmoscope. Appl Opt 10:128–1380
2. Webb RH, Hughes GW, Delori FC (1987) Confocal scanning laser ophthalmoscope. Appl Opt 26:1492–1499
3. Sharp PF, Manivannan A, Xu H, Forrester JV (2004) The scanning laser ophthalmoscope: a review of its role in bioscience and medicine. Phys Med Biol 49:1085–1096
4. Roorda A, Romero-Borja F, Donnelly WJ, Queener H, Hebert TJ, Campbell MCW (2002) Adaptive optics scanning laser ophthalmoscopy. Opt Express 10:405–412
5. Zhang Y, Poonja S, Roorda A (2006) MEMS-based adaptive optics scanning laser ophthalmoscopy. Opt Lett 31:1268–1270
6. Hammer DX, Ferguson RD, Iftimia NV, Ustun T, Burns SA (2005) Tracking adaptive optics scanning laser ophthalmoscope (TAOSLO). Invest Ophthalmol Vis Sci 46
7. Lu J, Yudong Z, Xuejun R, Guohua S, Hansheng Y, Can W (2007) Optical design of a confocal scanning laser ophthalmoscope based on adaptive optics. Proc SPIE 6624:6624–127
8. Li H, Lu J, Shi G, Zhang Y (2011) Measurement of oxygen saturation in small retinal vessels with adaptive optics confocal scanning laser ophthalmoscope. J Biomed Opt 16(11):110504
9. Donnelly WJ (2001) Improving imaging in the confocal scanning laser ophthalmoscope. M.S. dissertation. University of Houston, Houston

Chapter 51
Construction of 0.15 Tesla Overhauser Enhanced MRI

Yuumi Tokunaga, Motonao Nakao, Tatsuya Naganuma, and Kazuhiro Ichikawa

Abstract Overhauser enhanced MRI (OMRI) is one of the free radical imaging technologies and has been used in biomedical research such as for partial oxygen measurements in tumor, and redox status in acute oxidative diseases. The external magnetic field of OMRI is frequently in the range of 5–10 mTesla to ensure microwave penetration into small animals, and the S/N ratio is limited. In this study, a 0.15 Tesla OMRI was constructed and tested to improve the S/N ratio for a small sample, or skin measurement. Specification of the main magnet was as follows: 0.15 Tesla permanent magnet; gap size 160 mm; homogenous spherical volume of 80 mm in diameter. The OMRI resonator was designed based on TE_{101} cavity mode and machined from a phosphorus deoxidized copper block for electron spin resonance (ESR) excitation and a solenoid transmission/receive resonator for NMR detection. The resonant frequencies and Q values were 6.38 MHz/150 and 4.31–4.41 GHz/120 for NMR and ESR, respectively. The Q values were comparable to those of conventional low field OMRI resonators at 15 mTesla. As expected, the MRI S/N ratio was improved by a factor of 30. Triplet dynamic nuclear polarization spectra were observed for ^{14}N carboxy-PROXYL, along the excitation microwave sweep. In the current setup, the enhancement factor was ca. 0.5. In conclusion, the results of this preliminary evaluation indicate that the 0.15 Tesla OMRI could be useful for free radical measurement for small samples.

Keywords Free radical • Molecular imaging • OMRI • Redox status • Partial oxygen pressure

Y. Tokunaga • K. Ichikawa (✉)
Innovation Center for Medical Redox Navigation, Kyushu University, Fukuoka, Japan
e-mail: ichikawa.kazuhiro.684@m.kyushu-u.ac.jp

M. Nakao • T. Naganuma
Japan Redox Ltd., Fukuoka, Japan

H.J. Halpern et al. (eds.), *Oxygen Transport to Tissue XXXIX*, Advances in Experimental Medicine and Biology 977, DOI 10.1007/978-3-319-55231-6_51

1 Introduction

Measurement of partial oxygen pressure in living tissue has attracted considerable interest in biochemical and medical research and treatments, including cancer radiation therapy. A wide range of analytical methods has been developed for partial oxygen pressure, including imidazole derivatives and copper complex [1] or oxygen sensitive degradation protein [2], and the electrode method [3]. As measurement of partial oxygen pressure would be carried out repeatedly, the magnetic resonance approach is a promising candidate for this purpose.

Oxygen sensitive water-soluble contrast agents or fine particles, which have unpaired electrons, have been utilized for quantitative measurement of partial oxygen pressure in living tissues in combination with an electron spin/paramagnetic resonance (ESR/EPR) spectrometer or an Overhauser-enhanced MRI (OMRI) scanner. OMRI is a dynamic nuclear polarization technique for imaging free radicals based on the Overhauser effect [4]. ESR saturation of free radical results in enhanced nuclear magnetic resonance of water protons in the solution compared with thermal equilibrium without ESR excitation. OMRI takes advantage of the Overhauser effect to image free radical indirectly through a change in proton signal amplitude in the sample containing free radicals. Since the detection process is the same as MRI, high spatial resolution of a free radical image is obtained in a short time using OMRI. Oxygen sensitive contrast agents with unpaired electrons, such as nitroxides or trityl radicals, change their ESR spectra according to interaction with oxygen molecules [5–7] and tissue oxygen pressure is calculated from OMRI images [8].

Microwave penetration into a biological sample (skin depth) is dependent on the microwave frequency and dielectric loss of the sample [9]. Since the OMRI measurement process includes both ESR excitation and NMR detection, the external field strength is limited by the ESR microwave frequency for the object size of interest. For example, the ESR frequency of a typical small animal OMRI is 150-450 MHz, i.e. 5–15 mT. Thus, the MRI sensitivity of the OMRI is limited. For specific applications, including oxygen measurements in skin or a shallow area in muscle, the ESR frequency can be higher than that in a conventional small animal OMRI scanner to achieve high sensitivity. In this study, a 4 GHz OMRI resonator was designed and evaluated for use in a high resolution study of oxygen pressure in skin.

2 Methods

The main magnet was a 0.15 Tesla permanent magnet with gap size 160 mm, spherical volume of 80 mm in diameter (Hitachi Metal, Ltd) and equipped with gradient coils. The OMRI resonator was designed using a simulation software of the electromagnetic field, and for TE_{101} cavity mode. Designated cavities were machined from a phosphorus deoxidized copper block, with initial dimensions of $40 \times 70 \times 50$ mm^3.

A solenoid transmission/receive NMR resonator (i.d. 10–40 mm in diameter, 10–30 mm in length) was combined with the cavity. The resonator was equipped with an adjustable lid for fine tuning. The resonator was connected with a WR-229 rectangular waveguide and a coaxial-waveguide converter to a microwave amplifier (ZVE-3 W-83, Mini-Circuits). Resonant frequency was measured using a network analyzer (MS2026C, Antritsu Corp.) and output microwave power was examined using a power meter (E4418B, Agilent Technology) after 30 dB attenuation. All pulse sequence control was carried out using a custom-made OMRI control box and software. Typical OMRI parameters were as follows; TR/TE/ESR excitation time (Tesr) = 5000/40/1000 ms, flip angle FA = 90 degree, and FOV = 48.0 × 48.0 mm^2, Acq matrix 48 × 48 for 2D images. A solution of 3-carboxy-2,2,5,5-tetramethyl-1-pyrrolidine-1-oxyl (Carboxy- PROXYL, Sigma-Aldrich Co. LLC) was prepared in distilled water (0.01–10 mM) as a free radical sample. The free radical content in the sample was quantified before and after OMRI measurement, using an X-band ESR (JEOL Ltd.)

3 Results and Discussion

The OMRI resonant frequencies and Q_{empty} values were 6.38 MHz/150 and 4.32–4.44 GHz/120 for NMR and ESR, respectively. The OMRI resonator was placed in a 0.15 Tesla vertical MRI magnet, as shown in Fig. 51.1a. The cylindrical object in front of the rectangular cavity was a copper-radiofrequency shield for NMR tuning circuits. The sample object was placed from an insertion hole (40 mm i.d.) on the rear side (not shown in Fig. 51.1a). By carefully adjusting the physical height of the rectangular cavity using the adjustable lid, fine-tuning of the ESR frequency was carried out. The ESR frequency was adjustable in the range of 4.32–4.44 GHz (Fig. 51.1b), which covered the target ESR frequency of the system, i.e. 4.41 GHz.

The system was then used for acquisition of dynamic nuclear polarization spectra of ^{14}N-carboxy PROXYL solution. Conventional X-band ESR spectra of ^{14}N-carboxy PROXYL is shown in Fig. 51.2a as a reference. In this specific DNP spectra (Fig. 51.2b), ESR resonant frequency of the cavity was fixed to 4.41 GHz and the applied ESR microwave frequency was swept from 4.28-4.44 GHz. In this condition, the Q_{load} were 80 and 25 for NMR and ESR, respectively and 1D NMR spectra were obtained at each measured point. The frequency differences of the triplet DNP spectra were approximately 45 MHz, which correlated well with that observed with X-band ESR, indicating that the DNP spectra were clearly due to ^{14}N-Nitrogen splitting of Carboxy-PROXYL. The DNP intensity, i.e., changes of NMR signal intensity, was largest at around 4.415 GHz, to which the cavity resonant frequency was tuned, and gradually decreased at 4.37 and 4.325 GHz. At data points other than triplets, there was no significant difference in NMR intensities with and without ESR excitation (data not shown). These variations of OMRI intensity among the triplet ESR lines were possible because of the untuned status for 4.37 and 4.32 GHz, since we did not retune the ESR resonant frequency of the cavity for

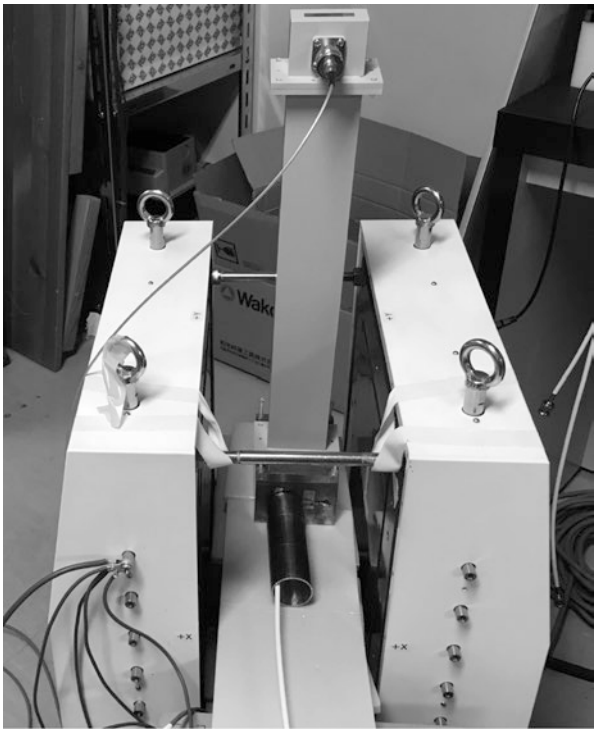

Fig. 51.1 Overview of the 0.15 Tesla OMRI system

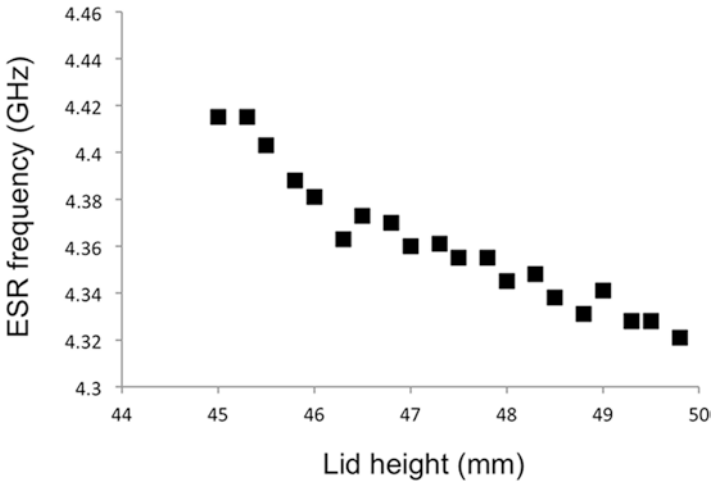

Fig. 51.2 Fine-tuning profile of the ESR cavity resonator. The adjustable lid was gradually moved to reach the target ESR resonant frequency. Optimum resonant frequencies and Q values were 6.38 MHz/150, 4.31-4.41 GHz/120 for NMR and ESR, respectively

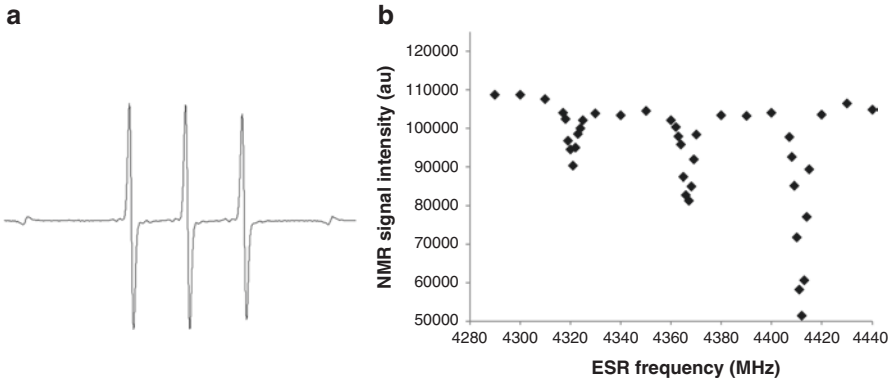

Fig. 51.3 OMRI image of 2 mM Carboxyl PROXYL phantom solution, (**a**) without and (**b**) with ESR excitation. *Arrows* indicate points of decrease in proton image intensity due to the Overhauser effect. The OMRI parameters were; NMR/ESR = 6.622 MHz/4.421 GHz, TR/TE/Tesr =1000 /25/0 to 1500 ms, FA = 90, FOV = 64x64 mm. Acq # = 64x64

each acquisition, but fixed it at 4.415 GHz, the off-resonance effect may contribute to the decrease in DNP intensities.

We then carried out a 2D OMRI scan at NMR and ESR frequencies of 6.38 MHz and 4.41 GHz, respectively. The image intensity of OMRI decreased significantly (Fig. 51.3b, arrows) compared with the MRI image (Fig. 51.3a). ESR microwave penetration was 3 to 5 mm in depth, based on estimation of 2D images. In the current setup, the decrease in the OMRI intensity was heterogeneous. However, when the region of interest was set for all circular regions in MRI and OMRI images, the total decrease in OMRI intensity was nearly half of the MRI intensity (data not shown), which agreed with the changes observed in 1D DNP spectra (Fig. 51.4b). A possible reason for the heterogeneous changes of OMRI intensity includes inhomogeneous ESR excitation due to interference of the NMR coil element on ESR homogeneity. Since we used a solenoid NMR coil element in the current setup, changes to the parallel coil element might improve the ESR homogeneity by minimizing the metal element of the NMR coil from the sample area.

4 Conclusions

A 0.15 T OMRI was designed and constructed. The OMRI cavity resonator has a comparable performance to the conventional OMRI resonator at low field. The result of this preliminary evaluation indicates that the 0.15 Tesla OMRI could be useful for free radical measurement of small samples, or of the skin.

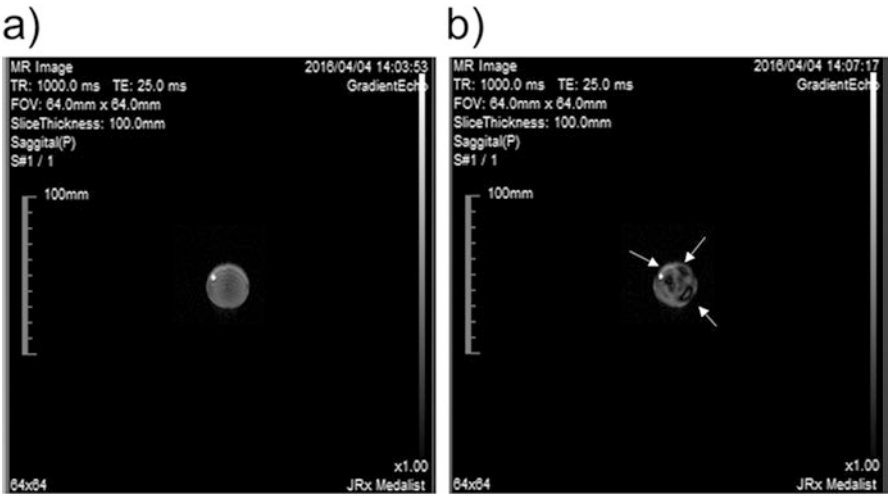

Fig. 51.4 (**a**) 0.01 mM X-band ESR spectra, and (**b**) dynamic nuclear polarization spectra of 2 mM ^{14}N Carboxy PROXYL solution at 0.15 Tesla OMRI. For DNP spectra acquisition, the ESR cavity was tuned to 4.41 GHz and 1D OMRI spectra were obtained with ESR frequency sweep. X-band ESR parameters: field strength of 0.33 Tesla, ESR power of 1 mW at 9.45 GHz, 100 kHz modulation frequency, 0.025 mTesla of modulation, 10mT of scan width. OMRI parameters: NMR/ESR = 6.622 MHz/4.28 to 4.48 GHz, TR/Tesr = 5000/2500 ms, FA = 60

Acknowledgments This work was in part supported by the funding program 'Creation of Innovation Centers for Advanced Interdisciplinary Research Areas' from JST (K.I.).

References

1. Fujibayashi Y, Taniuchi H, Yonekura Y et al (1997) Copper-62-ATSM: a new hypoxia imaging agent with high membrane permeability and low redox potential. J Nucl Med 38:1155–1160
2. Kudo T, Ueda M, Kuge Y et al (2009) Imaging of HIF-1-active tumor hypoxia using a protein effectively delivered to and specifically stabilized in HIF-1-active tumor cells. J Nucl Med 50(6):942–949
3. Hockel M, Schlenger K, Aral B et al (1996) Association between tumor hypoxia and malignant progression in advanced cancer of the uterine cervix. Cancer Res 56:4509–4515
4. Overhauser AW (1953) Paramagnetic relaxation in metals. Phys Rev 89:689–700
5. Halpern HJ, Yu C, Peric M et al (1994) Oxymetry deep in tissues with low-frequency electron paramagnetic resonance. Proc Natl Acad Sci U S A 91:13047–13051
6. Epel B, Bowman MK, Mailer C et al (2014) Absolute oxygen R_{1e} imaging in vivo with pulse electron paramagnetic resonance. Magn Reson Med 72:362–368
7. Khan N, How H, Eskey CJ et al (2015) Deep-tissue oxygen monitoring in the brain of rabbits for stroke research. Stroke 46:e62–e66
8. Matsumoto S, Yasui H, Batra S et al (2009) Simultaneous imaging of tumor oxygenation and microvascular permeability using Overhauser enhanced MRI. Proc Natl Acad Sci U S A 106:17898–17903
9. Roschmann P (1987) Radiofrequency penetration and absorption the human body: limitations to high-field whole-body nuclear magnetic resonance imaging. Med Phys 14(6):922–931

Chapter 52
Gold Nanoparticle-Based Fluorescent Contrast Agent with Enhanced Sensitivity

Kyung Aih Kang and Mai-Dung Nguyen

Abstract Gold nanoparticle (GNP) based contrast agents that are highly specific and sensitive for both optical and X-ray/CT imaging modalities are being developed for detecting the cancer expressing nucleolin and matrix metallo-proteinase 14 (MMP-14) on the cell membrane: Nucleolin is normally present in the nucleus. For many cancer cells, however, it is over-expressed on the cell membrane, having it to be a good cancer marker. Aptamer AS1411 is known to be an excellent target for nucleolin and also known to treat several cancer types; and MMP-14 in cancer is involved in tumor angiogenesis, blood vessel re-organization, and metastasis. In the proposed agent, AS1411 is selected as the cancer targeting molecule; and the unique property of GNPs of modulating fluorescence are utilized to allow the agent to trigger its fluorescence upon reacting with MMP-14, at an enhanced fluorescence level. GNPs are also natural X-ray/CT contrast agent. Here, as a part of on-going development of the dual-modality contrast agent, we report that conjugating a safe, NIR fluorophore Cypate at a precisely determined distance from the GNP enhanced the Cypate fluorescence up to two times. In addition, successful conjugation of the nucleolin target AS1411 onto the GNP was confirmed and among the GNPs size range 5–30 nm tested, 10 nm GNPs showed the highest X-ray/CT enhancement.

Keywords MDA-MB 231 • Breast Cancer Detection • Fluorescence Enhancement • Gold Nanoparticles • Cypate, MMP-14

1 Introduction

For the past decade, nano-biotechnology has been extensively studied in various aspects of disease detection/diagnoses and treatment, particularly for the cancer [1], because of its many beneficial properties; Nano-sized entity is small enough to perform its functions in a cellular or molecular level, but large enough to incorporate multiple functions in one entity, and retained longer in blood. Taking

K.A. Kang (✉) • M.-D. Nguyen
Department of Chemical Engineering, University of Louisville, Louisville, KY, USA
e-mail: kyung.kang@louisville.edu

H.J. Halpern et al. (eds.), *Oxygen Transport to Tissue XXXIX*, Advances in Experimental Medicine and Biology 977, DOI 10.1007/978-3-319-55231-6_52

advantage of these beneficial aspects of nanotechnology, we have been developing gold nanoparticle (GNP)-based, multifunctional contrast agent for a selected type of cancer, which is highly specific, sensitive and safe for both optical and X-ray/CT imaging modalities, as well as treating the cancer. Because optical imaging *via* fluorophores is known to be sensitive and X-ray/CT provides a good resolution [2] this agent is expect to provide clinicians with more complete information for early diagnosis and accurate prognosis.

The proposed contrast agent is for detecting the cancer producing nucleolin and enzyme matrix metalloproteinase 14 (MMP-14) on its cell membrane: Nucleolin is normally present in the cell nucleus but, for many cancers, it is over-expressed on the cell membrane surface. A DNA aptamer AS1411 is known to be a very good target for nucleolin and to treat several cancer types without harming normal cells [3]. MMP-14 is an enzyme expressed on the cell membrane and, for the cancer, it actively involves in tumor angiogenesis, blood vessel re-organization, and metastasis [4]. GNPs have a unique electromagnetic property that can influence the fluorescence emission of fluorophores placed nearby: when a fluorophore is on the surface of or very close to the GNP, its fluorescence is significantly or completely quenched. At a particular distance from the GNP surface (depending on the fluorophore properties and GNP size) its fluorescence can be significantly enhanced [5–10]. GNPs are also natural X-ray/CT contrast agent [11]. The completed agent is to target nucleolin on the cancer cell membrane; generate optical signal upon encountering MMP-14 on the target cancer at an amplified level, and enhance the X-ray/CT contrast; and also potentially treat the cancer.

For the model cancer cell line testing this contrast agent, we have selected breast cancer cell line MDA-MB 231. The cell line expresses both nucleolin and MMP-14. It is aggressive and does not well respond to the currently available, three main treatment regimens (i.e., triple negative).

The proposed contrast agent for both optical and CT imaging is shown in Fig. 52.1a. Its individual components are: GNPs; AS1411 as a target for nucleolin on the MDA-MB 231 cell membrane; sets of a short spacer (SS) composed of an MMP-14 substrate (amino-acid sequence) and a long spacer (LS); safe NIR-fluorophore Cypate (Cy; excitation and emission peaks at 780, and 830 nm, respectively) at the end of spacers [12]; and bio-polymer 11-mercaptoundecyl-tri-ethylene glycol (sPEG) to cover the GNP surface that is unoccupied by other moieties [6–10]. These components are carefully selected to assure the final product to be non-toxic and biocompatible. The SS is short by design and holds Cypate closely to the GNP; and the LS, at its full length, places Cypate at a distance from the GNP, where the Cypate fluorescence becomes maximally enhanced. This agent normally emits little fluorescence (Fig. 52.1a) until it binds to the cancer cell *via* AS1411 and also encounters MMP-14. Then the SS gets cleaved and Cypate is released from the SS, resulting in the distance between Cypate and the GNP to become the full LS length, and thus generating the enhanced fluorescence (Fig. 52.1b). Based on our previous studies, the GNP size best fitting to our purpose was found to be ~10 nm [8].

The design and performance of the SS-Cypate conjugated GNPs (dotted rectangle in Fig. 52.1A), i.e., conditionally fluorescing agent for MMP-14, have been previously reported [10]: The fluorescence of Cypate-SS-GNP became only 14–17%

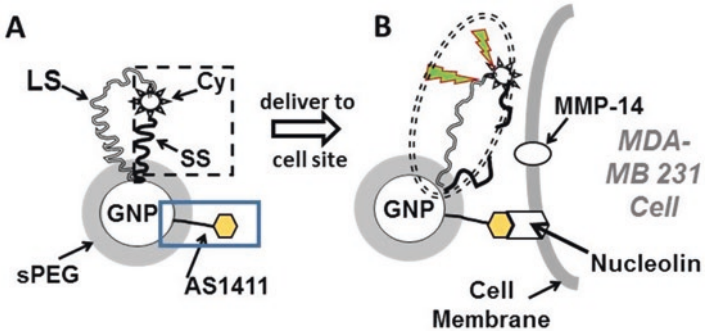

Fig. 52.1 Schematic diagram of GNP-based optical/CT contrast agent for MDA-MB 231: AS1411 is cancer cell target (*solid rectangle*) and Cypate is conjugated *via* SS/LS. (**A**) The agent normally emits little fluorescence because SS holds Cypate close to the GNP (*dotted rectagle*). (**B**) When the agent is delivered to the cancer cell site, AS1411 binds to the cell. MMP-14 on the cell membrane then cleaves SS, placing Cypate from the GNP at a distance of the fully stretched LS length (oval area), and Cypate fluoresces at an enhanced level

that of Cypate alone, and when Cypate-SS-GNP was reacted with MMP-14, the fluorescence was fully restored. In this article, as a next step toward completing our ultimate contrast agent, we report the study results of designing and testing various LSs (oval circle in Fig. 52.1B). Results on the AS1411 conjugation onto the GNPs (solid rectangle in Fig. 52.1A) and the X-ray/CT contrast enhancement with respect the GNP size are also briefly reported here.

2 Materials, Methods, and Instruments

In the process of developing the optimally functioning LS for our purpose, various candidates, including the hydrocarbon/polyethylene-glycol (PEG) combinations [7, 8] and amino-acid sequences were tested. For these candidates, however, the hydrophobicity of the resulting products was strong and they tended to aggregate easily. Therefore, more hydrophilic biomolecules were investigated and oligonucleotide sequences made of only deoxythymidines (T_s), to avoid them reacting with natural DNA sequences or enzymes in the body, were considered. DNA sequences also keep their lengths relatively constant, which was beneficial for predicting their lengths. Figure 52.2 shows the structures of five LS's composed of '*T*' only. The range of *T* numbers was 10–19, whose corresponding length ranges were 2.7–5.9 nm, estimated by computer simulation. This particular length (i.e., distance between a GNP and Cypate) range was selected based on our previous studies for the maximum Cypate fluorescence affected by 10 nm GNPs [6, 7]. For each oligonucleotide sequence studied, its *3′* end included an amine group (dotted circle) for Cypate conjugation and its *5′* end has an S-S group *via* dithiolphosphoramidite (DTPA), so that the reduced S-S, two thiol endings (−SH; solid circles) can bind

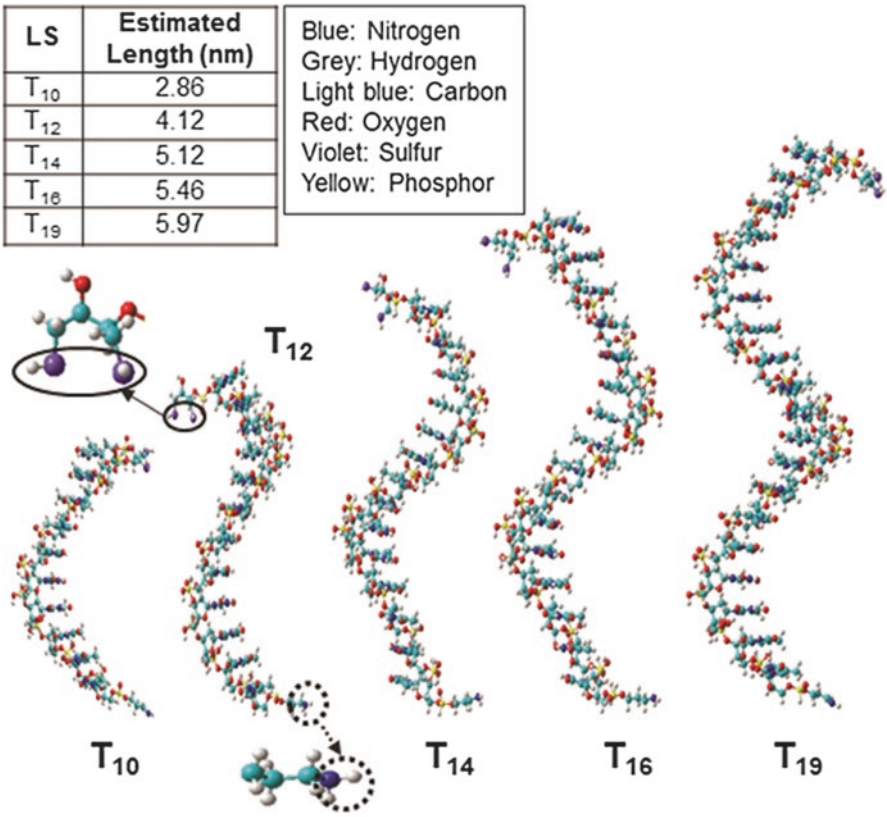

Fig. 52.2 Computer simulated structures of tested deoxy-thymidine (*T*) sequences (*T* numbers, 10–19) with *3′* and *5′* endings of an amine group (*dotted circle*) and two thiol groups (*solid circle*), respectively. The amine and thiol groups at the end of the sequence are enlarged for easier views. The estimated lengths of the LS are presented in the table. The subscribed number after 'T' denotes the number of *T*s in the sequence

onto the GNP surface. The actual construct is, therefore, *5′* (DTPA)-T_n-$(CH_2)_3NH_2$*3′*, where ***n*** denotes the number of '*T*.'

Conjugation of LS/sPEG onto GNP surface Spacers are usually conjugated onto GNPs together with sPEG [6–10]. However, the structure of oligo-nucleotides used in this study is spiral and has a potential for generating steric hindrance in the neighboring space broader than those of linear spacers. Because we wanted to bind a large number of the LS onto the GNP with minimal competition with other molecules, we conjugated the LS onto GNP first and then sPEG later.

Three (3) ml of 10 nm GNPs at 9.47 nM (Ted Pella; Redding, CA) was used to prepare the agent. Then, 64 nmoles (2 times that of available binding sites [13] on 10 nm GNPs) of LS (commissioned to TriLink Biotechnologies; San Diego, CA) were dissolved in 200 μL DI water, in a 1.5 ml Eppendorf tube. To activate the thiol

(-SH) group at the one end of the LS, 1 µl of 0.5 M (7 times the excess of LS) Tris(2-carboxyethyl) phosphine hydrochloride (TCEP; MW, 286.7; VWR; Batavia, IL) was added to the solution in the tube and the mixture was left at room temperature (RT) for 1 hr. Next, TCEP was removed from the solution by dialysis in a 400–500 µl cassette at a molecular cut-off (MWCO) 0.5–1 KD (SpectrumLabs; Rancho Dominguez, CA) in DI water (0.5 L) at RT for 1.5 hrs, changing the water four times. The solution in the cassette was then retrieved and its volume was adjusted to 1.5 ml with 0.1 mM PBS. It was then reacted with the GNP solution at RT overnight, stirring very slowly (~150 rpm). Next, to the resulting solution, 96 nmoles (3 times of binding sites on the 10 nm GNP surface) of sPEG (MW, 380.6; Sigma-Aldrich; St. Louis, MO) dissolved in 1.5 ml ethanol (Sigma-Aldrich) were added and reacted for 3 hrs at RT, stirring it slowly. The solution was then dialyzed in a ~ 12 ml dialysis cassette with 20 K MWCO (Fisher Scientific; Pittsburgh, PA) in 1.0 mM PBS for 3 hrs, changing the PBS four times. The solution was then centrifuged at 15,700 x g for 1 hr. (Eppendorf; Hauppauge, NY). The resulting GNP-LS/sPEG pellet was dispersed in 1.0 mM PBS, adjusting the final volume to 9 ml.

Cypateconjugation to the LS on the GNP All experiments dealing with Cypate were performed in dark to avoid its photo-bleaching. 0.2 µmoles (~3 times that of the LS) of Cypate (MW, 640; Diapeutix Chemicals; St. Louis, MO) was dissolved in 150 µl of N,N-Dimethylformamide (DMF; MW, 73.1; Sigma-Aldrich) in a 1.5 ml Eppendorf tube. Next, Cypate carboxyl groups were activated by adding 1.5 µmoles of N-(3-Dimethylaminopropyl)-N′-ethylcarbodiimide hydrochloride (EDC; MW, 191.7; Sigma-Aldrich) and 3.75 µmoles Sulfo-NHS (MW, 115.1; Sigma-Aldrich) in 100 µl of 0.1 M MES buffer at pH 5.5 (Sigma-Aldrich). The molar ratio of Cy:EDC:Sulfo-NHS was 1:8:20. The mixture was reacted gently on a rotator for 30 min at RT. Next, 50 µl of 0.35 M PBS was added to the mixture to adjust its pH 7.2–7.5, and then reacted with the amine group of the LS in the prepared GNP-LS/sPEG. The solution was then mixed with 3.0 ml ethanol on a stirrer and added slowly to the Cypate/ethanol mixture, then the coupling reaction was carried out at RT for 3 hrs. Next, the solution was placed in a dialysis cassette of 20 K MWCO (Fisher Scientific) and dialyzed in 1.0 mM PBS overnight. The resulting solution was centrifuged (Eppendorf) at 15,700 x g for 1 hr, twice. The GNP-LS/sPEG-Cy pellet was dispersed in 1.0 mM PBS and the product was characterized as described below.

Conjugation of AS1411/sPEG onto GNPs Conjugation of Cy5 labelled AS1411/sPEG was performed using the same method as for LS/sPEG conjugation, but replacing LS with AS1411 (Integrated DNA Technologies; Coralville, IA) with an amount 1/65 times that of available binding sites on the GNP surface and AS1411 binding was confirmed *via* the Cy5 fluorescence (the excitation and emission peaks at 647 and 665 nm, respectively).

Characterization of products GNP-LS/sPEG-Cy was characterized by UV-Vis spectrophotometer (Beckman Instruments; Fullerton, CA). The GNP in the product and the conjugated Cypate were quantified at 520 and 780 nm, respectively. The fluorescence emission of the product in 96-well Uniplates (Whatman; Florham Park, NJ) was quantified, with the control solution of Cypate alone, using a Spectra Gemini XPS Fluorometer (Molecular Devices; Sunnyvale, CA).

Theoretical studies Molecular simulations for oligo-nucleotides were performed using HyperChem 7.5 (Hypercube; Gainesville, FL), and fluorescence outputs influenced by GNPs were done using a computer code developed by our group [6–10].

3 Results and Discussion

Figure 52.3A shows absorption spectra of the product GNP-LS/sPEG-Cy (with T_{16} as an LS example for the figure), the GNP, and Cypate alone, normalized by their respective peak values. GNPs at 10 nm have an absorption peak at 520 nm. The peak of the GNP-LS/sPEG-Cy (triangle) is red-shifted by 5 nm, implying that the particle size increased due to the conjugation of LS/sPEG, which is consistent with our previous studies [5–7]. There is an increase in absorption at around 780 nm (arrow), indicating that Cypate is present in the products, *via* the LS. The amount of GNP and Cypate in the product was quantified by their absorptions at 520 and 780 nm, respectively, and the average molar ratio of Cypate to GNP was found to be 40:1. Assuming that a single Cypate molecule was conjugated to a single LS molecule on the GNP surface, this value is less than the ones for our SS, which were usually greater than 100 [10]. As previously stated, our SS is a short amino acid sequence. This lower binding ratio may be due to the spiral configuration of the oligo-nucleotide (LS) sequences, occupying more space and generating steric hindrance around the area. Also, oligo-nucleotides are negatively charged at a neutral pH and, therefore, they tend to repel each other when they are crowded in a small space of the GNP surface [14].

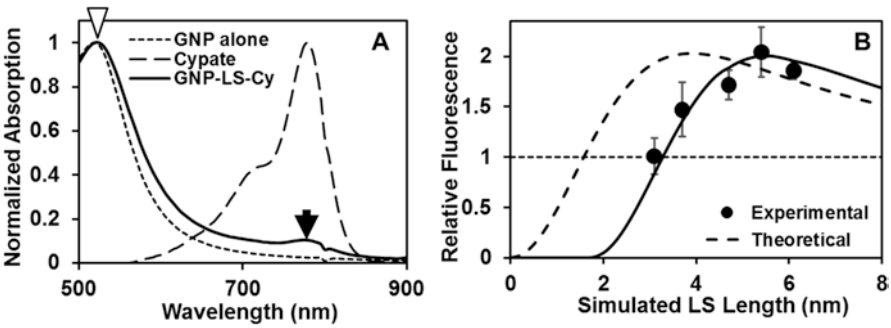

Fig. 52.3 (**A**) Normalized absorption spectra of GNP alone, Cypate alone, and product GNP-LS/sPEG-Cy. The spectrum of GNP-LS/sPEG-Cy was ~5 nm red-shifted (*pointed by the empty triangle*) indicating the particle size increase due to the conjugation of sPEG and/or LS on GNPs. The absorbance at 780 nm increased (*arrow*), implying the Cy at the end of the LS. (**B**) Fluorescence of Cy-conjugated-GNP *via* various LS's, relative to that of Cypate alone (*filled circle* and *solid line*), compared to the theoretically estimated fluorescence (*dotted line*). Fluorescence enhancement up to two times is shown in both the theoretical and the experimental results. The experimental results are, however, approximately 2 nm right-shifted from the theoretical predictions, which is phenomenon shown in our previous studies [5, 7]

Figure 52.3B shows the fluorescence level of the resulting product with the five LS sequences tested (filled circle) relative to that of the Cypate alone at the same concentration, along with the theoretically estimated fluorescence levels (dotted line), with respect to the estimated LS length (distance from the GNP surface). For T_{10}, which is the shortest, the fluorescence level was approximately the same as that of Cypate alone. As the length increased, the fluorescence also increased until the *T* number becomes 16 and its fluorescence level became approximately twice of that of the Cyapte alone. This implies the sensitivity of the Cypate using optical imaging can be doubled by carefully utilizing the electromagnetic energy generated by the GNP. When the length became longer than that of T_{16} (~5.5 nm) the level started to decrease, and it is expected that the level will return to 1.0 when the length exceeds the outer limit of the electromagnetic field by the GNP.

When the experimental result is compared to the theoretically predicted one, the levels of fluorescence for both are very close to each other, although the length of the experimental results is ~2 nm longer (Fig. 52.3B) than the theoretical ones. A similar phenomenon was observed in our previous studies with the hydrocarbon/PEG spacer for another cancer biomarker [5, 7]. This may be because the theoretical model is based on much simplified and ideal conditions.

Recently, there have been many studies on fluorescence level control of fluorophores using GNPs in order to produce more efficient optical contrast agents. They have been relatively qualitative, and focused mainly on quenching/de-quenching. This study result can, therefore, provide scientists with the information on more quantitative manipulation of fluorescence, not only for the quenching but also for the enhancement.

Two additional studies (data not shown in the article) completed until now are: thiolate AS1411 was also successfully conjugated onto GNPs. The contrast increase by the GNP for X-ray/CT was tested for the GNPs size range 5–30 nm and at a concentration range of 0–0.4 mg/ml. The GNP size showing the highest X-ray/CT contrast was 10 nm and the contrast increased linearly as the GNP concentration increased, in the range tested.

One of the most important issues on the products for *in vivo* biomedical application is their safety in both short and long terms. In that sense, our product being developed is safe because all components utilized for the final product are proven to be safe and the size of the GNP used and the GNP surface treatment of sPEG are appropriate for minimizing long-term toxicity, e.g., accumulation in excretory organs, generating immunogenicity; etc.

4 Conclusions

A safe, NIR fluorophore Cypate was linked to a 10 nm GNP *via* the DNA based LS and the optimized resulting product successfully enhanced Cypate sensitivity by two times. The cancer targeting agent AS1411 was successfully conjugated onto the GNP and, among the GNP particles, size ranging 5–30 nm, 10 nm GNPs showed the most contrast for X-ray/CT, for the same mass concentration.

With the study results reported in this article, the functionalities of individual components of our proposed nanoparticles are now confirmed to provide the positive results as a targeting, enhancing selectivity and sensitivity for optical and X-ray/CT imaging modality, and also treating breast cancer caused by MDA-MB 231. The immediate future studies to pursue are combining the components in one single entity; and test them, both in the cell and animal models, for its multi-functionalities.

The same concept used in present study can be effectively applied for other disease biomarkers, both for *in vitro* and *in vivo* molecular biosensing/imaging, as long as the biomarker changes the target molecule length, upon encountering the agent. Each of the individual components can also be used for various biomedical purposes.

Acknowledgments The authors acknowledge the financial supported with the NIH Grant 1R15CA173693. The authors also thank Dr. Rosendo Estrada for his advice on various chemical reactions involved in the development of this optical contrast agent.

References

1. National Cancer Institute of the U.S. National Insitute of Health (2015) Cancer nanotechnology plan 2015, https://nano.cancer.gov/objects/pdfs/caNanoPlan%202015%20-%20Front%20Matter%20(WEB_508).pdf
2. Cassidy PJ, Radda GK (2005) Molecular imaging perspectives. J R Soc Interface 2:133–144
3. Malik MT, O'Toole MG, Casson LK, Thomas SD, Bardi GT, Reyes-Reyes EM, Ng CK, Kang KA, Bates PJ (2015) AS1411-conjugated gold nanospheres and their potential for breast cancer therapy. Oncotarget 6(26):22270–22281
4. Curran S, Murray GI (1999) Matrix metalloproteinases in tumour invasion and metastasis. J Pathol 189:300–308
5. Kang KA, Wang JT, Jasinski JB et al (2011) Fluorescence manipulation by gold nanoparticles: from complete quenching to extensive enhancement. J Nanobiotechnol 9:16. doi:10.1186/1477-3155-9-16
6. Wang JT, Achilefu S, Nantz M, Kang KA (2011) Gold nanoparticle-fluorophore complex for conditionally fluorescing signal mediator. Anal Chim Acta 695:96–104
7. Wang JT, Moore J, Laulhe S, Nantz M, Achilefu S, Kang KA (2012) Fluorophore-gold nanoparticle complex for sensitive optical biosensing and imaging. Nanotechnology 23:095501. doi:10.1088/0957-4484/23/9/095501
8. Kang KA, Wang JT (2014a) Conditionally activating optical contrast agent with enhanced sensitivity via gold nanoparticle plasmon energy transfer: feasibility study. J Nanobiotechnol 12:56. doi:10.1186/s12951-014-0056-2
9. Kang KA, Wang JT (2014b) Smart dual-mode fluorescent gold nanoparticle agents. WIREs Nanomed Nanobiotechnol 6:398–409
10. Nguyen MD, Kang KA (2016) MMP-14 triggered fluorescence contrast agent. Adv Exp Med Biol 923:413–419
11. Chien C-C, Chen H-H, Lai S-F et al (2012) Gold nanoparticles as high-resolution X-ray imaging contrast agents for the analysis of tumor-related microvasculature. J Nanobiotechnol 10:10. doi:10.1186/1477-3155-10-10
12. Achilefu S, Dorshow RB, Bugaj JE, Rajagopalan R (2000) Novel receptor-targeted fluorescent contrast agents for in vivo tumor imaging. Investig Radiol 35:479–485

13. Duchesne L, Gentili D, Comes-Franchini M et al (2008) Robust ligand shells for biological applications of gold nanoparticles. Langmuir 24(23):13572–13580
14. Hurst SJ, Lytton-Jean AKR, Mirkin CA (2006) Maximizing DNA loading on a range of gold nanoparticle sizes. Anal Chem 78:8313–8318

Chapter 53
Potential Erythropoiesis in the Primo-Vascular System in Heart Failure

Chae Jeong Lim, Yiming Shen, So Yeong Lee, and Pan Dong Ryu

Abstract The primo-vascular system (PVS), composed of primo-nodes (PNs) and primo-vessels (PVs), has been identified in various animal models. However, little is known about its function. Here, we investigated the changes in gross morphology and cellular composition of the organ-surface PVS (osPVS) in rats with heart failure (HF) induced by myocardial infarction. The size of the PNs in rats with HF was larger than in sham rats (1.87 vs. 0.80 mm^2; $P < 0.01$) and the density of osPVS per rat was greater for the HF rats (28 of 6 rats vs. 19 of 9 rats; $P < 0.01$). In addition, the osPVS number containing red chromophore was greater in HF rats ($P < 0.001$). The chromophore was identified as hemoglobin. Transmission electron microscopy and H&E staining revealed that the osPVS of HF rats ($P < 0.001$) possessed more red blood cells (RBCs) than that of the sham rats. In particular, immature RBC number increased in the HF rats (90.7 vs. 42.3%; $P < 0.001$). Altogether, the results showed that the osPVS in HF rats increased in its size, density, and the proportion of immature RBCs in the PNs, which may indicate that the PVS has erythropoietic activity. Our study will help to elucidate the physiological roles of PVS in normal and disease states associated with HF.

Keywords Primo node • Organ-surface PVS • Erythrocyte • Reticulocyte • Myocardial infarction

1 Introduction

The primo-vascular system (PVS) was first reported in the 1960s by BH Kim as a novel vascular system corresponding to the acupuncture meridians [1]. The PVS consists of primo-nodes (PNs) and primo-vessels (PVs). Its existence has been confirmed on the surface of abdominal organs [2], inside the lymphatic vessel [3], and in the subcutaneous tissue layer [4] in rats, mice, and rabbits [2]. Recently, the PVS

C.J. Lim • Y. Shen • S.Y. Lee • P.D. Ryu (✉)
Department of Veterinary Pharmacology, College of Veterinary Medicine and Research Institute for Veterinary Science, Seoul National University, Seoul 08826, Republic of Korea
e-mail: pdryu@snu.ac.kr

H.J. Halpern et al. (eds.), *Oxygen Transport to Tissue XXXIX*, Advances in Experimental Medicine and Biology 977, DOI 10.1007/978-3-319-55231-6_53

was identified inside of a blood vessel in a human placenta [5]. In addition, various identification techniques were developed and applied to the PVS, such as the window chambers [6] and hollow gold nanospheres [7].

The trend in PVS research over the past 5 years has focused mostly on developing new methods to visualize the PVS in lymphatic vessels [6], understanding the associations between PVS and acupuncture meridians [4, 8], and identifying stem cells in the PVS [9]. These studies were mainly performed on the PVS in normal, healthy rats. PVS was also examined in cancer animal models [10, 11], however, the changes in PVS under various disease conditions are not yet well understood. In this study, we aimed to study morphological changes in the osPVS of the rats with heart failure (HF). We chose the osPVS because it can be identified without staining, which is different from other PVS subtypes [2, 12].

2 Materials and Methods

All animal experiments were performed in accordance with the Guide for the Laboratory Animal Care Advisory Committee of Seoul National University and approved by the Institute of Laboratory Animal Resource of Seoul National University (SNU-140926-2). Male Sprague-Dawley rats (5–7 weeks; $n = 15$, Orient Bio, Gyeonggi-do, Korea) used in this study were housed in a temperature-controlled environment (20–26 °C) under a 12-h light/dark cycle with water and food available *ad libitum*.

For the HF models, myocardial infarction was induced as described previously [13]. Briefly, rats were anesthetized by intramuscular injection of an anesthetic cocktail (tiletamine/zolazepam, 25 mg/kg; xylazine, 10 mg/kg), and intubated for mechanical ventilation (Harvard Apparatus, Holliston, MA). After the left thoracotomy, the heart was exteriorized, and the pericardium was incised. The left descending coronary artery was then ligated with 6–0 sterile silk suture. In the case of sham models, the same surgical procedure was performed, except for the coronary artery ligation.

The osPVS tissues were sampled at 8 weeks after the surgery. The rat abdomen was incised along the *linea alba*, and milky-colored PVS on the surface of large and small intestines was collected under a stereomicroscope (OSM-1, Dongwon, Seoul, Korea) [12]. In the three or four transverse sections (2 mm) of the heart, the infarct size was measured as ratio of the infarcted area to the mean left ventricular circumference with ImageJ software (developed at the National Institutes of Health) [13]. The rats with infarct size less than 30% were excluded from the analysis. For transmission electron microscopy (TEM), the samples were primary- and post-fixed, then *en bloc* stained. The samples were then dehydrated with graded ethanol, embedded in Spurr's resin, sectioned and observed by TEM (JEOL, JEM 1010, Tokyo, Japan) [4].

In this study, we defined the PN as the part PVS tissue that is markedly thicker (> 1.7 folds) than that of PV connected (0.09 ~ 0.57 mm), and excluded the tissue

samples without a PN. The size of the PNs was estimated based on the area of the tissue image measured with ImageJ software. For the staining of cells in PNs, hematoxylin and eosin (H&E) staining was performed by conventional protocols. The number of red blood cells (RBCs) counted from 20 TEM images (90 × 70 μm) of the PNs at magnification of 400x. All data are expressed as mean ± standard error and the Student *t*-test or Fisher's test used to analyzed the data (GraphPad Prism version 5.0).

3 Results

The results were based on the 19 osPVS tissue samples from 9 sham rats and 28 osPVS tissue samples from 6 HF rats. The mean infarct ratio of the heart was 38.0 ± 1.5% ($n = 6$) in the HF rats. Figure 53.1a shows a representative osPVS identified on the surface of the small intestine from sham rats, which is composed of the PV and the PNs. Figure 53.1b shows an enlarged PN attached to one end of a PV from the HF rats. The area of the PNs from the HF rats (1.87 ± 0.28 mm^2, $n = 28$) was significantly larger than the sham rats (0.80 ± 0.09 mm^2, $n = 19$; $P < 0.01$) (Fig. 53.1e). Figure 53.1f shows that the total number of osPVS samples per rat was increased by 2.2-times in the HF ($n = 28$) compared to the sham rats ($n = 19$). In addition, we often found a red chromophore inside some PNs and/or PVs. As illustrated in Figs. 53.1c, d, when the osPVS samples were considered in isolation, the osPVS number containing red chromophore was 4.0-times higher in the HF rats ($n = 17$, 60.7%) than sham rats ($n = 3$, 15%) (Fig. 53.1g).

To further examine the red chromophore inside the PN and PV, we sectioned the PVS, stained with H&E, and conducted TEM. Figures 53.2a, b illustrate typical examples of a PN slice (10 μm) stained with H&E. Inside of the PN of the HF rats the cells with reddish cytoplasm were grouped together. The cell number and the red color intensity in the PN of the HF rats (Fig. 53.2a, *asterisks*) were significantly greater than those of the sham rats (Fig. 53.2b, *asterisks*). As shown in Figs. 53.2c, d, the TEM images showed many dark cells, which is typical for iron containing cells, such as erythrocytes and reticulocytes (*asterisks*). In these TEM images, mature and immature RBCs displayed a rounded (Figs. 53.2c, d, dotted circles) and a distorted shape (Figs. 53.2c, d, dotted squares), respectively [14]. The number of mature and immature RBCs per osPVS of the HF rats was increased by 12.6-times of those of sham rats (Fig. 53.2e). Such difference was largely due to the increased number of immature RBCs in the HF rats (sham, 42.3% vs. HF, 90.7%; $P < 0.001$) (Fig. 53.2f).

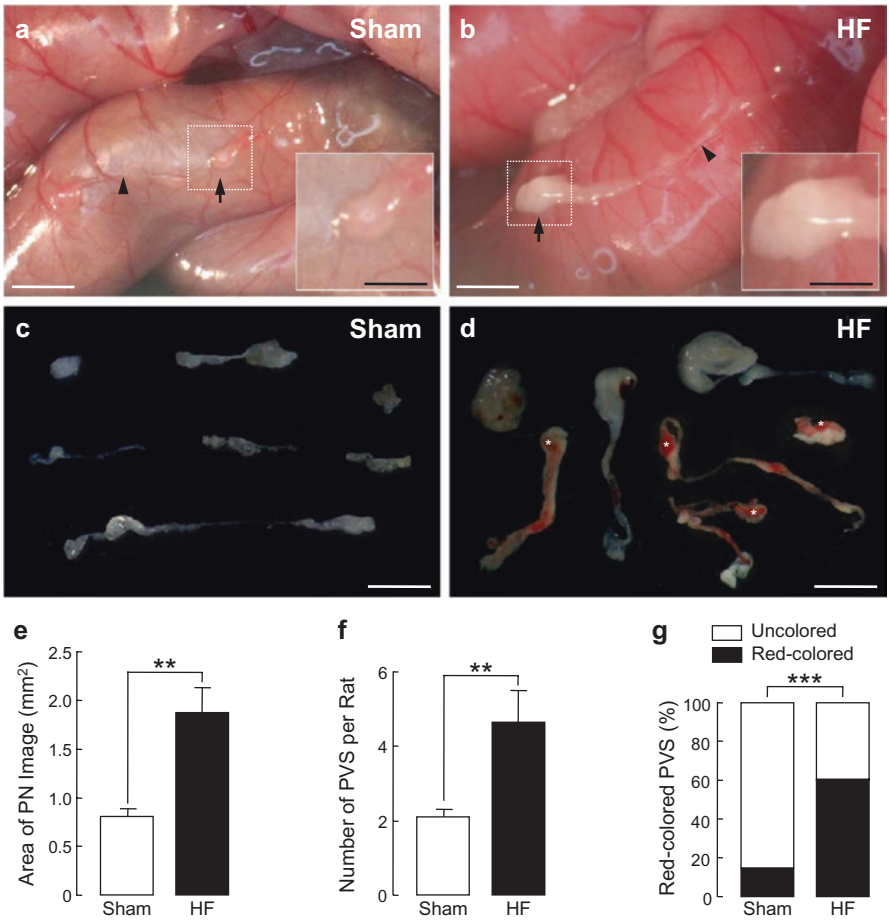

Fig. 53.1 Comparison of the morphological properties of the osPVS of two groups from sham and HF rats. **(a**, **b)** Representative images of intact osPVS tissue composed of PNs (*arrows*) and PVs (*arrowheads*) identified on the surface of the intestines from sham (**a**) and HF rats (**b**). Note the size of the PNs ((**a, b**), *insets*) of sham ((**a**), 0.91 × 0.77 mm) and HF rats ((**b**), 1.75 × 1.43 mm). Scale bars: 2 mm and 1 mm (*insets*). **(c**, **d)** Collection of isolated PVS specimens in saline solution from sham (**c**) and HF rats (**d**). Note the PVS contains a red chromophore ((**d**), *asterisks*) in HF rats. Scale bars: 2 mm. (**e**) The area of PN in sham (n = 19 from 9 rats) and HF rats (n = 28 from 6 rats). (**f**) The number of osPVS in sham (n = 19 from 9 rats) and HF rats (n = 28 from 6 rats). (**g**) The proportion of osPVS containing a red chromophore in sham (n = 19 from 9 rats) and HF rats (n = 28 from 6 rats). Values are mean ± standard error. $^{**}P < 0.01$, $^{***}P < 0.001$, by Student's t-test or Fisher's test

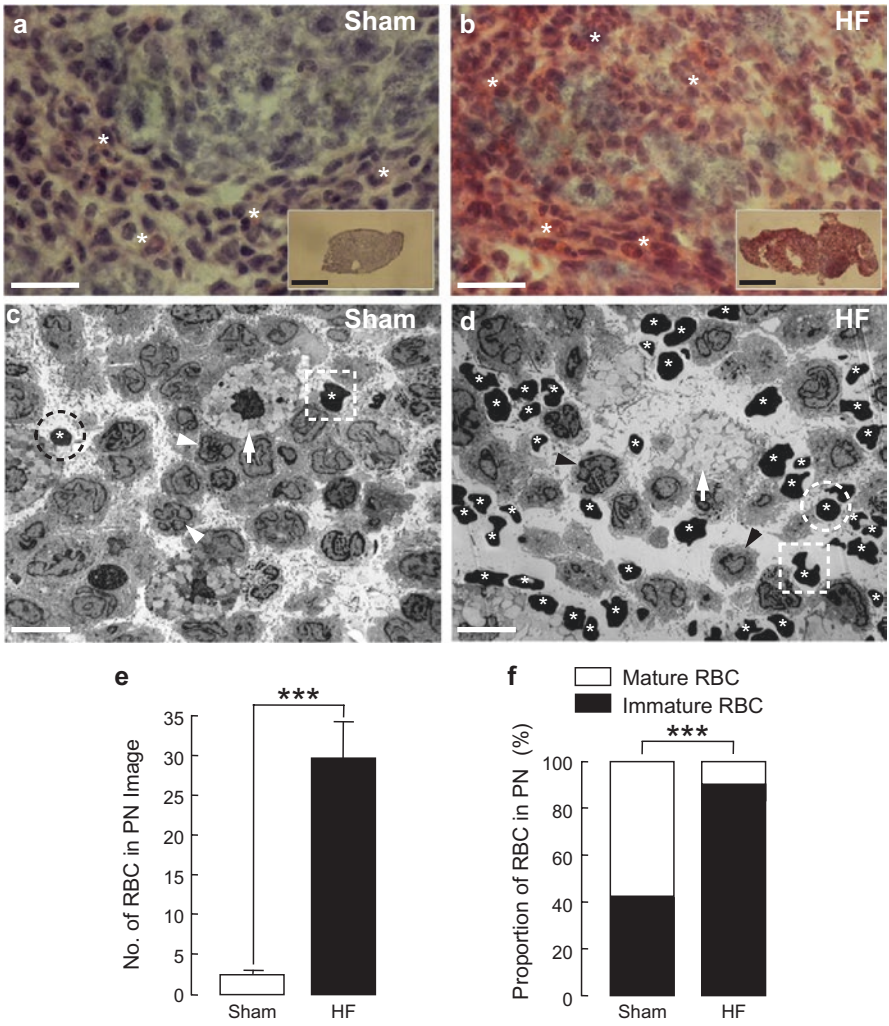

Fig. 53.2 Comparison of the cellular properties of the osPVS in sham and HF rats. (**a**, **b**) Representative images (400x) of the cross-sectioned PN slice (10 μm) stained by H&E from sham (**a**) and HF rats (**b**). *Insets* in (**a**) and (**b**) represents whole PN slices at low magnification (40x). Note the intensity of red chromophore is more clearly revealed in the PN from HF rats ((**b**), *asterisks*) than sham rats ((**a**), *asterisks*). Scale bars: 50 μm and 300 μm (*insets*). (**c**, **d**) Representative TEM images of a PN slice showing RBCs (*asterisks*), mast cells (*arrows*), and white blood cells (*arrowheads*) from sham (**c**) and HF rats (**d**). RBCs in dotted circles are mature RBCs and RBCs in dotted squares are immature RBCs. Scale bars: 10 μm. (**e**) The number of RBC in osPVS in sham ($n = 3$ from 3 rats) and HF rats ($n = 3$ from 3 rats). Individual RBCs in osPVS were counted from 20 rectangular fields (90 × 70 μm) in a TEM micrograph of the osPVS tissues. (**f**) The proportion of mature and immature RBCs in osPVS in sham and HF rats. Values are mean ± standard error. $^{***}P < 0.001$, by Student's t-test or Fisher's test

4 Discussion

Major findings of this study can be summarized as follows: the osPVS in the HF rats showed increases in the following parameters, 1) the PN size (in terms of the area): 2.1-times, 2) osPVS number per rat: 2.2-times, 3) total RBC number: 12.6-times, and 4) ratio of immature to mature RBCs: 2.1-times. These morphological and cytological changes indicate that significant erythropoiesis occurred inside the PN and PV of osPVS of the HF rats.

It is well-known that HF predisposes an individual to infections and anemia due to decreased hematopoiesis in bone marrow [15]. Chronic anemia or heart failure potentially precipitates extramedullary hematopoiesis, which occurs in the liver, spleen, lymph nodes, and hearts in HF [16, 17]. Therefore, it may suggest that the erythropoiesis inside the PN and PV in HF rats also resulted from the compensatory extramedullary hematopoiesis.

The existence of erythrocytes in the PVS of healthy rats was shown in our previous study [12]. The present study further demonstrates that PVS contains reticulocytes, which normally constitute approximately 1% of the total number of circulating erythrocytes [18]. The high percentage of reticulocytes (42.3% in sham rats) is a unique feature of the osPVS. Our observations are in agreement with BH Kim's report, in that PNs inside the blood vessels increased in its size (1.5 ~ 2-times), density, and the number of mature and immature RBCs in the anemic rabbits [19]. In the anemia model, Soh [2] also stated that the PVS became thicker and easier to detect. Recently, Kwon et al. [9] showed the presence of hematopoietic progenitor cells in the PVS. These findings strongly suggest that the PVS can function as a hematopoietic organ, which was claimed by BH Kim in 1965 [19]. More studies are required to further understand detailed mechanisms of the changes in the osPVS in HF and the role of the PVS in erythropoiesis in normal and disease states.

In conclusion, this study showed, for the first time, the morphological and cytological changes of erythropoiesis inside the PN and PV of the osPVS of a rat model of HF. Understanding the mechanism of HF-induced erythropoiesis changes in the PVS may help further elucidate the pathophysiology of the diseases associated with HF.

Acknowledgements This study was supported by the National Research Foundation of Korea funded by the Ministry of Education, Science and Technology (2016-937314, NRF-2015R1D1A1A02061732).

References

1. Kim BH (1963) On the Kyungrak system. J Acad Med Sci of Democratic People's Republic of Korea 90:1–41
2. Soh KS (2009) Bonghan circulatory system as an extension of acupuncture meridians. J Acupunct Meridian Stud 2:93–106
3. Lee C, Seol SK, Lee BC et al (2006) Alcian blue staining method to visualize Bonghan threads inside large caliber lymphatic vessels and x-ray microtomography to reveal their microchannels. Lymphat Res Biol 4:181–190

4. Lim CJ, Lee SY, Ryu PD (2015) Identification of primo-vascular system in abdominal subcutaneous tissue layer of rats. Evid Based Complement Alternat Med 2015:13 p Article ID 751937
5. Lee BS, Lee BC, Park JE et al (2014) Primo vascular system in human umbilical cord and placenta. J Acupunct Meridian Stud 7:291–297
6. Kim J, Kim DH, Jung SJ et al (2016) Monitoring the primo vascular system in lymphatic vessels by using window chambers. Biomed Opt Express 7:1251–1259
7. Carlson E, Perez-Abadia G, Adams S et al (2015) A novel technique for visualizing the intralymphatic primo vascular system by using hollow gold nanospheres. J Acupunct Meridian Stud 8:294–300
8. Jang H, Yoon J, Gil H et al (2016) Observation of a flowing duct in the abdominal wall by using nanoparticles. PLoS One 11:e0150423
9. Rai R, Chandra V, Kwon BS (2015) A hyaluronic acid-rich node and duct system in which pluripotent adult stem cells circulate. Stem Cells Dev 24:2243–2258
10. Yoo JS, Ayati MH, Kim HB et al (2010) Characterization of the primo-vascular system in the abdominal cavity of lung cancer mouse model and its differences from the lymphatic system. PLoS One 5:e9940
11. Kang KA, Maldonado C, Perez-Aradia G et al (2013) Primo vascular system and its potential role in cancer metastasis. Adv Exp Med Biol 789:289–296
12. Lim CJ, Yoo JH, Kim Y et al (2013) Gross morphological features of the organ surface primovascular system revealed by hemacolor staining. Evid Based Complement Alternat Med 2013:12 p Article ID 350815
13. Han TH, Lee K, Park JB et al (2010) Reduction in synaptic GABA release contributes to target-selective elevation of PVN neuronal activity in rats with myocardial infarction. Am J Physiol Regul Integr Comp Physiol 299:R129–R139
14. Fukuta K, Orui T, Tanaka K et al (2007) Novel erythrocyte pits in the small tropical ruminant, lesser mouse deer. Anat Histol Embryol 36:424–427
15. Iversen PO, Woldbaek PR, Tønnessen T et al (2002) Decreased hematopoiesis in bone marrow of mice with congestive heart failure. Am J Physiol Regul Integr Comp Physiol 282:R166–R172
16. Orphanidou-Vlachou E, Tziakouri-Shiakalli C, Georgiades CS (2014) Extramedullary hemopoiesis. Semin Ultrasound CT MR 35:255–262
17. Goldman BI, Wurzel J (2001) Hematopoiesis/erythropoiesis in myocardial infarcts. Mod Pathol 14:589–594
18. Junqueira LC, Carneiro J (2003) Basic histology, 10th edn. McGraw-Hill, New York
19. Kim BH (1965) Sanal and hematopoiesis. J Jo Sun Med 108:1–6

Addendum

Chapter 54
Quantitative Biology of Exercise-Induced Signal Transduction Pathways

Timon Cheng-Yi Liu*, Gang Liu*, Shao-Juan Hu*, Ling Zhu, Xiang-Bo Yang, and Quan-Guang Zhang

Abstract Exercise is essential in regulating energy metabolism. Exercise activates cellular, molecular, and biochemical pathways with regulatory roles in training response adaptation. Among them, endurance/strength training of an individual has been shown to activate its respective signal transduction pathways in skeletal muscle. This was further studied from the viewpoint of quantitative difference (QD). For the mean values, $\bar{x}$ *and* $\bar{y}$, of two sets of data, their QD is defined as $l = \left|\log_{\tau}\left(\bar{x}/\bar{y}\right)\right|$ ($\tau = \left(\sqrt{5}-1\right)/2 \approx 0.618$). The function-specific homeostasis (FSH) of a function of a biosystem is a negative-feedback response of the biosystem to maintain the function-specific conditions inside the biosystem so that the function is perfectly performed. A function in/far from its FSH is called a normal/dysfunctional function. A cellular normal function can resist the activation of other signal transduction pathways so that there are normal function-specific signal transduction pathways which full activation maintains the normal function. **Results**: An acute endurance/strength training may be dysfunctional, but its regular training may be normal. The normal endurance/strength training of an individual may resist the activation of other signal transduction pathways in skeletal muscle so that there may be normal endurance/strength training-specific signal transduction pathways (NEPs/NSPs) in skeletal muscle. The endurance/strength training may activate NSPs/NEPs, but the QD from the control is smaller than 0.80. The simultaneous activation of both NSPs and NEPs may enhance their respective activation, and the QD from the control is larger than 0.80. The low level laser irradiation pretreatment of rats may promote the activation of NSPs in endurance training skeletal muscle. **Conclusion**: There may be NEPs/NSPs in skeletal muscle trained by normal endurance/strength training.

*Timon Cheng-Yi Liu, Gang Liu, Shao-Juan Hu contributed equally to this work.

T.C.-Y. Liu (✉) • S.-J. Hu • L. Zhu • X.-B. Yang • Q.-G. Zhang
Laboratory of Laser Sports Medicine, South China Normal University, Guangzhou, China
e-mail: liutcy@scnu.edu.cn; liutcy@foxmail.com

G. Liu
Sports and Health College,Guangzhou University of Chinese Medicine, Guangzhou, China

H.J. Halpern et al. (eds.), *Oxygen Transport to Tissue XXXIX*, Advances in Experimental Medicine and Biology 977, DOI 10.1007/978-3-319-55231-6_54

Keywords Exercise • Skeletal muscle • Signal transduction pathways • Homeostasis • Self-similarity

1 Introduction

A signal transduction pathway is always signal-specific [1, 2], but it becomes special in exercise physiology, especially for regular exercise training. Hawley et al. [3] have reviewed the signal transduction pathway adaption in skeletal muscle from endurance- and strength-trained individuals. It was based on p-values, the 'gold standard' of statistical validity. However, p-values are not as reliable as many scientists assume [4]. Here, the signal transduction pathway adaption in skeletal muscle was further studied with the quantitative difference (QD) [5].

2 Quantitative Difference

For two sets of data, $\{x_{1i}, i=1,2,\ldots,m\}$ and $\{x_{2i}, i=1,2,\ldots,m\}$, the null hypothesis of their respective mean values, $\bar{x}_1=\sum x_{1i}/m$ and $\bar{x}_2=\sum x_{2i}/m$, is $\bar{x}_1=\bar{x}_2$ [4, 6]. The statistical significance, $P<0.05$, or 0.01, means that $\bar{x}_1\neq\bar{x}_2$. However, statistical significance is not the same as biological importance [6]. For genomics and proteinomics, the biological importance has been assessed with the well-known expression thresholds, 1.5-fold and 2.0-fold. In order to extend the ratio threshold, Liu et al. have introduced the QD [5], $l=\left|\log_\tau\left(\bar{x}_1/\bar{x}_2\right)\right|$ ($\tau=\left(\sqrt{5}-1\right)/2\approx 0.618$). It was found that there is QD thresholds (α,β) so that it is significant if $\alpha\le l<\beta$ and extraordinarily significant if $l\ge\beta$. The QD thresholds (α,β) at the level of cells, molecules or central nervous systems, the level of organs or tissue and the level of body are (0.80,1.22), (0.47, 0.80) and (0.27, 0.47), respectively. The QD of 1.5-fold or 2.0-fold, 0.84 or 1.44, is just larger than the QD threshold, 0.80 or 1.22, at the cellular or sub-cellular level. Our QD thresholds may be more fine than the well-known expression thresholds, which should be further verified.

The QD may be understood from the viewpoint of self-similarity. Self-similarity denotes a power-law relation between two variables x and y [7]: $y=Ax^\kappa$. The power law is historically referred to as an allometric relation between two observables. Typically an allometric equation relates two properties of a given organism. It may be used to discuss a process from 1 to 2: $(x_2/x_1)=(y_2/y_1)^{1/\kappa}$. We have $1/\kappa=\log_\tau(x_2/x_1)$ if $y_2/y_1=\tau$. Obviously, $l=|1/\kappa|$.

The QD thresholds (α,β) may be understood from the viewpoint of negative feedback [8]. The biological negative feedback response maintaining the specific conditions of a function so that the function is perfectly performed is called a function-specific homeostasis (FSH) of the function. A function in/far from its FSH is called a normal/dysfunctional function. A FSH-specific stress (FSS) disrupts the FSH. A FSS in/far from its FSS-specific homeostasis (FSSH) is called a successful/chronic stress. A

normal function or a successful stress can resist a disturbance under its threshold so that $l<\alpha$ for the disturbance-induced difference. A dysfunctional function or chronic stress sensitively depends on a disturbance so that the QD is significant if $\alpha \le l<\beta$ and extraordinarily significant if $l \ge \beta$ for the disturbance-induced difference.

Moreover, a cellular normal function not only resists an extra-cellular disturbance, but also maintains the full activation of its intracellular normal function-specific signal transduction pathways (NFPs) by suppressing the activation of other signal transduction pathways [8]. For a successful stress, $l \ge 0.80$ for the full activation of the NFPs, but $l<0.80$ for the partial activation of other pathways. A normal function may have several NFPs which are called redundant NFPs with one another. The full activation of one NFP can maintain a first-order normal function. The synergistic full activation of one NFP and its N - 1 redundant NFPs can upgrade the first-order normal function into the N^{th}-order normal function.

3 Normal Endurance Training-Specific Pathways

Exercise training is a global function of an individual. An acute training always induces dysfunctional delayed onset muscle soreness [9]. However, a regular training can be normal so that there may be normal training-specific signal transduction pathways in skeletal muscle. The normal endurance training-specific pathways (NEPs) are discussed in this section.

Generally endurance training induces changes in the metabolic properties of skeletal muscle by conferring an increased oxidative profile to the trained myofibers. As Hawley et al. have summarized [3], such effects are likely to involve a plethora of signaling cascades and transcription factors including, but not limited to, calcium signaling pathways involving calcineurin, calcium-calmodulin-dependent kinase (CaMK), p53, sirtuin 1 (SIRT1), p38 mitogen-activated protein kinase (MAPK) and the transcriptional cofactors peroxisome proliferator-activated receptor γ coactivator 1α (PGC-1α). As Bartlett et al. have summarized [10], CaMK, p53, SIRT1, and p38 MAPK are activated in an acute training. Philp et al. have found that SIRT1 deacetylase activity is not required for mitochondrial biogenesis or PGC-1α deacetylation following endurance exercise [11]. Geng et al. found that PGC-1α is required for complete skeletal muscle adaptations induced by endurance exercise in mice, such as mitochondrial biogenesis and angiogenesis [12]. Therefore, PGC-1α mediated pathway may be one of the NEPs.

4 Normal Strength Training-Specific Pathways

Strength training increases muscle fiber size (hypertrophy) and maximal tension output. These adaptations are attained by positive muscle protein balance and satellite cell addition to pre-existing fibers. Positive muscle protein balance occurs when the rate of new muscle protein synthesis exceeds that of breakdown. Activation of

mammalian target of rapamycin (mTOR) appears to be important for contraction-induced increases in muscle protein synthesis [13]. The phosphorylation of raptor bound to mTOR is significant, but the one of mTOR at Ser2446 is not, between control group and rapamycin group, according to QD.

The insulin-like growth factor 1 (IGF-1) mediated pathway may be one of the normal strength training-specific pathways (NSPs). IGF-1 has long been considered a key upstream regulator of mTOR [3]. Signaling activated by IGF-1 positively regulates skeletal muscle mass via induction of protein synthesis downstream of protein kinase B/Akt and the mTOR pathway. IGF-1 transmits signaling along the phosphatidylinositide 3-kinase (PI3K)/Akt pathway, resulting in the parallel activation of the mTOR pathway, producing a multitude of responses, including mRNA translation, ribosomal biogenesis, and nutrient metabolism.

5 Crosstalk Between Endurance and Strength Training

The simultaneous activation of both NSPs and NEPs may enhance their respective activation, and the QD from the control is larger than 0.80. Wang et al. found that strength exercise enhances the molecular signaling of mitochondrial biogenesis induced by endurance exercise in human skeletal muscle [14]. Ten healthy subjects regularly performed either only endurance exercise (E; 1-h cycling at ~ 65% of maximal oxygen uptake), or endurance exercise followed by resistance exercise (ER; 1-h cycling +6 sets of leg press at 70–80% of 1 repetition maximum) in a randomized cross-over design. Muscle biopsies were obtained before and after exercise (1 and 3 h postcycling). The mRNA difference of PGC-1α is not quantitatively significant 1 h postcycling, but is quantitatively significant 3 h postcycling, between the ER and E groups.

Liu found that low level laser irradiation (LLL) pre-irradiated regular endurance may inhibit rat Sarcopenia [15]. She has investigated the effects of moderate intensity low load endurance training (MIE), LLL(Ga-Al-As laser, 810 nm, 125 mW/cm^2, 30 s)and LLL pre-irradiation and then MIE (LMIE) on natural aging female rats aged 18 months by using QD. She found that MIE, LLL and LMIE significantly activated PGC-1α, nuclear respiratory factor 1(NRF-1) and mitochondrial transcription factor A (TFAM). She also found neither MIE nor LLL, but LMIE significantly activated IGF-1. Moreover, the activation of NRF-1 in LMIE group was significantly higher than the one in the control group, but was significantly lower than the one in the MIE group, which suggested that there was synergistic crosstalk between the IGF-1 pathway and the PGC-1α pathway in the LMIE group.

The endurance/strength training may activate NSPs/NEPs, but the QD from the control is smaller than 0.80. PGC-1α mediated pathway is one of the NEPs, but PGC-1α4 belongs the IGF-1 mediated pathway [16]. White et al. [16] found that regular endurance training non-significantly, but regular strength training significantly, activated PGC-1α4, according to QD. White et al. [16] also found neither regular endurance training nor regular strength training activated IGF-1 statistically, but regular strength training activated IGF-1 quantitatively.

6 Discussion

As reviewed above, there may be NEPs/NSPs in skeletal muscle trained by regular endurance/strength training. The NEPs/NSPs may be redundant with one another, and the synergistic full activation of several NEPs/NSPs may upgrade the performance maintained by the full activation of one NEP/NSP. A short-term training may fully activate one NEP/NSP, but a long-term training may fully activate several NEPs/NSPs and may then upgrade the short-term performance. These phenomena have not yet observed in skeletal muscle, but are suggested in mouse cardiac muscle [17, 18]. Isoproterenol (Iso) can induce cardiac fibrosis [17, 18]. Four-weeks swimming may partially resist Iso-induced cardiac fibrosis through activating the adenosine monophosphate-activated protein kinase (AMPK) pathway [17], but 13-weeks running on a motor-driven treadmill may completely resist Iso-induced cardiac fibrosis through activating kallikrein-kinin pathway [18]. As the AMPK activation did not depend on the kallikrein-kinin pathway [19], the AMPK may be redundant with the kallikrein-kinin pathway so that 13-weeks running may completely resist cardiac fibrosis through the synergistic activation of AMPK pathway and kallikrein-kinin pathway.

7 Conclusion

There may be normal endurance/strength training-specific signal transduction pathways in skeletal muscle trained by regular endurance/strength training.

Acknowledgments This work was supported by National Science Foundation of China (61575065, 11604104), Doctoral Fund of Ministry of Education of China (20124407110013), Guangdong Scientific Project (2012B031600004) and The Sports Scientific Project of Guangdong (GDSS2014103).

References

1. Rodbell M (1980) The role of hormone receptors and GTP-regulatory proteins in membrane transduction. Nature 284(5751):17–22
2. Levy ED, Landry CR, Michnick SW (2010) Cell signaling: signaling through cooperation. Science 328(5981):983–984
3. Hawley JA, Hargreaves M, Joyner MJ et al (2014) Integrative biology of exercise. Cell 159(4):738–749
4. Nuzzo R (2014) Scientific method: statistical errors. Nature 506(7487):150–152
5. Liu CY, Wu CY, Li FH et al (2017) Self-similarity constant and quantitative difference and their applications in sports science. J Phys Educ 24 (to be published in Chinese)
6. Whitlook MC, Schluter D (2015) The analysis of biological data, 2nd edn. Roberts and Company Publishers, Colorado, pp 176–177

7. West BJ (2010) Fractal physiology and the fractional calculus: a perspective. Front Physiol 1:12
8. Liu TCY, Wu DF, Zhu L et al (2014) Micro-environment dependent photobiomodulation on function-specific signal transduction pathways. Int J Photoenergy 2014: Article ID 904304, 8 p
9. Cheung K, Hume P, Maxwell L (2003) Delayed onset muscle soreness: treatment strategies and performance factors. Sports Med 33(2):145–164
10. Bartlett JD, Close GL, Drust B et al (2014) The emerging role of p53 in exercise metabolism. Sports Med 44(3):303–309
11. Philp A, Chen A, Lan D et al (2011) Sirtuin 1 (SIRT1) deacetylase activity is not required for mitochondrial biogenesis or peroxisome proliferator-activated receptor-gamma coactivator-1alpha (PGC-1alpha) deacetylation following endurance exercise. J Biol Chem 286(35):30561–30570
12. Geng T, Li P, Okutsu M et al (2010) PGC-1alpha plays a functional role in exercise-induced mitochondrial biogenesis and angiogenesis but not fiber-type transformation in mouse skeletal muscle. Am J Physiol Cell Physiol 298(3):C572–C579
13. Drummond MJ, Fry CS, Glynn EL et al (2009) Rapamycin administration in humans blocks the contraction-induced increase in skeletal muscle protein synthesis. J Physiol 587(Pt 7):1535–1546
14. Wang L, Mascher H, Psilander N et al (2011) Resistance exercise enhances the molecular signaling of mitochondrial biogenesis induced by endurance exercise in human skeletal muscle. J Appl Physiol (1985) 111(5):1335–1344
15. Liu YY (2015) Effects of low level laser pre-irradiation and exercise on skeletal muscle mitochondrial apoptosis pathways of aging rats and its mechanism. PhD thesis, South China Normal University
16. White JP, Wrann CD, Rao RR et al (2014) G protein-coupled receptor 56 regulates mechanical overload-induced muscle hypertrophy. Proc Natl Acad Sci U S A 11(44):15756–15761
17. Ma X, Fu Y, Xiao H et al (2015) Cardiac fibrosis alleviated by exercise training is AMPK-dependent. PLoS One 10(6):e0129971
18. Silva JA Jr, Santana ET, Manchini MT et al (2014) Exercise training can prevent cardiac hypertrophy induced by sympathetic hyperactivity with modulation of kallikrein-kinin pathway and angiogenesis. PLoS One 9(3):e91017
19. Schweitzer GG, Cartee GD (2011) Postexercise skeletal muscle glucose transport is normal in kininogen-deficient rats. Med Sci Sports Exerc 43(7):1148–1153

Index

H.J. Halpern et al. (eds.), *Oxygen Transport to Tissue XXXIX*, Advances in Experimental Medicine and Biology 977, DOI 10.1007/978-3-319-55231-6